Distinguishing hypothetical systems of PS beads by $g(s^*)$ analysis of simulated AUC data to which noise has been added, and quantifying the statistical significance of any observed distinguishability

INTRODUCTION

This work examines the effects of noise on the distinguishability of mixtures subjected to analytical ultracentrifugation (AUC). The mixtures are hypothetical, the AUC is simulated, and the noise, which consists of both systematic and random parts, is generated artificially. For each mixture, the AUC is simulated just once. Replicate samples of a mixture are created by the addition of noise to the simulated AUC data of that mixture. The added noise is unique to each replicate, and the set of replicates that pertains to a particular mixture is defined as a treatment group. Thus, the artificially generated noise is the only source of variation within a treatment group. Across treatment groups, the implicit solvent composition is identical, and the initial concentrations of comparable solutes are as much alike as possible. To ensure that, in the absence of noise, the composition of the system is the only source of variation between treatment groups, for each mixture, the simulated AUC method is identical with respect to parameters that depend on temperature, rotor speed and data collection. Across treatment groups, the simulated AUC data are recorded at identical radial positions at identical times, and the signal-to-mass ratios are identical for comparable materials.

A common observation is obtained for each replicate of each treatment group at three significantly different times. At each of the three times chosen for analysis, the population mean of the observations within one treatment group is compared to that within every other treatment group. One-way analysis of variance (ANOVA) is used to test whether there are any statistically

significant differences in the population means between any of the treatment groups at a given time. To quantify the statistical significance of a difference between any two treatment groups, a Bonferroni-adjusted *t*-test (2-tailed) is applied to pair-wise comparisons of the population means from different treatment groups at each time. Confidence intervals about the population means are determined and graphed to illustrate selected results from the Bonferroni-adjusted *t*-tests.

The data presented here were generated by simulations (Moody, 2012a). The method of simulation is an implementation of an integral, finite-element solution to the relevant continuity equation (Moody, 2011). The method is built on that which Claverie, Dreux and Cohen (1975) described in their solution to the Lamm equation, but differs in several respects. To correctly implement their concentration dependence, the transport coefficients are defined as spatially-independent parameters. To correctly evaluate the concentration-dependent transport coefficients at the time to be evaluated, the concentrations are calculated iteratively. By such an evaluation of the concentration-dependent transport coefficients at both the time already evaluated and the time being evaluated, the accuracy of each new set of concentrations is maximised. Computational artefacts are reduced by first calculating all concentrations in one order, then recalculating all concentrations in the opposite order, and averaging the results. For the cylindrical coordinate system of AUC, simpler results of integration are obtained by using one-half the square of the radial position, rather than the radial position, as the spatial parameter of the continuity equation. Additionally, a simple coupled-flow equation has been implemented.

DATA

An overview of the signal and the noise

For each treatment group, a single AUC simulation (Moody, 2011) yielded noise-free data at a set of radial positions and times. All such noise-free data were collected at the same simulated rotor speed of 60,000 RPM, and the same simulated temperature of 20.00°C. At each selected time, t, the noise-free data consist of the mass concentration (e.g. g/ml) of each potentially signal-generating solute, k, at each selected radial position, r, within the hypothetical system. The data were always recorded at the same radial positions, and at all times, the radial extrema, which are the innermost and outermost radial boundaries of the system, were the same for each replicate of each treatment group. Each recorded solute concentration, c_k, was multiplied by an appropriate signal-to-concentration ratio to best approximate what its contribution to the total signal would be, given the optical path-length (typically 0.3 cm or 1.2 cm) and the detection system being simulated. (Fringe displacement is the signal obtained from the Rayleigh interferometric (RI) detection system, which is that simulated here.) At a given time and at a given radial position, the sum of all such signal contributions is equal to the Noise-Free Signal (*NFS*). The *NFS* is the only concentration-dependent signal. Noise is defined as any contribution to the signal that is not concentration-dependent.

For a specific treatment group at a specific time, the set of concentration-dependent signals from all radial positions (i.e., the *NFS* at all radial positions of a treatment group at a given time) is equivalent to a noise-free scan of the system at that time, insofar as that which is called a scan in a real experiment would yield a record of the signal at each of many radial positions at a specific time. Within each treatment group, a scan of a replicate sample consists of a common noise-free scan plus the noise specific to the replicate.

Time-independent noise (*TIN*) is generated by a summation of logarithmic and cosine functions of radial position. As the name implies, *TIN* does not vary with time. The *TIN* does vary with radial position, however, and at any given radial position, can vary from one replicate to another. Thus, for a given replicate within a given treatment group, the same set of *TIN* values is added to the noise-free scan from each time at which data are recorded. The same set of *TIN* values applies to each scan of a replicate because the data for each replicate are always recorded at the same set of r for each replicate of each treatment group at all times. For each replicate, the *TIN* values are limited to a realistic range and pattern that would be expected for the detection system being simulated.

A unique set of radially independent noise (*RIN*) is generated for each data set of each replicate of each mixture. The noise, in this case, is an offset in the signal. As the name implies, *RIN* does not vary radially, so that, for a given replicate of a given treatment group at a given time, the same *RIN* value is added to the *NFS* at each radial position. The *RIN* does vary with time, however, and at any given time, can vary from one replicate to another. Thus, a different *RIN* value is added to each noise-free scan of each replicate. In each case, the *RIN* value is limited to a realistic range that would be expected for the detection system being simulated.

Generally random noise (*GRN*) is noise that varies randomly with respect to both time and radial position. At a given time and radial position, the *GRN* also varies randomly from replicate to replicate. Thus, at each radial position, a different *GRN* value is added to the *NFS* from each time of each replicate. The *GRN* values are limited to a realistic range that would be expected for the detection system being simulated.

Making use of the preceding definitions of the *NFS*, *TIN*, *RIN* and *GRN*, for replicate h within treatment group i, the noise-modified signal, *NMS*, at scanned radial position r and scanned time t can be written as

$$NMS_{i,h}(r,t) = NFS_i(r,t) + TIN_{i,h}(r) + RIN_{i,h}(t) + GRN_{i,h}(r,t), \quad (1a)$$

where the presence of r in parentheses indicates that the associated parameter is a function of r, the presence of t in parentheses indicates that the associated parameter is a function of t, the subscript i indicates that the associated parameter varies from one treatment group to another, and the subscript h indicates that the associated parameter varies within a treatment group from one replicate to another.

With t, i and h each held fixed, a simulated scan is identical to the set of all ordered triples, (r; $NMS_{i,h}(r;t)$, $N_{i,h}(r;t)$), where r is a radial position at which a signal is recorded, and where the third entry of the ordered triple,

$$N_{i,h}(r,t) = TIN_{i,h}(r) + RIN_{i,h}(t) + GRN_{i,h}(r,t), \quad (2a)$$

is the total noise at radial position r and scanned time t for replicate h within treatment group i. (For the results from simulations, the third entry of the ordered triple is a placeholder that is only needed if data are analysed with software that, in conformity with the output from some optical systems of an analytical ultracentrifuge, requires three columns of data.) Equations 1b and 2b will present less ambiguous versions of Equations 1a and 2a, respectively. For now, however, the characteristics of the simulated AUC data are summarised in terms of the notation used in Equations 1a and 2a.

At a given time, t, the application of the same set of $NFS_i(r;t)$ to all replicates within a given treatment group, i, is made possible by the consistent recording of data at a common set of radial positions for all replicates, and by making the radial extrema the same for all replicates. Similarly, for a given replicate, h, of a given treatment group, i, the application of the same set of $TIN_{i,h}(r)$ at all times is made possible by the consistent recording of data at a common set of radial positions at all times. In contrast, the choice of radial positions is irrelevant insofar as $RIN_{i,h}(t)$ is concerned and is of marginal interest (*Changing N and* r_j *values to keep* $\Delta s^*_{\varphi_\epsilon}$ *constant*) insofar as $GRN_{i,h}(r;t)$ is concerned.

Some differences between real experimental data and the simulated AUC data used here

To minimise the number of simulations required to generate data, and to eliminate the noise-free signals as a potential source of variability among replicates within a treatment group at any given time, the radial extrema were made identical for all replicates within a treatment group. Furthermore, to avoid arousing the suspicion that such a potential source of variation might account for any apparently significant differences between treatment groups, the radial extrema were made identical for all treatment groups. For the same reasons, the set of radial positions was made identical for all replicates of all treatment groups. Of these conditions, the invariance of radial extrema is admittedly unrealistic.

Subtracting $N_{i,h}(r;t)$ from $NMS_{i,h}(r;t)$ leaves $NFS_i(r;t)$. Within a given treatment group, i, at a given time, t, the set of $NFS_i(r;t)$ values at all r constitutes the noise-free scan for all replicates. Thus, within a treatment group, the set of all $N_{i,h}(r;t)$ values comprises all of the differences between replicates. This latter characteristic differs slightly from that which would be expected in a real

experiment. As mentioned above, and as discussed in more detail later (*An overview of the times chosen for analysis*, and *Simulation of* $TIN_{i,h}(r)$), the radial extrema of a replicate are the innermost and outermost radial boundaries of the system. In any real experiment, the radial extrema would generally differ from one replicate to another, as a result of which, within a given treatment group, i, at a given time, t, the set of $NFS_i(r,t)$ values at all r would generally differ from one replicate to another, even if the data were recorded at the same radial positions for each replicate.

In some real experiments, for a given replicate, h, within a given treatment group, i, the data may not be recorded at the same radial positions at each time, t, in which case, in place of r in Equations 1a and 2a, $r_{i,h,t}$ would apply, where $r_{i,h,t}$ denotes the radial position recorded at time t of replicate h within treatment group i. Such variability can be inherent to the detection system. Even a detection system, such as the RI-detection system simulated here, that can, within some small error inherent to the technology, repeatedly record data at one consistent set of radial positions may, following a recalibration, start repeatedly recording data at another consistent set of radial positions. Where unintentional and erratic, recording data at time-dependent radial positions would probably be considered disadvantageous. In some cases, however, it is conceivable that at least some advantage could be gained by imposing a systematic time dependence on the number and location of radial positions at which data are recorded. (For example, see *Changing N and* r_j *values to keep* $\Delta s^*_{\varphi_\epsilon}$ *constant*.)

An overview of the model systems from which the treatment groups are constructed

The treatment groups are constructed from two previously described model systems that were

contrived to exhibit dramatic Johnston-Ogston effects in AUC simulations (Moody, 2012a), selected data from which were subjected to analysis in a subsequent paper (Moody, 2012b). Each of the two previously described model systems constitutes one of the treatment groups. Every other treatment group consists of a mixture of the two previously described model systems.

The two previously described model systems are identical with respect to species, but distinguishable with respect to components. Both systems model buffered, part aqueous, part heavy-water solutions of polystyrene (PS) beads that, by varied substitutions of ^{1}H with deuterium, are polydisperse with respect to specific gravity (Moody, 2012a).

(The density of each solute particle is equal to its mass divided by its volume, and the ratio of that density to the density of water (at specified conditions of pressure and temperature) is the specific gravity of the particle. Likewise, the local density of the solution is equal to its local mass divided by its local volume, and the ratio of that density to the density of water (at specified conditions of pressure and temperature) is the local specific gravity of the solution.)

In each system, the PS beads are defined as the solutes, and the buffer is defined as the implicit solvent (Moody, 2012a). The solvent is treated as being incompressible, as is each solute particle. The transport coefficients of each solute are concentration-dependent (Moody, 2012a: Equations 5 to 18). The coupled-flow sedimentation (Moody, 2012a: Equations 27 to 30) and diffusion (Moody, 2012a: Equations 31 and 32) coefficients are equal to 1 for each type of solute with respect to itself, and are equal to 0 for each type of solute with respect to another (Moody, 2012a: Table 2, case 0). All temperature-dependent system properties, such as solution density, viscosity, specific gravities, transport coefficients and second virial coefficients, are based on an

expectation that the systems are maintained at 20.00°C (Moody, 2012a). Thus, 20.00°C, which equates to 293.15 K on the absolute temperature scale, is the hypothetical temperature of all of the simulated experiments. The simulated rotor speed of 60,000 RPM was treated as having been instantaneously achieved beginning at time $t_0 = 0$ s.

In each system, 26 of the 27 model PS beads are defined as isotropic spheres of 30 nm diameter, and a dimer of the most positively-buoyant and the most negatively-buoyant of these defines the remaining model PS bead, which is neutrally buoyant with respect to the implicit solvent at 20.00°C.

Together, the most positively-buoyant species, *H*, the most negatively-buoyant species, *L*, and the dimer, *LH*, account for 99% of the total mass concentration, $c = 0.1$ g/ml, of all PS-bead solutes in either system. Thus, the collection of all *H*, *L* and *LH* particles are described as the high-concentration solutes, and the collection of all particles from the other 24 PS-bead species are described as the low-concentration solutes. In the absence of concentration gradients, the molarity of species *LH* is half that of species *L* or *H*, while species *L* and *H* are equimolar, so that $c_L/M_L = c_H/M_H = 2(c_{LH}/M_{LH})$, where $M_L = 8{,}964{,}823$ g/mol $M_H = 9{,}462{,}869$ g/mol and $M_{LH} = 18{,}427{,}691$ g/mol are the molar masses of species *L*, *H* and, *LH*, respectively (Moody, 2012a: Table 1), and where c_L, c_H and c_{LH} are the mass concentrations of species *L*, *H* and *LH*, respectively. Given that $M_{LH} = M_L + M_H$, where both $c_L/M_L = c_H/M_H = 2(c_{LH}/M_{LH})$ and $c_L + c_H + c_{LH} = 0.99c$ hold, as they initially do prior to the development of concentration gradients anywhere in the system, $c_L = 0.99(2c/3)(M_L/M_{LH})$, $c_H = 0.99(2c/3)(M_H/M_{LH})$ and $c_{LH} = (c_L + c_H)/2 = 0.99(c/3)$ throughout the system. Thus, with $c = 0.1$ g/ml, the initially uniform concentrations of the high-concentration solutes, *L*, *H* and *LH*, respectively, are $c_L = 3.211$E-02

g/ml, $c_H = 3.389\text{E-}02$ g/ml and $c_{LH} = 3.300\text{E-}02$ g/ml.

The total concentration of each low-concentration solute is (0.001 g/ml)/24 in both systems. Among the 24 low-concentration solutes, 12 are positively-buoyant and 12 are negatively-buoyant (Moody, 2012a: Table 1) with respect to the implicit solvent at 20.00°C. The solute concentrations, the basic transport parameters (Moody, 2012a: Table 1) and the parameters that mediate concentration dependence (Moody, 2012a: Equations 14 to 18) are such that each of the low-concentration solutes exhibits Johnston-Ogston effects.

In one system, each of the 27 model PS beads, including *L*, *H* and *LH*, is a single-species component. In the other system, 24 of the model PS beads are single-species components, while *L* is a two-species component, *H* is a two-species component, and *LH* is the second species of both two-species components, for a total of 27 solute species among 26 components. In both systems, each of the low-concentration solutes is a single-species component.

For the system in which 26 components encompass 27 solute species, $K_A = 30.325$ ml/g is the association constant applied to the formation of *LH* from *L* and *H*. As previously described (Moody, 2012a), this value of K_A was calculated to ensure that, in the absence of concentration gradients, at 20.00°C, the concentrations of *L*, *H* and *LH* in the system with 27 solute species among 26 components would be everywhere equal to the concentrations of *L*, *H* and *LH*, respectively, in the system with 27 single-species components. Additionally, in the absence of concentration gradients, the concentration of each of the remaining 24 solute species in one system is everywhere equal to that in the other system. Thus, at 20.00°C, the two systems are indistinguishable prior to the formation of concentration gradients.

For the system in which *L*, *H* and *LH* are single-species components, K_A, the association constant that would otherwise apply to the formation of *LH* from *L* and *H*, is undefined, and henceforth, the two systems are identified by whether the K_A for the formation of *LH* from *L* and *H* is undefined or is equal to 30.325 ml/g at 20.00°C.

In the system for which $K_A = 30.325$ ml/g at 20.00°C, the applied forward rate constant is $k_{for} =$ 30,000 [ml/g]/s, and thus the applied reverse rate constant is $k_{rev} = k_{for}/K_A \cong 989.277$ s. Relative to the time increments applied to simulate AUC in this study, these rate constants are high enough to ensure the rapid equilibration of the chemical reaction linking *L*, *H* and *LH*. Thus, with the development of gradients in the concentrations of *L*, *H* and *LH*, the two systems behave differently enough to be easily distinguished at many points in time. In this study, the challenge lies in distinguishing simulated AUC data from similar treatment groups, each being a mixture of the two model systems, after realistic noise has been added to the data at each of three widely spaced points in time.

An overview of the treatment groups and the Noise-Free Signals

At a given radial position at a given time, the noise-free signal (Equation 4) is the product of the concentration of solutes found only in the sample, the specific fringe displacement of those solutes, and the optical path-length. For each replicate of each treatment group considered here, an optical path-length of $L = 0.3$ cm was used to calculate the noise-free signal.

Each treatment group consists of a mixture of the two previously described model systems

(Moody, 2012a). For each treatment group, the total mass concentration of all hypothetical PS beads is $c = 0.1$ g/ml, which is the same as that of the pure systems in the previous studies (Moody, 2012a and 2012b). For each species of PS bead, the signal-to-mass ratio is treated as being the same. Thus, each species of PS bead is assigned the same specific fringe displacement of $k_\lambda = 2{,}500$ fringe/[cm·g/ml], where 1 fringe is the unit of the signal obtained from the RI detection system, for which λ is the nominal wavelength of the light source.

For sample materials of a given composition, the specific fringe displacement is directly proportional to the refractive index increment and inversely proportional to λ (Moody, 2011: Equation E1). In Equation 4, the proportionality of the noise-free signal to the optical path-length stems from the proportionality of $k_{\lambda,q,a}$ to $1/\lambda$. As the refractive index increment is a function of λ, solvent properties, and such system properties as temperature, few experimental parameters can be altered without affecting $k_{\lambda,q,a}$.

The refractive index increment of the PS-bead solutions was calculated for a temperature of 20.00°C and a wavelength of $\lambda = 6.75\text{E-}5$ cm, which is the nominal wavelength of the RI detection system being simulated. (See *Data that formed the basis of* $GRN_{i,h}(r;t)$.) The implicit solvent (see below) of the PS-bead solutions was modelled as an aqueous buffer consisting of 71.23% D_2O, 0.15 M NaCl, 20 mM NH_4HCO_3 and pH 7.0 at 20.00°C (Moody, 2012a), where the amount of D_2O is given in volume-percent. The calculation of k_λ was then contrived to yield a fairly round number that, aside from neglecting (for the sake of a little simplicity) the effects of ^{1}H-to-D substitution on its value, was fairly evidence-based.

Based on such measurements for similar polymers with 0% ^{1}H-to-D substitution, the refractive

index of each PS-bead at 20.00°C was estimated as $n_{PS} = 1.50000$, despite the expectation that the true value would decrease slightly with increasing ^{1}H-to-D substitution. Based on such measurements for similar aqueous buffers with 0% D_2O, the refractive index of the model buffer at 20.00°C and $\lambda = 6.75$E-5 cm was estimated as $n_0 = 1.33125$, despite the expectation that the true value would decrease slightly with increasing D_2O content. The refractive index increment of the PS-bead solutions at 20.00°C and $\lambda = 6.75$E-5 cm was estimated as $(n_{PS} - n_0)/(1\text{ g/ml}) = 0.16875$, despite the expectation that its true value would only be found in the limit as the PS-bead concentration approached zero, and would also depend on the level of ^{1}H-to-D substitution among the PS-beads. The specific fringe displacement of the PS-bead solutions at 20.00°C and $\lambda =$ 6.75E-5 cm was then calculated as $k_\lambda = 0.16875/\lambda = 2{,}500$ fringe/[cm·g/ml].

(For the steadfastly fastidious, simply imagine that compensating but proprietary and thus undisclosed chemical substitutions were applied during the manufacture of each PS-bead component, such that, regardless of the extent of ^{1}H-to-D substitution, $k_\lambda = 2{,}500$ fringe/[cm·g/ml] for each such component in the model buffer at 20.00°C and $\lambda = 6.75$E-5 cm. Warning: Do not eat the PS-beads. And don't drink the buffer.)

RI detection requires a reference system for each sample system. At any given radial position, the signal is equal to the fringe displacement of the sample relative to the reference. Where the sample is identical to the reference, the expected fringe displacement is zero, as c, the concentration of components not found in the reference, is zero. Where the sample consists of the components of the reference plus the above-described hypothetical PS beads at $c = 0.1$ g/ml, and where the optical path-length through both the sample and the reference is $L = 0.3$ cm, the expected signal would be $cLk_\lambda = 75$ fringe.

In simulated AUC, the reference is implicit. For each treatment group of this study, the implicit reference is that which applied to the pure systems in the previous studies (Moody, 2012a and 2012b). The implicit reference system is treated as being devoid of PS beads, and all components other than PS beads are treated as being at equal chemical potential in the sample and reference systems, so that, at any given radial position at any given time, only the PS beads contribute to the *NFS*. In the best case of a real AUC experiment, the reference system would be identical to the dialysate that would be obtained after the sample system had been dialysed to equilibrium against the buffer of interest at the temperature of the AUC experiment. Such a reference system can be defined as the implicit solvent of the sample system. (The composition of the implicit solvent of this study is that given in the preceding calculation of the specific fringe displacement.)

Four treatment groups were subjected to intensive analysis. Two of the treatment groups consist of the pure systems of the previous studies (Moody, 2012a and 2012b), and one treatment group consists of a one-to-one mass-to-mass mixture of those previously described systems. On a mass-to-mass basis, the other treatment group is a 99-to-1 mixture of the previously described systems, with the major part of the mixture coming from the system for which $K_A = 30.325$ ml/g at 20.00°C.

The treatment groups and the number of their replicates were selected with the goal of detecting a 1% difference in composition at a confidence level of 95%, while also checking the significance of differences between treatment groups of widely divergent compositions. To this end, nine replicates were included in each treatment group that predominantly consisted of the system for which $K_A = 30.325$ ml/g at 20.00°C, and three replicates were included in each treatment group

that consisted of 50% or more of the system for which K_A is undefined at 20.00°C. Additionally, data from three widely divergent times were analysed to probe the time dependence of any differences between treatment groups.

An overview of the times chosen for analysis

The transport behaviour of the solutes is used to identify which AUC data might be especially worthy of analysis. At any given time during the simulated AUC, a solute exhibits net transport wherever the specific gravity of its particles differs from the specific gravity of the surrounding solution. Such net transport is centripetally directed where the specific gravity of the solute particles is less than the specific gravity of the surrounding solution, and centrifugally directed where the specific gravity of the solute particles is greater than the specific gravity of the surrounding solution.

The innermost and outermost radial positions of the system are its radial extrema. Whichever way the net transport of a solute is directed, it can be viewed as moving away from an apparent radial extremum of origin and towards an apparent radial extremum of accumulation. Where centripetally directed, the outermost radial position of the system is the apparent radial extremum of origin, while the innermost radial position of the system is the apparent radial extremum of accumulation. Where centrifugally directed, the innermost radial position of the system is the apparent radial extremum of origin, while the outermost radial position of the system is the apparent radial extremum of accumulation.

Where a solute exhibits net transport, a gradient develops in its concentration. While still distinct

from the radial extrema of accumulation, the concentration gradient of a solute is regarded as its boundary. Where the concentration of a solute increases with r, the boundary of that solute can be viewed as centrifugally directed. Where the concentration of a solute decreases with r, the boundary of that solute can be viewed as centripetally directed. Thus, at a given radial position and time, whichever way the net transport of a solute is directed, so too is the boundary of that solute directed.

The index ϵ is applied to times at which useful data are acquired (Equation 1b). For each treatment group, such data from three time points were chosen for analysis. The time points were chosen to be late enough that each centripetally or centrifugally directed boundary had cleared its radial extremum of origin, but early enough that no centripetally or centrifugally directed boundary had yet begun to merge with its radial extremum of accumulation. The earliest and latest data sets that meet these criteria, and that also exhibit minimal boundary overlap, were sought. The data set that meets these criteria while also exhibiting maximal boundary overlap was sought for the remaining time point. Accordingly, the data from $t_\epsilon = 2160$ s (36 min), $t_\epsilon = 3060$ s (51 min) and $t_\epsilon = 3960$ s (66 min) were chosen for analysis (Table 17).

The data set from the intermediate time point of $t_\epsilon = 3060$ s (51 min) is that which coincides with the approximate maximum extent of overlap between the centripetally and centrifugally directed boundaries. The time of such overlap had previously been noted as that at which, within one treatment group, the results of data analysis can be the most divergent of all times examined (Moody, 2012b), and was included here to check whether boundary overlap adversely affects the distinguishability of one treatment group from another.

For details regarding the AUC method that might have been applied had the systems been real, see **IMAGINARY EXPERIMENTAL PROTOCOL**.

DATA ANALYSIS: METHOD

The simulated AUC data, with and without the artificially generated noise described above, were analysed in terms of the apparent sedimentation coefficient, s^*, and its distribution function, $g(s^*)$. In this work, $g(s^*)$ was determined by a variation of the most direct method presented in a prior work (Moody, 2012b), in which a derivation of $g(s^*)$ from the continuity equation pertaining to AUC, an expression of $g(s^*)$ in terms of Dirac delta functions, and some practical methods by which $g(s^*)$ may be determined from experimentally obtained data, are described in detail, along with some of the history of such analysis. The method of analysis employed here is largely described in this section. Some aspects of the method are covered over the course of its application in subsequent sections, where tables and figures facilitate the use of examples.

For each replicate of each treatment group, the AUC data from three selected times were analysed. To correct for time-independent noise, for each replicate, the earliest data recorded were subtracted, radial-position-by-radial-position, from the data subsequently recorded at each of the three selected times. To show such operations clearly in equations, indices are assigned to both r and t. The index j, for which $1 \leq j \leq N$, is applied to the radial positions at which usable data are found, of which there are N in total. (Such indexing is discussed at length with respect to Equations 31 and 32.) The index ϵ is applied to times at which useful data are acquired. Useful data are defined as data that are fully described

$$NMS_{i,h}(r_j, t_\epsilon) = NFS_i(r_j, t_\epsilon) + TIN_{i,h}(r_j) + RIN_{i,h}(t_\epsilon) + GRN_{i,h}(r_j, t_\epsilon),$$

(1b)

of which the total noise is given by

$$N_{i,h}(r_j, t_\epsilon) = TIN_{i,h}(r_j) + RIN_{i,h}(t_\epsilon) + GRN_{i,h}(r_j, t_\epsilon).$$

(2b)

It is the application of the indices for radial position and time that makes Equations 1b and 2b less ambiguous forms of Equations 1a and 2a, respectively. The earliest recorded time at which useful data are acquired is specially denoted as $t_\epsilon = t_\alpha$.

For each treatment group considered here, at radial position r_j (Equation 32) and time t_ϵ (Table 17), $NFS_i(r_j,t_\epsilon)$ is invariant across replicates, for which all variation is found in $N_{i,h}(r_j,t_\epsilon)$. Thus, for each replicate of any given treatment group, i, considered here, at radial position r_j and time t_ϵ, the total concentration of all solute species is

$$c_i(r_j, t_\epsilon) = \sum_{k=1}^{n} c_k,$$

(3)

where n is the total number of solute species.

In general, the expected signal is identical to the noise-free signal. For each replicate of each treatment group considered here, the relationship between the noise-free signal and the total PS-bead concentration is the same, being given, for treatment group i at radial position r_j and time t_ϵ, by

$$NFS_i(r_j, t_\epsilon) = k_\lambda[c_i(r_j, t_\epsilon)]L,$$

(4)

where $k_\lambda = 2{,}500$ fringe/[cm·g/ml] is the specific fringe displacement, $c_i(r_j,t_\epsilon)$ is the total concentration of all solute species, and $L = 0.3$ cm is the optical path-length. (Also see Equation

154 and the associated discussion.) While the expected signal must be equal to $NFS_i(r_j,t_\epsilon)$, the observed signal need not be equal to $NMS_{i,h}(r_j,t_\epsilon)$ necessarily. If the observed signal does equal $NMS_{i,h}(r_j,t_\epsilon)$, it is deemed useful data.

Various optical effects, some of which can be categorised as noise, cause the observed signal to differ from the expected signal. Useful data are not obtained when and where some of these optical effects overwhelm the analytical effort to extract interpretable information about crucial characteristics of the expected signal. For example, noise due to reflections from system boundaries render the observed signal from affected radial positions uninterpretable. Worse, perhaps, is the potential for the observed signal to be misinterpreted, as can exist where solute concentrations lie outside the dynamic range of the detection system. Such bedevilling optical effects as these are assumed to be nonexistent, or at least negligible, where Equations 1b, 2b and 4 apply.

With the signal at radial position r_j and time t_ϵ denoted as $NMS_{i,h}(r_j,t_\epsilon)$ for replicate h of treatment group i, and the signal at radial position r_j and the earliest recorded time t_α denoted as $NMS_{i,h}(r_j,t_\alpha)$ for replicate h of treatment group i, the difference at radial position r_j is $NMS_{i,h}(r_j,t_\epsilon)$ - $NMS_{i,h}(r_j,t_\alpha)$. For replicate h of treatment group i at time t_ϵ, the set of all differences, $NMS_{i,h}(r_j,t_\epsilon)$ - $NMS_{i,h}(r_j,t_\alpha)$, is used to analyse the system as a collection of hypothetical solutes, each of which is defined as an imaginary, thermodynamically ideal, non-diffusing solute characterised by an apparent sedimentation coefficient and a constant of concentration.

At time t_ϵ (expressed in seconds), each radial position, r_j, is transformed to two values of the apparent sedimentation coefficient,

$$s^*_{\varphi_\epsilon} = \frac{1}{\omega^2 t_\epsilon} ln\left(\frac{r_j}{r_0}\right),$$

(5)

where r_0 is either equal to the innermost radial extremum, r_m, or the outermost radial extremum, r_b (Moody, 2012b), and where, for the N radial positions at which usable data exist, the $s^*_{\varphi_\epsilon}$ values are indexed by

$$\varphi_\epsilon = \left\{ \begin{matrix} j \; for \; r_0 = r_b, where \; r_b > r_j \\ j + N \; for \; r_0 = r_m, where \; r_m < r_j \end{matrix} \right\} \; in \; s^*_{\varphi_\epsilon} = \frac{1}{\omega^2 t_\epsilon} ln\left(\frac{r_j}{r_0}\right),$$

(6)

the sub-index of which, ϵ, being the index applied to time, serves as a reminder that, except where $s^*_{\varphi_\epsilon}$ and $s^*_{\varphi_{\tau\neq\epsilon}}$ are both zero, $s^*_{\varphi_\epsilon} \neq s^*_{\varphi_{\tau\neq\epsilon}}$, because $t_\epsilon \neq t_{\tau\neq\epsilon}$. (The subscripts associated with the radial extrema stem from the coincidence of r_m with the meniscus of the system, and the coincidence of r_b with the base of the system.) Thus, by Equation 6, the first N values of the index, φ_ϵ, are given by $\varphi_\epsilon = j$ for $r_0 = r_b$, where $r_b > r_j$ for all j, and the second N values of the index, φ_ϵ, are given by $\varphi_\epsilon = j + N$ for $r_0 = r_m$, where $r_m < r_j$ for all j.

For convenience, t_ϵ is sometimes expressed in terms of minutes, and is frequently denoted by the time in minutes, throughout the latter parts of this work. To calculate $s^*_{\varphi_\epsilon}$ in dimensions of seconds, however, t_ϵ must be expressed in seconds in Equation 5, where the angular velocity, ω (Equation 55), is assumed to be expressed in inverse seconds. Equation 5 also requires that r_j and r_0 share the same unit of length, with the centimetre being that chosen to express all radial positions in this work.

In Equation 5, setting r_0 equal to the innermost radial extremum, r_m, yields the set of all $s^*_{\varphi_\epsilon} < 0$. Conversely, setting r_0 equal to the outermost radial extremum, r_b, yields the set of all $s^*_{\varphi_\epsilon} > 0$. If it

were possible for r_j to equal either extremum represented by r_0, then $s^*_{\varphi_\epsilon}$ would equal 0 when r_j equalled r_0. However, in a real experiment, or in a simulation meant to generate realistic results, the radial extrema, r_m and r_b, lie outside the radial range of usable data, so that $r_b > r_j > r_m$ holds for each value of r_j. Thus, $\left|s^*_{\varphi_\epsilon}\right| > 0$ for all r_j values at which usable data exist. It therefore follows that, if the number of r_j values at which usable data exist is N, the number of $s^*_{\varphi_\epsilon}$ values at which usable data exist is $2N$.

With respect to Equation 5, it is also worth noting that, as $s^*_{\varphi_\epsilon}$ is inversely proportional to t_ϵ, $s^*_{\varphi_\epsilon}$ at $t_\epsilon = 0$ s is best evaluated by taking the limit as at t_ϵ approaches 0 s from above, in which case, $s^*_{\varphi_\epsilon}$ approaches -∞ for $r_0 = r_b$ and $s^*_{\varphi_\epsilon}$ approaches +∞ for $r_0 = r_m$.

For data obtained by the RI detection system, the N of $1 \leq j \leq N$ is time-independent, because, within the error of the measurement, and barring unforeseen disasters such as the loss of sample or reference volumes to the combined assaults of vacuum pumps and centrifugal forces, time does not change the radial positions, denoted as r_j, at which usable data are found for a given replicate of a given treatment group. The time-independence of N ensures that the set of all φ_ϵ is also time-independent.

A catastrophic loss of sample or reference volumes would warrant the rejection of the affected replicate, so the only acceptable source of a time dependence in N would be a detection system that records data at time-dependent radial positions. Data recorded at time-dependent radial positions would not be suitable for the analytical step described next, which consists of the point-by-point subtraction of data recorded at one time from data recorded at another time (Equation 7). With the replacement of N by a time-dependent counterpart, N_ϵ, however, Equation 6 would

be applicable to data recorded at time-dependent radial positions.

Point-by-point subtraction of data recorded at one time from data recorded at a later time

Provided that, as is the case here, the set of radial positions is identical for all replicates of all treatment groups, at each radial position, r_j, the data at one time can be subtracted from the data at any other time without resorting to extrapolation. Given such a commonality of radial positions for all data sets, within the data sets for a given replicate of a given treatment group, subtracting $NMS_{i,h}(r_j,t_\alpha)$ from $NMS_{i,h}(r_j,t_\epsilon)$ unambiguously eliminates $TIN_{i,h}(r_j)$ from the difference.

The weight-average apparent sedimentation coefficient within 5E-13 s $< \left|s^*_{\varphi_\epsilon}\right| <$ 10.625E-13 s, $s^*_{i,h,\epsilon}$ (Equation 13), is the observation obtained for each replicate, h, of each treatment group, i, at each time, t_ϵ, chosen for analysis. As will be shown (Equation 8), a differential step in the calculation of $s^*_{i,h,\epsilon}$ ensures that neither radially independent noise nor any radially independent portion of the signal contributes anything to the observation To also eliminate the contribution of time-independent noise to the observation, for each replicate, h, of each treatment group, i, $s^*_{i,h,\epsilon}$ is calculated from the set of differences (Equation 7), $NMS_{i,h}(r_j,t_\epsilon)$ - $NMS_{i,h}(r_j,t_\alpha)$, at each radial position, r_j, where $NMS_{i,h}(r_j,t_\epsilon)$ is the signal at a time, t_ϵ, of interest analytically, while $NMS_{i,h}(r_j,t_\alpha)$ is the signal at the earliest recorded time, t_α. As such, the signal, $NMS_{i,h}(r_j,t_\alpha)$, at the earliest recorded time, t_α, is treated as if it applied to time t_ϵ, even though, with $t_\epsilon \neq t_{\alpha\neq\epsilon}$, $s^*_{\varphi_\epsilon} \neq s^*_{\varphi_{\alpha\neq\epsilon}}$ at $\varphi_\epsilon = \varphi_{\alpha\neq\epsilon}$. However for t_ϵ not much greater than t_α, $NMS_{i,h}(r_j,t_{\epsilon\cong\alpha})$ is weakly time-dependent at most radial positions. Thus, it is argued that $NMS_{i,h}(r_j,t_\alpha)$ can be treated as if it applied to any time, t_ϵ, at which data are recorded.

The applicability of $NMS_{i,h}(r_j,t_\alpha)$ to data from later times can be justified by considering any time, t_β, within $t_\alpha \leq t_\beta \leq t_\gamma$, where t_α to t_γ is an early time period during which much of the system has yet to develop concentration gradients. Within $t_\alpha \leq t_\beta \leq t_\gamma$, $NMS_{i,h}(r_j,t_\beta) = k_\lambda[c_i(r_j,t_\beta)]L + N_{i,h}(r_j,t_\beta)$, where k_λ and L are constants (Equation 4), while away from unusable data near the extrema, $c_i(r_j,t_\beta)$ is independent of r_j and only weakly dependent on t_β. Thus, within the range of radial positions where usable data are found, $k_\lambda[c_i(r_j,t_{\beta=\alpha})]L$ makes no contribution to $s^*_{i,h,\epsilon}$ (Equation 13). Away from the extrema, most of the time dependence in $NMS_{i,h}(r_j,t_\beta)$ is found in $N_{i,h}(r_j,t_\beta)$, of which, by Equation 2b, $TIN_{i,h}(r_j)$ is the time-independent noise, $RIN_{i,h}(t_\beta)$ is the radially independent noise and $GRN_{i,h}(r_j,t_\beta)$ is the generally random noise. Of the three parts of $N_{i,h}(r_j,t_{\beta=\alpha})$, neither $TIN_{i,h}(r_j)$ nor $RIN_{i,h}(t_{\beta=\alpha})$ makes any contribution to $s^*_{i,h,\epsilon}$. Due to the variation of $GRN_{i,h}(r_j,t_\beta)$ with both radial position and time, $GRN_{i,h}(r_j,t_{\beta=\alpha})$ does make systematic contributions to $s^*_{i,h,\epsilon}$. As is shown in a later section (*Mitigation of data clipping*), however, the systematic contributions that $GRN_{i,h}(r_j,t_{\beta=\alpha})$ makes to $s^*_{i,h,\epsilon}$ can be minimised by excluding from analysis those data for which the absolute value of the difference (Equation 7), $NMS_{i,h}(r_j,t_\epsilon)$ - $NMS_{i,h}(r_j,t_\alpha)$, is small enough to be attributable to noise.

Letting Y denote the difference between two signals separated by time only, for radial position r_j of replicate h of treatment group i, the equation

$$Y_{i,h}(r_j,t_\epsilon) = NMS_{i,h}(r_j,t_\epsilon) - NMS_{i,h}(r_j,t_\alpha) \quad (7)$$

can be written for the difference between the signals at times t_ϵ and t_α. (Equation 111 is a more detailed expression of Equation 7.) The set of all such differences for replicate h of treatment group i is transformed by remapping $Y_{i,h}(r_j,t_\epsilon)$ versus r_j to $Y_{i,h}(s^*_{\varphi_\epsilon})$ versus $s^*_{\varphi_\epsilon}$, where $s^*_{\varphi_\epsilon}$ is

calculated from r_j and t_ϵ using Equation 5.

Despite its being equal to the difference between the signals at two times, t_ϵ and t_α, $Y_{i,h}(s^*_{\varphi_\epsilon})$ is treated as if it pertained solely to time t_ϵ, and as such, the partial derivative of $Y_{i,h}(s^*_{\varphi_\epsilon})$ is taken with respect to $s^*_{\varphi_\epsilon}$ at constant time, with t_ϵ effectively being the time held constant.

As the set of r_j values is finite, the set of $s^*_{\varphi_\epsilon}$ values is finite at each time, t_ϵ. Thus, any partial derivative with respect to r_j or $s^*_{\varphi_\epsilon}$ must be approximated if it cannot be evaluated analytically. The approximation used to evaluate the partial derivative of $Y_{i,h}(s^*_{\varphi_\epsilon})$ with respect to $s^*_{\varphi_\epsilon}$ at time t_ϵ is given by

$$\left(\frac{\partial Y_{i,h}\left(s^*_{\varphi_\epsilon}\right)}{\partial s^*_{\varphi_\epsilon}}\right)_t \cong \frac{1}{2}\left[\frac{Y_{i,h}\left(s^*_{\varphi_\epsilon}\right) - Y_{i,h}\left(s^*_{\varphi_\epsilon-1}\right)}{s^*_{\varphi_\epsilon} - s^*_{\varphi_\epsilon-1}} + \frac{Y_{i,h}\left(s^*_{\varphi_\epsilon+1}\right) - Y_{i,h}\left(s^*_{\varphi_\epsilon}\right)}{s^*_{\varphi_\epsilon+1} - s^*_{\varphi_\epsilon}}\right] \equiv \frac{\Delta Y_{i,h}\left(s^*_{\varphi_\epsilon}\right)}{\Delta s^*_{\varphi_\epsilon}}$$

(8a)

at φ_ϵ within $1 < \varphi_\epsilon < 2N$,

$$\left(\frac{\partial Y_{i,h}\left(s^*_{\varphi_\epsilon=1}\right)}{\partial s^*_{\varphi_\epsilon}}\right)_t \cong \frac{Y_{i,h}\left(s^*_{\varphi_\epsilon+1}\right) - Y_{i,h}\left(s^*_{\varphi_\epsilon}\right)}{s^*_{\varphi_\epsilon+1} - s^*_{\varphi_\epsilon}} \equiv \frac{\Delta Y_{i,h}\left(s^*_{\varphi_\epsilon=1}\right)}{\Delta s^*_{\varphi_\epsilon=1}}$$

(8b)

at $\varphi_\epsilon = 1$, and

$$\left(\frac{\partial Y_{i,h}\left(s^*_{\varphi_\epsilon=2N}\right)}{s^*_{\varphi_\epsilon}}\right)_t \cong \frac{Y_{i,h}\left(s^*_{\varphi_\epsilon}\right) - Y_{i,h}\left(s^*_{\varphi_\epsilon-1}\right)}{s^*_{\varphi_\epsilon} - s^*_{\varphi_\epsilon-1}} \equiv \frac{\Delta Y_{i,h}\left(s^*_{\varphi_\epsilon=2N}\right)}{\Delta s^*_{\varphi_\epsilon=2N}}$$

(8c)

at $\varphi_\epsilon = 2N$.

Equation 8 describes the differentiation method of Origin 6.0(Microcal Software, Inc), which was

applied to the signal-versus-transformed-radial-position data, in the form of $Y_{i,h}(s^*_{\varphi_\epsilon})$ plotted as a function of $s^*_{\varphi_\epsilon}$, to evaluate the partial derivative of $Y_{i,h}(s^*_{\varphi_\epsilon})$ with respect to $s^*_{\varphi_\epsilon}$ at time t_ϵ.

As $TIN_{i,h}(r_j)$ is identical in $NMS_{i,h}(r_j,t_\alpha)$ and $NMS_{i,h}(r_j,t_\epsilon)$ (Equation 1b), $TIN_{i,h}(r_j)$ vanishes in the difference, $NMS_{i,h}(r_j,t_\epsilon)$ - $NMS_{i,h}(r_j,t_\alpha)$, that yields $Y_{i,h}(r_j,t_\epsilon)$ (Equation 7). Therefore, $TIN_{i,h}(r_j)$ is absent from $Y_{i,h}(s^*_{\varphi_\epsilon})$. Thus, $TIN_{i,h}(r_j)$ does not contribute anything to the partial derivative of $Y_{i,h}(s^*_{\varphi_\epsilon})$ with respect to $s^*_{\varphi_\epsilon}$ at time t_ϵ (Equation 8). (Equation 107 is a formal expression of this characteristic of $TIN_{i,h}(r_j)$.)

As both $RIN_{i,h}(t_\alpha)$ and $RIN_{i,h}(t_\epsilon)$ are constant with r_j, both are also constant with $s^*_{\varphi_\epsilon}$. Therefore, $RIN_{i,h}(t_\alpha)$ and $RIN_{i,h}(t_\epsilon)$ merely contribute an $s^*_{\varphi_\epsilon}$-independent offset, equal to $RIN_{i,h}(t_\epsilon)$ - $RIN_{i,h}(t_\alpha)$ (Equations 1b and 7) to $Y_{i,h}(s^*_{\varphi_\epsilon})$. Thus, neither $RIN_{i,h}(t_\alpha)$ nor $RIN_{i,h}(t_\epsilon)$ contribute anything to the partial derivative of $Y_{i,h}(s^*_{\varphi_\epsilon})$ with respect to $s^*_{\varphi_\epsilon}$ at time t_ϵ (Equation 8). (Equation 108 is a formal expression of the difference, $RIN_{i,h}(t_\epsilon)$ - $RIN_{i,h}(t_\alpha)$.)

As both $GRN_{i,h}(r_j,t_\alpha)$ and $GRN_{i,h}(r_j,t_\epsilon)$ are randomly distributed with respect to r_j, neither $GRN_{i,h}(r_j,t_\alpha)$ nor $GRN_{i,h}(r_j,t_\epsilon)$ makes any systematic contribution to $Y_{i,h}(r_j,t_\epsilon)$. Rather, their contribution to $Y_{i,h}(r_j,t_\epsilon)$ consists of the difference, $GRN_{i,h}(r_j,t_\epsilon)$ - $GRN_{i,h}(r_j,t_\alpha)$ (Equations 1b and 7), that, with respect to r_j, is found to be randomly distributed with a standard deviation approximately equal to $2^{0.5}$ times the standard deviation in either $GRN_{i,h}(r_j,t_\alpha)$ or $GRN_{i,h}(r_j,t_\epsilon)$. (As will be discussed with respect to Figure 5 and Table 14, every set of $GRN_{i,h}(r_j,t_\epsilon)$ values has a standard deviation of approximately 0.01400 fringe.) Consequently, the standard deviation of the randomly distributed noise of $Y_{i,h}(r_j,t_\epsilon)$ is about $2^{0.5}$-fold greater than that of either $NMS_{i,h}(r_j,t_\alpha)$ or $NMS_{i,h}(r_j,t_\epsilon)$. (Equation 109 is a formal expression of the difference, $GRN_{i,h}(r_j,t_\epsilon)$ - $GRN_{i,h}(r_j,t_\alpha)$, and

the standard deviation of such differences is discussed in *Mitigation of data clipping*.)

Upon transformation of $Y_{i,h}(r_j,t_\epsilon)$ versus r_j to $Y_{i,h}(s^*_{\varphi_\epsilon})$ versus $s^*_{\varphi_\epsilon}$, the randomly distributed noise of the former with respect to r_j becomes the randomly distributed noise of the latter with respect to $s^*_{\varphi_\epsilon}$. The greater the randomly distributed noise of $Y_{i,h}(r_j,t_\epsilon)$ is with respect to $s^*_{\varphi_\epsilon}$, the more erratic the partial derivative of $Y_{i,h}(s^*_{\varphi_\epsilon})$ is with respect to $s^*_{\varphi_\epsilon}$ at time t_ϵ (Equation 8). Nevertheless, if the partial derivative of $Y_{i,h}(s^*_{\varphi_\epsilon})$ at time t_ϵ were taken with respect to the index (Equation 6), φ_ϵ, for which $\Delta\varphi_\epsilon$, the increment between consecutive values, is always equal to 1, the random noise of that approximated derivative, $\frac{\Delta Y_{i,h}(s^*_{\varphi_\epsilon})}{\Delta\varphi_\epsilon} \cong \left(\frac{\partial Y_{i,h}(s^*_{\varphi_\epsilon})}{\partial\varphi_\epsilon}\right)_t$, would be normally distributed with a $2^{0.5}$-fold smaller standard deviation than that in the random noise of $Y_{i,h}(s^*_{\varphi_\epsilon})$. As such, there is no cost of eliminating $TIN_{i,h}(r_j)$ and RIN by subtraction to first obtaining $Y_{i,h}(s^*_{\varphi_\epsilon})$, followed by approximated differentiation to then obtain $\frac{\Delta Y_{i,h}(s^*_{\varphi_\epsilon})}{\Delta\varphi_\epsilon}$. The parameter of interest is not $\frac{\Delta Y_{i,h}(s^*_{\varphi_\epsilon})}{\Delta\varphi_\epsilon}$, however. (The standard deviation of such approximated derivatives is discussed in *Mitigation of data clipping*.)

If, $\Delta s^*_{\varphi_\epsilon}$, the increment between consecutive values of $s^*_{\varphi_\epsilon}$, did not change over the full range of $s^*_{\varphi_\epsilon}$, the approximated derivative, $\frac{\Delta Y_{i,h}(s^*_{\varphi_\epsilon})}{\Delta s^*_{\varphi_\epsilon}} \cong \left(\frac{\partial Y_{i,h}(s^*_{\varphi_\epsilon})}{\partial s^*_{\varphi_\epsilon}}\right)_t$, would differ from $\frac{\Delta Y_{i,h}(s^*_{\varphi_\epsilon})}{\Delta\varphi_\epsilon}$ by an $s^*_{\varphi_\epsilon}$-independent magnitude, $\frac{\Delta\varphi_\epsilon}{\Delta s^*_{\varphi_\epsilon}}$. In the simulated AUC data presented here, and in real data of the sort simulated, the values of r_j are such that, upon the application of Equation 5, $\Delta s^*_{\varphi_\epsilon}$ will be a function of $s^*_{\varphi_\epsilon}$, in addition to which, $\Delta s^*_{\varphi_\epsilon}$ will be a function of t_ϵ. Thus, the random error in $\frac{\Delta Y_{i,h}(s^*_{\varphi_\epsilon})}{\Delta\varphi_\epsilon}$ becomes systematic error in $\frac{\Delta Y_{i,h}(s^*_{\varphi_\epsilon})}{\Delta s^*_{\varphi_\epsilon}}$, as $\frac{\Delta Y_{i,h}(s^*_{\varphi_\epsilon})}{\Delta s^*_{\varphi_\epsilon}}$ is equal to $\frac{\Delta\varphi_\epsilon}{\Delta s^*_{\varphi_\epsilon}}$ times $\frac{\Delta Y_{i,h}(s^*_{\varphi_\epsilon})}{\Delta\varphi_\epsilon}$, where

$\frac{\Delta\varphi_\epsilon}{\Delta s^*_{\varphi\epsilon}}$ depends on $s^*_{\varphi_\epsilon}$ and t_ϵ. As $\Delta\varphi_\epsilon$ remains equal to 1, $\Delta s^*_{\varphi_\epsilon}$ is the sole source of the dependence on $s^*_{\varphi_\epsilon}$ and t_ϵ. (See discussions following Equations 9 and 13.)

The nonredundant derivative and the elimination function

The application of Equation 8 yields $\left(\frac{\partial Y_{i,h}(s^*_{\varphi\epsilon})}{\partial s^*_{\varphi\epsilon}}\right)_t$ as the apparent signal that is subjected to further analysis. The nonredundant derivative of $Y_{i,h}(s^*_{\varphi_\epsilon})$ with respect to $s^*_{\varphi_\epsilon}$ at time t_ϵ for replicate h of treatment group i is

$$q_{i,h}(s^*_{\varphi_\epsilon}) = \left(\frac{\partial Y_{i,h}(s^*_{\varphi_\epsilon})}{\partial s^*_{\varphi_\epsilon}}\right)_t - e_{i,h}(s^*_{\varphi_\epsilon}),$$

(9a)

where the elimination function,

$$e_{i,h}(s^*_{\varphi_\epsilon}) = \begin{Bmatrix} 0 \; if \; s^*_{\varphi_\epsilon}\left(\frac{\partial Y_{i,h}(s^*_{\varphi_\epsilon})}{\partial s^*_{\varphi_\epsilon}}\right)_t \geq 0 \\ \left(\frac{\partial Y_{i,h}(s^*_{\varphi_\epsilon})}{\partial s^*_{\varphi_\epsilon}}\right)_t \; if \; s^*_{\varphi_\epsilon}\left(\frac{\partial Y_{i,h}(s^*_{\varphi_\epsilon})}{\partial s^*_{\varphi_\epsilon}}\right)_t < 0 \end{Bmatrix},$$

(9b)

provides the term by which redundant values of $\left(\frac{\partial Y_{i,h}(s^*_{\varphi\epsilon})}{\partial s^*_{\varphi\epsilon}}\right)_t$ are eliminated from $q_{i,h}(s^*_{\varphi_\epsilon})$ (Moody, 2012b). Equations 8a to 8c are used to approximately evaluate $\left(\frac{\partial Y_{i,h}(s^*_{\varphi\epsilon})}{\partial s^*_{\varphi\epsilon}}\right)_t$ as it appears in Equations 9a and 9b. For values of $\frac{\Delta Y_{i,h}(s^*_{\varphi\epsilon})}{\Delta s^*_{\varphi\epsilon}} \cong \left(\frac{\partial Y_{i,h}(s^*_{\varphi\epsilon})}{\partial s^*_{\varphi\epsilon}}\right)_t$ that survive as values of $q_{i,h}(s^*_{\varphi_\epsilon})$ upon the application of Equation 9, the systematic error in $\frac{\Delta Y_{i,h}(s^*_{\varphi\epsilon})}{\Delta s^*_{\varphi\epsilon}}$ becomes the systematic error in $\frac{\Delta Y_{i,h}(s^*_{\varphi\epsilon})}{\Delta s^*_{\varphi\epsilon}}$. (See discussions following Equations 8 and 13)

The apparent sedimentation coefficient distribution function

The apparent sedimentation coefficient distribution function for replicate h of treatment group i at time t_ϵ is

$$g_{i,h}\left(s^*_{\varphi_\epsilon}\right) = q_{i,h}\left(s^*_{\varphi_\epsilon}\right)\left(e^{2s^*_{\varphi_\epsilon}\omega^2 t_\epsilon}\right),$$

(10)

in which multiplication of $q_{i,h}\left(s^*_{\varphi_\epsilon}\right)$ by $e^{2s^*_{\varphi_\epsilon}\omega^2 t_\epsilon}$ yields a product, $g_{i,h}\left(s^*_{\varphi_\epsilon}\right)$, that is normalised for the hypothetical effects of radial dilution or radial concentration that the plateau of a hypothetical solute characterised by $s^*_{\varphi_\epsilon}$ would have accumulated by time t_ϵ (Moody, 2012b). (It is not possible to perfectly normalise for the real effects of radial dilution or radial concentration that the plateau of a real solute would have accumulated by time t_ϵ, because no real solute exhibits a diffusion coefficient of zero and behaves like an ideal solute from the start of the experiment to time t_ϵ.) As $e^{2s^*_{\varphi_\epsilon}\omega^2 t_\epsilon}$ is always positive, the signs of $g_{i,h}\left(s^*_{\varphi_\epsilon}\right)$ and $q_{i,h}\left(s^*_{\varphi_\epsilon}\right)$ are the same, so that $g_{i,h}\left(s^*_{\varphi_\epsilon}\right)$ differs from $q_{i,h}\left(s^*_{\varphi_\epsilon}\right)$ solely with respect to magnitude. For values of $\frac{\Delta Y_{i,h}\left(s^*_{\varphi_\epsilon}\right)}{\Delta s^*_{\varphi_\epsilon}} \cong \left(\frac{\partial Y_{i,h}\left(s^*_{\varphi_\epsilon}\right)}{\partial s^*_{\varphi_\epsilon}}\right)_t$ that survive as values of $q_{i,h}\left(s^*_{\varphi_\epsilon}\right)$ upon the application of Equation 9, $e^{2s^*_{\varphi_\epsilon}\omega^2 t_\epsilon}$ times the systematic error in $\frac{\Delta Y_{i,h}\left(s^*_{\varphi_\epsilon}\right)}{\Delta s^*_{\varphi_\epsilon}}$ becomes the systematic error in $\frac{\Delta Y_{i,h}\left(s^*_{\varphi_\epsilon}\right)}{\Delta s^*_{\varphi_\epsilon}}$. (See discussions following Equations 8, 9 and 13.)

The cumulative distribution function of the apparent sedimentation coefficient

The cumulative distribution function of the apparent sedimentation coefficient,

$$G_{i,h}\left(s^*_{\varphi_\epsilon}\right) = \int_{s^*_{\varphi_\epsilon=1}}^{s^*_{\varphi_\epsilon}} \left|g_{i,h}(s^*)\right| ds^*,$$

(11)

is a substantially time-normalised, but not entirely time-independent, measure of the total, initial signal from all solutes for which the apparent sedimentation coefficient is less than or equal to $s^*_{\varphi_\epsilon}$, but greater than or equal to $s^*_{\varphi_\epsilon=1}$ at time t_ϵ (Moody, 2012b). (This issue is revisited in the discussion surrounding Equation 80.) This integral was evaluated numerically from a baseline of zero using the trapezoidal rule, as implemented in Origin 6.0. Any systematic noise in $\left|g_{i,h}(s^*)\right|$ within the limits of integration is accumulated by $G_{i,h}\left(s^*_{\varphi_\epsilon}\right)$. (See discussions following Equations 8, 9, 10 and 13.)

The weight-average apparent sedimentation coefficient

The equation for the weight-average apparent sedimentation coefficient within $s^*_{\varphi_\epsilon-\alpha} \le s^*_{\varphi_\epsilon} \le s^*_{\varphi_\epsilon+\beta}$ can be written as

$$s^*_{i,h,\epsilon}\left(s^*_{\varphi_\epsilon-\alpha}, s^*_{\varphi_\epsilon+\beta}\right) = \frac{\int_{s^*_{\varphi_\epsilon-\alpha}}^{s^*_{\varphi_\epsilon+\beta}} s^*_{\varphi_\epsilon}\left|g_{i,h}\left(s^*_{\varphi_\epsilon}\right)\right| ds^*_{\varphi_\epsilon}}{G_{i,h}\left(s^*_{\varphi_\epsilon+\beta}\right) - G_{i,h}\left(s^*_{\varphi_\epsilon-\alpha}\right)}.$$

(12)

The integral in the numerator was evaluated numerically from a baseline of zero using the trapezoidal rule, as implemented in Origin 6.0. The terms in the denominator were evaluated using Equation 11.

The observation obtained for each replicate, *h*, of each treatment group, *i*, at each time, t_ϵ, chosen

for analysis was

$$s^*_{i,h,\epsilon} = s^*_{i,h,\epsilon}\left(s^*_{\varphi_\epsilon} > s^*_{min<0}, s^*_{\varphi_\epsilon} < s^*_{max<0}\right) + s^*_{i,h,\epsilon}\left(s^*_{\varphi_\epsilon} > s^*_{min>0}, s^*_{\varphi_\epsilon} < s^*_{max>0}\right),$$

(13)

where $s^*_{min<0}$ = -10.625E-13 s, $s^*_{max<0}$ = -5E-13 s, $s^*_{min>0}$ = 5E-13 s and $s^*_{max>0}$ = 10.625E-13 s. Equation 12 was used to evaluate the terms on the right-hand side, the inequalities of which reflect the fact that, as $s^*_{\varphi_\epsilon}$ values depend on t_ϵ, it is not possible to set the ranges of $s^*_{\varphi_\epsilon}$ to specific values without implying that Equation 13 applies to a specific time, which it does not. To provide the greatest possible comparability, for all replicates of all treatment groups at each time chosen for analysis, the same ranges of $s^*_{i,h,\epsilon}$ values were, to the closest extent possible, applied to the determination of $s^*_{i,h,\epsilon}$. The observations (the $s^*_{i,h,\epsilon}$values) from each time were analysed to assess the statistical significance of differences between treatment groups.

As shown later (*The signal-to-noise ratio of* $g_{i,h}\left(s^*_{\varphi_\epsilon}\right)$ *worsens in proportion to* $1/e^{2s^*_{\varphi_\epsilon}\omega^2 t_\epsilon}$ *as* $s^*_{\varphi_\epsilon}$ *increases*; *The accumulated error in* $G_{i,h}\left(s^*_{\varphi_\epsilon=2N}\right)$ *increases in proportion to the clipping of random noise*; *The accumulated error in* $\langle s^*_{i,\epsilon}\rangle$ *increases in proportion to the clipping of random noise*), $GRN_{i,h}(r_j,t_\alpha)$, would make the least systematic contribution to $s^*_{i,h,\epsilon}$ if, in going from $\left(\frac{\partial Y_{i,h}(s^*_{\varphi_\epsilon})}{\partial s^*_{\varphi_\epsilon}}\right)_t$ (Equation 8) to $q_{i,h}\left(s^*_{\varphi_\epsilon}\right)$ (Equation 9), the clipping of the positively signed and the negatively signed random noise were minimised (Figures 24 to 27). Even where the clipping of positively signed random noise within $-|s^*_a| < s^*_{\varphi_\epsilon} < -|s^*_z|$ is complemented by the clipping of negatively signed random noise within $|s^*_a| < s^*_{\varphi_\epsilon} < |s^*_z|$, the remaining random noise in those regions will contribute an offset to $s^*_{i,h,\epsilon}$, such that $\left|s^*_{i,h,\epsilon} - s^*_{i,\epsilon}\right| > 0$. As the results for treatment groups 1 to 4 (Tables 24 to 27; Figures 44 to 47) show, such an offset can be minimised by excluding, through the judicious selection of $s^*_{min<0}$, $s^*_{max<0}$, $s^*_{min>0}$ and $s^*_{max>0}$, regions of low

signal-to-noise from the ranges of $s^*_{\varphi_\epsilon}$ used to calculate $s^*_{i,h,\epsilon}$ (Equation13).

Statistical analysis

At each time chosen for analysis, the population mean of the observations from the replicates within each treatment group is calculated. One-way analysis of variance (ANOVA) is used to test whether there are any statistically significant differences in the population means between any of the treatment groups at a given time. To quantify the statistical significance of a difference between any two treatment groups, a Bonferroni-adjusted *t*-test (2-tailed) is applied to pair-wise comparisons of the population means from different treatment groups at each time. (For details, see: *One-way analyses of variance (ANOVA), Bonferroni adjusted t-test (2-tailed), and confidence intervals about mean values*.)

Expectation values

The expectation value of the observation for treatment group *i* at time t_ϵ is obtained by subjecting the corresponding $NFS_i(r_j,t_\epsilon)$ data to the same sort of analysis (Equations 7 to 13) that yields the observation for replicate *h* of treatment group *i* at time t_ϵ when applied to the corresponding $NMS_{i,h}(r_j,t_\epsilon)$ data. To apply the equations (Equations 7 to 13) developed for $NMS_{i,h}(r_j,t_\epsilon)$ to $NFS_i(r_j,t_\epsilon)$ without changing the notation, the $NFS_i(r_j,t_\epsilon)$ of treatment group *i* is designated as $NMS_i(r_j,t_\epsilon)$, where

$$NFS_i(r_j,t_\epsilon) \equiv NMS_i(r_j,t_\epsilon) = NFS_i(r_j,t_\epsilon) + TIN_i(r_j) + RIN_i(t_\epsilon) + GRN_i(r_j,t_\epsilon),$$

(1c)

of which the total noise is given by

$$N_i(r_j, t_\epsilon) = TIN_i(r_j) + RIN_i(t_\epsilon) + GRN_i(r_j, t_\epsilon) = 0,$$

(2c)

as each value of $TIN_i(r_j) = 0$, each value of $RIN_i(t_\epsilon) = 0$ and each value of $GRN_i(r_j, t_\epsilon) = 0$.

Absent the subscript h, Equations 7 to 13 are then applied. Applying Equation 7 to $NMS_i(r_j, t_\epsilon)$ and $NMS_i(r_j, t_\alpha)$ yields $Y_i(r_j, t_\epsilon)$ for the difference between the noise-free signals at times t_ϵ and t_α. (The difference, $NMS_{i,h}(r_j, t_\epsilon)$ - $NMS_{i,h}(r_j, t_\alpha)$, described again in Equation 110.) Transforming $Y_i(r_j, t_\epsilon)$ to $Y_i(s^*_{\varphi_\epsilon})$ and applying Equation 8 to $Y_i(s^*_{\varphi_\epsilon})$ yields $\left(\frac{\partial Y_i(s^*_{\varphi_\epsilon})}{\partial s^*_{\varphi_\epsilon}}\right)_t$, which is free of any effects due to random noise. Applying Equation 9 to $\left(\frac{\partial Y_i(s^*_{\varphi_\epsilon})}{\partial s^*_{\varphi_\epsilon}}\right)_t$ yields $q_i(s^*_{\varphi_\epsilon})$, applying Equation 10 to $q_i(s^*_{\varphi_\epsilon})$ yields $g_i(s^*_{\varphi_\epsilon})$, applying Equation 11 to $g_i(s^*_{\varphi_\epsilon})$ yields $G_i(s^*_{\varphi_\epsilon})$ and, lastly, applying Equations 12 and 13 to $G_i(s^*_{\varphi_\epsilon})$ yields $s^*_{i,\epsilon}$, which is the expectation value of the observation for treatment group i at time t_ϵ.

It is worth noting that, despite its alternate designation as $NMS_i(r_j, t_\epsilon)$, $NFS_i(r_j, t_\epsilon)$ is not a replicate of treatment group i. Parameters that apply to the noise-free data of treatment group i are distinguished by the absence of a subscript h. Parameters that apply to replicates of treatment group i are distinguished by the presence of a subscript h, where h is an integer within $1 \leq h \leq n_i$, in which n_i is the number of replicates of treatment group i. Thus, when calculating the population mean of the observations, $s^*_{i,h,\epsilon}$, from all replicates within treatment group i, the expectation value for treatment group i, $s^*_{i,\epsilon}$, is excluded, because the expectation value is not an observation from a replicate.

The Svedberg: a convenient unit for reporting $s^*_{\varphi_\epsilon}$ and the like

As measured sedimentation coefficients, apparent or otherwise, usually range from a little under 1E-13 s to not much over 100E-13 s, it is often convenient to report such values as multiples of 1E-13 s, for which purpose, the Svedberg was defined as equal to 1E-13 s. The Svedberg was named in honour of The Svedberg, who was the foremost pioneer of AUC. (Sometimes an ambiguity is won in translation.)

In this work, to conserve space in tables and graphs, the Svedberg is often applied to $s^*_{\varphi_\epsilon}$ (Equation 5). Likewise, the Svedberg is often applied to the particular weight average apparent sedimentation coefficient, $s^*_{i,h,\epsilon}$ (Equation 13), that is the observation sought from each replicate within a treatment group, and to the population mean of the replicate observations within a treatment group. Where convenient, the Svedberg is also applied to the particular weight average apparent sedimentation coefficient, $s^*_{i,\epsilon}$ (Equation 13, absent the subscript *h*), that is the expectation value of the observation.

RANDOM NOISE

GRN source and the Cumulative Distribution Function

The data used as the source of the *GRN* (Equation 2b) is shown in Figure 1. In that figure, χ_Z, is the random variable, in that it is randomly distributed with respect to the normalised index,

$$Z_m = \frac{Z}{m+1}, \tag{14}$$

where Z is the integral index of the χ_Z values, and m is the total number of χ_Z values, so that $m \geq 1$ and $1 \leq Z \leq m$. Thus, $0 < Z_m < 1$, and for any permitted value of m, the mean of all Z_m values is equal to 0.5.

Figure 1 also shows another normalised index,

$$\zeta_m = \frac{\zeta}{m+1},$$

(15)

plotted against χ_ζ, which consists of the χ_Z values placed in ascending order with respect to the integral index, ζ, where $1 \leq \zeta \leq m$ and where, being identical to the corresponding parameter in Equation 14, $m \geq 1$. As with Z_m, $0 < \zeta_m < 1$, and for any permitted value of m, the mean of all ζ_m values is equal to 0.5.

The values of χ_Z and χ_ζ are identical but differently ordered with respect to either their integral or normalised indices. As Z_m monotonically increases, χ_Z varies randomly; as ζ_m monotonically increases, χ_ζ monotonically increases. Thus, for $\zeta = Z$, $\chi_\zeta \neq \chi_Z$ in most instances (Tables 1 and 2). Among many data sets having m in common, the average frequency with which $\chi_\zeta = \chi_Z$ when $\zeta = Z$ is $1/m$, which equates to once per data set. Within any given data set, however, the frequency with which $\chi_\zeta = \chi_Z$ when $\zeta = Z$ may differ from $1/m$. For example, among the data shown in Figure 1, the frequency with which $\chi_\zeta = \chi_Z$ when $\zeta = Z$ is twice out of $m = 98{,}588$ chances (Table 3).

In the limit as m approaches infinity, a graph of ζ_m plotted as a function of χ_ζ becomes indistinguishable from a graph of the Cumulative Distribution Function plotted as a function of χ_Z. The Cumulative Distribution Function can be written as

$$CDF(\chi) = \frac{A}{2}\left\{1 + erf\left(\frac{\chi - \mu}{\sqrt{2\sigma^2}}\right)\right\} = \int_{-\infty}^{\chi} \Psi_{\mu,\sigma^2}(\alpha)d\alpha,$$

(16)

where χ is a random variable that can take on any real value, μ is the mean value of χ, σ is the standard deviation of χ about μ, A is the value of the CDF in the limit as χ approaches infinity, and $\Psi_{\mu,\sigma^2}(\chi)$ is the Probability Density Function (*PDF*; Equation 24; Figure 2). In Figure 1, the plot of $CDF(\chi_Z)$ versus χ_Z and the plot of $CDF(\chi_\zeta)$ versus χ_ζ are differently ordered but otherwise identical, relative to their differently ordered but otherwise identical arguments, χ_Z and χ_ζ, respectively. Figure 1 shows that a plot of ζ_m versus χ_ζ is practically indistinguishable from a plot of $CDF(\chi_Z)$ versus χ_Z. For both χ_Z and χ_ζ in Figure 1, $\mu = 0$ and $\sigma = 1$, while for both $CDF(\chi_Z)$ and $CDF(\chi_\zeta)$ in Figure 1, $A = 1$.

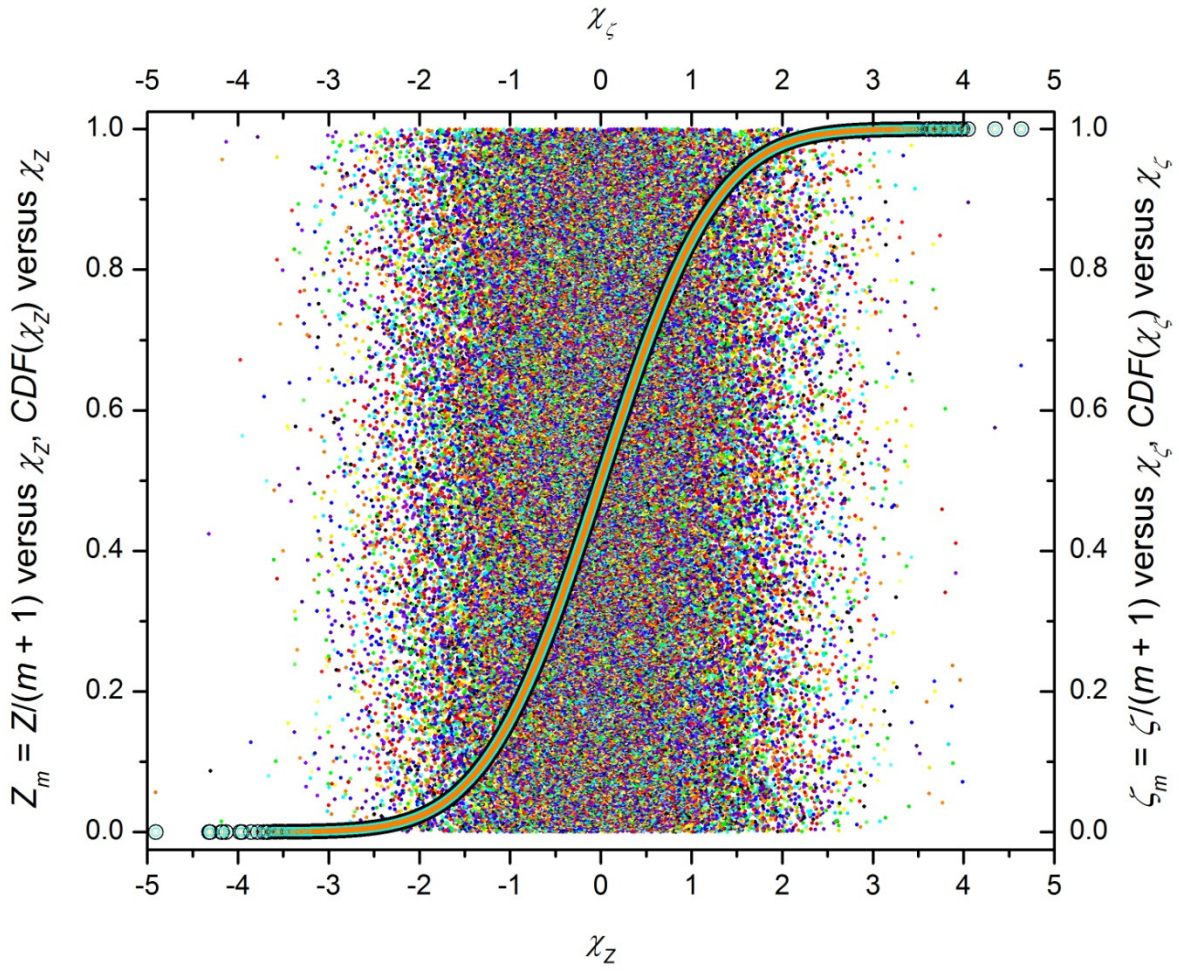

Figure 1. $CDF(\chi_Z)$ (○) versus χ_Z, $Z_m = Z/(m+1)$ (small dots, such as · and ·, in 24 evenly distributed colours) versus χ_Z, $CDF(\chi_\zeta)$ (○) versus χ_ζ, and $\zeta_m = \zeta/(m+1)$ (○) versus χ_ζ, where χ_Z and χ_ζ are differently ordered distributions of the same values, which number m in total. As Z_m monotonically increases, χ_Z varies randomly, while as ζ_m monotonically increases, χ_ζ monotonically increases. For the data in this figure, $m = 98{,}588$. For χ_Z, and thus too for χ_ζ, $\mu = 0$, and $\sigma = 1$, while for $CDF(\chi_Z)$, and thus too for $CDF(\chi_\zeta)$, $A = 1$. (See Equation 16.)

Origin 6.0 was used to generate the normally distributed random numbers that formed the basis of the values shown in Figure 1. The mean, μ_0, and the standard deviation, σ_0, of the numbers generated by Origin were calculated, μ_0 was subtracted from each number so generated, and the

difference was divided by σ_0 to obtain the χ_Z values shown. The adjustments applied to the numbers generated by Origin ensured that, for the χ_ζ values, μ would be as close as possible to 0 and σ would be as close as possible to 1.

Z	χ_Z	Z_m	$CDF(\chi_Z)$		ζ	χ_ζ	ζ_m	$CDF(\chi_\zeta)$
1	-0.28398	1.0143E-5	0.38821		1	-4.90662	1.0143E-5	4.6330E-7
2	1. 01070	2.0286E-5	0.84392		2	-4.31897	2.0286E-5	7.8381E-6
3	1. 51942	3.0429E-5	0.93567		3	-4.30438	3.0429E-5	8.3726E-6
…	…	…	…		…	…	…	…
24,646	-1.01704	0.249987	0.15457		24,646	-0.676711	0.249987	0.249295
24,647	-0.53198	0.249997	0.29737		24,647	-0.676708	0.249997	0.249296
24,648	-0.45924	0.250008	0.32303		24,648	-0.676705	0.250008	0.249297
…	…	…	…		…	…	…	…
49,294	1.19642	0.499995	0.88423		49,294	-0.001800	0.499995	0.499282
49,295	0.34601	0.500005	0.63533		49,295	-0.001793	0.500005	0.499285
…	…	…	…		…	…	…	…
49,363	0.07720	0.500695	0.53077		49,363	5.80928E-6	0.500695	0.500002
…	…	…	…		…	…	…	…
73,940	2.31231	0.749982	0.98962		73,940	0.672328	0.749982	0.749312
73,941	1.21134	0.749992	0.88712		73,941	0.672345	0.749992	0.749318
73,942	-0.13885	0.750003	0.44478		73,942	0.672378	0.750003	0.749328
…	…	…	…		…	…	…	…
98,586	0.41343	0.999970	0.66036		98,586	4.049212	0.999970	0.999974
98,587	0.43826	0.999980	0.66940		98,587	4.345309	0.999980	0.999993
98,588	-1.55481	0.999990	0.06000		98,588	4.634160	0.999990	0.999998

Table 1. Selected values of χ_Z and χ_ζ for which $\zeta = Z$. (In this table, and in the two tables that follow, data are shown at sufficient precision to distinguish close values.) Overall, the values of χ_Z and χ_ζ are identical but differently ordered, in that χ_ζ increases as ζ increases, while χ_Z varies randomly as Z increases. By chance, the lowest magnitude value of χ_ζ occurs at $\zeta = 49{,}363$, rather than, as might be expected, at one of the two most central positions, $\zeta = 49{,}294$ or $\zeta = 49{,}295$. Among the selected values in this table, there is no instance in which $\chi_\zeta = \chi_Z$ when $\zeta = Z$. For each of the selected values of χ_ζ in this table, Table 2 shows the value of Z for which $\chi_Z = \chi_\zeta$. Chance favours a $1/m$ frequency of instances in which $\chi_\zeta = \chi_Z$ when $\zeta = Z$. For the data shown in Figure 1,

the actual frequency of instances in which $\chi_\zeta = \chi_Z$ when $\zeta = Z$ is $2/m$ (Table 3).

ζ	χ_ζ	$CDF(\chi_\zeta)$		$Z - \zeta$		Z	χ_Z	$CDF(\chi_Z)$
1	-4.90662	4.6330E-7		5,563		5,564	-4.90662	4.6330E-7
2	-4.31897	7.8381E-6		41,810		41,812	-4.31897	7.8381E-6
3	-4.30438	8.3726E-6		8,589		8,592	-4.30438	8.3726E-6
…	…	…		…		…	…	…
24,646	-0.676711	0.249295		55,061		79,707	-0.676711	0.249295
24,647	-0.676708	0.249296		21,178		45,825	-0.676708	0.249296
24,648	-0.676705	0.249297		61228		85,876	-0.676705	0.249297
…	…	…		…		…	…	…
49,294	-0.001800	0.499282		37,270		86,564	-0.001800	0.499282
49,295	-0.001793	0.499285		-44,510		4,785	-0.001793	0.499285
…	…	…		…		…	…	…
49,363	5.8093E-6	0.500002		31,143		80,506	5.8093E-6	0.500002
…	…	…		…		…	…	…
73,940	0.672328	0.749312		-48,463		25,477	0.672328	0.749312
73,941	0.672345	0.749318		-11,189		62,752	0.672345	0.749318
73,942	0.672378	0.749328		1,819		75,761	0.672378	0.749328
…	…	…		…		…	…	…
98,586	4.049212	0.999974		-10,289		88,297	4.049212	0.999974
98,587	4.345309	0.999993		-41,898		56,689	4.345309	0.999993
98,588	4.634160	0.999998		-33,182		65,406	4.634160	0.999998

Table 2. The selected values of ζ, χ_ζ and $CDF(\chi_\zeta)$ from Table 1 versus the corresponding values of Z, χ_Z and $CDF(\chi_Z)$ for which $\chi_Z = \chi_\zeta$. Among values selected for this table, $\chi_{Z \neq \zeta} = \chi_{\zeta \neq Z}$ always holds, as there is no instance in which $Z = \zeta$ when $\chi_Z = \chi_\zeta$. Instances in which $Z = \zeta$ when $\chi_Z = \chi_\zeta$ are shown in Table 3.

ζ	χ_ζ	ζ_m	$CDF(\chi_\zeta)$		$Z - \zeta$		Z	χ_Z	Z_m	$CDF(\chi_Z)$
…	…	…	…		…		…	…	…	…
8,311	-1.37546	0.084299	0.084495		0		8,311	-1.37546	0.084299	0.084495
…	…	…	…		…		…	…	…	…
33,492	-0.41398	0.339713	0.339445		0		33,492	-0.41398	0.339713	0.339445
…	…	…	…		…		…	…	…	…

Table 3. The two instances, among 98,588 chances (Figure 1; Tables 1 and 2), for which $Z = \zeta$

when $\chi_Z = \chi_\zeta$, such that $\chi_{Z=\zeta} = \chi_{\zeta=Z}$. As m normally distributed random numbers can be ordered in any of $m!$ equally probable ways, the frequency of instances in which $\chi_{Z=\zeta} = \chi_{\zeta=Z}$ should approach an average value of $1/m$ as the number of data sets, each consisting of m values, approaches infinity. As in Tables 1 and 2, for a given value of ζ, the values of $CDF(\chi_\zeta)$ and ζ_m are close, but not identical. Relative to instances in which $\chi_{Z\neq\zeta} = \chi_{\zeta\neq Z}$, instances in which $\chi_{Z=\zeta} = \chi_{\zeta=Z}$ would be neither more nor less likely to coincide with an exact equality of $CDF(\chi_\zeta)$ to ζ_m, of which no instance is found among the data shown in Figure 1. As the set of all real numbers includes the set of all rational numbers and much else, there is almost no chance that an exact equality of $CDF(\chi_\zeta)$ to ζ_m would ever occur, though the two sets of values should become increasing indistinguishable as m approaches infinity.

THE 5 MEGILLAHS

As Table 1 illustrates, the set of all ordered pairs given by $(\chi_\zeta, CDF(\chi_\zeta))$ is not identical to the set of all ordered pairs given by (χ_ζ, ζ_m), despite the impression left by Figure 1 that the plot of $CDF(\chi_\zeta)$ versus χ_ζ might be identical to the plot of ζ_m versus χ_ζ. It might be supposed, however, that the similarity of the two plots would increase as m, and thus the number of χ_ζ values, increased. Taken to an extreme, it might be hypothesised that the two sets of ordered pairs, $(\chi_\zeta, CDF(\chi_\zeta))$ and (χ_ζ, ζ_m), would approach a state of indistinguishability as m increases to very large values. This hypothesis has been partly tested using 64 treatment groups for which the defining parameter, m, ranged from 1 to 39,000,000. Among the treatment groups, the number of replicates ranged from a high of 195,000,000 at $m = 1$ to a low of 5 at $m = 39{,}000{,}000$. (The 5 megillahs are the 5 replicates at $m = 39{,}000{,}000$.) With respect to these treatment groups, in this section, the general approach of the data analysis is summarised, and the main result is given. Further details of the

data generation and the results of data analysis are presented in the final section (**RANDOMNESS AS A FUNCTION OF THE TOTAL POPULATION OF OBSERVATIONS**) of this work. Some of the data analysis relies on the same statistical methods (*One-way analyses of variance (ANOVA), Bonferroni adjusted t-test (2-tailed), and confidence intervals about mean values*) that are applied to the simulated AUC data.

The 64 treatment groups are indexed by i, and within a given treatment group, there are n_i replicate data sets that are indexed by h. Within each replicate, h, of treatment group i, there is a population of m_i random variables that are denoted as $\chi_{Z_i,h}$ when in their original order given by the integral index, Z_i. When placed in ascending order, the m_i random variables within replicate h of treatment group i are denoted as $\chi_{\zeta_i,h}$, and their place in the ascending order is given by the integral index ζ_i. The normalised index of Z_i is given by $Z_{m_i} = Z_i/(m_i + 1)$, and the normalised index of ζ_i is given by $\zeta_{m_i} = \zeta_i/(m_i + 1)$. Thus, it follows that $1 \leq Z_i \leq m_i$, $1 \leq \zeta_i \leq m_i$, $0 < Z_{m_i} < 1$ and $0 < \zeta_{m_i} < 1$. It also follows that, for any permitted value of m_i, the mean of all Z_{m_i} values and the mean of all ζ_{m_i} values are both equal to 0.5.

The parameter m of Equations 14 and 15 is an instance of the parameter m_i that is unspecified with respect to treatment group. The parameters Z and Z_m of Equation 14, Figure 1 and Tables 1 to 3 are instances of the parameters Z_i and Z_{m_i}, respectively, that are unspecified with respect to treatment group. Likewise, the parameters ζ and ζ_m of Equation 15, Figure 1 and Tables 1 to 3 are instances of the parameters ζ_i and ζ_{m_i}, respectively, that are unspecified with respect to treatment group. Similarly, the parameters χ_Z and χ_ζ of Figure 1 and Tables 1 to 3 are instances of the parameters $\chi_{Z_i,h}$ and $\chi_{\zeta_i,h}$, respectively, that are unspecified with respect to either treatment

group or replicate.

The defining parameter of each treatment group i, is the population, m_i, of each replicate, h. With the set of all ζ_i consisting of each integer within 1 to m_i, the m_i values of ζ_{m_i} are identical for each replicate, h, within treatment group i. In contrast, within a given treatment group, i, each replicate, h, exhibits a unique set of m_i values of $\chi_{\zeta_i,h}$ that increase monotonically as either ζ_i or ζ_{m_i} increases, assuming $m_i > 1$. Thus, for $m_i > 1$, the set of m_i values of $CDF(\chi_{\zeta_i,h})$ will increase monotonically as ζ_{m_i} increases. In the limit as m_i approaches infinity, the set of all ζ_{m_i} values and the set of all $CDF(\chi_{\zeta_i,h})$ values should share the same range, according to the hypothesis being tested.

Within replicate h of treatment group i, there are m_i absolute differences, each given by

$$\delta_{i,h} = \left|\zeta_{m_i} - CDF\left(\chi_{\zeta_i,h}\right)\right| = \left|\frac{\zeta_i}{m_i + 1} - CDF\left(\chi_{\zeta_i,h}\right)\right|. \quad (17)$$

For any permissible value of m_i, the range of $\delta_{i,h}$ can be described by $0 \leq \delta_{i,h} < 1$, although for finite values of m_i, $\delta_{i,h}$ would very rarely equal zero.

Within replicate h of treatment group i, the mean of all m_i absolute differences is

$$A_{i,h} = \frac{1}{m_i}\sum_{\zeta=1}^{m_i}\delta_{i,h} = \frac{1}{m_i}\sum_{\zeta=1}^{m_i}\left|\zeta_{m_i} - CDF\left(\chi_{\zeta_i,h}\right)\right| = \frac{1}{m_i}\sum_{\zeta=1}^{m_i}\left|\frac{\zeta_i}{m_i + 1} - CDF\left(\chi_{\zeta_i,h}\right)\right|, \quad (18)$$

and within treatment group i, the mean of all $A_{i,h}$ is

$$A_i = \frac{1}{n_i}\sum_{h=1}^{n_i} A_{i,h}.$$

(19)

As n_i approaches infinity, A_i can be expected to converge toward a value that depends solely on m_i.

At $m_i = 1$, A_i approaches 0.25 as n_i approaches infinity

The values of $\chi_{\zeta_i,h}$ are obtained by placing the values of $\chi_{Z_i,h}$ in ascending order, and as above, it is assumed below that each value of $\chi_{Z_i,h}$ is randomly drawn from a set of real numbers for which the mean, $\mu_{i,h}$, is equal to zero and the standard deviation, $\sigma_{i,h}$, is equal to one (Equation 16). Given that assumption, and given sufficient information about the characteristics of $A_{i,h}$ and $CDF(\chi_{\zeta_i,h})$, the expectation value of A_i can be obtained for the case of n_i approaching infinity and $m_i = 1$.

At $m_i = 1$, ζ_i is restricted to a value of 1, and, by Equation 15, ζ_{m_i} is restricted to a value of 0.5. Furthermore, at $m_i = 1$, there is only one absolute difference per replicate in Equation 18. Thus, $A_{i,h} = |0.5 - CDF(\chi_{\zeta_i,h})|$ for each replicate, h, at $m_i = 1$. At $m_i = 1$, as n_i approaches infinity, the collection of all n_i of the $\chi_{\zeta_i,h}$ values is found to be normally distributed about a mean of $\mu_{i,h} = 0$ with an standard deviation of $\sigma_{i,h} = 1$ over a range that hypothetically includes all real numbers ($-\infty < \chi_{\zeta_i,h} < \infty$), so that the values of $CDF(\chi_{\zeta_i,h})$ become uniformly distributed over a hypothetical range given by $0 < CDF(\chi_{\zeta_i,h}) < 1$, within which the central value of $CDF(0) = 0.5$ is also the mean value. Defining $\delta_{0.5}$ as a real variable with a range given by $0 \leq \delta_{0.5} \leq 0.5$, for any given permissible value of $\delta_{0.5}$, the probability of finding $CDF(\chi_{\zeta_i,h}) = \delta_{0.5}$ is equal to the

probability of finding $CDF(\chi_{\zeta_i,h})$ - 0.5 = $\delta_{0.5}$. Exploiting these characteristics of $\chi_{\zeta_i,h}$, it is shown below that, at $m_i = 1$, A_i approaches 0.25 as n_i approaches infinity.

At $m_i = 1$, as n_i approaches infinity, in one half of all instances, $CDF(\chi_{\zeta_i,h}) \leq 0.5$, while in the other half of all instances, $CDF(\chi_{\zeta_i,h}) \geq 0.5$. Furthermore, as n_i approaches infinity, the mean value of all $CDF(\chi_{\zeta_i,h}) \leq 0.5$ approaches 0.25, while the mean value of all $CDF(\chi_{\zeta_i,h}) \geq 0.5$ approaches 0.75. (See notes following Equation 27.) Thus, as n_i approaches infinity, the mean of $n_i/2$ instances of $|0.5 - CDF(\chi_{\zeta_i,h})|$ will approach $|0.5 - 0.25| = 0.25$, while the mean of the other $n_i/2$ instances of $|0.5 - CDF(\chi_{\zeta_i,h})|$ will approach $|0.5 - 0.75| = 0.25$. Therefore, as n_i approaches infinity, the total value of all n_i instances of $|0.5 - CDF(\chi_{\zeta_i,h})|$ approaches $(0.25n_i/2 + 0.25n_i/2)$, so that the mean of all n_i instances of $|0.5 - CDF(\chi_{\zeta_i,h})|$ will approach $(0.25n_i/2 + 0.25n_i/2)/n_i = 0.25$.

Setting the index i to 1 for the treatment group characterised by a single absolute difference per replicate renders $m_{i=1} = 1$, which, due to $\zeta_{i=1}$ being restricted to 1, makes 0.5 the sole value that $\zeta_{m_{i=1}}$ exhibits. Thus, with $i = 1$, ζ_{m_1} can always be expressed as 0.5, $\chi_{\zeta_{i=1},h}$ can always be expressed as $\chi_{1,h}$, $A_{1,h}$ can always be expressed as $|0.5 - CDF(\chi_{1,h})|$, and in the limit as n_1 approaches infinity,

$$\lim_{n_1\to\infty} A_1 = \lim_{n_1\to\infty} \frac{1}{n_1}\sum_{h=1}^{n_1} A_{1,h} = \lim_{n_1\to\infty} \frac{1}{n_1}\sum_{h=1}^{n_1}\frac{1}{m_1}\sum_{\zeta=1}^{m_1}\left|\zeta_{m_1} - CDF\left(\chi_{\zeta_{i=1},h}\right)\right|$$

$$= \lim_{n_1\to\infty} \frac{1}{n_1}\sum_{h=1}^{n_1}\frac{1}{m_1}\sum_{\zeta=1}^{m_1=1}\left|\frac{\zeta_{i=1}}{m_1+1} - CDF\left(\chi_{\zeta_{i=1},h}\right)\right| = \lim_{n_1\to\infty} \frac{1}{n_1}\sum_{h=1}^{n_1}\left|0.5 - CDF\left(\chi_{1,h}\right)\right|$$

$$= \frac{1}{n_1}\sum_{h=1}^{n_1}\left(\frac{|0.5-0.25| + |0.5-0.75|}{2}\right) = \frac{1}{n_1}n_1\left(\frac{|0.5-0.25| + |0.5-0.75|}{2}\right)$$

$$= \frac{|0.5-0.25| + |0.5-0.75|}{2} = \frac{0.25+0.25}{2} = 0.25,$$

(20)

where, for n_i approaching infinity, |0.5 – 0.25| has been substituted for the mean of |0.5 - $CDF(\chi_{\zeta_i,h})$| in one half of all n_1 instances, and |0.5 – 0.75| has been substituted for the mean of |0.5 - $CDF(\chi_{\zeta_i,h})$| in the other half of all n_1 instances.

As m_i approaches ∞, A_i approaches 0, regardless of whether n_i approaches infinity

At the opposite extreme, it is expected that each value of $A_{i,h}$ approaches zero as m_i approaches infinity. Again, the values of $\chi_{\zeta_i,h}$ are obtained by placing the values of $\chi_{Z_i,h}$ in ascending order, and as above, it is again assumed below that each value of $\chi_{Z_i,h}$ is randomly drawn from a set of real numbers for which the mean, $\mu_{i,h}$, is equal to zero and the standard deviation, $\sigma_{i,h}$, is equal to one (Equation 16).

Letting ∞ represent i for the treatment group in which m_i approaches ∞, the key parameter of Equation 18 is m_∞. As a consequence of m_∞ approaching infinity, the set of all $\chi_{\zeta_\infty,h}$ comes as close as possible to resembling an infinite number of random numbers that are normally

distributed about $\mu = 0$ with $\sigma = 1$ over a range that hypothetically includes all real numbers ($-\infty < \chi_{\zeta_\infty,h} < \infty$), so that the values of $CDF(\chi_{\zeta_\infty,h})$ become uniformly distributed over a hypothetical range given by $0 < CDF(\chi_{\zeta_\infty,h}) < 1$, within which the central value of $CDF(0) = 0.5$ is also the mean value.

As another consequence of m_∞ approaching infinity, the collection of all m_∞ of the ζ_∞ values comes as close as possible to resembling the set of all positive integers, so that, by Equation 15, the set of all ζ_{m_∞} values comes as close as possible to resembling the set of every rational number between zero and one. As such, a value of ζ_{m_∞} can be found that is arbitrarily close to any given value of $CDF(\chi_{\zeta_\infty,h})$, the entire set of which comes as close as possible to resembling the set of all real numbers between 0 and 1. Furthermore, as the values of $\chi_{\zeta_\infty,h}$ are placed in ascending order with respect to ζ_∞, the values of $CDF(\chi_{\zeta_\infty,h})$, like the values of ζ_{m_∞}, also occur in ascending order with respect to ζ_∞. Thus, as m_∞ approaches ∞, ζ_{m_∞} approaches $CDF(\chi_{\zeta_\infty,h})$ at each value of ζ_∞, so that, by Equation 18,

$$A_{\infty,h} = \lim_{m_i \to \infty} A_{i,h} = \lim_{m_i \to \infty} \frac{1}{m_i} \sum_{\zeta=1}^{m_i} \left| \zeta_{m_i} - CDF\left(\chi_{\zeta_i,h}\right) \right| = \frac{1}{m_\infty} \sum_{\zeta=1}^{m_\infty} \left| \zeta_{m_\infty} - CDF\left(\chi_{\zeta_{i=\infty},h}\right) \right|$$

$$= \frac{1}{m_\infty} \sum_{\zeta=1}^{m_\infty} \left| \frac{\zeta_\infty}{m_\infty + 1} - CDF\left(\chi_{\zeta_\infty,h}\right) \right| = \frac{1}{m_\infty} \sum_{\zeta=1}^{m_\infty} 0 = 0.$$

(21)

Applying to this result to Equation 19, even in the absence of replicates, which is to say, where $n_\infty = 1$, $A_\infty = 0$ should be obtained. In the limit as both n_∞ and m_∞ approach infinity, therefore,

$$A_\infty = \lim_{i\to\infty} A_i = \lim_{n_\infty\to\infty} \frac{1}{n_\infty}\sum_{h=1}^{n_\infty} A_{\infty,h} = \lim_{n_\infty\to\infty} \frac{1}{n_\infty}\left(\lim_{m_i\to\infty} A_{i,h}\right)$$

$$= \lim_{n_\infty\to\infty} \frac{1}{n_\infty}\sum_{h=1}^{n_\infty}\left(\lim_{m_i\to\infty} \frac{1}{m_i}\sum_{\zeta=1}^{m_i}\left|\zeta_{m_i} - CDF\left(\chi_{\zeta_i,h}\right)\right|\right)$$

$$= \lim_{n_\infty\to\infty} \frac{1}{n_\infty}\sum_{h=1}^{n_\infty}\frac{1}{m_\infty}\sum_{\zeta=1}^{m_\infty}\left|\zeta_{m_\infty} - CDF\left(\chi_{\zeta_{i=\infty},h}\right)\right|$$

$$= \lim_{n_\infty\to\infty} \frac{1}{n_\infty}\sum_{h=1}^{n_\infty}\frac{1}{m_\infty}\sum_{\zeta=1}^{m_\infty}\left|\frac{\zeta_\infty}{m_\infty+1} - CDF\left(\chi_{\zeta_\infty,h}\right)\right| = \frac{1}{n_\infty}\sum_{h=1}^{n_\infty}\frac{1}{m_\infty}\sum_{\zeta=1}^{m_\infty} 0 = \frac{1}{n_\infty}\sum_{h=1}^{n_\infty} 0 = 0.$$

(22)

For $1 \le m_i$, up until the results become erratic at high values of m_i, it is found that

$$\lim_{n_i\to\infty} A_i = \lim_{n_i\to\infty} \frac{1}{n_i}\sum_{h=1}^{n_i} A_{i,h} = \lim_{n_i\to\infty} \frac{1}{n_i}\sum_{h=1}^{n_i}\frac{1}{m_i}\sum_{\zeta=1}^{m_i}\left|\zeta_{m_i} - CDF\left(\chi_{\zeta_i,h}\right)\right|$$

$$= \lim_{n_i\to\infty} \frac{1}{n_i}\sum_{h=1}^{n_i}\frac{1}{m_i}\sum_{\zeta=1}^{m_i}\left|\frac{\zeta_i}{m_i+1} - CDF\left(\chi_{\zeta_i,h}\right)\right| \ge \frac{\lim_{n_1\to\infty} A_1}{\sqrt{m_i}} = \frac{A_{ref}}{\sqrt{m_i}} = \frac{0.25}{\sqrt{m_i}},$$

(23)

where Equation 20 gives 0.25 exactly for the value of A_1 in the limit as n_1 approaches infinity, and A_{ref} is defined as $\lim_{n_1\to\infty} A_1$. Results that are fairly consistent with Inequality 23 are presented in the supplementary section, **RANDOMNESS AS A FUNCTION OF THE TOTAL POPULATION OF OBSERVATIONS**.

Based on linear regression results for data restricted to $m_i < 15{,}000$, it could be argued that $A_i = A_{ref}(m_i)^{-1/k} + \delta_i$, where $A_{ref} = A_{i=1} = 0.25$, $k = 2$ and δ_i increases from 0 at $m_i = m_1 = 1$ to approximately 0.02364 for $m_i = 3$, beyond which δ_i decreases to approximately 0.00065 at $m_i = 10{,}000$. Accordingly, A_i would be expected to approach $\delta_i < 0.00065$ as m_i approached infinity,

but this expectation is difficult to confirm, as the results are erratic for $m_i > 10{,}000$. Within $10{,}000 < m_i < 3{,}900{,}000$, A_i sometimes violates Inequality 23, and for the most populous treatment groups ($m_i = 3{,}900{,}000$ to $m_i = 39{,}000{,}000$), the values of A_i are not mutually distinguishable with appreciable confidence. An inverse proportionality of n_i to m_i, and a constrained precision of $\chi_{\zeta_i,h}$ in the face of m_i values that literally increase *ad infinitum*, are hypothetical causes of the erratic behaviour of A_i at high m_i. Thus, to more confidently address the functional relationship between A_i and m_i would perhaps require increasing the number of replicates at high m_i values, and increasing the precision of the $\chi_{\zeta_i,h}$ values.

Random noise and the Standard Normal Distribution

As shown in Equation 16, the *CDF* is obtained by integrating the *PDF* with respect to the random variable, χ, that, along with the variables μ, σ and A, the two functions share in common. The Standard Normal Distribution (Figure 2) is equal to the *PDF* in the case of $\mu = 0$, $\sigma = 1$ and $A = 1$, which are the values of μ, σ and A that apply to the *CDF*, either in the form of $CDF(\chi_Z)$ or $CDF(\chi_\zeta)$, shown in Figure 1.

Whether distributed randomly or in ascending order with respect to the *CDF* values, approximately 68.27% of all points are found within $-\sigma < \chi < \sigma$; approximately 95.45% of all points are found within $-2\sigma < \chi < 2\sigma$; and approximately 99.73% of all points are found within $-3\sigma < \chi < 3\sigma$.

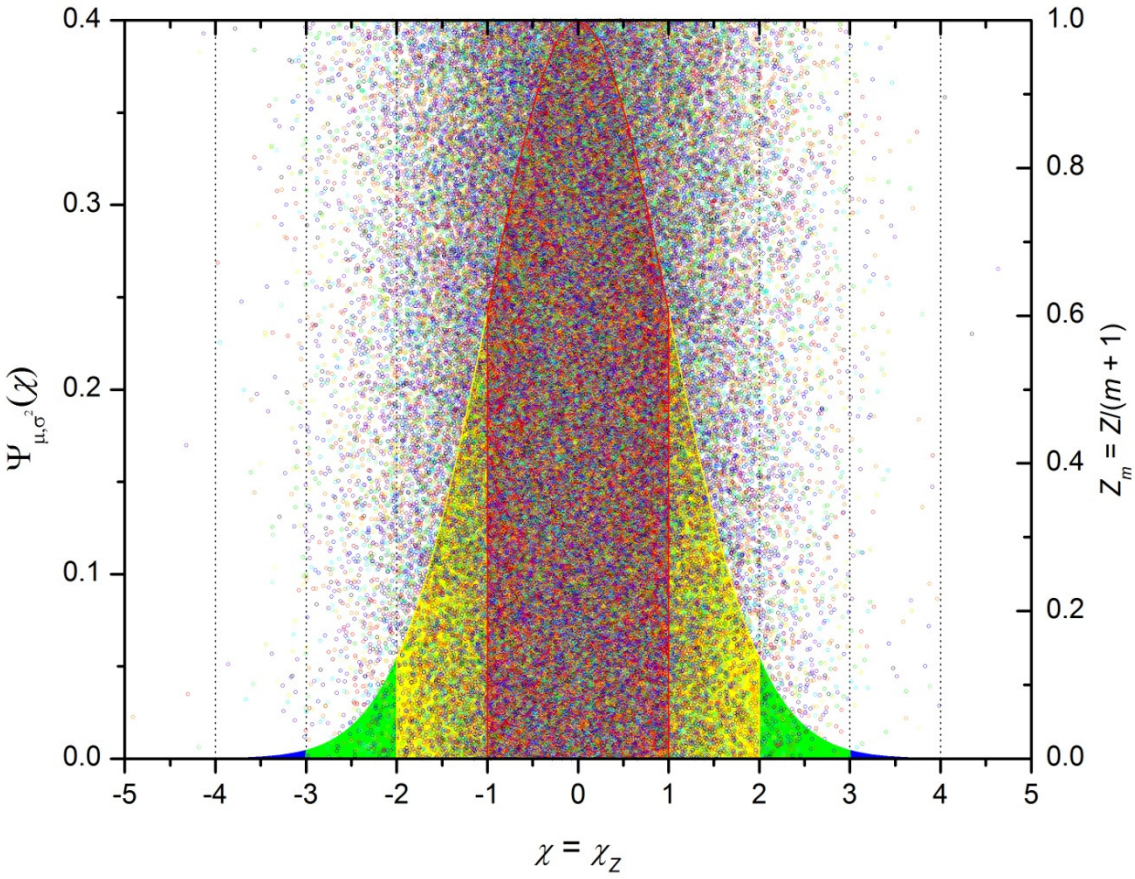

Figure 2. The Standard Normal Distribution (———), a special case of $PDF(\chi) = \Psi_{\mu,\sigma^2}(\chi)$, versus the real, random variable, χ. The normalised index, Z_m (small circles, such as ◦ and ◦, in 24 evenly distributed colours), versus χ is shown superimposed. (Where Z_m is superimposed against a coloured background, symbols of that colour cannot always be seen.)

The Standard Normal Distribution (*SND*) is a special case of the Probability Density Function (*PDF*; Equation 24). With μ (the mean value of χ) equal to 0, σ (the standard deviation of χ about μ) equal to 1 and A (the integral of the *PDF* from $\chi = -\infty$ to $\chi = \infty$; Equation 25) equal to 1, the *PDF* is equal to the *SND*. The probability of finding a randomly chosen, real number within $\chi_{min} < \chi < \chi_{max}$ is given by $p(\chi_{min}, \chi_{max})$, which is the normalised area obtained when the *PDF* is integrated from χ_{min} to χ_{max} (Equation 26). For $\mu = 0$ and $\sigma = 1$, $p(-\sigma, \sigma) \simeq 0.682689$, $p(-2\sigma, 2\sigma) \simeq$

0.954500, $p(-3\sigma, 3\sigma) \simeq 0.997300$, $p(-4\sigma, 4\sigma) \simeq 0.999937$, and $p(-5\sigma, 5\sigma) \simeq 0.999999$. For the *SND* illustrated in this figure, the area shown in red is equal to $p(-\sigma, \sigma)$, the sum of the areas shown in red and yellow is equal to $p(-2\sigma, 2\sigma)$, the sum of the areas shown in red, yellow and green is equal to $p(-3\sigma, 3\sigma)$, the sum of the areas shown in red, yellow, green and blue is equal to $p(-4\sigma, 4\sigma)$, and, although the areas in black are too small to be seen, the sum of the areas in black, red, yellow, green and blue is equal to $p(-5\sigma, 5\sigma)$.

The Probability Density Function (*PDF*), a special case of which, the Standard Normal Distribution (*SND*), is shown in Figure 2, is given by

$$PDF(\chi) = \Psi_{\mu,\sigma^2}(\chi) = \frac{A}{\sqrt{2\pi\sigma^2}}\left\{exp\left(-\left[\frac{\chi-\mu}{\sqrt{2\sigma^2}}\right]^2\right)\right\} = \frac{dCDF(\chi)}{d\chi},$$

(24)

where χ is a random variable that can take on any real value, μ is the mean value of χ, σ is the standard deviation of χ about μ, *CDF* is the Cumulative Distribution Function (Equation 16; Figure 1) and

$$A = \int_{-\infty}^{\infty} \Psi_{\mu,\sigma^2}(\alpha)d\alpha = \lim_{\chi\to\infty} \frac{A}{2}\left\{1 + erf\left(\frac{\chi-\mu}{\sqrt{2\sigma^2}}\right)\right\} = \lim_{\chi\to\infty} CDF(\chi)$$

(25)

is the area obtained when the *PDF* is integrated from $\chi = -\infty$ to $\chi = \infty$.

The probability of finding a randomly chosen, real number within $\chi_{min} < \chi < \chi_{max}$ is given by

$$p(\chi_{min}, \chi_{max}) = \frac{1}{A}\int_{\chi_{min}}^{\chi_{max}} \Psi_{\mu,\sigma^2}(\alpha)d\alpha = \frac{CDF(\chi_{max}) - CDF(\chi_{min})}{A},$$

(26)

which is the normalised area obtained when the *PDF* is integrated from χ_{min} to χ_{max}, with A

(Equation 25) being the normalisation factor. Applied to the *SND* (Figure 2), for which $\mu = 0$ and $\sigma = 1$, Equation 26 yields $p(-\sigma, \sigma) \simeq 0.682689$, $p(-2\sigma, 2\sigma) \simeq 0.954500$, $p(-3\sigma, 3\sigma) \simeq 0.997300$, $p(-4\sigma, 4\sigma) \simeq 0.999937$, and $p(-5\sigma, 5\sigma) \simeq 0.999999$. As $A = 1$ for the *SND*, in Figure 2, the area shown in red is equal to $p(-\sigma, \sigma)$, the sum of the areas shown in red and yellow is equal to $p(-2\sigma, 2\sigma)$, and the sum of the areas shown in red, yellow and green is equal to $p(-3\sigma, 3\sigma)$.

For $n_i \to \infty$, $\mu = 0$, $\sigma = 1$ and $\chi_{min} \leq \chi_{\zeta_i,h} \leq \chi_{max}$, the median and the mean of $CDF(\chi_{\zeta_i,h})$ are equal

It will now be shown that, for n_i approaching infinity, $\mu = 0$, $\sigma = 1$ and $\chi_{min} \leq \chi_{\zeta_i,h} \leq \chi_{max}$, the median and the mean of $CDF(\chi_{\zeta_i,h})$ approach the same value. The relatively general result obtained will be used to support the two previous statements, made with respect to Equation 20, that, for n_i approaching infinity, $\mu = 0$, $\sigma = 1$ and $A = 1$, the mean value of all $CDF(\chi_{\zeta_i,h}) \leq 0.5$ approaches 0.25, while the mean value of all $CDF(\chi_{\zeta_i,h}) \geq 0.5$ approaches 0.75. The specific cases of $CDF(\chi_{\zeta_i,h}) \leq 0.5$ and $CDF(\chi_{\zeta_i,h}) \geq 0.5$ will be explored with the aid of two landmarks, $\chi_{0.25}$ and $\chi_{0.75}$, among the $\chi_{\zeta_i,h}$ values.

For n_i approaching infinity, $\mu = 0$, $\sigma = 1$ and $A = 1$, $CDF(\chi_{\zeta_i,h})$ increases monotonically from just above 0 to just below 1 as $\chi_{\zeta_i,h}$ increases monotonically from just above -∞ to just below ∞, with $\chi_{\zeta_i,h}$ approaching -∞ from above, $\chi_{\zeta_i,h} = 0$ and $\chi_{\zeta_i,h}$ approaching ∞ from below constituting useful landmarks at which $CDF(-\infty) = 0$, $CDF(0) = 0.5$ and $CDF(\infty) = 1$, respectively. Two additional landmarks are now defined within the range of $\chi_{\zeta_i,h}$. Located among $\chi_{\zeta_i,h} \leq 0$, the landmark $\chi_{0.25}$ is defined such that $CDF(\chi_{0.25}) = 0.25$ when $\mu = 0$ and $\sigma = 1$. Located among $\chi_{\zeta_i,h} \geq 0$, the landmark $\chi_{0.75}$ is defined such that $CDF(\chi_{0.75}) = 0.75$ when $\mu = 0$ and $\sigma = 1$. As $SND(\chi_{0.25}) =$

$SND(\chi_{0.75})$, where $SND(\chi_{\zeta_i,h}) = PDF(\chi_{\zeta_i,h})$ in the special case of $\mu = 0$, $\sigma = 1$ and $A = 1$ (Equation 24), it can be seen (Figure 2) that $|\chi_{0.25} - 0| = |\chi_{0.75} - 0|$. Thus, being on opposite sides of zero, $\chi_{0.25} = -\chi_{0.75}$. (Numerically, $\chi_{0.25} \simeq -0.67448975$ and $\chi_{0.75} \simeq 0.67448975$.)

That $p(-\infty, \chi_{0.25}) = p(\chi_{0.25}, 0) = 0.25$ shows that, as n_i approaches infinity, the median value of all $CDF(\chi_{\zeta_i,h}) \leq 0.5$ approaches $CDF(\chi_{0.25}) = 0.25$. (That is, the probability of $\chi_{\zeta_i,h}$ being below $\chi_{0.25}$ is equal to the probability of $\chi_{\zeta_i,h}$ being between $\chi_{0.25}$ and 0.) Similarly, that $p(0, \chi_{0.75}) = p(\chi_{0.75}, \infty) = 0.25$ shows that, as n_i approaches infinity, the median value of all $CDF(\chi_{\zeta_i,h}) \geq 0.5$ approaches $CDF(\chi_{0.75}) = 0.75$. (That is, the probability of $\chi_{\zeta_i,h}$ being between 0 and $\chi_{0.75}$ is equal to the probability of $\chi_{\zeta_i,h}$ being above $\chi_{0.75}$.)

In the case of $\mu = 0$ and $\sigma = 1$, for $\chi_{\zeta_i,h}$ within $\chi_{min} \leq \chi_{\zeta_i,h} \leq \chi_{max}$, the median value of $CDF(\chi_{\zeta_i,h})$ is equal to the mean value of $CDF(\chi_{\zeta_i,h})$, the latter being given by

$$\overline{CDF}(\chi_{min}, \chi_{max}) = \frac{\int_{\chi_{min}}^{\chi_{max}} CDF(\alpha)\Psi_{\mu,\sigma^2}(\alpha)d\alpha}{\int_{\chi_{min}}^{\chi_{max}} \Psi_{\mu,\sigma^2}(\alpha)d\alpha} = \frac{\int_{\chi_{min}}^{\chi_{max}} CDF(\alpha)\Psi_{\mu,\sigma^2}(\alpha)d\alpha}{CDF(\chi_{max}) - CDF(\chi_{min})},$$

(27a)

which, using Equations 24, 25 and 26, can be rewritten as

$$\overline{CDF}(\chi_{min}, \chi_{max}) = \frac{\int_{\chi_{min}}^{\chi_{max}} CDF(\alpha)\mathrm{PDF}(\alpha)d\alpha}{CDF(\chi_{max}) - CDF(\chi_{min})} = \frac{\int_{\chi_{min}}^{\chi_{max}} CDF(\alpha)\frac{dCDF(\alpha)}{d\alpha}d\alpha}{CDF(\chi_{max}) - CDF(\chi_{min})}$$

$$= \frac{\int_{\chi_{min}}^{\chi_{max}} CDF(\alpha)dCDF(\alpha)}{CDF(\chi_{max}) - CDF(\chi_{min})} = \frac{1}{A}\frac{\int_{\chi_{min}}^{\chi_{max}} CDF(\alpha)dCDF(\alpha)}{p(\chi_{min}, \chi_{max})}.$$

(27b)

If χ_m is defined such that, in the case of $\mu = 0$ and $\sigma = 1$, $CDF(\chi_m) = \overline{CDF}(\chi_{min}, \chi_{max})$, then χ_m is the value of $\chi_{\zeta_i,h}$ at which $p(\chi_{min}, \chi_m) = p(\chi_m, \chi_{max})$, so that, as n_i approaches infinity, the median

value of all $CDF(\chi_{\zeta_i,h})$ within $CDF(\chi_{min}) \leq CDF(\chi_{\zeta_i,h}) \leq CDF(\chi_{max})$ approaches $CDF(\chi_m)$. (That is, the probability of $\chi_{\zeta_i,h}$ being between $\chi_{\min}$ and χ_m is equal to the probability of $\chi_{\zeta_i,h}$ being between χ_m and $\chi_{\max}$.)

In general, then, within $CDF(\chi_{min}) \leq CDF(\chi_{\zeta_i,h}) \leq CDF(\chi_{max})$, as n_i approaches infinity, the mean value of all $CDF(\chi_{\zeta_i,h})$ approaches the median value of all $CDF(\chi_{\zeta_i,h})$. Specifically, as n_i approaches infinity, within $\chi_{\zeta_i,h} \leq 0$, $CDF(\chi_{0.25}) = \overline{CDF}(-\infty, 0) = 0.25$ when $\mu = 0$ and $\sigma = 1$, $A = 1$. Likewise, as n_i approaches infinity, within $\chi_{\zeta_i,h} \geq 0$, $CDF(\chi_{0.75}) = \overline{CDF}(0, \infty) = 0.75$ when $\mu = 0$, $\sigma = 1$ and $A = 1$.

Some other consequences of $\chi_{\zeta_i,h}$, and $CDF(\chi_{\zeta_i,h})$ being distributed differently

Some other noteworthy consequences result from $\chi_{\zeta_i,h}$, and $CDF(\chi_{\zeta_i,h})$ being distributed differently. As n_i approaches infinity, the collection of all $\chi_{\zeta_i,h}$, values becomes normally distributed but the collection of all $CDF(\chi_{\zeta_i,h})$ values becomes uniformly distributed, as a result of which, for $CDF(\chi_b) - CDF(\chi_a) = CDF(\chi_d) - CDF(\chi_c) > 0$, the number of $\chi_{\zeta_i,h}$ values within $\chi_a \leq \chi_{\zeta_i,h} \leq \chi_b$ will be equal to the number of $\chi_{\zeta_i,h}$ values within $\chi_c \leq \chi_{\zeta_i,h} \leq \chi_d$, provided that m_i is sufficiently large to ensure there being many intervening $\chi_{\zeta_i,h}$ values between the extrema of the two intervals, χ_a to χ_b and χ_c to χ_d. For $CDF(\chi_b) - CDF(\chi_a) = CDF(\chi_d) - CDF(\chi_c) > 0$, with $\chi_d > \chi_c > \chi_b > \chi_a$, and with m_i approaching infinity, $\chi_b - \chi_a$ would only be found to equal $\chi_d - \chi_c$ in the special case of $(\chi_c - \mu) = (\mu - \chi_b)$, however.

Data that formed the basis of $GRN_{i,h}(r,t)$

The signal to be simulated is that which would be collected in an AUC experiment using the RI detection system. The *GRN* of the simulations was based on the characteristics of three sets of real AUC data collected at 3,000 RPM using the RI-detection system to scan the open spaces, visible below $r = 5.85$ cm and above $r = 7.15$ cm, of a radial-calibration centrepiece properly placed and aligned in position 8 of an 8-hole rotor. The selected scans were obtained under conditions of the closest discernible approach to thermal stability and the closest discernible approach to vacuum. For each scan, the rotor temperature recorded, being 20.00°C, was that which the instrument was set to maintain. (The temperature recorded during these scans is treated as being identical the simulation temperature, even though the latter, denoted as 20.00°C on the Celsius scale, is written with one more significant figure, which is done to avoid rounding when converting from or to 293.15 K on the absolute temperature scale.) No blank subtraction was applied to any of the scans. (This method describes the initial portion of an AUC velocity experiment. For a somewhat general method that applies to an AUC velocity experiment in its entirety, see **IMAGINARY EXPERIMENTAL PROTOCOL**.)

As applied to these scans, for which the nominal wavelength of the laser light source was 675 nm, the settings of the RI-detection system included an alignment angle of 0.00°, a laser delay of 248.50°, a laser duration of 0.40°, a laser gain (contrast) of 10, a laser offset (brightness) of 127, a vertical scaling factor of 21.75 points (pixel rows) per fringe, an inside radius of $r_{1st} = 5.7500$ cm and an outside radius of $r_{last} = 7.2140$ cm. The latter two parameters are used to calculate the horizontal scaling factor.

The vertical and horizontal scaling factors apply to the images to be recorded. For each such

image, horizontally oriented points (as pixel columns) can be considered those that are parallel to the radial axis, while vertically oriented points (as pixel rows) can be considered those that are perpendicular to the radial axis and perpendicular to the light path through the open spaces of the radial-calibration centrepiece. For the vertical scaling factor, 21.75 points (pixel rows) per fringe is the default setting. The horizontal scaling factor is equal to $(r_{last} - r_{1st})/(p_{last} - p_{1st})$, where p_{1st} is the first point (pixel column 1, by definition) of the image, p_{last} is the last point (pixel column 2022, in this case) of the image, r_{1st} is the inside radius that is assigned to p_{1st}, and r_{last} is the outside radius that is assigned to p_{last}. The default setting of the inside radius is $r_{1st} = 5.7500$ cm, and the default setting of the outside radius is $r_{last} = 7.2140$ cm. Using these default settings of r_{1st} and r_{last}, for $p_{1st} = 1$ pixel and $p_{last} = 2022$ pixel, a horizontal scaling factor of $(r_{last} - r_{1st})/(p_{last} - p_{1st}) \cong 7.2439\text{E-}4$ cm/pixel would be obtained. (As the actual value of r_{last} was 7.2145 cm, with r_{1st} equal to its expected value of 5.7500 cm, a horizontal scaling factor of approximately 7.2464E-4 cm/pixel was obtained instead.)

When directed through the open spaces of a radial-calibration centrepiece, the light from the RI detection system is unobstructed by any parts of the rotor or any components placed in the rotor. Except near their edges, which can give rise to optical artefacts, such open spaces should yield data that are dominated by *GRN* to the greatest possible extent, as the least systematic noise possible should be found where the fewest components lie in the optical path of the detection system.

Edited data sets were obtained by deleting any data that did not correspond with an open space. There being two open spaces per scan, each scan yielded one data set for the upper opening of the radial-calibration centrepiece, and another data set for the lower opening of the radial-

calibration centrepiece. Such once-edited data did not exclude optical artefacts from the edges of the openings. The once-edited data sets did exclude the first pixel column (r=5.7500 cm) of each scan, however, as its value was always found to be zero, and thus recorded neither signal nor noise. As such, the lower-most once-edited data set of each scan extended from pixel column 2 (r =5.7507 cm) to pixel column 139 (r=5.8500 cm), while the upper-most once-edited data set of each scan extended from pixel column 1933 (r=7.1500 cm) to pixel column 2022 (r=7.2145 cm).

From each once-edited data set, a further edited data set was obtained by deleting any data that looked to be affected by optical artefacts from the edges of the open spaces of the radial-calibration centrepiece. Only the two edges used to set the inner and outer radial calibration points, r_{inner} = 5.8500 cm and r_{outer} = 7.1500 cm, respectively, were within the range of the data. As such, the lower-most twice-edited data set of each scan extended from pixel column 2 (5.7507 cm) to pixel column 133 (5.8471 cm), while the upper-most twice-edited data set of each scan extended from pixel column 1949 (7.1616 cm) to pixel column 2022 (7.2145 cm). Only the twice-edited data were subjected to analysis, which followed the procedures described next.

To normalise the twice-edited data sets to a common mean of zero, within each such edited data set, the mean fringe displacement was subtracted from the individual fringe displacements (Figure 3). The so-normalised, twice-edited data sets were then combined, placed in ascending order and defined as the independent variable, χ_Z, against which, as in Figure 1, was plotted a dependent variable, ζ_m (Equation 15), for which m = 630 was the total number of χ_Z values. (Both χ_Z and ζ_m are indexed by Z, which takes on each integral value from 1 to m. As Z ranges from its lowest to highest value, so do χ_Z and ζ_m.) For the combined set of m = 630 χ_Z values, the

mean,

$$\mu_{\chi_z} = \frac{1}{m}\sum_{Z=1}^{m} \chi_Z,$$

(28)

and the standard deviation,

$$\sigma_{\chi_z} = \left\{\frac{1}{m-1}\left[\sum_{Z=1}^{m}\left(\chi_Z - \mu_{\chi Z}\right)^2\right]\right\}^{0.5},$$

(29)

were $\mu_{\chi_z} = 0$ fringe and $\sigma_{\chi_z} = 8.80480\text{E-}3$ fringe, respectively. The normalisation procedure ensured that μ_{χ_z} would equal zero.

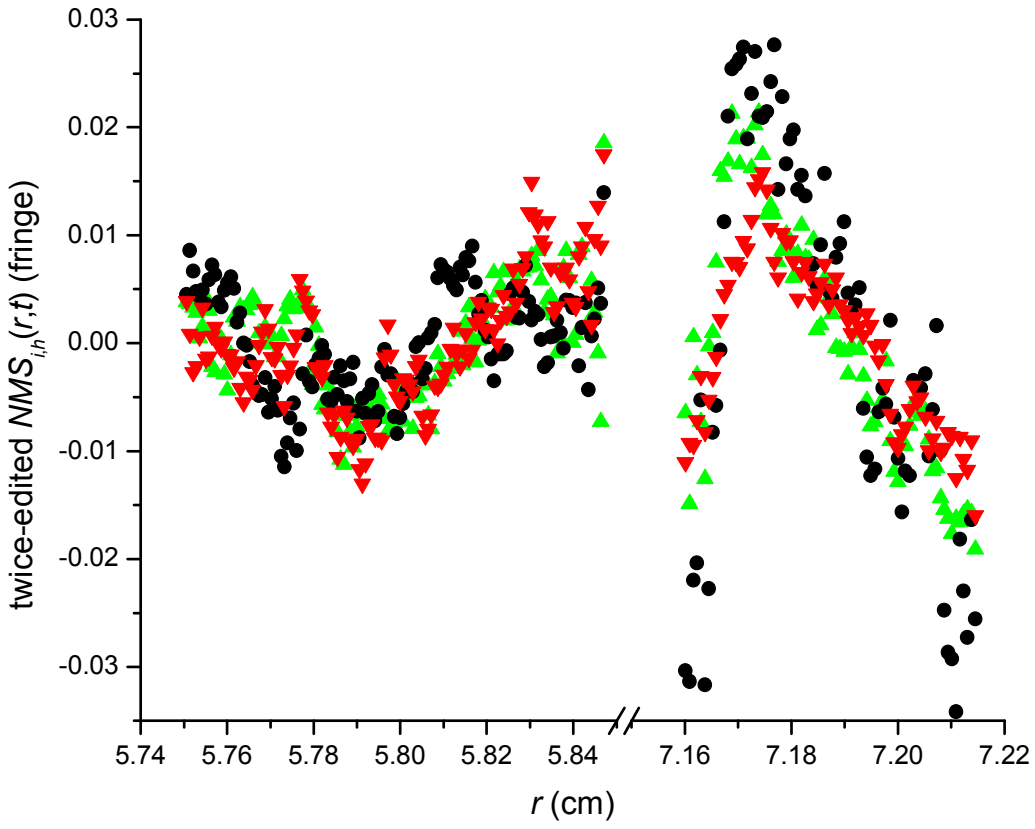

Figure 3. The twice-edited, normalised data sets, from scans $NMS_{i,h}(r,t_{2682\text{ s}})$ (▲),$NMS_{i,h}(r,t_{3182\text{ s}})$

(●) and $NMS_{i,h}(r;t_{3388\,s})$ (▼), versus r, where h and i can each be assigned the value 0 to denote the calibration centrepiece as replicate $h = 0$ of treatment group $i = 0$, and where $t_{2682\,s} = 2{,}682$ s, $t_{3182\,s} = 3{,}182$ s and $t_{3388\,s} = 3{,}388$ s. All of the data lie within the open holes of the calibration centrepiece. Thus, while systematic trends are evident, these data are assumed to exhibit the least systematic noise possible.

Data were fit via the nonlinear least-squares fitting (NLSF) utility of Origin 6.0. As a function of the presumed-to-be random variable, χ_Z, the dimensionless normalised index, ζ_m, was readily fit to the Cumulative Distribution Function, $CDF(\chi_Z)$ (Equation 16), to obtain, with A held fixed at 1 and μ held fixed at 0, $\sigma = (7.55901 \pm 0.01920)$E-3 fringe, a correlation coefficient of $R^2 = 0.99856$, and a reduced chi-squared statistic of $\chi^2/DoF = 1.2$E-4, where DoF, the degrees of freedom, should be 1 less than m - n_{param}, for which the number of fitted parameters is n_{param}. For the $CDF(\chi_Z)$, when only fitting σ, n_{param} is equal to just 1. In tests with several sets of χ_Z versus ζ_m data in which the NLSF was used to fit ζ_m as $CDF(\chi_Z)$, it was found that χ^2/DoF was indistinguishable from the sum of the squares of error (A.K.A. the mean square error),

$$e_{MS} = \frac{1}{m-1}\sum_{Z=1}^{m}[Z_m - CDF(\chi_Z)]^2, \tag{30}$$

for values of m ranging from 630 to 100,000. With respect to the data just discussed, which yielded $\chi^2/DoF = 1.2$E-4 for ζ_m fit as $CDF(\chi_Z)$, $e_{MS} = 1.20206$E-4 was obtained.

Denoting μ and σ from the NLSF as μ_{NLSF} and σ_{NLSF}, respectively, μ_{χ_z} can be equated to μ_{NLSF} exactly, while $\Delta\sigma\% = (100\%)\left|\sigma_{\chi_z} - \sigma_{NLSF}\right|/\sigma_{\chi_z} = 14.15\%$. The equivalence of μ_{χ_z} and μ_{NLSF} is due to both having been set equal to zero. The extent by which $\Delta\sigma\%$ exceeds zero can be considered a

measure of the extent to which χ_Z diverges from a normal distribution. Both visually (Figure 4) and statistically (given R^2 and χ^2/DoF), however, the fact that ζ_m (Equation 15)appears to be normally distributed with respect to χ_Z can be taken as evidence that χ_Z is normally distributed.

With $\sigma_{\chi_z} = 8.80480\text{E-}3$ fringe being slightly larger than $\sigma_{NLSF} = (7.55901 \pm 0.01920)\text{E-}3$ fringe, the former was used as the more liberal starting point to estimate σ_{RI}, the standard deviation used to scale the random noise. The standard deviation of the χ_Z values of the twice-edited data was rounded up from 8.80480E-3 fringe to 0.00900 fringe, which was multiplied by 3/2 to obtain 0.01350 fringe, which, in turn, was rounded up to obtain $\sigma_{RI} = 0.01400$ fringe.

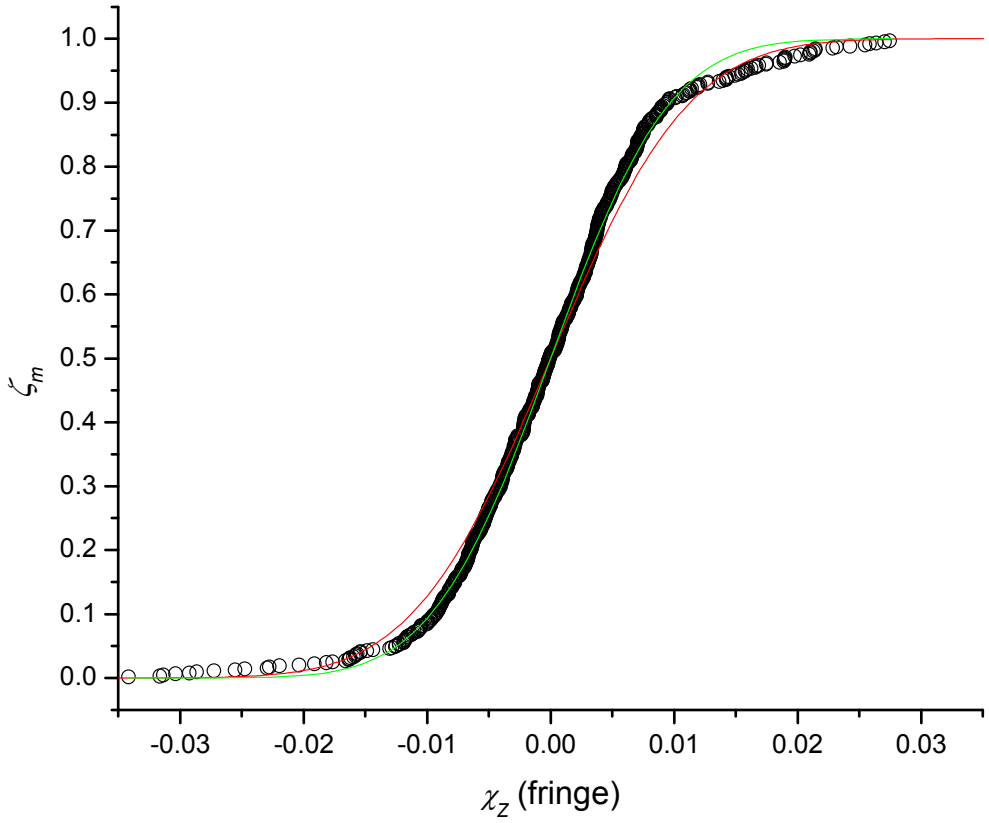

Figure 4. The dimensionless normalised index, ζ_m (○), versus the combined, twice-edited, normalised data sets, χ_Z. With A held fixed at 1 and μ held fixed at 0, ζ_m, was fit (——)to the

Cumulative Distribution Function, $CDF(\chi_Z)$ to obtain $R^2 = 0.99856$ and $\chi^2/DoF = 0.00012$ and $\sigma = \sigma_{NLSF} = (7.55901 \pm 0.01920)$E-3 fringe. Also shown is $CDF(\chi_Z)$ with $A = 1$, $\mu = 0$, and $\sigma = \sigma_{\chi_Z} =$ 8.80480E-3 fringe (——).

Construction of $GRN_{i,h}(r,t)$ data

The characteristics given the $GRN_{i,h}(r,t)$ data were based on the characteristics observed in representative noise from real AUC data collected with the RI detection system (*Data that formed the basis of $GRN_{i,h}(r,t)$*). The data shown in Figure 1 provided the raw material from which the $GRN_{i,h}(r,t)$ data were constructed. With respect to either its integral index, Z, or its normalised index, ζ_m (Equation 15), the dimensionless random variable, χ_Z, of Figure 1 is normally distributed with a standard deviation of $\sigma = 1$ about a mean value of $\mu = 0$.

As described in more detail later (*Simulation of $GRN_{i,h}(r,t)$*; Equation 42; Tables 14a and 14b), the 98,588 data points shown in Figure 1 were split into 49 groups, each comprised of 2,012 χ_Z values that, consecutively from 1st to 2,012th, were kept in the same order as that in which they occur with respect to Z in the original set of 98,588 values. Two adjustments were made to each group of 2,012 χ_Z values. In the first adjustment, the mean of each group of 2,012 χ_Z values was subtracted from each individual value of that group to obtain 2,012 normalised χ_Z values for which the mean was as close to zero as error allowed, and the standard deviation was approximately 1. In the second adjustment, each normalised χ_Z value of each group was multiplied by σ_{RI} to obtain a group of 2,012 δY_Z values with a standard deviation approximately equal to 0.01400 fringe, which is the sought after value for the standard deviation of the random noise. The collection of all such δY_Z values comprises the random fringe displacements shown in

Figure 5 versus $Z/2{,}012$. Each set of $GRN_{i,h}(r,t)$ was equated to a consecutive set of values within a single group of 2,012 δY_Z values, such that, with the radial positions and the random fringe displacements sharing a common index, $GRN_{i,h}(r_Z,t) = \delta Y_Z$, where $r_{Z\text{-}1} < r_Z < r_{Z+1}$ holds for all r_Z within the radial extrema.

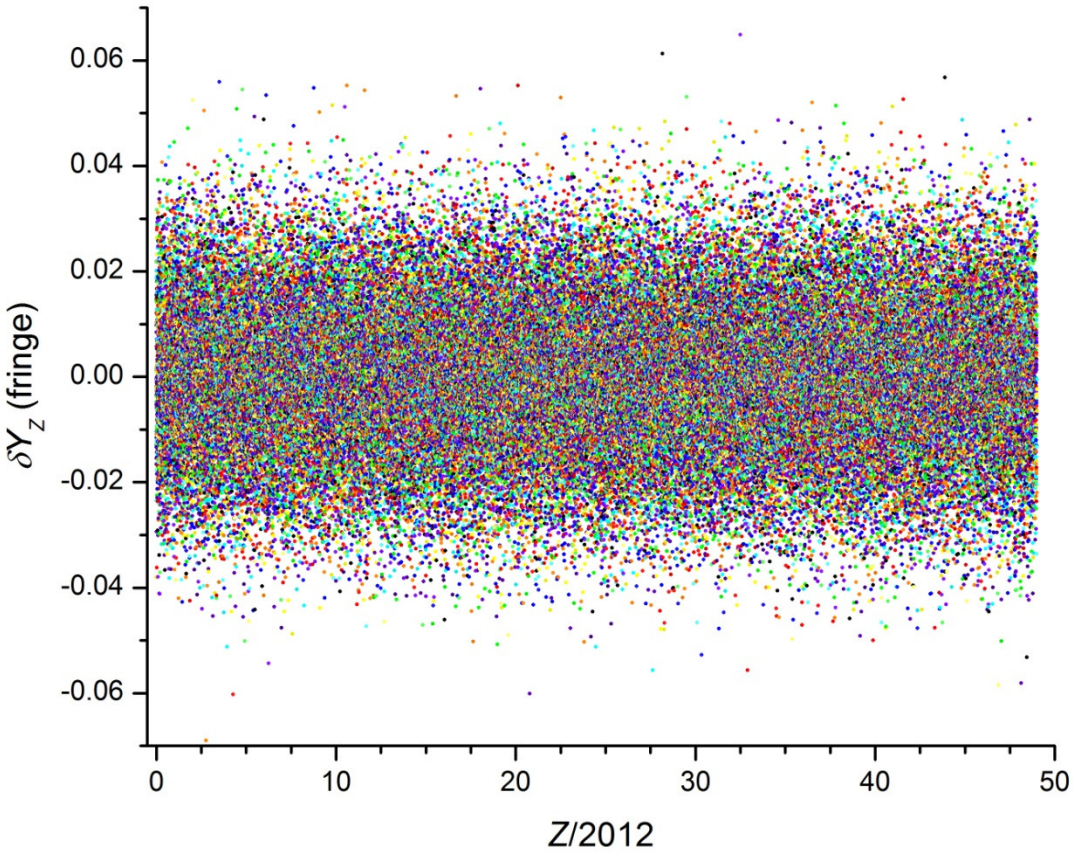

Figure 5. Simulated *GRN*, presented as the combined 49 groups of δY_Z values versus $Z/2{,}012$. Within each group of 2,012 values, the mean value and standard deviation of δY_Z are $\mu_{RI} = 0$ and $\sigma_{RI} = 0.01400$ fringe, respectively. To obtain the δY_Z values of this figure, first, the data shown in Figure 1 were, with no change in order relative to Z, split into 49 groups of 2,012 χ_Z values each. Within each group, the mean χ_Z-value was then subtracted from each individual χ_Z value, and

each resulting difference was multiplied by $\sigma_{RI} = 0.01400$ fringe to obtain a random fringe displacement, δY_Z. The division of Z by 2,012 scales the abscissa to the population of each group. As such, the δY_Z values are effectively plotted by group. Although the δY_Z values of each group bear a slightly different proportionality to the χ_Z values shown in Figure 1, the axes of Figure 5 can be viewed as the rescaled and exchanged axes of Figure 1.

TIN

Simulation of $TIN_{i,h}(r)$

Each system was simulated in terms of the gravitational-potential-space parameter, $\xi = r^2/2$, where r is the radial position in the centrifuge (Moody, 2011). For the purpose of data output, however, spatial data were saved in terms of radial position, $r = (2\xi)^{0.5}$. In terms of the radial position, $r = r_m = 6$ cm was chosen for the meniscus position that corresponds to the lower system boundary, and $r = r_b = 7.2$ cm was chosen for the base position that corresponds to the upper system boundary. (The lower and upper system boundaries are, respectively, identical to the innermost and outermost radial extrema of the system.) Starting from a time at which there are no concentration gradients, and proceeding at judiciously determined time intervals, concentration data for each system were repeatedly calculated at $N = 900$ spatial elements along the radial axis between the meniscus and the base of the system. In terms of ξ, the spatial increment, $\Delta\xi$, was the same ($\Delta\xi = 8.8\text{E-}3$ cm^2) for every pair of adjacent spatial elements. The N spatial elements are indexed by j, and in terms of ξ, each is given by

$$\xi_j = \xi_m + (j - 0.5)\Delta\xi, \tag{31}$$

where $1 \leq j \leq N$, and $\xi_m = r_m^2/2$ is the gravitational-potential-spatial position of the meniscus. With the gravitational-potential-spatial position of the base given by $\xi_b = r_b^2/2$, $\xi_m < \xi_j < \xi_b$ for any permitted value of j.

As the radial position is given by

$$r_j = \sqrt{2\xi_j} = \sqrt{2[\xi_m + (j - 0.5)\Delta\xi]},$$

(32)

and as $\Delta\xi = [\xi_{j+1} - \xi_{j-1}]/2$ is constant with j, the average distance between adjacent radial positions, $\Delta r_j = [(2\xi_{j+1})^{0.5} - (2\xi_{j-1})^{0.5}]/2$, decreases as j increases. (See Equation 113 and its accompanying discussion.) For the systems under study here, Δr_j ranges from $\Delta r_1 \cong 1.46631\text{E-}3$ cm to $\Delta r_{N=900} \cong 1.22243\text{E-}3$ cm.

The *TIN* was generated using combinations of logarithmic and cosine functions to which some common mathematical operations were applied. The initial function used to generate the *TIN* is

$$\varphi_q(x_j) = \alpha_{1,q}\left[ln\left(\alpha_{2,q} + \alpha_{3,q}cos\left(\frac{x_j}{\alpha_{4,q}}\right)\right)\right] + \sum_{\epsilon=1}^{3}\beta_{1,q,\epsilon}\left[cos\left(\frac{\pi}{\beta_{2,q,\epsilon}} + \frac{x_j}{\beta_{3,q,\epsilon}}\right)\right]^{\beta_{4,q,\epsilon}},$$

(33)

in which

$$x_j = N\left(\frac{j + \Delta j - 1}{x_{max} - 1}\right),$$

(34)

where x_{max} and Δj are positive integers. As applied here, $\Delta j = 500$ and $x_{max} = 2{,}012$. The index q applies to $\varphi_q(x_j)$, 7 variations of which were used as the basis of the *TIN*. Among the parameters of $\varphi_q(x_j)$, there is 1 set indexed by q, and 21 subsets that are indexed by q and u. The parameters

indexed by q alone, $\alpha_{1,q}$, $\alpha_{2,q}$, $\alpha_{3,q}$ and $\alpha_{4,q}$, are listed in Table 4a. The parameters indexed by both q and u, $\beta_{1,q,u}$, $\beta_{2,q,u}$ and $\beta_{3,q,u}$, are shown in Table 4b.

See Equations 33 and 34.				
	$\alpha_{1,q}\left[ln\left(\alpha_{2,q}+\alpha_{3,q}cos\left(\frac{x_j}{\alpha_{4,q}}\right)\right)\right]$			
q	$\alpha_{1,q}$	$\alpha_{2,q}$	$\alpha_{3,q}$	$\alpha_{4,q}$
1	-1	5.0	-0.3	220
2	1	4.0	0.9	200
3	1	6.0	-1.3	210
4	-1	7.0	1.6	230
5	1	8.0	-4.1	190
6	-1	3.8	-3.2	198
7	-1	8.7	2.5	215

Table 4a. Values chosen for parameters $\alpha_{1,q}$, $\alpha_{2,q}$, $\alpha_{3,q}$ and $\alpha_{4,q}$ of Equation 33.

See Equations 33 and 34.												
	$\beta_{1,q,u}\left[cos\left(\frac{\pi}{\beta_{2,q,u}}+\frac{x_j}{\beta_{3,q,u}}\right)\right]^{\beta_{4,q,u}}$											
	$u=2$				$u=2$				$u=3$			
q	$\beta_{1,q,u}$	$\beta_{2,q,u}$	$\beta_{3,q,u}$	$\beta_{4,q,u}$	$\beta_{1,q,u}$	$\beta_{2,q,u}$	$\beta_{3,q,u}$	$\beta_{4,q,u}$	$\beta_{1,q,u}$	$\beta_{2,q,u}$	$\beta_{3,q,u}$	$\beta_{4,q,u}$
1	0.12	1	190	1	0.020	1.6	110	1	0.013	2.1	50	2
2	0.10	1	200	1	0.025	2.0	100	1	0.010	2.0	60	2
3	0.16	1	217	1	-0.045	1.8	128	1	0.031	1.8	39	2
4	-0.27	1	232	1	0.081	1.5	84	1	-0.022	2.1	45	2
5	-0.16	1	221	1	-0.066	2.1	117	1	0.026	1.5	53	2
6	0.21	1	-208	1	0.072	2.3	-107	1	-0.018	1.3	-66	2
7	-0.33	1	-212	1	-0.037	1.3	-93	1	-0.029	2.3	-70	2

Table 4b. Values chosen for parameters $\beta_{1,q,u}$, $\beta_{2,q,u}$, $\beta_{3,q,u}$ and $\beta_{4,q,u}$ of Equation 33, where $u=1$, $u=2$ or $u=3$.

Subjecting each instance of Equation 33 to various operations involving exponentiation, multiplication and addition yields

$$A_q(x_j) = \gamma_{1,q} + \gamma_{2,q}\left[\sum_{p=1}^{7} \gamma_{3,q,p}\left[\varphi_q(x_j)\right]^{\gamma_{4,q,p}}\right].$$

(35)

The index q applies to $A_q(x_j)$, 7 variations of which were carried forward to generate the *TIN*. Among the parameters of $A_q(x_j)$, there is 1 set indexed by q, and 49 subsets that are indexed by q and p. The parameters indexed by q alone, $\gamma_{1,q}$ and $\gamma_{2,q}$, are listed in Table 5a. The parameters indexed by both q and p, $\gamma_{3,q,p}$ and $\gamma_{3,q,p}$, are shown in Table 5b.

See Equation 35.		
q	$\gamma_{1,q}$	$\gamma_{2,q}$
1	-29	-0.05
2	17	0.09
3	-11	0.06
4	6	-0.04
5	-15	0.36
6	32	-0.13
7	-5	-0.07

Table 5a. Values chosen for parameters $\gamma_{1,q}$ and $\gamma_{2,q}$ of Equation 35.

See Equation 35.														
	$p = 1$		$p = 2$		$p = 3$		$p = 4$		$p = 5$		$p = 6$		$p = 7$	
q	$\gamma_{3,q,p}$	$\gamma_{4,q,p}$	$\gamma_{3,q,p}$	$\gamma_{4,q,p}$	$\gamma_{3,q,p}$	$\gamma_{4,q,p}$	$\gamma_{3,q,p}$	$\gamma_{4,q,p}$	$\gamma_{3,q,p}$	$\gamma_{4,q,p}$	$\gamma_{3,q,p}$	$\gamma_{4,q,p}$	$\gamma_{3,q,p}$	$\gamma_{4,q,p}$

1	2	-1	-8	-2	-5	-1	5	-2	-1	-1	-7	2	6	1
2	7	-2	-8	-1	-1	-2	-5	-1	2	-2	3	1	7	2
3	-5	-2	5	-2	-3	-2	-9	-2	-9	-1	-5	1	1	2
4	8	-2	-1	-1	1	-2	-2	-1	-5	-1	7	2	-4	2
5	-4	-2	7	-1	2	-1	-1	-2	-7	-2	2	1	-2	1
6	-6	-2	5	-2	9	-1	8	-1	4	-2	4	2	-9	1
7	2	-1	-3	-1	-4	-2	6	-2	-3	-2	-9	2	5	1

Table 5b. Values chosen for parameters $\gamma_{3,q,p}$ and $\gamma_{4,q,p}$ of Equation 35.

Pairs of results from $A_q(x_j)$ were combined to obtain $B_q(x_j)$ (Table 6), pairs of results from $B_q(x_j)$ were combined to obtain $C_q(x_j)$ (Table 7), pairs of results from $C_q(x_j)$ were combined to obtain $D_q(x_j)$ (Table 8), and pairs of results from $D_q(x_j)$ were combined to obtain $E_q(x_j)$ (Table 9).

Equation 36

$$B_q(x_j) = \left[0.4A_q(x_j) + 0.6A_{p\neq q}(x_j)\right]\kappa_{B_q} + \lambda_{B_q}$$

q	p	κ_{B_q}	λ_{B_q}
1	2	5.00	22
2	3	3.00	-22
3	4	2.60	0
4	5	1.25	0
5	6	0.90	0
6	7	1.60	-46
7	1	0.90	7

Table 6. Values chosen for parameters κ_{B_q} and λ_{B_q} of Equation 36, for which $p = q + 1$ if $(q + 1) \leq 7$, and $p = (q - 7) + 1$ if $(q + 1) > 7$, were the rules used to select the ordered pairs of indices p and q. For $A_q(x_j)$ and $A_{p\neq q}(x_j)$, see Equation 35 and Table 5.

Equation 37			
$C_q(x_j) = [0.4B_q(x_j) + 0.6B_{p\neq q}(x_j)]\kappa_{C_q} + \lambda_{C_q}$			
q	p	κ_{C_q}	λ_{C_q}
1	3	2.2	-5
2	4	3.0	10
3	5	1.3	0
4	6	5.5	150
5	7	3.0	0
6	1	1.0	0
7	2	1.0	-22

Table 7. Values chosen for parameters κ_{C_q} and λ_{C_q} of Equation 37, for which $p = q + 2$ if $(q + 2) \leq 7$, and $p = (q - 7) + 2$ if $(q + 2) > 7$, were the rules used to select the ordered pairs of indices p and q. For $B_q(x_j)$ and $B_{p\neq q}(x_j)$, see Equation 36 and Table 6.

Equation 38			
$D_q(x_j) = [0.4C_q(x_j) + 0.6C_{p\neq q}(x_j)]\kappa_{D_q} + \lambda_{D_q}$			
q	p	κ_{D_q}	λ_{D_q}
1	5	1.2	27
2	6	1.0	0
3	7	2.6	16
4	1	1.4	-11
5	2	2.5	37
6	3	3.5	-55
7	4	1.2	-7

Table 8. Values chosen for parameters κ_{D_q} and λ_{D_q} of Equation 38, for which $p = q + 4$ if $(q + 4) \leq 7$, and $p = (q - 7) + 4$ if $(q + 4) > 7$, were the rules used to select the ordered pairs of indices p

and q. For $C_q(x_j)$ and $C_{p\neq q}(x_j)$, see Equation 37 and Table 7.

Equation 39

$$E_q(x_j) = \left[0.4D_q(x_j) + 0.6D_{p\neq q}(x_j)\right]\kappa_{E_q} + \lambda_{E_q}$$

q	p	κ_{E_q}	λ_{E_q}
1	7	1.0	-7
2	1	1.2	0
3	2	1.3	0
4	3	1.0	0
5	4	1.0	0
6	5	1.5	10
7	6	1.3	0

Table 9. Values chosen for parameters κ_{E_q} and λ_{E_q} of Equation 39, for which $p = q + 6$ if $(q + 6) \leq 7$, and $p = (q - 7) + 6$ if $(q + 6) > 7$, were the rules used to select the ordered pairs of indices p and q. For $D_q(x_j)$ and $D_{p\neq q}(x_j)$, see Equation 38 and Table 8.

Combinations of results from $A_q(x_j)$ (Table 5), $B_q(x_j)$ (Table 6), $C_q(x_j)$ (Table 7), $D_q(x_j)$ (Table 8), and $E_q(x_j)$ (Table 9) were used to obtain $F_q(x_j)$ (Table 10), and pairs of results from $F_q(x_j)$ were combined to obtain $G_q(x_j)$ (Table 11).

Equation 40

$$F_q(x_j) = \left[A_q(x_j) + B_r(x_j) + C_s(x_j) + D_t(x_j) + E_u(x_j)\right]\kappa_{F_q} + \lambda_{F_q}$$

q	r	s	t	u	κ_{F_q}	λ_{F_q}
1	2	3	4	5	0.3	30
2	3	4	5	6	0.4	–3
3	4	5	6	7	0.6	10

4	5	6	7	1	0.7	−20
5	6	7	1	2	0.4	−10
6	7	1	2	3	0.5	0
7	1	2	3	4	0.3	0

Table 10. Values chosen for parameters κ_{F_q} and λ_{F_q} of Equation 40, in which the ordered quintuples of indices *q*, *r*, *s*, *t* and *u* are selected so that no index value is repeated in any given ordered quintuple, and each of the 7 possible index values appears 5 times among all ordered quintuples. For $A_q(x_j)$, $B_r(x_j)$, $C_s(x_j)$, $D_t(x_j)$ and $E_u(x_j)$, see Equations 35 to 39 and Tables 5 to 9, respectively.

Equation 41

$$G_q(x_j) = \left[\frac{F_q(x_j) + F_{p\neq q}(x_j)}{2}\right] + \lambda_{G_q}$$

q	p	λ_{G_q}
1	5	-14
2	6	16
3	7	0
4	1	3
5	2	0
6	3	-7
7	4	-40

Table 11. Values chosen for parameter λ_{G_q} Equation 41, for which $p = q + 4$ if $(q + 4) \leq 7$, and $p = (q - 7) + 4$ if $(q + 4) > 7$, were the rules used to select the ordered pairs of indices *p* and *q*. For $F_q(x_j)$ and $F_{q\neq p}(x_j)$, see Equation 40 and Table 10.

Each replicate, *h*, of each treatment group, *i*, was assigned a unique $TIN_{i,h}(r_j)$ function consisting

of one of the results from $D_q(x_j)$, $E_q(x_j)$, $F_q(x_j)$ and $G_q(x_j)$ (Table 12). For a given replicate, h, of a given treatment group, i, the same $TIN_{i,h}(r_j)$ function was added to the signal from each time, t_ϵ, at which data were analysed.

$K_A = 30.325$ ml/g		$\xi_m = 18$ cm^2, $\Delta\xi = 0.0088$ cm^2, $N = 900$					
treatment group		$TIN_{i,h}(r_j)$ of replicates					
% $K_A > 0$	i	$h = 1$	$h = 2$	$h = 3$			
100	1	$G_1(x_j)$	$G_2(x_j)$	$G_3(x_j)$			
99	2	$G_7(x_j)$	$F_7(x_j)$	$F_6(x_j)$			
50	3	$F_2(x_j)$	$F_1(x_j)$	$E_7(x_j)$			
0	4	$G_4(x_j)$	$G_5(x_j)$	$G_6(x_j)$			
% $K_A > 0$	i	$h = 4$	$h = 5$	$h = 6$	$h = 7$	$h = 8$	$h = 9$
100	1	$F_5(x_j)$	$F_4(x_j)$	$F_3(x_j)$	$D_7(x_j)$	$D_6(x_j)$	$D_5(x_j)$
99	2	$E_3(x_j)$	$E_2(x_j)$	$E_1(x_j)$	$E_6(x_j)$	$E_5(x_j)$	$E_4(x_j)$

Table 12. Functions chosen for $TIN_{i,h}(r_j)$ of each replicate, h, of each treatment group, i. These functions are shown in Figures 6 and 7.

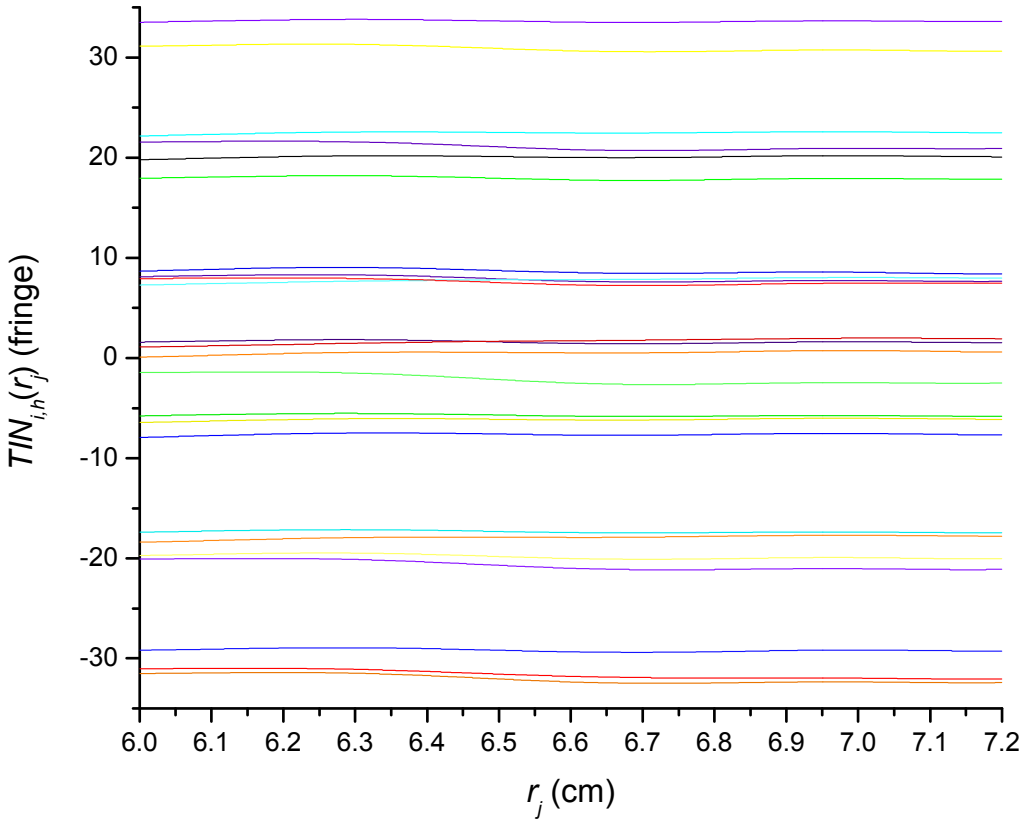

Figure 6. $TIN_{i,h}(r_j)$ versus r_j for each replicate, h, of each treatment group, i. For $i = 1$: $h = 9$ (——), $h = 8$ (——), $h = 7$ (——), $h = 6$ (——), $h = 5$ (——), $h = 4$ (——), $h = 3$ (——), $h = 2$ (——), $h = 1$ (——); for $i = 2$: $h = 9$ (——), $h = 8$ (——), $h = 7$ (——), $h = 6$ (——), $h = 5$ (——), $h = 4$ (——), $h = 3$ (——), $h = 2$ (——), $h = 1$ (——); for $i = 3$: $h = 3$ (——), $h = 2$ (——), $h = 1$ (——); for $i = 4$: $h = 3$ (——), $h = 2$ (——), $h = 1$ (——).

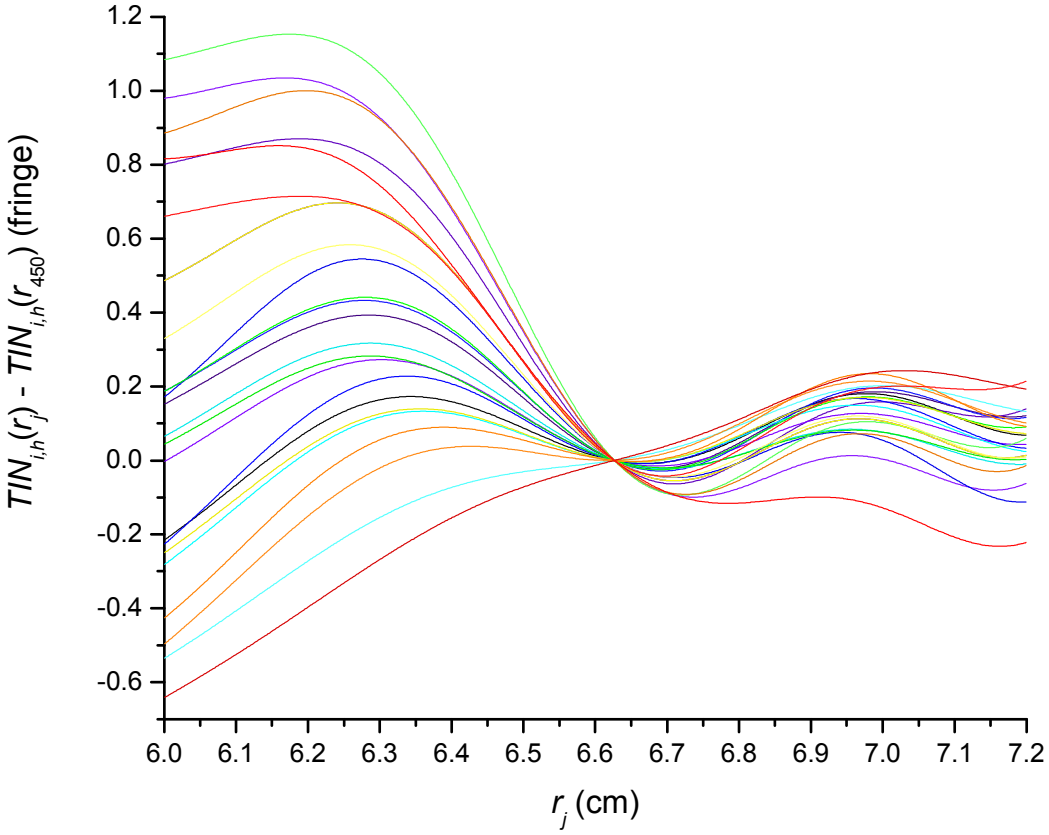

Figure 7. $TIN_{i,h}(r_j)$ - $TIN_{i,h}(r_{450})$, where $r_{450} \cong 6.62655$ cm, versus r_j for each replicate, h, of each treatment group, i. For $i = 1$: $h = 9$ (——), $h = 8$ (——), $h = 7$ (——), $h = 6$ (——), $h = 5$ (——), $h = 4$ (——), $h = 3$ (——), $h = 2$ (——), $h = 1$ (——); for $i = 2$: $h = 9$ (——), $h = 8$ (——), $h = 7$ (——), $h = 6$ (——), $h = 5$ (——), $h = 4$ (——), $h = 3$ (——), $h = 2$ (——), $h = 1$ (——); for $i = 3$: $h = 3$ (——), $h = 2$ (——), $h = 1$ (——); for $i = 4$: $h = 3$ (——), $h = 2$ (——), $h = 1$ (——).

RIN

Simulation of $RIN_{i,h}(t)$

For each replicate, h, of each treatment group, i, a unique $RIN_{i,h}(t_\epsilon)$ function was assigned to each

time, t_ϵ, at which data were analysed (Table 12). Each $RIN_{i,h}(t_\epsilon)$ function consists of nothing more than an offset value (Table 13) that is added to the corresponding signal at every radial position, r_j.

		$RIN_{i,h}(t_\epsilon)$, in fringe, at $t_{36} = 2160$ s, $t_{51} = 3060$ s, $t_{66} = 3960$ s.					
% K_A > 0	i	$h = 1$	$h = 2$	$h = 3$			
		t_{36}, t_{51}, t_{66}	t_{36}, t_{51}, t_{66}	t_{36}, t_{51}, t_{66}			
100	1	-30, 17, -18	-30, -25, -42	18, 25, 37			
99	2	-4, 55, 31	19, -6, 38	4, -41, 17			
50	3	-10, -51, 7	-65, -22, -34	-4, 38, 47			
0	4	14, -49, -23	-22, 17, 7	-9, -36, -12			
% K_A > 0	i	$h = 4$	$h = 5$	$h = 6$	$h = 7$	$h = 8$	$h = 9$
		t_{36}, t_{51}, t_{66}	t_{36}, t_{51}, t_{66}	t_{36}, t_{51}, t_{66}	t_{36}, t_{51}, t_{66}	t_{36}, t_{51}, t_{66}	t_{36}, t_{51}, t_{66}
100	1	16, 48, -9	-7, -21, 13	62, 24, 42	-12, -28, 26	15, 54, 3	21, -26, -32
99	2	-15, 46, 13	11, -12, -43	6, -39, 23	20, -8, -23	-43, 14, -19	7, -28, 18

Table 13a. The $RIN_{i,h}(t_\epsilon)$ functions, each of which is simply an offset value that is added to the signal at every radial position, r_j, of replicate h of treatment group i at time t_ϵ. For $RIN_{i,h}(t_1)$, where t_1 is the earliest time at which data were recorded, see Table 13b. In minutes, $t_{36} = 2160$ s corresponds to 36 min, $t_{51} = 3060$ s corresponds to 51 min, $t_{66} = 3960$ s corresponds to 66 min.

By Equation 4, at each radial position, r_j, $NFS_i(r_j,t_0) = (0.1 \text{ g/ml})Lk_\lambda = 75$ fringe, where, for any treatment group, i, 0.1 g/ml is the total solute concentration at each radial position at t_0. By definition, $RIN_{i,h}(t_0) = NMS_{i,h}(r_j,t_0) - NFS_i(r_j,t_0) - TIN_{i,h}(r_j) - GRN_{i,h}(r_j,t_0)$.

Equation 7 gives the substantially noise-cancelled signal for replicate h of treatment group i at

radial position r_j and time t_ϵ as $Y_{i,h}(r_j,t_\epsilon) = NMS_{i,h}(r_j,t_\epsilon)$ - $NMS_{i,h}(r_j,t_\alpha)$, where $NMS_{i,h}(r_j,t_\epsilon)$ is the actual signal at a time t_ϵ, while $NMS_{i,h}(r_j,t_\alpha)$ is the signal at the earliest recorded time, t_α. For each treatment group, the earliest recorded time was at 1 minute. Thus, t_α of Equation 7 is equated to $t_1 = 60$ s.

In a real experiment, a few minutes would elapse before the rotor reached the speed of 60,000 RPM that applies to the simulated AUC presented here. Thus, in a real experiment, the effective centrifugation time upon reaching a chosen RPM would always be less than the actual time to reach it (Moody, 2012b: Equation 12). For the simulated AUC presented here, the rotor speed was treated as accelerating from 0 to 60,000 RPM at the instant the simulated experiment started, so $t_1 = 60$ s is the effective centrifugation time, for which the actual time would probably be 120 s to 180 s.

Times as late as 11 min could have been chosen for t_α while still providing that the region devoid of concentration gradients completely encompassed the radial positions at which data were analysed at all subsequent times (Moody, 2012a: Figures 1 and 2, for which $K_A = 30.325$ ml/g, and Figures 8 and 9, for which K_A is undefined), which is all that is required of data that must serve as $NMS_{i,h}(r_j,t_\alpha)$ in Equation 4. Graphically, however, setting t_α to $t_1 = 60$ s maximises the distinction between the data from t_α and the data from each subsequent time, $t_\epsilon >> 60$ s. Thus, t_α was set to $t_1 = 60$ s solely for looks (Figures 12 to 19).

At t_1, the total solute concentration, $c_i(r_j,t_1)$, of any treatment group, i, will no longer be uniform with respect to radial position, and thus the values of $NFS_i(r_j,t_1) = c_i(r_j,t_1)Lk_\lambda$ will have changed from their respective values at t_0, with the most significant changes occurring near the extrema.

Away from a small percentage of positions that lie near the extrema, however, the total solute concentration, $c_i(r_j,t_1)$, will be uniform, and will differ from $c_i(r_j,t_0)$ only slightly.

Table 13b gives the values of $RIN_{i,h}(t_1)$, which are equated to $-NFS_i(r_{450},t_1)$. Thus, for each replicate, h, of treatment group, i, $RIN_{i,h}(t_1)$ is equated to -1 times the value of $NFS_i(r_j,t_1)$ in the region where it is uniform. As such, $RIN_{i,h}(t_1) + NFS_i(r_j,t_1) = 0$ in the region where $NFS_i(r_j,t_1)$ is uniform, so that $NMS_{i,h}(r_j,t_1) = TIN_{i,h}(r_j) + GRN_{i,h}(r_j,t_1)$ at most radial positions. (By definition, $NMS_{i,h}(r_j,t_1) = TIN_{i,h}(r_j) + GRN_{i,h}(r_j,t_1) + RIN_{i,h}(t_1) + NFS_i(r_j,t_1)$.)

	$NMS_{i,h}(r_j,t_1) = TIN_{i,h}(r_j) + GRN_{i,h}(r_j,t_1)$ where $RIN_{i,h}(t_1) + NFS_i(r_j,t_1) = 0$			
% $K_A > 0$	i	h	r_j where $RIN_{i,h}(t_1) + NFS_i(r_j,t_1) = 0$	$RIN_{i,h}(t_1)$ (fringe)
100	1	$1 \le h \le 9$	$r_{42} < r_j < r_{858}$	-74.995439436203660
99	2	$1 \le h \le 9$	$r_{41} < r_j < r_{859}$	-74.995427091651645
50	3	$1 \le h \le 3$	$r_{43} < r_j < r_{858}$	-74.995072449176778
0	4	$1 \le h \le 3$	$r_{31} < r_j < r_{864}$	-74.995439436203897

Table 13b. The $RIN_{i,h}(t_1)$ functions, each of which is simply an offset value that is added to the signal at every radial position, r_j, of replicate h of treatment group i at time $t_1 = 60$ s (1 min). Away from the radial extrema, the $NFS_i(r_j,t_1)$ values are constant with r_j, and are little changed from the $NFS_i(r_j,t_0)$ values. (At each radial position, r_j, $NFS_i(r_j,t_0) = (0.1\text{ g/ml})Lk_\lambda = 75$ fringe.)

Between the elimination of redundant values of $\left(\frac{\partial Y_{i,h}(s^*_{\varphi\epsilon})}{\partial s^*_{\varphi\epsilon}}\right)_t$ (Equation 8; Figures 24 to 27) from $q_{i,h}(s^*_{\varphi\epsilon})$ (Equation 9b; Figures 28 to 31) and the application of masks (Figures 20 to 23; Figure 32) to $g(s^*)$ (Figures 33 to 36), analysis was limited to data that lay well within radial positions

where $NMS_{i,h}(r_j,t_1) = TIN_{i,h}(r_j) + GRN_{i,h}(r_j,t_1)$ held (Table 13b).

GRN

Simulation of $GRN_{i,h}(r,t)$

For each replicate, h, of each treatment group, i, a unique set of $GRN_{i,h}(r_j,t_\epsilon)$ values was assigned to each time, t_ϵ, at which data were analysed (Table 12a). Each set of $GRN_{i,h}(r_j,t_\epsilon)$ consists of a subset of N of the δY_Z values shown in Figure 5, such that the index Z of δY_Z is equal to $\Delta Z_{i,h}(t_\epsilon)$ plus the index j of r_j, where $\Delta Z_{i,h}(t_\epsilon)$ is an offset value that is unique to each time, t_ϵ, for each replicate, h, of each treatment group, i, and where the $\Delta Z_{i,h}(t_\epsilon)$ values are chosen to ensure that no δY_Z value is equated to more than one $GRN_{i,h}(r_j,t_\epsilon)$ value. The 96 $\Delta Z_{i,h}(t_\epsilon)$ values used can be calculated from the information given in Table 14a and its legend, but do not follow a consistent pattern with respect to i, h or t_ϵ, as no extraordinary effort was made to follow a pattern during the process of assembling illustrative treatment groups. That process was iterative, and in each iteration of it, the pattern of $\Delta Z_{i,h}(t_\epsilon)$ assignments was disrupted as replicates were added to some treatment groups and removed from others. (In the last iteration of the process, one entire treatment group was eliminated, and its replicates distributed to another treatment group.) Using Table 14b, however, each value of $\Delta Z_{i,h}(t_\epsilon)$ can readily be mapped to an equivalent offset given by

$$\Delta Z(\Phi, N, N_{extra}) = \sum_{\varphi=1}^{\Phi}([\varphi - 1]N + [\{\varphi - 1\}\ mod\ 2]N_{extra}),$$

(42)

where $N = 900$ and $N_{extra} = 212$. The range of Φ is limited to $1 \leq \Phi \leq \Phi_{\max}$, where

$$\Phi_{\max} = 2 + \tau \sum_{i=1}^{g} \sum_{h=1}^{n_i} n_i,$$

(43)

where g is the total number of treatment groups, n_i is the number of replicates of treatment group i, and τ is the number of times at which data are collected. Including the earliest recorded time, $\tau = 4$. With $g = 4$, $n_1 = 9$, $n_2 = 9$, $n_3 = 3$ and $n_4 = 4$, Equation 43 yields $\Phi_{\max} = 98$. As can be seen from the entries in Table 14b, the two highest values of Φ, 97 and 98, were not needed, as the last 2,012 random numbers were not used.

For each replicate, h, of each treatment group, i.						
	$GRN_{i,h}(r_j,t_\epsilon)$ at t_ϵ equal to $t_1 = 60$ s, $t_{36} = 2160$ s, $t_{51} = 3060$ s and $t_{66} = 3960$ s.					
i	$h = 1$	$h = 2$	$h = 3$			
	t_1, t_{36}, t_{51}, t_{66}	t_1, t_{36}, t_{51}, t_{66}	t_1, t_{36}, t_{51}, t_{66}			
1	${}^1a$, ${}^2a$, ${}^3a$, ${}^4a$	${}_1a$, ${}_2a$, ${}_3a$, ${}_4a$	${}^5a$, ${}^6a$, ${}^7a$, ${}_5a$			
2	${}^6b$, ${}_6b$, ${}^7b$, ${}_7b$	${}^1c$, ${}_1c$, ${}^2c$, ${}_2c$	${}^3c$, ${}_3c$, ${}^4c$, ${}_4c$			
3	${}^4d$, ${}_4d$, ${}^5d$, ${}_5d$	${}^6d$, ${}_6d$, ${}^7d$, ${}_7d$	${}^1e$, ${}_1e$, ${}^2e$, ${}_2e$			
4	${}_6a$, ${}_7a$, ${}^1b$, ${}_1b$	${}^2b$, ${}_2b$, ${}^3b$, ${}_3b$	${}^4b$, ${}_4b$, ${}^5b$, ${}_5b$			
i	$h = 4$	$h = 5$	$h = 6$	$h = 7$	$h = 8$	$h = 9$
	t_1, t_{36}, t_{51}, t_{66}	t_1, t_{36}, t_{51}, t_{66}	t_1, t_{36}, t_{51}, t_{66}	t_1, t_{36}, t_{51}, t_{66}	t_1, t_{36}, t_{51}, t_{66}	t_1, t_{36}, t_{51}, t_{66}
1	${}^5c$, ${}_5c$, ${}^6c$, ${}_6c$	${}^7c$, ${}_7c$, ${}^1d$, ${}_1d$	${}^2d$, ${}_2d$, ${}^3d$, ${}_3d$	${}^1g$, ${}_1g$, ${}^2g$, ${}_2g$	${}^3g$, ${}_3g$, ${}^4g$, ${}_4g$	${}^5g$, ${}_5g$, ${}^6g$, ${}_6g$
2	${}^2f$, ${}_2f$, ${}^3f$, ${}_3f$	${}^4f$, ${}_4f$, ${}^5f$, ${}_5f$	${}^6f$, ${}_6f$, ${}^7f$, ${}_7f$	${}^3e$, ${}_3e$, ${}^4e$, ${}_4e$	${}^5e$, ${}_5e$, ${}^6e$, ${}_6e$	${}^7e$, ${}_7e$, ${}^1f$, ${}_1f$

Table 14a. Sets of $GRN_{i,h}(r_j,t_\epsilon)$. The δY_Z values shown in Figure 5 were sequentially organised with respect to the index Z into 7 groups, a, b, c, d, f, and g, each consisting of 7 columns of 2,012 numbers. The columns of each group were numbered 1 through 7. Each column was populated with 2,102 δY_Z values that, consecutively from the 1st to the 2,012th column entry, were ordered

as they occur with respect to Z in the original set of 98,588 values. Columns were filled in numerical order from 1 to 7 within each group, and groups were filled in alphabetical order from *a* to *g*. (With respect to Z, the first set of 2,012 δY_Z values were placed in column 1 of group *a*, the second set of 2,012 δY_Z values were placed in column 2 of group *a*, etcetera, until, penultimately, the forty-eighth set of 2,012 δY_Z values were placed in column 6 of group *g*, and, lastly, the forty-ninth set of 2,012 δY_Z values were placed in column 7 of group *g*.) Either the first 900 or the second 900 entries of a column were equated to $GRN_{i,h}(r,t)$ and added to the 900 signal values of an $NFS_i(r_j,t_\epsilon)$ being evaluated. Where the first 900 entries of a column were added to the $NFS_i(r_j,t_\epsilon)$ values, the number of that column is shown as a superscript preceding the letter of the group to which the column pertains. Where the second 900 entries of a column were added to the $NFS_i(r_j,t_\epsilon)$ values, the number of that column is shown as a subscript preceding the letter of the group to which the column pertains. No column entry was added to more than one $NFS_i(r_j,t_\epsilon)$ signal. The last 212 values of each column were never used, and none of the values from column 7 of group *g* was ever used.

For each replicate, h, of each treatment group, i.						
	$GRN_{i,h}(r_j,t_\epsilon)$ at t_ϵ equal to $t_1 = 60$ s, $t_{36} = 2160$ s, $t_{51} = 3060$ s and $t_{66} = 3960$ s.					
i	$h = 1$	$h = 2$	$h = 3$			
	t_1, t_{36}, t_{51}, t_{66}	t_1, t_{36}, t_{51}, t_{66}	t_1, t_{36}, t_{51}, t_{66}			
1	^{1}, ^{3}, ^{5}, ^{7}	2, 4, 6, 8	^{9}, ^{11}, ^{13}, 10			
2	^{25}, 26, ^{27}, 28	^{29}, 30, ^{31}, 32	^{33}, 34, ^{35}, 36			
3	^{49}, 50, ^{51}, 52	^{53}, 54, ^{55}, 56	^{57}, 58, ^{59}, 60			
4	12, 14, ^{15}, 16	^{17}, 18, ^{19}, 20	^{21}, 22, ^{23}, 24			

i	$h = 4$	$h = 5$	$h = 6$	$h = 7$	$h = 8$	$h = 9$
	t_1, t_{36}, t_{51}, t_{66}	t_1, t_{36}, t_{51}, t_{66}	t_1, t_{36}, t_{51}, t_{66}	t_1, t_{36}, t_{51}, t_{66}	t_1, t_{36}, t_{51}, t_{66}	t_1, t_{36}, t_{51}, t_{66}
1	$^{37}_{38}$, $^{39}_{40}$	$^{41}_{42}$, $^{43}_{44}$	$^{45}_{46}$, $^{47}_{48}$	$^{85}_{86}$, $^{87}_{88}$	$^{89}_{90}$, $^{91}_{92}$	$^{93}_{94}$, $^{95}_{96}$
2	$^{73}_{74}$, $^{75}_{76}$	$^{77}_{78}$, $^{79}_{80}$	$^{81}_{82}$, $^{83}_{84}$	$^{61}_{62}$, $^{63}_{64}$	$^{65}_{66}$, $^{67}_{68}$	$^{69}_{70}$, $^{71}_{72}$

Table 14b. The Φ value corresponding to each set of $GRN_{i,h}(r_j,t_\epsilon)$. Using Equation 42, the tabulated values of Φ are used to calculate $\Delta Z(\Phi,N,N_{extra})$, where $N = 900$ and $N_{extra} = 212$. Given the tabulated values of Φ, i, h and t_ϵ, each value of $\Delta Z_{i,h}(t_\epsilon)$ can be assigned its equivalent value of $\Delta Z(\Phi,N,N_{extra})$. Following the pattern in Table 14a, where the first 900 adjusted random numbers of a column were equated to $GRN_{i,h}(r,t)$ and added to the $NFS_i(r_j,t_\epsilon)$ values, the corresponding Φ value is superscripted, where the second 900 adjusted random numbers of a column were equated to $GRN_{i,h}(r,t)$ and added to the $NFS_i(r_j,t_\epsilon)$ values, the corresponding Φ value is subscripted. In minutes, $t_1 = 60$ s corresponds to 1 min, $t_{36} = 2160$ s corresponds to 36 min, $t_{51} = 3060$ s corresponds to 51 min, $t_{66} = 3960$ s corresponds to 66 min.

As previously noted, the δY_Z values of Figure 5 were obtained from the χ_Z values in Figure 1. Thus, if in place of the δY_Z values of Figure 5, the corresponding χ_Z values in Figure 1 were placed into the columns given by Tables 14a and 14b, two adjustments to each column of χ_Z values would yield each column of δY_Z values. In the first adjustment, the mean of each column of 2,012 χ_Z values would be subtracted from each individual column value to obtain a column of normalised χ_Z values for which the mean was as close to zero as error allowed, and the standard deviation was approximately 1. In the second adjustment, each normalised χ_Z value of each column would be multiplied by σ_{RI} to obtain a column of δY_Z values having a standard deviation approximately equal to the sought after value of 0.01400 fringe.

NFS

Details regarding the model systems from which the treatment groups are constructed

Two imaginary, aqueous systems were designed. It was assumed that T = 20.00°C throughout both systems at all times. In each system, the buffer is defined as the implicit solvent, which is modelled as having sufficient D_2O to render its density, ρ_0, equal to the mean density,

$$\mu_\rho = \frac{1}{n}\sum_{k=1}^{n} \rho_k,$$

(44)

of the particles of all PS-bead species, where ρ_k is the density (as particle mass per particle volume) of PS-bead species k. The ρ_k values are shown in Table 15, and their mean value is $\mu_\rho =$ 1.08225 g/ml. (As used here, the density of a solute species is equal to the mass of one of its particles divided by the volume of one of its particles.)

The aqueous buffer chosen as the model for the implicit solvent consists of 71.23% D_2O, 0.15 M NaCl, 20 mM NH_4HCO_3 and pH 7.0 at 20.00°C (Moody, 2012a), where the amount of D_2O is given in volume-percent. At 20.00°C, the calculated density, ρ_0, of this buffer equals the desired value of $\mu_\rho =$ 1.08225 g/ml. (The density of such a buffer at 20.00°C would be 1.00594 g/ml at 0% D_2O.) The calculated viscosity, η, of this buffer at 20.00°C is 0.010196 poise. These density and viscosity calculations were performed using the Sedimentation Interpretation Program, Sednterp (Laue et al., 1992), version 1.09. (Sednterp is available at http://www.rasmb.bbri.org/software/, the Analytical Ultracentrifugation Software Archive of the Reversible Associations in Structural and Molecular Biology (RASMB) website.)

name	index k	c_k (mg/ml) at t = 0	ρ_k (g/ml)	$\bar{v}_k^0 = \frac{1}{\rho_k}$ (ml/g)	M_k (g/mol)	σ_k^0 (cm^{-2}) at 60,000 RPM	s_k^0 (Svedberg)
H	1	33.891892	1.11150	0.89969	9,462,869	403.343	9.324
	2	0.041667	1.11075	0.90029	9,456,483	393.001	9.084
	3	0.041667	1.11000	0.90090	9,450,098	382.659	8.845
	4	0.041667	1.10925	0.90151	9,443,713	372.316	8.606
	5	0.041667	1.10850	0.90212	9,437,328	361.974	8.367
	6	0.041667	1.10775	0.90273	9,430,943	351.632	8.128
	7	0.041667	1.10700	0.90334	9,424,557	341.290	7.889
	8	0.041667	1.10625	0.90395	9,418,172	330.948	7.650
	9	0.041667	1.10550	0.90457	9,411,787	320.606	7.411
	10	0.041667	1.10475	0.90518	9,405,402	310.264	7.172
	11	0.041667	1.10400	0.90580	9,399,017	299.922	6.933
	12	0.041667	1.10325	0.90641	9,392,631	289.579	6.694
	13	0.041667	1.10250	0.90703	9,386,246	279.237	6.455
LH	14	33.000000	1.08225	0.92400	18,427,691	0	0
	15	0.041667	1.06200	0.94162	9,041,445	-279.237	-6.455
	16	0.041667	1.06125	0.94229	9,035,060	-289.579	-6.694
	17	0.041667	1.06050	0.94295	9,028,675	-299.922	-6.933
	18	0.041667	1.05975	0.94362	9,022,290	-310.264	-7.172
	19	0.041667	1.05900	0.94429	9,015,904	-320.606	-7.411
	20	0.041667	1.05825	0.94496	9,009,519	-330.948	-7.651
	21	0.041667	1.05750	0.94563	9,003,134	-341.290	-7.889
	22	0.041667	1.05675	0.94630	8,996,749	-351.632	-8.128
	23	0.041667	1.05600	0.94697	8,990,364	-361.974	-8.367
	24	0.041667	1.05525	0.94764	8,983,978	-372.316	-8.606
	25	0.041667	1.05450	0.94832	8,977,593	-382.659	-8.845
	26	0.041667	1.05375	0.94899	8,971,208	-393.001	-9.084
L	27	32.108108	1.05300	0.94967	8,964,823	-403.343	-9.324

Table 15. The major distinguishing characteristics of the model solute particles. Except for species 14 (*LH*), all particles are modelled as monomeric spheres. At 20.00°C, ρ_0, the density of

the hypothetical buffer, is equal to ρ_{14}, the density of species 14. Equation 47 describes ρ_k, the inverse of which is equated to $\bar{v}_k^0$, the partial specific volume of species k in the zero-concentration limit (Equation 54). Equation 50 describes M_k, Equation 54 describes σ_k^0, and Equations 56 to 58 describe s_k^0. Further details about the characteristics of the model particles and the hypothetical buffer have been described previously (Moody, 2012a).

The empirical formula of polystyrene (PS) at 0% ^{1}H-to-D substitution is CH, and the empirical formula of PS at 100% ^{1}H-to-D substitution is CD. With m defined as the applicable multiplicity of the empirical formula, the molecular formula of PS at 0% ^{1}H-to-D substitution is $(\mathrm{CH})_m$, for which the molar mass is denoted as $M_{(\mathrm{CH})_m}$, and molecular formula of PS at 100% ^{1}H-to-D substitution is $(\mathrm{CD})_m$, for which the molar mass is denoted as $M_{(\mathrm{CD})_m}$. A PS molecule with a ^{1}H-to-D substitution between 0% and 100% will have a molar mass that lies within $M_{(\mathrm{CH})_m} \leq M_{[(\mathrm{CH})_{m-\Delta m}+(\mathrm{CD})_{\Delta m}]} \leq M_{(\mathrm{CD})_m}$, where $0 \leq \Delta m \leq m$, a general formula for which can be written as

$$M_{[(\mathrm{CH})_{m-\Delta m}+(\mathrm{CD})_{\Delta m}]} \cong (m-\Delta m)(M_\mathrm{C}+M_\mathrm{H})+(\Delta m)(M_\mathrm{C}+M_\mathrm{D}),$$

(45a)

where $M_\mathrm{C} \cong 12.0111$ g/mol is an approximate average molar mass for all isotopes of carbon found on Earth, $M_\mathrm{H} \cong 1.007947$ g/mol is an approximate average molar mass for all isotopes of hydrogen found on Earth, and $M_\mathrm{D} \cong 2.014102$ g/mol is the approximate molar mass of deuterium. For PS molecules of equal multiplicity m, the ratio of the molar mass of those at 100% ^{1}H-to-D substitution to these at 0% ^{1}H-to-D substitution, $M_{(\mathrm{CD})_m} : M_{(\mathrm{CH})_m}$, is estimated as

$$\frac{M_{(\mathrm{CD})_m}}{M_{(\mathrm{CH})_m}} = \frac{M_{(\mathrm{CD})_1}}{M_{(\mathrm{CH})_1}} = \frac{M_\mathrm{CD}}{M_\mathrm{CH}} = \frac{M_\mathrm{C}+M_\mathrm{D}}{M_\mathrm{C}+M_\mathrm{H}} \cong 1.07728.$$

(45b)

For a 30 nm diameter PS bead at any level of ^{1}H-to-D substitution, $m \cong 688{,}593$, assuming

atmospheric pressure applies and T = 293.15 K.

In the AUC simulations conducted for this study, it was assumed that the elevated pressures found within the pressure gradients of a part aqueous, part heavy-water system subjected to AUC would not affect the size or shape of the PS beads. With g_E, the cgs standard acceleration due to gravity, being approximately 981 cm/s^2 at sea level on Earth, At a given radial position, r, the relative centrifugal force, RCF, is given by $(r\omega^2/g_E) \times g_E$., where ω is the angular velocity (Equation 55) of the rotor. At 60,000 RPM, the RCF ranges from 233,410 $\times g_E$ at r = 5.8 cm, which is close to the innermost detectable point, to 289,750 $\times g_E$ at r = 7.2 cm, which is close to the outermost detectable point. (For the calculation of ω from RPM, see Equation 55.)

At $\xi = r^2/2$ (Equation 31), where $r_m < r < r_b$. Due to the net flow of matter within the system prior to reaching equilibrium, ρ, the density of the solution, depends on t and ξ. At any given time, however, the ξ dependence of the pressure can be approximately described by treating the system as if it were hydrostatic. For a system subjected to AUC, the hydrostatic pressure of a solution of ξ-dependent density ρ is given by the applicable form of Bernoulli's equation (Moody, 2011: Equation A8), $P = P_0 + \omega^2 \int_{\xi_m}^{\xi_a} \rho d\xi$, where P_0, the pressure at r_m, is assumed equal to 1.013E+6 dyne/cm^2, which is the cgs-equivalent of 1 atmosphere. For the systems described here, if ρ were everywhere equal to ρ_0 = 1.08225 g/ml, then at 60,000 RPM, P/P_0 would range from 1 at r_m = 6 cm to approximately 385 at r_b = 7.2 cm. (The density of the hypothetical buffer at 20.00°C and $P = P_0$ is ρ_0 = 1.08225 g/ml.)

With %D defined at the percent of ^{1}H-to-D substitution, the density of a PS bead of %D is

$$\rho_{\%D} = \rho_{0\%} + \frac{(\rho_{100\%} - \rho_{0\%})\%D}{100\%},$$

(46)

where $\rho_{0\%} = \rho_L = 1.05300$ g/ml and $\rho_{100\%} = \rho_{CD} = \rho_{0\%} M_{CD}/M_{CH} = 1.13438$ g/ml. The PS-bead species with the highest density is $\rho_H = \rho_{76\%} = 1.11150$ g/ml. Figure 8 shows $\rho_{\%D}$ as a function of %D. Figure 9 shows ρ_k as a function of k, an equation for which is

$$\rho_k = \rho_n + [(n-1)(3-\alpha_k) + 1 - k]\Delta\rho,$$

(47)

where $\Delta\rho = 0.00075$ g/ml is an increment of the density, $n = 27$ is the upper value of k, $\alpha_{k<14} = 0$, $\alpha_{k=14} = 1$ and $\alpha_{k>14} = 2$. This equation yields the values of ρ_k, including $\rho_{n=27} = 1.05300$ g/ml, shown in Table 15.

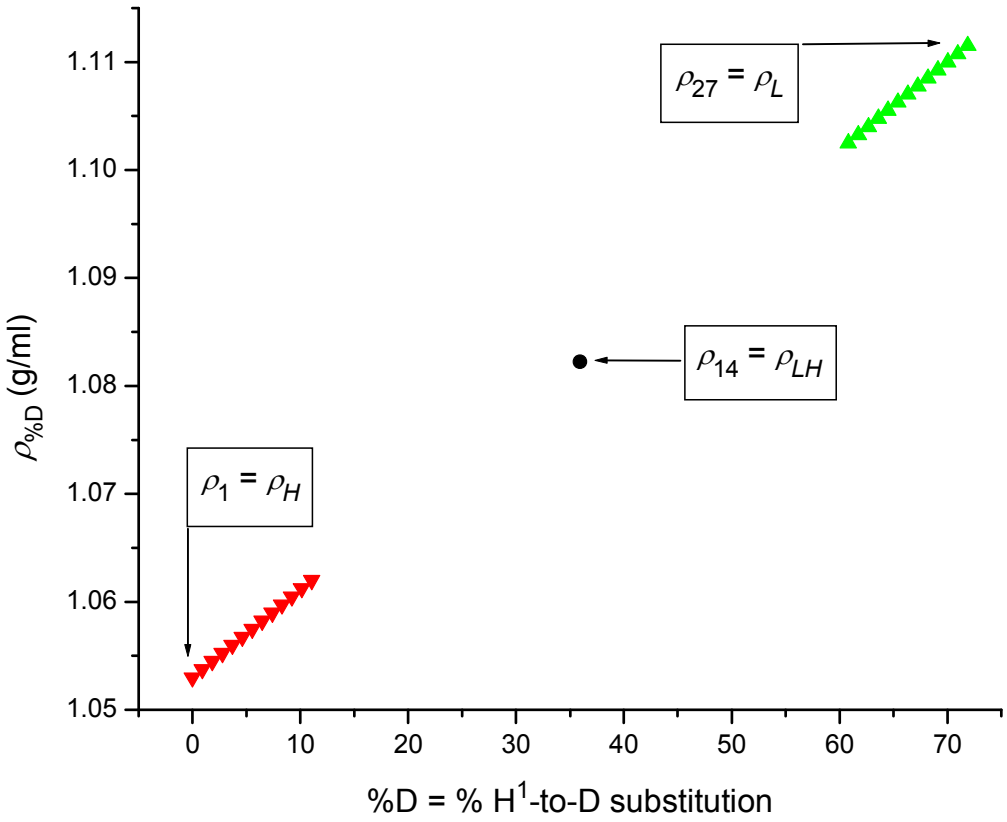

Figure 8. Density, $\rho_{\%D}$, versus %D, with $\rho_{\%D>36\%} > \rho_0$ (▲), $\rho_{\%D=36\%} = \rho_0$ (●) and $\rho_{\%D<36\%} < \rho_0$ (▼). The relationship is given by Equation 46, $\rho_{\%D} = \rho_{0\%} + \frac{(\rho_{100\%} - \rho_{0\%})\%D}{100\%}$, where $\rho_{0\%} = \rho_L =$ 1.05300 g/ml, $\rho_{100\%} =$ 1.13438 g/ml. The PS-bead species with the highest density is $\rho_H = \rho_{76\%} =$ 1.11150 g/ml.

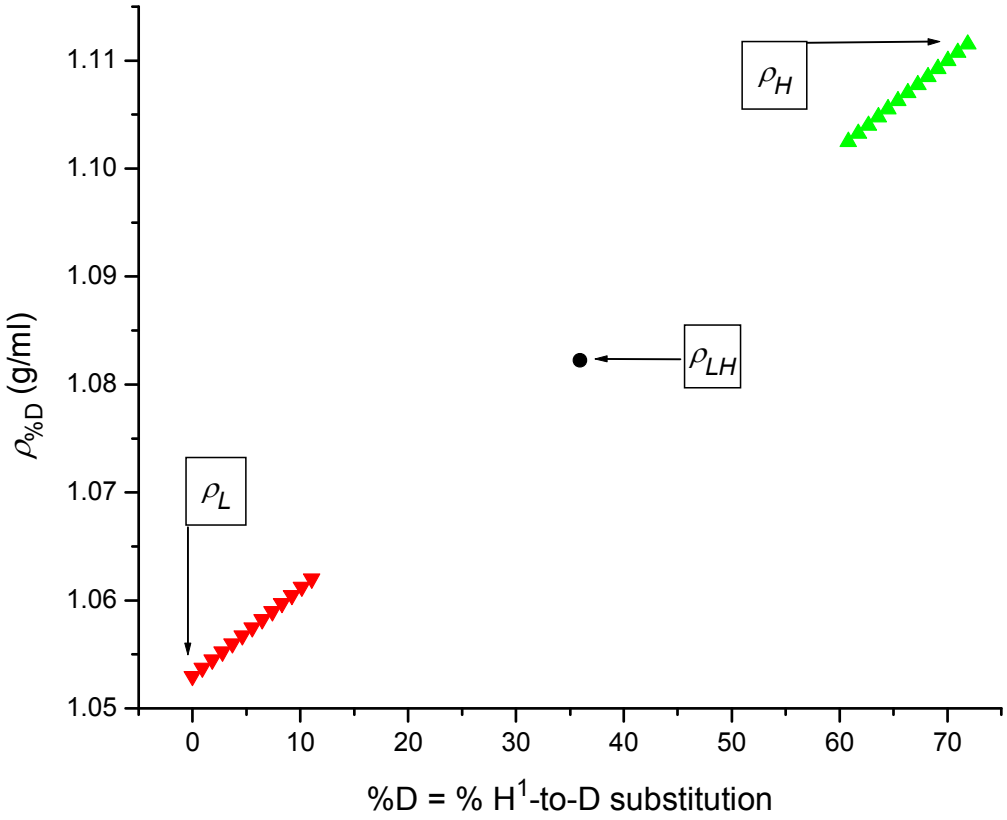

Figure 9. Density, ρ_k, versus k, with $\rho_{k<14} > \rho_0$ (▲), $\rho_{k=14} = \rho_0$ (●) and $\rho_{k>14} < \rho_0$ (▼). The relationship is given by Equation 47, $\rho_k = \rho_n + [(n-1)(3-\alpha_k) + 1 - k]\Delta\rho$, where $n = 27$, $\rho_n = \rho_L =$ 1.05300 g/ml, $\Delta\rho =$ 0.00075 g/ml, $\alpha_{k<14} = 0$, $\alpha_{k=14} = 1$ and $\alpha_{k>14} = 2$. The values of all ρ_k are shown in Table 15.

Being composed of one part L, the volume of which is V_L, and one part H, the volume of which is V_H, the density of LH is

$$\rho_{LH} = \frac{V_L\rho_L + V_H\rho_H}{V_L + V_H} = \frac{V_L\rho_L + V_H\rho_H}{V_{LH}},$$

(48)

where $V_{LH} = V_L + V_H$ is the volume of *LH*. For every species except $LH\,(k = 14)$, the solute particles are spheres with an anhydrous radius of $R_{k\neq14} = 1.5\text{E-}6$ cm, so that

$$V_{k\neq14} = \frac{4\pi R_{k\neq14}^3}{3}$$

(49)

is approximately equal to 1.41372E-17 ml. With $V_{27} = V_L$ and $V_1 = V_H$, $V_{LH} = V_L + V_H$ is the volume of *LH*, as previously noted with respect to the denominator of Equation 48.

With Avogadro's number represented by N_A, the molar mass of every species is given by

$$M_k = N_A\rho_k V_k,$$

(50)

the values of which are listed in Table 15.

PS-bead species $LH\,(k = 14)$ is defined as a dimer composed of two spherical particles, PS-bead species $L\,(k = 27)$ and PS-bead species $H\,(k = 1)$. As such, PS-bead species *LH* would not be spherical, but for simplicity of calculation, the anhydrous radius of its equivalent sphere is defined as

$$R_{LH} \equiv \sqrt[3]{\frac{3M_{LH}}{4\pi N_A\rho_{LH}}} = \sqrt[3]{\frac{3(M_L + M_H)}{4\pi N_A\rho_{LH}}} \cong 1.88988\text{E} - 6 \text{ cm},$$

(51)

where ρ_{LH} is given by Equation 49. By virtue of this definition,

$$V_k = \frac{4\pi R_k^3}{3}$$

(52)

holds for each species, including LH ($k = 14$).

Using R_k, the diffusion coefficient of each solute in the zero-concentration limit is calculated as

$$\lim_{c\to 0} D_k = D_k^0 = \frac{RT}{6\pi N_A \eta h_k R_k},$$

(53)

where R is the ideal gas constant, $T = 293.15$ K is the absolute temperature, D_k is the diffusion coefficient of solute species k, and h_k is the hydration factor of solute species k in the limit as c, the total solute concentration, approaches zero. With $h_k = 1/0.65$ used for each solute species, k, $D_{k\neq 14}^0 = 9.12567\text{E-}8$ cm^2/s and $D_{14}^0 = D_{LH}^0 = 7.24305\text{E-}8$ cm^2/s.

The reduced molar mass of each solute in the zero-concentration limit is calculated as

$$\lim_{c\to 0} \sigma_k = \sigma_k^0 = \frac{M_k\left(1 - \frac{\rho_0}{\rho_k}\right)\omega^2}{RT},$$

(54)

where σ_k is the reduced molar mass of solute species k, $T = 293.15$ K is (again) the absolute temperature, $\rho_0 = 1.08225$ g/ml is the density of the solution in the limit as c approaches zero, $1/\rho_k = \bar{v}_k^0$ is the partial specific volume of species k in the limit as c approaches zero, and ω is the angular velocity of the rotor, which is calculated from the rotor speed in RPM (rotations per minute) as

$$\omega = 2\pi\left(\frac{\text{RPM}}{60\ \text{s/min}}\right).$$

(55)

During the full course of each simulated AUC experiment presented here, the simulated rotor speed was 60,000 RPM. Thus, the start of each experiment at $t_0 = 0$ s marks the time at which the rotor was modelled as having instantly accelerated from 0 RPM to 60,000 RPM.

The sedimentation coefficient of species k in the limit as c approaches zero is

$$s_k^0 = \frac{\sigma_k^0 D_k^0}{\omega^2}.$$

(56)

With the right-hand sides of Equation 54 for σ_k^0 and Equation 53 for D_k^0 substituted into the preceding equation for s_k^0 results in

$$s_k^0 = \frac{M_k\left(1 - \frac{\rho_0}{\rho_k}\right)}{6\pi N_A \eta h_k R_k}.$$

(57)

Substituting the right-hand side of Equation 50 for M_k in Equation 57, and then substituting the right-hand side of Equation 52 for V_k in the result, yields

$$s_k^0 = \frac{2R_k^2(\rho_k - \rho_0)}{9\eta h_k}.$$

(58)

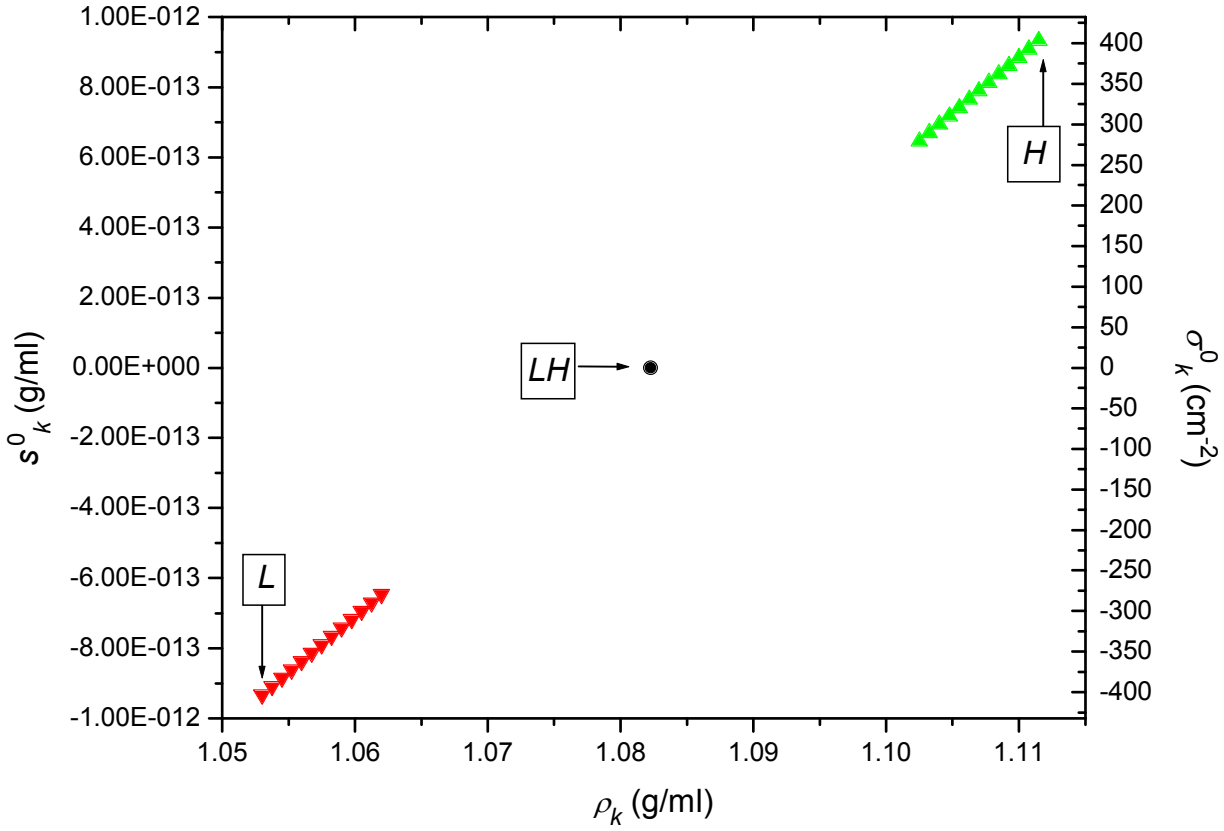

Figure 10. On the left-hand ordinate: s_k^0 (s), the sedimentation coefficient of species k in the limit as c approaches zero (Equations 56 to 58), versus ρ_k (g/ml), with $s_{k>14}^0 > 0$ (△), $s_{k=14}^0 = s_{LH}^0 = 0$ (○) and $s_{k<14}^0 < 0$ (▽). The highest value of s_k^0 is that of solute species H ($k = 1$). The lowest value of s_k^0 is that of solute species L ($k = 27$). The values of all s_k^0 are shown in Table 15. On the right-hand ordinate: σ_k^0 (cm^{-2}), the reduced molar mass of species k in the limit as c approaches zero (Equation 54), versus ρ_k (g/ml), with $\sigma_{k>14}^0 > 0$ (▲), $\sigma_{k=14}^0 = \sigma_{LH}^0 = 0$ (●) and $\sigma_{k<14}^0 < 0$ (▼). The highest value of σ_k^0 is that of solute species H ($k = 1$). The lowest value of σ_k^0 is that of solute species L ($k = 27$). The values of all σ_k^0 are shown in Table 15. For the solute species in question, the ordinate axes can be, and in this case are, scaled so that, for each value of k, the

symbol for σ_k^0 is superimposed on the symbol for s_k^0.

The transport of species k is coupled to the effect of species q on the thermodynamic nonideality of the system through $y_{k,q}c_q$, where c_q is the concentration of species q,

$$y_{k,q} = \frac{4}{\rho_q}$$

(59)

and ρ_q is the density of species q.

The transport of species k is coupled to the effect of species q on the viscosity of the system through $h_{k,q}c_q$, where c_q is the concentration of species q,

$$h_{k,q} = \frac{2.5}{\rho_q}$$

(60)

and ρ_q is the density of species q.

For all k, the c-dependent diffusion coefficient is

$$D_k = D_k^0 \left(\frac{1 + \sum_{q=1}^{n} y_{k,q} c_q}{1 + \sum_{q=1}^{n} h_{k,q} c_q} \right).$$

(61)

At $t = 0$, $c_{1<k<14} = c_{14<k<27} = 4.16667\text{E-}5$ g/ml, $c_H = c_1 = 3.38918\text{E-}2$ g/ml, $c_{LH} = c_{14} = 3.30000\text{E-}2$ g/ml and $c_L = c_{27} = 3.2108\text{E-}2$ g/ml throughout the system, so that $D_{k\neq14} = 9.12567\text{E-}8$ cm^2/s and $D_{14} = D_{LH} = 7.24305\text{E-}8$ cm^2/s everywhere at $t = 0$.

The volume fraction of each species q is

$$\varphi_q = \frac{c_q}{\rho_q} < \left[\varphi_q\right]_{max} \leq 1,$$

(62)

where c_q is the mass concentration of solute species q, ρ_q is the density of species q and $\left[\varphi_q\right]_{max}$ is the maximum volume fraction of solute species q. With ρ_q assumed to be c-independent for all solutes, $\left[\varphi_q\right]_{max}$ is given by

$$\lim_{c_{k\neq q}\to 0}\left[\lim_{c_q\to\left[c_q\right]_{max}} \varphi_q\right] = \lim_{c\to\left[c_q\right]_{max}} \varphi_q = \frac{\left[c_q\right]_{max}}{\rho_q} = \left[\varphi_q\right]_{max},$$

(63)

where $\left[c_q\right]_{max}$ is the maximum concentration of solute species q in the limit as every $c_{k\neq q}$ approaches zero. (A measure of $\left[c_q\right]_{max}$ is presented in the discussion that follows Equation 66, and an alternative definition of $\left[\varphi_q\right]_{max}$ is given by Equation 67.) For each solute species, $\left[\varphi_q\right]_{max}$ is assigned a value of 0.5. (In general, $0 \leq \left[\varphi_q\right]_{max} \leq 1$.) Thus, for each solute species, $\left[\varphi_q\right]_{max}$ is treated as if it were a constant.

The transport of species $k \neq 14$ is coupled to the effect of species q on the density of the system through $p_{k\neq 14,q}c_q$, where c_q is the concentration of species q,

$$p_{k\neq 14,q} = \frac{1}{\rho_q\left[\varphi_q\right]_{max}}\left[\frac{\left(1-\frac{\rho_q}{\rho_k}\right)-\left(1-\frac{\rho_0}{\rho_k}\right)}{\left(1-\frac{\rho_0}{\rho_k}\right)}\right] = \frac{-1}{\rho_q\left[\varphi_q\right]_{max}}\left[\frac{\rho_q-\rho_0}{\rho_k-\rho_0}\right],$$

(64)

ρ_k is the density of species k, ρ_q is the density of species q, and ρ_0 is the density of the implicit solvent.

The transport of any solute species, including $k = 14$, is coupled to the effect of species q on the density of the system through $(\sigma p)_{k,q} c_q$, where c_q is the concentration of species q,

$$(\sigma p)_{k,q} = \sigma_k^0 p_{k,q} = \frac{\omega^2 M_k}{RT\rho_k}\left[\frac{\rho_0 - \rho_q}{\rho_q [\varphi_q]_{max}}\right],$$

(65)

ρ_k is the density of species k, ρ_q is the density of species q, ρ_0 is the density of the implicit solvent, σ_k^0 is the reduced molar mass of species k in the limit as c approaches zero (Equation 54) and the rest of the parameters are as defined previously.

For $k \neq 14$, the c-dependent reduced molar mass is given

$$\sigma_{k\neq 14} = \sigma_k^0 \left(\frac{1 + \sum_{q=1}^{n} p_{k,q} c_q}{1 + \sum_{q=1}^{n} y_{k,q} c_q}\right).$$

(66)

For $k \neq 14$, substituting the right-hand side of Equation 64 for $p_{k,q}$ shows that $\sigma_k = 0$ when $c_k = \rho_k [\varphi_k]_{max}$ and each $c_{q\neq k} = 0$. (As $p_{k,q=14} = 0$ for all k, $\sigma_{k\neq 14} = 0$ when $c_{k\neq 14} = \rho_k [\varphi_k]_{max}$ even if $c_{q=14}$ is greater than zero, provided that every other $c_{q\neq k} = 0$.) As the sedimentation coefficient (Equation 70) of solute species k is zero when $\sigma_k = 0$, there is no net transport of species k where $(\partial c_k / \partial r)_t = 0$ and $\sigma_k = 0$. Thus, for $k \neq 14$, $\rho_k [\varphi_k]_{max}$ can be viewed as a measure of $[c_k]_{max}$.

If solute species q could be concentrated to the point that no solvent remained in its presence, then $[c_q]_{max}$ would be equal to ρ_q, provided that, as is assumed here, no voids took the place of the missing solvent. Thus, the actual $[c_q]_{max}$ is equal to its theoretical maximum of ρ_q minus the mass of solvent that cannot be removed from a given volume in which no further concentration of solute species q is possible. Applying this concept to $[\varphi_q]_{max}$ in Equation 63 results in

$$\left[\varphi_q\right]_{max} = \frac{\left[c_q\right]_{max}}{\rho_q} = \frac{\rho_q - \left[H_q\right]_{max}\rho_0}{\rho_q},$$

(67)

where $\left[H_q\right]_{max}$ is defined as the (dimensionless) hydration factor of solute species q, such that $\left[H_q\right]_{max}\rho_0$ is the amount of solvent that cannot be removed from the particles of solute species q at $c = c_q = \left[c_q\right]_{max}$. Solving Equation 67 for $\left[H_q\right]_{max}$ yields

$$\left[H_q\right]_{max} = \frac{\rho_q}{\rho_0}\left(1 - \left[\varphi_q\right]_{max}\right) = \frac{\rho_q - \left[c_q\right]_{max}}{\rho_0}.$$

(68)

As the solvent and the solute particles are all treated as being incompressible, ρ_0 and each value of ρ_q are constants. Furthermore, as each value of $\left[\varphi_q\right]_{max}$ is treated as being a constant, each value of $\left[c_q\right]_{max}$ is a constant. Thus, each value of $\left[H_q\right]_{max}$ is also a constant.

For any solute species, including $k = 14$, the c-dependent reduced molar mass is given by

$$\sigma_k = \frac{\sigma_k^0 + \sum_{q=1}^{n}(\sigma p)_{k,q}c_q}{1 + \sum_{q=1}^{n} y_{k,q}c_q}.$$

(69)

For $k \neq 14$, Equation 69 yields the same results as Equation 66. Thus, Equation 69 works for all k, and is more general than Equation 66. Moreover, it is by virtue of Equation 69 that $\sigma_{k=14}$ can be nonzero even though $\sigma_{k=14}^0 = 0$.

For any solute species, k, the c-dependent sedimentation coefficient is given by

$$s_k = \frac{\sigma_k D_k}{\omega^2}.$$

(70)

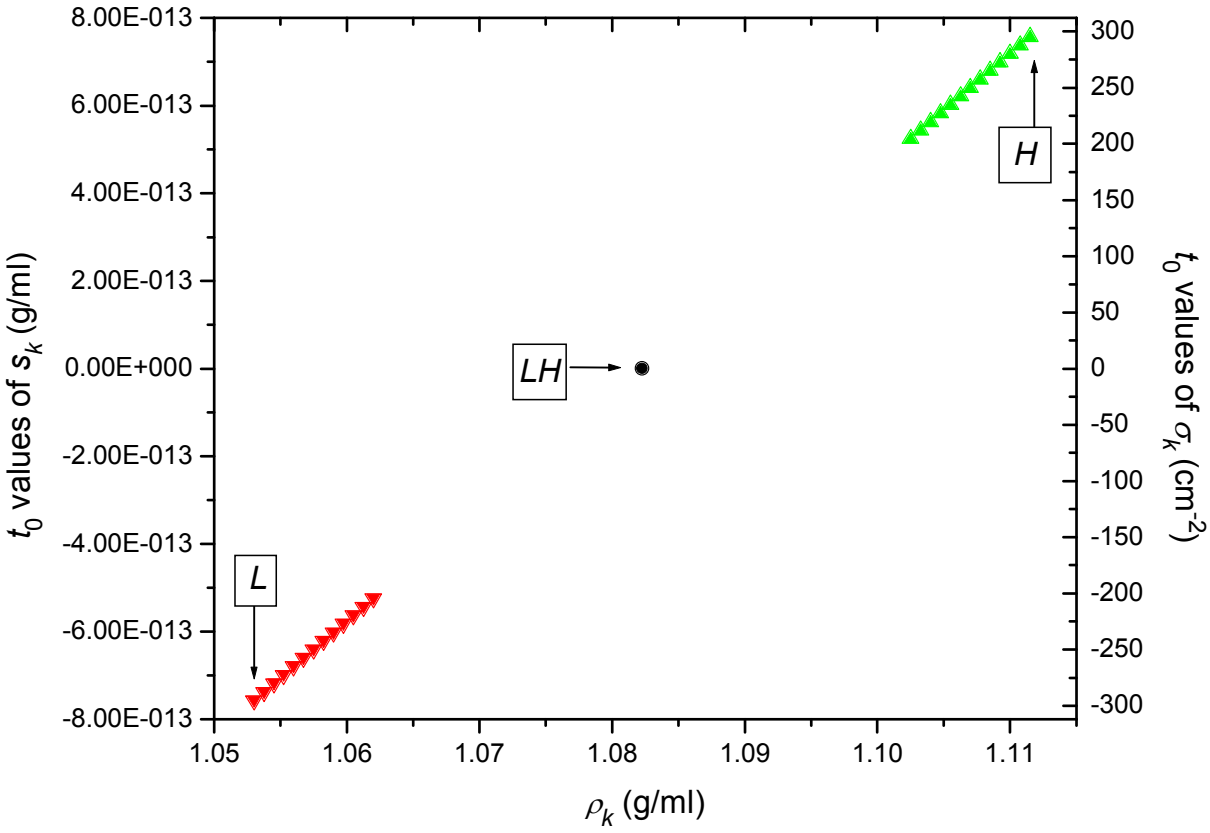

Figure 11. On the left-hand ordinate: s_k (s), the concentration-dependent sedimentation coefficient of species k at $t = 0$ (Equation 70), versus ρ_k (g/ml), with $s_{k>14} > 0$ (△), $s_{k=14} = s_{LH} = 0$ (○) and $s_{k<14} < 0$ (▽). The highest value of s_k is that of solute species H ($k = 1$). The lowest value of s_k is that of solute species L ($k = 27$). On the right-hand ordinate: σ_k (cm^{-2}), the concentration-dependent reduced molar mass of species k at $t = 0$ (Equations 66 and 69), versus ρ_k (g/ml), with $\sigma_{k>14} > 0$ (▲), $\sigma_{k=14} = \sigma_{LH} = 0$ (●) and $\sigma_{k<14} < 0$ (▼). The highest value of σ_k is that of solute species H ($k = 1$). The lowest value of σ_k is that of solute species L ($k = 27$). At $t = 0$, the solute concentrations (column c_k of Table 15) are invariant with radial position. For the solute species in question, the ordinate axes can be, and in this case are, scaled so that, for each

value of k, the symbol for σ_k is superimposed on the symbol for s_k.

Henceforth, as needed to distinguish the reactive species from their single-species-component counterparts, the reactive species of H, LH and L are denoted as H_+, LH_+ and L_+, respectively, and the single-species components of H, LH and L are denoted as H_-, LH_- and L_-, respectively. Thus, the mass-action association/dissociation reaction for which $K_A = 30.325$ ml/g at 20.00°C is written as

$$H_+ + L_+ \underset{k_{r+}>0}{\overset{k_{f+}>0}{\rightleftharpoons}} LH_+, \tag{71}$$

where $k_{f+} = 30{,}000$ [ml/g]/s and $k_{r+} = k_{f+}/K_A \cong 989.277$ s are the forward and reverse rate constants, respectively, while the corresponding interaction for which K_A is undefined at 20.00°C would be written as

$$H_- + L_- \underset{k_{r-}=0}{\overset{k_{f-}=0}{\rightleftharpoons}} LH_-, \tag{72}$$

where $k_{f-} = 0$ [ml/g]/s and $k_{r-} = 0$ s are the forward and reverse rate constants, respectively.

The concentrations of H_+, LH_+ and L_+ are written as c_{H+}, c_{LH+} and c_{L+}, respectively. The concentrations of H_-, LH_- and L_- are written as c_{H-}, c_{LH-} and c_{L-}, respectively. The concentrations of H, LH and L are redefined as $c_H = c_{H-} + c_{H+}$, $c_{LH} = c_{LH-} + c_{LH+}$ and $c_L = c_{L-} + c_{L+}$, respectively. As such, it remains true that, in the absence of concentration gradients, $c_H/M_H = 2(c_{LH}/M_{LH}) = c_L/M_L$. Table 16 and its accompanying legend present the concentrations of all solute species of each treatment group at $t = 0$.

i	c_{H-} (g/ml)	c_{LH-} (g/ml)	c_{L-} (g/ml)	c_{H+} (g/ml)	c_{LH+} (g/ml)	c_{L+} (g/ml)
(% $K_A > 0$)	$c_{H-} + c_{LH-} + c_{L-}$			$c_{H+} + c_{LH+} + c_{L+}$		
1	0	0	0	3.38918E-2	3.30000E-2	3.2108E-2
(100%)	$c_{H-} + c_{LH-} + c_{L-} = 0$			$c_{H+} + c_{LH+} + c_{L+} = 0.099$ g/ml		
2	3.38918E-4	3.30000E-4	3.2108E-4	3.36372E-2	3.25059E-2	3.18668E-2
(99%)	$c_{H-} + c_{LH-} + c_{L-} = 0.00099$ g/ml			$c_{H+} + c_{LH+} + c_{L+} = 0.09801$ g/ml		
3	1.69549E-2	1.65000E-2	1.60541E-2	1.96959E-2	1.11448E-2	1.86593E-2
(50%)	$c_{H-} + c_{LH-} + c_{L-} = 0.0495$ g/ml			$c_{H+} + c_{LH+} + c_{L+} = 0.0495$ g/ml		
4	3.38918E-2	3.30000E-2	3.2108E-2	0	0	0
(0%)	$c_{H-} + c_{LH-} + c_{L-} = 0.099$ g/ml			$c_{H+} + c_{LH+} + c_{L+} = 0$		

Table 16. Concentrations of c_H, c_{LH} and c_L at $t = 0$ for each treatment group, i. The solute species that participate in the mass-action association/dissociation reaction described by Equation 71 are denoted as H_+, LH_+ and L_+ to distinguish them from their respective single-species-component counterparts, H_-, LH_- and L_-. By definition, at all times, at point in the system, $c_H = c_{H-} + c_{H+}$, $c_{LH} = c_{LH-} + c_{LH+}$, $c_L = c_{L-} + c_{L+}$ and $c_H = c_{LH} + c_L$ for each treatment group. At $t = 0$, at each point in the system, $c_H = 3.38918\text{E-}2$ g/ml, $c_{LH} = 3.30000\text{E-}2$ g/ml, $c_L = 3.2108\text{E-}2$ g/ml, $c_H = 0.099$ g/ml, $c_H/M_H = 2(c_{LH}/M_{LH}) = c_L/M_L$ and $c_{1<k<14} = c_{14<k<27} = 4.16667\text{E-}5$ g/ml for each treatment group. For each treatment group, at $t = 0$, it also holds that $c_{H-}/M_H = 2(c_{LH-}/M_{LH}) = c_{L-}/M_L$ and $c_{H+}/M_H = c_{L+}/M_L$ throughout the system.

Details regarding the treatment groups, the Noise-Free Signals and the times chosen for analysis

For each system, 71.23% (by volume) D_2O, 0.15 M NaCl and 20 mM NH_4HCO_3 define the

imaginary aqueous buffer, for which, at T = 20.00°C, the pH is neutral, the density is $\rho_0 = 1.08225$ g/ml and the viscosity is $\eta = 1.0196$ cP. Despite its multiple components, the buffer is defined as the implicit solvent, and as such, it is treated as if it were just one component. It is therefore assumed that each system can be adequately modelled without the need to keep track of each buffer component (the H_2O, D_2O, NaCl and NH_4HCO_3) individually, as would be required if each buffer component were treated explicitly.

Every explicit solute species of every system is imagined as a spherical, 30 nm diameter PS bead, or a dimer of two such beads, and each explicit solute species can be defined by its extent of deuteration (Figure 8) or its consequent density (Table 15). Each system includes the implicit solvent plus as many as 30 explicit solute species. Of those 30 explicit solute species, 27 are single-species components that include L_-, H_-, and LH_- (Table 16), plus each of the 24 PS-bead species present at low concentration ($1 < k < 14$ or $14 < k < 27$, Table 15). The 3 remaining explicit solute species, L_+, H_+ and LH_+, arise from 2 two-species components, L_+ and H_+, that share 1 product, LH_+, in common (Table 16).

Each treatment group (Table 16) is a mixture of the two previously described systems (Figures 12 and 16) that differ with respect to K_A (Equations 71 and 72). In a given treatment group, % $K_A > 0$ denotes the mass-percent of the mixture drawn from the system in which H, LH and L consist entirely of the reactive species, H_+, LH_+ and L_+ (Equation 71; Table 16; Figure 12). Likewise, in a given treatment group, the mass-percent of the mixture drawn from the system in which H, LH and L consist entirely of the nonreactive species, H_-, LH_- and L_- (Equation 72; Table 16; Figure 16), is denoted as % K_A undefined, which is equal to 100% - (% $K_A > 0$).

At 0% $K_A > 0$, the explicit solute species consist entirely of the 27 single-species components that include L_-, H_-, and LH_- (Equation 72; Table 16; Figure 16). At 100% $K_A > 0$, the explicit solute species consist entirely of the 3 explicit solute species (L_+, H_+ and LH_+) that arise from the 2 two-species components (L_+ and H_+) that share 1 product (LH_+) in common (Equation 71; Table 16; Figure 12), plus the 24 single-species components present at low concentration ($1 < k < 14$ or $14 < k < 27$, Table 15). Between 0% $K_A > 0$ and 100% $K_A > 0$, all 30 explicit solute species are present.

As the model renders the solution density sensitive to the concentration of each explicit solute species (Equations 62 to 70), the implicit solvent is treated as displaceable by the explicit solutes. With the implicit solvent being treated as a single component, however, it is assumed that the composition of any implicit solvent displaced is identical to the composition of the buffer in the reference solution. The implicit solvent is also treated as the implicit reference system of each AUC simulation. In the simulated AUC, all components other than PS beads are treated as being at equal chemical potential in a given solute-containing system and its implicit reference system, so that only the PS beads contribute to the Noise-Free Signal.

The set of all treatment groups number $g = 4$ in total. The treatment groups are indexed by i, and their composition in terms of % $K_A > 0$ is shown in Table 17. Table 17 also lists n_i, which is the number of replicates, h, per treatment group, i. In addition, Table 17 gives the times, t_ϵ, at which AUC data from each replicate of each treatment group were analysed. The within-group results of the analysis were used in pair-wise comparisons between treatment groups.

treatment group		n_i	t_ϵ analysed (reference: t_1)		
% $K_A > 0$	i				
100	1	9	t_{36}	t_{51}	t_{66}
99	2	9	t_{36}	t_{51}	t_{66}
50	3	3	t_{36}	t_{51}	t_{66}
0	4	3	t_{36}	t_{51}	t_{66}

Table 17. Treatment groups, number of replicates and times chosen for analysis. Each treatment group is a mixture for which the % $K_A > 0$ is the mass-percent drawn from the system for which *H*, *LH* and *L* consist entirely of H_+, LH_+ and L_+ (Equation 71; Table 16). The number of replicates, *h*, per treatment group, *i*, is n_i. At each of the times chosen, AUC data from each replicate of each treatment group were analysed, and the within-group results of the analysis were used in pair-wise comparisons between treatment groups.

By Equation 3, for treatment group *i* at radial position r_j and time t_ϵ, the total concentration of all solute species is $c_i(r_j, t_\epsilon) = \sum_{k=1}^{n} c_k$, where *n* is the total number of solute species. At t_0, for each treatment group, *i*, $c_i(r_j,t_0,) = 0.1$ g/ml at each radial position, r_j. (See *An overview of the method of data analysis*.) For consistency of indexing among similar species across treatment groups, when counting species, c_{H-}, c_{H+}, c_{LH-}, c_{LH+}, c_{L-} and c_{L+} are regarded as subspecies. As in the legend of Table 16, $c_H = c_{H-} + c_{H+}$, $c_{LH} = c_{LH-} + c_{LH+}$ and $c_L = c_{L-} + c_{L+}$, where, following the system presented in Table 15, $c_H = c_1$, $c_{LH} = c_{14}$ and $c_L = c_{27}$. Thus, as in Table 15, $n = 27$ for all *i*, even though there are really 30 species among the 24 single-species components and the 6 subspecies of each treatment group within $1 < i < 4$. For $i = 1$, there really are 27 species among 24 single-species components plus a pair of components that comprises 3 subspecies. For $i = 4$ as well, there really are 27 species, each of which is a single-species component.

An overview of the times chosen for analysis describes the basic guidelines for choosing the times at which data are analysed. With the further constraint that the same time points be chosen for each treatment group, the earliest, the most central and the latest time points that fall within those guidelines were chosen for analysis to try to maximise the likelihood of detecting any time-dependent system behaviour. (In general, the ideal time points that meet such criteria would be expected to vary with treatment group, but for the treatment groups in Table 17, these time points are very similar.) The earliest time point, t_{36}, occurs shortly after the last of the solute boundaries has cleared its radial extremum of origin. The latest time point, t_{66}, occurs shortly before the first of the solute boundaries has begun to merge with its radial extremum of accumulation. The central time point, t_{51}, occurs at or near the maximum extent of overlap between the centripetally and centrifugally directed boundaries (Moody, 2012a; 2012b).

Figures 12 to 15 show $NFS_i(r_j,t_\epsilon)$ versus r_j for each treatment group at each time, t_ϵ, chosen for analysis (Table 17). As previously noted, the optical path-length was assigned a value of $L = 0.3$ cm for each treatment group, and each PS-bead species was assigned a specific fringe displacement of $k_\lambda = 2{,}500$ fringe/[cm·g/ml]. Thus, by Equation 4, with $c_i(r_j,t_\epsilon)$ denoting the total PS-bead concentration of treatment group i at radial position r_j and time t_ϵ, and with L denoting the optical path-length, $NFS_i(r_j,t_\epsilon) = k_\lambda[c_i(r_j,t_\epsilon)]L$ is the noise-free portion of the signal that would be obtained using the RI detection system. (See *An overview of the method of data analysis*.)

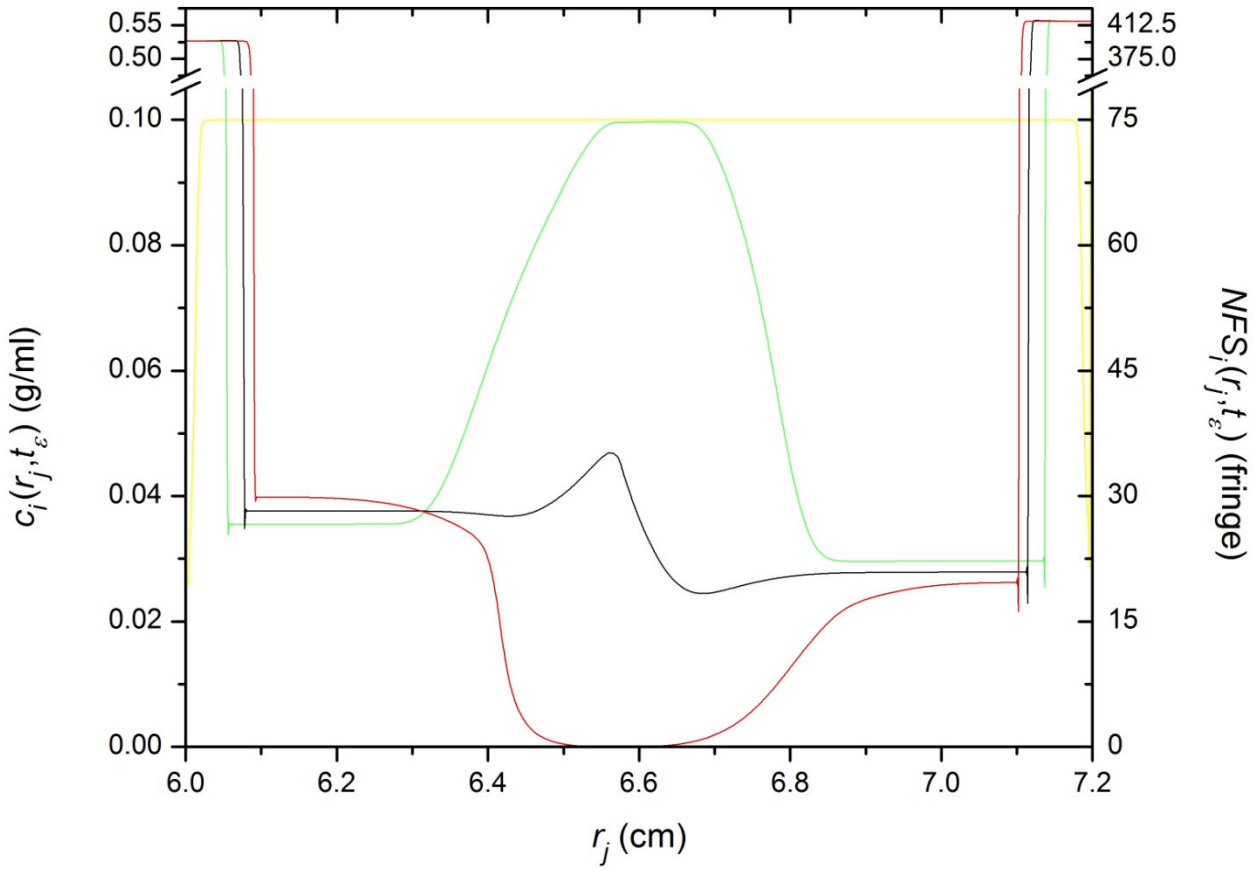

Figure 12. $c_i(r_j,t_\epsilon)$ and $NFS_i(r_j,t_\epsilon)$ versus r_j for $i = 1$ (100% $K_A > 0$, 0% K_A undefined) at t_1 (——), t_{36} (——), t_{51} (——) and t_{66} (——). For all i, at all r_j, $NFS_i(r_j,t_0) = c_i(r_j,t_0)Lk_\lambda = 75$ fringe, where $c_i(r_j,t_0) = 0.1$ g/ml, $L = 0.3$ cm and $k_\lambda = 2{,}500$ fringe/[cm·g/ml]. Treatment group $i = 1$ is one of the two previously described model systems that were contrived to exhibit dramatic Johnston-Ogston effects in AUC simulations (Moody, 2012a), selected data from which were subjected to analysis in a subsequent paper (Moody, 2012b).

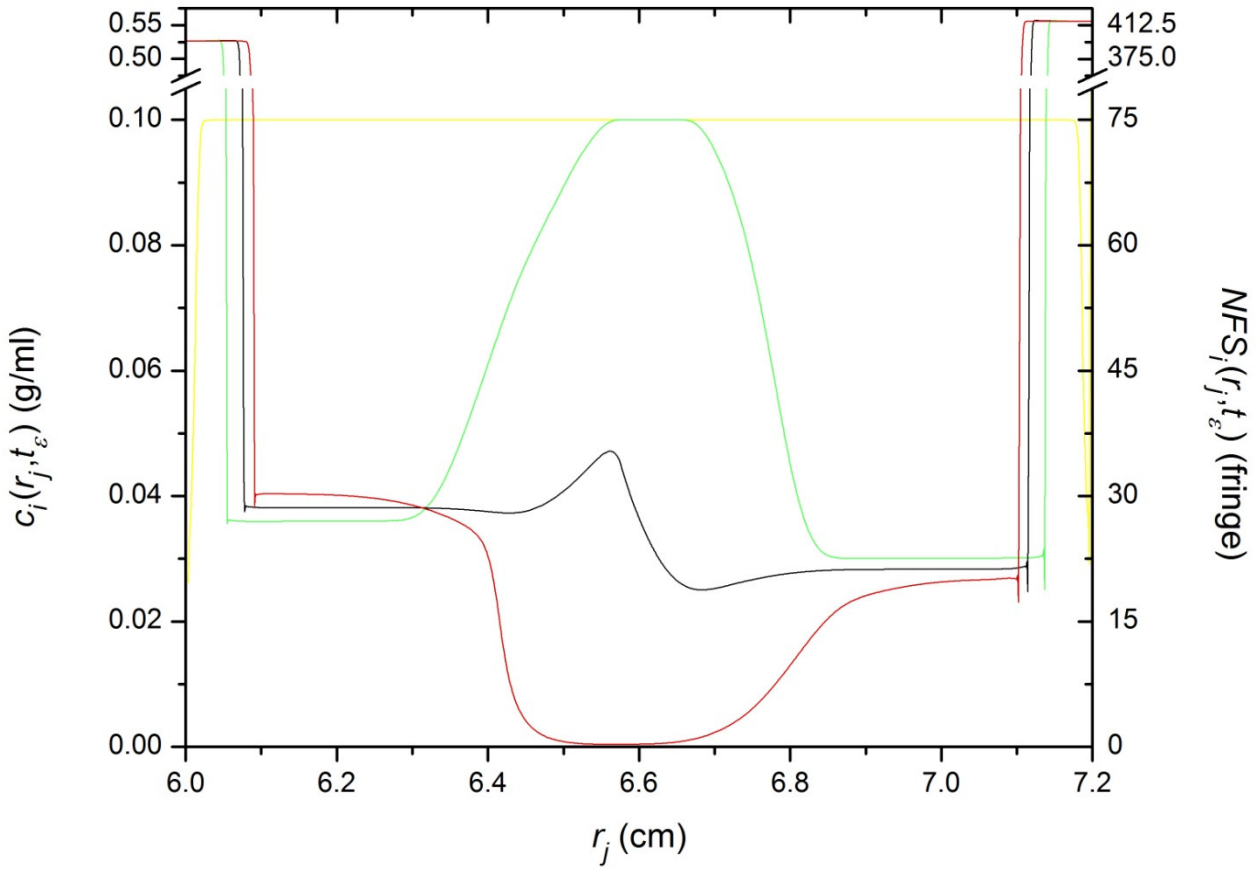

Figure 13. $c_i(r_j,t_\epsilon)$ and $NFS_i(r_j,t_\epsilon)$ versus r_j for $i = 2$ (99% $K_A > 0$, 1% K_A undefined) at t_1 (——), t_{36} (——), t_{51} (——) and t_{66} (——). For all i, at all r_j, $NFS_i(r_j,t_0) = c_i(r_j,t_0)Lk_\lambda = 75$ fringe, where $c_i(r_j,t_0) = 0.1$ g/ml, $L = 0.3$ cm and $k_\lambda = 2{,}500$ fringe/[cm·g/ml].

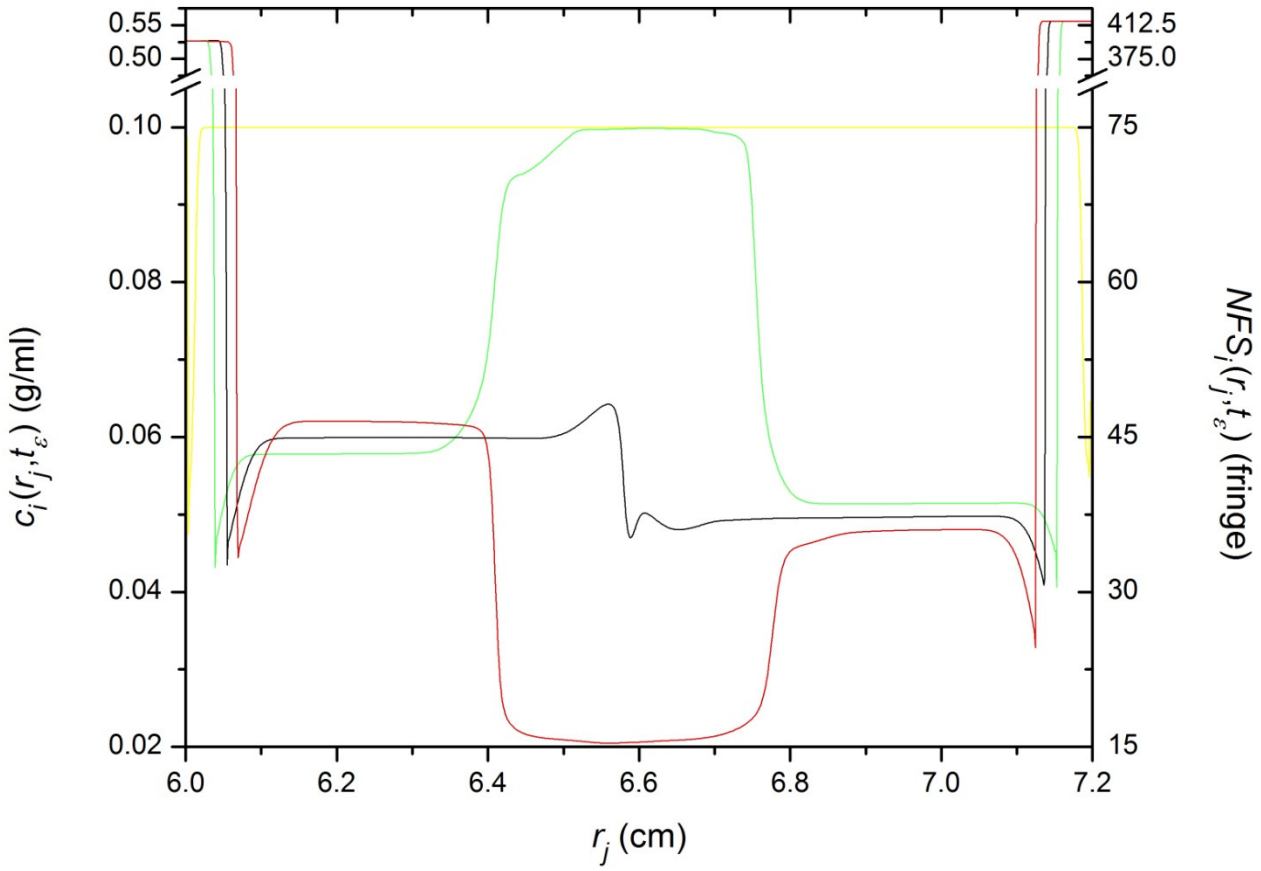

Figure 14. $c_i(r_j,t_\epsilon)$ and $NFS_i(r_j,t_\epsilon)$ versus r_j for $i = 3$ (50% $K_A > 0$, 50% K_A undefined) at t_1 (——), t_{36} (——), t_{51} (——) and t_{66} (——). For all i, at all r_j, $NFS_i(r_j,t_0) = c_i(r_j,t_0)Lk_\lambda = 75$ fringe, where $c_i(r_j,t_0) = 0.1$ g/ml, $L = 0.3$ cm and $k_\lambda = 2{,}500$ fringe/[cm·g/ml].

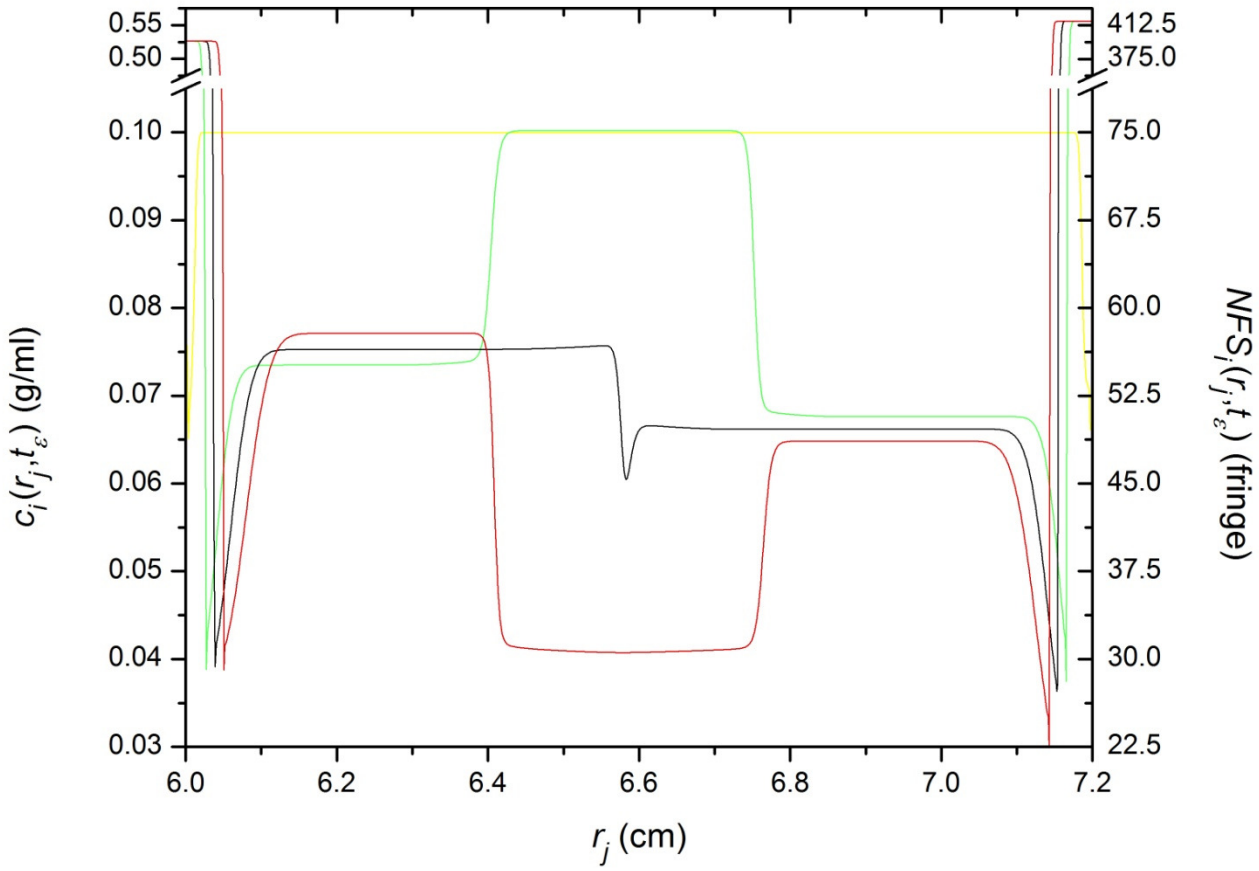

Figure 15. $c_i(r_j,t_\epsilon)$ and $NFS_i(r_j,t_\epsilon)$ versus r_j for $i = 4$ (0% $K_A > 0$, 100% K_A undefined) at t_1 (——), t_{36} (——), t_{51} (——) and t_{66} (——). For all i, at all r_j, $NFS_i(r_j,t_0) = c_i(r_j,t_0)Lk_\lambda = 75$ fringe, where $c_i(r_j,t_0) = 0.1$ g/ml, $L = 0.3$ cm and $k_\lambda = 2{,}500$ fringe/[cm·g/ml]. Treatment group $i = 4$ is one of the two previously described model systems that were contrived to exhibit dramatic Johnston-Ogston effects in AUC simulations (Moody, 2012a), selected data from which were subjected to analysis in a subsequent paper (Moody, 2012b).

For treatment group i at radial position r_j and time t_ϵ, the concentrations of all solute species other than c_H, c_{LH} and c_L is

$$[c_i(r_j, t_\epsilon)]_{low} = \sum_{k=2}^{13} c_k + \sum_{k=15}^{26} c_k,$$

(73)

where, as in the legend of Table 16, $c_H = c_{H-} + c_{H+}$, $c_{LH} = c_{LH-} + c_{LH+}$ and $c_L = c_{L-} + c_{L+}$. Figures 16 to 19 show $[c_i(r_j,t_\epsilon)]_{low}$ versus r for each treatment group at each time chosen for analysis (Table 17). At t_0, for each treatment group, i, $[c_i(r_j,t_0)]_{low} = 0.001$ g/ml at each radial position, r_j.

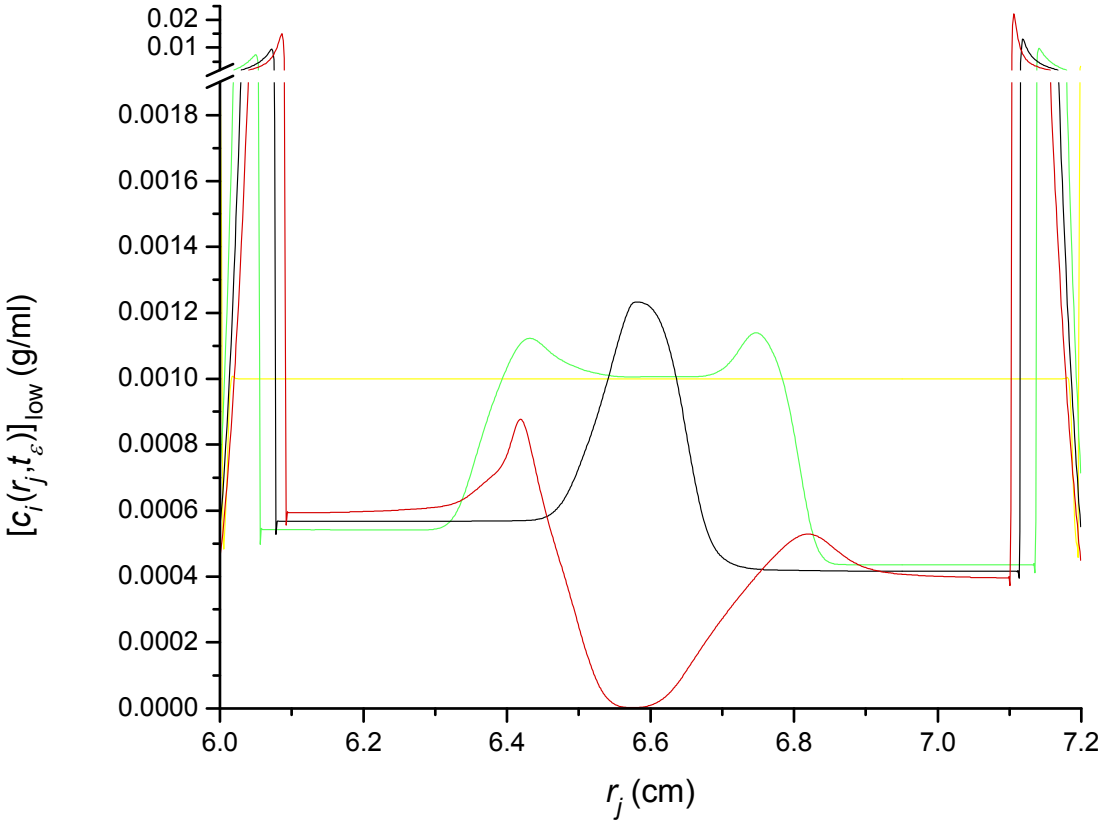

Figure 16. $[c_i(r_j,t_\epsilon)]_{low}$ versus r_j for $i = 1$ (100% $K_A > 0$, 0% K_A undefined) at t_1 (——), t_{36} (——), t_{51} (——) and t_{66} (——). As $[c_i(r_j,t_\epsilon)]_{low}$ (Equation 73) is included within $c_i(r_j,t_\epsilon)$, the data in this figure contribute to the $NMS_i(r_j,t_\epsilon)$ data shown in Figure 12, albeit almost imperceptibly, due to $c_i(r_j,t_\epsilon)$ being dominated by the c_H, c_{LH} and c_L (Tables 15 and 16). This treatment group is one of the two

previously described model systems that were contrived to exhibit dramatic Johnston-Ogston effects in AUC simulations (Moody, 2012a), selected data from which were subjected to analysis in a subsequent paper (Moody, 2012b).

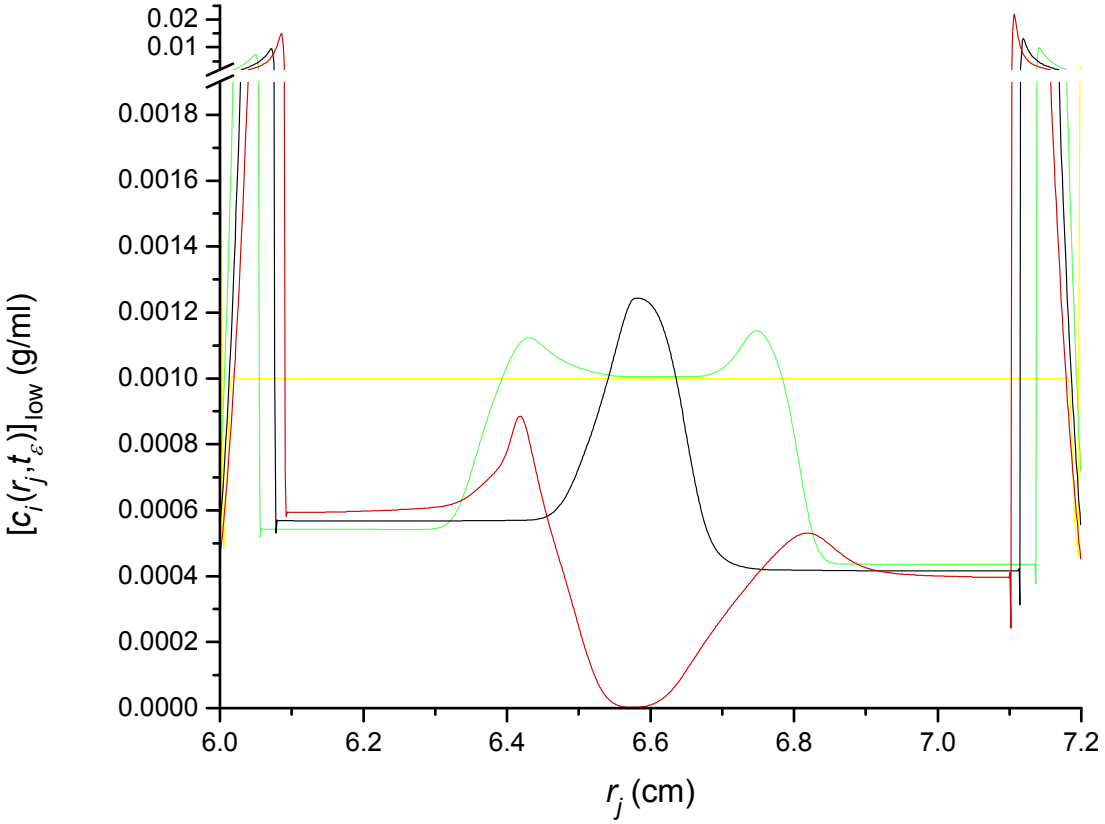

Figure 17. $[c_i(r_j,t_\epsilon)]_{low}$ versus r_j for $i = 2$ (99% $K_A > 0$, 1% K_A undefined) at t_1 (——), t_{36} (——), t_{51} (——) and t_{66} (——). As $[c_i(r_j,t_\epsilon)]_{low}$ (Equation 73) is included within $c_i(r_j,t_\epsilon)$, the data in this figure contribute to the $NMS_i(r_j,t_\epsilon)$ data shown in Figure 13, albeit almost imperceptibly, due to $c_i(r_j,t_\epsilon)$ being dominated by the c_H, c_{LH} and c_L (Tables 15 and 16).

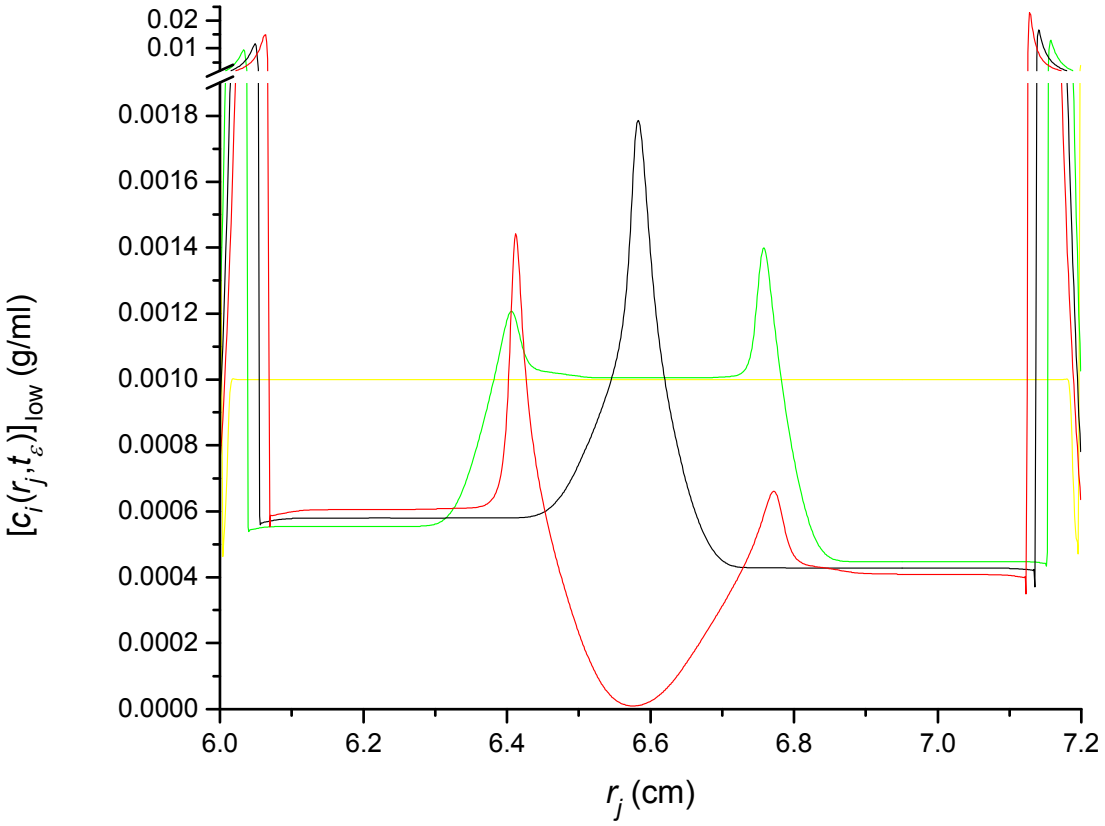

Figure 18. $[c_i(r_j,t_\epsilon)]_{low}$ versus r_j for $i = 3$ (50% $K_A > 0$, 50% K_A undefined) at t_1 (——), t_{36} (——), t_{51} (——) and t_{66} (——). As $[c_i(r_j,t_\epsilon)]_{low}$ (Equation 73) is included within $c_i(r_j,t_\epsilon)$, the data in this figure contribute to the $NMS_i(r_j,t_\epsilon)$ data shown in Figure 14, albeit almost imperceptibly, due to $c_i(r_j,t_\epsilon)$ being dominated by the c_H, c_{LH} and c_L (Tables 15 and 16).

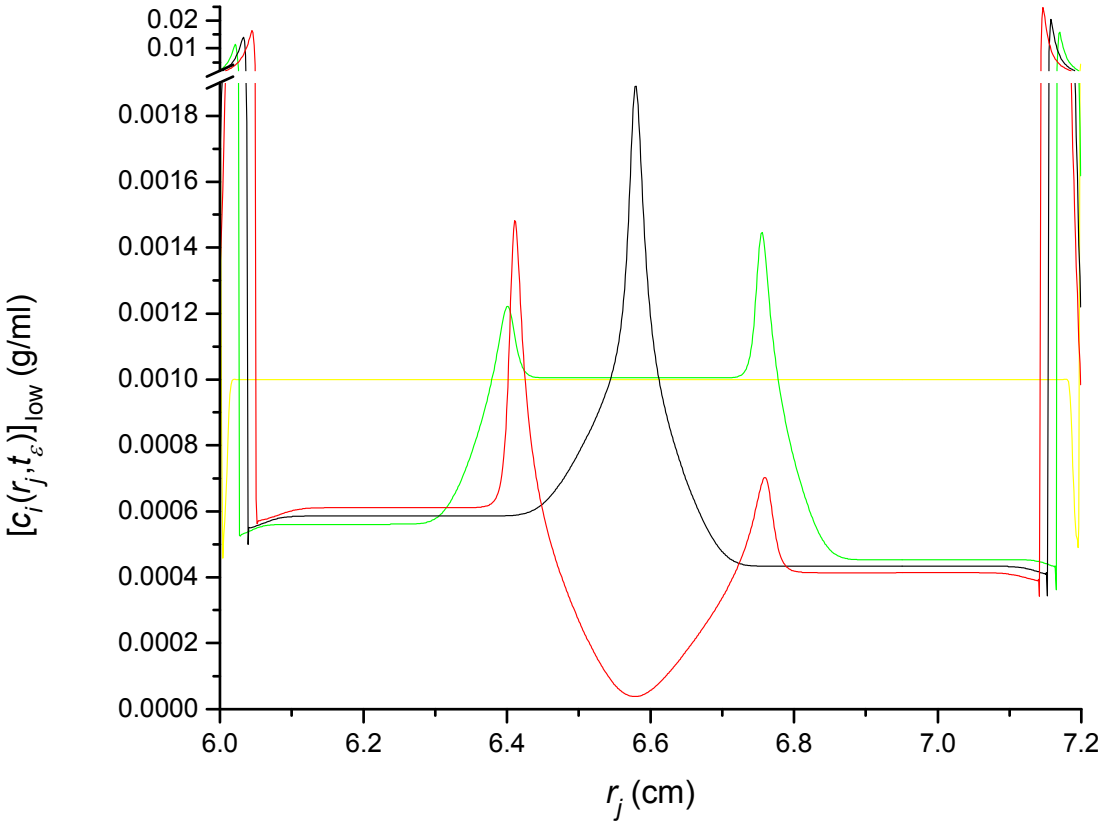

Figure 19. $[c_i(r_j,t_\epsilon)]_{low}$ versus r_j for $i = 4$ (0% $K_A > 0$, 100% K_A undefined) at t_1 (——), t_{36} (——), t_{51} (——) and t_{66} (——). As $[c_i(r_j,t_\epsilon)]_{low}$ (Equation 73) is included within $c_i(r_j,t_\epsilon)$, the data in this figure contribute to the $NMS_i(r_j,t_\epsilon)$ data shown in Figure 15, albeit almost imperceptibly, due to $c_i(r_j,t_\epsilon)$ being dominated by the c_H, c_{LH} and c_L (Tables 15 and 16). This treatment group is one of the two previously described model systems that were contrived to exhibit dramatic Johnston-Ogston effects in AUC simulations (Moody, 2012a), selected data from which were subjected to analysis in a subsequent paper (Moody, 2012b).

That $c_{LH} = c_{LH-} + c_{LH+}$ for $i = 3$ (50% $K_A > 0$, 50% K_A undefined; Figures 14 and 18) is nearer to $c_{LH} = c_{LH-} + c_{LH+}$ for $i = 4$ (0% $K_A > 0$, 100% K_A undefined; Figures 15 and 19) than it is to $c_{LH} = c_{LH-} + c_{LH+}$ for $i = 1$ (100% $K_A > 0$, 0% K_A undefined; Figures 12 and 16) is shown by the much

stronger resemblance Figure 18 (50% $K_A > 0$) bears to Figure 19 (0% $K_A > 0$) than to Figure 16 (100% $K_A > 0$). Evidence of the same is less obviously shown by the stronger resemblance Figure 14 (50% $K_A > 0$) bears to Figure 15 (0% $K_A > 0$) than to Figure 12 (100% $K_A > 0$).

NMS AND DATA TRANSFORMATION

Transformations from r_j and t_ϵ *to* $s^*_{\varphi_\epsilon}$, *from* $Y_i(r_j,t_\epsilon)$ to $Y_i(s^*_{\varphi_\epsilon})$ *and from* $Y_{i,h}(r_j,t_\epsilon)$ to $Y_{i,h}(s^*_{\varphi_\epsilon})$

To provide the greatest possible comparability, for each treatment groups at each time chosen for analysis, the same ranges of $s^*_{\varphi_\epsilon}$ values were, to the closest extent possible, applied to determine the expectation value, $s^*_{i,\epsilon}$, and the observation, $s^*_{i,h,\epsilon}$, for each replicate (Equation 13). By Equation 5, $s^*_{\varphi_\epsilon} = \frac{1}{\omega^2 t_\epsilon} ln\left(\frac{r_j}{r_0}\right)$, where the first N values of the index, φ_ϵ, are given by $\varphi_\epsilon = j$ for $r_0 = r_b > r_j$, and the second N values of the index, φ_ϵ, are given by $\varphi_\epsilon = j + N$ for $r_0 = r_m < r_j$ (Equation 6). As $s^*_{\varphi_\epsilon}$ values depend on both r_j and t_ϵ (Equation 5), and as the r_j values are both discrete (Equation 32) and invariant with t_ϵ, it is not possible to set a range of $s^*_{\varphi_\epsilon}$ to specific values that apply to more than one specific times. Rather, both the values and the full range (Table 18) of all $s^*_{\varphi_\epsilon}$ values vary with time, while the number of $s^*_{\varphi_\epsilon}$ values within a limited range (Table 19) also varies with time.

j	r_j (cm)	φ_ϵ	$s^*_{\varphi_\epsilon}$ (Svedberg); ϵ gives t_ϵ in minutes		
			$s^*_{\varphi_{36}}$	$s^*_{\varphi_{51}}$	$s^*_{\varphi_{66}}$
1	6.00073	1	-21.3665	-15.0822	-11.6545
900	7.19939	900	-0.00100	-0.00070	-0.00054

1	6.00073	901	0.00143	0.00101	0.00078
900	7.19939	1,800	21.3709	15.0853	11.6568

Table 18. The full range, at each time, t_ϵ, of all $s^*_{\varphi_\epsilon}$ values, and, within each such range, the nearest approaches of $s^*_{\varphi_\epsilon}$ to 0 from below and above. The $s^*_{\varphi_\epsilon}$ values are calculated as shown by Equation 5, where, at each time, t_ϵ, each of the $N = 900$ radial positions, r_j, is applied once to the outermost extremum, $r_0 = r_b = 7.12000$ cm, and once to the innermost extremum, $r_0 = r_m = 6.00000$ cm. The $2N$ values of the index φ_ϵ are calculated from N and the index j, as shown by Equation 6. (The first N values of φ_ϵ are equal to j for $r_0 = r_b$, and the second N values of φ_ϵ are equal to $\varphi_\epsilon = j + N$ for $r_0 = r_m$.)

j	r_j (cm)	φ_ϵ	$s^*_{\varphi_\epsilon}$ (Svedberg); ϵ gives t_ϵ in minutes		
			$s^*_{\varphi_{36}}$	$s^*_{\varphi_{51}}$	$s^*_{\varphi_{66}}$
68	6.09820	68	-19.4771	-13.7486	**-10.6239**
234	6.33321	234	-1.50426	**-10.6183**	-8.20504
413	6.57723	413	**-10.6090**	-7.48873	-5.78675
474	6.65835	474	-9.17163	-6.47409	**-5.00271**
565	6.77755	565	-7.09074	**-5.00523**	-3.86768
659	6.89852	659	**-5.01609**	-3.54077	-2.73605
183	6.26195	1083	**5.01117**	3.5373	2.73337
264	6.37476	1164	7.10508	**5.01535**	3.8755
347	6.48833	1247	9.17583	6.47706	**5.00500**
406	6.56786	1306	**10.6046**	7.48558	5.78431

599	6.82155	1499	1.5049	**10.6228**	8.20854
806	7.08356	1706	1.94688	1.37427	**10.6193**
all points within limits			471	668	867

Table 19. Selected $s^*_{\varphi_\epsilon}$ values that, at each time, t_ϵ, lie within the limits applied to the calculation of $s^*_{i,\epsilon}$ and $s^*_{i,h,\epsilon}$ (Equation 13). For each time t_ϵ, the 4 $s^*_{\varphi_\epsilon}$ values shown in bold type are those that most closely approach those limits, and as such, are those values of $s^*_{\varphi_\epsilon}$ that lie just over $s^*_{min<0}$ = -10.625E-13 s, just under $s^*_{max<0}$ = -5E-13 s, just over $s^*_{min>0}$ = 5E-13 s or just under $s^*_{max>0}$ = 10.625E-13 s. Of the 10 $s^*_{\varphi_\epsilon}$ values shown for each time t_ϵ, the 8 that lie between either $s^*_{min<0}$ and $s^*_{max<0}$ or $s^*_{min>0}$ and $s^*_{max>0}$ are highlighted in yellow. For each time, t_ϵ, the number of all points that lie within the limits are highlighted in blue.

By Equation 7, $Y_{i,h}(r_j,t_\epsilon) = NMS_{i,h}(r_j,t_\epsilon)$ - $NMS_{i,h}(r_j,t_\alpha)$, where $t_\alpha = t_1$. The set of all such differences for replicate h of treatment group i is transformed by remapping $Y_{i,h}(r_j,t_\epsilon)$ versus r_j to $Y_{i,h}(s^*_{\varphi_\epsilon})$ versus $s^*_{\varphi_\epsilon}$, where $s^*_{\varphi_\epsilon}$ is calculated from r_j and t_ϵ using Equation 5. The $NFS_i(r_j,t_\epsilon)$ of treatment group i is designated as $NMS_i(r_j,t_\epsilon)$ (Equation 1c), to which the application of Equation 7 yields, absent the subscript h, $Y_i(r_j,t_\epsilon) = NMS_i(r_j,t_\epsilon)$ - $NMS_i(r_j,t_\alpha)$, where, again, $t_\alpha = t_1$. The set of all such differences for treatment group i is transformed by remapping $Y_i(r_j,t_\epsilon)$ versus r_j to $Y_i(s^*_{\varphi_\epsilon})$ versus $s^*_{\varphi_\epsilon}$, where, again, $s^*_{\varphi_\epsilon}$ is calculated from r_j and t_ϵ using Equation 5.

Figures 20 to 23 show $Y_i(s^*_{\varphi_\epsilon})$ versus $s^*_{\varphi_\epsilon}$ and $Y_{i,h}(s^*_{\varphi_\epsilon})$ versus $s^*_{\varphi_\epsilon}$ for treatment groups $i = 1$ to $i = 4$ at t_{36}, t_{51} and t_{66}. (For convenience, t_ϵ is denoted by the time in minutes. To calculate $s^*_{\varphi_\epsilon}$ (Equation 5) in dimensions of seconds, however, t_ϵ (Table 17) must be expressed in seconds.) These figures appear pair-wise, with the first of each pair showing the $Y_i(s^*_{\varphi_\epsilon})$ values obtained

from the noise-free data, and the second first of each pair showing the $Y_{i,h}(s^*_{\varphi_\epsilon})$ values obtained from the noise-modified data.

At each time, t_6, a mask was applied to select the ranges (Table 19) of data used to calculate the expectation value, $s^*_{i,\epsilon}$, and each replicate observation, $s^*_{i,h,\epsilon}$ (Equation 13), of each treatment group, *i*. The dimensionless values of each mask are set equal to 1 at all $s^*_{\varphi_\epsilon}$ within 5E-13 s $< |s^*_{\varphi_\epsilon}| <$ 10.625E-13 s, and are set equal to 0 everywhere else. Such a mask is shown throughout Figures 20 to 23.

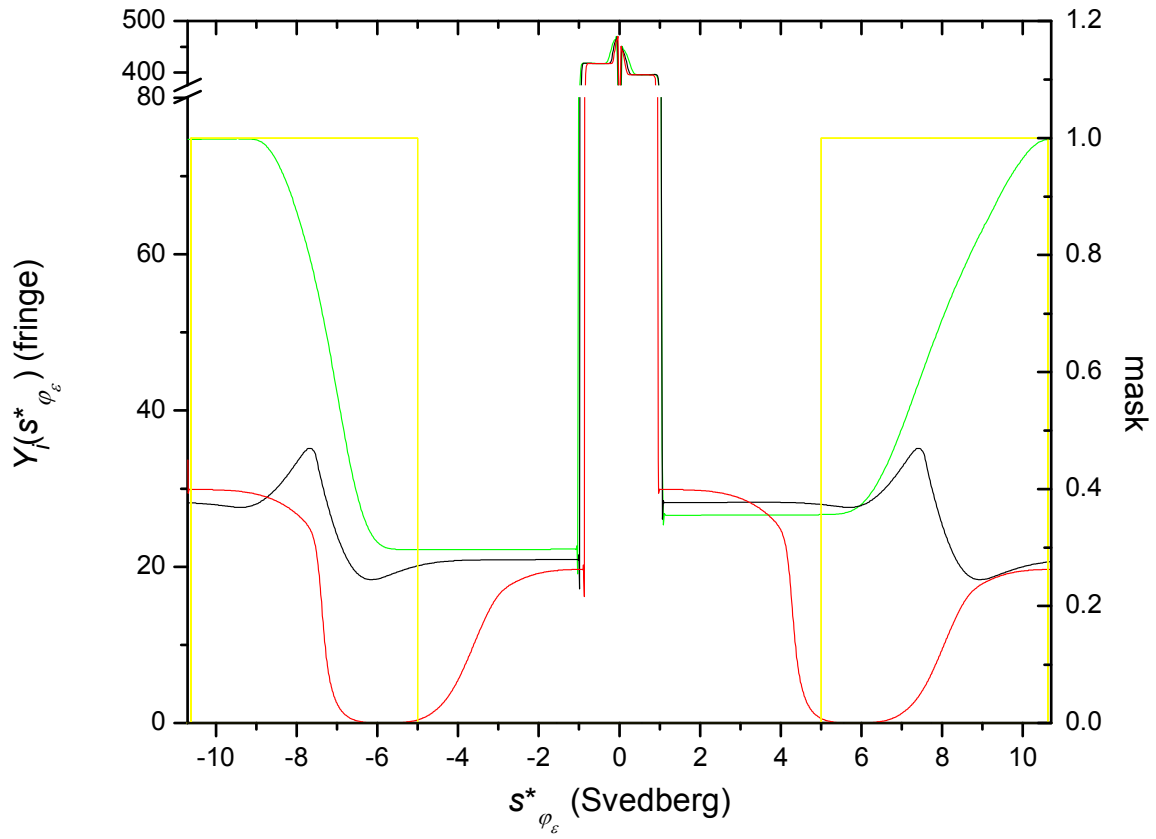

Figure 20a. Noise-free $Y_i(s^*_{\varphi_\epsilon})$ versus $s^*_{\varphi_\epsilon}$ for $i = 1$ (100% $K_A > 0$, 0% K_A undefined) at t_{36} (——), t_{51} (——) and t_{66} (——). For the mask shown (——), the dimensionless values are set equal to 1 at

all $s^*_{\varphi_\epsilon}$ within 5E-13 s < $|s^*_{\varphi_\epsilon}|$ < 10.625E-13 s, and are set equal to 0 everywhere else (Figure 32).

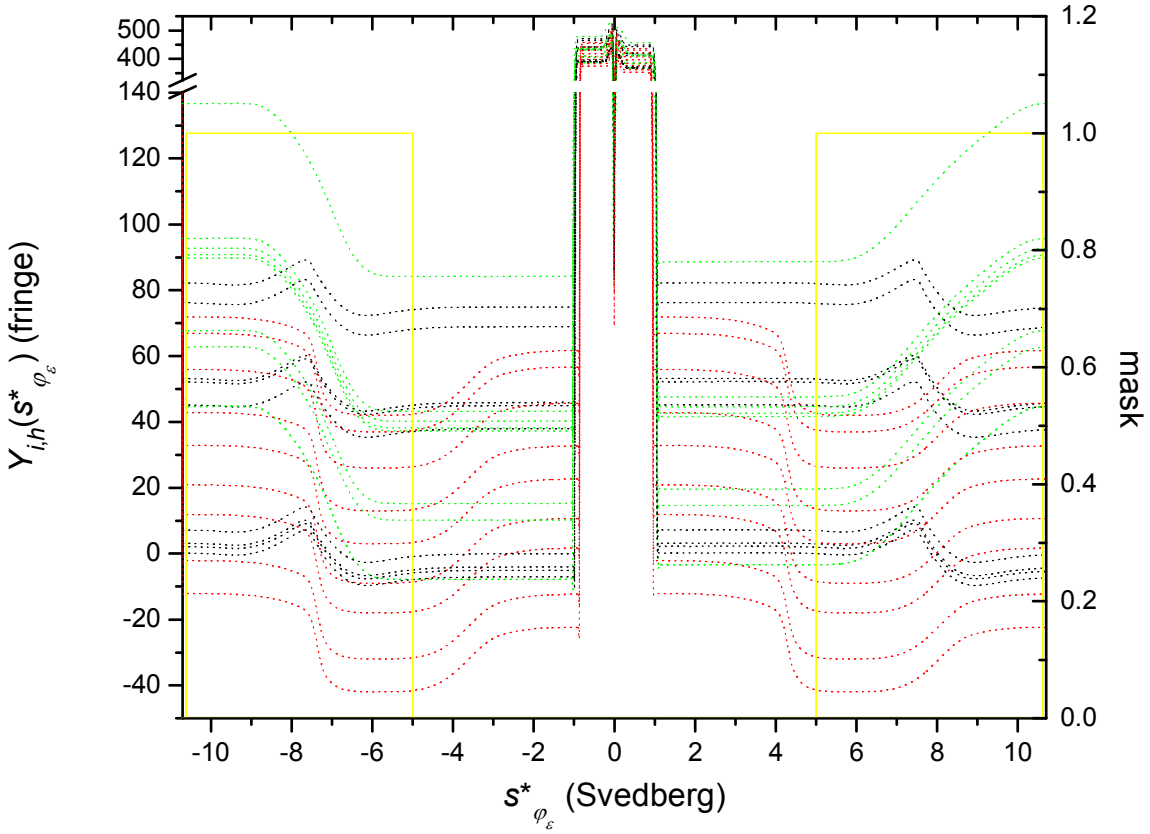

Figure 20b. $Y_{i,h}(s^*_{\varphi_\epsilon})$ versus $s^*_{\varphi_\epsilon}$ for $i = 1$ (100% $K_A > 0$, 0% K_A undefined) and $1 \leq h \leq 9$ at t_{36} (·····), t_{51} (·····) and t_{66} (·····). For the mask shown (——), the dimensionless values are set equal to 1 at all $s^*_{\varphi_\epsilon}$ within 5E-13 s < $|s^*_{\varphi_\epsilon}|$ < 10.625E-13 s, and are set equal to 0 everywhere else (Figure 32).

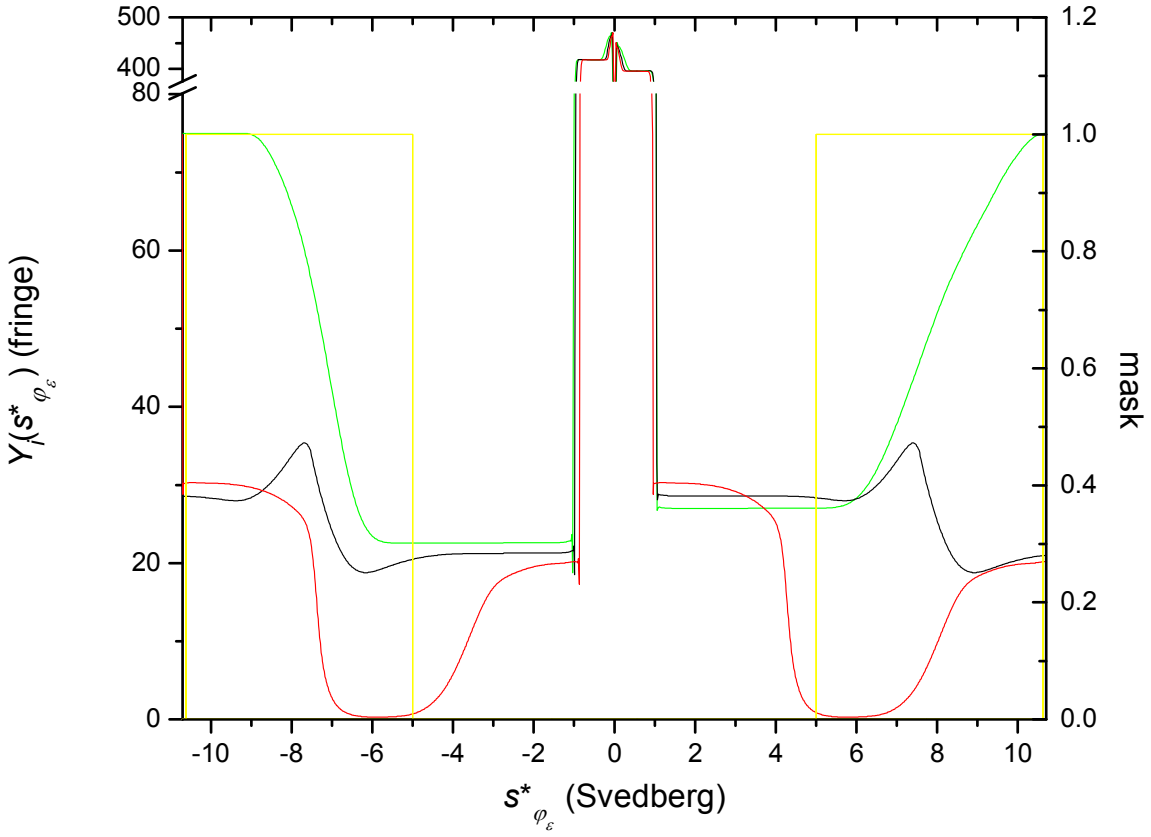

Figure 21a. Noise-free $Y_i(s^*_{\varphi_\epsilon})$ versus $s^*_{\varphi_\epsilon}$ for $i = 2$ (99% $K_A > 0$, 1% K_A undefined) at t_{36} (——), t_{51} (——) and t_{66} (——). For the mask shown (——), the dimensionless values are set equal to 1 at all $s^*_{\varphi_\epsilon}$ within 5E-13 s $< |s^*_{\varphi_\epsilon}| <$ 10.625E-13 s, and are set equal to 0 everywhere else (Figure 32).

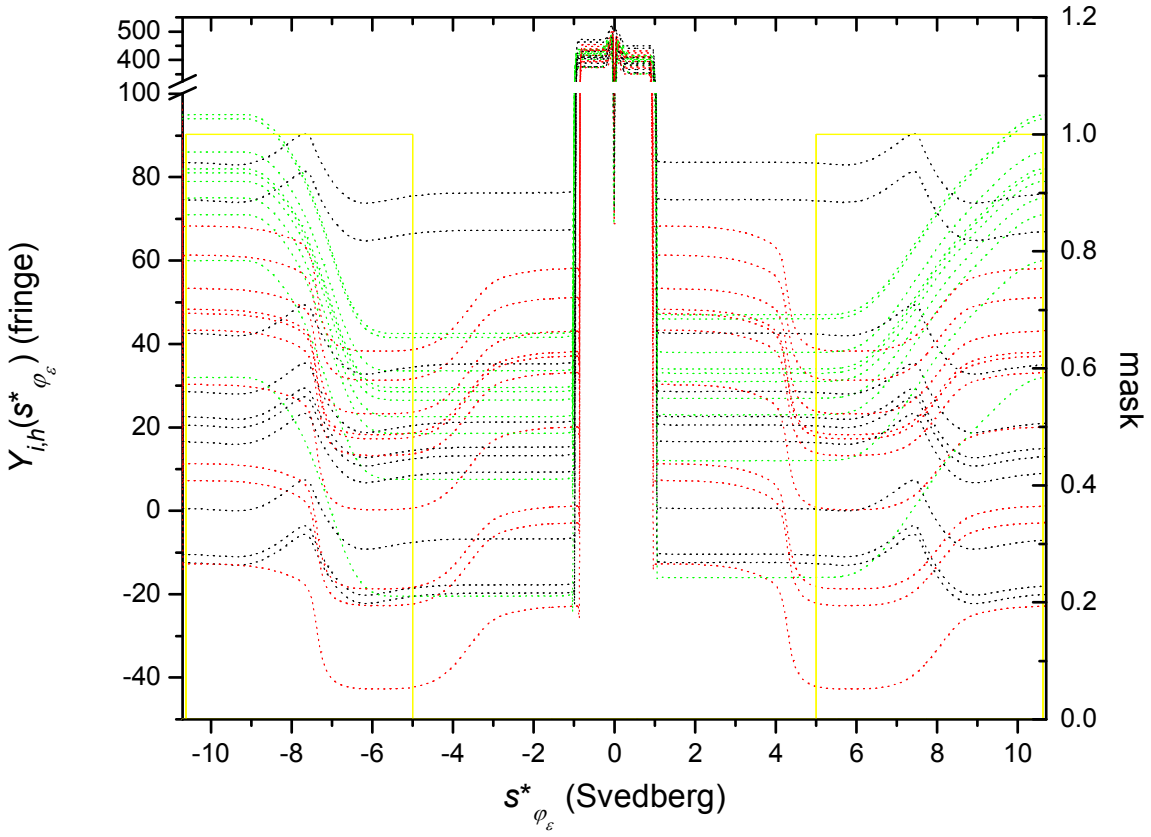

Figure 21b. $Y_{i,h}(s^*_{\varphi_\epsilon})$ versus $s^*_{\varphi_\epsilon}$ for $i = 2$ (99% $K_A > 0$, 1% K_A undefined) and $1 \leq h \leq 9$ at t_{36} (·····), t_{51} (·····) and t_{66} (·····). For the mask shown (——), the dimensionless values are set equal to 1 at all $s^*_{\varphi_\epsilon}$ within 5E-13 s $< \left|s^*_{\varphi_\epsilon}\right| <$ 10.625E-13 s, and are set equal to 0 everywhere else (Figure 32).

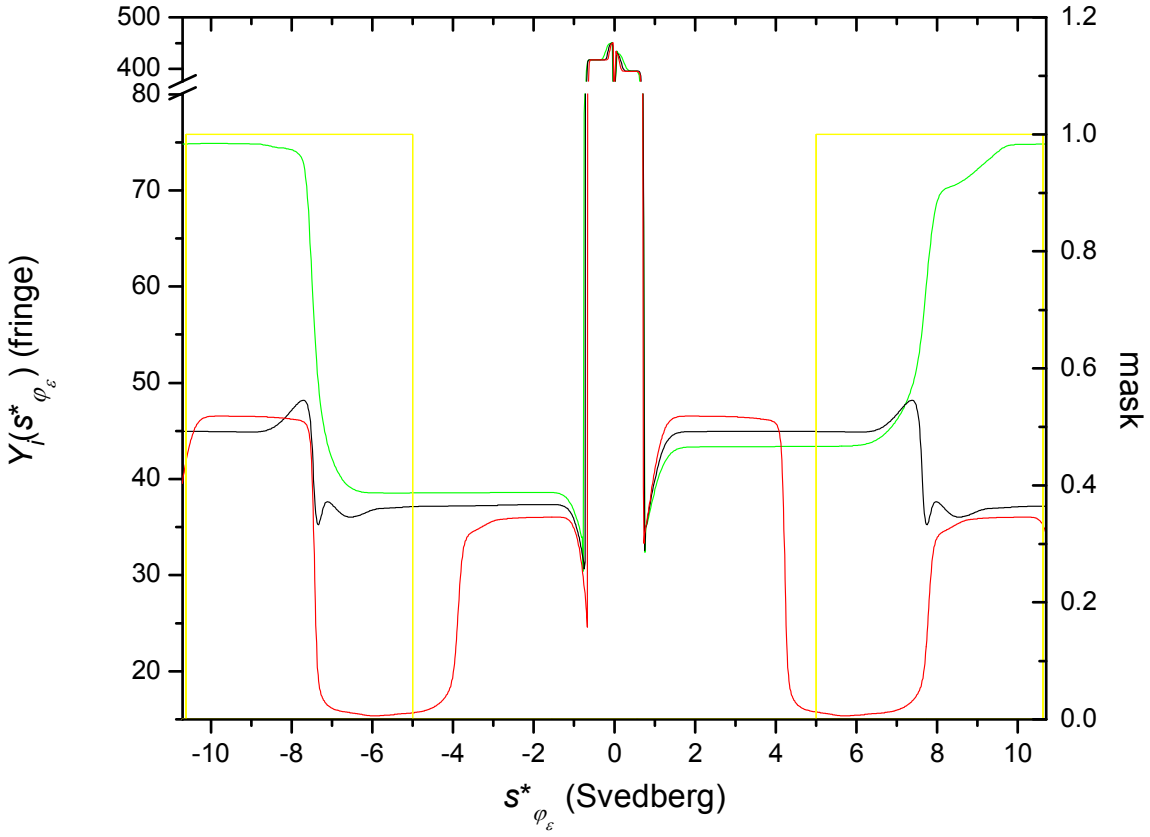

Figure 22a. Noise-free $Y_i(s^*_{\varphi_\epsilon})$ versus $s^*_{\varphi_\epsilon}$ for $i = 3$ (50% $K_A > 0$, 50% K_A undefined) at t_{36} (——), t_{51} (——) and t_{66} (——). For the mask shown (——), the dimensionless values are set equal to 1 at all $s^*_{\varphi_\epsilon}$ within 5E-13 s $< |s^*_{\varphi_\epsilon}| <$ 10.625E-13 s, and are set equal to 0 everywhere else (Figure 32).

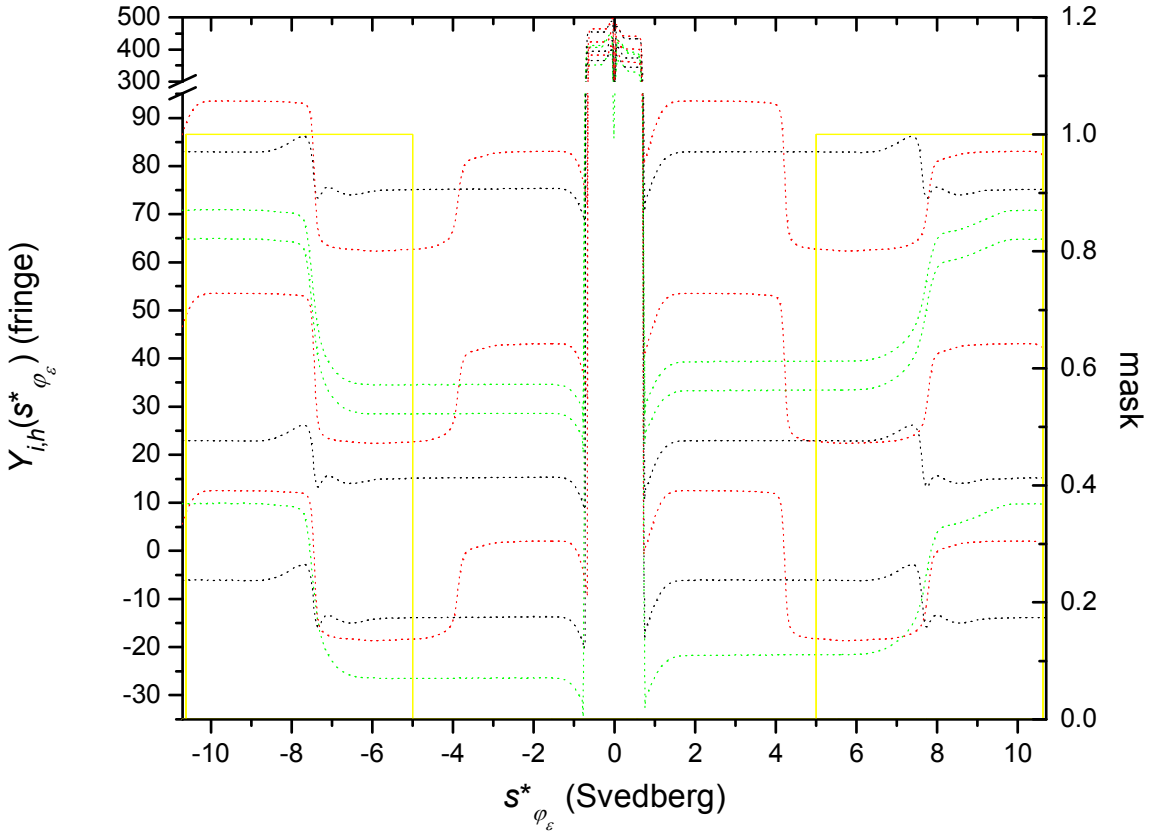

Figure 22b. $Y_{i,h}(s^*_{\varphi_\epsilon})$ versus $s^*_{\varphi_\epsilon}$ for $i = 3$ (50% $K_A > 0$, 50% K_A undefined) and $1 \leq h \leq 3$ at t_{36} (·····), t_{51} (·····) and t_{66} (·····). For the mask shown (——), the dimensionless values are set equal to 1 at all $s^*_{\varphi_\epsilon}$ within 5E-13 s $< \left|s^*_{\varphi_\epsilon}\right| <$ 10.625E-13 s, and are set equal to 0 everywhere else (Figure 32).

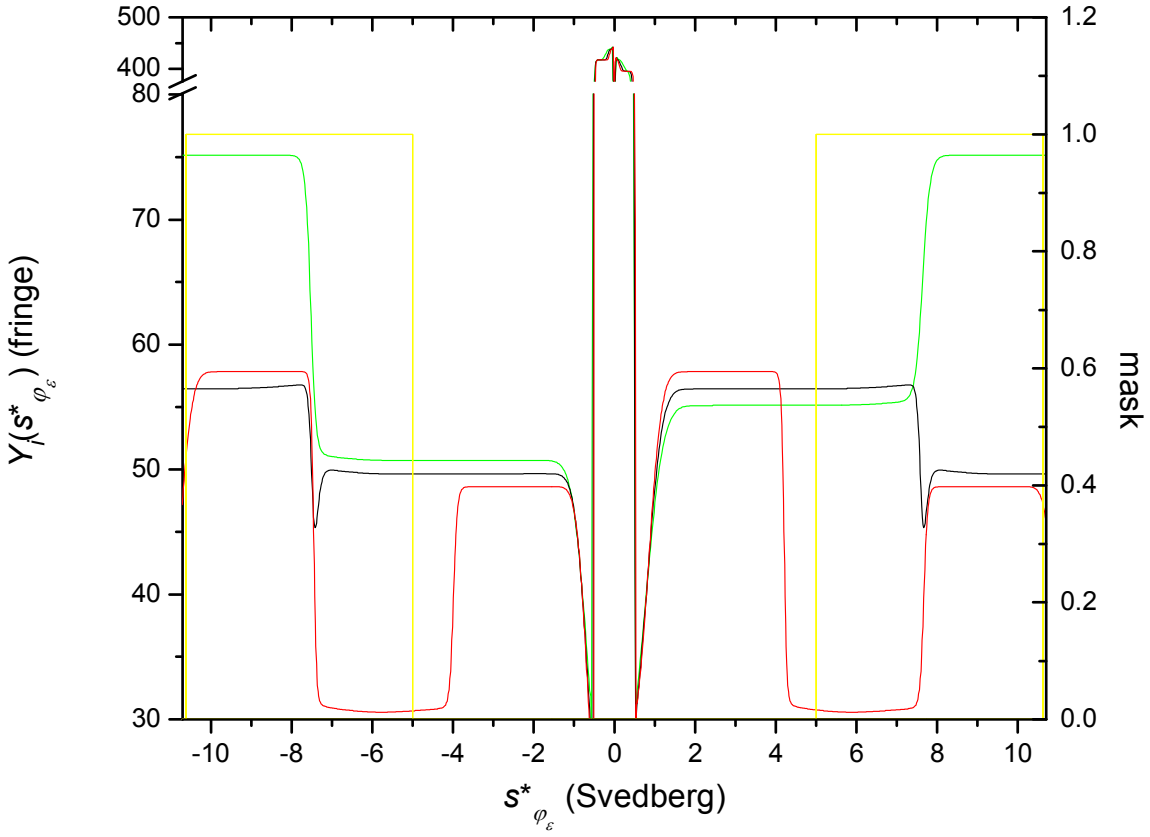

Figure 23a. Noise-free $Y_i(s^*_{\varphi_\epsilon})$ versus $s^*_{\varphi_\epsilon}$ for $i = 4$ (0% $K_A > 0$, 100% K_A undefined) at t_{36} (——), t_{51} (——) and t_{66} (——). For the mask shown (——), the dimensionless values are set equal to 1 at all $s^*_{\varphi_\epsilon}$ within 5E-13 s $< |s^*_{\varphi_\epsilon}| <$ 10.625E-13 s, and are set equal to 0 everywhere else (Figure 32).

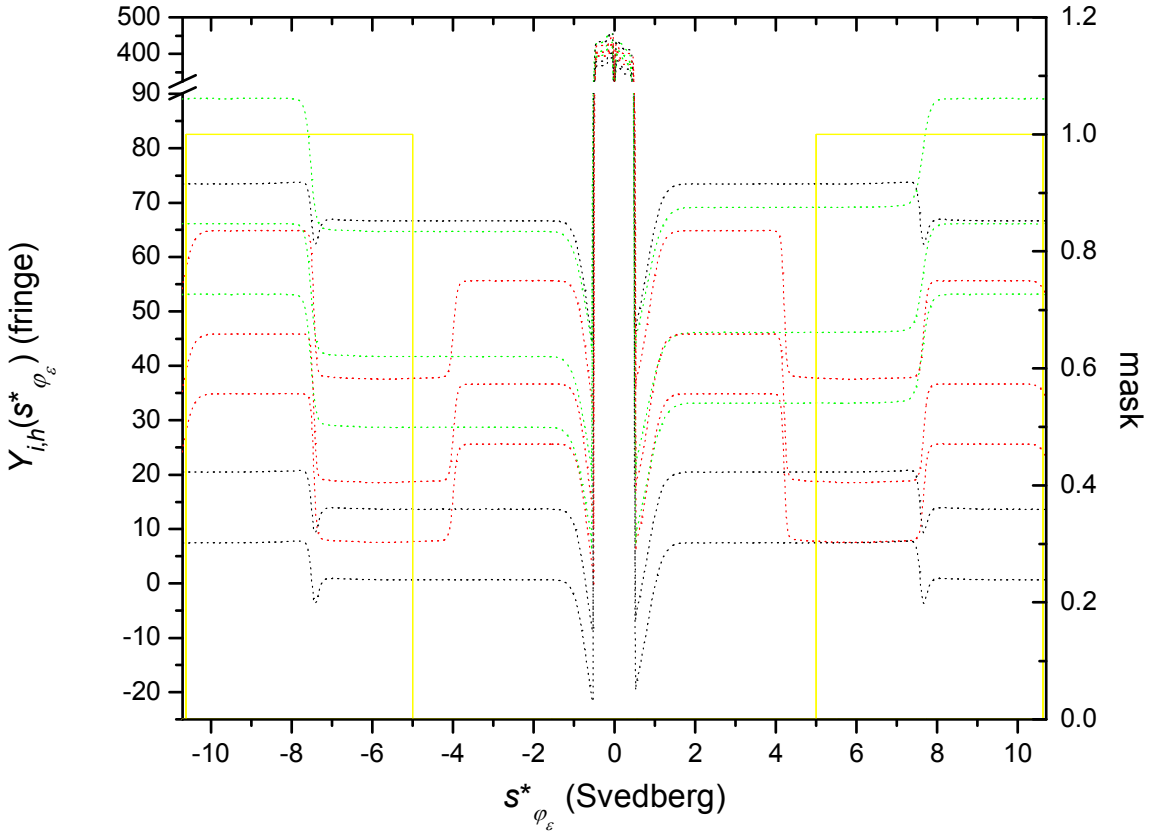

Figure 23b. $Y_{i,h}(s^*_{\varphi_\epsilon})$ versus $s^*_{\varphi_\epsilon}$ for $i = 4$ (0% $K_A > 0$, 100% K_A undefined) and $1 \leq h \leq 3$ at t_{36} (·····), t_{51} (·····) and t_{66} (·····). For the mask shown (——), the dimensionless values are set equal to 1 at all $s^*_{\varphi_\epsilon}$ within 5E-13 s $< \left|s^*_{\varphi_\epsilon}\right| <$ 10.625E-13 s, and are set equal to 0 everywhere else (Figure 32).

DATA ANALYSIS: APPLICATION

The derivative of the signal with respect to $s^*_{\varphi_\epsilon}$ *(Equation 8):* $\left(\frac{\partial Y_{i,h}(s^*_{\varphi_\epsilon})}{\partial s^*_{\varphi_\epsilon}}\right)_t$

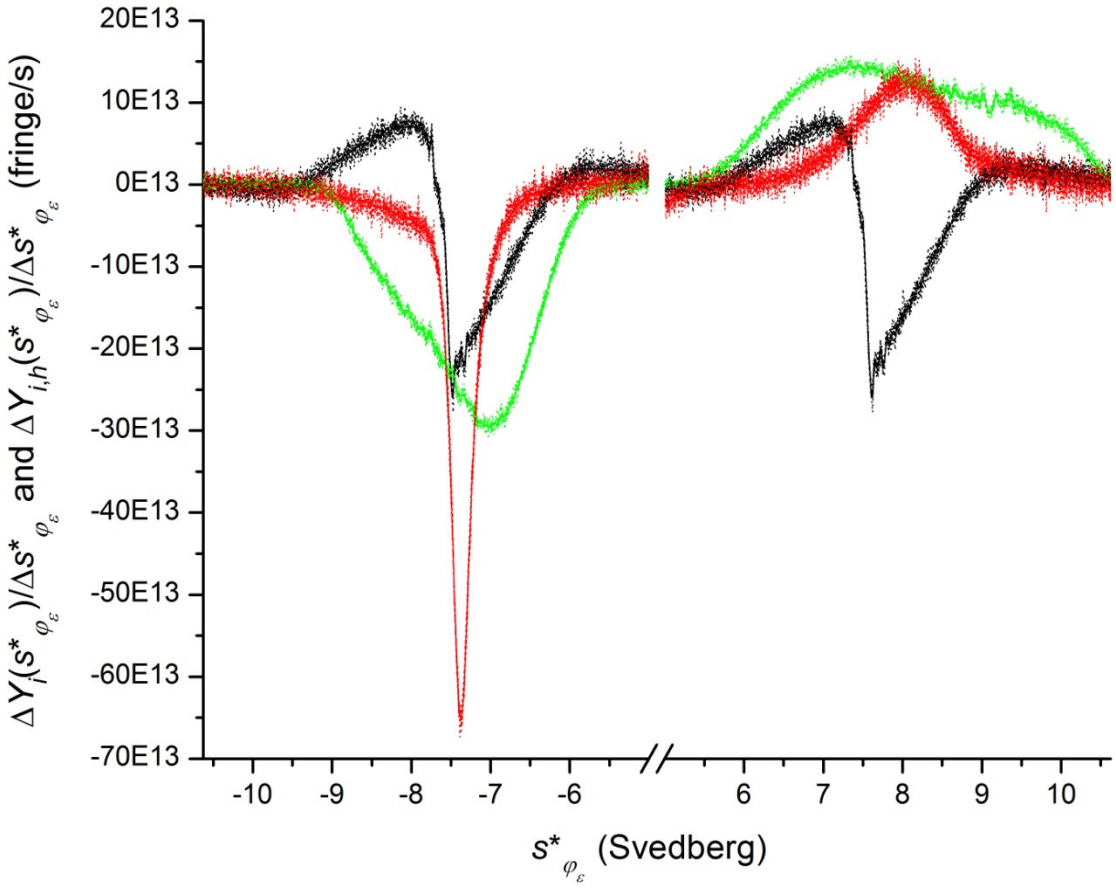

Figure 24. For $i = 1$ (100% $K_A > 0$, 0% K_A undefined), $\left(\frac{\partial Y_i(s^*_{\varphi\epsilon})}{\partial s^*_{\varphi\epsilon}}\right)_t$ at t_{36} (——), t_{51} (——) and t_{66} (——), along with $\left(\frac{\partial Y_{i,h}(s^*_{\varphi\epsilon})}{\partial s^*_{\varphi\epsilon}}\right)_t$ for each replicate ($1 \leq h \leq 9$) at t_{36} (·····), t_{51} (·····) and t_{66} (·····), all plotted against $s^*_{\varphi_\epsilon}$ restricted to the regions (5E-13 s $< \left|s^*_{\varphi_\epsilon}\right| <$ 10.625E-13 s) in which the mask shown in Figure 20 is equal to 1.

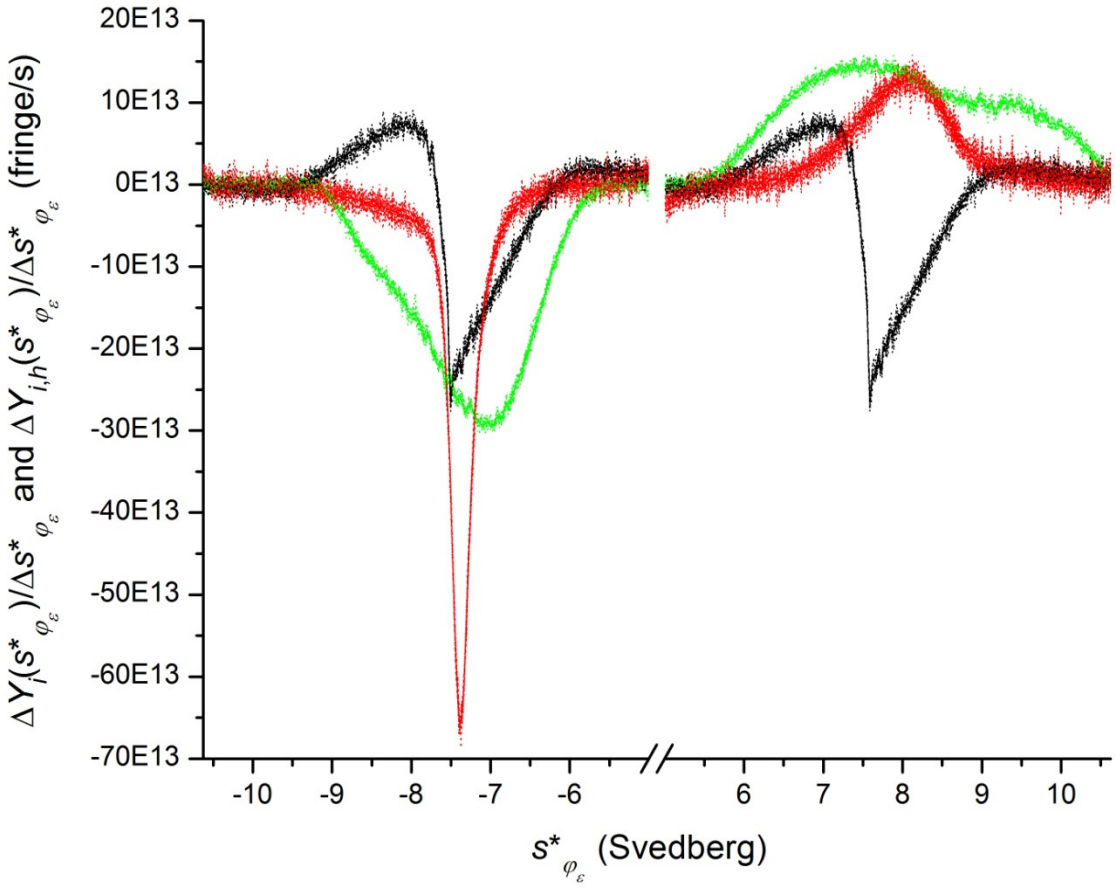

Figure 25. For $i = 2$ (99% $K_A > 0$, 1% K_A undefined), $\left(\frac{\partial Y_i(s^*_{\varphi\epsilon})}{\partial s^*_{\varphi\epsilon}}\right)_t$ at t_{36} (——), t_{51} (——) and t_{66} (——), along with $\left(\frac{\partial Y_{i,h}(s^*_{\varphi\epsilon})}{\partial s^*_{\varphi\epsilon}}\right)_t$ for each replicate ($1 \le h \le 9$) at t_{36} (·····), t_{51} (·····) and t_{66} (·····), all plotted against $s^*_{\varphi_\epsilon}$ restricted to the regions (5E-13 s $< \left|s^*_{\varphi_\epsilon}\right| <$ 10.625E-13 s) in which the mask shown in Figure 21 is equal to 1.

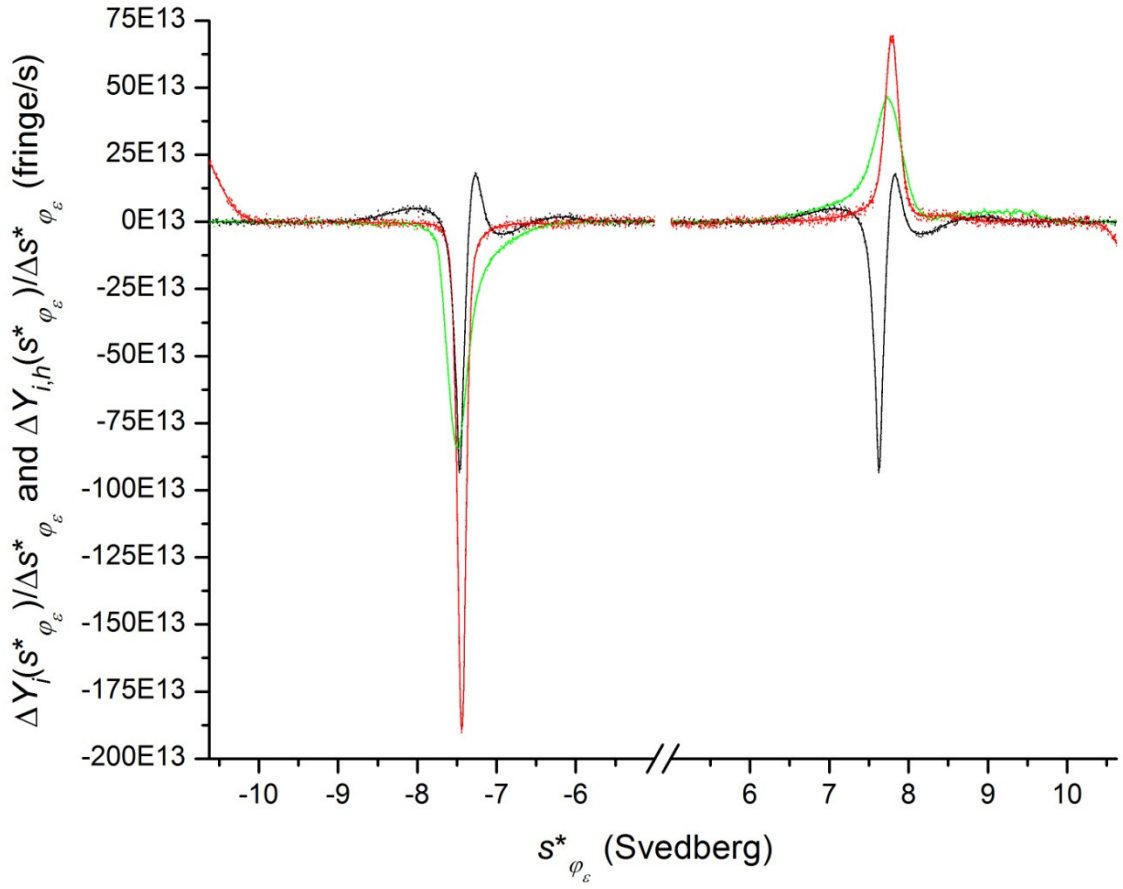

Figure 26. For $i = 3$ (50% $K_A > 0$, 50% K_A undefined), $\left(\frac{\partial Y_i(s^*_{\varphi\epsilon})}{\partial s^*_{\varphi\epsilon}}\right)_t$ at t_{36} (——), t_{51} (——) and t_{66} (——), along with $\left(\frac{\partial Y_{i,h}(s^*_{\varphi\epsilon})}{\partial s^*_{\varphi\epsilon}}\right)_t$ for each replicate ($1 \le h \le 3$) at t_{36} (·····), t_{51} (·····) and t_{66} (·····), all plotted against $s^*_{\varphi_\epsilon}$ restricted to the regions (5E-13 s $< \left|s^*_{\varphi_\epsilon}\right| <$ 10.625E-13 s) in which the mask shown in Figure 22 is equal to 1.

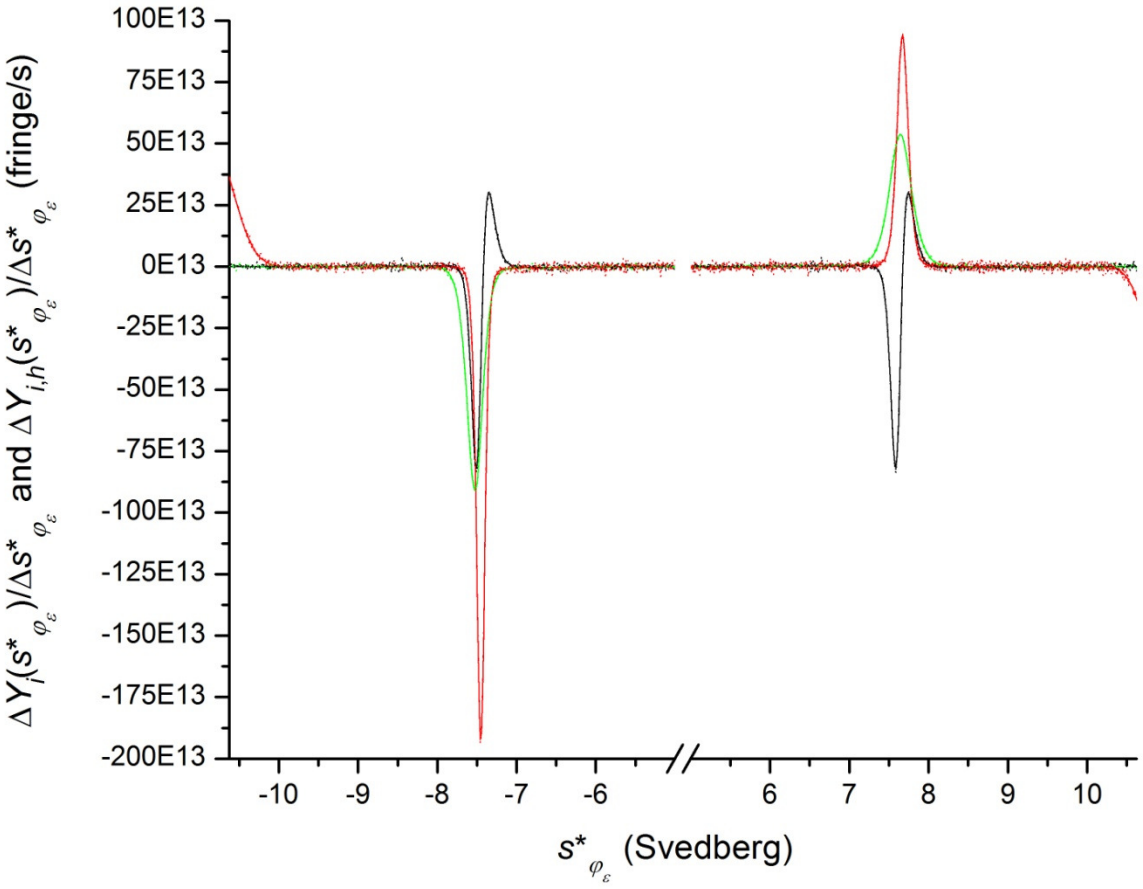

Figure 27. For $i = 4$ (0% $K_A > 0$, 100% K_A undefined), $\left(\frac{\partial Y_i(s^*_{\varphi\epsilon})}{\partial s^*_{\varphi\epsilon}}\right)_t$ at t_{36} (——), t_{51} (——) and t_{66} (——), along with $\left(\frac{\partial Y_{i,h}(s^*_{\varphi\epsilon})}{\partial s^*_{\varphi\epsilon}}\right)_t$ for each replicate ($1 \le h \le 3$) at t_{36} (·····), t_{51} (·····) and t_{66} (·····), all plotted against $s^*_{\varphi_\epsilon}$ restricted to the regions (5E-13 s $< \left|s^*_{\varphi_\epsilon}\right| <$ 10.625E-13 s) in which the mask shown in Figure 23 is equal to 1.

The nonredundant derivative (Equation 9): $q_{i,h}(s^*_{\varphi_\epsilon}) = \left(\frac{\partial Y_{i,h}(s^*_{\varphi\epsilon})}{\partial s^*_{\varphi\epsilon}}\right)_t - e_{i,h}(s^*_{\varphi_\epsilon})$

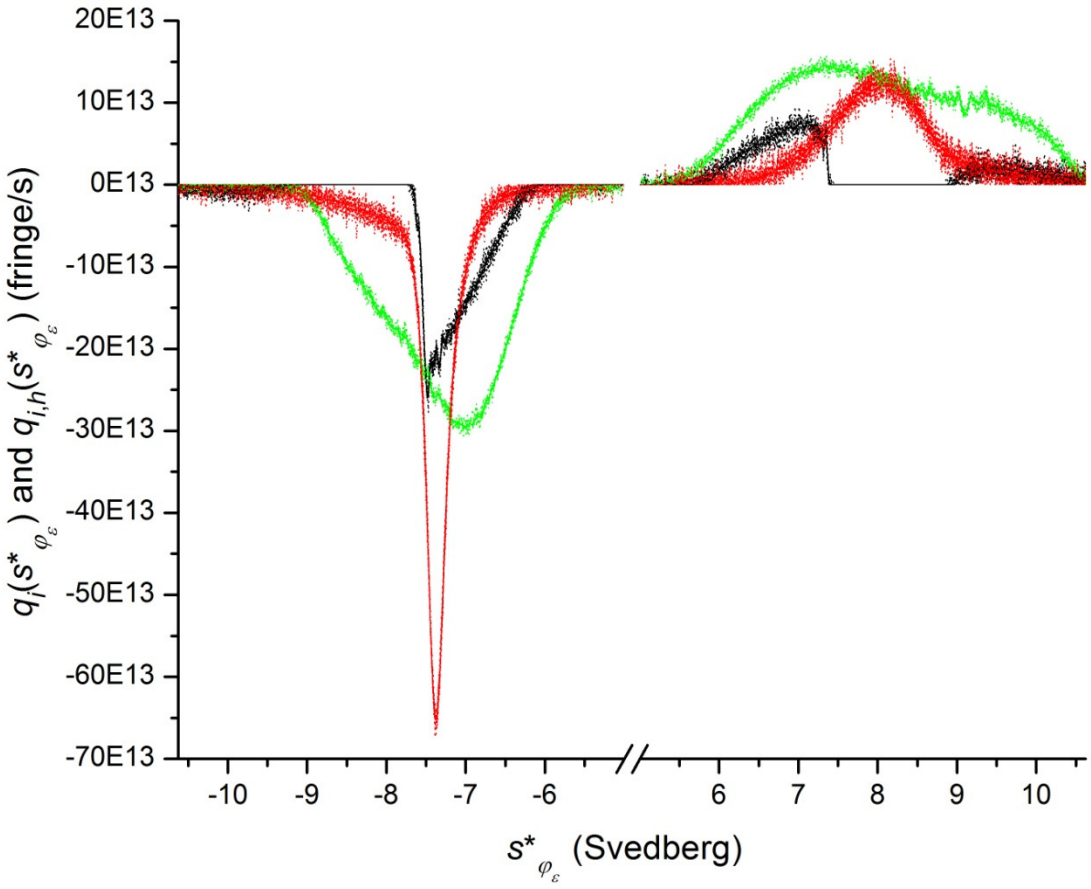

Figure 28. For $i = 1$ (100% $K_A > 0$, 0% K_A undefined), $q_i\left(s^*_{\varphi_\epsilon}\right)$ at t_{36} (——), t_{51} (——) and t_{66} (——), along with $q_{i,h}\left(s^*_{\varphi_\epsilon}\right)$ for each replicate ($1 \leq h \leq 9$) at t_{36} (·····), t_{51} (·····) and t_{66} (·····), all plotted against $s^*_{\varphi_\epsilon}$ restricted to the regions (5E-13 s $< \left|s^*_{\varphi_\epsilon}\right| <$ 10.625E-13 s) in which the mask shown in Figure 20 is equal to 1.

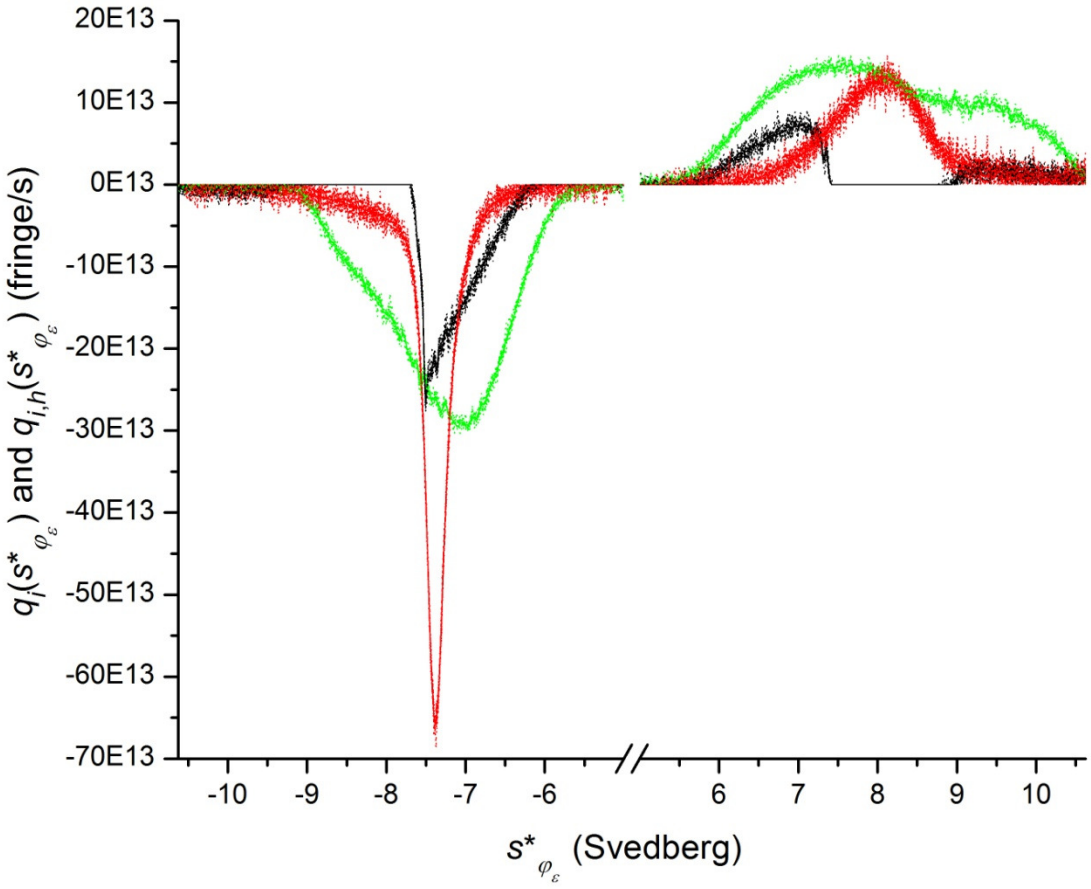

Figure 29. For $i = 2$ (99% $K_A > 0$, 1% K_A undefined), $q_i\left(s^*_{\varphi_\epsilon}\right)$ at t_{36} (——), t_{51} (——) and t_{66} (——), along with $q_{i,h}\left(s^*_{\varphi_\epsilon}\right)$ for each replicate ($1 \leq h \leq 9$) at t_{36} (·····), t_{51} (·····) and t_{66} (·····), all plotted against $s^*_{\varphi_\epsilon}$ restricted to the regions (5E-13 s $< \left|s^*_{\varphi_\epsilon}\right| <$ 10.625E-13 s) in which the mask shown in Figure 21 is equal to 1.

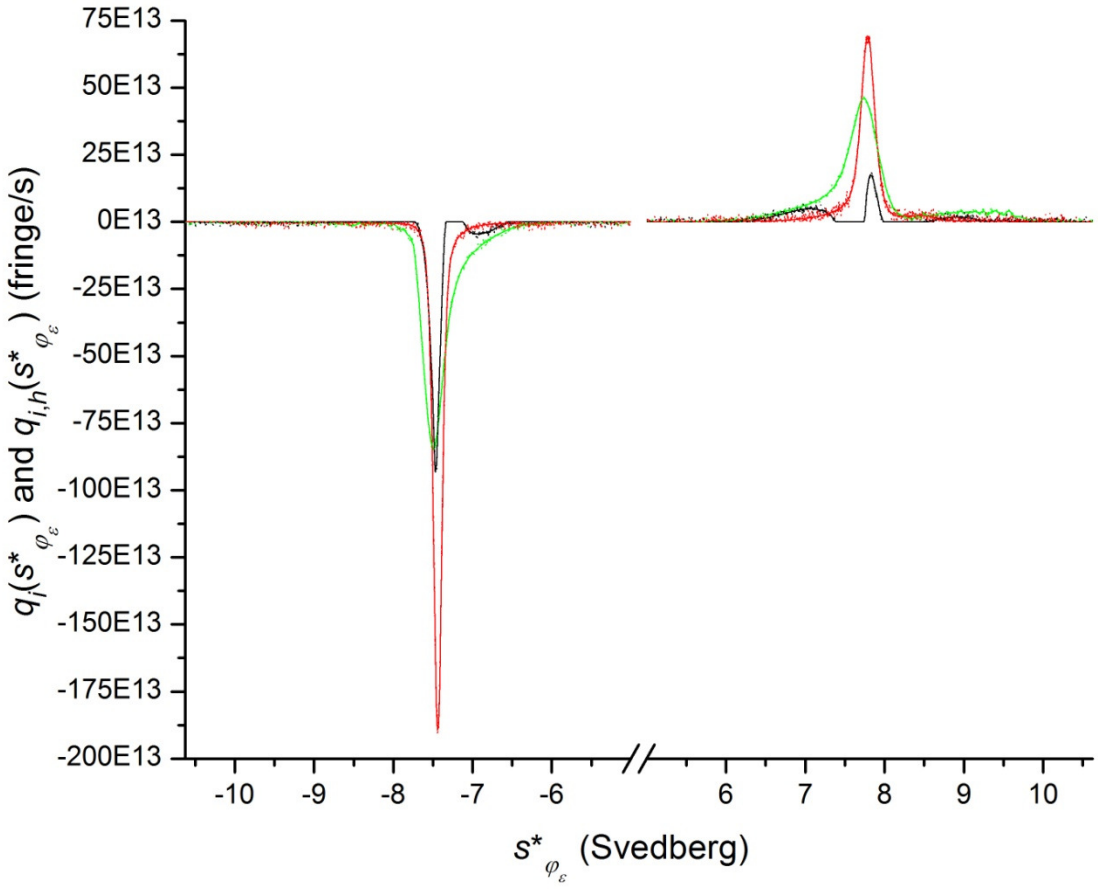

Figure 30. For $i = 3$ (50% $K_A > 0$, 50% K_A undefined), $q_i\left(s^*_{\varphi_\epsilon}\right)$ at t_{36} (——), t_{51} (——) and t_{66} (——), along with $q_{i,h}\left(s^*_{\varphi_\epsilon}\right)$ for each replicate ($1 \leq h \leq 3$) at t_{36} (·····), t_{51} (·····) and t_{66} (·····), all plotted against $s^*_{\varphi_\epsilon}$ restricted to the regions (5E-13 s $< \left|s^*_{\varphi_\epsilon}\right| <$ 10.625E-13 s) in which the mask shown in Figure 22 is equal to 1.

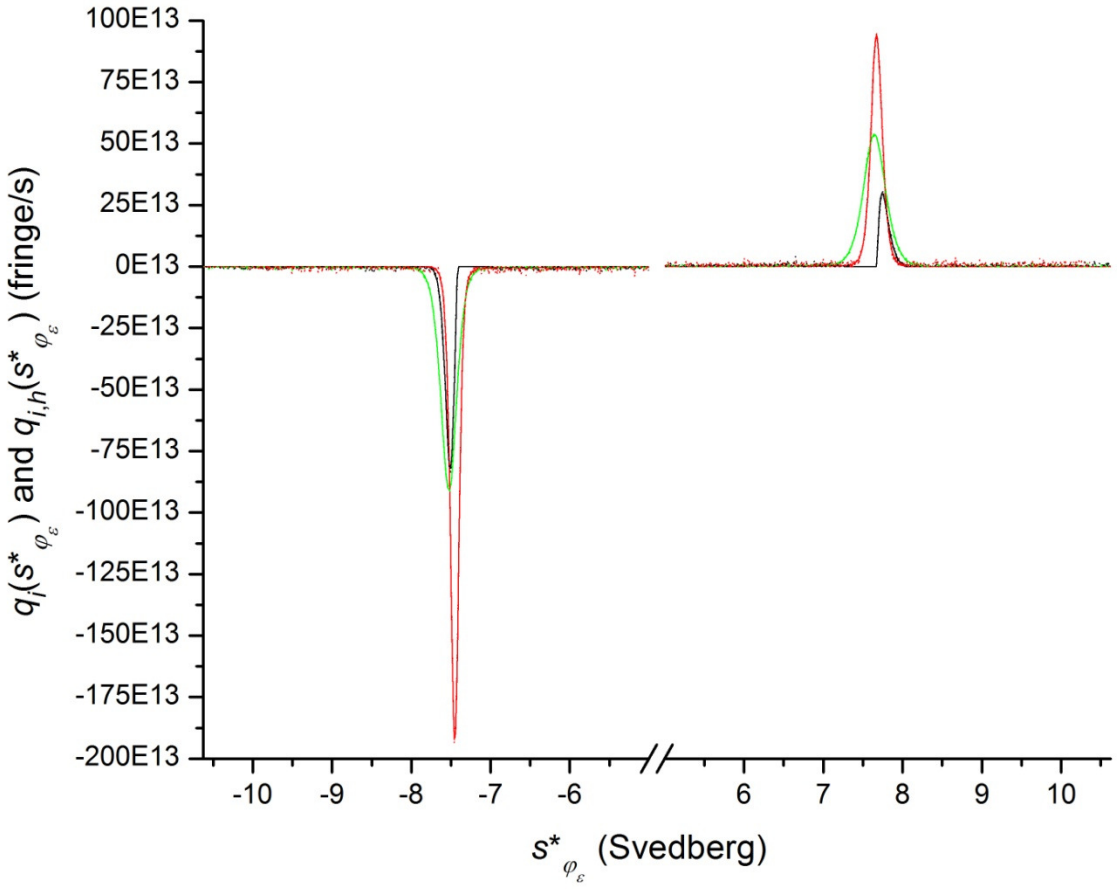

Figure 31. For $i = 4$ (0% $K_A > 0$, 100% K_A undefined), $q_i\left(s^*_{\varphi_\epsilon}\right)$ at t_{36} (——), t_{51} (——) and t_{66} (——), along with $q_{i,h}\left(s^*_{\varphi_\epsilon}\right)$ for each replicate ($1 \leq h \leq 3$) at t_{36} (·····), t_{51} (·····) and t_{66} (·····), all plotted against $s^*_{\varphi_\epsilon}$ restricted to the regions (5E-13 s $< \left|s^*_{\varphi_\epsilon}\right| <$ 10.625E-13 s) in which the mask shown in Figure 23 is equal to 1.

The time-corrected distribution function (Equation 10): $g_{i,h}\left(s^*_{\varphi_\epsilon}\right) = q_{i,h}\left(s^*_{\varphi_\epsilon}\right)\left(e^{2s^*_{\varphi_\epsilon}\omega^2 t_\epsilon}\right)$

At any given $s^*_{\varphi_\epsilon}$ value, the dimensionless factor $e^{2s^*_{\varphi_\epsilon}\omega^2 t_\epsilon}$ (Equation 10; Figure 32) increasingly diverges from 1 with increasing time, except at $s^*_{\varphi_\epsilon} = 0$ s, where $e^{2s^*_{\varphi_\epsilon}\omega^2 t_\epsilon}$ is always equal to 1.

Using Equation 5 to substitute for $s^*_{\varphi_\epsilon}$,

$$e^{2s^*_{\varphi_\epsilon}\omega^2 t_\epsilon} = e^{2ln\left(\frac{r_j}{r_0}\right)} = \left(\frac{r_j}{r_0}\right)^2 = \begin{Bmatrix} \left(\frac{r_j}{r_b}\right)^2 \; for\; r_j \; < r_0 \\ \left(\frac{r_j}{r_m}\right)^2 \; for\; r_j \; > r_0 \end{Bmatrix}$$

(74)

is obtained, where r_0 is equal either to its maximum value of r_b or its minimum value of r_m. Thus, at each time, $t_\epsilon > 0$, as $s^*_{\varphi_\epsilon}$ decreases from 0 toward its time-dependent minimum value of $\frac{1}{\omega^2 t_\epsilon} ln\left(\frac{r_m}{r_b}\right)$, $e^{2s^*_{\varphi_\epsilon}\omega^2 t_\epsilon}$ decreases from 1 toward its time-independent minimum value of $\left(\frac{r_m}{r_b}\right)^2$, while as $s^*_{\varphi_\epsilon}$ increases from 0 toward its time-dependent maximum value of $\frac{1}{\omega^2 t_\epsilon} ln\left(\frac{r_b}{r_m}\right)$, $e^{2s^*_{\varphi_\epsilon}\omega^2 t_\epsilon}$ increases from 1 toward its time-independent maximum value of $\left(\frac{r_b}{r_m}\right)^2$.

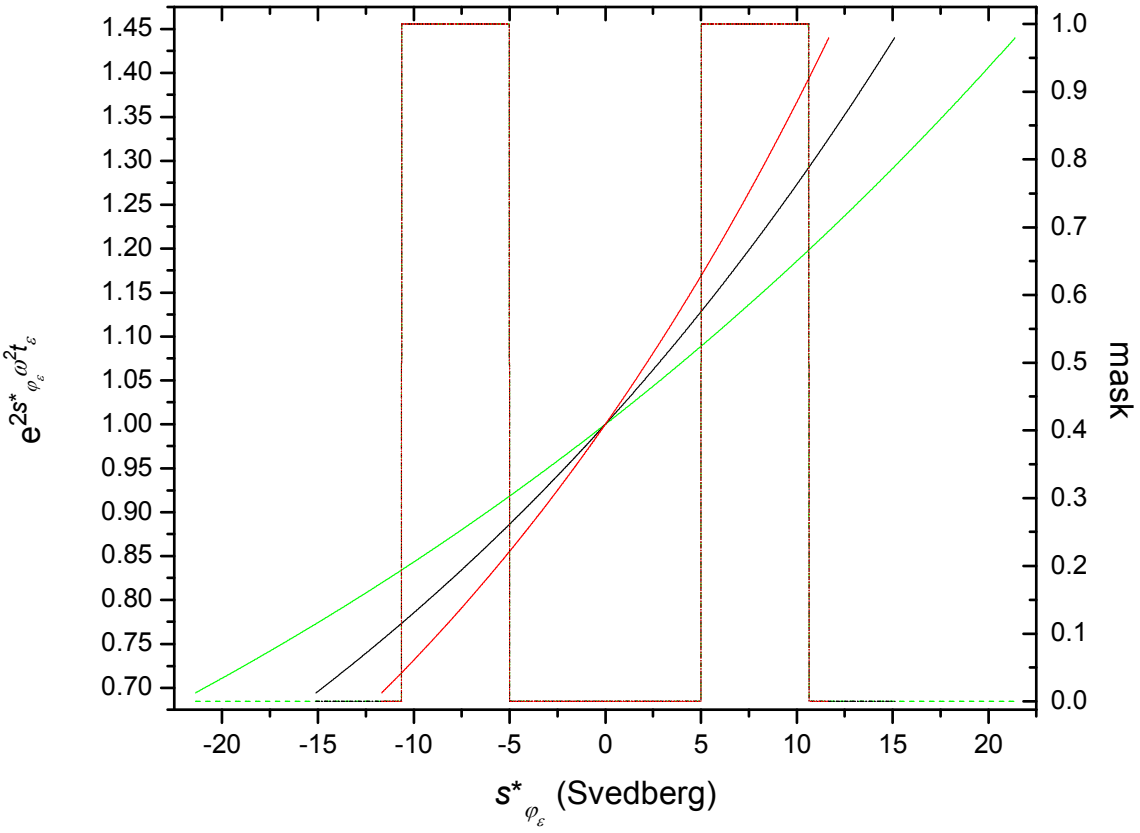

Figure 32a. The full range of the dimensionless factor $e^{2s^*_{\varphi_\epsilon}\omega^2 t_\epsilon}$ versus $s^*_{\varphi_\epsilon}$ at t_{36} (——), t_{51} (——) and t_{66} (——); and the full range of the dimensionless mask versus $s^*_{\varphi_\epsilon}$ at t_{36} (– – –), t_{51} (·–·–·) and t_{66} (·····). (Although the Svedberg is used for the dimension of the ordinate, $e^{2s^*_{\varphi_\epsilon}\omega^2 t_\epsilon}$ was calculated using $s^*_{\varphi_\epsilon}$ in seconds, t_ϵ in seconds, and ω in inverse seconds.)

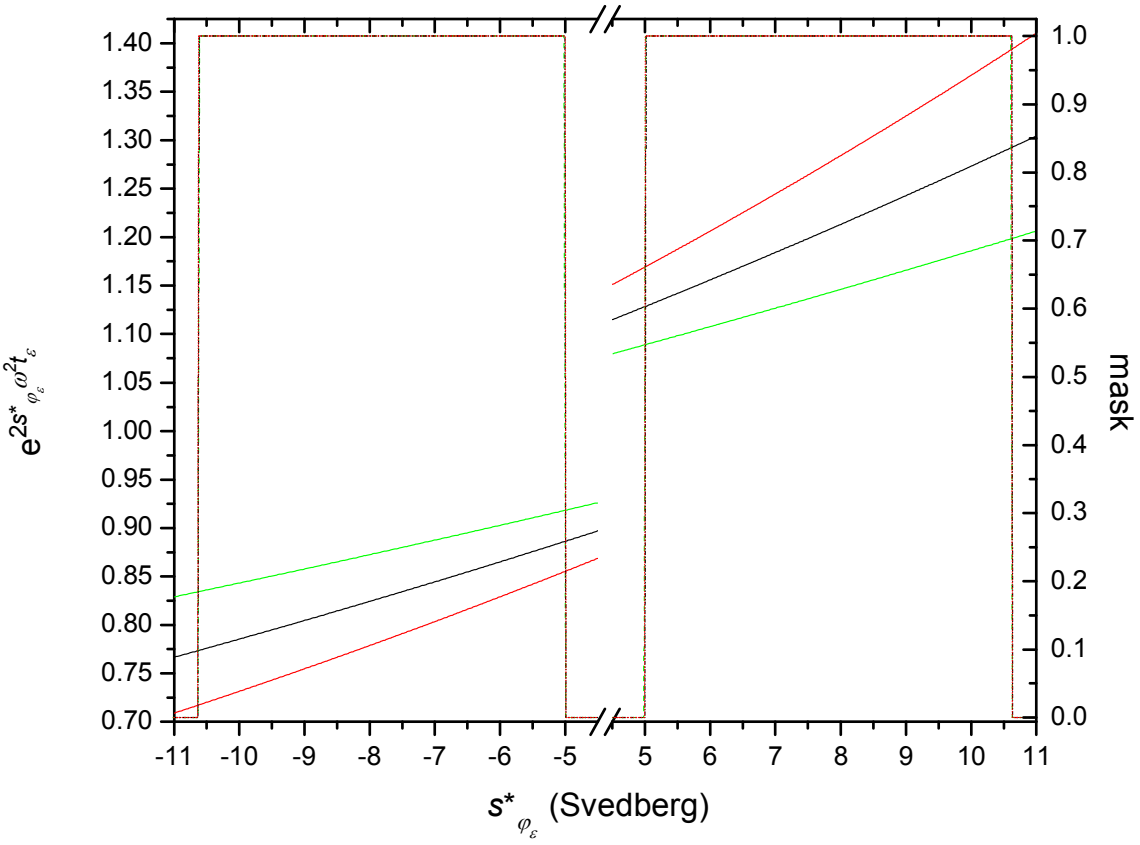

Figure 32b. The dimensionless factor $e^{2s^*_{\varphi_\epsilon}\omega^2 t_\epsilon}$ versus selected $s^*_{\varphi_\epsilon}$ values at t_{36} (——), t_{51} (——) and t_{66} (——); and the dimensionless mask versus selected $s^*_{\varphi_\epsilon}$ values at t_{36} (– – – –), t_{51} (·–·–·) and t_{66} (·····). The selected $s^*_{\varphi_\epsilon}$ values shown are those at which mask values of 1 predominate.

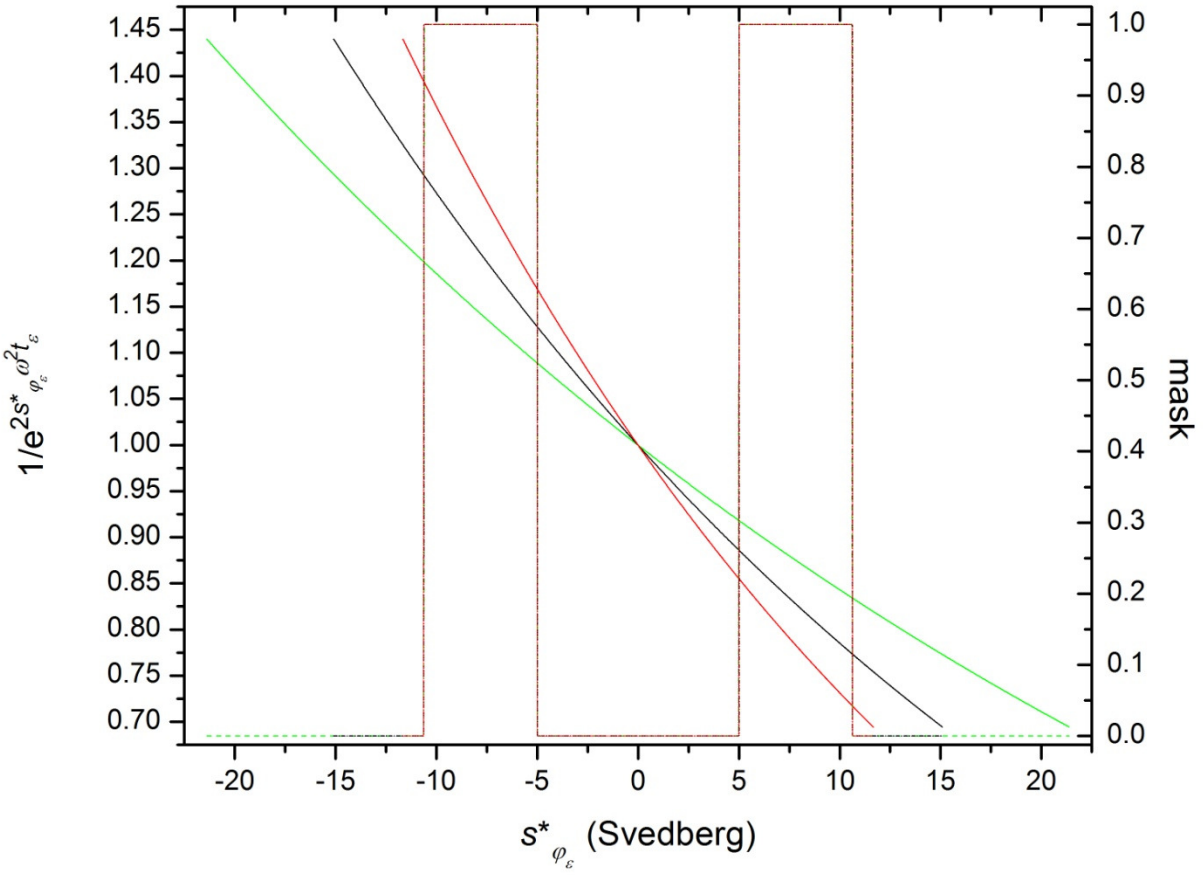

Figure 32c. The full range of $1/e^{2s^*_{\varphi_\epsilon}\omega^2 t_\epsilon}$ versus $s^*_{\varphi_\epsilon}$ at t_{36} (——), t_{51} (——) and t_{66} (——); and the full range of the dimensionless mask versus $s^*_{\varphi_\epsilon}$ at t_{36} (– – – –), t_{51} (·–·–·) and t_{66} (·····).

The signal-to-noise ratio of $g_{i,h}(s^*_{\varphi_\epsilon})$ *worsens in proportion to* $1/e^{2s^*_{\varphi_\epsilon}\omega^2 t_\epsilon}$ *as* $s^*_{\varphi_\epsilon}$ *increases*

The application of Equation 8 yields $\left(\frac{\partial Y_{i,h}(s^*_{\varphi_\epsilon})}{\partial s^*_{\varphi_\epsilon}}\right)_t$ as the apparent signal that is subjected to further analysis. The application of Equation 9 yields $q_{i,h}(s^*_{\varphi_\epsilon})$, which is equal to those values of $\left(\frac{\partial Y_{i,h}(s^*_{\varphi_\epsilon})}{\partial s^*_{\varphi_\epsilon}}\right)_t$ that do not appear to be redundant. Relative to the signal-to-noise ratio of $q_{i,h}(s^*_{\varphi_\epsilon})$,

at any given time, t_ϵ, the signal-to-noise ratio of $g_{i,h}(s^*_{\varphi_\epsilon})$ increases in proportion to $1/e^{2s^*_{\varphi_\epsilon}\omega^2 t_\epsilon}$ (Figure 32c) as $s^*_{\varphi_\epsilon}$ decreases from 0, while the signal-to-noise ratio of $g_{i,h}(s^*_{\varphi_\epsilon})$ decreases in proportion to $1/e^{2s^*_{\varphi_\epsilon}\omega^2 t_\epsilon}$ as $s^*_{\varphi_\epsilon}$ increases from 0. Also relative to the signal-to-noise ratio of $q_{i,h}(s^*_{\varphi_\epsilon})$, at any given $s^*_{\varphi_\epsilon} < 0$, the signal-to-noise ratio of $g_{i,h}(s^*_{\varphi_\epsilon})$ increases in proportion to $1/e^{2s^*_{\varphi_\epsilon}\omega^2 t_\epsilon}$ as t_ϵ increases, while at any given $s^*_{\varphi_\epsilon} > 0$, the signal-to-noise ratio of $g_{i,h}(s^*_{\varphi_\epsilon})$ decreases in proportion to $1/e^{2s^*_{\varphi_\epsilon}\omega^2 t_\epsilon}$ as t_ϵ increases. Such effects can be seen by comparing each of the figures for $q_{i,h}(s^*_{\varphi_\epsilon})$ (Figures 28 to 31) with its corresponding figure for $g_{i,h}(s^*_{\varphi_\epsilon})$ (Figures 33 to 36).

With respect to optimising the signal-to-noise ratio, its proportionality to $1/e^{2s^*_{\varphi_\epsilon}\omega^2 t_\epsilon}$ shows that the analysis of centripetally directed boundaries would benefit from utilising the latest possible data, while the analysis of centrifugally directed boundaries would benefit from utilising the earliest possible data. Where a boundary direction can be changed from centrifugal to centripetal through the use of D_2O or other substitutions that would make the implicit solvent more dense than the solutes, doing so would also be expected to optimise the signal-to-noise ratio, all else being equal. Such substitutions were, in fact, imagined to be made for treatment groups 1 to 4.

In the simulated AUC of treatment groups 1 to 4, the 71.23% D_2O (volume-percent) of the implicit solute ensured that, for any given replicate of a given treatment group, $|g_{i,h}(s^*_{\varphi_\epsilon})|$ would reflect approximately equal contributions from centripetally and centrifugally directed boundaries would at any given time, as a given mass of a solute of positive buoyancy is always counterbalanced by an approximately equal mass of a solute of negative buoyancy, such that the net buoyancy of the pair is close to zero. As a result, for the two treatment groups, $i = 1$ (100% K_A

> 0) and $i = 2$ (99% $K_A > 0$), with the strongest signal-to-noise characteristics, the net signal-to-noise ratio of $\left|g_{i,h}\left(s^*_{\varphi_\epsilon}\right)\right|$ is relatively stable with time, as compared to treatment groups 3 and 4.

Treatment groups 1 and 2 have the strongest signal-to-noise characteristics because their high signal-to-noise regions were selected as the negative-$s^*_{\varphi_\epsilon}$ and the positive-$s^*_{\varphi_\epsilon}$ ranges, -10.625E-13 s $< s^*_{\varphi_\epsilon} <$ -5E-13 s and 5E-13 s $< s^*_{\varphi_\epsilon} <$ 10.625E-13 s, respectively, over which to integrate both $\left|g_{i,h}\left(s^*_{\varphi_\epsilon}\right)\right|$ in the calculation of $G_{i,h}\left(s^*_{\varphi_\epsilon}\right)$ (Equation 11), and $s^*_{\varphi_\epsilon}\left|g_{i,h}\left(s^*_{\varphi_\epsilon}\right)\right|$ in the calculation of $s^*_{i,h,\epsilon}$ (Equations 12 and 13). In comparison, treatment group 3 has weaker signal-to-noise characteristics because a relatively larger portion of its low signal-to-noise regions lie within the utilised ranges of $s^*_{\varphi_\epsilon}$, 5E-13 s $< \left|s^*_{\varphi_\epsilon}\right| <$ 10.625E-13 s. Treatment group 4 has the weakest signal-to-noise characteristics because its high signal-to-noise regions are concentrated in two narrow segments within the utilised ranges of $s^*_{\varphi_\epsilon}$.

Over any given range of $s^*_{\varphi_\epsilon}$, regions with signal-to-noise ratios approaching zero are subject to data clipping, which results in roughly half the noise in such regions being counted as signal. The more predominant the noise is within the utilised ranges of $s^*_{\varphi_\epsilon}$, the more the noise becomes mistaken for signal via data clipping. (See *Mitigation of data clipping*.)

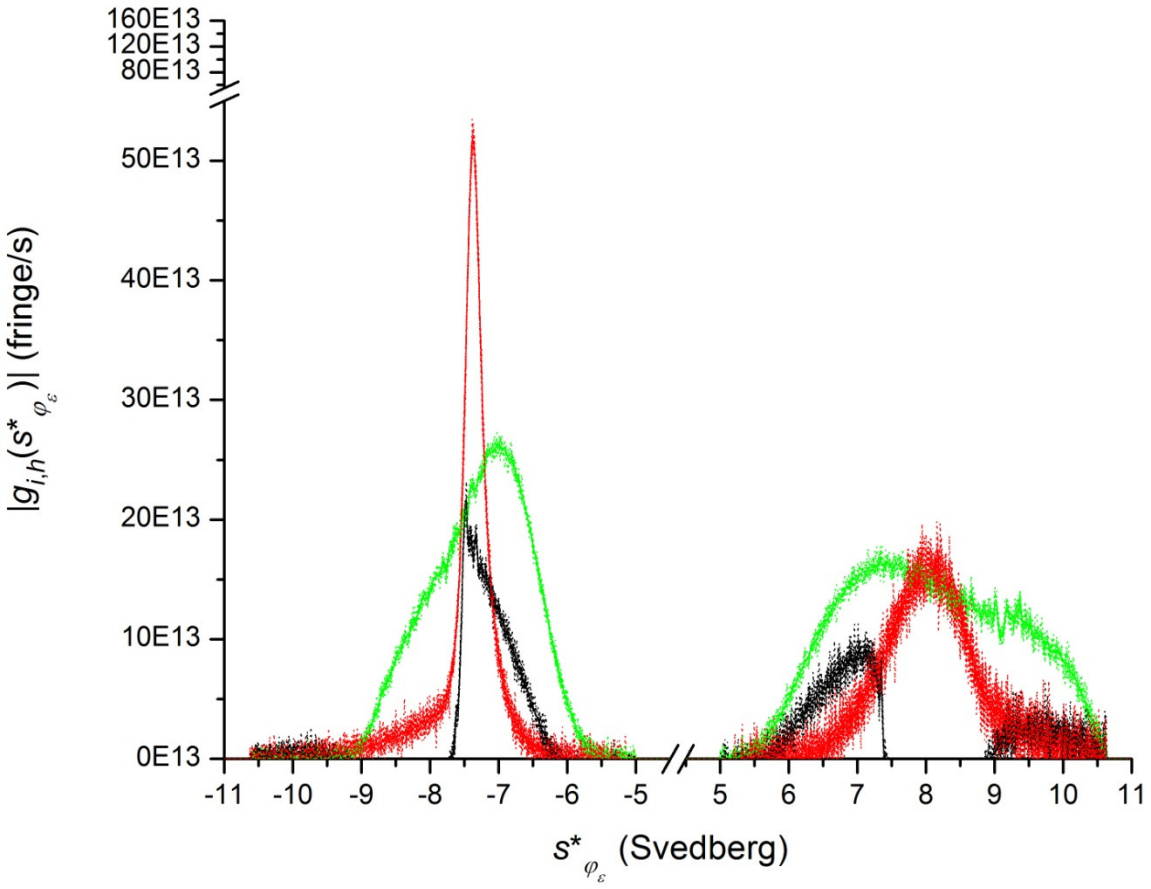

Figure 33. For $i = 1$ (100% $K_A > 0$, 0% K_A undefined), $\left|g_i\left(s^*_{\varphi_\epsilon}\right)\right|$ at t_{36} (——), t_{51} (——) and t_{66} (——), along with $\left|g_{i,h}\left(s^*_{\varphi_\epsilon}\right)\right|$ for each replicate ($1 \leq h \leq 9$) at t_{36} (·····), t_{51} (·····) and t_{66} (·····), all plotted against $s^*_{\varphi_\epsilon}$. Multiplication of $g_i\left(s^*_{\varphi_\epsilon}\right)$ and $g_{i,h}\left(s^*_{\varphi_\epsilon}\right)$ by the mask (Figure 32) for the corresponding time, t_{36}, t_{51} or t_{66}, left $g_i\left(s^*_{\varphi_\epsilon}\right)$ and $g_{i,h}\left(s^*_{\varphi_\epsilon}\right)$ unchanged wherever 5E-13 s $< \left|s^*_{\varphi_\epsilon}\right| <$ 10.625E-13 s, and set them to zero everywhere else. Figure 39 shows the integral of each of these curves with respect to $s^*_{\varphi_\epsilon}$.

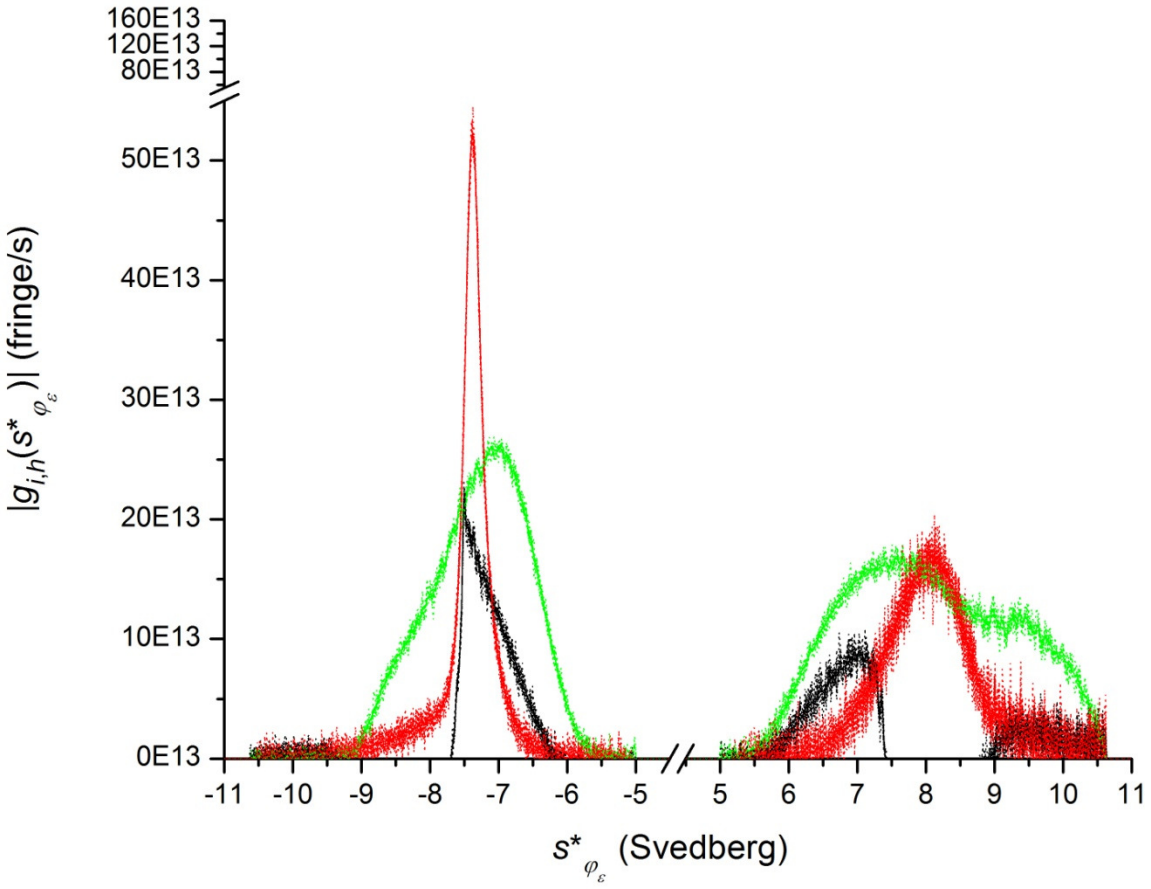

Figure 34. For $i = 2$ (99% $K_A > 0$, 1% K_A undefined), $\left|g_i\left(s^*_{\varphi_\epsilon}\right)\right|$ at t_{36} (——), t_{51} (——) and t_{66} (——), along with $\left|g_{i,h}\left(s^*_{\varphi_\epsilon}\right)\right|$ for each replicate ($1 \leq h \leq 9$) at t_{36} (·····), t_{51} (·····) and t_{66} (·····), all plotted against $s^*_{\varphi_\epsilon}$. Multiplication of $g_i\left(s^*_{\varphi_\epsilon}\right)$ and $g_{i,h}\left(s^*_{\varphi_\epsilon}\right)$ by the mask (Figure 32) for the corresponding time, t_{36}, t_{51} or t_{66}, left $g_i\left(s^*_{\varphi_\epsilon}\right)$ and $g_{i,h}\left(s^*_{\varphi_\epsilon}\right)$ unchanged wherever 5E-13 s $< \left|s^*_{\varphi_\epsilon}\right| <$ 10.625E-13 s, and set them to zero everywhere else. Figure 40 shows the integral of each of these curves with respect to $s^*_{\varphi_\epsilon}$.

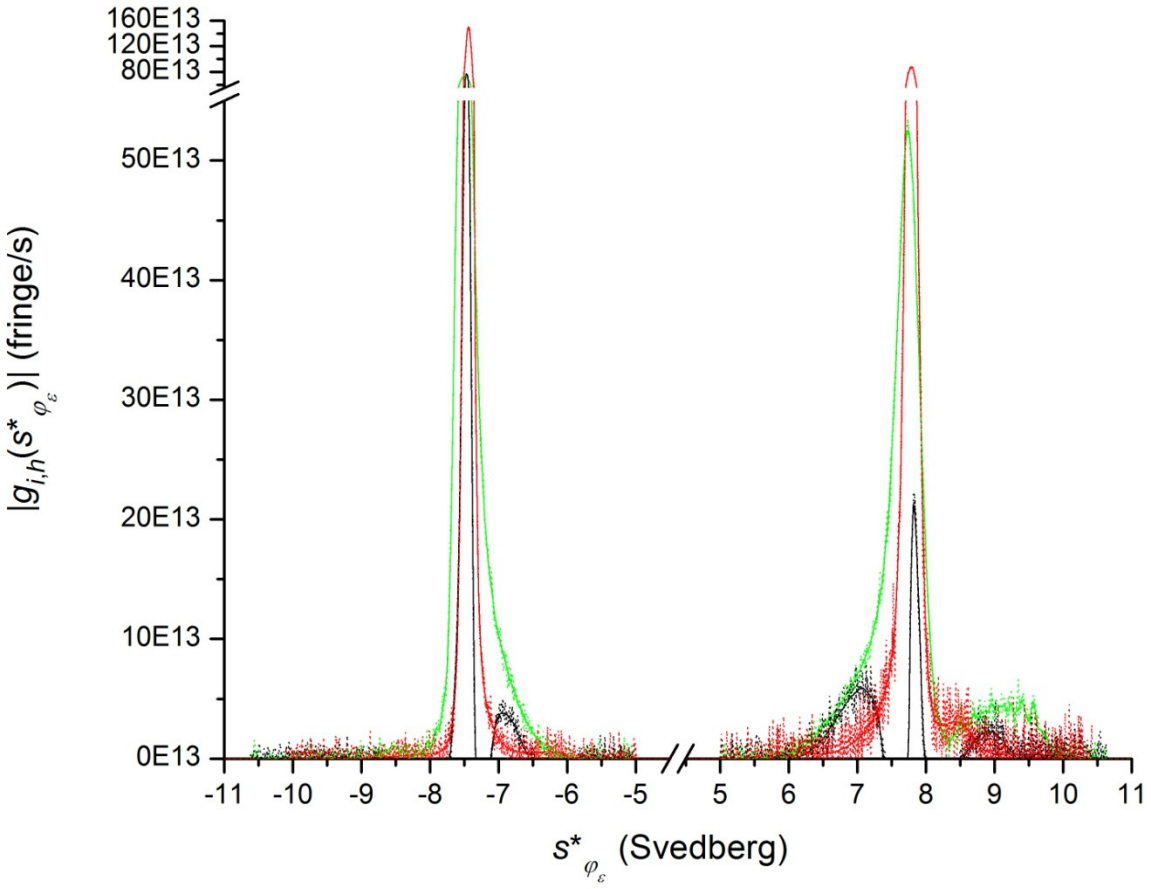

Figure 35. For $i = 3$ (50% $K_A > 0$, 50% K_A undefined), $\left|g_i\left(s^*_{\varphi_\epsilon}\right)\right|$ at t_{36} (——), t_{51} (——) and t_{66} (——), along with $\left|g_{i,h}\left(s^*_{\varphi_\epsilon}\right)\right|$ for each replicate ($1 \leq h \leq 3$) at t_{36} (·····), t_{51} (·····) and t_{66} (·····), all plotted against $s^*_{\varphi_\epsilon}$. Multiplication of $g_i\left(s^*_{\varphi_\epsilon}\right)$ and $g_{i,h}\left(s^*_{\varphi_\epsilon}\right)$ by the mask (Figure 32) for the corresponding time, t_{36}, t_{51} or t_{66}, left $g_i\left(s^*_{\varphi_\epsilon}\right)$ and $g_{i,h}\left(s^*_{\varphi_\epsilon}\right)$ unchanged wherever 5E-13 s $< \left|s^*_{\varphi_\epsilon}\right| <$ 10.625E-13 s, and set them to zero everywhere else. Figure 41 shows the integral of each of these curves with respect to $s^*_{\varphi_\epsilon}$.

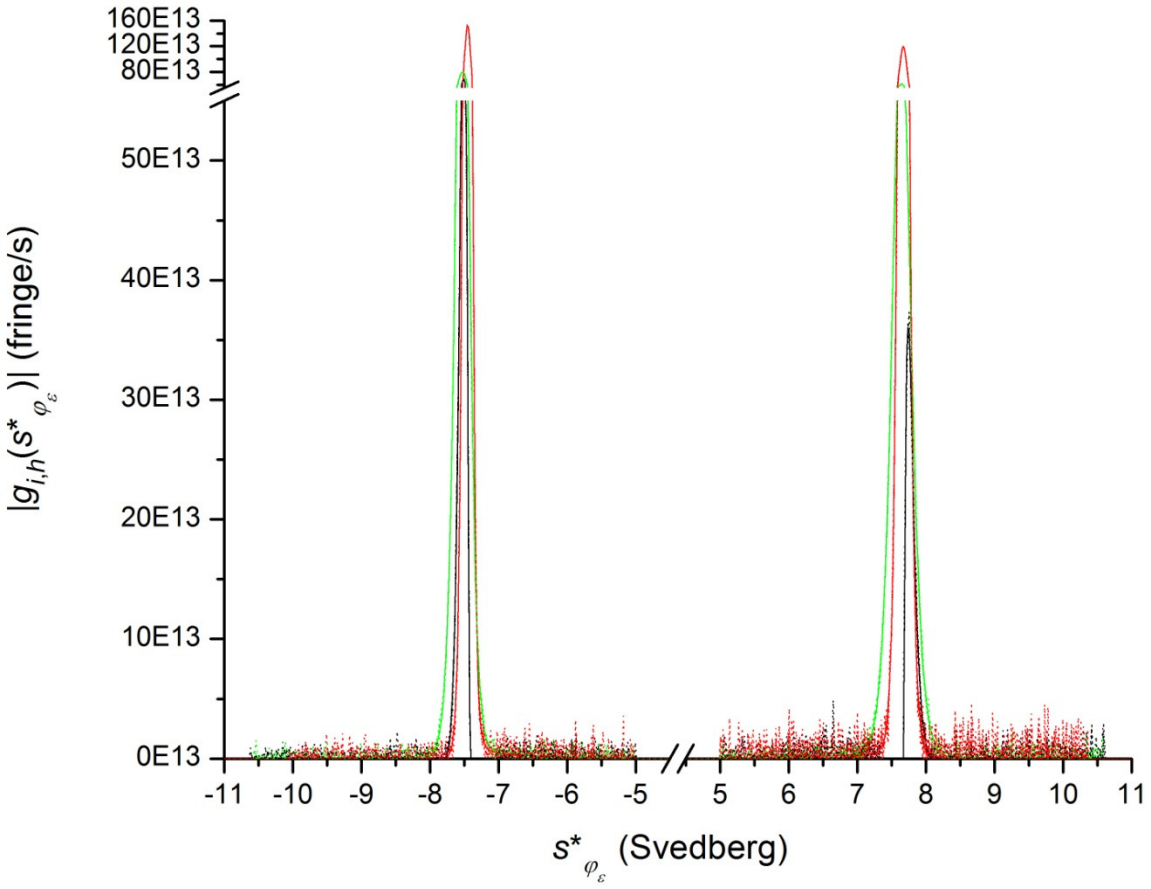

Figure 36. For $i = 4$ (0% $K_A > 0$, 100% K_A undefined), $\left|g_i\left(s^*_{\varphi_\epsilon}\right)\right|$ at t_{36} (——), t_{51} (——) and t_{66} (——), along with $\left|g_{i,h}\left(s^*_{\varphi_\epsilon}\right)\right|$ for each replicate ($1 \leq h \leq 3$) at t_{36} (·····), t_{51} (·····) and t_{66} (·····), all plotted against $s^*_{\varphi_\epsilon}$. Multiplication of $g_i\left(s^*_{\varphi_\epsilon}\right)$ and $g_{i,h}\left(s^*_{\varphi_\epsilon}\right)$ by the mask (Figure 32) for the corresponding time, t_{36}, t_{51} or t_{66}, left $g_i\left(s^*_{\varphi_\epsilon}\right)$ and $g_{i,h}\left(s^*_{\varphi_\epsilon}\right)$ unchanged wherever 5E-13 s $< \left|s^*_{\varphi_\epsilon}\right| <$ 10.625E-13 s, and set them to zero everywhere else. Figure 42 shows the integral of each of these curves with respect to $s^*_{\varphi_\epsilon}$.

The cumulative distribution function (Equation 11): $G_{i,h}\left(s^*_{\varphi_\epsilon}\right) = \int_{s^*_{\varphi_\epsilon=1}}^{s^*_{\varphi_\epsilon}} \left|g_{i,h}\left(\varsigma^*_{\varphi_\epsilon}\right)\right| d\varsigma^*_{\varphi_\epsilon}$

For replicate h of treatment group i at time t_ϵ, the cumulative distribution function of the apparent sedimentation coefficient, $G_{i,h}\left(s^*_{\varphi_\epsilon}\right)$, equates to a substantially time-normalised, but not entirely time-independent, measure of the total, initial signal from signal of all solutes for which the apparent sedimentation coefficient is less than or equal to some specified value of interest, but greater than its time-dependent minimum value, of $\frac{1}{\omega^2 t_\epsilon} ln\left(\frac{r_m}{r_b}\right)$. (See the discussion following Equation 74.) As $s^*_{\varphi_\epsilon=1} = \frac{1}{\omega^2 t_\epsilon} ln\left(\frac{r_1}{r_b}\right)$ is the nearest value to the time-dependent minimum of $s^*_{\varphi_\epsilon}$ (Equations 5 and 6), $s^*_{\varphi_\epsilon=1}$ is the lower limit of the integral (Equation 11) that yields $G_{i,h}\left(s^*_{\varphi_\epsilon}\right)$.

It is the dimensionless factor $e^{2s^*_{\varphi_\epsilon}\omega^2 t_\epsilon}$ (Equations 10 and 74; Figure 32) that serves to somewhat normalise $g_{i,h}\left(s^*_{\varphi_\epsilon}\right)$, and thus also $G_{i,h}\left(s^*_{\varphi_\epsilon}\right)$, with respect to time. That $G_{i,h}\left(s^*_{\varphi_\epsilon}\right)$ is time-normalised can be seen from the discrepancy between the change in $Y_{i,h}\left(s^*_{\varphi_\epsilon}\right)$ and the change in $G_{i,h}\left(s^*_{\varphi_\epsilon}\right)$ over a given range of $s^*_{\varphi_\epsilon}$. (Compare Figures 20 to 23 with Figures 39 to 42, respectively.)

For a system, $i = x$-, in which there is just one solute, and in which that solute behaves exactly like a distribution of nondiffusing solutes for which $s_{x\text{-}}$, the would-be weight-average sedimentation coefficient, is less than zero and is invariant with either radial position or time, the factor $e^{2s^*_{\varphi_\epsilon}\omega^2 t_\epsilon}$ would, in the absence of noise, render $G_{i=x\text{-}}\left(s^*_{\varphi_\epsilon=2N}\right)$ exactly equal to $Y_{i=x\text{-}}\left(s^*_{\varphi_0}\right)$, the signal produced by the solute at time t_0, thus compensating for the radial concentration effect having caused the signal across the centripetally directed boundary to increase by $Y_{i=x\text{-}}\left(s^*_{\varphi_0}\right)\left[e^{-2s_{x\text{-}}\omega^2 t_\epsilon} - e^{-2s_{x\text{-}}\omega^2 t_0}\right]$ from time t_0 to time t_ϵ, assuming that, at t_ϵ, the boundary would have remained distinct from the radial extremum at which the solute accumulates.

For a system, $i = x+$, in which there is just one solute, and in which that solute behaves exactly like a distribution of nondiffusing solutes for which s_{x+}, the would-be weight-average sedimentation coefficient, is greater than zero and is invariant with either radial position or time, the factor $e^{2s^*_{\varphi_\epsilon}\omega^2 t_\epsilon}$ would, in the absence of noise, render $G_{i=x+}\left(s^*_{\varphi_\epsilon=2N}\right)$ exactly equal to $Y_{i=x+}\left(s^*_{\varphi_0}\right)$, the signal produced by the solute at time t_0, thus compensating for the radial dilution effect having caused the signal across the centrifugally directed boundary to decrease by $Y_{i=x+}\left(s^*_{\varphi_0}\right)\left[e^{-2s_{x+}\omega^2 t_\epsilon} - e^{-2s_{x+}\omega^2 t_0}\right]$ from time t_0 to time t_ϵ, assuming that, at t_ϵ, the boundary would have remained distinct from the radial extremum at which the solute accumulates.

Treatment groups 1 to 4 are realistic enough systems with realistic enough solutes that the factor $e^{2s^*_{\varphi_\epsilon}\omega^2 t_\epsilon}$ only approximately compensates for the radial concentration or radial concentration effects. Nevertheless, predictable trends are seen in the data for these treatment groups. Due to the proportionality of $g_{i,h}\left(s^*_{\varphi_\epsilon}\right)$ to $e^{2s^*_{\varphi_\epsilon}\omega^2 t_\epsilon}$, $G_{i,h}\left(s^*_{\varphi_\epsilon=b}\right) - G_{i,h}\left(s^*_{\varphi_\epsilon=a}\right)$ tends to be significantly less than $Y_{i,h}\left(s^*_{\varphi_\epsilon=a}\right) - Y_{i,h}\left(s^*_{\varphi_\epsilon=b}\right)$ across a centripetally directed boundary spanning $s^*_{\varphi_\epsilon=a}$ to $s^*_{\varphi_\epsilon=b}$, where $s^*_{\varphi_\epsilon=a} < s^*_{\varphi_\epsilon=b} < 0$. Contrariwise, but again due to the proportionality of $g_{i,h}\left(s^*_{\varphi_\epsilon}\right)$ to $e^{2s^*_{\varphi_\epsilon}\omega^2 t_\epsilon}$ $G_{i,h}\left(s^*_{\varphi_\epsilon=d}\right) - G_{i,h}\left(s^*_{\varphi_\epsilon=c}\right)$ tends to be significantly greater than $Y_{i,h}\left(s^*_{\varphi_\epsilon=d}\right) - Y_{i,h}\left(s^*_{\varphi_\epsilon=c}\right)$ across a centrifugally directed boundary spanning $s^*_{\varphi_\epsilon=c}$ to $s^*_{\varphi_\epsilon=d}$, where $0 < s^*_{\varphi_\epsilon=c} < s^*_{\varphi_\epsilon=d}$. Such trends in $Y_{i,h}\left(s^*_{\varphi_\epsilon}\right)$, $g_{i,h}\left(s^*_{\varphi_\epsilon}\right)$, and $G_{i,h}\left(s^*_{\varphi_\epsilon}\right)$ are also seen in seen in $Y_i\left(s^*_{\varphi_\epsilon}\right)$, $g_i\left(s^*_{\varphi_\epsilon}\right)$, and $G_i\left(s^*_{\varphi_\epsilon}\right)$.

Figure 39 shows $G_i\left(s^*_{\varphi_\epsilon}\right)$ versus $s^*_{\varphi_\epsilon}$ and $G_{i,h}\left(s^*_{\varphi_\epsilon}\right)$ versus $s^*_{\varphi_\epsilon}$ for $i = 1$ (100% $K_A > 0$, 0% K_A undefined), and Figure 42 shows $G_i\left(s^*_{\varphi_\epsilon}\right)$ versus $s^*_{\varphi_\epsilon}$ and $G_{i,h}\left(s^*_{\varphi_\epsilon}\right)$ versus $s^*_{\varphi_\epsilon}$ for $i = 4$ (0% $K_A > 0$, 100% K_A undefined). Data at 5-minute intervals for the high-concentration species, *L*, *H* and *LH*,

that dominate those results are presented in the initial paper that described the AUC simulation of treatment group $i = 1$ (Moody, 2012a: Figures 3 to 5, $K_A = 30.325$ ml/g) and treatment group $i = 4$ (Moody, 2012a: Figures 10 to 12, K_A undefined). Additional figures presented here show c_L, c_H and c_{LH} versus r_i at t_{36}, t_{51} and t_{66} only (Figures 37 and 38), and for $i = 1$, also show the component concentrations of L and H versus r_i at t_{36} and two earlier times (Figure 37). The additional figures, and a review of treatment groups 1 through 4, with a focus on treatment groups 1 and 2, provide the background needed to consider the $G_i\left(s^*_{\varphi_\epsilon}\right)$ versus $s^*_{\varphi_\epsilon}$ and $G_{i,h}\left(s^*_{\varphi_\epsilon}\right)$ versus $s^*_{\varphi_\epsilon}$ for results for all four treatment groups (Figures 39 to 42; Table 20).

Treatment groups 1 to 4 reviewed

Treatment groups 1 and 2, the replicates of which consist, respectively, of the 100% $K_A > 0$ and 99% $K_A > 0$ solutions (Table 16), behave so similarly that, as will be shown (*Statistical analysis of AUC simulation results for any given time of analysis, t_ϵ*), distinguishing one group from the other at a confidence level of 95% requires considerable effort. For $i = 1$ and $i = 2$, the oppositely directed mass transport of L_+ and H_+ ensures that, from the radial extrema inward, c_{LH+} goes to zero with time. For $i = 2$, 1% (by mass) of LH is present as LH_-, which is all the LH that persists after c_{LH+} has declined to zero everywhere. A fairly thorough description of treatment group 1 is presented in a section (*Treatment group 1 reviewed in detail*) below. That section includes Figure 37, which shows the high-concentration species of treatment group 1 at the times analysed (t_{36}, t_{51} and t_{66}).

Treatment group 3 (Figure 18), the replicates of which consist of the 50% $K_A > 0$ solution, resembles the two treatment groups, 1 (100% $K_A > 0$) and 4 (0% $K_A > 0$), of which it is a 1-to-1

(mass-to-mass) mixture, but behaves more like the latter (Figure 19) than the former (Figure 16), as from the start (t_0), for $i = 3$ (Table 16), the mass-action equilibrium (Equation 71) is poised such that the concentration of dissociable dimer ($c_{LH+} = 1.11448\text{E-}2$ g/ml at t_0) is significantly less than the concentration of non-dissociable dimer ($c_{LH-} = 1.65000\text{E-}2$ g/ml at t_0). As with treatment group 1, for $i = 3$, the oppositely directed mass transport of L_+ and H_+ ensures that, from the radial extrema inward, c_{LH+} goes to zero with time. The 50% (by mass) of LH present as LH_-, is percentage of LH that persists after c_{LH+} has declined to zero everywhere. Figure 43 shows the high-concentration species of this group at the times analysed (t_{36}, t_{51} and t_{66}).

Treatment group 4, the replicates of which consist of the 0% $K_A > 0$ solution (Table 16), has no dissociable dimer present anywhere at any time. Instead, for $i = 4$, all particles of LH are in the form of LH_-, which persist permanently and redistribute subtly. A fairly thorough description of this group is presented in a section (*Treatment group 4 reviewed in detail*) below. That section includes Figure 38, which shows the high-concentration species of this group at the times analysed (t_{36}, t_{51} and t_{66}).

Treatment group 1 reviewed in detail

As previously stated (*Details regarding the treatment groups, the Noise-Free Signals and the times chosen for analysis*), the explicit solute species of treatment group 1 consist of 24 single-species components present at low concentration ($1 < k < 14$ or $14 < k < 27$, Table 15), plus 3 species, L_+, H_+ and LH_+, that are present at high concentration. The high-concentration species arise from 2 two-species components, L_+ and H_+, that share 1 product, LH_+, in common (Table

16). Equation 71 describes the mass-action association/dissociation reaction in which L_+ and H_+ are defined as the reactants and LH_+ is defined as the product. For that reaction at 20.00°C, $K_A =$ 30.325 ml/g, $k_{f+} = 30{,}000$ [ml/g]/s and $k_{r+} = k_{f+}/K_A \cong 989.277$ s. There being no L_-, H_- or LH_- present in treatment group 1, L_+ is simply referred to as L, H_+ is simply referred to as H and LH_+ is simply referred to as LH. Every explicit solute species other than LH is modelled as a spherical, 30 nm diameter PS bead, and LH is modelled as a dimer of L and H. The particles are modelled as varying in the extent of deuteration (Figure 8) and consequent density (Table 15).

The high-concentration species, L, H and LH, are responsible for the major effects observed in the replicates of treatment group 1. Furthermore, the effects of low-concentration species 2 to 13 on species L and LH are similar to the effects of species H on species L and LH, while the effects of low-concentration species 15 to 26 on species H and LH are similar to the effects of species L on species H and LH. The net effects of the low-concentration species are thus small enough to permit the system to be described as if only species L, H and LH were present. This fact is exploited here to describe treatment group 1 as simply as possible. Figure 37a, which shows, among other things, c_L, c_H and c_{LH} versus r_j at times t_{36}, t_{51} and t_{66}, illustrates the behaviour of species L, H and LH described below. Figure 37c shows the nearest equivalent to Figure 37a for the case of each $y_{k,q}$, each $h_{k,q}$, each $p_{k,q}$, each $(\sigma p)_{k,q}$ and each c_k of $[c_i(r_j,t_\epsilon)]_{low}$ set to zero. Other figures cited refer to a previous work (Moody, 2012a).

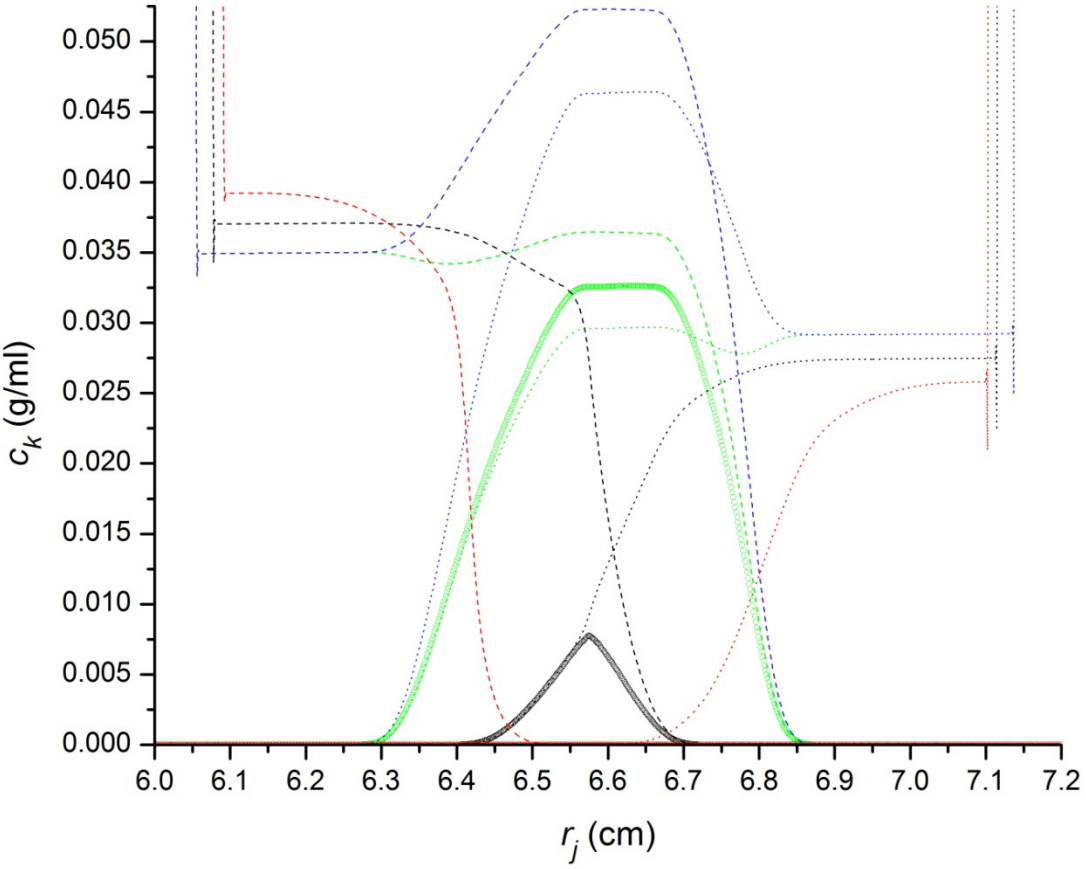

Figure 37a. Treatment group $i = 1$ (100% $K_A > 0$) at $t_{36} = 2160$ s (36 min), $t_{51} = 3060$ s (51 min) and $t_{66} = 3960$ s (min), which are the times analysed. Shown are the species concentrations of L, H and LH, c_L (dashed lines), c_H (dotted lines) and c_{LH} (small, open circles), respectively, versus r_j at times t_{36} (green), t_{51} (black) and t_{66} (red). Also shown are component concentration of L, $c_{L,LH} = c_L + c_{LH}M_L/M_{LH}$ (Equation 75), at t_{36} (dashed blue line); and the component concentration of H, $c_{H,LH} = c_H + c_{LH}M_H/M_{LH}$ (Equation 76), at t_{36} (dotted blue line). In the region of the dip in c_L along the boundary of H, the component concentration of L ($c_{L,LH}$) takes the form of the leading edge of a peak produced by a negatively buoyant solute undergoing a density-gradient-driven Johnston-Ogston effect (Moody, 2012a: Figure 7, Ka = 30.325 ml/g), but migrates centrifugally (Figure 37b) as a consequence of its form owing its existence to the centrifugally migrating boundary of

H. In the region of the dip in c_H along the boundary of *L*, the component concentration of *H* ($c_{H,LH}$) takes the form of the leading edge of a peak produced by a positively buoyant solute undergoing a density-gradient-driven Johnston-Ogston effect (Moody, 2012a: Figure 6, Ka = 30.325 ml/g), but migrates centripetally (Figure 37b) as a consequence of its form owing its existence to the centripetally migrating boundary of *L*.

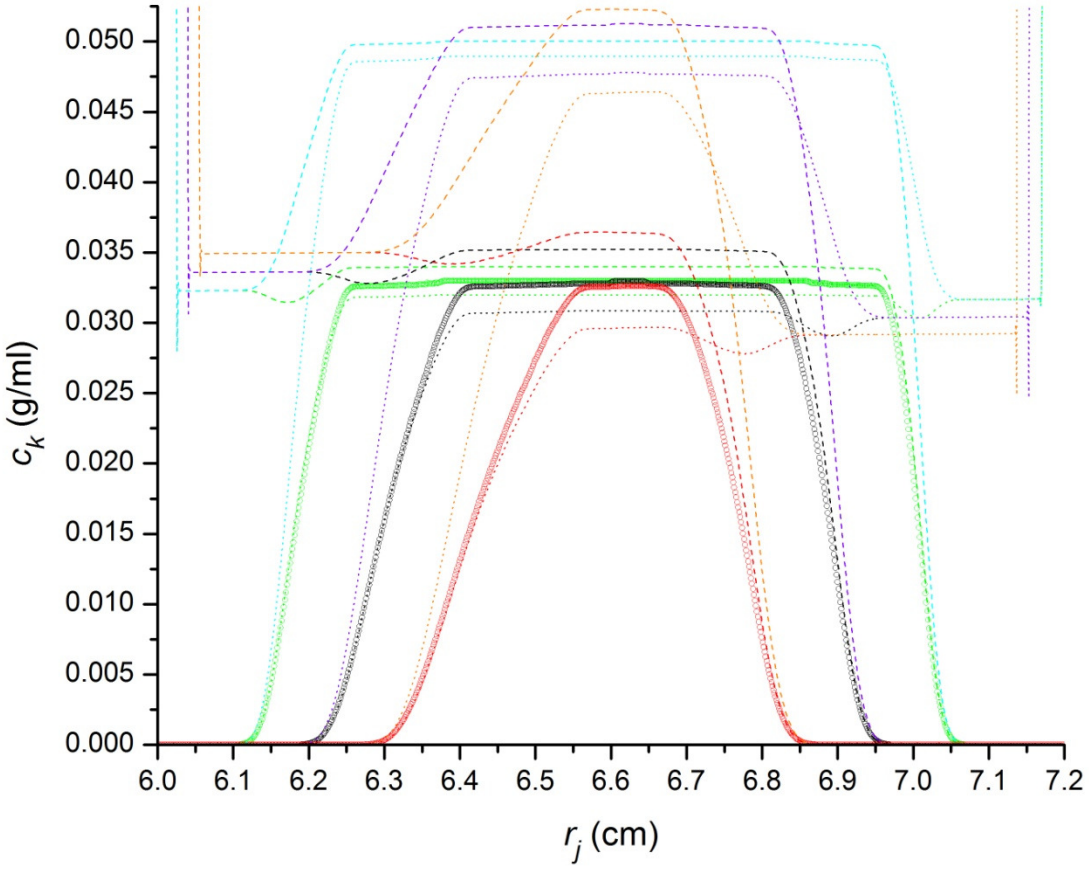

Figure 37b. Treatment group $i = 1$ (100% $K_A > 0$) at $t_{16} = 960$ s (16 min), $t_{26} = 1560$ s (26 min) and $t_{36} = 2160$ s (36 min). Shown are the component concentration of *L*, $c_{L,LH} = c_L + c_{LH}M_L/M_{LH}$ (Equation 75), at t_{16} (dashed cyan line), t_{26} (dashed violet line) and t_{36} (dashed orange line); and the component concentration of *H*, $c_{H,LH} = c_H + c_{LH}M_H/M_{LH}$ (Equation 76), at t_{16} (dotted cyan

line), t_{26} (dotted violet line) and t_{36} (dotted orange line). Also shown are the species concentrations of *L*, *H* and *LH*, which are c_L (dashed lines), c_H (dotted lines) and c_{LH} (small, open circles), respectively, versus r_j at times t_{16} (green), t_{26} (black) and t_{36} (red). At any given time, $c_{L,LH}$ resembles the truncated peak of a negatively buoyant solute undergoing a density-gradient-driven Johnston-Ogston effect (Moody, 2012a: Figure 7, Ka = 30.325 ml/g), but unlike such a peak, the apparent peak in $c_{L,LH}$ narrows with time as its leading edge co-migrates with the centrifugally directed boundary of *H* and its trailing edge co-migrates with the centripetally directed boundary of *L*. At any given time, $c_{H,LH}$ resembles the truncated peak of a positively buoyant solute undergoing a density-gradient-driven Johnston-Ogston effect (Moody, 2012a: Figure 6, Ka = 30.325 ml/g), but unlike such a peak, the apparent peak in $c_{H,LH}$ narrows with time as its leading edge co-migrates with the centripetally directed boundary of *L* and its trailing edge co-migrates with the centrifugally directed boundary of *H*.

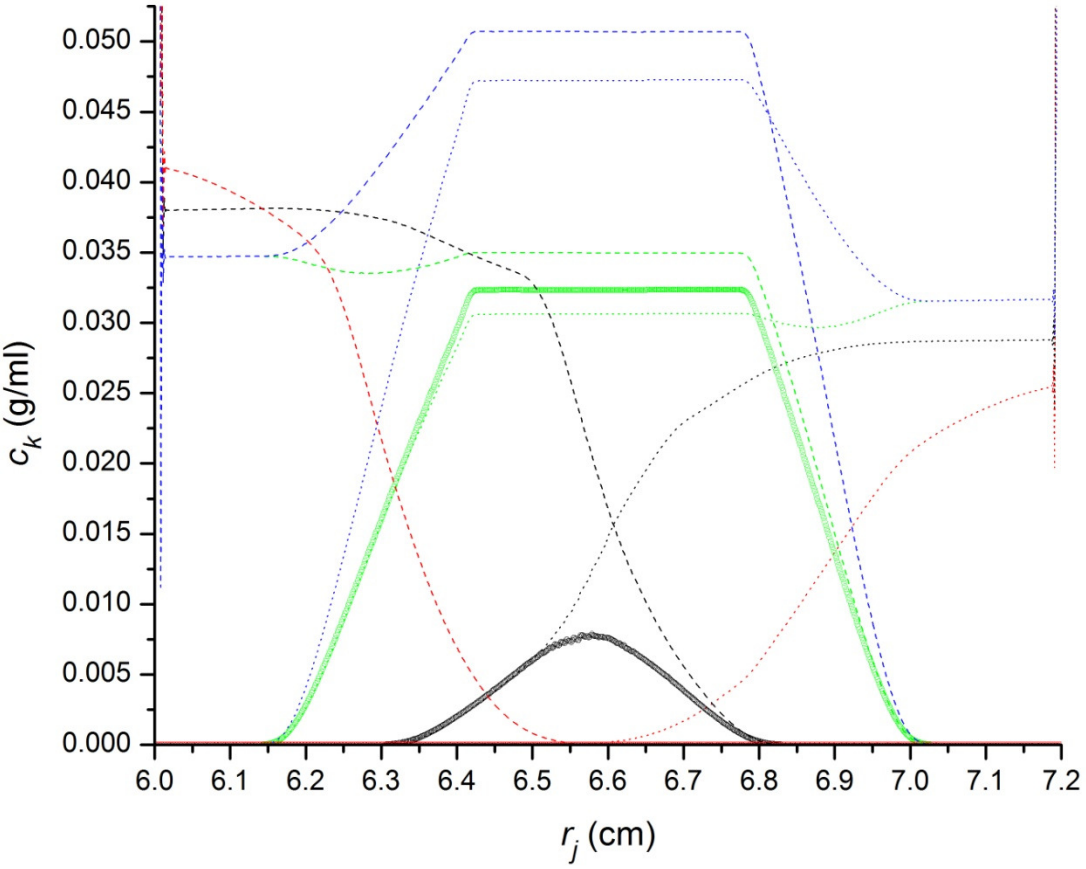

Figure 37c. The nearest equivalent to Figure 37a for the case of each $y_{k,q}$, each $h_{k,q}$, each $p_{k,q}$, each $(\sigma p)_{k,q}$ and each c_k of $[c_i(r_j,t_\epsilon)]_{low}$ set to zero. Shown are the species concentrations of L, H and LH, c_L (dashed lines), c_H (dotted lines) and c_{LH} (small, open circles), respectively, versus r_j at times t_{21} (green), t_{41} (black) and t_{61} (red), where $t_{21} = 1260$ s (21 min), $t_{41} = 2460$ s (41 min) and $t_{61} = 3660$ s (61 min). Also shown are the component concentration of L, $c_{L,LH} = c_L + c_{LH}M_L/M_{LH}$ (Equation 75), at t_{21} (dashed blue line); and the component concentration of H, $c_{H,LH} = c_H + c_{LH}M_H/M_{LH}$ (Equation 76), at t_{21} (dotted blue line). At all times, $s_k = s_k^0$ (Table 15; Equation 70) and $D_k = D_k^0$ (Equation 61) for each species, k, where $k = 1$ for H, $k = 14$ for LH and $k = 27$ for L. For the reaction in which L and H are defined as the reactants and LH is defined as the product (Equation 71), $K_A = 30.325$ ml/g, $k_{f+} = 30{,}000$ [ml/g]/s and $k_{r+} = k_{f+}/K_A \cong 989.277$ s.

Component concentrations $c_{L,LH}$ and $c_{H,LH}$ in this case can be described by the same text applied to their counterparts in Figure 37a.

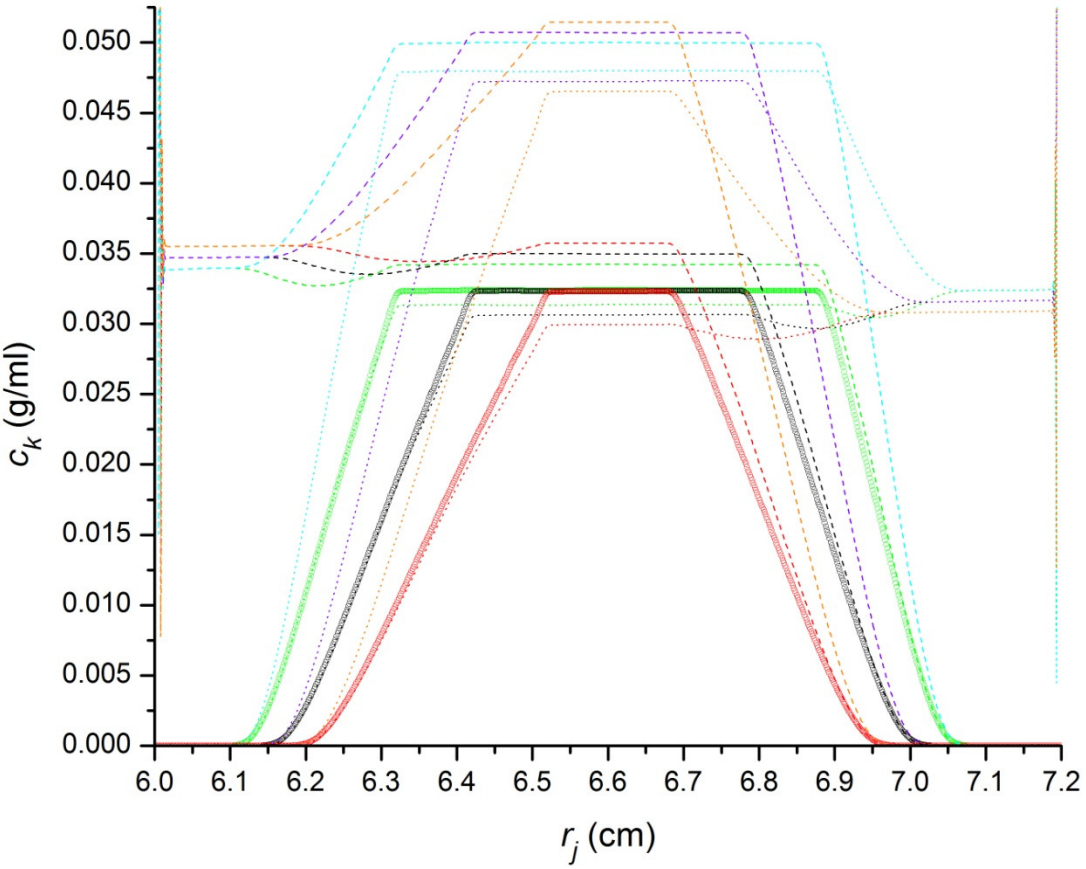

Figure 37d. The nearest equivalent to Figure 37b for the case of each $y_{k,q}$, each $h_{k,q}$, each $p_{k,q}$, each $(\sigma p)_{k,q}$ and each c_k of $[c_i(r_j,t_\epsilon)]_{low}$ set to zero. Shown are the component concentration of L, $c_{L,LH} = c_L + c_{LH}M_L/M_{LH}$ (Equation 75), at t_{16} (dashed cyan line), t_{21} (dashed violet line) and t_{26} (dashed orange line); and the component concentration of H, $c_{H,LH} = c_H + c_{LH}M_H/M_{LH}$ (Equation 76), at t_{16} (dotted cyan line), t_{21} (dotted violet line) and t_{26} (dotted orange line), where $t_{16} = 960$ s, $t_{21} = 1260$ s and $t_{26} = 1560$ s. Also shown are the species concentrations of L, H and LH, which are c_L (dashed lines), c_H (dotted lines) and c_{LH} (small, open circles), respectively, versus r_j at times t_{16}

(green), t_{21} (black) and t_{26} (red). The time-dependent behaviour of $c_{L,LH}$ and $c_{H,LH}$ in this case can be described by the same text applied to their counterparts in Figure 37b.

In a system of treatment group 1(100% $K_A > 0$), at a time from t_0 to a few minutes after t_{36}, there is always a plateau region (where $\left(\frac{\partial c}{\partial r}\right)_t \cong 0$) around the radial centre of the system. This plateau region narrows with time as the centripetally directed boundary of L (Moody, 2012a: Figure 4, $K_A = 30.325$ ml/g) migrates into it from above and the centrifugally directed boundary of H (Moody, 2012a: Figure 3, $K_A = 30.325$ ml/g) migrates into it from below. Within this narrowing plateau region, c_{LH} slowly decreases with time (Moody, 2012a: Figure 5, $K_A = 30.325$ ml/g), while c_L increases with time due to the radial concentration effect and c_H decreases with time due to the radial dilution effect.

In a system of treatment group 1(100% $K_A > 0$), at a time from t_0 to a few minutes after t_{36}, from r_b inward along the radial axis, following a region where $c_L = 0$, c_L increases broadly and almost linearly with decreasing r across the boundary of L to the plateau region where $\left(\frac{\partial c_L}{\partial r}\right)_t \cong 0$, and c_L then dips across the region occupied by the boundary of H, beyond which c_L rebounds to a level somewhat shy of its plateau concentration, at which level it remains until the innermost zone of accumulation, where c_L approaches its maximum possible value, $[c_L]_{max}$ (Equation 63).

In a system of treatment group 1(100% $K_A > 0$), at a time from t_0 to a few minutes after t_{36}, from r_m outward along the radial axis, following a region where $c_H = 0$, c_H increases broadly and almost linearly with increasing r across the boundary of H to the plateau region where $\left(\frac{\partial c_H}{\partial r}\right)_t \cong 0$, and c_H then dips across the region occupied by the boundary of L, beyond which c_H rebounds to

a level somewhat exceeding its plateau concentration, at which level it remains until the outermost zone of accumulation, where c_H approaches its maximum possible value, $[c_H]_{max}$ (Equation 63). The outermost zone of accumulation is occupied by the pellet.

In a system of treatment group 1($100\%\ K_A > 0$), at a time from t_0 to a few minutes after t_{36}, the mass-transport boundaries of L and H are also reaction boundaries along which c_{LH} is directly proportional to c_L within the boundary of L or c_H within the boundary of H. Denoting the component concentration of L by $c_{L,LH}$,

$$c_{L,LH} = c_L + c_{LH}\frac{M_L}{M_{LH}}$$

(75)

where $M_L = M_{k=27}$ and $M_{LH} = M_{k=14}$ are the molar masses (Equation 50; Table 15) of L and LH, respectively. Denoting the component concentration of H by $c_{H,LH}$,

$$c_{H,LH} = c_H + c_{LH}\frac{M_H}{M_{LH}}$$

(76)

where $M_H = M_{k=1}$ and $M_{LH} = M_{k=14}$ are the molar masses (Equation 50; Table 15) of H and LH, respectively.

In the region of the dip in c_L along the boundary of H, the component concentration of L, $c_{L,LH}$ (Equation 75; Figure 37a), takes the form of the leading edge of a peak produced by a negatively buoyant solute undergoing a density-gradient-driven Johnston-Ogston effect (Moody, 2012a: Figure 7, Ka = 30.325 ml/g), but migrates centrifugally (Figure 37b) as a consequence of its form owing its existence to the centrifugally migrating boundary of H. In the region of the dip in c_H along the boundary of L, the component concentration of H, $c_{H,LH}$ (Equation 76; Figure 37a), takes

the form of the leading edge of a peak produced by a positively buoyant solute undergoing a density-gradient-driven Johnston-Ogston effect (Moody, 2012a: Figure 6, Ka = 30.325 ml/g), but migrates centripetally (Figure 37b) as a consequence of its form owing its existence to the centripetally migrating boundary of *L*. As the effect is seen even with each $y_{k,q}$ (Equation 59), each $h_{k,q}$ (60), each $p_{k,q}$ (Equation 64), each $(\sigma p)_{k,q}$ (Equation 65) and each c_k of $[c_i(r_j,t_\epsilon)]_{low}$ ($1 < k < 14$ and $14 < k < 27$ of Equation 73) set to zero (Figures 37c and 37d), it can be entirely attributed to the solutes predominant solutes, *L*, *H* and *LH*, being sedimentationally polydisperse participants in a mass-action association/dissociation reaction (Equation 71).

In a system of treatment group 1(100% $K_A > 0$), at a few minutes after t_{36}, the centripetally directed boundary of the floating solute *L* (Moody, 2012a: Figure 4, $K_A = 30.325$ ml/g) and the centrifugally directed boundary of the sedimenting solute *H* (Moody, 2012a: Figure 3, $K_A =$ 30.325 ml/g) meet near the radial centre of the system, and are maximally superimposed at about t_{51}. By a few minutes before t_{71}, the centripetally directed boundary of *L* and the centrifugally directed boundary of *H* have largely passed through each other, leaving, from the approximate radial centre of the system outwards, a continuously broadening region where c_H and c_L both approach zero. For treatment group 1, wherever either c_H or c_L is zero, c_{LH} is zero, and the oppositely directed mass transport of *L* and *H* thus ensures that, from the radial extrema inward, c_{LH} goes to zero with time.

Treatment group 4 reviewed in detail

As previously stated (*Details regarding the treatment groups, the Noise-Free Signals and the times chosen for analysis*), the explicit solute species of treatment group 4 consist of 27 single-

species components, of which 24 are present at low concentration ($1 < k < 14$ or $14 < k < 27$, Table 15), and 3, L_-, H_- and LH_-, are present at high concentration (Table 16). There being no L_+, H_+ or LH_+ present in treatment group 1, L_- is simply referred to as L, H_- is simply referred to as H and LH_- is simply referred to as LH. Every explicit solute species other than LH is modelled as a spherical, 30 nm diameter PS bead, and LH is modelled as a dimer of L and H. The particles are modelled as varying in the extent of deuteration (Figure 8) and consequent density (Table 15).

The high-concentration species, L, H and LH, are responsible for the major effects observed in the replicates of treatment group 4. Furthermore, the effects of low-concentration species 2 to 13 on species L and LH are similar to the effects of species H on species L and LH, while the effects of low-concentration species 15 to 26 on species H and LH are similar to the effects of species L on species H and LH. The net effects of the low-concentration species are thus small enough to permit the system to be described as if only species L, H and LH were present. This fact is exploited here to describe treatment group 4 as simply as possible. Figure 38, which shows c_L, c_H and c_{LH} versus r_j at times t_{36}, t_{51} and t_{66}, illustrates the behaviour of species L, H and LH described below. Other figures cited refer to a previous work (Moody, 2012a).

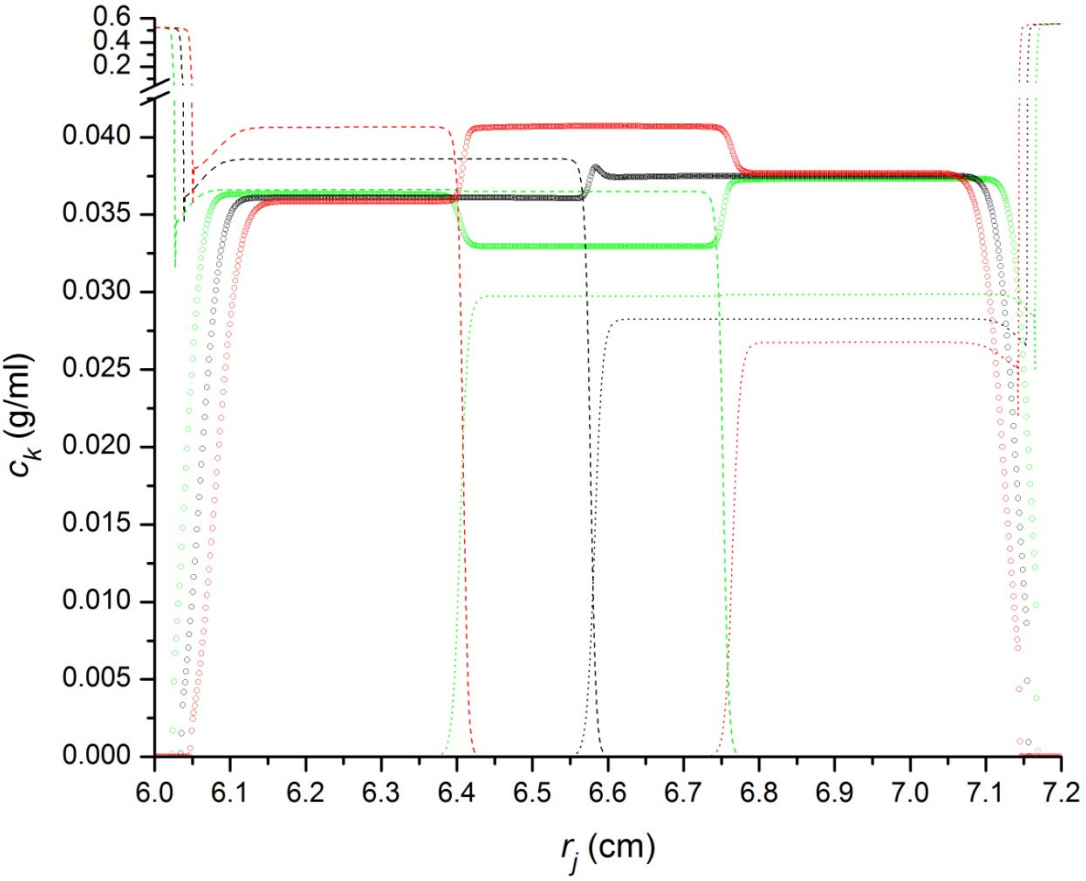

Figure 38. Treatment group $i = 4$ (0% $K_A > 0$). Shown are the species concentrations of L, H and LH, which are c_L (dashed lines), c_H (dotted lines) and c_{LH} (small, open circles), respectively, versus r_j at times t_{36} (green), t_{51} (black) and t_{66} (red).

Changes in c_{LH} (Moody, 2012a: Figure 12, K_A undefined) are entirely driven by changes in the concentrations of the system's other solute species, particularly c_H (Moody, 2012a: Figure 10, K_A undefined) and c_L (Moody, 2012a: Figure 11, K_A undefined). As c_H increases, s_{LH} becomes more negative, where $s_{LH} = s_{k=14}$ (Equation 70). As c_L increases, s_{LH} becomes more positive. Thus, where c_H accumulates in the pellet (the outermost zone of accumulation) or c_L accumulates in the supernatant (the innermost zone of accumulation), c_{LH} decreases.

Changes in c_{LH} have subtle effects on the mass flow of the other solute species. With respect to solute species H and L, as c_{LH} decreases, $|s_H|$ and $|s_L|$ increase, where $s_H = s_{k=1}$ and $s_L = s_{k=27}$ (Equation 70). Thus, the small decrease in c_H toward the pellet of species H (Moody, 2012a: Figure 10, K_A undefined), and the small decrease in c_L toward the supernatant of species L (Moody, 2012a: Figure 11, K_A undefined), are driven by the large decreases in c_{LH} toward the pellet and supernatant, respectively (Moody, 2012a: Figure 12, K_A undefined).

As L (Moody, 2012a: Figure 11, K_A undefined) migrates away from the pellet region, it leaves behind part of the plateau of H (Moody, 2012a: Figure 10, K_A undefined). The presence of H and the loss of L raise the local density of the solution, which confers a negative sedimentation coefficient on any LH present (Moody, 2012a: Figure 12, K_A undefined). Thus, the large decrease in c_{LH} toward the pellet is a centripetally directed boundary of LH. Between the centripetally directed boundary of LH and the centripetally directed boundary of L is a broadening plateau region in which c_{LH} is increased by a Johnston-Ogston effect of L on LH. This Johnston-Ogston-affected plateau region broadens with time because the centripetally directed boundary of L migrates much faster than the centripetally directed boundary of LH. The concentration of this Johnston-Ogston-affected plateau region increases with time due to the underlying effect of radial concentration on the centripetally migrating LH.

As H (Moody, 2012a: Figure 10, K_A undefined) migrates away from the supernatant region, it leaves behind part of the plateau of L (Moody, 2012a: Figure 11, K_A undefined). The presence of L and the loss of H lower the local density of the solution, which confers a positive sedimentation coefficient on any LH present (Moody, 2012a: Figure 12, K_A undefined). Thus, the large decrease

in c_{LH} toward the supernatant is a centrifugally directed boundary of *LH*. Between the centrifugally directed boundary of *LH* and the centrifugally directed boundary of *H* is a broadening plateau region in which c_{LH} is increased by a Johnston-Ogston effect of *H* on *LH*. This Johnston-Ogston-affected plateau region broadens with time because the centrifugally directed boundary of *H* migrates much faster than the centrifugally directed boundary of *LH*. The concentration of this Johnston-Ogston-affected plateau region decreases with time due to the underlying effect of radial dilution on the centrifugally migrating *LH*.

Before the centripetally directed boundary of *L* (Moody, 2012a: Figure 11, K_A undefined) and the centrifugally directed boundary of *H* (Moody, 2012a: Figure 10, K_A undefined) become superimposed, c_{LH} (Moody, 2012a: Figure 12, K_A undefined) barely changes from its initial concentration in the space remaining between its broadening Johnston-Ogston-affected plateau regions, as in that space, the balance between c_L and c_H changes slowly enough to keep *LH* close to neutral buoyancy. (The radial concentration effect increases c_L with time, and the radial dilution effect decreases c_H with time, causing $s_{LH} = s_{k=14}$ (Equation 70) between the Johnston-Ogston-affected plateau regions at t_{36} to approach 0.2 Svedberg, which is negligibly low.)

After the centripetally directed boundary of *L* (Moody, 2012a: Figure 11, K_A undefined) and the centrifugally directed boundary of *H* (Moody, 2012a: Figure 10, K_A undefined) have passed beyond superimposition and are migrating away from each other, the space between them is overlapped by the two Johnston-Ogston-affected plateau regions of c_{LH} (Moody, 2012a: Figure 12, K_A undefined). The overlap in the two Johnston-Ogston-affected plateau regions of c_{LH} broadens as the space between the centripetally directed boundary of *L* and the centrifugally directed boundary of *H* broadens. As both c_L and c_H are nearly zero where the Johnston-Ogston-affected

plateau regions of c_{LH} overlap, LH is extremely close to neutral buoyancy there, so that c_{LH} remains nearly constant with time there, at least until the time scale extends to days and weeks (Moody, 2012a: Figure 16, K_A undefined).

A consideration of the results for $G_i(s^*_{\varphi_\epsilon})$ and $G_{i,h}(s^*_{\varphi_\epsilon})$

Multiplication of the sedimentation coefficient distribution functions (Equation 10), $g_i(s^*_{\varphi_\epsilon})$ and $g_{i,h}(s^*_{\varphi_\epsilon})$, by the mask (Figure 32) for the corresponding time, t_{36}, t_{51} or t_{66}, left $g_i(s^*_{\varphi_\epsilon})$ and $g_{i,h}(s^*_{\varphi_\epsilon})$ unchanged wherever 5E-13 s $< |s^*_{\varphi_\epsilon}| <$ 10.625E-13 s, and set them to zero everywhere else (Figures 33 to 36). In effect, then, Figures 39 to 42 show the cumulative distribution function (Equation 11) of the apparent sedimentation coefficient within the limits (Table 19) applied to the calculation of $s^*_{i,\epsilon}$ and $s^*_{i,h,\epsilon}$ (Equation 13), in that

$$G_{i,h}(s^*_{\varphi_\epsilon=2N}) = \int_{s^*_{\varphi_\epsilon=1}}^{s^*_{\varphi_\epsilon=2N}} |g_{i,h}(s^*_{\varphi_\epsilon})| ds^*_{\varphi_\epsilon} \equiv \int_{s^*_{min<0}}^{s^*_{max<0}} |g_{i,h}(s^*_{\varphi_\epsilon})| ds^*_{\varphi_\epsilon} + \int_{s^*_{min>0}}^{s^*_{max>0}} |g_{i,h}(s^*_{\varphi_\epsilon})| ds^*_{\varphi_\epsilon}$$

$$= G_{i,h}(s^*_{max>0}) - G_{i,h}(s^*_{min>0}) + G_{i,h}(s^*_{max<0}) - G_{i,h}(s^*_{min<0}),$$

(77)

where $s^*_{min<0}$ = -10.625E-13 s, $s^*_{max<0}$ = -5E-13 s, $s^*_{min>0}$ = 5E-13 s and $s^*_{max>0}$ = 10.625E-13 s. Dropping the subscript h in Equation 77 yields the corresponding equation for the expectation value, $G_i(s^*_{\varphi_\epsilon=2N})$.

The equivalence of $G_{i,h}(s^*_{\varphi_\epsilon=2N})$ to $G_{i,h}(s^*_{max>0}) - G_{i,h}(s^*_{min>0}) + G_{i,h}(s^*_{max<0}) - G_{i,h}(s^*_{min<0})$ is not general, and thus Equation 77 is not general, as it only applies if all $g_{i,h}(s^*_{\varphi_\epsilon} < s^*_{min<0}) = 0$, all $g_{i,h}(s^*_{max<0} < s^*_{\varphi_\epsilon} < s^*_{min>0}) = 0$ and all $g_{i,h}(s^*_{\varphi_\epsilon} > s^*_{max>0}) = 0$, as is the case here after the

application of the masks (Figure 32) for t_{36}, t_{51} and t_{66}.

Within treatment group i, the mean of all $G_{i,h}(s^*_{\varphi_\epsilon})$ is given by

$$\langle G_i(s^*_{\varphi_\epsilon})\rangle = \frac{1}{n_i}\sum_{h=1}^{n_i} G_{i,h}(s^*_{\varphi_\epsilon}),$$

(78)

where n_i is the number of replicates for treatment group i. For treatment group i, the difference between the within-group mean, $\langle G_i(s^*_{\varphi_\epsilon})\rangle$, and the expectation value, $G_i(s^*_{\varphi_\epsilon})$, is denoted as

$$e_{G_i}(s^*_{\varphi_\epsilon}) = \langle G_i(s^*_{\varphi_\epsilon})\rangle - G_i(s^*_{\varphi_\epsilon}),$$

(79)

and is a measure of the accumulated error in $\langle G_i(s^*_{\varphi_\epsilon})\rangle$.

Tables 20 to 23 show, for $i = 1$ to 4, respectively, $G_i(s^*_{\varphi_\epsilon})$, $G_{i,h}(s^*_{\varphi_\epsilon})$, $\langle G_i(s^*_{\varphi_\epsilon})\rangle$, and $e_{G_i}(s^*_{\varphi_\epsilon})$ at $s^*_{\varphi_\epsilon} = 2N$ at each time, t_ϵ, analysed. The $G_i(s^*_{\varphi_{\epsilon=2N}})$ values of Tables 20 to 23 are equal to $G_i(s^*_{\varphi_\epsilon})$ at $s^*_{\varphi_\epsilon} \geq s^*_{max>0}$ in Figures 39 to 42, respectively, and the $G_{i,h}(s^*_{\varphi_{\epsilon=2N}})$ values of Tables 20 to 23 are equal to $G_{i,h}(s^*_{\varphi_\epsilon})$ at $s^*_{\varphi_\epsilon} \geq s^*_{max>0}$ in Figures 39 to 42, respectively.

$i = 1$	$t_\epsilon = t_{36} = 2160$ s	$t_\epsilon = t_{51} = 3060$ s	$t_\epsilon = t_{66} = 3960$ s
$G_i(s^*_{\varphi_{\epsilon=2N}})$	101.49655 fringe	26.34547 fringe	48.93778 fringe
h	$G_{i,h}(s^*_{\varphi_{36=2N}})$ (fringe)	$G_{i,h}(s^*_{\varphi_{51=2N}})$ (fringe)	$G_{i,h}(s^*_{\varphi_{66=2N}})$ (fringe)
1	101.91105	26.76412	50.45937
2	101.91331	26.80589	50.39927
3	101.94551	26.84282	50.53779
4	101.92266	26.92670	50.42958
5	101.95705	26.87394	50.57732

6	101.93849	26.84627	50.44268
7	101.90956	26.73099	50.44577
8	101.78902	26.78315	50.41757
9	101.95661	26.92200	50.38844
$\langle G_i(s^*_{\varphi_\epsilon=2N})\rangle$	101.91592 fringe	26.83288 fringe	50.45531 fringe
$e_{G_i}(s^*_{\varphi_\epsilon=2N})$	0.41937 fringe	0.48740 fringe	1.51753 fringe

Table 20. $G_i(s^*_{\varphi_\epsilon})$, $G_{i,h}(s^*_{\varphi_\epsilon})$, $\langle G_i(s^*_{\varphi_\epsilon})\rangle$, and $e_{G_i}(s^*_{\varphi_\epsilon})$ for $i = 1$ at $s^*_{\varphi_\epsilon=2N}$ at the times analysed: $t_\epsilon = t_{36}$, $t_\epsilon = t_{51}$ and $t_\epsilon = t_{66}$. The expectation values (Equation 77), $G_i(s^*_{\varphi_\epsilon=2N})$, are highlighted in blue. The replicate values (Equation 77), $G_{i,h}(s^*_{\varphi_\epsilon=2N})$, are not highlighted. The within-group mean values (Equation 78), $\langle G_i(s^*_{\varphi_\epsilon=2N})\rangle$, are highlighted in yellow. The accumulated error values (Equation 79), $e_{G_i}(s^*_{\varphi_\epsilon=2N})$, each being the difference between the mean and the expectation value, are highlighted in red. The $G_i(s^*_{\varphi_\epsilon=2N})$ values of this table are equal to $G_i(s^*_{\varphi_\epsilon})$ at $s^*_{\varphi_\epsilon} \geq s^*_{max>0}$ in Figure 39, and the $G_{i,h}(s^*_{\varphi_\epsilon=2N})$ values of this table are equal to $G_{i,h}(s^*_{\varphi_\epsilon})$ at $s^*_{\varphi_\epsilon} \geq s^*_{max>0}$ in Figure 39.

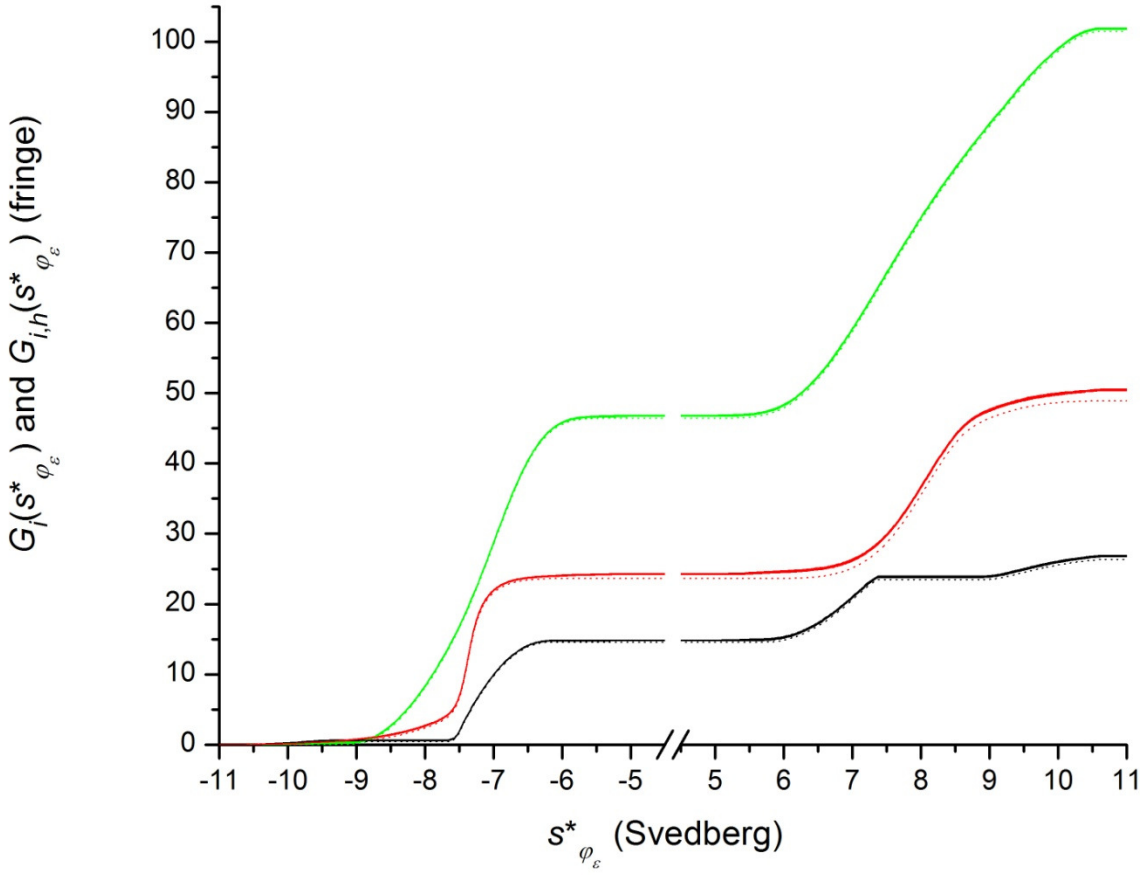

Figure 39. For $i = 1$ (100% $K_A > 0$, 0% K_A undefined), $G_i(s^*_{\varphi_\epsilon})$ at t_{36} (·····), t_{51} (·····) and t_{66} (·····), along with $G_{i,h}(s^*_{\varphi_\epsilon})$ for each replicate ($1 \leq h \leq 9$) at t_{36} (——), t_{51} (——) and t_{66} (——), all plotted against $s^*_{\varphi_\epsilon}$. These curves were obtained by integrating (Equation 77) those shown in Figure 33 with respect to $s^*_{\varphi_\epsilon}$. The $G_i(s^*_{\varphi_{\epsilon=2N}})$ values of Table 20 are equal to $G_i(s^*_{\varphi_\epsilon})$ at $s^*_{\varphi_\epsilon} \geq s^*_{max>0}$ in this figure, and the $G_{i,h}(s^*_{\varphi_{\epsilon=2N}})$ values of Table 20 are equal to $G_{i,h}(s^*_{\varphi_\epsilon})$ at $s^*_{\varphi_\epsilon} \geq s^*_{max>0}$ in this figure. Note: In Figures 20 to 31 and Figures 33 to 36, the results from noise-free data were shown as solid lines, while the results from noise-modified data were shown as dotted lines. Here, in Figures 39 to 42, as well as in Figures 44 to 47, that pattern is reversed to maximise distinguishability.

$i = 2$	$t_\epsilon = t_{36} = 2160$ s	$t_\epsilon = t_{51} = 3060$ s	$t_\epsilon = t_{66} = 3960$ s
$G_i\left(s^*_{\varphi_\epsilon=2N}\right)$	101.30369 fringe	25.87534 fringe	49.33616 fringe
h	$G_{i,h}\left(s^*_{\varphi_{36}=2N}\right)$ (fringe)	$G_{i,h}\left(s^*_{\varphi_{51}=2N}\right)$ (fringe)	$G_{i,h}\left(s^*_{\varphi_{66}=2N}\right)$ (fringe)
1	101.79919	26.30583	50.87075
2	101.81909	26.37697	50.63553
3	101.73783	26.26706	50.89893
4	101.85379	26.30790	50.97201
5	101.74203	26.33117	50.77086
6	101.82609	26.39495	50.77068
7	101.80078	26.37696	50.97742
8	101.67093	26.32227	50.93179
9	101.81939	26.35256	50.78000
$\langle G_i\left(s^*_{\varphi_\epsilon=2N}\right)\rangle$	101.78546 fringe	26.33730 fringe	50.84533 fringe
$e_{G_i}\left(s^*_{\varphi_\epsilon=2N}\right)$	0.48177 fringe	0.46196 fringe	1.50917 fringe

Table 21. $G_i\left(s^*_{\varphi_\epsilon}\right)$, $G_{i,h}\left(s^*_{\varphi_\epsilon}\right)$, $\langle G_i\left(s^*_{\varphi_\epsilon}\right)\rangle$, and $e_{G_i}\left(s^*_{\varphi_\epsilon}\right)$ for $i = 2$ at $s^*_{\varphi_\epsilon=2N}$ at the times analysed: $t_\epsilon = t_{36}$, $t_\epsilon = t_{51}$ and $t_\epsilon = t_{66}$. The expectation values (Equation 77), $G_i\left(s^*_{\varphi_\epsilon=2N}\right)$, are highlighted in blue. The replicate values (Equation 77), $G_{i,h}\left(s^*_{\varphi_\epsilon=2N}\right)$, are not highlighted. The within-group mean values (Equation 78), $\langle G_i\left(s^*_{\varphi_\epsilon=2N}\right)\rangle$, are highlighted in yellow. The accumulated error values (Equation 79), $e_{G_i}\left(s^*_{\varphi_\epsilon=2N}\right)$, each being the difference between the mean and the expectation value, are highlighted in red. The $G_i\left(s^*_{\varphi_\epsilon=2N}\right)$ values of this table are equal to $G_i\left(s^*_{\varphi_\epsilon}\right)$ at $s^*_{\varphi_\epsilon} \geq s^*_{max>0}$ in Figure 40, and the $G_{i,h}\left(s^*_{\varphi_\epsilon=2N}\right)$ values of this table are equal to $G_{i,h}\left(s^*_{\varphi_\epsilon}\right)$ at $s^*_{\varphi_\epsilon} \geq s^*_{max>0}$ in Figure 40.

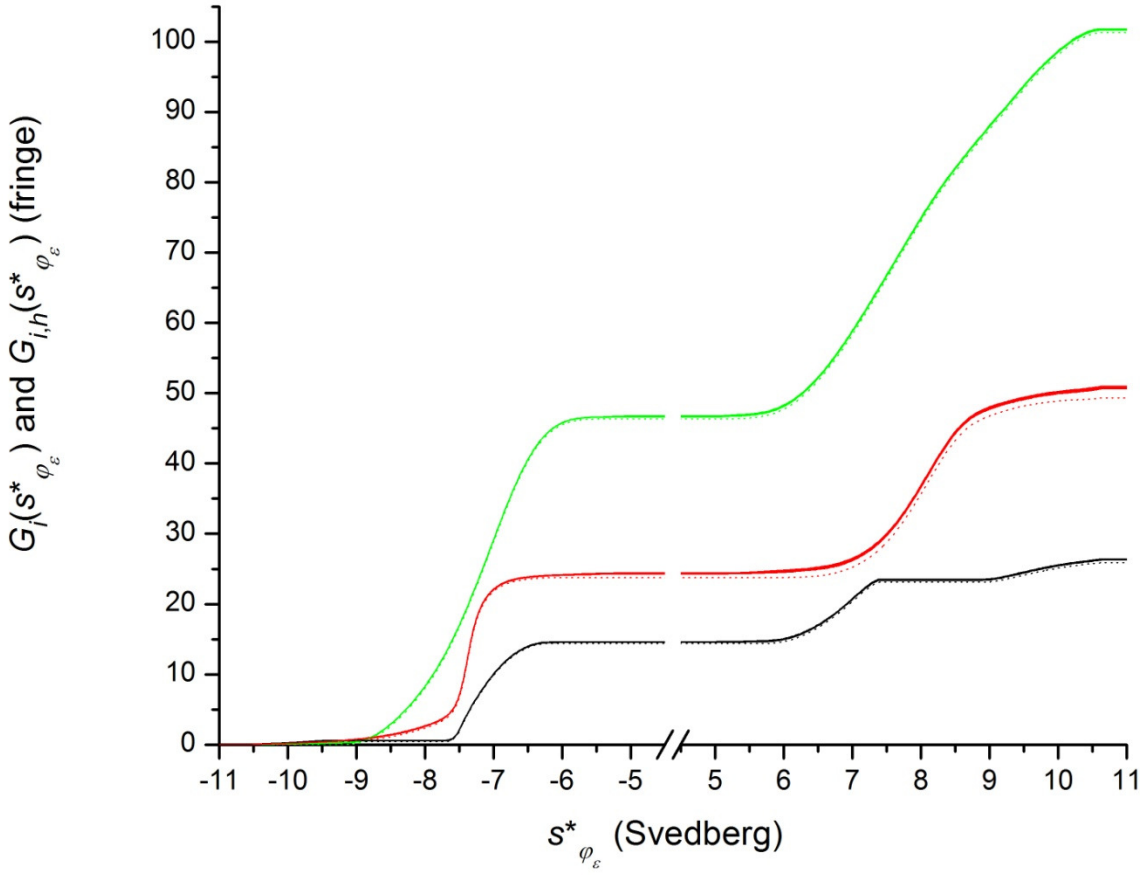

Figure 40. For $i = 2$ (99% $K_A > 0$, 1% K_A undefined), $G_i(s^*_{\varphi_\epsilon})$ at t_{36} (·····), t_{51} (·····) and t_{66} (·····), along with $G_{i,h}(s^*_{\varphi_\epsilon})$ for each replicate ($1 \leq h \leq 9$) at t_{36} (——), t_{51} (——) and t_{66} (——), all plotted against $s^*_{\varphi_\epsilon}$. (At Figure 39, see note regarding line markings.) These curves were obtained by integrating (Equation 77) those shown in Figure 34 with respect to $s^*_{\varphi_\epsilon}$. The $G_i(s^*_{\varphi_{\epsilon=2N}})$ values of Table 21 are equal to $G_i(s^*_{\varphi_\epsilon})$ at $s^*_{\varphi_\epsilon} \geq s^*_{max>0}$ in this figure, and the $G_{i,h}(s^*_{\varphi_{\epsilon=2N}})$ values of Table 21 are equal to $G_{i,h}(s^*_{\varphi_\epsilon})$ at $s^*_{\varphi_\epsilon} \geq s^*_{max>0}$ in this figure.

$i = 3$	$t_\epsilon = t_{36} = 2160$ s	$t_\epsilon = t_{51} = 3060$ s	$t_\epsilon = t_{66} = 3960$ s

$G_i\left(s^*_{\varphi_\epsilon=2N}\right)$	67.96545 fringe	20.42996 fringe	51.12734 fringe
h	$G_{i,h}\left(s^*_{\varphi_{36}=2N}\right)$ (fringe)	$G_{i,h}\left(s^*_{\varphi_{51}=2N}\right)$ (fringe)	$G_{i,h}\left(s^*_{\varphi_{66}=2N}\right)$ (fringe)
1	69.01049	22.03582	53.57553
2	69.03946	21.84881	53.23323
3	68.82548	22.26766	53.66466
$\langle G_i\left(s^*_{\varphi_\epsilon=2N}\right)\rangle$	68.95847 fringe	22.05076 fringe	53.49114 fringe
$e_{G_i}\left(s^*_{\varphi_\epsilon=2N}\right)$	0.99303 fringe	1.62080 fringe	2.36380 fringe

Table 22. $G_i\left(s^*_{\varphi_\epsilon}\right)$, $G_{i,h}\left(s^*_{\varphi_\epsilon}\right)$, $\langle G_i\left(s^*_{\varphi_\epsilon}\right)\rangle$, and $e_{G_i}\left(s^*_{\varphi_\epsilon}\right)$ for $i = 3$ at $s^*_{\varphi_\epsilon=2N}$ at the times analysed: $t_\epsilon = t_{36}$, $t_\epsilon = t_{51}$ and $t_\epsilon = t_{66}$. The expectation values (Equation 77), $G_i\left(s^*_{\varphi_\epsilon=2N}\right)$, are highlighted in blue. The replicate values (Equation 77), $G_{i,h}\left(s^*_{\varphi_\epsilon=2N}\right)$, are not highlighted. The within-group mean values (Equation 78), $\langle G_i\left(s^*_{\varphi_\epsilon=2N}\right)\rangle$, are highlighted in yellow. The accumulated error values (Equation 79), $e_{G_i}\left(s^*_{\varphi_\epsilon=2N}\right)$, each being the difference between the mean and the expectation value, are highlighted in red. The $G_i\left(s^*_{\varphi_\epsilon=2N}\right)$ values of this table are equal to $G_i\left(s^*_{\varphi_\epsilon}\right)$ at $s^*_{\varphi_\epsilon} \geq s^*_{max>0}$ in Figure 41, and the $G_{i,h}\left(s^*_{\varphi_\epsilon=2N}\right)$ values of this table are equal to $G_{i,h}\left(s^*_{\varphi_\epsilon}\right)$ at $s^*_{\varphi_\epsilon} \geq s^*_{max>0}$ in Figure 41.

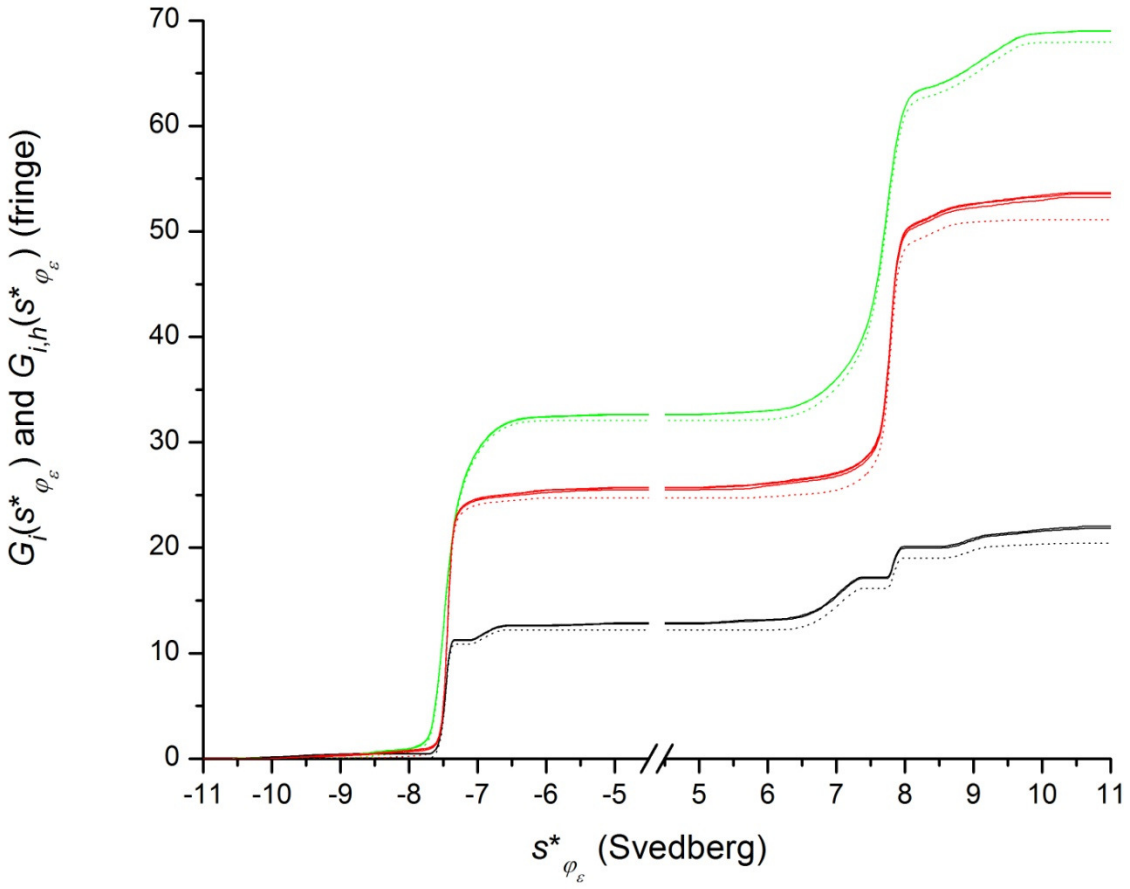

Figure 41. For $i = 3$ (50% $K_A > 0$, 50% K_A undefined), $G_i(s^*_{\varphi_\epsilon})$ at t_{36} (·····), t_{51} (·····) and t_{66} (·····), along with $G_{i,h}(s^*_{\varphi_\epsilon})$ for each replicate ($1 \leq h \leq 3$) at t_{36} (——), t_{51} (——) and t_{66} (——), all plotted against $s^*_{\varphi_\epsilon}$. (At Figure 39, see note regarding line markings.) These curves were obtained by integrating (Equation 77) those shown in Figure 35 with respect to $s^*_{\varphi_\epsilon}$. The $G_i(s^*_{\varphi_{\epsilon=2N}})$ values of Table 22 are equal to $G_i(s^*_{\varphi_\epsilon})$ at $s^*_{\varphi_\epsilon} \geq s^*_{max>0}$ in this figure, and the $G_{i,h}(s^*_{\varphi_{\epsilon=2N}})$ values of Table 22 are equal to $G_{i,h}(s^*_{\varphi_\epsilon})$ at $s^*_{\varphi_\epsilon} \geq s^*_{max>0}$ in this figure.

$i = 4$	$t_\epsilon = t_{36} = 2160$ s	$t_\epsilon = t_{51} = 3060$ s	$t_\epsilon = t_{66} = 3960$ s
$G_i(s^*_{\varphi_{\epsilon=2N}})$	44.29047 fringe	15.63733 fringe	44.59381 fringe
h	$G_{i,h}(s^*_{\varphi_{36=2N}})$ (fringe)	$G_{i,h}(s^*_{\varphi_{51=2N}})$ (fringe)	$G_{i,h}(s^*_{\varphi_{66=2N}})$ (fringe)

1	46.13008	18.18701	48.42823
2	46.16479	18.32052	48.28043
3	46.27128	18.67235	48.31607
$\langle G_i(s^*_{\varphi_\epsilon=2N})\rangle$	46.18872 fringe	18.39329 fringe	48.34158 fringe
$e_{G_i}(s^*_{\varphi_\epsilon=2N})$	1.89825 fringe	2.75596 fringe	3.74777 fringe

Table 23. $G_i(s^*_{\varphi_\epsilon})$, $G_{i,h}(s^*_{\varphi_\epsilon})$, $\langle G_i(s^*_{\varphi_\epsilon})\rangle$, and $e_{G_i}(s^*_{\varphi_\epsilon})$ for $i = 4$ at $s^*_{\varphi_\epsilon=2N}$ at the times analysed: $t_\epsilon = t_{36}$, $t_\epsilon = t_{51}$ and $t_\epsilon = t_{66}$. The expectation values (Equation 77), $G_i(s^*_{\varphi_\epsilon=2N})$, are highlighted in blue. The replicate values (Equation 77), $G_{i,h}(s^*_{\varphi_\epsilon=2N})$, are not highlighted. The within-group mean values (Equation 78), $\langle G_i(s^*_{\varphi_\epsilon=2N})\rangle$, are highlighted in yellow. The accumulated error values (Equation 79), $e_{G_i}(s^*_{\varphi_\epsilon=2N})$, each being the difference between the mean and the expectation value, are highlighted in red. The $G_i(s^*_{\varphi_\epsilon=2N})$ values of this table are equal to $G_i(s^*_{\varphi_\epsilon})$ at $s^*_{\varphi_\epsilon} \geq s^*_{max>0}$ in Figure 42, and the $G_{i,h}(s^*_{\varphi_\epsilon=2N})$ values of this table are equal to $G_{i,h}(s^*_{\varphi_\epsilon})$ at $s^*_{\varphi_\epsilon} \geq s^*_{max>0}$ in Figure 42.

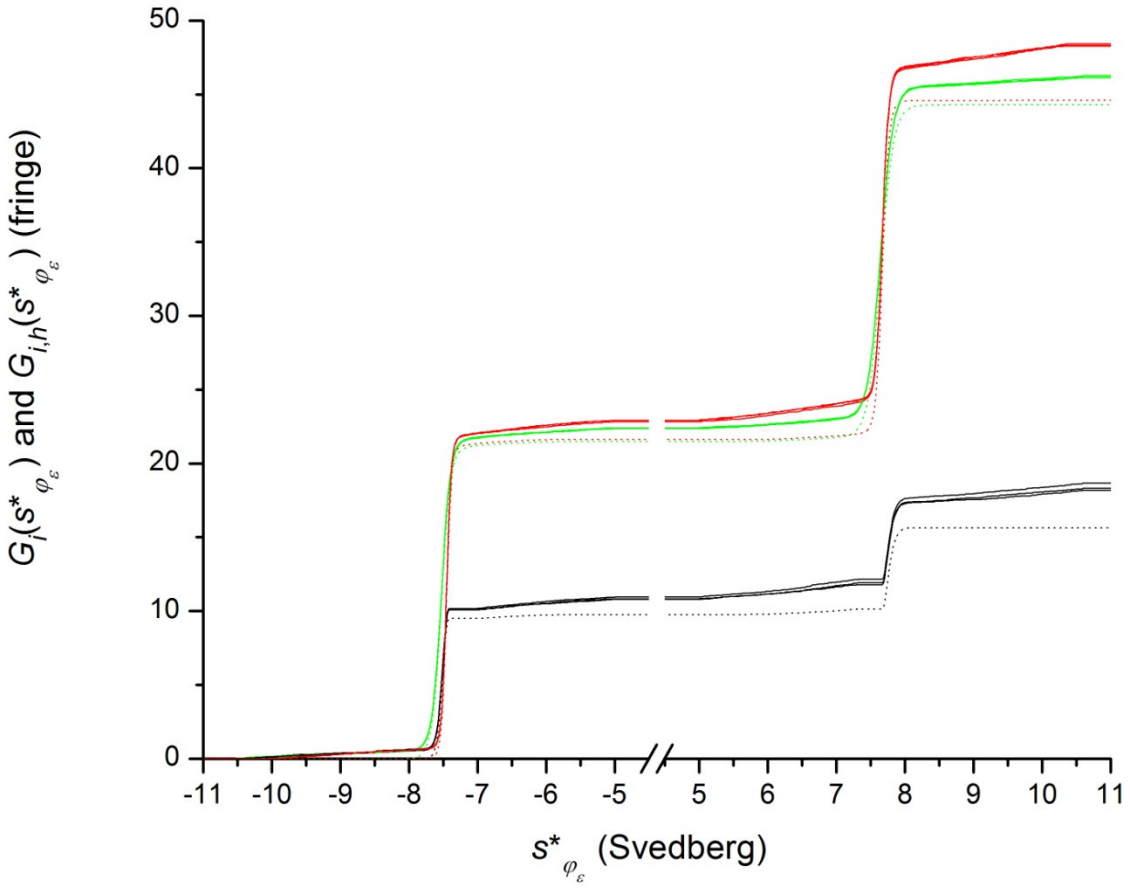

Figure 42. For $i = 4$ (0% $K_A > 0$, 100% K_A undefined), $G_i(s^*_{\varphi_\epsilon})$ at t_{36} (·····), t_{51} (·····) and t_{66} (·····), along with $G_{i,h}(s^*_{\varphi_\epsilon})$ for each replicate ($1 \leq h \leq 3$) at t_{36} (——), t_{51} (——) and t_{66} (——), all plotted against $s^*_{\varphi_\epsilon}$. (At Figure 39, see note regarding line markings.) These curves were obtained by integrating (Equation 77) those shown in Figure 36 with respect to $s^*_{\varphi_\epsilon}$. The $G_i(s^*_{\varphi_{\epsilon=2N}})$ values of Table 23 are equal to $G_i(s^*_{\varphi_\epsilon})$ at $s^*_{\varphi_\epsilon} \geq s^*_{max>0}$ in this figure, and the $G_{i,h}(s^*_{\varphi_{\epsilon=2N}})$ values of Table 23 are equal to $G_{i,h}(s^*_{\varphi_\epsilon})$ at $s^*_{\varphi_\epsilon} \geq s^*_{max>0}$ in this figure.

The accumulated error in $G_{i,h}(s^*_{\varphi_{\epsilon=2N}})$ increases in proportion to the clipping of random noise

A survey of Tables 20 to 23 reveals that the within-group mean (Equation 78), $\langle G_i\left(s^*_{\varphi_\epsilon=2N}\right)\rangle$, is always greater than the expectation value (Equation 77), $G_i\left(s^*_{\varphi_\epsilon=2N}\right)$. Thus, the accumulated error (Equation 79), $e_{G_i}\left(s^*_{\varphi_\epsilon=2N}\right)$, is always greater than zero. For any given time, t_ϵ, treatment groups 1 and 2 exhibit similar values of $e_{G_i}\left(s^*_{\varphi_\epsilon=2N}\right)$, as would be expected, given the small differences between those two treatment groups.

For any given time, t_ϵ, treatment groups 1 and 2 also exhibit the smallest values of $e_{G_i}\left(s^*_{\varphi_\epsilon=2N}\right)$, which is not surprising, given that the ranges of $s^*_{\varphi_\epsilon}$ over which $g_{i,h}\left(s^*_{\varphi_\epsilon}\right)$ and $g_i\left(s^*_{\varphi_\epsilon}\right)$ are integrated were chosen (Figure 32b) to maximise the signal-to-noise ratio of $g_{i,h}\left(s^*_{\varphi_\epsilon}\right)$ within treatment groups 1 and 2, and thereby optimise the confidence with which those two extremely similar treatment groups could be distinguished. The cost of such optimisation for treatment groups 1 and 2 is relatively poor signal-to-noise characteristics for treatment groups 3 and 4. The greater the regions of low signal-to-noise within the ranges of $s^*_{\varphi_\epsilon}$ used to calculate $g_{i,h}\left(s^*_{\varphi_\epsilon}\right)$, the greater the accumulated net noise in $G_{i,h}\left(s^*_{\varphi_\epsilon}\right)$. As i increases from 2 to 4, so does the prevalence of low signal-to-noise regions within the ranges of $s^*_{\varphi_\epsilon}$ used to calculate $g_{i,h}\left(s^*_{\varphi_\epsilon}\right)$ and $g_i\left(s^*_{\varphi_\epsilon}\right)$ any given time, t_ϵ. Thus, for any given time, t_ϵ, $e_{G_i}\left(s^*_{\varphi_\epsilon=2N}\right)$ increases as i increases from 2 to 4.

Treatment groups 3 and 4 include broad swathes of $s^*_{\varphi_\epsilon}$ values over which the derivative of the noise-free signal, $Y_i\left(s^*_{\varphi_\epsilon}\right)$, with respect to $s^*_{\varphi_\epsilon}$ at time t_ϵ is zero, and the more the limits of analysis ($s^*_{min<0}$ = -10.625E-13 s, $s^*_{max<0}$ = -5E-13 s, $s^*_{min>0}$ = 5E-13 s and $s^*_{max>0}$ = 10.625E-13 s of Table 19 and Equation 77) include such $s^*_{\varphi_\epsilon}$ values, the more $e_{G_i}\left(s^*_{\varphi_\epsilon=2N}\right)$ is increased. The effect stems from data clipping in going from $\left(\frac{\partial Y_{i,h}\left(s^*_{\varphi_\epsilon}\right)}{\partial s^*_{\varphi_\epsilon}}\right)_t$ to $q_{i,h}\left(s^*_{\varphi_\epsilon}\right)$. (See *Analysis of data for which*

the noise-free signal is always zero everywhere and *Mitigation of data clipping*.)

Over a range of $s^*_{\varphi_\epsilon}$ values throughout which $\left(\frac{\partial Y_{i,h}(s^*_{\varphi_\epsilon})}{\partial s^*_{\varphi_\epsilon}}\right)_t$ (Equation 8) is either above zero or below zero exclusively, and throughout which $s^*_{\varphi_\epsilon}\left(\frac{\partial Y_{i,h}(s^*_{\varphi_\epsilon})}{\partial s^*_{\varphi_\epsilon}}\right)_t < 0$ holds, the elimination function (Equation 9b), $e_{i,h}(s^*_{\varphi_\epsilon})$, would evaluate to $\left(\frac{\partial Y_{i,h}(s^*_{\varphi_\epsilon})}{\partial s^*_{\varphi_\epsilon}}\right)_t$ at each value of $s^*_{\varphi_\epsilon}$, and thus, by Equation 9a, $q_{i,h}(s^*_{\varphi_\epsilon}) = \left(\frac{\partial Y_{i,h}(s^*_{\varphi_\epsilon})}{\partial s^*_{\varphi_\epsilon}}\right)_t - e_{i,h}(s^*_{\varphi_\epsilon})$ would evaluate to zero at each value of $s^*_{\varphi_\epsilon}$, with the result that neither the signal, $\left(\frac{\partial Y_i(s^*_{\varphi_\epsilon})}{\partial s^*_{\varphi_\epsilon}}\right)_t$, nor the noise, $\left(\frac{\partial Y_{i,h}(s^*_{\varphi_\epsilon})}{\partial s^*_{\varphi_\epsilon}}\right)_t - \left(\frac{\partial Y_i(s^*_{\varphi_\epsilon})}{\partial s^*_{\varphi_\epsilon}}\right)_t$, would propagate to $g_{i,h}(s^*_{\varphi_\epsilon}) = q_{i,h}(s^*_{\varphi_\epsilon})e^{2s^*_{\varphi_\epsilon}\omega^2 t_\epsilon}$ (Equation 10) at any value of $s^*_{\varphi_\epsilon}$. Instead, with $q_{i,h}(s^*_{\varphi_\epsilon}) = 0$ everywhere throughout a range of $s^*_{\varphi_\epsilon}$ values in which $s^*_{\varphi_\epsilon}\left(\frac{\partial Y_{i,h}(s^*_{\varphi_\epsilon})}{\partial s^*_{\varphi_\epsilon}}\right)_t < 0$, $g_{i,h}(s^*_{\varphi_\epsilon}) = 0$ would be obtained everywhere, in which case, the signal and the net noise accumulated by $G_{i,h}(s^*_{\varphi_\epsilon})$ upon integration (Equations 11 and 77) of $\left|g_{i,h}(s^*_{\varphi_\epsilon})\right|$ would be zero.

Over a range of $s^*_{\varphi_\epsilon}$ values throughout which $\left(\frac{\partial Y_{i,h}(s^*_{\varphi_\epsilon})}{\partial s^*_{\varphi_\epsilon}}\right)_t$ (Equation 8) is either above zero or below zero exclusively, and throughout which $s^*_{\varphi_\epsilon}\left(\frac{\partial Y_{i,h}(s^*_{\varphi_\epsilon})}{\partial s^*_{\varphi_\epsilon}}\right)_t > 0$ holds, the elimination function (Equation 9b), $e_{i,h}(s^*_{\varphi_\epsilon})$, would evaluate to zero at each value of $s^*_{\varphi_\epsilon}$, and thus, by Equation 9a, $q_{i,h}(s^*_{\varphi_\epsilon}) = \left(\frac{\partial Y_{i,h}(s^*_{\varphi_\epsilon})}{\partial s^*_{\varphi_\epsilon}}\right)_t - e_{i,h}(s^*_{\varphi_\epsilon})$ would evaluate to $\left(\frac{\partial Y_{i,h}(s^*_{\varphi_\epsilon})}{\partial s^*_{\varphi_\epsilon}}\right)_t$ at each value of $s^*_{\varphi_\epsilon}$, with the result that both the signal, $\left(\frac{\partial Y_i(s^*_{\varphi_\epsilon})}{\partial s^*_{\varphi_\epsilon}}\right)_t$, and the noise, $\left(\frac{\partial Y_{i,h}(s^*_{\varphi_\epsilon})}{\partial s^*_{\varphi_\epsilon}}\right)_t - \left(\frac{\partial Y_i(s^*_{\varphi_\epsilon})}{\partial s^*_{\varphi_\epsilon}}\right)_t$, would propagate to $g_{i,h}(s^*_{\varphi_\epsilon}) = q_{i,h}(s^*_{\varphi_\epsilon})e^{2s^*_{\varphi_\epsilon}\omega^2 t_\epsilon}$ (Equation 10) at each value of $s^*_{\varphi_\epsilon}$. The noise in $\left(\frac{\partial Y_{i,h}(s^*_{\varphi_\epsilon})}{\partial s^*_{\varphi_\epsilon}}\right)_t$ would

include points where $\left(\frac{\partial Y_{i,h}(s^*_{\varphi\epsilon})}{\partial s^*_{\varphi\epsilon}}\right)_t - \left(\frac{\partial Y_i(s^*_{\varphi\epsilon})}{\partial s^*_{\varphi\epsilon}}\right)_t > 0$ and points where $\left(\frac{\partial Y_{i,h}(s^*_{\varphi\epsilon})}{\partial s^*_{\varphi\epsilon}}\right)_t - \left(\frac{\partial Y_i(s^*_{\varphi\epsilon})}{\partial s^*_{\varphi\epsilon}}\right)_t < 0$ such that the sum of all such differences would approach zero as the number of points within the range of $s^*_{\varphi_\epsilon}$ approached infinity. Thus, with $q_{i,h}(s^*_{\varphi_\epsilon}) = \left(\frac{\partial Y_{i,h}(s^*_{\varphi\epsilon})}{\partial s^*_{\varphi\epsilon}}\right)_t$ everywhere throughout a range of $s^*_{\varphi_\epsilon}$ values in which $s^*_{\varphi_\epsilon}\left(\frac{\partial Y_{i,h}(s^*_{\varphi\epsilon})}{\partial s^*_{\varphi\epsilon}}\right)_t > 0$, $g_{i,h}(s^*_{\varphi_\epsilon}) = \left(\frac{\partial Y_{i,h}(s^*_{\varphi\epsilon})}{\partial s^*_{\varphi\epsilon}}\right)_t e^{2s^*_{\varphi_\epsilon}\omega^2 t_\epsilon}$ would be obtained everywhere, in which case, the signal and the net noise accumulated by $G_{i,h}(s^*_{\varphi_\epsilon})$ upon integration (Equations 11 and 77) of $\left|g_{i,h}(s^*_{\varphi_\epsilon})\right|$ would be minimal, as for $\left|g_{i,h}(s^*_{\varphi_\epsilon}) - g_i(s^*_{\varphi_\epsilon})\right|$ of any given magnitude, $g_{i,h}(s^*_{\varphi_\epsilon}) - g_i(s^*_{\varphi_\epsilon}) > 0$ would be as likely an outcome as $g_{i,h}(s^*_{\varphi_\epsilon}) - g_i(s^*_{\varphi_\epsilon}) < 0$, where $g_i(s^*_{\varphi_\epsilon}) = q_i(s^*_{\varphi_\epsilon})e^{2s^*_{\varphi_\epsilon}\omega^2 t_\epsilon}$, $q_i(s^*_{\varphi_\epsilon}) = \left(\frac{\partial Y_i(s^*_{\varphi\epsilon})}{\partial s^*_{\varphi\epsilon}}\right)_t - e_i(s^*_{\varphi_\epsilon})$, $\left(\frac{\partial Y_i(s^*_{\varphi\epsilon})}{\partial s^*_{\varphi\epsilon}}\right)_t$ is the noise-free signal, and, given $s^*_{\varphi_\epsilon}\left(\frac{\partial Y_i(s^*_{\varphi\epsilon})}{\partial s^*_{\varphi\epsilon}}\right)_t > 0$, $e_i(s^*_{\varphi_\epsilon}) = 0$.

Where the data largely consist of broad ranges of $s^*_{\varphi_\epsilon}$ values throughout which $\left(\frac{\partial Y_{i,h}(s^*_{\varphi\epsilon})}{\partial s^*_{\varphi\epsilon}}\right)_t$ is either above zero or below zero exclusively, no data clipping occurs, regardless of whether $s^*_{\varphi_\epsilon}\left(\frac{\partial Y_{i,h}(s^*_{\varphi\epsilon})}{\partial s^*_{\varphi\epsilon}}\right)_t < 0$ or $s^*_{\varphi_\epsilon}\left(\frac{\partial Y_{i,h}(s^*_{\varphi\epsilon})}{\partial s^*_{\varphi\epsilon}}\right)_t > 0$. Over a range of $s^*_{\varphi_\epsilon}$ values throughout which $\left(\frac{\partial Y_{i,h}(s^*_{\varphi\epsilon})}{\partial s^*_{\varphi\epsilon}}\right)_t$ (Equation 8) is either above zero or below zero exclusively, all of the data are replaced with zeroes if $s^*_{\varphi_\epsilon}\left(\frac{\partial Y_{i,h}(s^*_{\varphi\epsilon})}{\partial s^*_{\varphi\epsilon}}\right)_t < 0$ holds throughout, and all of the data are retained if $s^*_{\varphi_\epsilon}\left(\frac{\partial Y_{i,h}(s^*_{\varphi\epsilon})}{\partial s^*_{\varphi\epsilon}}\right)_t > 0$ holds throughout. In contrast, in data clipping, which is a phenomenon restricted to ranges of $s^*_{\varphi_\epsilon}$ within which $\left(\frac{\partial Y_{i,h}(s^*_{\varphi\epsilon})}{\partial s^*_{\varphi\epsilon}}\right)_t$ is noise that varies randomly between positive and negative values, a random set of approximately half the data yield $s^*_{\varphi_\epsilon}\left(\frac{\partial Y_{i,h}(s^*_{\varphi\epsilon})}{\partial s^*_{\varphi\epsilon}}\right)_t >$

0 and are accordingly retained, while the rest of the data yield $s^*_{\varphi_\epsilon}\left(\frac{\partial Y_{i,h}(s^*_{\varphi_\epsilon})}{\partial s^*_{\varphi_\epsilon}}\right)_t < 0$ and are accordingly replaced with zeroes.

In general, $s^*_{\varphi_\epsilon}\left(\frac{\partial Y_{i,h}(s^*_{\varphi_\epsilon})}{\partial s^*_{\varphi_\epsilon}}\right)_t > 0$ holds for all $\left(\frac{\partial Y_{i,h}(s^*_{\varphi_\epsilon})}{\partial s^*_{\varphi_\epsilon}}\right)_t$ data that are retained, and all data that are retained are described as belonging to the data-retention category, while $s^*_{\varphi_\epsilon}\left(\frac{\partial Y_{i,h}(s^*_{\varphi_\epsilon})}{\partial s^*_{\varphi_\epsilon}}\right)_t < 0$ holds for all $\left(\frac{\partial Y_{i,h}(s^*_{\varphi_\epsilon})}{\partial s^*_{\varphi_\epsilon}}\right)_t$ data that are replaced with zeroes, and all data that are replaced with zeroes are described as belonging to the data-replacement (with zeroes) category. A value of $\left(\frac{\partial Y_{i,h}(s^*_{\varphi_\epsilon})}{\partial s^*_{\varphi_\epsilon}}\right)_t$ in the data-retention category yields, by Equation 9a, $q_{i,h}(s^*_{\varphi_\epsilon}) = \left(\frac{\partial Y_{i,h}(s^*_{\varphi_\epsilon})}{\partial s^*_{\varphi_\epsilon}}\right)_t$, which, by Equation 10, propagates to $g_{i,h}(s^*_{\varphi_\epsilon}) = q_{i,h}(s^*_{\varphi_\epsilon})e^{2s^*_{\varphi_\epsilon}\omega^2 t_\epsilon}$ as $\left(\frac{\partial Y_{i,h}(s^*_{\varphi_\epsilon})}{\partial s^*_{\varphi_\epsilon}}\right)_t e^{2s^*_{\varphi_\epsilon}\omega^2 t_\epsilon}$, and thence, by Equation 11 or 77, contributes to the noise accumulated by $G_{i,h}(s^*_{\varphi_\epsilon})$ upon integration of $\left|g_{i,h}(s^*_{\varphi_\epsilon})\right|$. A value of $\left(\frac{\partial Y_{i,h}(s^*_{\varphi_\epsilon})}{\partial s^*_{\varphi_\epsilon}}\right)_t$ in the data-replacement category yields $q_{i,h}(s^*_{\varphi_\epsilon}) = 0$, which renders $g_{i,h}(s^*_{\varphi_\epsilon})$ equal to zero, and thence contributes nothing to $G_{i,h}(s^*_{\varphi_\epsilon})$ upon integration of $\left|g_{i,h}(s^*_{\varphi_\epsilon})\right|$, provided that, as it is often found, $g_{i,h}(s^*_{\varphi_\epsilon-1})$ and $g_{i,h}(s^*_{\varphi_\epsilon+1})$ are also equal to zero.

Over a range of $s^*_{\varphi_\epsilon}$ values throughout which $\left(\frac{\partial Y_i(s^*_{\varphi_\epsilon})}{\partial s^*_{\varphi_\epsilon}}\right)_t = 0$, $\left(\frac{\partial Y_{i,h}(s^*_{\varphi_\epsilon})}{\partial s^*_{\varphi_\epsilon}}\right)_t$ will consist solely of noise that will be greater than zero at a randomly distributed set of approximately half of the $s^*_{\varphi_\epsilon}$ values, and will be less than zero at the rest of the $s^*_{\varphi_\epsilon}$ values, assuming, as is likely, that $\left(\frac{\partial Y_{i,h}(s^*_{\varphi_\epsilon})}{\partial s^*_{\varphi_\epsilon}}\right)_t$ would only equal zero very rarely. Within a range of $s^*_{\varphi_\epsilon}$ values throughout which

$\left(\frac{\partial Y_i(s^*_{\varphi\epsilon})}{\partial s^*_{\varphi\epsilon}}\right)_t = 0$, $\left(\frac{\partial Y_{i,h}(s^*_{\varphi\epsilon})}{\partial s^*_{\varphi\epsilon}}\right)_t$ values will fall into either the data-retention category or the data-replacement (with zeroes) category.

Where $s^*_{\varphi\epsilon}\left(\frac{\partial Y_{i,h}(s^*_{\varphi\epsilon})}{\partial s^*_{\varphi\epsilon}}\right)_t > 0$, $\left(\frac{\partial Y_{i,h}(s^*_{\varphi\epsilon})}{\partial s^*_{\varphi\epsilon}}\right)_t$ falls into the data-retention category. Within a range of $s^*_{\varphi\epsilon}$ values throughout which $\left(\frac{\partial Y_i(s^*_{\varphi\epsilon})}{\partial s^*_{\varphi\epsilon}}\right)_t = 0$, at a randomly distributed set of approximately half of the $s^*_{\varphi\epsilon}$ values, $s^*_{\varphi\epsilon}\left(\frac{\partial Y_{i,h}(s^*_{\varphi\epsilon})}{\partial s^*_{\varphi\epsilon}}\right)_t > 0$ would hold. Where $s^*_{\varphi\epsilon}\left(\frac{\partial Y_{i,h}(s^*_{\varphi\epsilon})}{\partial s^*_{\varphi\epsilon}}\right)_t > 0$ held, by Equation 9, $e_{i,h}(s^*_{\varphi\epsilon}) = 0$ would apply to the calculation of $q_{i,h}(s^*_{\varphi\epsilon}) = \left(\frac{\partial Y_{i,h}(s^*_{\varphi\epsilon})}{\partial s^*_{\varphi\epsilon}}\right)_t - e_{i,h}(s^*_{\varphi\epsilon})$, from which $q_{i,h}(s^*_{\varphi\epsilon}) = \left(\frac{\partial Y_{i,h}(s^*_{\varphi\epsilon})}{\partial s^*_{\varphi\epsilon}}\right)_t$ would be obtained. By Equation 10, $g_{i,h}(s^*_{\varphi\epsilon}) = q_{i,h}(s^*_{\varphi\epsilon})e^{2s^*_{\varphi\epsilon}\omega^2 t_\epsilon}$. Thus, $g_{i,h}(s^*_{\varphi\epsilon}) = \left(\frac{\partial Y_{i,h}(s^*_{\varphi\epsilon})}{\partial s^*_{\varphi\epsilon}}\right)_t e^{2s^*_{\varphi\epsilon}\omega^2 t_\epsilon}$ would be obtained at any value of $s^*_{\varphi\epsilon}$ where $q_{i,h}(s^*_{\varphi\epsilon}) = \left(\frac{\partial Y_{i,h}(s^*_{\varphi\epsilon})}{\partial s^*_{\varphi\epsilon}}\right)_t$, and the noise, which is all that $\left(\frac{\partial Y_{i,h}(s^*_{\varphi\epsilon})}{\partial s^*_{\varphi\epsilon}}\right)_t$ constitutes wherever $\left(\frac{\partial Y_i(s^*_{\varphi\epsilon})}{\partial s^*_{\varphi\epsilon}}\right)_t = 0$, would be a source of the net noise accumulated by $G_{i,h}(s^*_{\varphi\epsilon})$ upon integration (Equations 11 and 77) of $\left|g_{i,h}(s^*_{\varphi\epsilon})\right|$.

Where $s^*_{\varphi\epsilon}\left(\frac{\partial Y_{i,h}(s^*_{\varphi\epsilon})}{\partial s^*_{\varphi\epsilon}}\right)_t < 0$, $\left(\frac{\partial Y_{i,h}(s^*_{\varphi\epsilon})}{\partial s^*_{\varphi\epsilon}}\right)_t$ falls into the data-replacement (with zeroes) category. Within a range of $s^*_{\varphi\epsilon}$ values throughout which $\left(\frac{\partial Y_i(s^*_{\varphi\epsilon})}{\partial s^*_{\varphi\epsilon}}\right)_t = 0$, at a randomly distributed set of approximately half of the $s^*_{\varphi\epsilon}$ values, $s^*_{\varphi\epsilon}\left(\frac{\partial Y_{i,h}(s^*_{\varphi\epsilon})}{\partial s^*_{\varphi\epsilon}}\right)_t < 0$ would hold. Where $s^*_{\varphi\epsilon}\left(\frac{\partial Y_{i,h}(s^*_{\varphi\epsilon})}{\partial s^*_{\varphi\epsilon}}\right)_t < 0$ held, by Equation 9, $e_{i,h}(s^*_{\varphi\epsilon}) = \left(\frac{\partial Y_{i,h}(s^*_{\varphi\epsilon})}{\partial s^*_{\varphi\epsilon}}\right)_t$ would apply to the calculation of $q_{i,h}(s^*_{\varphi\epsilon}) =$

$\left(\frac{\partial Y_{i,h}(s^*_{\varphi\epsilon})}{\partial s^*_{\varphi\epsilon}}\right)_t - e_{i,h}(s^*_{\varphi_\epsilon})$, from which $q_{i,h}(s^*_{\varphi_\epsilon}) = 0$ would be obtained. By Equation 10, $g_{i,h}(s^*_{\varphi_\epsilon}) = q_{i,h}(s^*_{\varphi_\epsilon})e^{2s^*_{\varphi\epsilon}\omega^2 t_\epsilon}$. Thus, $g_{i,h}(s^*_{\varphi_\epsilon}) = 0$ would be obtained at any value of $s^*_{\varphi\epsilon}$ where $q_{i,h}(s^*_{\varphi_\epsilon}) = 0$, and the noise, which is all that $\left(\frac{\partial Y_{i,h}(s^*_{\varphi\epsilon})}{\partial s^*_{\varphi\epsilon}}\right)_t$ constitutes wherever $\left(\frac{\partial Y_i(s^*_{\varphi\epsilon})}{\partial s^*_{\varphi\epsilon}}\right)_t = 0$, would not be a source of the net noise accumulated by $G_{i,h}(s^*_{\varphi_\epsilon})$ upon integration (Equations 11 and 77) of $\left|g_{i,h}(s^*_{\varphi_\epsilon})\right|$.

Thus, over a range of $s^*_{\varphi_\epsilon}$ values throughout which $\left(\frac{\partial Y_i(s^*_{\varphi\epsilon})}{\partial s^*_{\varphi\epsilon}}\right)_t = 0$, the noise, $\left(\frac{\partial Y_{i,h}(s^*_{\varphi\epsilon})}{\partial s^*_{\varphi\epsilon}}\right)_t$, is clipped. Approximately half the noise would be in the data-retention category, for which $s^*_{\varphi_\epsilon}\left(\frac{\partial Y_{i,h}(s^*_{\varphi\epsilon})}{\partial s^*_{\varphi\epsilon}}\right)_t > 0$. Only the noise in the data-retention category would propagate to $g_{i,h}(s^*_{\varphi_\epsilon})$, and thence contribute to the noise accumulated by $G_{i,h}(s^*_{\varphi_\epsilon})$ upon integration of $\left|g_{i,h}(s^*_{\varphi_\epsilon})\right|$. The rest of the noise, being in the data-replacement category, would render $g_{i,h}(s^*_{\varphi_\epsilon})$ equal to zero, and thence contribute nothing to $G_{i,h}(s^*_{\varphi_\epsilon})$ upon integration of $\left|g_{i,h}(s^*_{\varphi_\epsilon})\right|$. The problem with data clipping is not that roughly half the data yield $g_{i,h}(s^*_{\varphi_\epsilon}) = 0$ over a range of $s^*_{\varphi_\epsilon}$ values throughout which $\left(\frac{\partial Y_i(s^*_{\varphi\epsilon})}{\partial s^*_{\varphi\epsilon}}\right)_t = 0$. The problem with data clipping is that roughly half the data yield $g_{i,h}(s^*_{\varphi_\epsilon}) = \left(\frac{\partial Y_{i,h}(s^*_{\varphi\epsilon})}{\partial s^*_{\varphi\epsilon}}\right)_t e^{2s^*_{\varphi\epsilon}\omega^2 t_\epsilon}$ over a range of $s^*_{\varphi_\epsilon}$ values throughout which $\left(\frac{\partial Y_i(s^*_{\varphi\epsilon})}{\partial s^*_{\varphi\epsilon}}\right)_t = 0$. If instead, all the data yielded $g_{i,h}(s^*_{\varphi_\epsilon}) = 0$ over any range of $s^*_{\varphi_\epsilon}$ values throughout which $\left(\frac{\partial Y_i(s^*_{\varphi\epsilon})}{\partial s^*_{\varphi\epsilon}}\right)_t = 0$, the net contribution of noise to $G_{i,h}(s^*_{\varphi_\epsilon})$ would be minimal. (See *Mitigation of data clipping*.)

For treatment groups 1 (Figure 33) and 2 (Figure 34) at most times (t_ϵ) of analysis (t_{36}, t_{51}, t_{66}) and at most values of $s^*_{\varphi_\epsilon}$ within the limits of analysis (Table 19; Figure 32b; Equation 77), the data largely consist of broad ranges of $s^*_{\varphi_\epsilon}$ values throughout which $\left(\frac{\partial Y_{i,h}(s^*_{\varphi_\epsilon})}{\partial s^*_{\varphi_\epsilon}}\right)_t$ is either above zero or below zero exclusively. Thus, replicates of treatment groups 1 and 2 exhibit only minor effects of data clipping. At times (t_ϵ) of analysis (t_{36}, t_{51}, t_{66}) and at most values of $s^*_{\varphi_\epsilon}$ within the limits of analysis (Table 19; Figure 32b; Equation 77), the data for treatment group 3 (Figure 35) include significant ranges of $s^*_{\varphi_\epsilon}$ in which $\left(\frac{\partial Y_{i,h}(s^*_{\varphi_\epsilon})}{\partial s^*_{\varphi_\epsilon}}\right)_t$ equals or closely approaches zero, while the data for treatment group 4 (Figure 36) include even larger ranges of $s^*_{\varphi_\epsilon}$ in which $\left(\frac{\partial Y_{i,h}(s^*_{\varphi_\epsilon})}{\partial s^*_{\varphi_\epsilon}}\right)_t$ equals or closely approaches zero. Thus, replicates of treatment group 3 exhibit substantial effects of data clipping, and replicates of treatment group 4 exhibit the greatest effects of data clipping.

$G_i\left(s^*_{\varphi_\epsilon=2N}\right)$ *results*

A comparison across treatment groups at each time of analysis shows (Tables 20 to 23) that at $t_\epsilon = t_{66}$, $G_i\left(s^*_{\varphi_\epsilon=2N}\right)$ ranges from $G_4\left(s^*_{\varphi_{66}=2N}\right) = 44.59381$ fringe (Table 23; Figure 42) to $G_3\left(s^*_{\varphi_{66}=2N}\right) = 51.12134$ fringe (Table 22; Figure 41). These results stem largely from the difference in the signal across the centripetally and centrifugally directed boundaries (Figures 12 to 15), to which species *L* and *H*, respectively, are the major contributors.

A comparison of treatment group 4 (Figure 38) and treatment group 3 (Figure 43) at $t_\epsilon = t_{66}$ shows that the differences across the boundaries of c_L and c_H are slightly greater for treatment

group 3, while between those boundaries, the intervening Johnston-Ogston-affected plateau region of c_{LH} is slightly greater for treatment group 4, hence $G_3\left(s^*_{\varphi_{66}=2N}\right) > G_4\left(s^*_{\varphi_{66}=2N}\right)$.

For each treatment group, $c_{L+H} = c_L + c_H = 0.066$ g/ml overall, from which, given $L = 0.3$ cm and $k_\lambda = 2{,}500$ fringe/[cm·g/ml], a signal of $c_{L+H}Lk_\lambda = 49.5$ fringe can be calculated. Adding to this $c_{low}Lk_\lambda = 0.75$ fringe, where $c_{low} = 0.001$ g/ml is the overall concentration of all solute species other than c_H, c_{LH} and c_L in each system (Equation 73), yields a calculated signal of 50.25 fringe for all species other than LH.

For $c_{LH} = 0$ everywhere, as it does for treatment group 1 at $t_\epsilon = t_{66}$ (Figure 37), and where the centripetally and centrifugally directed boundaries are within the effective limits (Table 19; Equation 77) that apply to the calculation of $G_i\left(s^*_{\varphi_{\epsilon}=2N}\right)$, as they are for treatment group 1 at $t_\epsilon = t_{66}$ (Figure 20), it might be expected that $G_i\left(s^*_{\varphi_{\epsilon}=2N}\right)$ would equal 50.25 fringe, then. As $G_1\left(s^*_{\varphi_{66}=2N}\right) = 48.93778$ fringe, such is nearly the case for treatment group 1 at $t_\epsilon = t_{66}$ (Table 20; Figure 39). As $G_2\left(s^*_{\varphi_{66}=2N}\right) = 49.33616$ fringe, such is also nearly the case for treatment group 2 at $t_\epsilon = t_{66}$ (Table 21; Figure 40).

As $G_i\left(s^*_{\varphi_\epsilon}\right)$ is insensitive to any radially independent signal, it might be expected that $G_i\left(s^*_{\varphi_{\epsilon}=2N}\right)$ would likewise equal 50.25 fringe for data in which c_{LH} is invariant with r_j. The results from treatment group 4 are those for which c_{LH} varies the least with r_j at any given time, of which $t_\epsilon = t_{66}$ is discussed above. At $t_\epsilon = t_{36}$, $G_4\left(s^*_{\varphi_{36}=2N}\right) = 44.29047$ fringe. At $t_\epsilon = t_{66}$, $G_4\left(s^*_{\varphi_{66}=2N}\right) = 44.59381$ fringe. Between the boundaries of c_L and c_H at $t_\epsilon = t_{36}$, an intervening Johnston-Ogston-affected plateau region of c_{LH} reduces the apparent height of those boundaries (Figure 38), so

that $G_4\left(s^*_{\varphi_{66}=2N}\right) = 44.59381$ fringe (Table 23; Figure 42). Likewise, centrifugal to the boundary of c_L and centripetal to the boundary of c_H at $t_\epsilon = t_{36}$, a Johnston-Ogston-affected plateau region of c_{LH} reduces the apparent height of those boundaries (Figure 38), so that $G_4\left(s^*_{\varphi_{36}=2N}\right) = 44.29047$ fringe (Table 23; Figure 42).

Were it not for the formation of Johnston-Ogston-affected plateau regions arising from the redistribution of c_{LH}, $G_4\left(s^*_{\varphi_\epsilon=2N}\right)$ would be much closer to 50.25 fringe at both $t_\epsilon = t_{36}$ and $t_\epsilon = t_{66}$. At $t_\epsilon = t_{51}$, however, the differences across the boundaries of c_L and c_H are obscured due to their superimposition at that time, and this effect, coupled with the converging Johnston-Ogston-affected plateau regions of c_{LH} at $t_\epsilon = t_{51}$, yields the lowest value of $G_i\left(s^*_{\varphi_\epsilon=2N}\right)$, $G_4\left(s^*_{\varphi_{51}=2N}\right) =$ 18.18701 fringe (Table 23; Figure 42), of all times analysed for any treatment group (Tables 20 to 23; Figures 39 to 42).

At $t_\epsilon = t_{51}$, treatment group 3 (Figure 43) exhibits many of the same characteristics as treatment group 4 (Figure 38), but treatment group 3 has just slightly more than half the dimer concentration of treatment group 4 by $t_\epsilon = t_{51}$. As a result, the converging Johnston-Ogston-affected plateau regions of c_{LH} at $t_\epsilon = t_{51}$ of treatment group 3 are roughly half the magnitude of those in treatment group 4. At $t_\epsilon = t_{51}$, then, the effects seen in treatment group 3 are less extreme than those seen in treatment group 4. Thus, $G_3\left(s^*_{\varphi_{51}=2N}\right) = 20.42996$ fringe (Table 22; Figure 41) is the second lowest value of $G_i\left(s^*_{\varphi_\epsilon=2N}\right)$ of all times analysed for any treatment group (Tables 20 to 23; Figures 39 to 42).

At $t_\epsilon = t_{36}$, treatment group 3 (Figure 43) exhibits some of the same characteristics as treatment

group 1 (Figure 37), but does so moderately, as the concentration of non-dissociating dimer in treatment group 3 is half the initial concentration of the entirely dissociable dimer of treatment group 1. Thus, at $t_\epsilon = t_{36}$, treatment group 3 (Figure 43) also exhibits some of the same characteristics as treatment group 4 (Figure 38), but likewise does so moderately. Thus, $G_3\left(s^*_{\varphi_{36}=2N}\right) = 67.96545$ fringe (Table 22; Figure 41) is a bit closer to $G_4\left(s^*_{\varphi_{36}=2N}\right) = 44.29047$ fringe (Table 23; Figure 42) than it is to $G_1\left(s^*_{\varphi_{36}=2N}\right) = 101.49655$ fringe (Table 20; Figure 39).

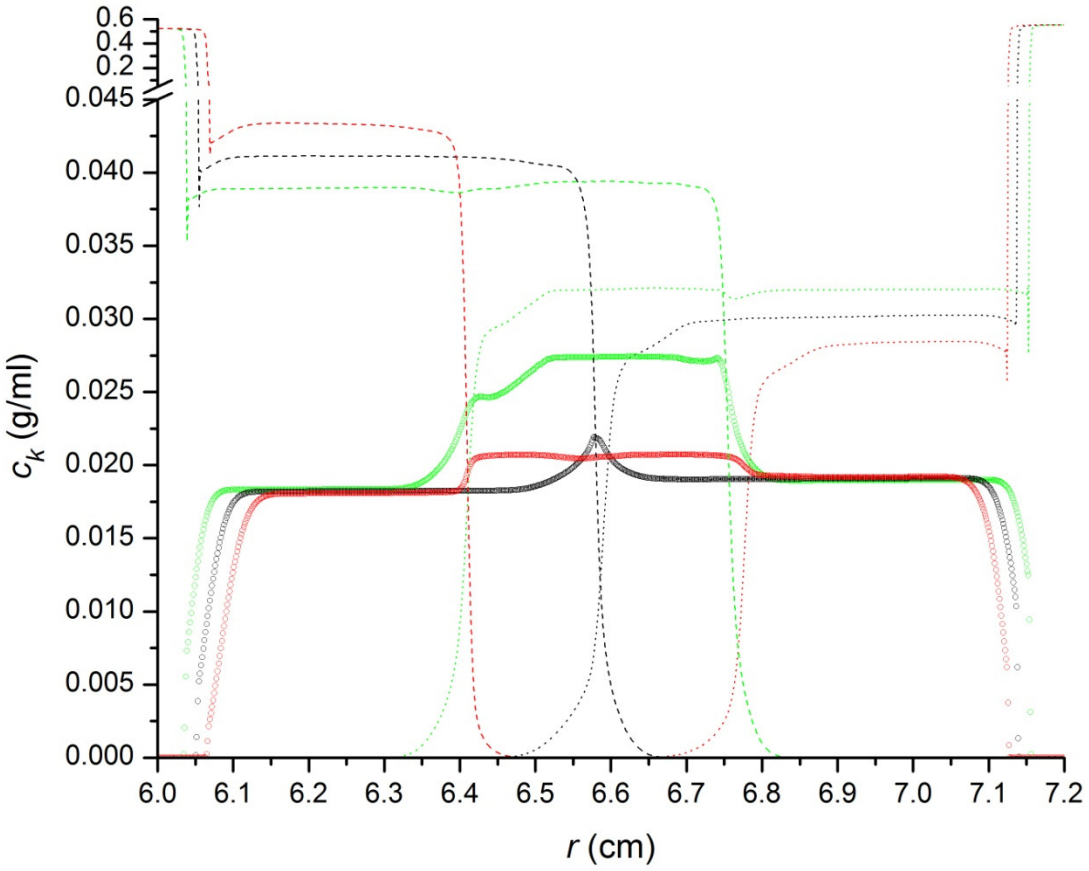

Figure 43a. Treatment group $i = 3$ (50% $K_A > 0$), L, H and LH. Shown are the concentrations of L, H and LH, which are $c_L = c_{L-} + c_{L+}$ (dashed lines, centripetally directed boundaries), $c_H = c_{H-} + c_{H+}$ (dotted lines, centrifugally directed boundaries) and $c_{LH} = c_{LH-} + c_{LH+}$ (small, open circles), respectively, versus r_j at times t_{36} (green), t_{51} (black) and t_{66} (red). Figure 43b shows c_{L-}, c_{H-} and

c_{LH-}. Figure 43c shows c_{L+}, c_{H+} and c_{LH+}.

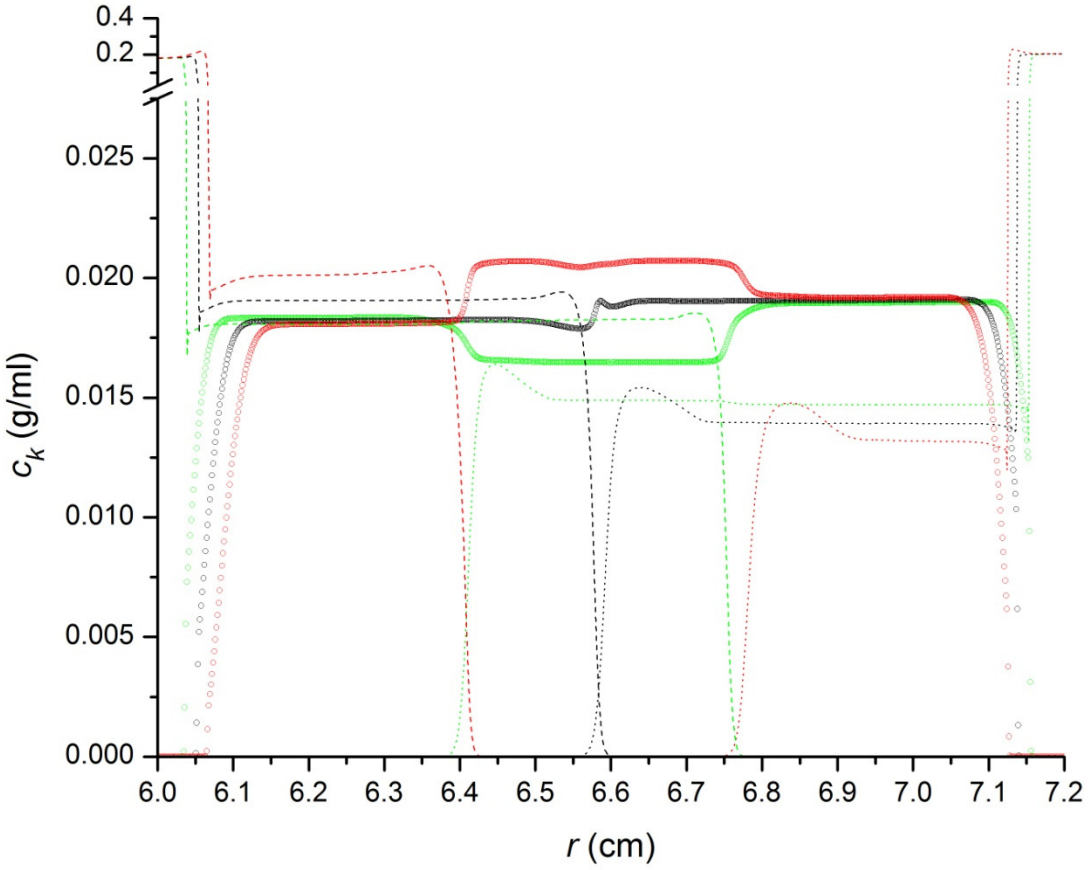

Figure 43b. Treatment group $i = 3$ (50% $K_A > 0$), L_-, H_- and LH_-. Shown are the species concentrations of L_-, H_- and LH_-, which are c_{L-} (dashed lines, centripetally directed boundaries), c_{H-} (dotted lines) and c_{LH-} (small, open circles, centrifugally directed boundaries), respectively, versus r_j at times t_{36} (green), t_{51} (black) and t_{66} (red). Figure 43a shows $c_L = c_{L-} + c_{L+}$, $c_H = c_{H-} + c_{H+}$ and $c_{LH} = c_{LH-} + c_{LH+}$. Figure 43c shows c_{L+}, c_{H+} and c_{LH+}.

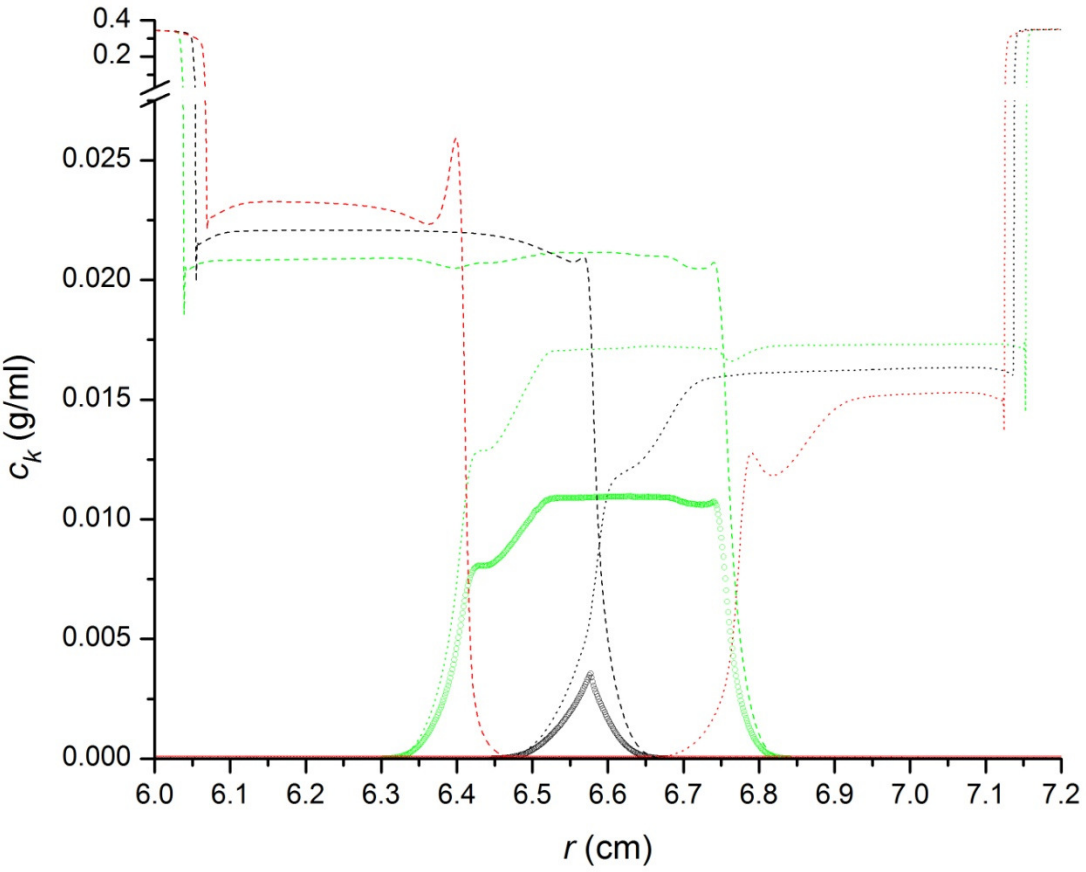

Figure 43c. Treatment group $i = 3$ (50% $K_A > 0$), L_+, H_+ and LH_+. Shown are the species concentrations of L_+, H_+ and LH_+, which are c_{L+} (dashed lines, centripetally directed boundaries), c_{H+} (dotted lines, centrifugally directed boundaries) and c_{LH+} (small, open circles), respectively, versus r_j at times t_{36} (green), t_{51} (black) and t_{66} (red). Figure 43a shows $c_L = c_{L-} + c_{L+}$, $c_H = c_{H-} + c_{H+}$ and $c_{LH} = c_{LH-} + c_{LH+}$. Figure 43b shows c_{L-}, c_{H-} and c_{LH-}.

As treatment group 2 (Table 21; Figure 40) overwhelmingly resembles treatment group 1 (Table 20; Figure 39), the results for each are very similar. The small differences seen must be attributable to treatment group 2 having slightly less dissociable dimer than treatment group 1 at any given time, and to treatment group 2 having a small amount of the non-dissociating dimer

that is completely absent from treatment group 1.

For treatment group 1 at $t_\epsilon = t_{51}$, the differences across the boundaries of c_L and c_H are obscured due to their superimposition at that time, and this effect reduces the value of $G_1\left(s^*_{\varphi_{51}=2N}\right)$ to 26.34547 fringe (Table 20; Figure 39). That $G_1\left(s^*_{\varphi_{51}=2N}\right) > G_3\left(s^*_{\varphi_{51}=2N}\right) > G_4\left(s^*_{\varphi_{51}=2N}\right)$ can be attributed to treatment group 1 being free from converging Johnston-Ogston-affected plateau regions of c_{LH} at $t_\epsilon = t_{51}$. (Compare Tables 20 to 23, and Figures 39 to 42.)

At $t_\epsilon = t_{36}$, for treatment group 1 (Figure 37), a centripetally directed boundary of *LH* co-migrates with the centripetally directed boundary of *L*, while a centrifugally directed boundary of *LH* co-migrates with the centrifugally directed boundary of *H*. With respect to the concentrations of these species as a function of r_j at $t_\epsilon = t_{36}$ (Figure 37), the radial concentration effect has rendered the absolute value of the difference across the centripetally directed boundary of *L* about 11.76% higher than the absolute value of the difference across the centripetally directed boundary of *LH*, and the radial dilution effect has rendered the absolute value of the difference across the centrifugally directed boundary of *H* about 8.95% lower than the absolute value of the difference across the centrifugally directed boundary of *LH* (Figure 37). The absolute value of the difference across the centripetally directed boundary of *LH* is always equal to the absolute value of the difference across the centrifugally directed boundary of *LH*, and at $t_\epsilon = t_{36}$, the value of each is of 0.032619 g/ml.

Given $L = 0.3$ cm and $k_\lambda = 2{,}500$ fringe/[cm·g/ml], a signal of $c_k L k_\lambda$ can be calculated from a concentration, c_k, of species *k* expressed in g/ml. With respect to the overall signals of the boundaries as a function of r_j at $t_\epsilon = t_{36}$ (Figure 12), the absolute value of the difference across

the sum of the centripetally directed boundaries of L and LH is approximately 51.81 fringe, the absolute value of the difference across the sum of the centrifugally directed boundaries of H and LH is approximately 46.74 fringe, and the grand total of these sums is approximately 98.55 fringe. Adding to this $c_{low}Lk_\lambda = 0.75$ fringe, where $c_{low} = 0.001$ g/ml is the overall concentration of all solute species other than c_H, c_{LH} and c_L (Equation 73), yields 99.30 fringe for the sum of the absolute values of the signal differences across the boundaries of all species. Johnston-Ogston effects on c_{low} (Figure 16) increase the signal differences across the boundaries of the low-concentration species, and should do so roughly in proportion to the extent by which the Johnston-Ogston peaks in c_{low} exceed the intervening local minimum in c_{low}. At $t_\epsilon = t_{36}$, such Johnston-Ogston effects on c_{low} would raise the sum of the absolute values of the signal differences across the boundaries of all species to 99.50 fringe, which can be considered the predicted value of $G_1\left(s^*_{\varphi_{36}=2N}\right)$.

When plotted as $Y_i(s^*_{\varphi_\epsilon})$ versus $s^*_{\varphi_\epsilon}$ (Figure 20a), the sum of the centripetally directed boundaries of L and LH is found to lie within $s^*_{min<0}$ to $s^*_{max<0}$ (Table 19; Equation 77), and thus, by Equation 9b, contributes to $\left|g_i\left(s^*_{\varphi_\epsilon}\right)\right|$ at t_{36} (Figure 33). Likewise, when plotted as $Y_i(s^*_{\varphi_\epsilon})$ versus $s^*_{\varphi_\epsilon}$ (Figure 20a), the sum of the centrifugally directed boundaries of H and LH is found to lie within $s^*_{min>0}$ to $s^*_{max>0}$ (Table 19; Equation 77) and thus, by Equation 9b, also contributes to $\left|g_i\left(s^*_{\varphi_\epsilon}\right)\right|$ at t_{36} (Figure 33). When $\left|g_i\left(s^*_{\varphi_\epsilon}\right)\right|$ at t_{36} is integrated (Equation 77) the result obtained, $G_1\left(s^*_{\varphi_{36}=2N}\right) = 101.49655$ fringe (Table 20; Figure 39), is about 2% greater than the predicted value of 99.50 fringe.

As $G_1\left(s^*_{\varphi_{36}=2N}\right)$ integrates both the centripetally and centrifugally directed boundaries of LH, and

as the magnitude of each of those boundaries is approximately equal to $c_{LH}(r_j,t_0)Lk_\lambda = 24.75$ fringe, where $c_{LH}(r_j,t_0) = 0.033$ g/ml is the initial concentration of LH throughout the system, the apparent signal from LH at t_{36} is approximately $2(24.75 \text{ fringe}) = 49.50$ fringe. In effect, at t_{36}, what would have been the initial signal of LH is counted twice. Meanwhile, the apparent signal from L and the apparent signal from H are each counted once at t_{36}. Given $c_{L+H} = c_L + c_H = 0.066$ g/ml overall and $c_{low} = 0.001$ g/ml overall (Equation 73), the total signal of from all of the boundaries could be estimated as $(2c_{LH}(r_j,t_0) + c_{L+H} + c_{low})Lk_\lambda = 99.75$ fringe, which is within 0.3% of 99.50 fringe.

The approximately 2% difference in $G_1\left(s^*_{\varphi_{36=2N}}\right)$ from that predicted is likely due to $g_i\left(s^*_{\varphi_\epsilon}\right)$ being uncorrected for concentration-dependent transport, except in trivial and unrealistic cases of concentration-dependent transport in a system of time-independent concentration, which should sound like an oxymoron because such cases are restricted to systems in which all solutes are neutrally buoyant at all times. As a review of Equations 8 to 11 shows,

$$g_i\left(s^*_{\varphi_\epsilon}\right) \neq \left(\frac{\partial Y_i\left(s^*_{\varphi_\epsilon}\right)}{\partial s^*_{\varphi_\epsilon}}\right)_t$$

(80)

except at $t_0 = 0$ s, at which time $\left(\frac{\partial Y_i\left(s^*_{\varphi_\epsilon}\right)}{\partial s^*_{\varphi_\epsilon}}\right)_t = 0$ at all $s^*_{\varphi_\epsilon}$.

In general, then, $G_i\left(s^*_{\varphi_\epsilon}\right)$ is an estimate of the total, initial signal from all solutes for which the apparent sedimentation coefficient is less than or equal to $s^*_{\varphi_\epsilon}$, but greater than or equal to $s^*_{\varphi_{\epsilon=1}}$ at time t_ϵ (Equations 11 and 77). The more time-independent the behaviour of those solutes, the more accurate an estimate of the sum of their initial signals $G_i\left(s^*_{\varphi_\epsilon}\right)$ becomes. Thus, as mentioned

with respect to Equation 11, $G_i\left(s^*_{\varphi_\epsilon}\right)$ is a substantially time-normalised, but not entirely time-independent, measure of that initial signal.

For a sense of how poorly $G_i\left(s^*_{\varphi_\epsilon}\right)$ can reflect the initial signal, consider, that, by Equation 4, at each radial position, r_j, $NFS_i(r_j,t_0) = (0.1\text{ g/ml})\,Lk_\lambda = 75$ fringe, where, for any treatment group, i, 0.1 g/ml is the total solute concentration at each radial position at t_0. Thus, $NFS_i(r_j,t_0) = 75$ fringe can be considered the true value of the initial signal for each treatment group. As a search through Tables 20 to 23 shows, however, $G_4\left(s^*_{\varphi_{51}}\right)$ is almost 76% smaller than $NFS_i(r_j,t_0)$, and $G_2\left(s^*_{\varphi_{36}}\right)$ is over 35% bigger than $NFS_i(r_j,t_0)$, while of all the $G_i\left(s^*_{\varphi_\epsilon}\right)$ values, $G_2\left(s^*_{\varphi_{36}}\right)$, which is 9.3794% smaller than $NFS_i(r_j,t_0)$, comes closest to the true value of the initial signal.

Thanks to the tenuous relationship of $G_i\left(s^*_{\varphi_\epsilon}\right)$ to $NFS_i(r_j,t_0)$, there is a lot of information to be found within $G_i\left(s^*_{\varphi_\epsilon}\right)$ results, and an accurate description of a treatment group might emerge from such results if they were extensive enough to show the dependence of $G_i\left(s^*_{\varphi_\epsilon}\right)$ on time and other critical parameters. Collecting data from a dilution series and altering any other conditions to which a specific system might be especially sensitive would probably be required to compensate for the likely absence of the sort of prior knowledge and solute-by-solute signal data that are readily available and heavily exploited here.

A consideration of the results for $s^*_{i,\epsilon}$ and $s^*_{i,h,\epsilon}$

Analysis of the noise-free $Y_i(s^*_{\varphi_\epsilon})$ versus $s^*_{\varphi_\epsilon}$ data within each treatment group yields $s^*_{i,\epsilon}$ (Equation 13), which is the expectation value of the observations at time t_ϵ. Analysis of the $Y_{i,h}(s^*_{\varphi_\epsilon})$ versus $s^*_{\varphi_\epsilon}$ data from the noise-modified replicates within each treatment group yields

the set of $s^*_{i,h,\epsilon}$ (Equation 13), which is the set of observations at time t_ϵ, used to probe the significance of differences between treatment groups. For treatment groups 1 to 4, respectively, Tables 24 to 27 show $s^*_{i,\epsilon}$ and the set of all $s^*_{i,h,\epsilon}$. Likewise for treatment groups 1 to 4, respectively, Figures 44 to 47 show $s^*_{i,h,\epsilon}\left(s^*_{\varphi_\epsilon=1}, s^*_{\varphi_\epsilon}\right)$ versus $s^*_{\varphi_\epsilon}$ and $s^*_{i,\epsilon}\left(s^*_{\varphi_\epsilon=1}, s^*_{\varphi_\epsilon}\right)$ versus $s^*_{\varphi_\epsilon}$, which, via Equation 81, are equal to $s^*_{i,h,\epsilon}$ and $s^*_{i,\epsilon}$, respectively, for $s^*_{\varphi_\epsilon} \geq s^*_{max>0}$. Figures 44 to 47 also show $s^*_{\varphi_\epsilon}\left|g_{i,h}\left(s^*_{\varphi_\epsilon}\right)\right|$ versus $s^*_{\varphi_\epsilon}$, $s^*_{\varphi_\epsilon}\left|g_i\left(s^*_{\varphi_\epsilon}\right)\right|$ versus $s^*_{\varphi_\epsilon}$, and results of their integration with respect to $s^*_{\varphi_\epsilon}$.

As previously noted (Equation 77), multiplication of the sedimentation coefficient distribution functions (Equation 10), $g_i\left(s^*_{\varphi_\epsilon}\right)$ and $g_{i,h}\left(s^*_{\varphi_\epsilon}\right)$, by the mask (Figure 32) for the corresponding time, t_{36}, t_{51} or t_{66}, left $g_i\left(s^*_{\varphi_\epsilon}\right)$ and $g_{i,h}\left(s^*_{\varphi_\epsilon}\right)$ unchanged wherever 5E-13 s $< \left|s^*_{\varphi_\epsilon}\right| <$ 10.625E-13 s, and set them to zero everywhere else (Figures 33 to 36).

With $g_{i,h}\left(s^*_{\varphi_\epsilon}\right)$ multiplied by the mask (Figure 32) for time t_ϵ, $s^*_{i,h,\epsilon}\left(s^*_{\varphi_\epsilon=1}, s^*_{\varphi_\epsilon=2N}\right)$, the weight-average apparent sedimentation coefficient (Equation 12) for replicate h of treatment group i within the entire range of $s^*_{\varphi_\epsilon}$ at time t_ϵ, becomes indistinguishable from $s^*_{i,h,\epsilon}$ (Equation 13), the observation for replicate h of treatment group i at time t_ϵ, which is calculated within the limits (Table 19) applied to construct the mask for time t_ϵ. Thus,

$$s^*_{i,h,\epsilon} = s^*_{i,h,\epsilon}\left(s^*_{\varphi_\epsilon} > s^*_{min<0}, s^*_{\varphi_\epsilon} < s^*_{max<0}\right) + s^*_{i,h,\epsilon}\left(s^*_{\varphi_\epsilon} > s^*_{min>0}, s^*_{\varphi_\epsilon} < s^*_{max>0}\right)$$

$$= \frac{\int_{s^*_{min<0}}^{s^*_{max<0}} s^*_{\varphi_\epsilon}\left|g_{i,h}\left(s^*_{\varphi_\epsilon}\right)\right| ds^*_{\varphi_\epsilon}}{G_{i,h}\left(s^*_{max<0}\right) - G_{i,h}\left(s^*_{min<0}\right)} + \frac{\int_{s^*_{min>0}}^{s^*_{max>0}} s^*_{\varphi_\epsilon}\left|g_{i,h}\left(s^*_{\varphi_\epsilon}\right)\right| ds^*_{\varphi_\epsilon}}{G_{i,h}\left(s^*_{max>0}\right) - G_{i,h}\left(s^*_{min>0}\right)}$$

$$\equiv \frac{\int_{s^*_{\varphi_\epsilon=1}}^{s^*_{\varphi_\epsilon=2N}} s^*_{\varphi_\epsilon}\left|g_{i,h}\left(s^*_{\varphi_\epsilon}\right)\right| ds^*_{\varphi_\epsilon}}{G_{i,h}\left(s^*_{\varphi_\epsilon=2N}\right) - G_{i,h}\left(s^*_{\varphi_\epsilon=1}\right)} = s^*_{i,h,\epsilon}\left(s^*_{\varphi_\epsilon=1}, s^*_{\varphi_\epsilon=2N}\right),$$

(81a)

where $s^*_{min<0}$ = -10.625E-13 s, $s^*_{max<0}$ = -5E-13 s, $s^*_{min>0}$ = 5E-13 s and $s^*_{max>0}$ = 10.625E-13 s. The equivalence of $s^*_{i,h,\epsilon}$ to $s^*_{i,h,\epsilon}\left(s^*_{\varphi_\epsilon=1}, s^*_{\varphi_\epsilon=2N}\right)$ is not general, and thus Equation 81a is not general, as it only applies if all $g_{i,h}\left(s^*_{\varphi_\epsilon} < s^*_{min<0}\right) = 0$, all $g_{i,h}\left(s^*_{max<0} < s^*_{\varphi_\epsilon} < s^*_{min>0}\right) = 0$ and all $g_{i,h}\left(s^*_{\varphi_\epsilon} > s^*_{max>0}\right) = 0$, as is the case here after the application of the masks (Figure 32) for t_{36}, t_{51} and t_{66}.

Likewise, with $g_i\left(s^*_{\varphi_\epsilon}\right)$ multiplied by the mask (Figure 32) for time t_ϵ, $s^*_{i,\epsilon}\left(s^*_{\varphi_\epsilon=1}, s^*_{\varphi_\epsilon=2N}\right)$, the weight-average apparent sedimentation coefficient (Equation 12) for the noise-free signal of treatment group i within the entire range of $s^*_{\varphi_\epsilon}$ at time t_ϵ, becomes indistinguishable from $s^*_{i,\epsilon}$ (Equation 13), the expectation value of treatment group i at time t_ϵ, which is also calculated within the limits (Table 19) applied to construct the mask for time t_ϵ. Thus,

$$s^*_{i,\epsilon} = s^*_{i,\epsilon}\left(s^*_{\varphi_\epsilon} > s^*_{min<0}, s^*_{\varphi_\epsilon} < s^*_{max<0}\right) + s^*_{i,\epsilon}\left(s^*_{\varphi_\epsilon} > s^*_{min>0}, s^*_{\varphi_\epsilon} < s^*_{max>0}\right)$$

$$= \frac{\int_{s^*_{min<0}}^{s^*_{max<0}} s^*_{\varphi_\epsilon}\left|g_i\left(s^*_{\varphi_\epsilon}\right)\right| ds^*_{\varphi_\epsilon}}{G_i\left(s^*_{max<0}\right) - G_i\left(s^*_{min<0}\right)} + \frac{\int_{s^*_{min>0}}^{s^*_{max>0}} s^*_{\varphi_\epsilon}\left|g_i\left(s^*_{\varphi_\epsilon}\right)\right| ds^*_{\varphi_\epsilon}}{G_i\left(s^*_{max>0}\right) - G_i\left(s^*_{min>0}\right)} \equiv \frac{\int_{s^*_{\varphi_\epsilon=1}}^{s^*_{\varphi_\epsilon=2N}} s^*_{\varphi_\epsilon}\left|g_i\left(s^*_{\varphi_\epsilon}\right)\right| ds^*_{\varphi_\epsilon}}{G_i\left(s^*_{\varphi_\epsilon=2N}\right) - G_i\left(s^*_{\varphi_\epsilon=1}\right)}$$

$$= s^*_{i,\epsilon}\left(s^*_{\varphi_\epsilon=1}, s^*_{\varphi_\epsilon=2N}\right),$$

(81b)

where $s^*_{min<0}$ = -10.625E-13 s, $s^*_{max<0}$ = -5E-13 s, $s^*_{min>0}$ = 5E-13 s and $s^*_{max>0}$ = 10.625E-13 s. The equivalence of $s^*_{i,\epsilon}$ to $s^*_{i,\epsilon}\left(s^*_{\varphi_\epsilon=1}, s^*_{\varphi_\epsilon=2N}\right)$ is not general, and thus Equation 81b is not general, as it only applies if all $g_i\left(s^*_{\varphi_\epsilon} < s^*_{min<0}\right) = 0$, all $g_i\left(s^*_{max<0} < s^*_{\varphi_\epsilon} < s^*_{min>0}\right) = 0$ and all $g_i\left(s^*_{\varphi_\epsilon} > s^*_{max>0}\right) = 0$, as is the case here after the application of the masks (Figure 32) for t_{36}, t_{51} and t_{66}.

Within treatment group *i*, the mean of all $s^*_{i,h,\epsilon}$ is given by

$$\langle s^*_{i,\epsilon} \rangle = \frac{1}{n_i} \sum_{h=1}^{n_i} s^*_{i,h,\epsilon},$$

(82)

where n_i is the number of replicates for treatment group *i*. For treatment group *i*, the difference between the within-group mean, $\langle s^*_{i,\epsilon} \rangle$, and the expectation value, $s^*_{i,\epsilon}$, is denoted as

$$e_{s^*_{i,\epsilon}} = \langle s^*_{i,\epsilon} \rangle - s^*_{i,\epsilon},$$

(83)

and is a measure of the accumulated error in $\langle s^*_{i,\epsilon} \rangle$.

Excluding regions of minimal signal from analysis minimises systematic contributions of the random noise, $GRN_{i,h}(r_j,t_\alpha)$, to each $s^*_{i,h,\epsilon}$ within a treatment group, and thus minimises $e_{s^*_{i,\epsilon}}$. As previously discussed (*The signal-to-noise ratio of* $g_{i,h}(s^*_{\varphi_\epsilon})$ *worsens in proportion to* $1/e^{2s^*_{\varphi_\epsilon}\omega^2 t_\epsilon}$ *as* $s^*_{\varphi_\epsilon}$ *increases*; *The accumulated error in* $G_{i,h}(s^*_{\varphi_\epsilon=2N})$ *increases in proportion to the clipping of random noise*; *The accumulated error in* $\langle s^*_{i,\epsilon} \rangle$ *increases in proportion to the clipping of random noise*; *Mitigation of data clipping*), $GRN_{i,h}(r_j,t_\alpha)$, makes the least systematic contribution to $s^*_{i,h,\epsilon}$ when, in going from $\left(\frac{\partial Y_{i,h}(s^*_{\varphi_\epsilon})}{\partial s^*_{\varphi_\epsilon}}\right)_t$ to $q_{i,h}(s^*_{\varphi_\epsilon})$, the clipping of the positively signed and the negatively signed random noise is minimised (Figures 24 to 27). Even when the clipping of positively signed random noise within $-|s^*_a| < s^*_{\varphi_\epsilon} < -|s^*_z|$ is complemented by the clipping of negatively signed random noise within $|s^*_a| < s^*_{\varphi_\epsilon} < |s^*_z|$, the net effect of the clipped random noise is likely to be an offset in $s^*_{i,h,\epsilon}$ of each replicate at time t_ϵ, such that, given $e_{s^*_{i,\epsilon}} = \langle s^*_{i,\epsilon} \rangle - s^*_{i,\epsilon}$ (Equation 83), $\left|e_{s^*_{i,\epsilon}}\right|$ will be significantly greater than zero. The relatively small values of $e_{s^*_{i,\epsilon}}$ for

treatment groups 1 and 2 (Tables 24 and 25; Figures 44 and 45) show that such offsets were minimised by excluding, through the judicious selection of $s^*_{min<0}$, $s^*_{max<0}$, $s^*_{min>0}$ and $s^*_{max>0}$, regions of low signal-to-noise from the ranges of $s^*_{\varphi_\epsilon}$ used to calculate $s^*_{i,h,\epsilon}$ (Equation 13). The relatively large values of $e_{s^*_{i,\epsilon}}$ for treatment groups 3 and 4 (Tables 26 and 27; Figures 46 and 47), result from these treatment groups having substantial regions of low signal-to-noise within the ranges of $s^*_{\varphi_\epsilon}$ used to calculate $s^*_{i,h,\epsilon}$.

$i = 1$	$t_\epsilon = t_{36} = 2160$ s	$t_\epsilon = t_{51} = 3060$ s	$t_\epsilon = t_{66} = 3960$ s
$s^*_{i,\epsilon}$	1.03097 Svedberg	-0.651551 Svedberg	0.56977 Svedberg
h	$s^*_{i,h,36}$ (Svedberg)	$s^*_{i,h,51}$ (Svedberg)	$s^*_{i,h,66}$ (Svedberg)
1	1.00390	-0.65433	0.59981
2	1.00218	-0.62807	0.61294
3	0.99784	-0.64450	0.60679
4	1.00230	-0.65377	0.58309
5	0.99148	-0.63713	0.58187
6	1.00150	-0.64263	0.57528
7	0.99895	-0.65521	0.58263
8	1.00689	-0.62817	0.57904
9	1.00976	-0.63846	0.60184
$\langle s^*_{i,\epsilon} \rangle$	1.00165 Svedberg	-0.64247 Svedberg	0.59148 Svedberg
$e_{s^*_{i,\epsilon}}$	-0.02933 Svedberg	0.00908 Svedberg	0.02171 Svedberg

Table 24. $s^*_{i,h,\epsilon}$, $s^*_{i,\epsilon}$, $\langle s^*_{i,\epsilon} \rangle$, and $e_{s^*_{i,\epsilon}}$ for $i = 1$ at the times analysed: $t_\epsilon = t_{36}$, $t_\epsilon = t_{51}$ and $t_\epsilon = t_{66}$. The expectation values, $s^*_{i,\epsilon}$, are highlighted in blue. The replicate values (Equation 13), $s^*_{i,h,\epsilon}$, are not highlighted. The within-group mean values (Equation 82), $\langle s^*_{i,\epsilon} \rangle$, are highlighted in yellow. The accumulated error values (Equation 83), $e_{s^*_{i,\epsilon}}$, each being the difference between the mean and the expectation value, are highlighted in red. The $s^*_{i,\epsilon}$ values of this table are equal to $s^*_{i,\epsilon}\left(s^*_{\varphi_\epsilon=1}, s^*_{\varphi_\epsilon}\right)$ at $s^*_{\varphi_\epsilon} \geq s^*_{max>0}$ in Figure 44, and the $s^*_{i,h,\epsilon}$ values of this table are equal to

$s^*_{i,h,\epsilon}\left(s^*_{\varphi_\epsilon=1}, s^*_{\varphi_\epsilon}\right)$ at $s^*_{\varphi_\epsilon} \geq s^*_{max>0}$ in Figure 44.

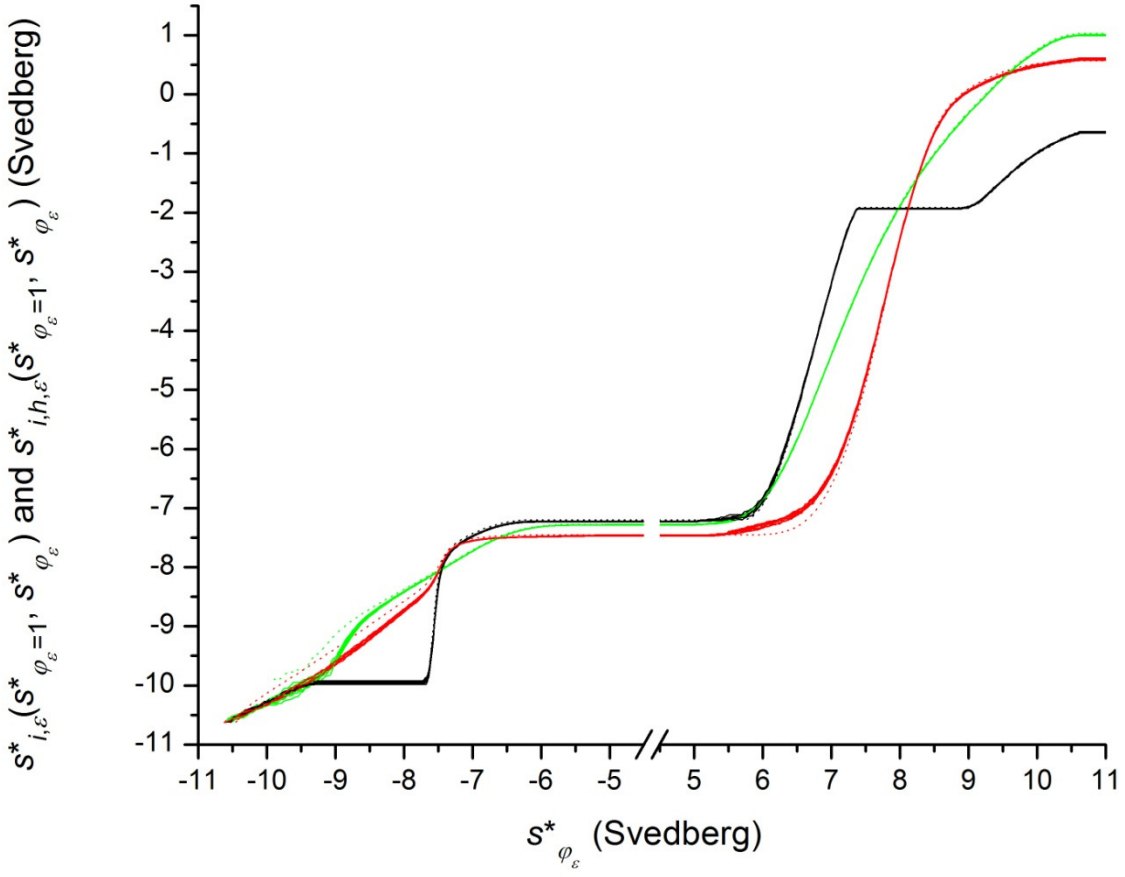

Figure 44a. For $i = 1$ (100% $K_A > 0$, 0% K_A undefined), $s^*_{i,\epsilon}\left(s^*_{\varphi_\epsilon=1}, s^*_{\varphi_\epsilon=2N}\right)$ at t_{36} (·····), t_{51} (·····) and t_{66} (·····), along with $s^*_{i,h,\epsilon}\left(s^*_{\varphi_\epsilon=1}, s^*_{\varphi_\epsilon=2N}\right)$ for each replicate ($1 \leq h \leq 9$) at t_{36} (——), t_{51} (——) and t_{66} (——), all plotted against $s^*_{\varphi_\epsilon}$. Given the masks (Figure 32) that render all $g_{i,h}\left(s^*_{\varphi_\epsilon}\right) = 0$ and all $g_i\left(s^*_{\varphi_\epsilon}\right) = 0$ outside of 5E-13 s $< \left|s^*_{\varphi_\epsilon}\right| <$ 10.625E-13 s at t_{36}, t_{51} and t_{66}, by Equation 81, $s^*_{i,h,\epsilon} \equiv s^*_{i,h,\epsilon}\left(s^*_{\varphi_\epsilon=1}, s^*_{\varphi_\epsilon=2N}\right)$ and $s^*_{i,\epsilon} \equiv s^*_{i,\epsilon}\left(s^*_{\varphi_\epsilon=1}, s^*_{\varphi_\epsilon=2N}\right)$.

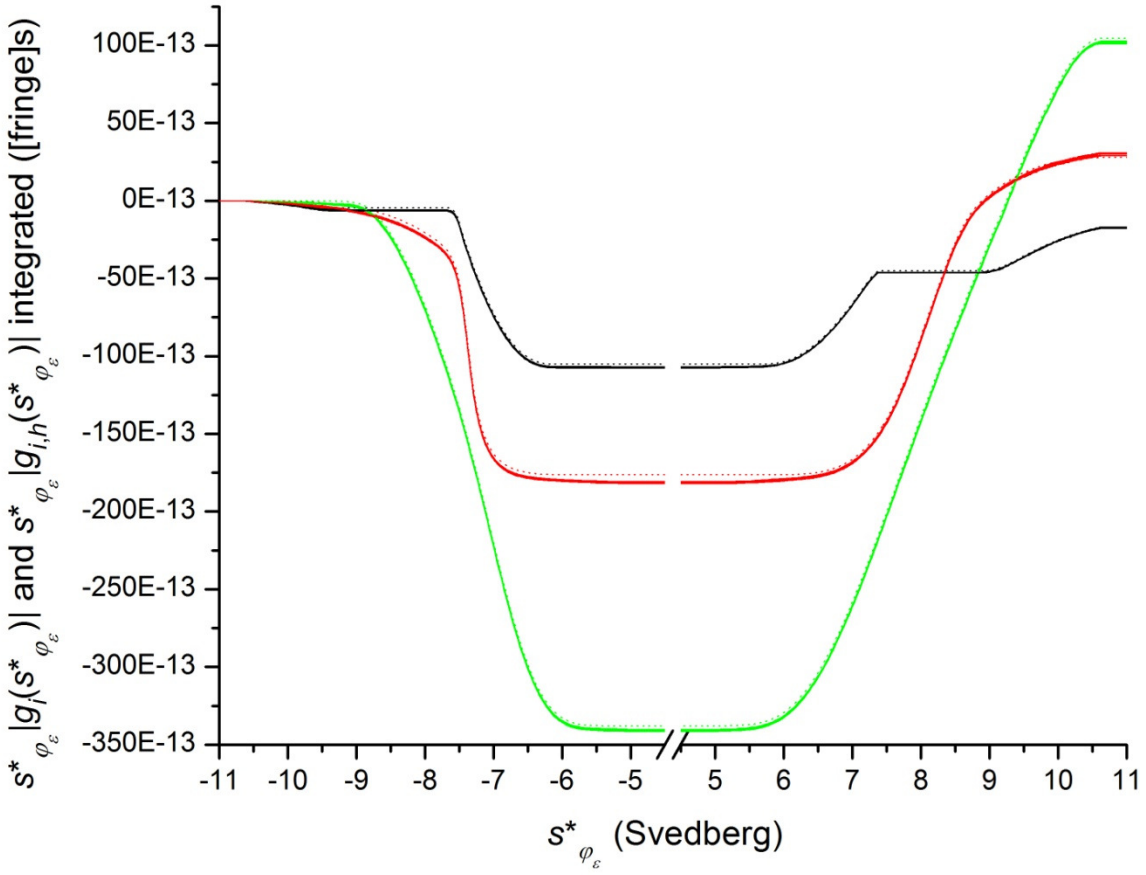

Figure 44b. For $i = 1$ (100% $K_A > 0$, 0% K_A undefined), $\int_{s^*_{\varphi\epsilon=1}}^{s^*_{\varphi\epsilon=2N}} s^*_{\varphi\epsilon} \left| g_i\left(s^*_{\varphi\epsilon}\right) \right| ds^*_{\varphi\epsilon}$ at t_{36} (·····), t_{51} (·····) and t_{66} (·····), along with $\int_{s^*_{\varphi\epsilon=1}}^{s^*_{\varphi\epsilon=2N}} s^*_{\varphi\epsilon} \left| g_{i,h}\left(s^*_{\varphi\epsilon}\right) \right| ds^*_{\varphi\epsilon}$ for each replicate ($1 \leq h \leq 9$) at t_{36} (——), t_{51} (——) and t_{66} (——), all plotted against $s^*_{\varphi\epsilon}$. The integrals are the numerators of Equation 81 that apply when all $g_{i,h}\left(s^*_{\varphi\epsilon}\right) = 0$ and all $g_i\left(s^*_{\varphi\epsilon}\right) = 0$ outside of 5E-13 s $< \left|s^*_{\varphi\epsilon}\right| <$ 10.625E-13 s at t_{36}, t_{51} and t_{66}, as ensured here through the use of masks (Figure 32).

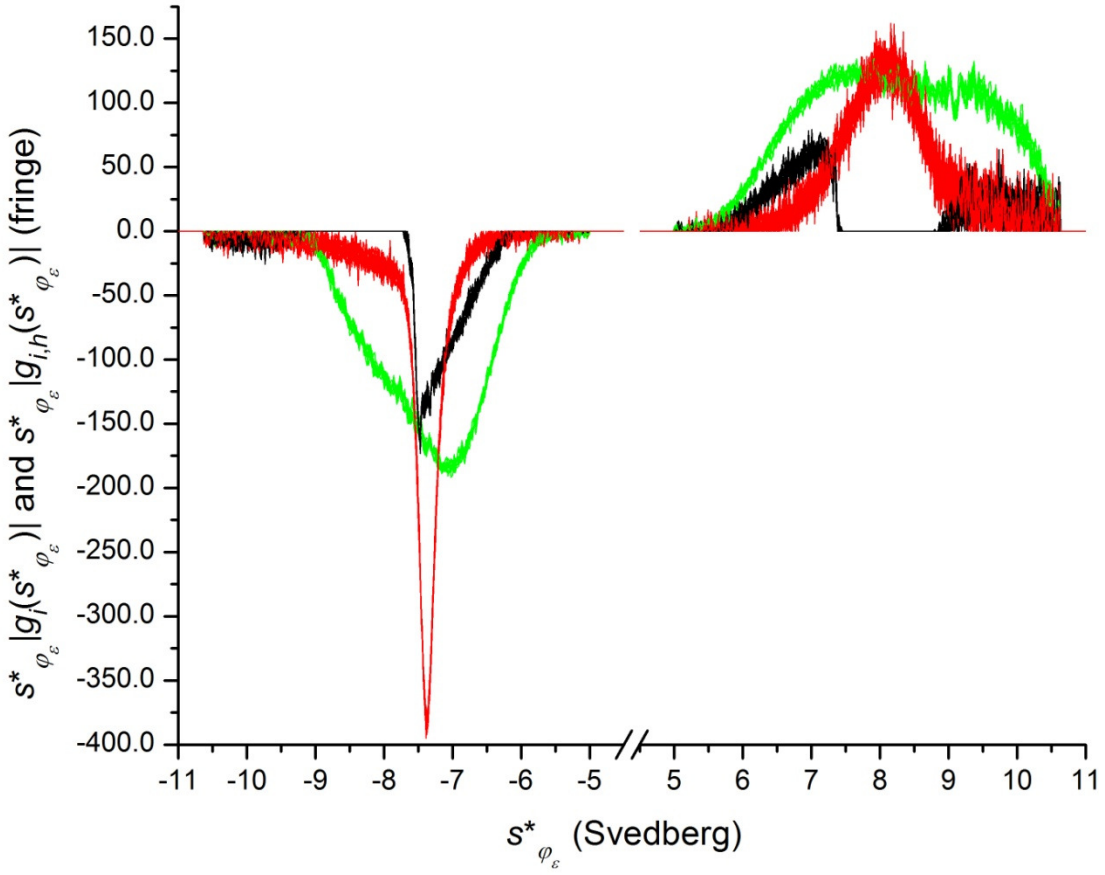

Figure 44c. For $i = 1$ (100% $K_A > 0$, 0% K_A undefined), $s^*_{\varphi_\epsilon}\left|g_i\left(s^*_{\varphi_\epsilon}\right)\right|$ at t_{36} (·····), t_{51} (·····) and t_{66} (·····), along with $s^*_{\varphi_\epsilon}\left|g_{i,h}\left(s^*_{\varphi_\epsilon}\right)\right|$ for each replicate ($1 \le h \le 9$) at t_{36} (——), t_{51} (——) and t_{66} (——), all plotted against $s^*_{\varphi_\epsilon}$. Masks (Figure 32) render all $g_{i,h}\left(s^*_{\varphi_\epsilon}\right) = 0$ and all $g_i\left(s^*_{\varphi_\epsilon}\right) = 0$ outside of 5E-13 s $< \left|s^*_{\varphi_\epsilon}\right| <$ 10.625E-13 s at t_{36}, t_{51} and t_{66}.

$i = 2$	$t_\epsilon = t_{36} = 2160$ s	$t_\epsilon = t_{51} = 3060$ s	$t_\epsilon = t_{66} = 3960$ s
$s^*_{i,\epsilon}$	1.03727 Svedberg	-0.70853 Svedberg	0.59763 Svedberg
h	$s^*_{i,h,36}$ (Svedberg)	$s^*_{i,h,51}$ (Svedberg)	$s^*_{i,h,66}$ (Svedberg)
1	1.00594	-0.72455	0.60207
2	1.00404	-0.68164	0.62118
3	1.00333	-0.68886	0.61163

4	0.99920	-0.71285	0.61302
5	1.00427	-0.71804	0.62930
6	0.99889	-0.69683	0.61586
7	1.00475	-0.68697	0.65109
8	1.00881	-0.65340	0.61016
9	0.99785	-0.69806	0.61644
$\langle s^*_{i,\epsilon} \rangle$	1.00301 Svedberg	-0.69569 Svedberg	0.61897 Svedberg
$e_{s^*_{i,\epsilon}}$	-0.03427 Svedberg	0.01284 Svedberg	0.02134 Svedberg

Table 25. $s^*_{i,h,\epsilon}$, $s^*_{i,\epsilon}$, $\langle s^*_{i,\epsilon} \rangle$, and $e_{s^*_{i,\epsilon}}$ for $i = 2$ at the times analysed: $t_\epsilon = t_{36}$, $t_\epsilon = t_{51}$ and $t_\epsilon = t_{66}$. The expectation values, $s^*_{i,\epsilon}$, are highlighted in blue. The replicate values (Equation 13), $s^*_{i,h,\epsilon}$, are not highlighted. The within-group mean values (Equation 82), $\langle s^*_{i,\epsilon} \rangle$, are highlighted in yellow. The accumulated error values (Equation 83), $e_{s^*_{i,\epsilon}}$, each being the difference between the mean and the expectation value, are highlighted in red. The $s^*_{i,\epsilon}$ values of this table are equal to $s^*_{i,\epsilon}\left(s^*_{\varphi_\epsilon=1}, s^*_{\varphi_\epsilon}\right)$ at $s^*_{\varphi_\epsilon} \geq s^*_{max>0}$ in Figure 45, and the $s^*_{i,h,\epsilon}$ values of this table are equal to $s^*_{i,h,\epsilon}\left(s^*_{\varphi_\epsilon=1}, s^*_{\varphi_\epsilon}\right)$ at $s^*_{\varphi_\epsilon} \geq s^*_{max>0}$ in Figure 45.

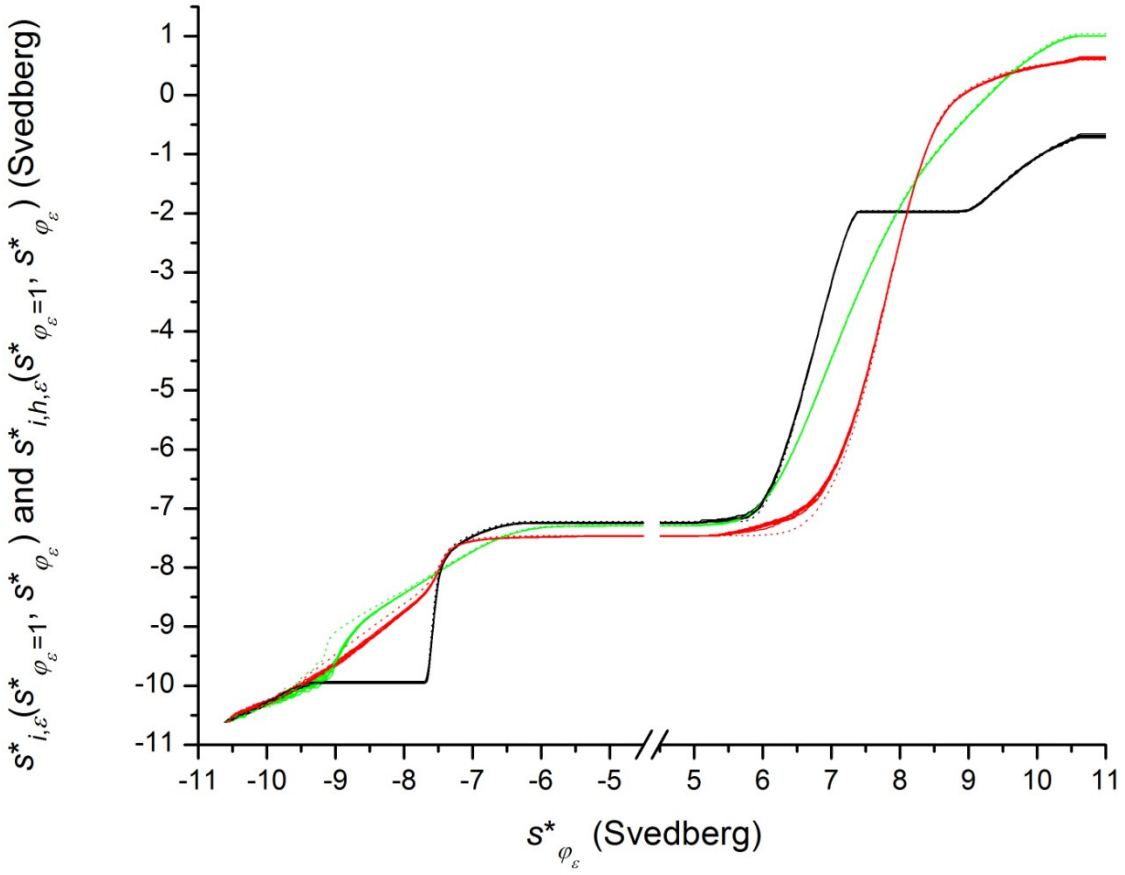

Figure 45a. For $i = 2$ (99% $K_A > 0$, 1% K_A undefined), $s^*_{i,\epsilon}\left(s^*_{\varphi_\epsilon=1}, s^*_{\varphi_\epsilon=2N}\right)$ at t_{36} (·····), t_{51} (·····) and t_{66} (·····), along with $s^*_{i,h,\epsilon}\left(s^*_{\varphi_\epsilon=1}, s^*_{\varphi_\epsilon=2N}\right)$ for each replicate ($1 \leq h \leq 9$) at t_{36} (——), t_{51} (——) and t_{66} (——), all plotted against $s^*_{\varphi_\epsilon}$. Given the masks (Figure 32) that render all $g_{i,h}\left(s^*_{\varphi_\epsilon}\right) = 0$ and all $g_i\left(s^*_{\varphi_\epsilon}\right) = 0$ outside of 5E-13 s $< \left|s^*_{\varphi_\epsilon}\right| <$ 10.625E-13 s at t_{36}, t_{51} and t_{66}, by Equation 81, $s^*_{i,h,\epsilon} \equiv s^*_{i,h,\epsilon}\left(s^*_{\varphi_\epsilon=1}, s^*_{\varphi_\epsilon=2N}\right)$ and $s^*_{i,\epsilon} \equiv s^*_{i,\epsilon}\left(s^*_{\varphi_\epsilon=1}, s^*_{\varphi_\epsilon=2N}\right)$.

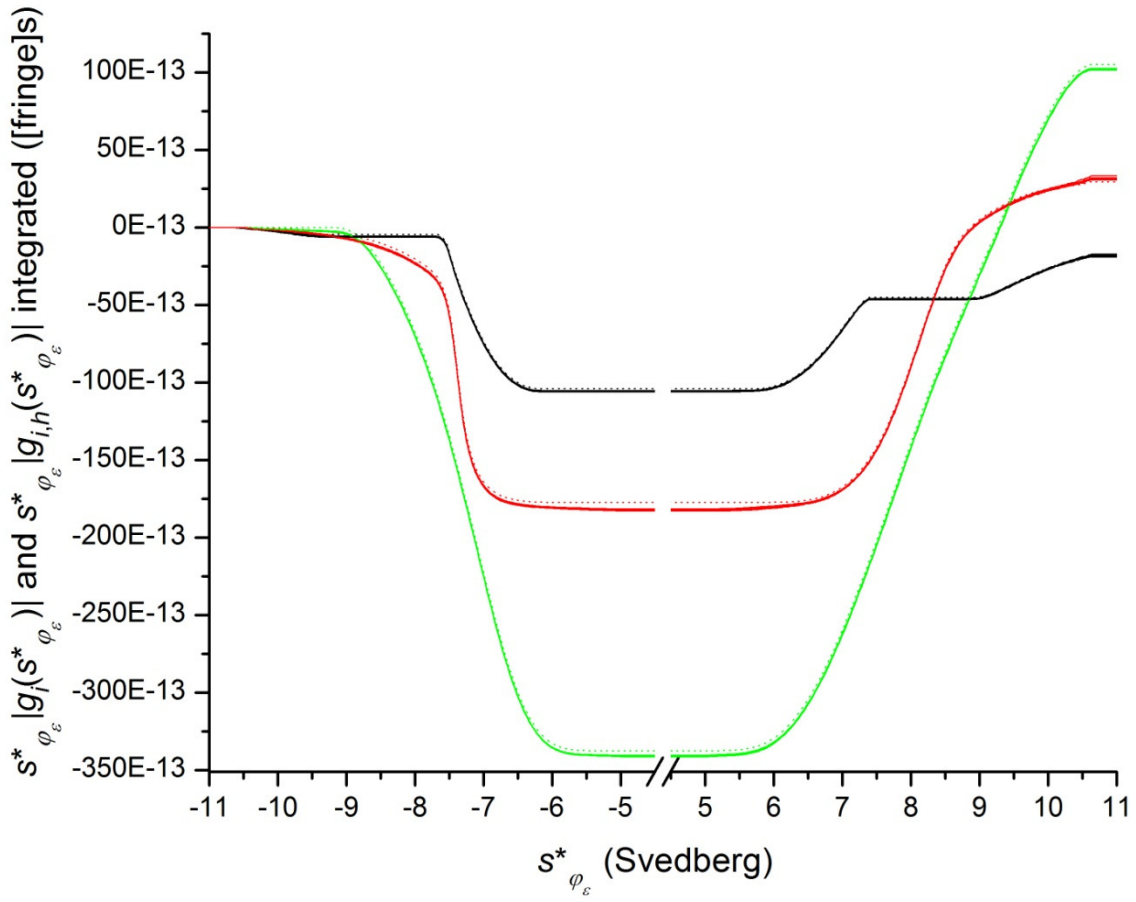

Figure 45b. For $i = 2$ (99% $K_A > 0$, 1% K_A undefined), $\int_{s^*_{\varphi\epsilon=1}}^{s^*_{\varphi\epsilon=2N}} s^*_{\varphi\epsilon}\left|g_i\left(s^*_{\varphi\epsilon}\right)\right| ds^*_{\varphi\epsilon}$ at t_{36} (·····), t_{51} (·····) and t_{66} (·····), along with $\int_{s^*_{\varphi\epsilon=1}}^{s^*_{\varphi\epsilon=2N}} s^*_{\varphi\epsilon}\left|g_{i,h}\left(s^*_{\varphi\epsilon}\right)\right| ds^*_{\varphi\epsilon}$ for each replicate ($1 \leq h \leq 9$) at t_{36} (——), t_{51} (——) and t_{66} (——), all plotted against $s^*_{\varphi\epsilon}$. The integrals are the numerators of Equation 81 that apply when all $g_{i,h}\left(s^*_{\varphi\epsilon}\right) = 0$ and all $g_i\left(s^*_{\varphi\epsilon}\right) = 0$ outside of 5E-13 s $< \left|s^*_{\varphi\epsilon}\right| <$ 10.625E-13 s at t_{36}, t_{51} and t_{66}, as ensured here through the use of masks (Figure 32).

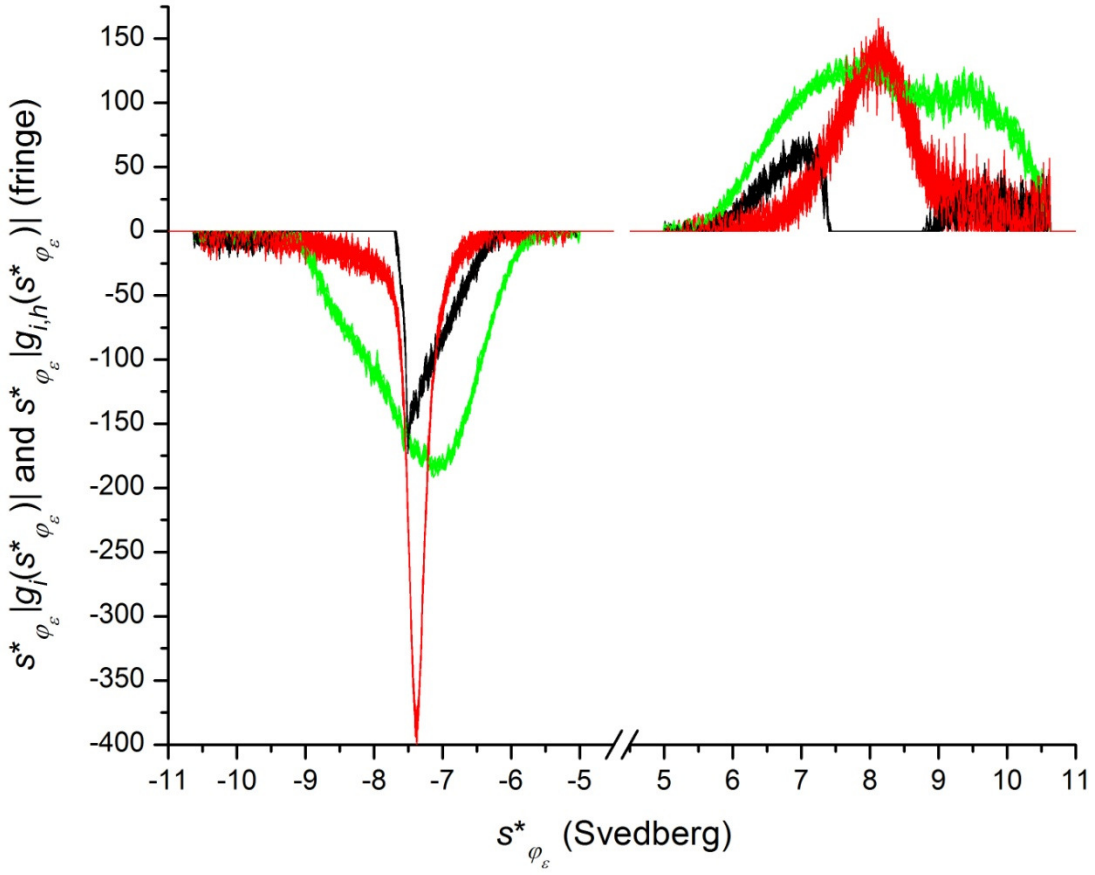

Figure 45c. For $i = 1$ (99% $K_A > 0$, 1% K_A undefined), $s^*_{\varphi_\epsilon}\left|g_i\left(s^*_{\varphi_\epsilon}\right)\right|$ at t_{36} (·····), t_{51} (·····) and t_{66} (·····), along with $s^*_{\varphi_\epsilon}\left|g_{i,h}\left(s^*_{\varphi_\epsilon}\right)\right|$ for each replicate ($1 \le h \le 9$) at t_{36} (——), t_{51} (——) and t_{66} (——), all plotted against $s^*_{\varphi_\epsilon}$. Masks (Figure 32) render all $g_{i,h}\left(s^*_{\varphi_\epsilon}\right) = 0$ and all $g_i\left(s^*_{\varphi_\epsilon}\right) = 0$ outside of 5E-13 s $< \left|s^*_{\varphi_\epsilon}\right| <$ 10.625E-13 s at t_{36}, t_{51} and t_{66}.

$i = 3$	$t_\epsilon = t_{36} = 2160$ s	$t_\epsilon = t_{51} = 3060$ s	$t_\epsilon = t_{66} = 3960$ s
$s^*_{i,\epsilon}$	0.62213 Svedberg	-1.37829 Svedberg	0.42570 Svedberg
h	$s^*_{i,h,36}$ (Svedberg)	$s^*_{i,h,51}$ (Svedberg)	$s^*_{i,h,66}$ (Svedberg)
1	0.60630	-1.18811	0.49612
2	0.59558	-1.19151	0.50404
3	0.58635	-1.15177	0.49197

$\langle s^*_{i,\epsilon} \rangle$	0.59608 Svedberg	-1.17713 Svedberg	0.49738 Svedberg
$e_{s^*_{i,\epsilon}}$	-0.02606 Svedberg	0.20116 Svedberg	0.07167 Svedberg

Table 26. $s^*_{i,h,\epsilon}$, $s^*_{i,\epsilon}$, $\langle s^*_{i,\epsilon} \rangle$, and $e_{s^*_{i,\epsilon}}$ for $i = 3$ at the times analysed: $t_\epsilon = t_{36}$, $t_\epsilon = t_{51}$ and $t_\epsilon = t_{66}$. The expectation values, $s^*_{i,\epsilon}$, are highlighted in blue. The replicate values (Equation 13), $s^*_{i,h,\epsilon}$, are not highlighted. The within-group mean values (Equation 82), $\langle s^*_{i,\epsilon} \rangle$, are highlighted in yellow. The accumulated error values (Equation 83), $e_{s^*_{i,\epsilon}}$, each being the difference between the mean and the expectation value, are highlighted in red. The $s^*_{i,\epsilon}$ values of this table are equal to $s^*_{i,\epsilon}\left(s^*_{\varphi_\epsilon=1}, s^*_{\varphi_\epsilon}\right)$ at $s^*_{\varphi_\epsilon} \geq s^*_{max>0}$ in Figure 46, and the $s^*_{i,h,\epsilon}$ values of this table are equal to $s^*_{i,h,\epsilon}\left(s^*_{\varphi_\epsilon=1}, s^*_{\varphi_\epsilon}\right)$ at $s^*_{\varphi_\epsilon} \geq s^*_{max>0}$ in Figure 46.

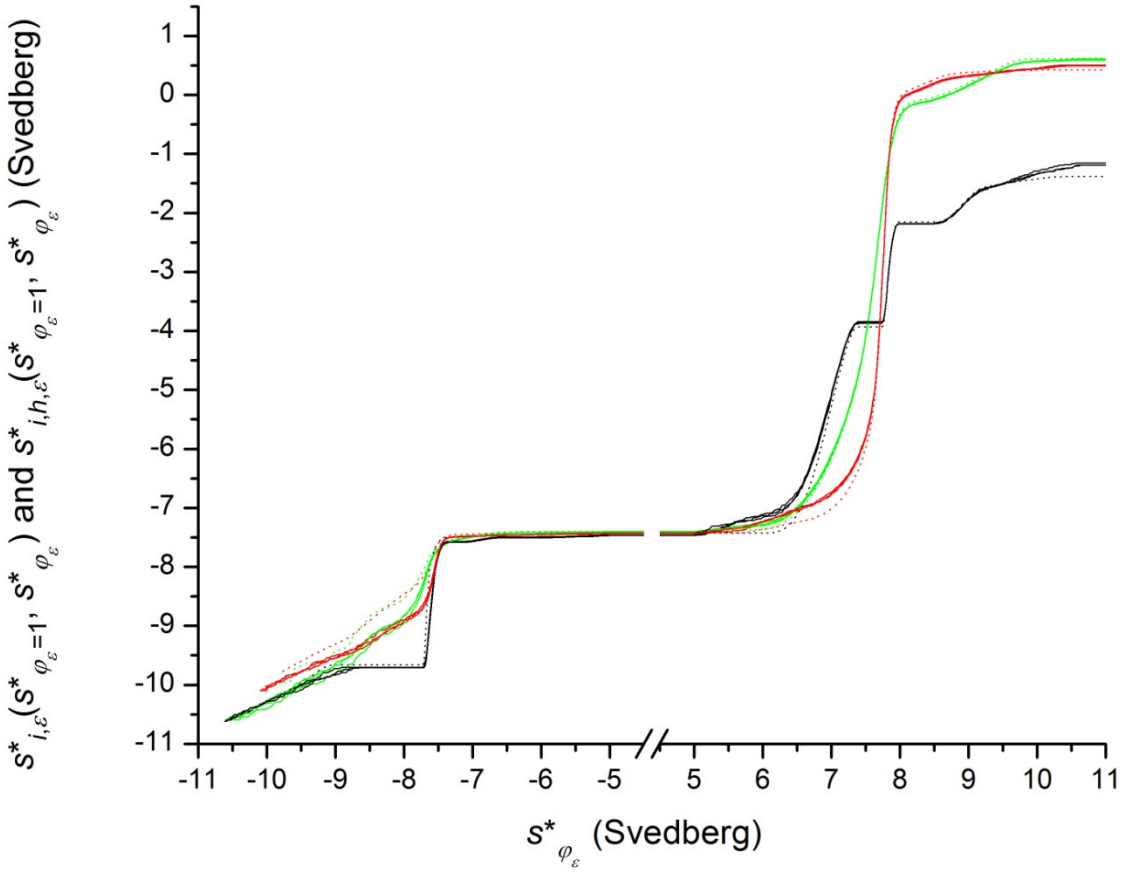

Figure 46a. For $i = 3$ (50% $K_A > 0$, 50% K_A undefined), $s^*_{i,\epsilon}\left(s^*_{\varphi_\epsilon=1}, s^*_{\varphi_{\epsilon=2N}}\right)$ at t_{36} (·····), t_{51} (·····)

and t_{66} (·····), along with $s^*_{i,h,\epsilon}\left(s^*_{\varphi_\epsilon=1}, s^*_{\varphi_\epsilon=2N}\right)$ for each replicate ($1 \leq h \leq 3$) at t_{36} (——), t_{51} (——) and t_{66} (——), all plotted against $s^*_{\varphi_\epsilon}$. Given the masks (Figure 32) that render all $g_{i,h}\left(s^*_{\varphi_\epsilon}\right) = 0$ and all $g_i\left(s^*_{\varphi_\epsilon}\right) = 0$ outside of 5E-13 s $< \left|s^*_{\varphi_\epsilon}\right| <$ 10.625E-13 s at t_{36}, t_{51} and t_{66}, by Equation 81, $s^*_{i,h,\epsilon} \equiv s^*_{i,h,\epsilon}\left(s^*_{\varphi_\epsilon=1}, s^*_{\varphi_\epsilon=2N}\right)$ and $s^*_{i,\epsilon} \equiv s^*_{i,\epsilon}\left(s^*_{\varphi_\epsilon=1}, s^*_{\varphi_\epsilon=2N}\right)$.

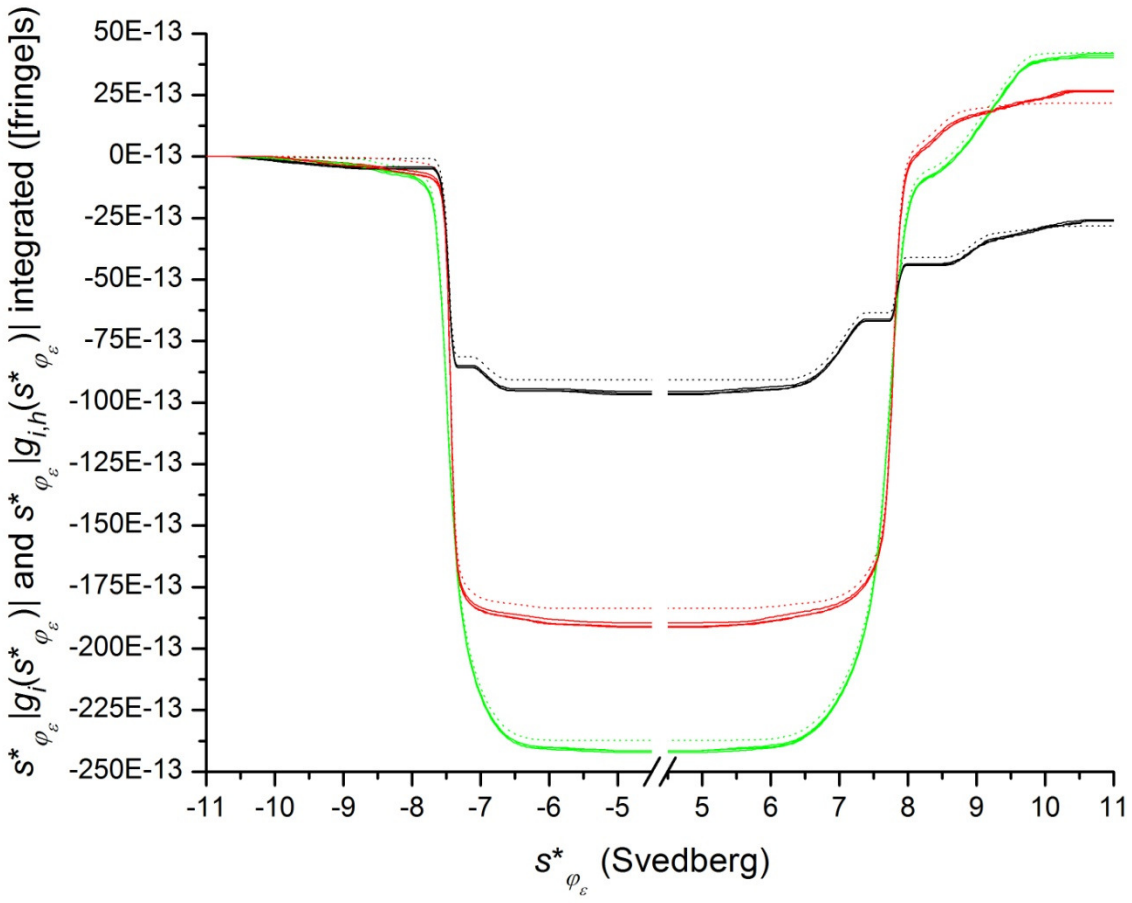

Figure 46b. For $i = 2$ (50% $K_A > 0$, 50% K_A undefined), $\int_{s^*_{\varphi_\epsilon=1}}^{s^*_{\varphi_\epsilon=2N}} s^*_{\varphi_\epsilon}\left|g_i\left(s^*_{\varphi_\epsilon}\right)\right| ds^*_{\varphi_\epsilon}$ at t_{36} (·····), t_{51} (·····) and t_{66} (·····), along with $\int_{s^*_{\varphi_\epsilon=1}}^{s^*_{\varphi_\epsilon=2N}} s^*_{\varphi_\epsilon}\left|g_{i,h}\left(s^*_{\varphi_\epsilon}\right)\right| ds^*_{\varphi_\epsilon}$ for each replicate ($1 \leq h \leq 3$) at t_{36} (——), t_{51} (——) and t_{66} (——), all plotted against $s^*_{\varphi_\epsilon}$. The integrals are the numerators of Equation 81 that apply when all $g_{i,h}\left(s^*_{\varphi_\epsilon}\right) = 0$ and all $g_i\left(s^*_{\varphi_\epsilon}\right) = 0$ outside of 5E-13 s $< \left|s^*_{\varphi_\epsilon}\right| <$ 10.625E-13 s at t_{36}, t_{51} and t_{66}, as ensured here through the use of masks (Figure 32).

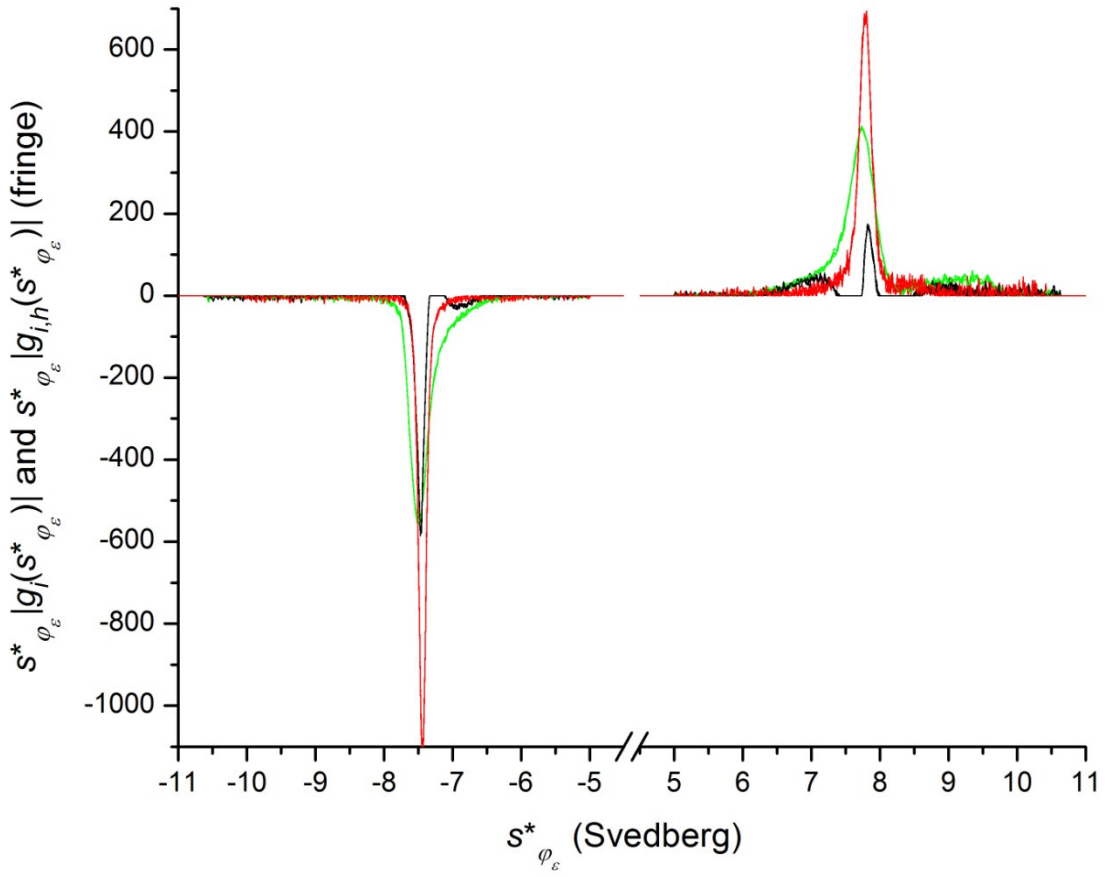

Figure 46c. For $i = 1$ (50% $K_A > 0$, 50% K_A undefined), $s^*_{\varphi_\epsilon}\left|g_i\left(s^*_{\varphi_\epsilon}\right)\right|$ at t_{36} (┈┈), t_{51} (┈┈) and t_{66} (┈┈), along with $s^*_{\varphi_\epsilon}\left|g_{i,h}\left(s^*_{\varphi_\epsilon}\right)\right|$ for each replicate ($1 \le h \le 3$) at t_{36} (——), t_{51} (——) and t_{66} (——), all plotted against $s^*_{\varphi_\epsilon}$. Masks (Figure 32) render all $g_{i,h}\left(s^*_{\varphi_\epsilon}\right) = 0$ and all $g_i\left(s^*_{\varphi_\epsilon}\right) = 0$ outside of 5E-13 s $< \left|s^*_{\varphi_\epsilon}\right| <$ 10.625E-13 s at t_{36}, t_{51} and t_{66}.

$i = 4$	$t_\epsilon = t_{36} = 2160$ s	$t_\epsilon = t_{51} = 3060$ s	$t_\epsilon = t_{66} = 3960$ s
$s^*_{i,\epsilon}$	0.28140 Svedberg	-1.78094 Svedberg	0.33734 Svedberg
h	$s^*_{i,h,36}$ (Svedberg)	$s^*_{i,h,51}$ (Svedberg)	$s^*_{i,h,66}$ (Svedberg)
1	0.29238	-1.30647	0.53019
2	0.29510	-1.26882	0.53799
3	0.30031	-1.20425	0.50524

$\langle s^*_{i,\epsilon} \rangle$	0.29593 Svedberg	-1.25985 Svedberg	0.52447 Svedberg
$e_{s^*_{i,\epsilon}}$	0.01453 Svedberg	0.52110 Svedberg	0.18713 Svedberg

Table 27. $s^*_{i,h,\epsilon}$, $s^*_{i,\epsilon}$, $\langle s^*_{i,\epsilon} \rangle$, and $e_{s^*_{i,\epsilon}}$ for $i = 4$ at the times analysed: $t_\epsilon = t_{36}$, $t_\epsilon = t_{51}$ and $t_\epsilon = t_{66}$. The expectation values, $s^*_{i,\epsilon}$, are highlighted in blue. The replicate values (Equation 13), $s^*_{i,h,\epsilon}$, are not highlighted. The within-group mean values (Equation 82), $\langle s^*_{i,\epsilon} \rangle$, are highlighted in yellow. The accumulated error values (Equation 83), $e_{s^*_{i,\epsilon}}$, each being the difference between the mean and the expectation value, are highlighted in red. The $s^*_{i,\epsilon}$ values of this table are equal to $s^*_{i,\epsilon}\left(s^*_{\varphi_\epsilon=1}, s^*_{\varphi_\epsilon}\right)$ at $s^*_{\varphi_\epsilon} \geq s^*_{max>0}$ in Figure 47, and the $s^*_{i,h,\epsilon}$ values of this table are equal to $s^*_{i,h,\epsilon}\left(s^*_{\varphi_\epsilon=1}, s^*_{\varphi_\epsilon}\right)$ at $s^*_{\varphi_\epsilon} \geq s^*_{max>0}$ in Figure 47.

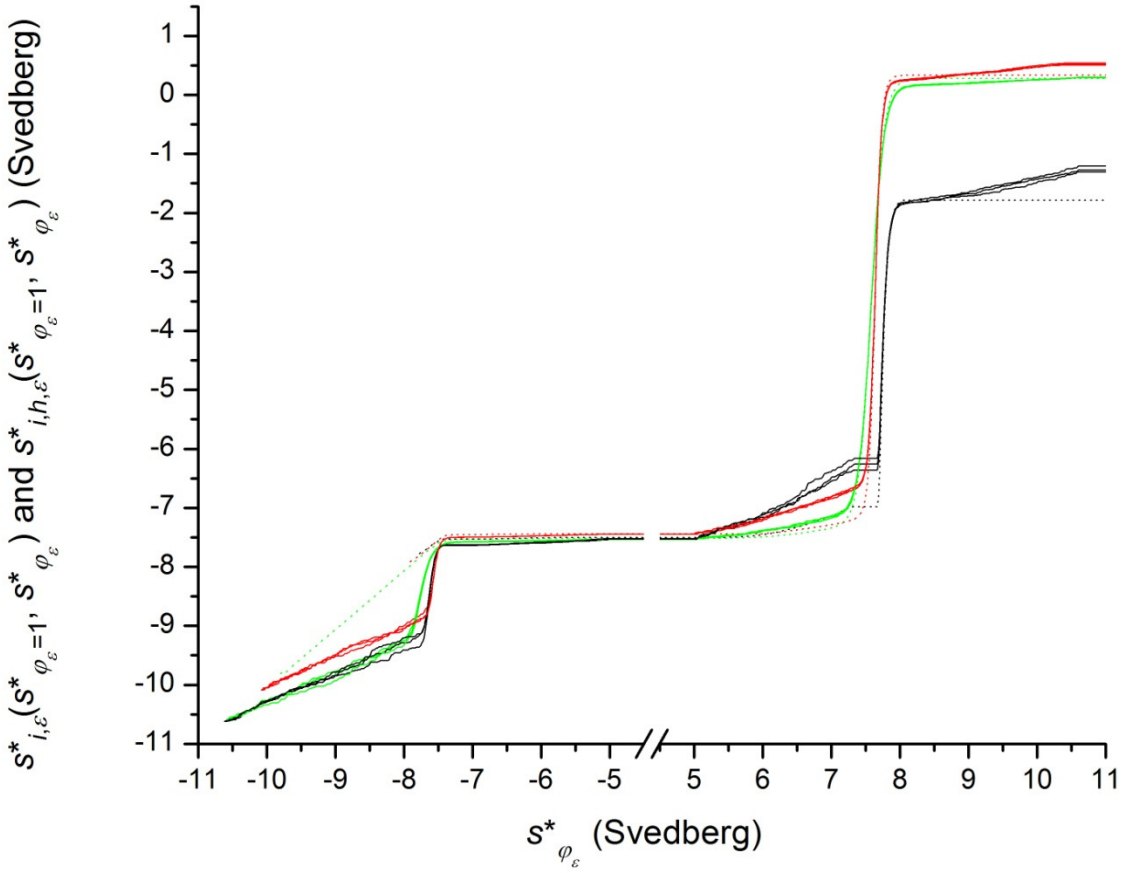

Figure 47a. For $i = 4$ (0% $K_A > 0$, 100% K_A undefined), $s^*_{i,\epsilon}\left(s^*_{\varphi_\epsilon=1}, s^*_{\varphi_{\epsilon=2N}}\right)$ at t_{36} (·····), t_{51} (·····)

and t_{66} (·····), along with $s^*_{i,h,\epsilon}\left(s^*_{\varphi_\epsilon=1}, s^*_{\varphi_\epsilon=2N}\right)$ for each replicate ($1 \leq h \leq 3$) at t_{36} (——), t_{51} (——) and t_{66} (——), all plotted against $s^*_{\varphi_\epsilon}$. Given the masks (Figure 32) that render all $g_{i,h}\left(s^*_{\varphi_\epsilon}\right) = 0$ and all $g_i\left(s^*_{\varphi_\epsilon}\right) = 0$ outside of 5E-13 s $< \left|s^*_{\varphi_\epsilon}\right| <$ 10.625E-13 s at t_{36}, t_{51} and t_{66}, by Equation 81, $s^*_{i,h,\epsilon} \equiv s^*_{i,h,\epsilon}\left(s^*_{\varphi_\epsilon=1}, s^*_{\varphi_\epsilon=2N}\right)$ and $s^*_{i,\epsilon} \equiv s^*_{i,\epsilon}\left(s^*_{\varphi_\epsilon=1}, s^*_{\varphi_\epsilon=2N}\right)$.

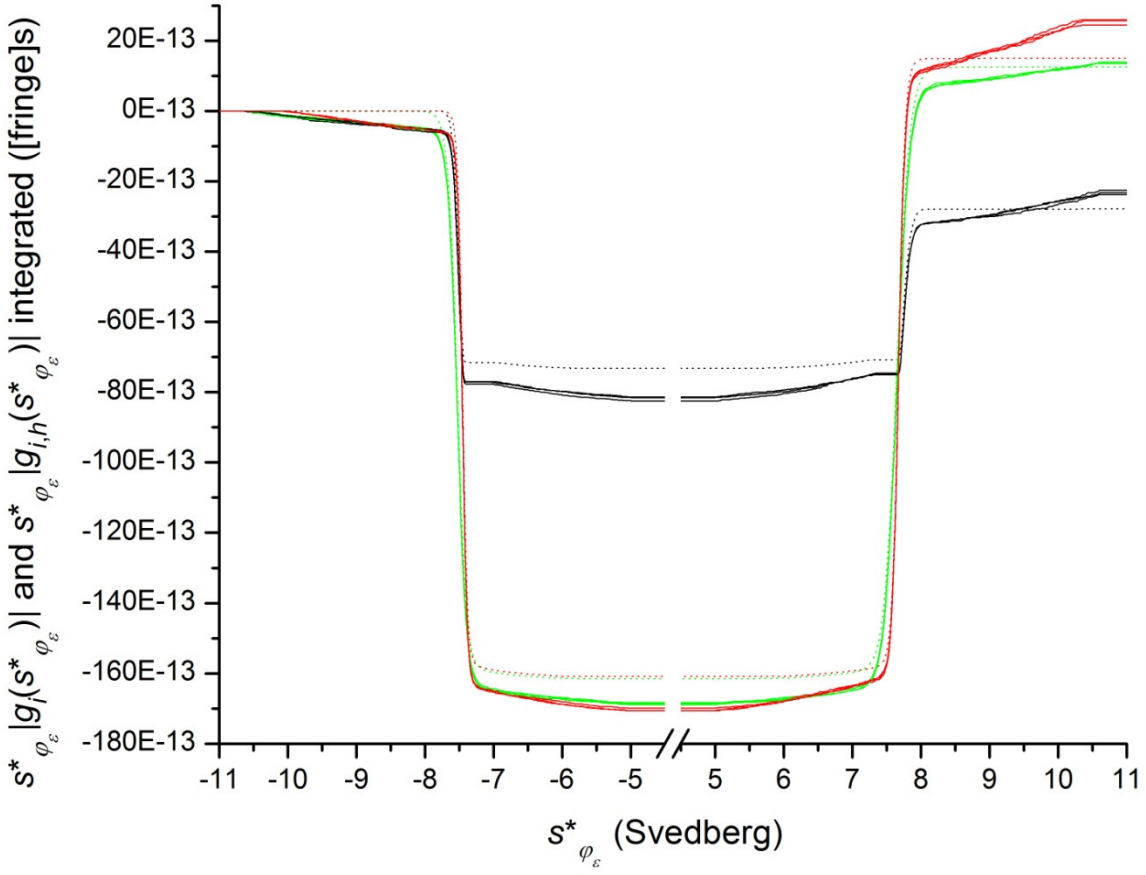

Figure 47b. For $i = 2$ (1-0% $K_A > 0$, 0% K_A undefined), $\int_{s^*_{\varphi_\epsilon=1}}^{s^*_{\varphi_\epsilon=2N}} s^*_{\varphi_\epsilon}\left|g_i\left(s^*_{\varphi_\epsilon}\right)\right| ds^*_{\varphi_\epsilon}$ at t_{36} (·····), t_{51} (·····) and t_{66} (·····), along with $\int_{s^*_{\varphi_\epsilon=1}}^{s^*_{\varphi_\epsilon=2N}} s^*_{\varphi_\epsilon}\left|g_{i,h}\left(s^*_{\varphi_\epsilon}\right)\right| ds^*_{\varphi_\epsilon}$ for each replicate ($1 \leq h \leq 3$) at t_{36} (——), t_{51} (——) and t_{66} (——), all plotted against $s^*_{\varphi_\epsilon}$. The integrals are the numerators of Equation 81 that apply when all $g_{i,h}\left(s^*_{\varphi_\epsilon}\right) = 0$ and all $g_i\left(s^*_{\varphi_\epsilon}\right) = 0$ outside of 5E-13 s $< \left|s^*_{\varphi_\epsilon}\right| <$ 10.625E-13 s at t_{36}, t_{51} and t_{66}, as ensured here through the use of masks (Figure 32).

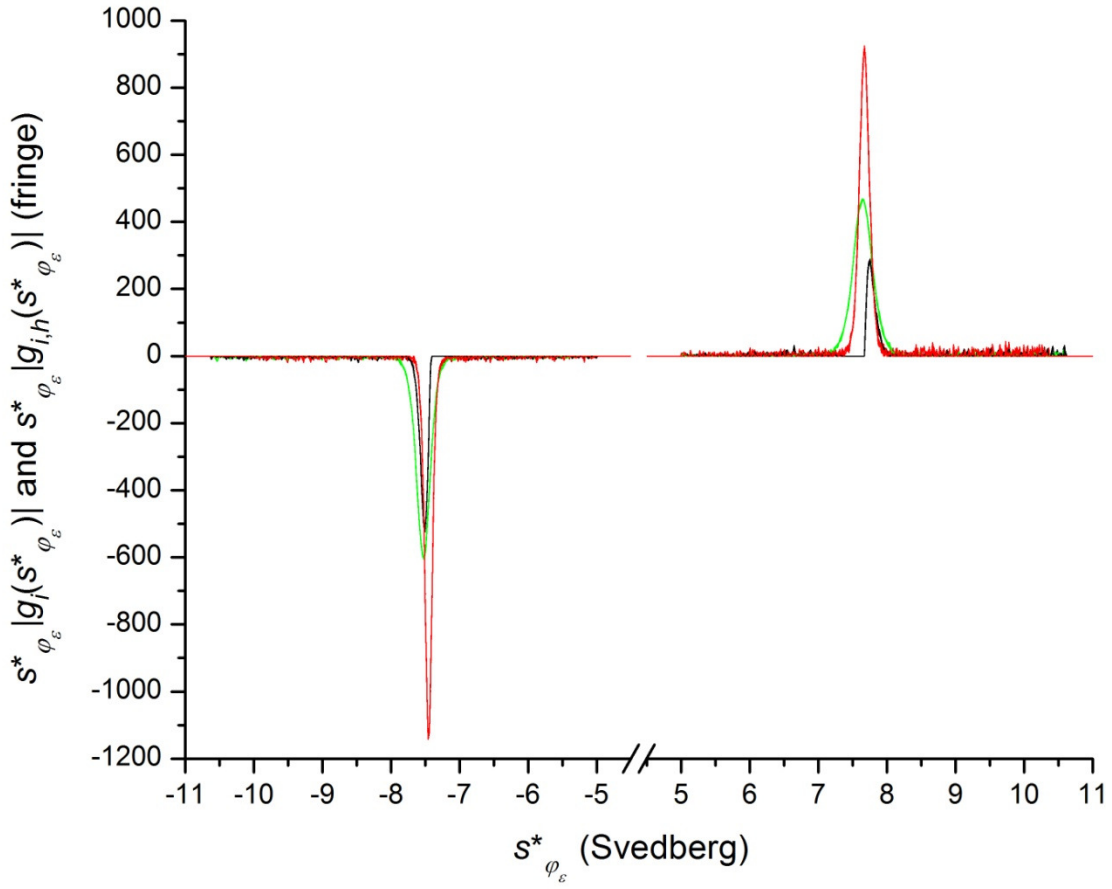

Figure 47c. For $i = 1$ (100% $K_A > 0$, 0% K_A undefined), $s^*_{\varphi\epsilon}\left|g_i\left(s^*_{\varphi\epsilon}\right)\right|$ at t_{36} (·····), t_{51} (·····) and t_{66} (·····), along with $s^*_{\varphi\epsilon}\left|g_{i,h}\left(s^*_{\varphi\epsilon}\right)\right|$ for each replicate ($1 \le h \le 3$) at t_{36} (——), t_{51} (——) and t_{66} (——), all plotted against $s^*_{\varphi\epsilon}$. Masks (Figure 32) render all $g_{i,h}\left(s^*_{\varphi\epsilon}\right) = 0$ and all $g_i\left(s^*_{\varphi\epsilon}\right) = 0$ outside of 5E-13 s $< \left|s^*_{\varphi\epsilon}\right| <$ 10.625E-13 s at t_{36}, t_{51} and t_{66}.

STATISTICAL ANALYSIS

One-way analyses of variance (ANOVA), Bonferroni adjusted t-test (2-tailed), and confidence intervals about mean values

This material is largely drawn from the work of Hembree (2006) and Prins et al. (2006).

ANOVA

A one-way analyses of variance (ANOVA) is used to test for statistically significant differences in population means between treatment groups. To discuss the ANOVA and subsequent analyses, a few definitions and explanations of notation are needed.

The treatment groups are indexed by i, and n_i denotes the number of observations (A.K.A. replicates) in treatment group i. Thus, for g treatment groups in a total population of N_{tot} observations, $1 \leq i \leq g$, and

$$N_{tot} = \sum_{i=1}^{g} n_i .$$

(84)

The degrees of freedom for treatment (A.K.A. the degrees of freedom among, or between, groups) is $[g - 1]$, and the degrees of freedom for error (A.K.A. the degrees of freedom within groups) is $[N_{tot} - g]$. The observations within each group are indexed by h. Thus, $1 \leq h \leq n_i$ within a treatment group, for which the mean of the observations is given by

$$\mu_i = \frac{1}{n_i} \sum_{h=1}^{n_i} A_{i,h} ,$$

(85)

where $A_{i,h}$ is the value of observation h within treatment group i.

It is assumed that the observations fit a model given by

$$A_{i,h} = \mu + \Delta\mu_i + e_{i,h} = \left(\frac{1}{g}\sum_{i=1}^{g}\mu_i\right) + \Delta\mu_i + e_{i,h}\,,$$

(86a)

where μ is the grand mean, $\Delta\mu_i$ is the deviation of the mean of treatment group i from the grand mean ($\Delta\mu_i = \mu_i - \mu$), and $e_{i,h}$ is the residual, which must be normally distributed (Equation 24) about $\mu + \Delta\mu_i$ with a standard deviation that does not vary from one treatment group to another. Thus, each observation, $A_{i,h}$, is the sum of a deterministic component, $\mu + \Delta\mu_i$, and a random component, $e_{i,h}$. As $\Delta\mu_i = \mu_i - \mu$,

$$\sum_{i=1}^{g}\Delta\mu_i = \sum_{i=1}^{g}(\mu_i - \mu) = \left(\sum_{i=1}^{g}\mu_i\right) - g\mu = 0.$$

(86b)

The deterministic component is assumed to be a function of an independent variable that defines each treatment group, i.

Provided that that $e_{i,h}$ follows "a Gaussian distribution with fixed location and spread" (Hembree, 2006), as it should if Equation 86 is applicable to the observations, then the ratio of the mean of the sum of squares of treatments with [g - 1] degrees of freedom, T_{MSb} (Equation 92), to the mean of the sum of squares of error with [N_{tot} - g] degrees of freedom, e_{MSw} (Equation 91), follows an F distribution with corresponding degrees of freedom ([g - 1] and [N_{tot} - g]). Therefore, at a chosen level of confidence, an F-test can be used to judge whether $\Delta\mu_i$ is significantly different from zero in one or more treatment groups.

All observations within all treatment groups are included in both the raw sum,

$$A_{tot} = \sum_{i=1}^{g} \sum_{h=1}^{n_i} A_{i,h} = \sum_{i=1}^{g} n_i \mu_i,$$

(87)

and the raw sum of squares,

$$A_{sq} = \sum_{i=1}^{g} \sum_{h=1}^{n_i} \left(A_{i,h}\right)^2 .$$

(88)

The mean of the raw sum squared is

$$\mu_{sq} = \frac{(A_{tot})^2}{N_{tot}},$$

(89)

and the correction term of the mean is

$$\mu_{corr} = \sum_{i=1}^{g} \frac{1}{n_i} (n_i \mu_i)^2 .$$

(90)

The mean of the sum of squares of error (A.K.A. the mean square error within groups) is

$$e_{MSw} = \left(A_{sq} - \mu_{corr}\right) \frac{1}{N_{tot} - g},$$

(91)

and the mean of the sum of squares of treatments is

$$T_{MSb} = \left(\mu_{corr} - \mu_{sq}\right) \frac{1}{g - 1}.$$

(92)

The denominator of Equation 91 is equal to the [N_{tot} - g] degrees of freedom in e_{MSw}, and the denominator of Equation 92 is equal to the [g - 1] degrees of freedom in T_{MSb}.

The F statistic, $F([g - 1],[N_{tot} - g])$, is equal to T_{MSb}/e_{MSw}, and is expressed as a function of the degrees of freedom in T_{MSb} and e_{MSw}. The F statistic is greater than 1 when the variance between two or more groups is greater than the variance within groups. (The greater the variance between groups, and the lower the variance within groups, the higher the value of the F statistic will be.) The statistical significance of the variation between groups can be expressed as the probability, p, that the variation is due solely to chance. That probability ($0 \leq p \leq 1$) is equal to 1 minus the integral of the probability density function (*F-PDF*) for the F distribution evaluated from 0 to $F([g - 1],[N_{tot} - g])$. The integral of the *F-PDF* is the corresponding cumulative probability distribution, (*F-CPD*), which takes as its arguments the F statistic, $[g - 1]$ and $[N_{tot} - g]$, and returns 1 minus the corresponding p value. The inverse *F-CPD* takes as its arguments $(1 - p)$, $[g - 1]$ and $[N_{tot} - g]$, and returns the corresponding F statistic. Thus, the inverse *F-CPD* is used to determine the lowest value of the F statistic that, at $[g - 1]$ degrees of freedom of treatment and $[N_{tot} - g]$ degrees of freedom of error, corresponds to a p value less than or equal to an acceptable limit.

The acceptable limit of the p value is the applied level of confidence, which will be denoted here as $(1 - \alpha)$. Thus, the significance level, α, is the accepted risk that the effects of treatments on observations are due solely to chance. If the treatments have a significant effect on the observations, then T_{MSb}/e_{MSw} should be greater than the F statistic returned by the inverse *F-CPD* at $(1 - p) = (1 - \alpha)$ with $[g - 1]$ degrees of freedom of treatment and $[N_{tot} - g]$ degrees of freedom of error. In terms of probability, if the treatments have a significant effect on the observations, then α should be greater than the p value returned by 1 - *F-CPD* at $F([g - 1],[N_{tot} - g]) = T_{MSb}/e_{MSw}$, where the $[g - 1]$ degrees of freedom of treatment and the $[N_{tot} - g]$ degrees of freedom of error

correspond to the degrees of freedom in T_{MSb} and e_{MSw}, respectively.

Bonferroni adjusted t-test (2-tailed)

Provided that the ANOVA has demonstrated their significance beforehand, differences between treatment groups are assessed by the Bonferroni adjusted *t*-test (2-tailed), which is a post-hoc test that controls for the family-wise error rate. Comparisons between different treatment groups are made pair-wise. Using i and j to index two treatment groups in a pair-wise comparison, for g treatment groups, $1 \leq i \leq g$ and $1 \leq j \leq g$. A comparison between i and j is considered identical to a comparison between j and i, and i cannot equal j in any comparison. Thus, for g treatment groups, there are $q = g(g - 1)/2$ unique, pair-wise comparisons between different treatment groups.

Denoting the means of treatment groups i and j as μ_i and μ_j, respectively, their mean difference,

$$\Delta\mu_{ij} = \mu_i - \mu_j,$$

(93)

is calculated for each unique, pair-wise comparison between different ($i \neq j$) treatment groups. As $\Delta\mu_{ij} = -\Delta\mu_{ji}$, there are $2q$ such parameters in g treatment groups, but as $|\Delta\mu_{ij}| = |-\Delta\mu_{ji}|$, half of those parameters can be viewed as redundant.

Denoting the number of replicates in treatment groups i and j as n_i and n_j, respectively, the mean square error within groups, e_{MSw} (Equation 91), is used to calculate the standard error of the mean difference,

$$e_{\Delta\mu_{ij}} = \left(e_{MSw}\left[1/n_i + 1/n_j\right]\right)^{0.5},$$

(94)

for each unique, pair-wise comparison between different ($i \neq j$) treatment groups. As $e_{\Delta\mu_{ij}} = e_{\Delta\mu_{ji}}$, there are q such parameters in g treatment groups.

A critical value (A.K.A. test statistic), given by

$$t\big([n_i - 1], [n_j - 1]\big) = \frac{\Delta\mu_{ij}}{e_{\Delta\mu_{ij}}},$$

(95)

is then calculated for each unique, pair-wise comparison between different ($i \neq j$) treatment groups. The number of critical values is equal to the number of mean differences.

Integrating Student's t-distribution function from -|t([n_i - 1] + [n_j - 1])| to |t([n_i - 1] + [n_j - 1])| at [N_{tot} - g] degrees of freedom, and subtracting the result from 1, yields p_{LSD}, which is the least-square-difference probability that the difference in the means of treatment groups i and j could be due to chance. Multiplying p_{LSD} by q yields p_{Bonf}, which is the Bonferroni-adjusted probability that the difference in the means of treatment groups i and j could be due to chance. As p_{Bonf} exceeds p_{LSD} by a factor of q whenever q is greater than 1, and as q is equal to the number of comparisons between treatment groups, p_{Bonf} accounts for an expectation that the risk of mistaking noise for information increases as the number of comparisons increases.

Confidence intervals about $\Delta\mu_{ij}$

Any given observation, h, within treatment group i is denoted as $A_{i,h}$, of which the deterministic component is $\mu + \Delta\mu_i$, where $\Delta\mu_i = \mu_i$ - μ (Equation 86). Likewise, any given observation, h, within

treatment group j is denoted as $A_{j,h}$, of which the deterministic component is $\mu + \Delta\mu_j$, where $\Delta\mu_j = \mu_j - \mu$. Thus, the mean difference between the deterministic components for groups i and j is equal to $(\mu + \Delta\mu_i) - (\mu + \Delta\mu_j) = \Delta\mu_i - \Delta\mu_j = \mu_i - \mu_j = \Delta\mu_{ij}$, which is the difference between the means of treatment groups i and j (Equation 93).

A true value of the parameter sought must underlie each observation, $A_{i,h}$, within treatment group i. Denoting such a true value as A_i (Equations 104 and 105), then if Equation 86 holds, A_i can be equated to $\mu + \Delta\mu_i$ in the limit as the number of replicates within each treatment group approaches infinity. Likewise, if Equation 86 holds, A_j can be equated to $\mu + \Delta\mu_j$ in the limit as the number of replicates within each treatment group approaches infinity. As such, A_j denotes the true value that must underlie each observation, $A_{j,h}$, within treatment group j. Thus, ΔA_{ij}, the mean difference between the true values for groups i and j, is equal to $A_i - A_j$.

The $(1 - \alpha)100\%$ confidence interval about each $\Delta\mu_{ij}$ is given by

$$\pm C_{\Delta\mu_{ij}} = \Delta\mu_{ij} \pm e_{\Delta\mu_{ij}} t([\alpha/2q], [N_{tot} - g]),$$

(96)

where $t([\alpha/2q],[N_{tot} - g])$ is the upper critical value of Student's t-distribution at $[N_{tot} - g]$ degrees of freedom and a Bonferroni-adjusted significance level of $[\alpha/2q]$ for a two-sided test. (If $\alpha = 0.05$, 95% confidence intervals are obtained.) At $[N_{tot} - g]$ degrees of freedom, the integral of Student's t-distribution from $-t([\alpha/2q],[N_{tot} - g])$ to $t([\alpha/2q],[N_{tot} - g])$ is equal to $(1 - 2[\alpha/2q])$. If no correction for the effects of multiple comparisons were needed, $(1 - 2[\alpha/2q])$ would be considered the probability that $\Delta\mu_{ij}$ will be found within $\pm C_{\Delta\mu_{ij}}$ in cases where ΔA_{ij} is found within $\pm C_{\Delta\mu_{ij}}$. Corrected for the effects of multiple comparisons, $(1 - 2q[\alpha/2q])$ is the probability that $\Delta\mu_{ij}$ will be found within $\pm C_{\Delta\mu_{ij}}$ in cases where ΔA_{ij} is found within $\pm C_{\Delta\mu_{ij}}$. Differences

between means are considered significant if $p_{Bonf} < \alpha$.

The independent variable on which the deterministic component of $A_{i,h}$ depends

A generic parameter, P, is henceforth treated as the sole independent variable on which, for the results under consideration, the deterministic component, $\mu + \Delta\mu_i$, of each observation, $A_{i,h}$ (Equation 86), depends. The value of P that corresponds to treatment group i is denoted as P_i. As such, P_i is the value of P that defines treatment group i.

Confidence intervals about μ_i, based on the standard error of the mean

The standard error of the mean is

$$e_{\mu_i} = (e_{MSw}[1/n_i])^{0.5},$$

(97)

where n_i is the number of replicates in the group for which μ_i is the mean. Using e_{μ_i}, a $(1 - \alpha)100\%$ confidence interval about each μ_i can be defined as $\pm C_{\mu_i} = \mu_i \pm \delta_i$, with the error in μ_i given by

$$\delta_i = e_{\mu_i} t([\alpha/2], [N_{tot} - g]).$$

(98)

At $[N_{tot} - g]$ degrees of freedom, the integral of Student's t-distribution function from $-t([\alpha/2],[N_{tot} - g])$ to $t([\alpha/2],[N_{tot} - g])$ is equal to $(1 - 2[\alpha/2])$,which can be viewed as the probability that μ_i will be found within $\pm C_{\mu_i}$ in cases where A_i is found within $\pm C_{\mu_i}$.

On graphs of μ_i and $\pm C_{\mu_i}$ versus the parameter, P_i, by which treatment groups are defined, an

overlap in the confidence intervals for different values of P_i would indicate a failure of the e_{μ_i}-based (1 - α)100% confidence level test. However, the Bonferroni adjusted t-test may fail to show a significant difference between two means, μ_a and μ_b, where, for $\mu_a < \mu_b$, the comparable confidence intervals, $+C_{\mu_a}$ and $-C_{\mu_b}$, do not overlap. Alternatively, in some cases, the Bonferroni adjusted t-test may show that there is a significant difference between two means, μ_a and μ_b, where, for $\mu_a < \mu_b$, the comparable confidence intervals, $+C_{\mu_a}$ and $-C_{\mu_b}$, do overlap. To graphically present the results of the Bonferroni adjusted t-tests, a $e_{\Delta\mu_{ij}}$-based (1 - α)100% confidence level test must be used.

Confidence intervals about μ_i, based on the standard errors of the mean difference

A $e_{\Delta\mu_{ij}}$-based (1 - α)100% confidence interval about each μ_i can be defined as

$$\pm C_{\mu_{ij}} = \mu_i \pm \delta_{ij},$$

(99)

with the error in μ_i given by

$$\delta_{ij} = \frac{e_{\Delta\mu_{ij}} t([\alpha/2q], [N_{tot} - g])}{2}.$$

(100)

By this approach, on graphs of μ_i and $\pm C_{\mu_{ij}}$ versus P_i, the parameter by which treatment groups are defined, an overlap in the confidence intervals for different values of P_i would indicate a failure of both the $e_{\Delta\mu_{ij}}$-based (1 - α)100% confidence level test and the corresponding Bonferroni-adjusted t-test, while the absence of an overlap would indicate that neither the test based on the standard error of the mean (Equations 97 and 98) nor the Bonferroni-adjusted t-test had failed. Such tests are most likely to fail in pair-wise comparisons of means that are most

alike. In some cases, the means that are most alike will be those from treatment groups that are most alike with respect to the independent variable, P_i. If P_i monotonically decreases as i increases, or if P_i monotonically increases as i increases, P_i will be most alike to $P_{[i-1]}$ or $P_{[i+1]}$. (For P_i monotonically decreasing as i increases, $P_1 > P_2 > \ldots P_{[i-1]} > P_i > P_{[i+1]\ldots} > P_{[g-1]} > P_g$. For P_i monotonically increasing as i increases, $P_1 < P_2 < \ldots P_{[i-1]} < P_i < P_{[i+1]\ldots} < P_{[g-1]} < P_g$.)

For P_i monotonically decreasing as i increases, or for P_i monotonically increasing as i increases, if it is also true that μ_i monotonically increases as i increases, so that $\mu_1 < \mu_2 < \ldots \mu_{[i-1]} < \mu_i < \mu_{[i+1]} \ldots < \mu_{[g-1]} < \mu_g$, then graphs are constructed using $-C_{\mu_{i[i-1]}}$ and $+C_{\mu_{i[i+1]}}$ for the lower bound and upper bound, respectively, of the confidence interval about μ_i with two exceptions within $1 \leq i \leq g$: $-C_{\mu_{1,g}}$ is used for the lower bound of the confidence interval about μ_1; and $+C_{\mu_{g,1}}$ is used for the upper bound of the confidence interval about μ_g.

For P_i monotonically decreasing as i increases, or for P_i monotonically increasing as i increases, if it is also true that μ_i monotonically decreases as i increases, so that $\mu_1 > \mu_2 > \ldots \mu_{[i-1]} > \mu_i > \mu_{[i+1]} \ldots > \mu_{[g-1]} > \mu_g$, then graphs are constructed using $-C_{\mu_{i[i+1]}}$ and $+C_{\mu_{i[i-1]}}$ for the lower bound and upper bound, respectively, of the confidence interval about μ_i with two exceptions within $1 \leq i \leq g$: $+C_{\mu_{1,g}}$ is used for the upper bound of the confidence interval about μ_1; and $-C_{\mu_{g,1}}$ is used for the lower bound of the confidence interval about μ_g.

Where μ_i neither monotonically increases nor monotonically decreases as P_i increases, the lower and upper bounds of the confidence interval about μ_i must be constructed on a more localised basis. For example, within $1 < i < g$, the confidence interval about the mean, μ_i, can be expressed

as either $-C_{\mu_{P,P-}} < \mu_P < +C_{\mu_{P,P+}}$ or $-C_{\mu_{P,P+}} < \mu_P < +C_{\mu_{P,P-}}$, in which the index i is replaced by P, such that $P_{[i\mp1]} = P\text{-} < P = P_i < P\text{+} = P_{[i\pm1]}$, where P is assumed to monotonically increase or decrease with i. At $P_{[i\mp1]} = P\text{-}$, $\mu_{[i\mp1]} = \mu_{P-}$. At $P = P_i$, $\mu_i = \mu_P$. At $P_{[i\pm1]} = P\text{+}$, $\mu_{[i\pm1]} = \mu_{P+}$. For $\mu_{P-} > \mu_P > \mu_{P+}$, $-C_{\mu_{i[i\mp1]}} = -C_{\mu_{P,P+}}$ and $+C_{\mu_{i[i\pm1]}} = +C_{\mu_{P,P-}}$. For $\mu_{P-} < \mu_P < \mu_{P+}$, $-C_{\mu_{i[i\mp1]}} = -C_{\mu_{P,P-}}$ and $+C_{\mu_{i[i\pm1]}} = +C_{\mu_{P,P+}}$. Of the four other possible inequalities relating μ_{P-}, μ_P and μ_{P+}, the nearest value to μ_P determines the confidence interval about μ_P. For either $\mu_{P+} > \mu_{P-} > \mu_P$ or $\mu_P < \mu_{P+} < \mu_{P-}$, $-C_{\mu_{P,P-}}$ and $+C_{\mu_{P,P+}}$. For either $\mu_{P-} > \mu_{P+} > \mu_P$ or $\mu_P < \mu_{P-} < \mu_{P+}$, $-C_{\mu_{P,P+}}$ and $+C_{\mu_{P,P-}}$. It is assumed that P_1 and P_g are the extrema of P at which special cases arise, as there is no P- relative to the minimum value of P, and there is no P+ relative to the maximum value of P. As such, for the lowest value of P at which data exist, P- is equated to the highest value of P at which data exist. Similarly, for the highest value of P at which data exist, P+ is equated to the lowest value of P at which data exist.

Statistical analysis of AUC simulation results for any given time of analysis, t_ϵ

At each time of analysis, the Bonferroni adjusted t-test (2-tailed) is used to place confidence intervals about the mean value of the observations in each treatment group. Tables 24 to 27 present the observations, the mean value and the expectation value for each treatment group at each time of analysis. As a significance level of $\alpha = 0.05$ is applied in all analyses, a $(1 - \alpha)100\% = 95\%$ confidence interval about each mean difference, $\Delta\mu_{ij}$ (Equation 96), and about each mean, μ_i (Equation 99), is obtained. These confidence intervals constitute the comparative statistics by which the significance of the difference between any two mean values is judged.

The notation of the section on statistical analysis (Equations 84 to 100) can be equated, or at least related, to the parameters previously defined to describe the results of AUC simulation for the various treatment groups. At time t_ϵ, both $A_{i,h}$ and (Equation 86) $s^*_{i,h,\epsilon}$ (Equation 81a) denote the observation for replicate h of treatment group i. At time t_ϵ, then,

$$A_{i,h} \equiv s^*_{i,h,\epsilon},$$

(101)

the values of which are tabulated for each treatment group, i, at time, t_ϵ (Tables 24 to 27). Likewise, at time t_ϵ, both μ_i (Equation 85) and $\langle s^*_{i,\epsilon} \rangle$ (Equation 82) denote the within-group mean value for treatment group i. Thus, at time t_ϵ,

$$\mu_i \equiv \langle s^*_{i,\epsilon} \rangle,$$

(102)

the value of which is tabulated for each treatment group, i, at time, t_ϵ (Tables 24 to 27).

The generic parameter, P, was previously defined as the sole independent variable on which, for the results under consideration, the deterministic component, $\mu + \Delta\mu_i$, of each observation, $A_{i,h}$ (Equation 86), depends. Just prior to the description of the various confidence intervals (Equations 96 to 100), the value of P that corresponds to treatment group i was denoted as P_i. Applying such notation to the systems originally described as dependent on $\%K_A > 0$, and choosing a normalised scale for the alternate independent variable, yields the dimensionless

$$P = \frac{\%K_A > 0}{100\%}.$$

(103a)

Table 28 shows the interrelationships between P_i, i and $\%K_A > 0$, which can be summarised as

$$P_i = \frac{(\%K_A > 0)_i}{100\%},$$

(103b)

where $(\%K_A > 0)_i$ is the $\%K_A > 0$ that defines treatment group i (Tables 17 and 28). Likewise, P_i is the value of P that defines treatment group i (Tables 17 and 28). Thus, $(\%K_A > 0)_i$ and P_i are alternative parameters by which to define each treatment group.

Just prior to Equation 96, which describes the (1 - α)100% confidence interval about each $\Delta\mu_{ij}$, A_i was defined as the true value that must underlie each observation, $A_{i,h}$, within treatment group i. In Equations 104 and 105, which follow next, A_i is redefined as the expectation value of the observations within treatment group i. The two definitions are mutually compatible, however, in that, for treatment group i, A_i is always the expectation value, and A_i is also the true value if Equation 86 holds. Where A_i satisfies both definitions, at time t_ϵ, A_i is equal to the known expectation value, $s^*_{i,\epsilon}$, as $s^*_{i,\epsilon}$, by virtue of being determined from noise-free data, is the true value that underlies each observation, $A_{i,h}$, within treatment group i at time t_ϵ.

At a given time, t_ϵ, in the limit as the number of replicates, n_i and each $n_{j\neq i}$, in all treatment groups, i and each $j \neq i$, approaches infinity, the deterministic component, $\mu + \Delta\mu_i$, of each observation, $A_{i,h}$ (Equation 86), of treatment group i, should approach the expectation value, A_i, of treatment group i. Thus, at a given time, t_ϵ,

$$\lim_{\substack{n_i\to\infty \\ and\ each \\ n_{j\neq i}\to\infty}} (\mu + \Delta\mu_i) = A_i.$$

(104a)

Additionally, if the data strictly conform to the model described by Equation 86, then at time t_ϵ, A_i is also the true value that underlies each observation, $A_{i,h}$, within treatment group i, in which case,

$$A_i \equiv s^*_{i,\epsilon},$$

(104b)

where $s^*_{i,\epsilon}$ (Equation 81b) is both the true value and the known expectation value of treatment group i at time t_ϵ (Tables 24 to 27).

Where $A_i \neq s^*_{i,\epsilon}$, A_i nevertheless remains the deterministic expectation value obtained when $\mu + \Delta\mu_i$ is subjected to the limit applied in Equation 104a, and as such, A_i simply differs from $s^*_{i,\epsilon}$ by an offset arising from the presence of noise of a sort that is not included in the model represented by Equation 86. Thus, the wholly deterministic analogue of Equation 86 is given by

$$A_i = A + \Delta A_i = \left(\frac{1}{g}\sum_{i=1}^{g} A_i\right) + \Delta A_i,$$

(105a)

where A_i (Equation 104a) is the expectation value of treatment group i, A is the grand mean of the expectation values of all treatment groups, and ΔA_i is the deviation of A_i from A, such that $\Delta A_i = A_i - A$. Consequently,

$$\sum_{i=1}^{g} \Delta A_i = \sum_{i=1}^{g} (A_i - A) = \left(\sum_{i=1}^{g} A_i\right) - gA = 0.$$

(105b)

At two of the three times analysed, μ_i changes more desultorily than monotonically as P_i increases. Thus, at each time of analysis, t_ϵ, μ_i is sometimes expressed as μ_P, and the $e_{\Delta\mu_{ij}}$-based $(1 - \alpha)100\%$ confidence interval about μ_i is sometimes expressed as either $-C_{\mu_{P,P-}} < \mu_P < +C_{\mu_{P,P+}}$ or $-C_{\mu_{P,P+}} < \mu_P < +C_{\mu_{P,P-}}$. A detailed description of this notation, in which the index i is replaced by P, is given at the end of the section describing the $e_{\Delta\mu_{ij}}$-based $(1 - \alpha)100\%$ confidence interval about μ_i (Equation 99). In general, any parameter indexed by i can be indexed by the

corresponding value of $P = P_i$, which is shown as a function of i in Table 28. For example, in the legends of figures that show $-C_{\mu_{P,P-}} < \mu_P < +C_{\mu_{P,P+}}$ or $-C_{\mu_{P,P+}} < \mu_P < +C_{\mu_{P,P-}}$, the expectation value is equated to $s^*_{i,\epsilon}$ and is expressed as $s^*_{P,\epsilon}$, where $s^*_{P,\epsilon} = s^*_{i,\epsilon}$ (Equation 81b) at $P = P_i$. Likewise, if Equation 86 held, $s^*_{P,\epsilon}$ would be equal to A_P, where $A_P = A_i$ (Equations 104 and 105) at $P = P_i$.

In addition to the comparative statistics, descriptive statistics are presented for each treatment group at each time. Among the descriptive statistics presented, all but the standard deviation of the replicate observations about their mean have been described already. Within each treatment group, i, at each time, t_ϵ, the n_i (Table 28) replicate observations, of which $A_{i,h} = s^*_{i,h,\epsilon}$ is that of replicate h, are distributed about their mean value, $\mu_i = \langle s^*_{i,\epsilon} \rangle$, with a standard deviation of

$$\sigma_i = \left\{ \frac{1}{n_i - 1} \left[\sum_{h=1}^{n_i} \left(A_{i,h} - \mu_i \right)^2 \right] \right\}^{0.5} . \quad (106)$$

Common statistical parameters

Tables 28 and 29 show parameters that apply to all times of analysis. Table 28 lists the value of P_i (Equation 103) for each treatment group, i. Table 29 lists commonly applied statistical parameters and their values, all of which are dimensionless.

i	$(\%K_A > 0)_i$	P_i	n_i
1	100	1.00	$n_1 = 9$

2	99	0.99	$n_2 = 9$
3	50	0.50	$n_3 = 3$
4	0	0.00	$n_4 = 3$

Table 28. Parameters that apply to all times analysed, where all but $(\%K_A > 0)_i$ are dimensionless. The calculation of P_i from $(\%K_A > 0)_i$ is given by Equation 103.

statistic	notation	value
total population (of all replicates)	N_{tot}	24
number of treatment groups	g	4
degrees of freedom of error	$[N_{tot} - g]$	20
degrees of freedom of treatment	$[g - 1]$	3
pair-wise between-group comparisons	q	6
significance level	α	0.05
Bonferroni-adjusted significance level	$[\alpha/2q]$	4.16667E--3
upper critical value of Student's t-distribution	$t([\alpha/2q],[N_{tot} - g])$	2.92712

Table 29. Dimensionless statistical parameters that apply at all times analysed. The total population is given by Equation 84. The upper critical value of Student's t-distribution at $[N_{tot} - g]$ degrees of freedom and a Bonferroni-adjusted significance level of $[\alpha/2q]$ for a two-sided test is $t([\alpha/2q],[N_{tot} - g])$, which is applied first to the $(1 - \alpha)100\%$ confidence interval about each $\Delta\mu_{ij}$ in Equation 96, and is applied later to the $e_{\Delta\mu_{ij}}$-based $(1 - \alpha)100\%$ confidence interval about μ_i in Equations 99 and 100.

Statistical analysis of AUC simulation results for t_{36}

The statistical analysis of the data for t_{36} in Tables 24 to 27 yielded the results presented in Tables 30 to 33. Table 30 collects statistical parameters that apply to all treatment groups at $t_\epsilon = t_{36}$. Table 31 lists descriptive statistical parameters that apply to each treatment group at $t_\epsilon = t_{36}$. Table 32 lists the comparative statistical parameters that apply to the (1 - α)100% confidence interval about each pair-wise mean difference, $\Delta\mu_{ij}$ (Equation 96), between treatment groups at $t_\epsilon = t_{36}$. Table 33 lists the comparative statistical parameters that constitute the $e_{\Delta\mu_{ij}}$-based (1 - α)100% confidence interval about the mean, μ_i, of each treatment group at $t_\epsilon = t_{36}$. Figure 48 shows, as a function of P, the $e_{\Delta\mu_{ij}}$-based (1 - α)100% confidence interval about the mean, either as $-C_{\mu_{P,P-}} < \mu_P < +C_{\mu_{P,P+}}$ or $-C_{\mu_{P,P+}} < \mu_P < +C_{\mu_{P,P-}}$ (Table 33), along with the known expectation value, $s^*_{P,\epsilon}$ (Equation 81b), at $t_\epsilon = t_{36}$. Where Equation 86 holds, A_P (Equations 104 and 105) is identical to $s^*_{P,\epsilon}$ at $t_\epsilon = t_{36}$.

Table 32 gives the value of the Bonferroni adjusted t-test (2-tailed), p_{Bonf}, for each pair-wise mean difference, $\Delta\mu_{ij}$ at $t_\epsilon = t_{36}$. Less than (1 - α)100% confidence is accorded to the difference between any two means for which the comparison yields $p_{Bonf} > \alpha$, and by this measure, with $\alpha = 0.05$, $\mu_{P=1.00}$ (identical to $\mu_{i=1}$) and $\mu_{P=0.99}$ (identical to $\mu_{i=2}$) are considered indistinguishable, as their comparison yields $p_{Bonf} = q(p_{LSD}) = 6(0.59182) > 1$. Likewise, in Table 33 and in Figure 48, less than (1 - α)100% confidence is accorded to the difference between any two means with overlapping confidence intervals, and by this measure as well, $\mu_{P=1.00}$ (identical to $\mu_{i=1}$) and $\mu_{P=0.99}$ (identical to $\mu_{i=2}$) are considered indistinguishable.

Equation	statistic		value
87	raw sum	A_{tot}	2.07179E-12 s
88	raw sum of squares	A_{sq}	1.94131E-25 s^2

89	mean of the raw sum squared	μ_{sq}	1.78846E-25 s^2
90	correction term of the mean	μ_{corr}	1.94125E-25 s^2
91	mean square error within groups	e_{MSw}	2.81014E-31 s^2
92	mean of the sum of squares of treatments	T_{MSb}	5.09288E-27 s^2

Table 30. Statistical parameters that apply to treatment groups 1 to 4 at $t_\epsilon = t_{36}$ only. The ratio of two of these statistics, T_{MSb} and e_{MSw}, yield $F = T_{MSb}/e_{MSw} = 18{,}123$. The results in this table are calculated using the replicate observations for t_{36}, which are the sets of all $A_{i,h} \equiv s^*_{i,h,36}$ given in Tables 24 to 27.

treatment group	$\%K_A > 0$	replicates	mean (Svedberg)	standard deviation (Svedberg)	e_{μ_i}-based (1 - α)100% confidence interval (Svedberg)	
i	$(P_i)100\%$	n_i	$\mu_i = \langle s^*_{i,\epsilon} \rangle$	σ_i	$-C_{\mu_i}$	$+C_{\mu_i}$
1	100	9	1.00165	5.29334E-3	9.96473E-1	1.00682
2	99	9	1.00301	3.64291E-3	9.97835E-1	1.00818
3	50	3	5.96079E-1	9.98079E-3	5.87121E-1	6.05038E-1
4	0	3	2.95930E-1	4.02948E-3	2.86971E-1	3.04888E-1

Table 31. The descriptive statistics, μ_i, σ_i and, with $\alpha = 0.05$ (Equation 98), the 95% confidence interval about μ_i, $\pm C_{\mu_i}$, determined using the standard error of the mean, e_{μ_i} (Equation 97). In turn, the standard error of the mean was determined using e_{MSw} (Table 30). Each statistic in this table applies to just one treatment group at $t_\epsilon = t_{36}$ only.

P_i	n_i	P_j	n_j	$\Delta\mu_{ij} = \mu_i - \mu_j$ (Svedberg)	$e_{\Delta\mu_{ij}}$ (Svedberg)	$-C_{\Delta\mu_{ij}}$ (Svedberg)	$+C_{\Delta\mu_{ij}}$ (Svedberg)	p_{Bonf}

1.00	9	0.99	9	-1.36176E-3	2.49895E-3	-8.67649E-3	5.95296E-3	> 1
1.00	9	0.50	3	4.05566E-1	3.53405E-3	3.95221E-1	4.15911E-1	< 1E-6
1.00	9	0.00	3	7.05716E-1	3.53405E-3	6.95371E-1	7.16060E-1	< 1E-6
0.99	9	0.50	3	4.06928E-1	3.53405E-3	3.96583E-1	4.17272E-1	< 1E-6
0.99	9	0.00	3	7.07077E-1	3.53405E-3	6.96733E-1	7.17422E-1	< 1E-6
0.50	3	0.00	3	3.00150E-1	4.32831E-3	2.87480E-1	3.12819E-1	< 1E-6

Table 32. Comparative statistical parameters. Each statistic applies to just one pair-wise comparison between two treatment groups at $t_\epsilon = t_{36}$ only. Equation 95 gives the critical value, $t\left(\left[n_i - 1\right], \left[n_j - 1\right]\right) = \frac{\Delta\mu_{ij}}{e_{\Delta\mu_{ij}}}$, for each pair-wise comparison. The probability obtained from the Bonferroni adjusted *t*-test (2-tailed) is p_{Bonf}. Less than (1 - α)100% confidence is accorded to the difference between any two means for which the comparison yields $p_{Bonf} > \alpha$. The difference between $\mu_{P=1.00}$ (identical to $\mu_{i=1}$) and $\mu_{P=0.99}$ (identical to $\mu_{i=2}$) yields $p_{Bonf} = q(p_{LSD}) = 6(0.59182)$, which is tabulated as $p_{Bonf} > 1$, as no real probability can exceed 1, and it is only by virtue of p_{LSD} being greater than $1/q$ that $p_{Bonf} = q(p_{LSD}) > 1$. Values of p_{Bonf} that lie below 1 – $p(-5\sigma, 5\sigma) \simeq$ 1E-6 (Figure 2; Equation 26) are tabulated as $p_{Bonf} <$ 1E-6.

i	$P = P_i$	$+C_{\mu_{P,P-}} = +C_{\mu_{i,j}}$	$-C_{\mu_{P,P+}} = -C_{\mu_{i,j}}$		i	$P = P_i$	$-C_{\mu_{P,P-}} = -C_{\mu_{i,j}}$	$+C_{\mu_{P,P+}} = +C_{\mu_{i,j}}$
1	1.00	$+C_{\mu_{i=1,j=2}}$	$-C_{\mu_{i=1,j=4}}$		1	1.00		
2	0.99	$+C_{\mu_{i=2,j=3}}$	$-C_{\mu_{i=2,j=1}}$		2	0.99		
3	0.50				3	0.50	$-C_{\mu_{i=3,j=4}}$	$+C_{\mu_{i=3,j=2}}$
4	0.00				4	0.00	$-C_{\mu_{i=4,j=1}}$	$+C_{\mu_{i=4,j=3}}$

Table 33a. For $t_\epsilon = t_{36}$, the identities of the $e_{\Delta\mu_{ij}}$-based (1 - α)100% confidence interval about μ_i, which are expressed as either $-C_{\mu_{P,P-}} < \mu_P < +C_{\mu_{P,P+}}$ or $-C_{\mu_{P,P+}} < \mu_P < +C_{\mu_{P,P-}}$, that are shown in

Figure 48.

i	$P = P_i$	$+C_{\mu_{P,P-}}$ (s)	$-C_{\mu_{P,P+}}$ (s)		i	$P = P_i$	$-C_{\mu_{P,P-}}$ (s)	$+C_{\mu_{P,P+}}$ (s)
1	1.00	1.00530E-13	9.96473E-14		1	1.00		
2	0.99	1.00818E-13	9.99350E-14		2	0.99		
3	0.50				3	0.50	5.89745E-14	6.01252E-14
4	0.00				4	0.00	2.90757E-14	3.02264E-14

Table 33b. For $t_\epsilon = t_{36}$, selected values of the $e_{\Delta\mu_{ij}}$-based (1 - α)100% confidence interval about μ_i, which are expressed as either $-C_{\mu_{P,P-}} < \mu_P < +C_{\mu_{P,P+}}$ or $-C_{\mu_{P,P+}} < \mu_P < +C_{\mu_{P,P-}}$. These are the confidence intervals presented graphically in Figure 48. Less than (1 - α)100% confidence is accorded to the difference between any two means with overlapping confidence intervals. By this measure, $\mu_{P=1.00}$ (identical to $\mu_{i=1}$) and $\mu_{P=0.99}$ (identical to $\mu_{i=2}$) are considered indistinguishable.

j and n_j apply to $-C_{\mu_{ij}}$			i and n_i apply to both $-C_{\mu_{ij}}$ and $+C_{\mu_{ij}}$					j and n_j apply to $+C_{\mu_{ij}}$	
j	n_j	$-C_{\mu_{ij}}$ (s)	μ_i (s)	i	P_i	n_i	$s^*_{i,\epsilon}$ (s)	$+C_{\mu_{ij}}$ (s)	j	n_j
4	3	9.96473E-14	1.00165E-13	1	1.00	9	1.03097E-13	1.00530E-13	2	9
1	9	9.99350E-14	1.00301E-13	2	0.99	9	1.03727E-13	1.00818E-13	3	3
4	3	5.89745E-14	5.96079E-14	3	0.50	3	6.22135E-14	6.01252E-14	2	9
1	9	2.90757E-14	2.95930E-14	4	0.00	3	2.81395E-14	3.02264E-14	3	3

Table 33c. For $t_\epsilon = t_{36}$, the known expectation value, $s^*_{i,\epsilon}$; the mean, μ_i; and the $e_{\Delta\mu_{ij}}$-based (1 - α)100% confidence interval about μ_i, $-C_{\mu_{i,j}} < \mu_i < +C_{\mu_{i,j}}$, shown in Figure 48. These parameters are plotted as a function of P in Figure 48. As noted with respect to Equations 104 and 105, the deterministic expectation value, A_i, can only be equated to the known expectation

value, $s^*_{i,\epsilon}$, if Equation 86 holds.

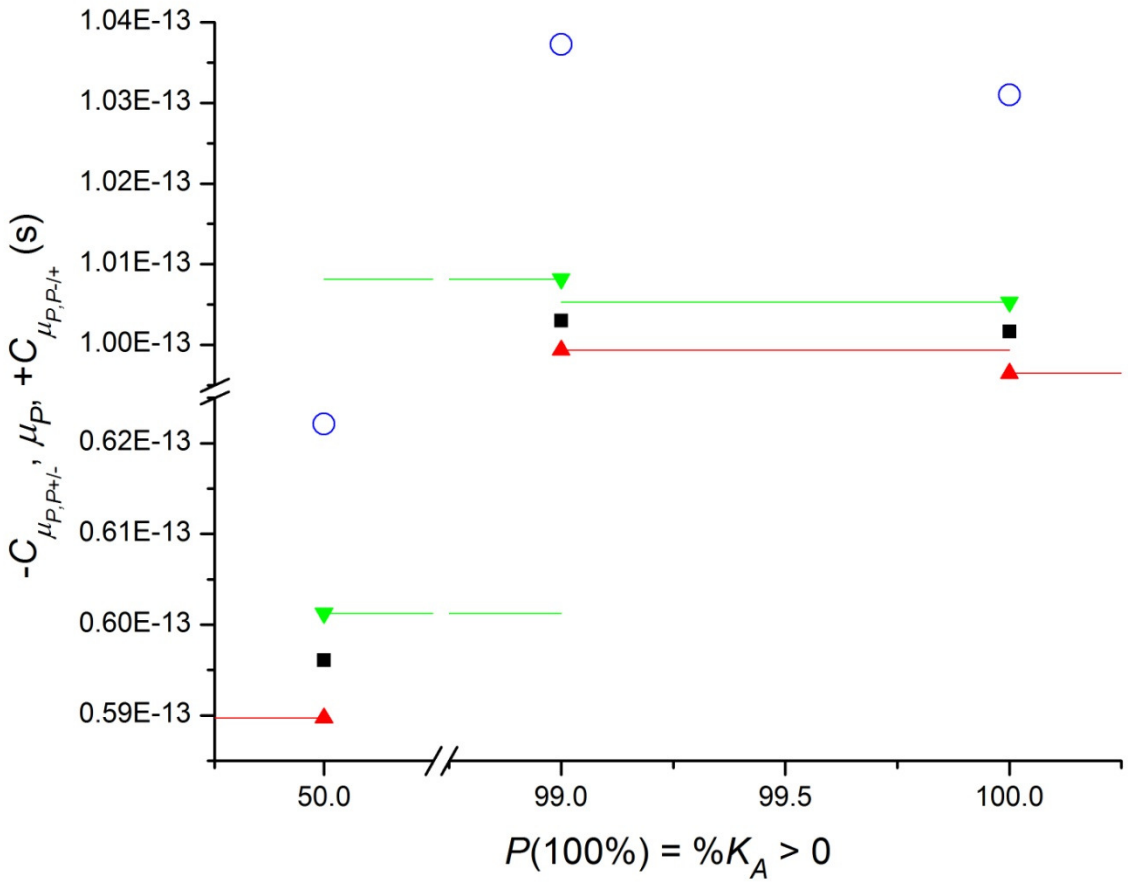

Figure 48a. For $t_\epsilon = t_{36}$, the known expectation value, $s^*_{P,\epsilon}$ (○), and the $e_{\Delta\mu_{ij}}$-based (1 - α)100% confidence interval about μ_P, $-C_{\mu_{P,P-}}$ (—▲) < μ_P (■) < $+C_{\mu_{P,P+}}$ (▼—) or $-C_{\mu_{P,P+}}$ (▲—) < μ_P (■) < $+C_{\mu_{P,P-}}$ (—▼) within $0.50 \leq P \leq 1.00$. Where Equation 86 holds, A_P (Equations 104 and 105) is identical to $s^*_{P,\epsilon}$ (Equation 81b) at $t_\epsilon = t_{36}$. The confidence intervals shown here are tabulated in Table 33. Less than (1 - α)100% confidence is accorded to the difference between any two means with overlapping confidence intervals. By this measure, $\mu_{P=1.00}$ (identical to $\mu_{i=1}$) and $\mu_{P=0.99}$ (identical to $\mu_{i=2}$) are considered indistinguishable.

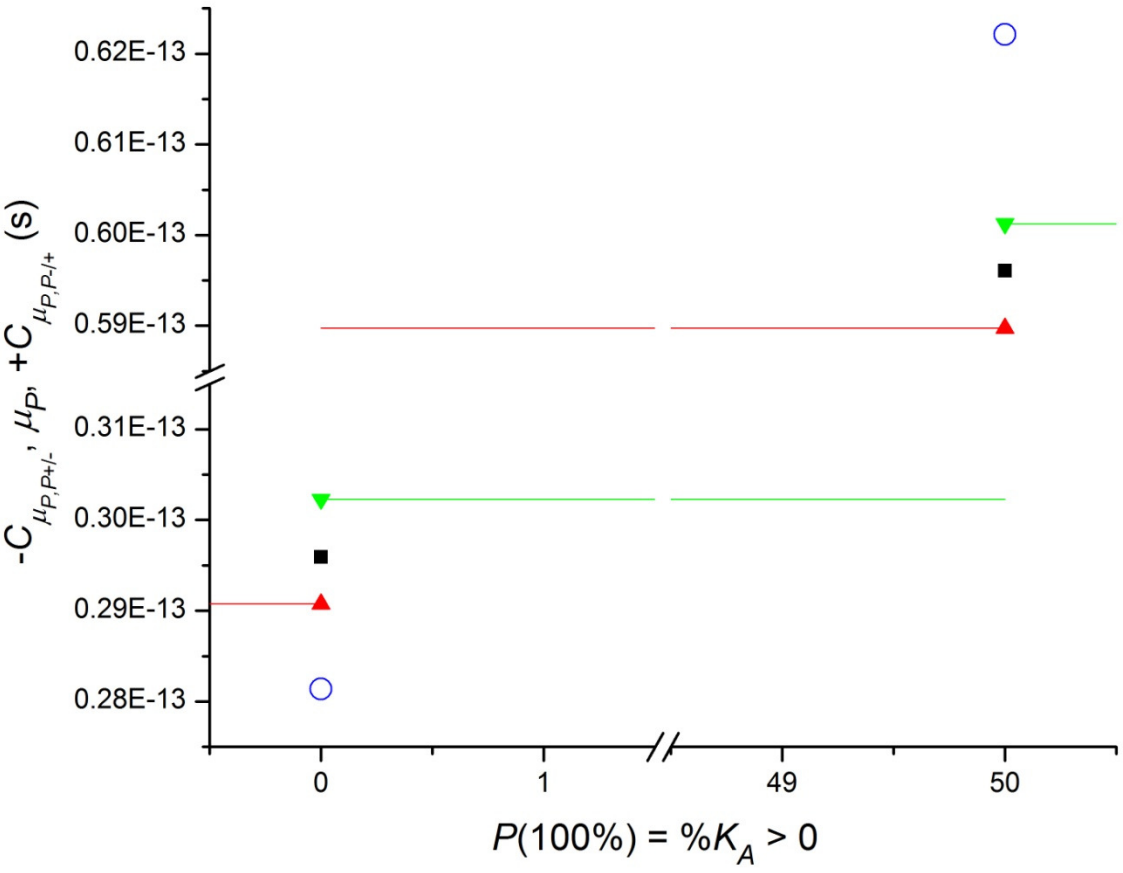

Figure 48b. For $t_\epsilon = t_{36}$, the known expectation value, $s^*_{P,\epsilon}$ (○), and the $e_{\Delta\mu_{ij}}$-based (1 - α)100% confidence interval about μ_P, $-C_{\mu_{P,P-}}$ (—▲) < μ_P (■) < $+C_{\mu_{P,P+}}$ (▼—) or $-C_{\mu_{P,P+}}$ (▲—) < μ_P (■) < $+C_{\mu_{P,P-}}$ (—▼), as a function of P within $0.00 \leq P \leq 0.50$. Where Equation 86 holds, A_P (Equations 104 and 105) is identical to $s^*_{P,\epsilon}$ (Equation 81b) at $t_\epsilon = t_{36}$. The confidence intervals shown here are tabulated in Table 33.

Statistical analysis of AUC simulation results for t_{51}

The statistical analysis of the data for t_{51} in Tables 24 to 27 yielded the results presented in Tables 34 to 37. Table 34 collects statistical parameters that apply to all treatment groups at $t_\epsilon = t_{51}$. Table 35 lists descriptive statistical parameters that apply to each treatment group at $t_\epsilon = t_{51}$. Table 36 lists the comparative statistical parameters that apply to the (1 - α)100% confidence interval about each pair-wise mean difference, $\Delta\mu_{ij}$ (Equation 96), between treatment groups at $t_\epsilon = t_{51}$. Table 37 lists the comparative statistical parameters that constitute the $e_{\Delta\mu_{ij}}$-based (1 - α)100% confidence interval about the mean, μ_i, of each treatment group at $t_\epsilon = t_{51}$. Figure 49 shows, as a function of P, the $e_{\Delta\mu_{ij}}$-based (1 - α)100% confidence interval about the mean, either as $-C_{\mu_{P,P-}} < \mu_P < +C_{\mu_{P,P+}}$ or $-C_{\mu_{P,P+}} < \mu_P < +C_{\mu_{P,P-}}$ (Table 37), along with the known expectation value, $s^*_{P,\epsilon}$ (Equation 81b), at $t_\epsilon = t_{51}$. Where Equation 86 holds, A_P (Equations 104 and 105) is identical to $s^*_{P,\epsilon}$ at $t_\epsilon = t_{51}$.

Table 36 gives the value of the Bonferroni adjusted t-test (2-tailed), p_{Bonf}, for each pair-wise mean difference, $\Delta\mu_{ij}$ at $t_\epsilon = t_{51}$. Less than (1 - α)100% confidence is accorded to the difference between any two means for which the comparison yields $p_{Bonf} > \alpha$, and by this measure, with $\alpha = 0.05$, each mean value, μ_P (identical to μ_i), is considered distinguishable from every other mean value, as each pair-wise comparison yields $p_{Bonf} < \alpha$. Likewise, in Table 37 and in Figure 49, less than (1 - α)100% confidence is accorded to the difference between any two means with overlapping confidence intervals, and by this measure as well, each mean value is considered distinguishable from every other mean value.

Equation	statistic		value
87	raw sum	A_{tot}	-1.93544E-12 s
88	raw sum of squares	A_{sq}	1.70003E-25 s^2

89	mean of the raw sum squared	μ_{sq}	1.56080E-25 s^2
90	correction term of the mean	μ_{corr}	1.69893E-25 s^2
91	mean square error within groups	e_{MSw}	5.47537E-30 s^2
92	mean of the sum of squares of treatments	T_{MSb}	4.60440E-27 s^2

Table 34. Statistical parameters that apply to treatment groups 1 to 4 at $t_\epsilon = t_{51}$ only. The ratio of two of these statistics, T_{MSb} and e_{MSw}, yield $F = T_{MSb}/e_{MSw} = 840.93$. The results in this table are calculated using the replicate observations for t_{51}, which are the sets of all $A_{i,h} \equiv s^*_{i,h,51}$ given in Tables 24 to 27.

treatment group	$\%K_A > 0$	replicates	mean (Svedberg)	standard deviation (Svedberg)	e_{μ_i}-based (1 - α)100% confidence interval (Svedberg)	
i	$(P_i)100\%$	n_i	$\mu_i = \langle s^*_{i,\epsilon} \rangle$	σ_i	$-C_{\mu_i}$	$+C_{\mu_i}$
1	100	9	-6.42474E-1	1.05574E-2	-6.65306E-1	-6.19643E-1
2	99	9	-6.95688E-1	2.16304E-2	-7.18519E-1	-6.72857E-1
3	50	3	-1.17713	2.20316E-2	-1.21667	-1.13758
4	0	3	-1.25985	5.16977E-2	-1.29939	-1.22030

Table 35. The descriptive statistics, μ_i, σ_i and, with $\alpha = 0.05$ (Equation 98), the 95% confidence interval about μ_i, $\pm C_{\mu_i}$, determined using the standard error of the mean, e_{μ_i} (Equation 97). In turn, the standard error of the mean was determined using e_{MSw} (Table 34). Each statistic in this table applies to just one treatment group at $t_\epsilon = t_{51}$ only.

P_i	n_i	P_j	n_j	$\Delta\mu_{ij} = \mu_i - \mu_j$ (Svedberg)	$e_{\Delta\mu_{ij}}$ (Svedberg)	$-C_{\Delta\mu_{ij}}$ (Svedberg)	$+C_{\Delta\mu_{ij}}$ (Svedberg)	p_{Bonf}

1.00	9	0.99	9	5.32139E-2	1.10306E-2	2.09259E-2	8.55019E-2	6.18454E-4
1.00	9	0.50	3	5.34655E-1	1.55997E-2	4.88993E-1	5.80317E-1	< 1E-6
1.00	9	0.00	3	6.17372E-1	1.55997E-2	5.71710E-1	6.63034E-1	< 1E-6
0.99	9	0.50	3	4.81441E-1	1.55997E-2	4.35779E-1	5.27103E-1	< 1E-6
0.99	9	0.00	3	5.64158E-1	1.55997E-2	5.18496E-1	6.09820E-1	< 1E-6
0.50	3	0.00	3	8.27170E-2	1.91056E-2	2.67926E-2	1.38641E-1	1.95399E-3

Table 36. Comparative statistical parameters. Each statistic applies to just one pair-wise comparison between two treatment groups at $t_\epsilon = t_{51}$ only. Equation 95 gives the critical value, $t\left(\left[n_i - 1\right], \left[n_j - 1\right]\right) = \frac{\Delta\mu_{ij}}{e_{\Delta\mu_{ij}}}$, for each pair-wise comparison. The probability obtained from the Bonferroni adjusted *t*-test (2-tailed) is p_{Bonf}. Less than (1 - α)100% confidence is accorded to the difference between any two means for which the comparison yields $p_{Bonf} > \alpha$. Values of p_{Bonf} that lie below 1 – $p(-5\sigma, 5\sigma) \simeq$ 1E-6 (Figure 2; Equation 26) are tabulated as $p_{Bonf} <$ 1E-6.

i	$P = P_i$	$+C_{\mu_{P,P-}} = +C_{\mu_{i,j}}$	$-C_{\mu_{P,P+}} = -C_{\mu_{i,j}}$		i	$P = P_i$	$-C_{\mu_{P,P-}} = -C_{\mu_{i,j}}$	$+C_{\mu_{P,P+}} = +C_{\mu_{i,j}}$
1	1.00				1	1.00	$-C_{\mu_{i=1,j=2}}$	$+C_{\mu_{i=1,j=4}}$
2	0.99				2	0.99	$-C_{\mu_{i=2,j=3}}$	$+C_{\mu_{i=2,j=1}}$
3	0.50				3	0.50	$-C_{\mu_{i=3,j=4}}$	$+C_{\mu_{i=3,j=2}}$
4	0.00				4	0.00	$-C_{\mu_{i=4,j=1}}$	$+C_{\mu_{i=4,j=3}}$

Table 37a. For $t_\epsilon = t_{51}$, the identities of the $e_{\Delta\mu_{ij}}$-based (1 - α)100% confidence interval about μ_i, which are expressed as either $-C_{\mu_{P,P-}} < \mu_P < +C_{\mu_{P,P+}}$ or $-C_{\mu_{P,P+}} < \mu_P < +C_{\mu_{P,P-}}$, that are shown in Figure 49.

i	$P = P_i$	$+C_{\mu_{P,P-}}$ (s)	$-C_{\mu_{P,P+}}$ (s)		i	$P = P_i$	$-C_{\mu_{P,P-}}$ (s)	$+C_{\mu_{P,P+}}$ (s)
1	1.00				1	1.00	-6.58618E-14	-6.19643E-14
2	0.99				2	0.99	-7.18519E-14	-6.79544E-14
3	0.50				3	0.50	-1.20509E-13	-1.15430E-13
4	0.00				4	0.00	-1.28268E-13	-1.23188E-13

Table 37b. For $t_\epsilon = t_{51}$, selected values of the $e_{\Delta\mu_{ij}}$-based (1 - α)100% confidence interval about μ_i, which are expressed as either $-C_{\mu_{P,P-}} < \mu_P < +C_{\mu_{P,P+}}$ or $-C_{\mu_{P,P+}} < \mu_P < +C_{\mu_{P,P-}}$. These are the confidence intervals presented graphically in Figure 49. Less than (1 - α)100% confidence is accorded to the difference between any two means with overlapping confidence intervals.

j and n_j apply to -$C_{\mu_{ij}}$			i and n_i apply to both -$C_{\mu_{ij}}$ and $+C_{\mu_{ij}}$					j and n_j apply to $+C_{\mu_{ij}}$		
j	n_j	-$C_{\mu_{ij}}$ (s)	μ_i (s)	i	P_i	n_i	$s^*_{i,\epsilon}$ (s)	$+C_{\mu_{ij}}$ (s)	j	n_j
2	9	-6.58618E-14	-6.42474E-14	1	1.00	9	-6.51551E-14	-6.19643E-14	4	3
3	3	-7.18519E-14	-6.95688E-14	2	0.99	9	-7.08527E-14	-6.79544E-14	1	9
4	3	-1.20509E-13	-1.17713E-13	3	0.50	3	-1.37829E-13	-1.15430E-13	2	9
1	9	-1.28268E-13	-1.25985E-13	4	0.00	3	-1.78094E-13	-1.23188E-13	3	3

Table 37c. For $t_\epsilon = t_{51}$, the known expectation value, $s^*_{i,\epsilon}$; the mean, μ_i; and the $e_{\Delta\mu_{ij}}$-based (1 - α)100% confidence interval about μ_i, $-C_{\mu_{i,j}} < \mu_i < +C_{\mu_{i,j}}$, shown in Figure 49. These parameters are plotted as a function of P in Figure 49. As noted with respect to Equations 104 and 105, the deterministic expectation value, A_i, can only be equated to the known expectation value, $s^*_{i,\epsilon}$, if Equation 86 holds.

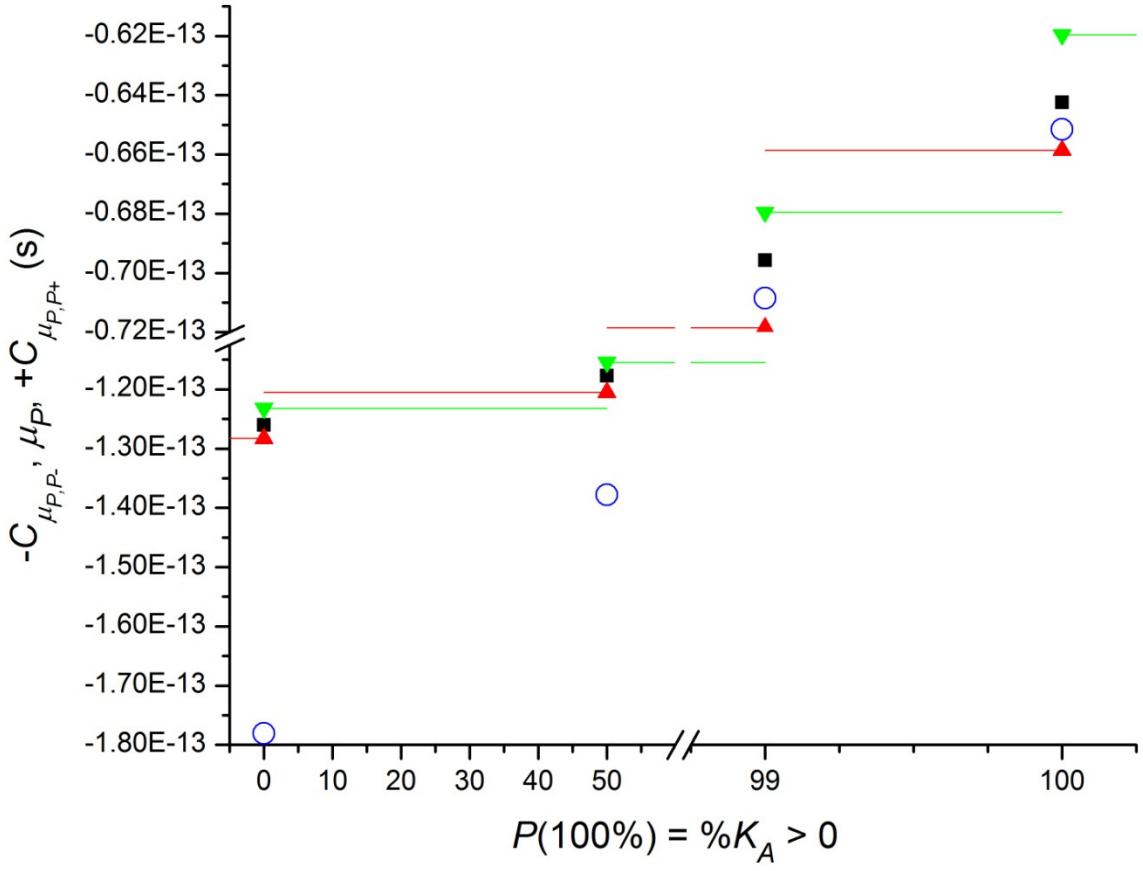

Figure 49. For $t_\epsilon = t_{51}$, the known expectation value, $s^*_{P,\epsilon}$ (○), and the $e_{\Delta\mu_{ij}}$-based (1 - α)100% confidence interval about μ_P, $-C_{\mu_{P,P-}}$ (—▲) < μ_P (■) < $+C_{\mu_{P,P+}}$ (▼—). Where Equation 86 holds, A_P (Equations 104 and 105) is identical to $s^*_{P,\epsilon}$ (Equation 81b) at $t_\epsilon = t_{51}$. The confidence intervals shown here are tabulated in Table 37.

Statistical analysis of AUC simulation results for t_{66}

The statistical analysis of the data for t_{66} in Tables 24 to 27 yielded the results presented in Tables 38 to 41. Table 38 collects statistical parameters that apply to all treatment groups at $t_\epsilon = t_{66}$. Table 39 lists descriptive statistical parameters that apply to each treatment group at $t_\epsilon = t_{66}$.

Table 40 lists the comparative statistical parameters that apply to the (1 - α)100% confidence interval about each pair-wise mean difference, $\Delta\mu_{ij}$ (Equation 96), between treatment groups at $t_\epsilon = t_{66}$. Table 41 lists the comparative statistical parameters that constitute the $e_{\Delta\mu_{ij}}$-based (1 - α)100% confidence interval about the mean, μ_i, of each treatment group at $t_\epsilon = t_{66}$. Figure 50 shows, as a function of P, the $e_{\Delta\mu_{ij}}$-based (1 - α)100% confidence interval about the mean, either as $-C_{\mu_{P,P-}} < \mu_P < +C_{\mu_{P,P+}}$ or $-C_{\mu_{P,P+}} < \mu_P < +C_{\mu_{P,P-}}$ (Table 41), along with the known expectation value, $s^*_{P,\epsilon}$ (Equation 81b), at $t_\epsilon = t_{66}$. Where Equation 86 holds, A_P (Equations 104 and 105) is identical to $s^*_{P,\epsilon}$ at $t_\epsilon = t_{66}$.

Table 40 gives the value of the Bonferroni adjusted t-test (2-tailed), p_{Bonf}, for each pair-wise mean difference, $\Delta\mu_{ij}$ at $t_\epsilon = t_{66}$. Less than (1 - α)100% confidence is accorded to the difference between any two means for which the comparison yields $p_{Bonf} > \alpha$, and by this measure, with $\alpha =$ 0.05, $\mu_{P=0.00}$ (identical to $\mu_{i=4}$) and $\mu_{P=0.50}$ (identical to $\mu_{i=3}$) are considered indistinguishable, as their comparison yields $p_{Bonf} =$ 1.55280E-1. Likewise, in Table 41 and in Figure 50, less than (1 - α)100% confidence is accorded to the difference between any two means with overlapping confidence intervals, and by this measure as well, $\mu_{P=0.00}$ (identical to $\mu_{i=4}$) and $\mu_{P=0.50}$ (identical to $\mu_{i=3}$) are considered indistinguishable.

Equation	statistic		value
87	raw sum	A_{tot}	1.39596E-12 s
88	raw sum of squares	A_{sq}	8.16790E-26 s^2
89	mean of the raw sum squared	μ_{sq}	8.11958E-26 s^2
90	correction term of the mean	μ_{corr}	8.16410E-26 s^2
91	mean square error within groups	e_{MSw}	1.90127E-30 s^2

92	mean of the sum of squares of treatments	T_{MSb}	1.48404E-28 s^2

Table 38. Statistical parameters that apply to treatment groups 1 to 4 at $t_\epsilon = t_{66}$ only. The ratio of two of these statistics, T_{MSb} and e_{MSw}, yield $F = T_{MSb}/e_{MSw} = 78.055$. The results in this table are calculated using the replicate observations for t_{66}, which are the sets of all $A_{i,h} \equiv s^*_{i,h,66}$ given in Tables 24 to 27.

treatment group	$\%K_A > 0$	replicates	mean (Svedberg)	standard deviation (Svedberg)	e_{μ_i}-based (1 - α)100% confidence interval (Svedberg)	
i	$(P_i)100\%$	n_i	$\mu_i = \langle s^*_{i,\epsilon} \rangle$	σ_i	$-C_{\mu_i}$	$+C_{\mu_i}$
1	100	9	5.91476E-1	1.38295E-2	5.78023E-1	6.04930E-1
2	99	9	6.18973E-1	1.41951E-2	6.05519E-1	6.32426E-1
3	50	3	4.97375E-1	6.13183E-3	4.74073E-1	5.20677E-1
4	0	3	5.24471E-1	1.71072E-2	5.01168E-1	5.47773E-1

Table 39. The descriptive statistics, μ_i, σ_i and, with $\alpha = 0.05$ (Equation 98), the 95% confidence interval about μ_i, $\pm C_{\mu_i}$, determined using the standard error of the mean, e_{μ_i} (Equation 97). In turn, the standard error of the mean was determined using e_{MSw} (Table 38). Each statistic in this table applies to just one treatment group at $t_\epsilon = t_{66}$ only.

P_i	n_i	P_j	n_j	$\Delta\mu_{ij} = \mu_i - \mu_j$ (Svedberg)	$e_{\Delta\mu_{ij}}$ (Svedberg)	$-C_{\Delta\mu_{ij}}$ (Svedberg)	$+C_{\Delta\mu_{ij}}$ (Svedberg)	p_{Bonf}
1.00	9	0.99	9	-2.74964E-2	6.50003E-3	-4.65228E-2	-8.47004E-3	2.46370E-3
1.00	9	0.50	3	9.41013E-2	9.19244E-3	6.71939E-2	1.21009E-1	$<$ 1E-6
1.00	9	0.00	3	6.70055E-2	9.19244E-3	4.00981E-2	9.39129E-2	$<$ 1E-6

0.99	9	0.50	3	1.21598E-1	9.19244E-3	9.46903E-2	1.48505E-1	< 1E-6
0.99	9	0.00	3	9.45019E-2	9.19244E-3	6.75946E-2	1.21409E-1	< 1E-6
0.50	3	0.00	3	-2.70958E-2	1.12584E-2	-6.00504E-2	5.85886E-3	1.55280E-1

Table 40. Comparative statistical parameters. Each statistic applies to just one pair-wise comparison between two treatment groups at $t_\epsilon = t_{66}$ only. Equation 95 gives the critical value, $t\left([n_i - 1], [n_j - 1]\right) = \frac{\Delta\mu_{ij}}{e_{\Delta\mu_{ij}}}$, for each pair-wise comparison. The probability obtained from the Bonferroni adjusted *t*-test (2-tailed) is p_{Bonf}. Less than (1 - α)100% confidence is accorded to the difference between any two means for which the comparison yields $p_{Bonf} > \alpha$. Values of p_{Bonf} that lie below 1 – $p(-5\sigma, 5\sigma) \simeq$ 1E-6 (Figure 2; Equation 26) are tabulated as $p_{Bonf} <$ 1E-6. By this measure, $\mu_{P=0.00}$ (identical to $\mu_{i=4}$) and $\mu_{P=0.50}$ (identical to $\mu_{i=3}$) are considered indistinguishable.

i	$P = P_i$	$+C_{\mu_{P,P-}} = +C_{\mu_{i,j}}$	$-C_{\mu_{P,P+}} = -C_{\mu_{i,j}}$		i	$P = P_i$	$-C_{\mu_{P,P-}} = -C_{\mu_{i,j}}$	$+C_{\mu_{P,P+}} = +C_{\mu_{i,j}}$
1	1.00	$+C_{\mu_{i=1,j=2}}$	$-C_{\mu_{i=1,j=4}}$		1	1.00		
2	0.99	$+C_{\mu_{i=2,j=3}}$	$-C_{\mu_{i=2,j=1}}$		2	0.99		
3	0.50	$+C_{\mu_{i=3,j=4}}$	$-C_{\mu_{i=3,j=2}}$		3	0.50		
4	0.00	$+C_{\mu_{i=4,j=1}}$	$-C_{\mu_{i=4,j=3}}$		4	0.00		

Table 41a. For $t_\epsilon = t_{66}$, the identities of the $e_{\Delta\mu_{ij}}$-based (1 - α)100% confidence interval about μ_i, which are expressed as either $-C_{\mu_{P,P-}} < \mu_P < +C_{\mu_{P,P+}}$ or $-C_{\mu_{P,P+}} < \mu_P < +C_{\mu_{P,P-}}$, that are shown in Figure 50.

i	$P = P_i$	$+C_{\mu_{P,P-}}$ (s)	$-C_{\mu_{P,P+}}$ (s)		i	$P = P_i$	$-C_{\mu_{P,P-}}$ (s)	$+C_{\mu_{P,P+}}$ (s)
1	1.00	6.00990E-14	5.78023E-14		1	1.00		

2	0.99	6.32426E-14	6.09460E-14		2	0.99		
3	0.50	5.13852E-14	4.83921E-14		3	0.50		
4	0.00	5.37925E-14	5.07994E-14		4	0.00		

Table 41b. For $t_\epsilon = t_{66}$, selected values of the $e_{\Delta\mu_{ij}}$-based (1 - α)100% confidence interval about μ_i, which are expressed as either $-C_{\mu_{P,P-}} < \mu_P < +C_{\mu_{P,P+}}$ or $-C_{\mu_{P,P+}} < \mu_P < +C_{\mu_{P,P-}}$. These are the confidence intervals presented graphically in Figure 50. Less than (1 - α)100% confidence is accorded to the difference between any two means with overlapping confidence intervals. By this measure, $\mu_{P=0.00}$ (identical to $\mu_{i=4}$) and $\mu_{P=0.50}$ (identical to $\mu_{i=3}$) are considered indistinguishable.

j and n_j apply to $-C_{\mu_{ij}}$			i and n_i apply to both $-C_{\mu_{ij}}$ and $+C_{\mu_{ij}}$					j and n_j apply to $+C_{\mu_{ij}}$		
j	n_j	$-C_{\mu_{ij}}$ (s)	μ_i (s)	i	P_i	n_i	$s^*_{i,\epsilon}$ (s)	$+C_{\mu_{ij}}$ (s)	j	n_j
4	3	5.78023E-14	5.91476E-14	1	1.00	9	5.69770E-14	6.00990E-14	2	9
1	9	6.09460E-14	6.18973E-14	2	0.99	9	5.97635E-14	6.32426E-14	3	3
2	3	4.83921E-14	4.97375E-14	3	0.50	3	4.25702E-14	5.13852E-14	4	3
3	3	5.07994E-14	5.24471E-14	4	0.00	3	3.37342E-14	5.37925E-14	1	9

Table 41c. For $t_\epsilon = t_{66}$, the known expectation value, $s^*_{i,\epsilon}$; the mean, μ_i; and the $e_{\Delta\mu_{ij}}$-based (1 - α)100% confidence interval about μ_i, $-C_{\mu_{i,j}} < \mu_i < +C_{\mu_{i,j}}$, shown in Figure 50. These parameters are plotted as a function of P in Figure 50. As noted with respect to Equations 104 and 105, the deterministic expectation value, A_i, can only be equated to the known expectation value, $s^*_{i,\epsilon}$, if Equation 86 holds.

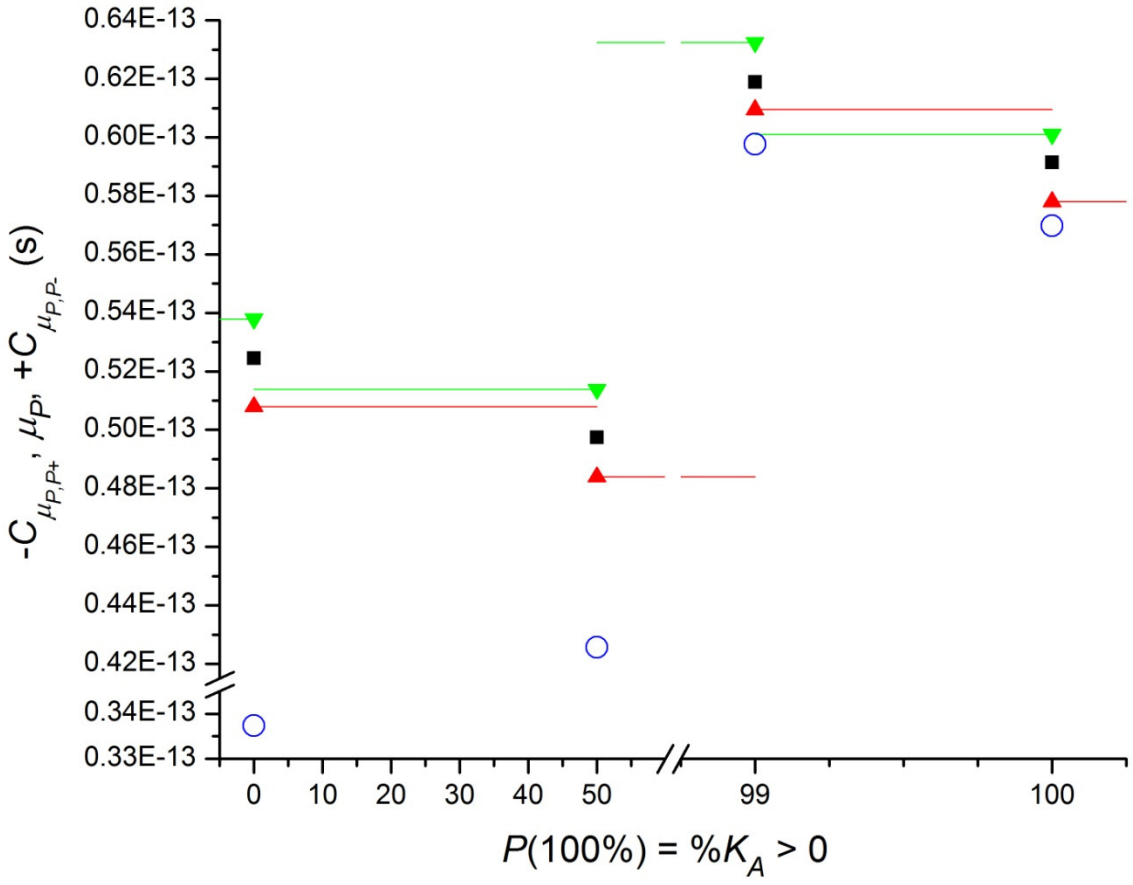

Figure 50. For $t_\epsilon = t_{66}$, the known expectation value, $s^*_{P,\epsilon}$ (○), and the $e_{\Delta\mu_{ij}}$-based (1 - α)100% confidence interval about μ_P, $-C_{\mu_{P,P+}}$ (▲——) < μ_P (■) < $+C_{\mu_{P,P-}}$ (——▼). Where Equation 86 holds, A_P (Equations 104 and 105) is identical to $s^*_{P,\epsilon}$ (Equation 81b) at $t_\epsilon = t_{66}$. The confidence intervals shown here are tabulated in Table 41. Less than (1 - α)100% confidence is accorded to the difference between any two means with overlapping confidence intervals. By this measure, $\mu_{P=0.00}$ (identical to $\mu_{i=4}$) and $\mu_{P=0.50}$ (identical to $\mu_{i=3}$) are considered indistinguishable.

Regarding the statistical analysis of AUC simulation results for t_{36}, t_{51} and t_{66}

An underlying assumption of the statistical analysis just presented was that the observations fit a

model given by $A_{i,h} = \mu + \Delta\mu_i + e_{i,h}$ (Equation 86), where μ is the grand mean, $\Delta\mu_i$ is the deviation of the mean of treatment group i from the grand mean ($\Delta\mu_i = \mu_i - \mu$), and $e_{i,h}$ is the residual that, as the random component of each observation, must be normally distributed (Equation 24) about $\mu + \Delta\mu_i$ with a standard deviation that does not vary from one treatment group to another. In the limit as the number of replicates in each treatment group approaches infinity, the deterministic component, $\mu + \Delta\mu_i$, of each observation should approach the known expectation value, $s^*_{i,\epsilon}$ (Equation 81b), for each treatment group, provided that the data strictly conform to the model described by Equation 86.

Regardless of whether Equation 86 holds, in the limiting case of virtually infinite replicates within each treatment group, the deterministic expectation value, A_i (Equations 104 and 105), can be equated to $\mu + \Delta\mu_i$. Where Equation 86 also holds, A_i at time t_ϵ can be equated to $s^*_{i,\epsilon}$. Doubt is cast on the validity of comparisons between the treatment groups for which A_i at time t_ϵ cannot be equated to $s^*_{i,\epsilon}$. The results (Tables 24 to 27; Tables 33, 37 and 41; Figures 44 to 50) provide evidence of there being systematic noise present in the observations, in which case, $A_{i,h} - (\mu + \Delta\mu_i)$ would not equal $e_{i,h}$ as defined for Equation 86, and A_i at time t_ϵ could not be equated to $s^*_{i,\epsilon}$, although for the two most similar treatment groups, $P_{i=2} = 0.99$ and $P_{i=1} = 1.00$, equating A_i at time t_{51} to $s^*_{i,51}$ would yield values of $A_{P=0.99}$ and $A_{P=1.00}$ that lie within the confidence intervals about the mean for their respective treatment groups, such that $-C_{\mu_{P=0.99,P=0.50}} < A_{P=0.99} < +C_{\mu_{P=0.99,P=1.00}}$, and $-C_{\mu_{P=1.00,P=0.99}} < A_{P=1.00} < +C_{\mu_{P=1.00,P=0.00}}$. Thus, for treatment groups $P_{i=2} = 0.99$ and $P_{i=1} = 1.00$ at time t_{51}, $A_{i,h} - (\mu + \Delta\mu_i)$ values may closely approach $e_{i,h}$ as defined.

Only in the cases of treatment groups $P_{i=2} = 0.99$ and $P_{i=1} = 1.00$ at time t_{51} (Table 37; Figure 49) would equating A_i to $s^*_{i,\epsilon}$ place A_P within the confidence interval about μ_P. Of all the other cases

(Tables 33, 37 and 41; Figures 48 to 50), the next closest are for treatment groups $P_{i=2} = 0.99$ and $P_{i=1} = 1.00$ at time t_{66} (Table 41; Figure 50), in which equating A_i to $s^*_{i,\epsilon}$ place A_P just below the confidence interval about μ_P. By this measure, the comparisons between treatment groups $P_{i=2} = 0.99$ and $P_{i=1} = 1.00$ at times t_{51} and t_{66} might be thought the first and second most convincing, respectively. In both of those comparisons, there is no overlap between the confidence intervals about the mean values (Tables 37 and 41; Figures 49 and 50).

Greater than $p(-3\sigma, 3\sigma)100\% \simeq 99.73\%$ confidence (Figure 2; Equation 26) can be accorded to the difference between $\mu_{P=0.99}$ and $\mu_{P=1.00}$, for which $(1 - p_{Bonf}) = 0.99754$ at t_{66} (Table 40), and $(1 - p_{Bonf}) = 0.99938$ at t_{51} (Table 36). Graphically, the confidence intervals of $\mu_{P=0.99}$ and $\mu_{P=1.00}$ at t_{66} would still not overlap at $(1 - \alpha) = 0.99754$, and the confidence intervals of $\mu_{P=0.99}$ and $\mu_{P=1.00}$ at t_{51} would still not overlap at $(1 - \alpha) = 0.99938$. Thus, even if 0.0025 were chosen for α, $\mu_{P=0.99}$ and $\mu_{P=1.00}$ would still pass the distinguishability test at times t_{51} and t_{66}. This, coupled with the relative nearness of the expectation values to μ_P for treatment groups $P_{i=2} = 0.99$ and $P_{i=1} = 1.00$ at t_{51} and t_{66}, can be taken as evidence that, given enough replicates and a large enough difference between the expectation values of the observations for the different treatment groups at one or more of the times chosen for analysis, suitable methods of AUC can be used to distinguish some systems that differ in composition by as little as 1% (volume percent).

As previously discussed (*The signal-to-noise ratio of* $g_{i,h}(s^*_{\varphi_\epsilon})$ *worsens in proportion to* $1/e^{2s^*_{\varphi_\epsilon}\omega^2 t_\epsilon}$ *as* $s^*_{\varphi_\epsilon}$ *increases*; *The accumulated error in* $G_{i,h}(s^*_{\varphi_\epsilon=2N})$ *increases in proportion to the clipping of random noise*; *The accumulated error in* $\langle s^*_{i,\epsilon}\rangle$ *increases in proportion to the clipping of random noise*), $GRN_{i,h}(r_j, t_\alpha)$, makes the least systematic contribution to $s^*_{i,h,\epsilon}$ when, in

going from $\left(\frac{\partial Y_{i,h}(s^*_{\varphi_\epsilon})}{\partial s^*_{\varphi_\epsilon}}\right)_t$ to $q_{i,h}(s^*_{\varphi_\epsilon})$, the clipping of the positively signed and the negatively signed random noise is minimised (Figures 24 to 27). The less comprehensive such minimisation, the more $s^*_{i,\epsilon}$ will differ from μ_i at any given time (Tables 24 to 27; Tables 33, 37 and 41; Figures 44 to 50). Even where the clipping of positively signed random noise within $-|s^*_a| < s^*_{\varphi_\epsilon} < -|s^*_z|$ is complemented by the clipping of negatively signed random noise within $|s^*_a| < s^*_{\varphi_\epsilon} < |s^*_z|$, the remaining random noise will be imbalanced in such a way that $s^*_{i,h,\epsilon}$ accumulates systematic noise.

The results for treatment groups 1 and 2 (Tables 24 and 25; Tables 37 and 41; Figures 44 and 45; Figures 49 and 50) show that the accumulation of systematic noise from data clipping can be minimised by excluding, through the judicious selection of $s^*_{min<0}$, $s^*_{max<0}$, $s^*_{min>0}$ and $s^*_{max>0}$, regions of low signal-to-noise from the ranges of $s^*_{\varphi_\epsilon}$ used to calculate $s^*_{i,h,\epsilon}$ (Equation13). In contrast, the results for treatment groups 3 and 4 (Tables 26 and 27; Figures 46 and 47) show that the accumulation of systematic noise from data clipping can be readily observed when large regions of low signal-to-noise are present within the ranges of $s^*_{\varphi_\epsilon}$ used to calculate $s^*_{i,h,\epsilon}$.

The process by which data clipping becomes a source of systematic noise is most easily shown through an example in which the noise-free signal, $NFS_i(r_j,t_\epsilon)$, is equal to zero at all radial positions and times, and where $s^*_{min<0} = s^*_{\varphi_\epsilon=1}$, $s^*_{max<0} = 0$, $s^*_{min>0} = 0$ and $s^*_{max>0} = s^*_{\varphi_\epsilon=2N}$ are the limits applied to the integrals that yield $G_{i,h}(s^*_{\varphi_\epsilon=2N})$ (Equation 77) and $s^*_{i,h,\epsilon}(s^*_{\varphi_\epsilon=1}, s^*_{\varphi_\epsilon=2N})$ (Equation 81a). Before presenting such an example (*Analysis of data for which the noise-free signal is always zero everywhere*), some background information, in which consideration is given to more general cases in which the observations can deviate from the model represented by

Equation 86 (*Deviation of the observations from the model represented by Equation 86*), is presented.

Deviation of the observations from the model represented by Equation 86

To equate an observation, $s^*_{i,h,\epsilon}\left(s^*_{\varphi_\epsilon=1}, s^*_{\varphi_\epsilon=2N}\right)$, to $A_{i,h}$ of Equation 86, all such observations, which are those resulting from the analysis of data obtained at the same time, t_ϵ, must fit the model represented by $A_{i,h} = \mu + \Delta\mu_i + e_{i,h}$, where $e_{i,h}$ is the random component of each observation, and as such, $e_{i,h}$ must be normally distributed (Equation 24) about $\mu + \Delta\mu_i$ with a standard deviation that does not vary from one treatment group to another.

Where the primary data are fully described by Equation 1b,$NMS_{i,h}(r_j, t_\epsilon) = NFS_i(r_j, t_\epsilon) + TIN_{i,h}(r_j) + RIN_{i,h}(t_\epsilon) + GRN_{i,h}(r_j, t_\epsilon)$, of which the total noise is given by $N_{i,h}(r_j, t_\epsilon) = TIN_{i,h}(r_j) + RIN_{i,h}(t_\epsilon) + GRN_{i,h}(r_j, t_\epsilon)$. By definition (Figure 5), the generally random noise, $GRN(r_j, t_\epsilon)$, is normally distributed with a standard deviation approaching $\sigma_{RI} = 0.01400$ fringe about a mean value approaching $\mu_{\mathrm{RI}} = 0$ fringe.

For radial position r_j of replicate h of treatment group i, Equation 7 gives the difference between two signals separated by time as $Y_{i,h}(r_j, t_\epsilon) = NMS_{i,h}(r_j, t_\epsilon) - NMS_{i,h}(r_j, t_\alpha)$, where $NMS_{i,h}(r_j, t_\alpha) = NFS_i(r_j, t_\alpha) + TIN_{i,h}(r_j) + RIN_{i,h}(t_\alpha) + GRN_{i,h}(r_j, t_\alpha)$. At each radial position, the difference in the time-independent noise is

$$\Delta TIN_{i,h}(r_j) = TIN_{i,h}(r_j) - TIN_{i,h}(r_j) = 0, \tag{107}$$

and the difference in the radially independent noise,

$$\Delta RIN_{i,h}(t_\epsilon) = RIN_{i,h}(t_\epsilon) - RIN_{i,h}(t_\alpha) = k_{i,h,\epsilon},$$

(108)

is equal to a radially independent offset, $k_{i,h,\epsilon}$, that contributes zero when differentiated with respect to either r_j or $s^*_{\varphi_\epsilon}$ at time t_ϵ. As both $GRN_{i,h}(r_j,t_\alpha)$ and $GRN_{i,h}(r_j,t_\epsilon)$ are randomly distributed with respect to r_j, neither $GRN_{i,h}(r_j,t_\alpha)$ nor $GRN_{i,h}(r_j,t_\epsilon)$ makes any systematic contribution to $Y_{i,h}(r_j,t_\epsilon)$. Rather, their contribution to $Y_{i,h}(r_j,t_\epsilon)$ consists of the difference,

$$\Delta GRN_{i,h}(r_j,t_\epsilon) = GRN_{i,h}(r_j,t_\epsilon) - GRN_{i,h}(r_j,t_\alpha)$$

(109)

that, with respect to r_j, is found to be randomly distributed with a standard deviation approximately $2^{0.5}$ times that of either $GRN_{i,h}(r_j,t_\alpha)$ or $GRN_{i,h}(r_j,t_\epsilon)$. (The standard deviation of such approximated differences is discussed in *Mitigation of data clipping*.) Consequently, the randomly distributed noise of $Y_{i,h}(r_j,t_\epsilon)$ is normally distributed with a standard deviation approaching $2^{0.5}\sigma_{RI} = 1.97990\text{E-}2$ fringe about a mean value approaching $\mu_{RI} = 0$ fringe. Other than the radially independent offset, $\Delta RIN_{i,h}(t_\epsilon) = k_{i,h,\epsilon}$, the only systematic part of $Y_{i,h}(r_j,t_\epsilon)$ is the difference in the noise-free signal,

$$\Delta NFS_i(r_j,t_\epsilon) = NFS_i(r_j,t_\epsilon) - NFS_i(r_j,t_\alpha),$$

(110)

which, at over 90% of all radial positions (Table 13b), consists of $NFS_i(r_j,t_\epsilon)$ minus a radially independent offset, with the exceptions limited to radial positions so close to the extrema that they are excluded from analysis. (Table 13b gives the values of $RIN_{i,h}(t_1)$, which are equated to $-NFS_i(r_{450},t_1)$, where $t_1 = t_\alpha$.) Using Equations 107 to 110, Equation 7 can be rewritten as

$$Y_{i,h}(r_j,t_\epsilon) = \Delta NFS_i(r_j,t_\epsilon) + \Delta TIN_{i,h}(r_j) + \Delta RIN_{i,h}(t_\epsilon) + \Delta GRN_{i,h}(r_j,t_\epsilon)$$

$$= \Delta NFS_i(r_j,t_\epsilon) + 0 + k_{i,h,\epsilon} + \Delta GRN_{i,h}(r_j,t_\epsilon).$$

(111a)

The signal difference, $Y_{i,h}(r_j,t_\epsilon)$, is remapped from $Y_{i,h}(r_j,t_\epsilon)$ versus r_j to $Y_{i,h}(s^*_{\varphi_\epsilon})$ versus $s^*_{\varphi_\epsilon}$, where $s^*_{\varphi_\epsilon}$ is calculated from r_j and t_ϵ using Equation 5. In the process, the difference in the time-independent noise is remapped from $\Delta TIN_{i,h}(r_j) = 0$ versus r_j to $\Delta TIN_{i,h}(s^*_{\varphi_\epsilon}) = 0$ versus $s^*_{\varphi_\epsilon}$, the difference in the radially independent noise is remapped from $\Delta RIN_{i,h}(t_\epsilon) = k_{i,h,\epsilon}$ versus r_j to $\Delta RIN_{i,h}(s^*_{\varphi_\epsilon}) = k_{i,h,\epsilon}$ versus $s^*_{\varphi_\epsilon}$, the difference in the noise-free signal is remapped from $\Delta NFS_i(r_j,t_\epsilon)$ versus r_j to $\Delta NFS_i(s^*_{\varphi_\epsilon})$ versus $s^*_{\varphi_\epsilon}$, and the difference in the randomly distributed noise is remapped from $\Delta GRN_{i,h}(r_j,t_\epsilon)$ versus r_j to $\Delta GRN_{i,h}(s^*_{\varphi_\epsilon})$ versus $s^*_{\varphi_\epsilon}$. Thus,

$$Y_{i,h}(s^*_{\varphi_\epsilon}) = \Delta NFS_i(s^*_{\varphi_\epsilon}) + \Delta TIN_{i,h}(s^*_{\varphi_\epsilon}) + \Delta RIN_{i,h}(s^*_{\varphi_\epsilon}) + \Delta GRN_{i,h}(s^*_{\varphi_\epsilon})$$
$$= \Delta NFS_i(s^*_{\varphi_\epsilon}) + 0 + k_{i,h,\epsilon} + \Delta GRN_{i,h}(s^*_{\varphi_\epsilon}).$$

(111b)

As with $\Delta GRN_{i,h}(r_j,t_\epsilon)$, $\Delta GRN_{i,h}(s^*_{\varphi_\epsilon})$ is normally distributed with a standard deviation approaching $2^{0.5}\sigma_{RI} =$ 1.197990E-2 fringe about a mean value approaching $\mu_{\mathrm{RI}} = 0$ fringe.

Systemic noise arising from $\Delta GRN_{i,h}(s^*_{\varphi_\epsilon})$ has its first source in the derivative, $\left(\frac{\partial Y_{i,h}(s^*_{\varphi_\epsilon})}{\partial s^*_{\varphi_\epsilon}}\right)_t$. The approximation used to evaluate the partial derivative of $Y_{i,h}(s^*_{\varphi_\epsilon})$ with respect to $s^*_{\varphi_\epsilon}$ at time t_ϵ is given by Equation 8, of which the part that applies to $\Delta GRN_{i,h}(s^*_{\varphi_\epsilon})$ is given by

$$\left(\frac{\partial \Delta GRN_{i,h}(s^*_{\varphi_\epsilon})}{\partial s^*_{\varphi_\epsilon}}\right)_t \cong \frac{1}{2}\left[\frac{\Delta GRN_{i,h}(s^*_{\varphi_\epsilon}) - \Delta GRN_{i,h}(s^*_{\varphi_\epsilon-1})}{s^*_{\varphi_\epsilon} - s^*_{\varphi_\epsilon-1}} + \frac{\Delta GRN_{i,h}(s^*_{\varphi_\epsilon+1}) - \Delta GRN_{i,h}(s^*_{\varphi_\epsilon})}{s^*_{\varphi_\epsilon+1} - s^*_{\varphi_\epsilon}}\right]$$
$$\equiv \frac{\Delta\Delta GRN_{i,h}(s^*_{\varphi_\epsilon})}{\Delta s^*_{\varphi_\epsilon}}$$

(112a)

at φ_ϵ within $1 < \varphi_\epsilon < 2N$,

$$\left(\frac{\partial \Delta GRN_{i,h}\left(s^*_{\varphi_\epsilon=1}\right)}{\partial s^*_{\varphi_\epsilon}}\right)_t \cong \frac{\Delta GRN_{i,h}\left(s^*_{\varphi_\epsilon+1}\right) - \Delta GRN_{i,h}\left(s^*_{\varphi_\epsilon}\right)}{s^*_{\varphi_\epsilon+1} - s^*_{\varphi_\epsilon}} \equiv \frac{\Delta\Delta GRN_{i,h}\left(s^*_{\varphi_\epsilon=1}\right)}{\Delta s^*_{\varphi_\epsilon=1}}$$

(112b)

at $\varphi_\epsilon = 1$, and

$$\left(\frac{\partial \Delta GRN\left(s^*_{\varphi_\epsilon=2N}\right)}{\partial s^*_{\varphi_\epsilon}}\right)_t \cong \frac{\Delta GRN\left(s^*_{\varphi_\epsilon}\right) - \Delta GRN_{i,h}\left(s^*_{\varphi_\epsilon-1}\right)}{s^*_{\varphi_\epsilon} - s^*_{\varphi_\epsilon-1}} \equiv \frac{\Delta\Delta GRN_{i,h}\left(s^*_{\varphi_\epsilon=2N}\right)}{\Delta s^*_{\varphi_\epsilon=2N}}$$

(112c)

at $\varphi_\epsilon = 2N$.

With $\left(\frac{\partial \Delta GRN_{i,h}(s^*_{\varphi_\epsilon})}{\partial s^*_{\varphi_\epsilon}}\right)_t$ approximated by $\frac{\Delta\Delta GRN_{i,h}(s^*_{\varphi_\epsilon})}{\Delta s^*_{\varphi_\epsilon}}$ or its equivalents at $\varphi_\epsilon = 1$ and $\varphi_\epsilon = 2N$ (Equation 112), $\Delta s^*_{\varphi_\epsilon}$ must be constant with φ_ϵ to keep the standard deviation of $\frac{\Delta\Delta GRN_{i,h}(s^*_{\varphi_\epsilon})}{\Delta s^*_{\varphi_\epsilon}}$ constant with φ_ϵ. The spacing between $s^*_{\varphi_\epsilon}$ values determines $\Delta s^*_{\varphi_\epsilon}$, and $s^*_{\varphi_\epsilon} = \frac{1}{\omega^2 t_\epsilon} ln\left(\frac{r_j}{r_0}\right)$ (Equations 5 and 6), where ϵ is the index applied to time, and where, with $1 \leq j \leq N$, $\varphi_\epsilon = j$ when r_0 is equal to the outermost radial extremum, r_b, while $\varphi_\epsilon = N + j$ when r_0 is equal to the innermost radial extremum, r_m. Thus, the spacing between $s^*_{\varphi_\epsilon}$ values depends on both t_ϵ and the spacing between r_j values.

As will be shown (Equations 113 to 117), $1/\Delta s^*_{\varphi_\epsilon=j} = 1/\Delta s^*_{\varphi_\epsilon=N+j} = \omega^2 t_\epsilon r_j/\Delta r_j$, where Δr_j is the average distance between adjacent radial positions about r_j. Furthermore, as implemented here, Δr_j decreases as j increases (Equation 113). Figure 51 shows the effects of $1/\Delta s^*_{\varphi_\epsilon}$ being proportional to $t_\epsilon r_j/\Delta r_j$, where Δr_j decreases as j increases.

To keep the standard deviation of $\frac{\Delta\Delta GRN_{i,h}(s^*_{\varphi_\epsilon})}{\Delta s^*_{\varphi_\epsilon}}$ constant with φ_ϵ, $\Delta s^*_{\varphi_\epsilon}$ would have to be kept

constant with φ_ϵ, and to keep $\Delta s^*_{\varphi_\epsilon}$ constant with φ_ϵ, the total number of r_j values and the spacing between adjacent r_j values would have to change with time in a facilitating manner (*Changing N and r_j values to keep $\Delta s^*_{\varphi_\epsilon}$ constant*), but even if that were done, it would still result in an $s^*_{\varphi_\epsilon}$-dependent the signal-to-noise ratio of $\frac{e^{2s^*_{\varphi_\epsilon}\omega^2 t_\epsilon}}{\Delta s^*_{\varphi_\epsilon}}$, albeit with $\Delta s^*_{\varphi_\epsilon}$ constant (compare with Figure 51), once $q_{i,h}(s^*_{\varphi_\epsilon})$ is multiplied by $e^{2s^*_{\varphi_\epsilon}\omega^2 t_\epsilon}$ to render the product, $g_{i,h}(s^*_{\varphi_\epsilon})$, hypothetically normalised for the effects of radial dilution or radial concentration. Nor would keeping $\Delta s^*_{\varphi_\epsilon}$ constant with φ_ϵ reduce the occurrence of data clipping, which is more problematic than an $s^*_{\varphi_\epsilon}$ dependence in the signal-to-noise ratio. Instead, it is simpler and more practical to edit the data such that $Y_{i,h}(s^*_{\varphi_\epsilon})$ is set to zero wherever its value is likely to be dominated by $\Delta GRN_{i,h}(s^*_{\varphi_\epsilon})$, thereby preventing most instances of data clipping. One such editing method will be described (*Mitigation of data clipping*) after covering other faults found with the method employed in this work.

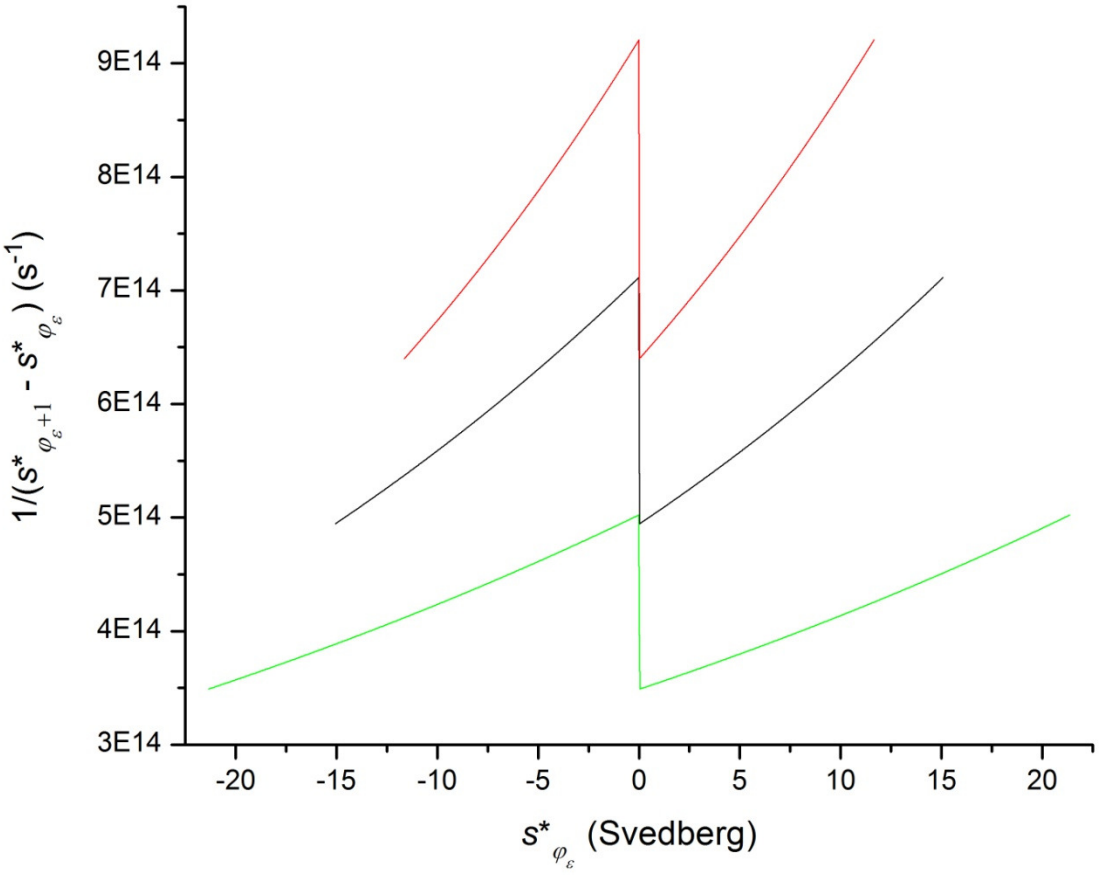

Figure 51. The full range of $1/\left(s^*_{\varphi_\epsilon+1} - s^*_{\varphi_\epsilon}\right)$ versus $s^*_{\varphi_\epsilon}$ at t_{36} (——), t_{51} (——) and t_{66} (——), where $\left(s^*_{\varphi_\epsilon+1} - s^*_{\varphi_\epsilon}\right)$ is equal to one of the $\Delta s^*_{\varphi_\epsilon}$ terms of Equations 8 and 112. The other $\Delta s^*_{\varphi_\epsilon}$ term of Equations 8 and 112, $\left(s^*_{\varphi_\epsilon} - s^*_{\varphi_\epsilon-1}\right)$, if used in place of $\left(s^*_{\varphi_\epsilon+1} - s^*_{\varphi_\epsilon}\right)$ to plot $1/\Delta s^*_{\varphi_\epsilon}$ versus $s^*_{\varphi_\epsilon}$, would yield indistinguishable results at the scales shown in this figure. Equation 117 states that $1/\Delta s^*_{\varphi_\epsilon=j} = 1/\Delta s^*_{\varphi_\epsilon=N+j} = \omega^2 t_\epsilon r_j/\Delta r_j$, where Δr_j is the average distance between adjacent radial positions about r_j. In a further complication, as implemented here, Δr_j decreases as j increases (Equation 113).

Why Δr_j decreases as j increases

For all the simulated AUC data in this study, $r_j = \sqrt{2\xi_j}$ (Equation 32) and $\xi_j = \xi_m + (j - 0.5)\Delta\xi$ (Equation 31), where $1 \leq j \leq N$, $\xi_j = r_j^2/2$ is the gravitational-potential-spatial element indexed by j, $\xi_m = r_m^2/2$ is the gravitational-potential-spatial position of the meniscus, and $\Delta\xi = [\xi_{j+1} - \xi_{j-1}]/2$ is constant at 8.8E-3 cm^2 with j. As $\Delta\xi$ is constant with j, the average distance between adjacent radial positions,

$$\Delta r_j = \frac{(r_{j+1} - r_j) + (r_j - r_{j-1})}{2} = \frac{r_{j+1} - r_{j-1}}{2},$$

(113a)

decreases as j increases. When applying Equation 113 to Δr_1, r_{j-1} could be calculated as $\sqrt{2\xi_0}$ (Equation 32), where $\xi_0 \equiv \xi_m + (0 - 0.5)\Delta\xi$ (Equation 31). When applying Equation 113 to Δr_N, r_{N+1} could be calculated as $\sqrt{2\xi_{N+1}}$ (Equation 32), where $\xi_{N+1} \equiv \xi_m + (N + 1 - 0.5)\Delta\xi$ (Equation 31). Here, however, Δr_1 and Δr_N are treated as special cases in which

$$\Delta r_1 = r_2 - r_1 \cong 0.00146631\ cm$$

(113b)

and

$$\Delta r_N = r_N - r_{N-1} \cong 0.0012224\ cm,$$

(113c)

respectively.

Why $1/\Delta s^*_{\varphi_\epsilon = j} = 1/\Delta s^*_{\varphi_\epsilon = N+j} = \omega^2 t_\epsilon r_j/\Delta r_j$

Either the partial derivative of r_j with respect to $s^*_{\varphi_\epsilon}$ or the partial derivative of $s^*_{\varphi_\epsilon}$ with respect to r_j can be used to obtain an equation that describes $1/\Delta s^*_{\varphi_\epsilon}$ as a function of $s^*_{\varphi_\epsilon}$. Equation 5, which

describes $s^*_{\varphi_\epsilon}$ as a function of t_ϵ and r_j, yields $\left(\frac{\partial s^*_{\varphi_\epsilon}}{\partial r_j}\right)_t$ when differentiated with respect to r_j at constant time, and Equation 6 can be used to apply the appropriate values of r_0 and j for a given value of φ_ϵ. To evaluate $\left(\frac{\partial r_j}{\partial s^*_{\varphi_\epsilon}}\right)_t$ requires an expression of r_j as a function of t_ϵ and $s^*_{\varphi_\epsilon}$. Solving Equation 5 for r_j results in,

$$r_j = r_0 e^{s^*_{\varphi_\epsilon}\omega^2 t_\epsilon},$$

(114)

where, in correspondence with Equation 6,

$$r_0 = \left\{ \begin{matrix} r_b \; for \; \varphi_\epsilon = j \\ r_m \; for \; \varphi_\epsilon = j + N \end{matrix} \right\} \; in \; r_j = r_0 e^{s^*_{\varphi_\epsilon}\omega^2 t_\epsilon}.$$

(115)

Equation 114, which describes r_j as a function of t_ϵ and $s^*_{\varphi_\epsilon}$, yields $\left(\frac{\partial r_j}{\partial s^*_{\varphi_\epsilon}}\right)_t$ when differentiated with respect to $s^*_{\varphi_\epsilon}$ at constant time, and Equation 115 can be used to apply the appropriate values of r_0 and φ_ϵ for a given value of j.

As the set of r_j values is finite, the set of $s^*_{\varphi_\epsilon}$ values is finite at each time, t_ϵ. Thus, any partial derivative with respect to r_j or $s^*_{\varphi_\epsilon}$ must be approximated if it cannot be evaluated analytically. At φ_ϵ within $1 < \varphi_\epsilon < 2N$ and j within $1 < j < N$, the analytical solution and the approximation used to evaluate the partial derivative of r_j with respect to $s^*_{\varphi_\epsilon}$ at time t_ϵ are given by

$$\left(\frac{\partial r_j}{\partial s^*_{\varphi_\epsilon}}\right)_t = r_0 \left(\frac{\partial e^{s^*_{\varphi_\epsilon}\omega^2 t_\epsilon}}{\partial s^*_{\varphi_\epsilon}}\right)_t = \left(r_0 e^{s^*_{\varphi_\epsilon}\omega^2 t_\epsilon}\right)\omega^2 t_\epsilon = r_j \omega^2 t_\epsilon \cong \frac{1}{2}\left[\frac{r_j - r_{j-1}}{s^*_{\varphi_\epsilon} - s^*_{\varphi_\epsilon - 1}} + \frac{r_{j+1} - r_j}{s^*_{\varphi_\epsilon + 1} - s^*_{\varphi_\epsilon}}\right]$$

$$= \frac{1}{2}\left[\frac{e^{s^*_{\varphi_\epsilon}\omega^2 t_\epsilon} - e^{s^*_{\varphi_\epsilon - 1}\omega^2 t_\epsilon}}{s^*_{\varphi_\epsilon} - s^*_{\varphi_\epsilon - 1}} + \frac{e^{s^*_{\varphi_\epsilon + 1}\omega^2 t_\epsilon} - e^{s^*_{\varphi_\epsilon}\omega^2 t_\epsilon}}{s^*_{\varphi_\epsilon + 1} - s^*_{\varphi_\epsilon}}\right] r_0 \equiv \frac{\Delta r_j}{\Delta s^*_{\varphi_\epsilon}},$$

(116a1)

while the analytical solution and the approximation used to evaluate the partial derivative of $s^*_{\varphi_\epsilon}$ with respect to r_j at time t_ϵ are given by

$$\left(\frac{\partial s^*_{\varphi_\epsilon}}{\partial r_j}\right)_t = \frac{1}{\omega^2 t_\epsilon}\left(\frac{\partial ln\left(\frac{r_j}{r_0}\right)}{\partial r_j}\right)_t = \frac{1}{r_j \omega^2 t_\epsilon} \cong \frac{1}{2}\left[\frac{s^*_{\varphi_\epsilon} - s^*_{\varphi_\epsilon - 1}}{r_j - r_{j-1}} + \frac{s^*_{\varphi_\epsilon + 1} - s^*_{\varphi_\epsilon}}{r_{j+1} - r_j}\right]$$

$$= \frac{1}{2}\left[\frac{ln\left(\frac{r_j}{r_0}\right) - ln\left(\frac{r_{j-1}}{r_0}\right)}{r_j - r_{j-1}} + \frac{ln\left(\frac{r_{j+1}}{r_0}\right) - ln\left(\frac{r_j}{r_0}\right)}{r_{j+1} - r_j}\right]\frac{1}{\omega^2 t_\epsilon} = \frac{1}{2}\left[\frac{ln\left(\frac{r_j}{r_{j-1}}\right)}{r_j - r_{j-1}} + \frac{ln\left(\frac{r_{j+1}}{r_j}\right)}{r_{j+1} - r_j}\right]\frac{1}{\omega^2 t_\epsilon}$$

$$\equiv \frac{\Delta s^*_{\varphi_\epsilon}}{\Delta r_j}.$$

(116a2)

Equations 116a1 and 116a2 each yield the inverse of the other, as can be seen by expressing $s^*_{\varphi_\epsilon}$ in terms of r_j in Equation 116a1, or by expressing r_j in terms of $s^*_{\varphi_\epsilon}$ in Equation 116a2.

At $\varphi_\epsilon = 1$ and $j = 1$, the analytical solution and the approximation used to evaluate the partial derivative of r_j with respect to $s^*_{\varphi_\epsilon}$ at time t_ϵ are given by

$$\left(\frac{\partial r_{j=1}}{\partial s^*_{\varphi_\epsilon}}\right)_t = r_b\left(\frac{\partial e^{s^*_{\varphi_\epsilon}\omega^2 t_\epsilon}}{\partial s^*_{\varphi_\epsilon}}\right)_t = \left(r_b e^{s^*_1 \omega^2 t_\epsilon}\right)\omega^2 t_\epsilon = r_1 \omega^2 t_\epsilon \cong \left[\frac{r_2 - r_1}{s^*_2 - s^*_1}\right] = \left[\frac{e^{s^*_2 \omega^2 t_\epsilon} - e^{s^*_1 \omega^2 t_\epsilon}}{s^*_2 - s^*_1}\right] r_b$$

$$\equiv \frac{\Delta r_{j=1}}{\Delta s^*_{\varphi_\epsilon = 1}},$$

(116b1)

while the analytical solution and the approximation used to evaluate the partial derivative of $s^*_{\varphi_\epsilon}$ with respect to r_j at time t_ϵ are given by

$$\left(\frac{\partial s^*_{\varphi_\epsilon=1}}{\partial r_j}\right)_t = \frac{1}{\omega^2 t_\epsilon}\left(\frac{\partial ln\left(\frac{r_j}{r_b}\right)}{\partial r_j}\right)_t = \frac{1}{r_{j=1}\omega^2 t_\epsilon} \cong \left[\frac{s^*_2 - s^*_1}{r_2 - r_1}\right] = \frac{1}{2}\left[\frac{ln\left(\frac{r_2}{r_b}\right) - ln\left(\frac{r_1}{r_b}\right)}{r_2 - r_1}\right]\frac{1}{\omega^2 t_\epsilon}$$

$$= \left[\frac{ln\left(\frac{r_2}{r_1}\right)}{r_2 - r_1}\right]\frac{1}{\omega^2 t_\epsilon} \equiv \frac{\Delta s^*_{\varphi_\epsilon=1}}{\Delta r_{j=1}}.$$

(116b2)

Equations 116b1 and 116b2 each yield the inverse of the other, as can be seen by expressing $s^*_{\varphi_\epsilon}$ in terms of r_j in Equation 116b1, or by expressing r_j in terms of $s^*_{\varphi_\epsilon}$ in Equation 116b2.

At $\varphi_\epsilon = 2N$ and $j = N$, the analytical solution and the approximation used to evaluate the partial derivative of r_j with respect to $s^*_{\varphi_\epsilon}$ at time t_ϵ are given by

$$\left(\frac{\partial r_{j=N}}{\partial s^*_{\varphi_\epsilon}}\right)_t = r_m\left(\frac{\partial e^{s^*_{\varphi_\epsilon}\omega^2 t_\epsilon}}{\partial s^*_{\varphi_\epsilon}}\right)_t = \left(r_m e^{s^*_{2N}\omega^2 t_\epsilon}\right)\omega^2 t_\epsilon = r_N\omega^2 t_\epsilon \cong \left[\frac{r_N - r_{N-1}}{s^*_{2N} - s^*_{2N-1}}\right]$$

$$= \left[\frac{e^{s^*_{2N}\omega^2 t_\epsilon} - e^{s^*_{2N-1}\omega^2 t_\epsilon}}{s^*_{2N} - s^*_{2N-1}}\right] r_m \equiv \frac{\Delta r_{j=N}}{\Delta s^*_{\varphi_\epsilon=2N}},$$

(116c1)

while the analytical solution and the approximation used to evaluate the partial derivative of $s^*_{\varphi_\epsilon}$ with respect to r_j at time t_ϵ are given by

$$\left(\frac{\partial s^*_{\varphi_\epsilon=2N}}{\partial r_j}\right)_t = \frac{1}{\omega^2 t_\epsilon}\left(\frac{\partial ln\left(\frac{r_j}{r_m}\right)}{\partial r_j}\right)_t = \frac{1}{r_N\omega^2 t_\epsilon} \cong \left[\frac{s^*_{2N} - s^*_{2N-1}}{r_N - r_{N-1}}\right] = \frac{1}{2}\left[\frac{ln\left(\frac{r_N}{r_m}\right) - ln\left(\frac{r_{N-1}}{r_m}\right)}{r_N - r_{N-1}}\right]\frac{1}{\omega^2 t_\epsilon}$$

$$= \left[\frac{ln\left(\frac{r_N}{r_{N-1}}\right)}{r_{j=N} - r_{N-1}}\right]\frac{1}{\omega^2 t_\epsilon} \equiv \frac{\Delta s^*_{\varphi_\epsilon=2N}}{\Delta r_{j=N}}.$$

(116c2)

Equations 116c1 and 116c2 each yield the inverse of the other, as can be seen by expressing $s^*_{\varphi_\epsilon}$

in terms of r_j in Equation 116c1, or by expressing r_j in terms of $s^*_{\varphi_\epsilon}$ in Equation 116c2.

At $\varphi_\epsilon = 1 + N$ and $j = 1$, the analytical solution and the approximation used to evaluate the partial derivative of r_j with respect to $s^*_{\varphi_\epsilon}$ at time t_ϵ are given by

$$\left(\frac{\partial r_{j=1}}{\partial s^*_{\varphi_\epsilon}}\right)_t = r_m\left(\frac{\partial e^{s^*_{\varphi_\epsilon}\omega^2 t_\epsilon}}{\partial s^*_{\varphi_\epsilon}}\right)_t = \left(r_m e^{s^*_{1+N}\omega^2 t_\epsilon}\right)\omega^2 t_\epsilon = r_1\omega^2 t_\epsilon \cong \left[\frac{r_2 - r_j}{s^*_{2+N} - s^*_{1+N}}\right]$$

$$= \left[\frac{e^{s^*_{2+N}\omega^2 t_\epsilon} - e^{s^*_{1+N}\omega^2 t_\epsilon}}{s^*_{2+N} - s^*_{1+N}}\right] r_m \equiv \frac{\Delta r_{j=1}}{\Delta s^*_{\varphi_\epsilon=1+N}},$$

(116d1)

while the analytical solution and the approximation used to evaluate the partial derivative of $s^*_{\varphi_\epsilon}$ with respect to r_j at time t_ϵ are given by

$$\left(\frac{\partial s^*_{\varphi_\epsilon=1+N}}{\partial r_j}\right)_t = \frac{1}{\omega^2 t_\epsilon}\left(\frac{\partial ln\left(\frac{r_j}{r_m}\right)}{\partial r_j}\right)_t = \frac{1}{r_1\omega^2 t_\epsilon} \cong \left[\frac{s^*_{2+N} - s^*_{1+N}}{r_2 - r_1}\right] = \frac{1}{2}\left[\frac{ln\left(\frac{r_2}{r_m}\right) - ln\left(\frac{r_1}{r_m}\right)}{r_2 - r_1}\right]\frac{1}{\omega^2 t_\epsilon}$$

$$= \left[\frac{ln\left(\frac{r_2}{r_1}\right)}{r_2 - r_1}\right]\frac{1}{\omega^2 t_\epsilon} \equiv \frac{\Delta s^*_{\varphi_\epsilon=1}}{\Delta r_{j=1}}.$$

(116d2)

Equations 116d1 and 116d2 each yield the inverse of the other, as can be seen by expressing $s^*_{\varphi_\epsilon}$ in terms of r_j in Equation 116d1, or by expressing r_j in terms of $s^*_{\varphi_\epsilon}$ in Equation 116d2. Furthermore, Equations 116b2 and 116d2 yield identical results, as information about r_0 is lost upon partial differentiation, at constant time, of $s^*_{\varphi_\epsilon}$ with respect to r_j.

At $\varphi_\epsilon = N$ and $j = N$, the analytical solution and the approximation used to evaluate the partial derivative of r_j with respect to $s^*_{\varphi_\epsilon}$ at time t_ϵ are given by

$$\left(\frac{\partial r_{j=N}}{\partial s^*_{\varphi_\epsilon}}\right)_t = r_b\left(\frac{\partial e^{s^*_{\varphi_\epsilon}\omega^2 t_\epsilon}}{\partial s^*_{\varphi_\epsilon}}\right)_t = \left(r_b e^{s^*_{\varphi_\epsilon=N}\omega^2 t_\epsilon}\right)\omega^2 t_\epsilon = r_{j=N}\omega^2 t_\epsilon \cong \left[\frac{r_N - r_{N-1}}{s^*_{\varphi_\epsilon=N} - s^*_{\varphi_\epsilon=N-1}}\right]$$

$$= \left[\frac{e^{s^*_{\varphi_\epsilon=N}\omega^2 t_\epsilon} - e^{s^*_{\varphi_\epsilon=N-1}\omega^2 t_\epsilon}}{s^*_{\varphi_\epsilon=N} - s^*_{\varphi_\epsilon=N-1}}\right] r_b \equiv \frac{\Delta r_{j=N}}{\Delta s^*_{\varphi_\epsilon=N}},$$

(116e1)

while the analytical solution and the approximation used to evaluate the partial derivative of $s^*_{\varphi_\epsilon}$ with respect to r_j at time t_ϵ are given by

$$\left(\frac{\partial s^*_{\varphi_\epsilon=N}}{\partial r_j}\right)_t = \frac{1}{\omega^2 t_\epsilon}\left(\frac{\partial ln\left(\frac{r_j}{r_b}\right)}{\partial r_j}\right)_t = \frac{1}{r_{j=N}\omega^2 t_\epsilon} \cong \left[\frac{s^*_{\varphi_\epsilon=N} - s^*_{\varphi_\epsilon=N-1}}{r_N - r_{N-1}}\right] = \frac{1}{2}\left[\frac{ln\left(\frac{r_N}{r_b}\right) - ln\left(\frac{r_{N-1}}{r_b}\right)}{r_N - r_{N-1}}\right]\frac{1}{\omega^2 t_\epsilon}$$

$$= \left[\frac{ln\left(\frac{r_N}{r_{N-1}}\right)}{r_N - r_{N-1}}\right]\frac{1}{\omega^2 t_\epsilon} \equiv \frac{\Delta s^*_{\varphi_\epsilon=N}}{\Delta r_{j=N}}.$$

(116e2)

Equations 116e1 and 116e2 each yield the inverse of the other, as can be seen by expressing $s^*_{\varphi_\epsilon}$ in terms of r_j in Equation 116e1, or by expressing r_j in terms of $s^*_{\varphi_\epsilon}$ in Equation 116e2. Furthermore, Equations 116c2 and 116e2 yield identical results, as information about r_0 is lost upon partial differentiation, at constant time, of $s^*_{\varphi_\epsilon}$ with respect to r_j.

Equation 116 shows that the analytical solutions, $\left(\frac{\partial s^*_{\varphi_\epsilon}}{\partial r_j}\right)_t = \frac{1}{r_j\omega^2 t_\epsilon}$ and $\left(\frac{\partial r_j}{\partial s^*_{\varphi_\epsilon}}\right)_t = r_j\omega^2 t_\epsilon$, are each the inverse of the other. Equation 116 also shows that the approximate solutions, $\frac{\Delta s^*_{\varphi_\epsilon}}{\Delta r_j}$ and $\frac{\Delta r_j}{\Delta s^*_{\varphi_\epsilon}}$, are each an alternative expression of the inverse of the other. Dividing the analytical solution for the partial derivative of r_j with respect to $s^*_{\varphi_\epsilon}$ at time t_ϵ, (Equation 116) by Δr_j (Equation 113) yields

$$\frac{1}{\Delta s^*_{\varphi_\epsilon=j}} = \frac{1}{\Delta s^*_{\varphi_\epsilon=N+j}} = \left(\frac{\partial r_j}{\partial s^*_{\varphi_\epsilon}}\right)_t \frac{1}{\Delta r_j} = \frac{r_j \omega^2 t_\epsilon}{\Delta r_j} = \frac{r_j \omega^2 t_\epsilon}{(r_{j+1} - r_{j-1})/2}$$

(117a)

for $1 < j < N$,

$$\frac{1}{\Delta s^*_{\varphi_\epsilon=1}} = \frac{1}{\Delta s^*_{\varphi_\epsilon=1+N}} = \left(\frac{\partial r_{j=1}}{\partial s^*_{\varphi_\epsilon}}\right)_t \frac{1}{\Delta r_{j=1}} = \frac{r_1 \omega^2 t_\epsilon}{\Delta r_1} = \frac{r_1 \omega^2 t_\epsilon}{r_2 - r_1}$$

(117b)

for $j = 1$ and

$$\frac{1}{\Delta s^*_{\varphi_\epsilon=N}} = \frac{1}{\Delta s^*_{\varphi_\epsilon=2N}} = \left(\frac{\partial r_{j=N}}{\partial s^*_{\varphi_\epsilon}}\right)_t \frac{1}{\Delta r_{j=N}} = \frac{r_N \omega^2 t_\epsilon}{\Delta r_N} = \frac{r_N \omega^2 t_\epsilon}{r_N - r_{N-1}}$$

(117c)

for $j = N$.

Analysis of data for which the noise-free signal is always zero everywhere

To illustrate how the method of data analysis can turn normally distributed noise in the noise-modified signals, those being the sets of all $NMS_{i,h}(r_j, t_\epsilon)$, into systematic noise in the observations, those being the sets of all $s^*_{i,h,\epsilon}\left(s^*_{\varphi_\epsilon=1}, s^*_{\varphi_\epsilon=2N}\right)$, such analysis is applied to data that are devoid of a noise-free signal. The index value $i = 0$ is assigned to the treatment group for which the data that are devoid of a noise-free signal, and within treatment group $i = 0$, just one replicate, $h = 1$, is examined. Thus, at each radial position, r_j, at each time, t_ϵ, $NFS_i(r_j, t_\epsilon) = 0$ holds for any replicate of treatment group $i = 0$. With $NFS_i(r_j, t_\epsilon) = 0$ at each radial position, r_j, at each time, t_ϵ, Equation 8 becomes identical to Equation 112, so that

$$\left(\frac{\partial Y_{i,h}\left(s^*_{\varphi_\epsilon}\right)}{\partial s^*_{\varphi_\epsilon}}\right)_t = \left(\frac{\partial \Delta GRN_{i,h}\left(s^*_{\varphi_\epsilon}\right)}{\partial s^*_{\varphi_\epsilon}}\right)_t \equiv \frac{\Delta\Delta GRN_{i,h}\left(s^*_{\varphi_\epsilon}\right)}{\Delta s^*_{\varphi_\epsilon}}$$

(118)

for any replicate of treatment group $i = 0$. As, by Equation 8, $\left(\frac{\partial Y_{i,h}(s^*_{\varphi_\epsilon})}{\partial s^*_{\varphi_\epsilon}}\right)_t \cong \frac{\Delta Y_{i,h}(s^*_{\varphi_\epsilon})}{\Delta s^*_{\varphi_\epsilon}}$, in the absence of a noise-free signal, $\Delta Y_{i,h}(s^*_{\varphi_\epsilon}) = \Delta\Delta GRN_{i,h}(s^*_{\varphi_\epsilon})$.

In what follows, several pairs of statistics, each consisting of a mean and a standard deviation of a parameter, arise frequently enough to warrant description. What is often of interest is whether the standard deviation of a parameter about its mean varies systematically from one narrow range of the spatially relevant independent variable to another at a given time, t_ϵ. Where the spatially relevant independent variable is the radial position, r_j, the index j is convenient for defining each narrow range. Where the spatially relevant independent variable is the apparent sedimentation coefficient, $s^*_{\varphi_\epsilon}$, the index φ_ϵ is convenient for defining each narrow range.

With respect to the N radial positions, at time t_ϵ, for a sequence of contiguous ranges that each comprises an equal number of r_j values, the standard deviation of a parameter about its mean within one narrow range, $a < j < b$, would be compared with the standard deviation of a parameter about its mean within the next narrow range, $b < j < c$, and the next narrow range, $c < j < d$, etcetera, where $b - a = c - b = d - c << N - 1$. With respect to the $2N$ apparent sedimentation coefficients, at time t_ϵ, for a sequence of contiguous ranges that each comprises an equal number of $s^*_{\varphi_\epsilon}$ values, the standard deviation of a parameter about its mean within one narrow range, $a < \varphi_\epsilon < b$, would be compared with the standard deviation of a parameter about its mean within the next narrow range, $b < \varphi_\epsilon < c$, and the next narrow range, $c < \varphi_\epsilon < d$, etcetera, where $b - a = c - b = d - c << 2N - 1$.

Within r_a to r_b of replicate h of treatment group i at time t_ϵ, the mean of $NMS_{i,h}(r_j, t_\epsilon)$ is given by

$$\langle NMS_{i,h}([r_a, r_b], t_\epsilon)\rangle = \frac{1}{b-a+1}\sum_{j=a}^{j=b} NMS_{i,h}(r_j, t_\epsilon),$$

(119a)

and the standard deviation of $NMS_{i,h}(r_j, t_\epsilon)$ about its mean, $\langle NMS_{i,h}([r_a, r_b], t_\epsilon)\rangle$, is given by

$$\sigma_{i,h}\left(NMS_{i,h}([r_a, r_b], t_\epsilon)\right) = \left\{\frac{1}{b-a-1}\left[\sum_{j=a}^{j=b}\left(NMS_{i,h}(r_j, t_\epsilon) - \langle NMS_{i,h}([r_a, r_b], t_\epsilon)\rangle\right)^2\right]\right\}^{0.5},$$

(119b)

where $1 \le a < b \le 2N$. Thus, at time t_ϵ, within the full range of r_j values, $\sigma_{i,h}\left(NMS_{i,h}([r_1, r_N], t_\epsilon)\right)$ is equal to the standard deviation about $\langle NMS_{i,h}([r_1, r_N], t_\epsilon)\rangle$, which is equal to the mean of all $NMS_{i,h}(r_j, t_\epsilon)$.

Within r_a to r_b of replicate h of treatment group i at time t_ϵ, the mean of $Y_{i,h}(r_j, t_\epsilon)$ is given by

$$\langle Y_{i,h}([r_a, r_b], t_\epsilon)\rangle = \frac{1}{b-a+1}\sum_{j=a}^{j=b} Y_{i,h}(r_j, t_\epsilon),$$

(120a)

and the standard deviation of $Y_{i,h}(r_j, t_\epsilon)$ about its mean, $\langle Y_{i,h}([r_a, r_b], t_\epsilon)\rangle$, is given by

$$\sigma_{i,h}\left(Y_{i,h}([r_a, r_b], t_\epsilon)\right) = \left\{\frac{1}{b-a-1}\left[\sum_{j=a}^{j=b}\left(Y_{i,h}(r_j, t_\epsilon) - \langle Y_{i,h}([r_a, r_b], t_\epsilon)\rangle\right)^2\right]\right\}^{0.5},$$

(120b)

where $1 \le a < b \le 2N$. Thus, at time t_ϵ, within the full range of r_j values, $\sigma_{i,h}\left(Y_{i,h}([r_1, r_N], t_\epsilon)\right)$ is equal to the standard deviation about $\langle Y_{i,h}([r_1, r_N], t_\epsilon)\rangle$, which is equal to the mean of all

$Y_{i,h}(r_j, t_\epsilon)$.

Within $s^*_{\varphi_\epsilon=a}$ to $s^*_{\varphi_\epsilon=b}$ of replicate h of treatment group i at time t_ϵ, the mean of $Y_{i,h}(s^*_{\varphi_\epsilon})$ is given by

$$\langle Y_{i,h}([s^*_{\varphi_\epsilon=a}, s^*_{\varphi_\epsilon=b}])\rangle = \frac{1}{b-a+1}\sum_{\varphi_\epsilon=a}^{\varphi_\epsilon=b} Y_{i,h}(s^*_{\varphi_\epsilon}),$$

(121a)

and the standard deviation of $Y_{i,h}(s^*_{\varphi_\epsilon})$ about its mean, $\langle Y_{i,h}([s^*_{\varphi_\epsilon=a}, s^*_{\varphi_\epsilon=b}])\rangle$, is given by

$$\sigma_{i,h}\left(Y_{i,h}([s^*_{\varphi_\epsilon=a}, s^*_{\varphi_\epsilon=b}])\right) = \left\{\frac{1}{b-a-1}\left[\sum_{\varphi_\epsilon=a}^{\varphi_\epsilon=b}\left(Y_{i,h}(s^*_{\varphi_\epsilon}) - \langle Y_{i,h}([s^*_{\varphi_\epsilon=a}, s^*_{\varphi_\epsilon=b}])\rangle\right)^2\right]\right\}^{0.5},$$

(121b)

where $1 \le a < b \le 2N$. Thus, at time t_ϵ, within the full range of $s^*_{\varphi_\epsilon}$ values that apply at that time, $\sigma_{i,h}\left(Y_{i,h}([s^*_{\varphi_\epsilon=1}, s^*_{\varphi_\epsilon=2N}])\right)$ is equal to the standard deviation about $\langle Y_{i,h}([s^*_{\varphi_\epsilon=1}, s^*_{\varphi_\epsilon=2N}])\rangle$, which is equal to the mean of all $Y_{i,h}(s^*_{\varphi_\epsilon})$.

Within $s^*_{\varphi_\epsilon=a}$ to $s^*_{\varphi_\epsilon=b}$ of replicate h of treatment group i at time t_ϵ, the mean of $\Delta Y_{i,h}(s^*_{\varphi_\epsilon})/\Delta s^*_{\varphi_\epsilon}$ is given by

$$\langle \Delta Y_{i,h}([s^*_{\varphi_\epsilon=a}, s^*_{\varphi_\epsilon=b}])/\Delta s^*_{\varphi_\epsilon}\rangle = \frac{1}{b-a+1}\sum_{\varphi_\epsilon=a}^{\varphi_\epsilon=b} \Delta Y_{i,h}(s^*_{\varphi_\epsilon})/\Delta s^*_{\varphi_\epsilon},$$

(122a)

and the standard deviation of $\Delta Y_{i,h}(s^*_{\varphi_\epsilon})/\Delta s^*_{\varphi_\epsilon}$ about its mean, $\langle \Delta Y_{i,h}([s^*_{\varphi_\epsilon=a}, s^*_{\varphi_\epsilon=b}])/\Delta s^*_{\varphi_\epsilon}\rangle$, is given by

$$\sigma_{i,h}\left(\Delta Y_{i,h}\left(\left[s^*_{\varphi_\epsilon=a}, s^*_{\varphi_\epsilon=b}\right]\right)/\Delta s^*_{\varphi_\epsilon}\right)$$

$$= \left\{\frac{1}{b-a-1}\left[\sum_{\varphi_\epsilon=a}^{\varphi_\epsilon=b}\left(\Delta Y_{i,h}\left(s^*_{\varphi_\epsilon}\right)/\Delta s^*_{\varphi_\epsilon} - \left\langle \Delta Y_{i,h}\left(\left[s^*_{\varphi_\epsilon=a}, s^*_{\varphi_\epsilon=b}\right]\right)/\Delta s^*_{\varphi_\epsilon}\right\rangle\right)^2\right]\right\}^{0.5},$$

(122b)

where $1 \le a < b \le 2N$. Thus, at time t_ϵ, within the full range of $s^*_{\varphi_\epsilon}$ values that apply at that time, $\sigma_{i,h}\left(\Delta Y_{i,h}\left(\left[s^*_{\varphi_\epsilon=1}, s^*_{\varphi_\epsilon=2N}\right]\right)/\Delta s^*_{\varphi_\epsilon}\right)$ is equal to the standard deviation about $\left\langle \Delta Y_{i,h}\left(\left[s^*_{\varphi_\epsilon=1}, s^*_{\varphi_\epsilon=2N}\right]\right)/\Delta s^*_{\varphi_\epsilon}\right\rangle$, which is equal to the mean of all $\Delta Y_{i,h}\left(s^*_{\varphi_\epsilon}\right)/\Delta s^*_{\varphi_\epsilon}$.

Within $s^*_{\varphi_\epsilon=a}$ to $s^*_{\varphi_\epsilon=b}$ of replicate h of treatment group i at time t_ϵ, the mean of $g_{i,h}\left(s^*_{\varphi_\epsilon}\right)$ is given by

$$\left\langle g_{i,h}\left(\left[s^*_{\varphi_\epsilon=a}, s^*_{\varphi_\epsilon=b}\right]\right)\right\rangle = \frac{1}{b-a+1}\sum_{\varphi_\epsilon=a}^{\varphi_\epsilon=b} g_{i,h}\left(s^*_{\varphi_\epsilon}\right),$$

(124a)

and the standard deviation of $g_{i,h}\left(s^*_{\varphi_\epsilon}\right)$ about its mean, $\left\langle g_{i,h}\left(\left[s^*_{\varphi_\epsilon=a}, s^*_{\varphi_\epsilon=b}\right]\right)\right\rangle$, is given by

$$\sigma_{i,h}\left(g_{i,h}\left(\left[s^*_{\varphi_\epsilon=a}, s^*_{\varphi_\epsilon=b}\right]\right)\right) = \left\{\frac{1}{b-a-1}\left[\sum_{\varphi_\epsilon=a}^{\varphi_\epsilon=b}\left(g_{i,h}\left(s^*_{\varphi_\epsilon}\right) - \left\langle g_{i,h}\left(\left[s^*_{\varphi_\epsilon=a}, s^*_{\varphi_\epsilon=b}\right]\right)\right\rangle\right)^2\right]\right\}^{0.5},$$

(124b)

where $1 \le a < b \le 2N$. Thus, at time t_ϵ, within the full range of $s^*_{\varphi_\epsilon}$ values that apply at that time, $\sigma_{i,h}\left(g_{i,h}\left(\left[s^*_{\varphi_\epsilon=1}, s^*_{\varphi_\epsilon=2N}\right]\right)\right)$ is equal to the standard deviation about $\left\langle g_{i,h}\left(\left[s^*_{\varphi_\epsilon=1}, s^*_{\varphi_\epsilon=2N}\right]\right)\right\rangle$, which is equal to the mean of all $g_{i,h}\left(s^*_{\varphi_\epsilon}\right)$.

Within $s^*_{\varphi_\epsilon=a}$ to $s^*_{\varphi_\epsilon=b}$ of replicate h of treatment group i at time t_ϵ, the mean of $\left|g_{i,h}\left(s^*_{\varphi_\epsilon}\right)\right|$ is given

by

$$\langle\left|g_{i,h}\left(\left[s^*_{\varphi_\epsilon=a}, s^*_{\varphi_\epsilon=b}\right]\right)\right|\rangle = \frac{1}{b-a+1}\sum_{\varphi_\epsilon=a}^{\varphi_\epsilon=b}\left|g_{i,h}\left(s^*_{\varphi_\epsilon}\right)\right|,$$

(125a)

and the standard deviation of $\left|g_{i,h}\left(s^*_{\varphi_\epsilon}\right)\right|$ about its mean, $\langle\left|g_{i,h}\left(\left[s^*_{\varphi_\epsilon=a}, s^*_{\varphi_\epsilon=b}\right]\right)\right|\rangle$, is given by

$$\sigma_{i,h}\left(\left|g_{i,h}\left(\left[s^*_{\varphi_\epsilon=a}, s^*_{\varphi_\epsilon=b}\right]\right)\right|\right) = \left\{\frac{1}{b-a-1}\left[\sum_{\varphi_\epsilon=a}^{\varphi_\epsilon=b}\left(\left|g_{i,h}\left(s^*_{\varphi_\epsilon}\right)\right| - \langle\left|g_{i,h}\left(\left[s^*_{\varphi_\epsilon=a}, s^*_{\varphi_\epsilon=b}\right]\right)\right|\rangle\right)^2\right]\right\}^{0.5},$$

(125b)

where $1 \le a < b \le 2N$. Thus, at time t_ϵ, within the full range of $s^*_{\varphi_\epsilon}$ values that apply at that time, $\sigma_{i,h}\left(\left|g_{i,h}\left(\left[s^*_{\varphi_\epsilon=1}, s^*_{\varphi_\epsilon=2N}\right]\right)\right|\right)$ is equal to the standard deviation about $\langle\left|g_{i,h}\left(\left[s^*_{\varphi_\epsilon=1}, s^*_{\varphi_\epsilon=2N}\right]\right)\right|\rangle$, which is equal to the mean of all $\left|g_{i,h}\left(s^*_{\varphi_\epsilon}\right)\right|$.

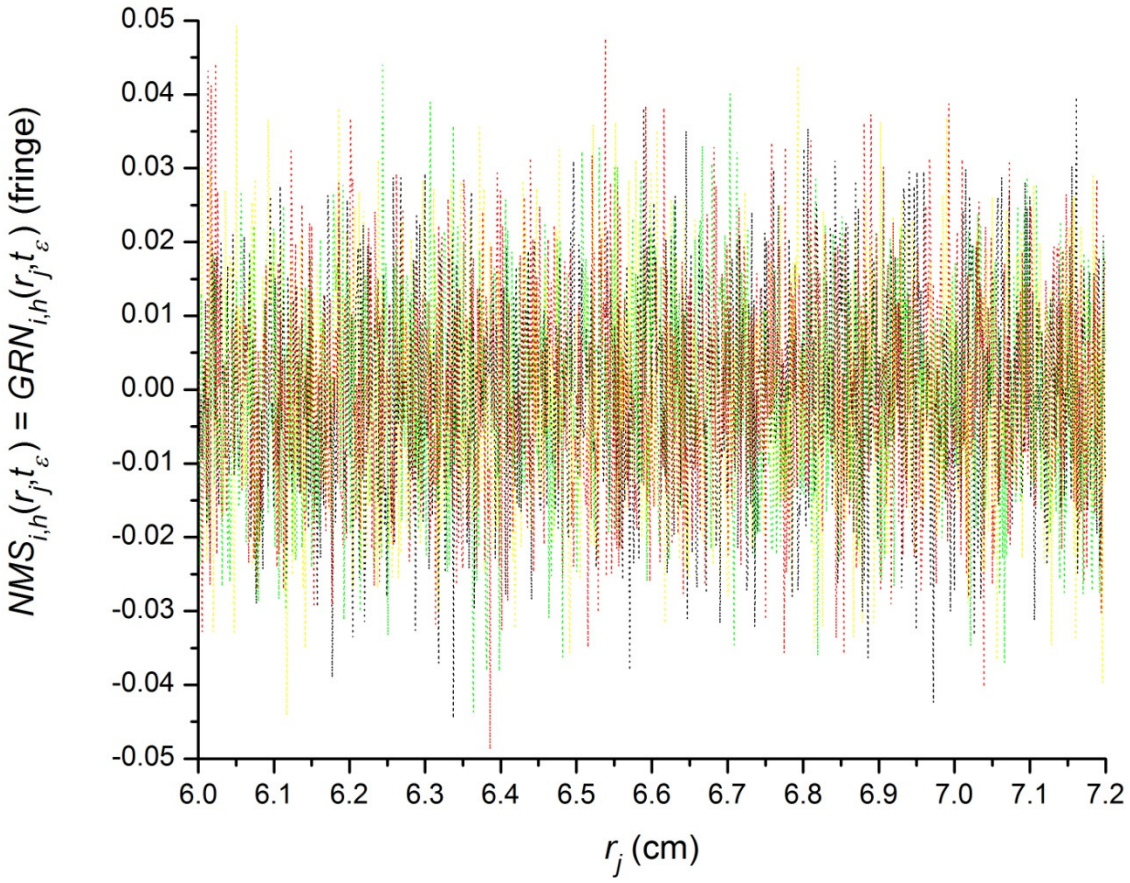

Figure 52. The sets of $NMS_{i,h}(r_j,t_\epsilon) = GRN_{i,h}(r_j,t_\epsilon)$, of which $NMS_{i,h}(r_j,t_\alpha) = GRN_{i,h}(r_j,t_\alpha)$ is a subset, versus r_j at $t_\epsilon = t_\alpha = t_1$ (·····), $t_\epsilon = t_{36}$ (·····), $t_\epsilon = t_{51}$ (·····) and $t_\epsilon = t_{66}$ (·····), where $i = 0$ and $h = 1$. The sets of $GRN_{i,h}(r_j,t_\epsilon)$ previously applied to replicate $h = 1$ of treatment group $i = 4$ were equated to the sets of $NMS_{0,1}(r_j,t_\epsilon)$ shown in this figure. Thus, as for $h = 1$ of $i = 4$ in Table 14a, set ${}_6a$ was used for $NMS_{0,1}(r_j,t_\alpha)$, set ${}_7a$ was used for $NMS_{0,1}(r_j,t_{36})$, set ${}_1b$ was used for $NMS_{0,1}(r_j,t_{51})$, and set ${}_1b$ was used for $NMS_{0,1}(r_j,t_{66})$. To a close approximation, each set of $NMS_{0,1}(r_j,t_\epsilon)$ values is normally distributed about a mean of $\langle NMS_{i,h}([r_1,r_{2N}],t_\epsilon)\rangle = \mu_{RI} = 0$ fringe with a standard deviation of $\sigma_{i,h}\left(NMS_{i,h}([r_1,r_{2N}],t_\epsilon)\right) = \sigma_{RI} = 0.01400$ fringe (Figure 5; Table 14). More importantly, at any given time, the standard deviation (Equation 119b) of $NMS_{0,1}(r_j,t_\epsilon)$ about its mean (Equation 119a) does not vary systematically from one narrow range of r_j values to

another.

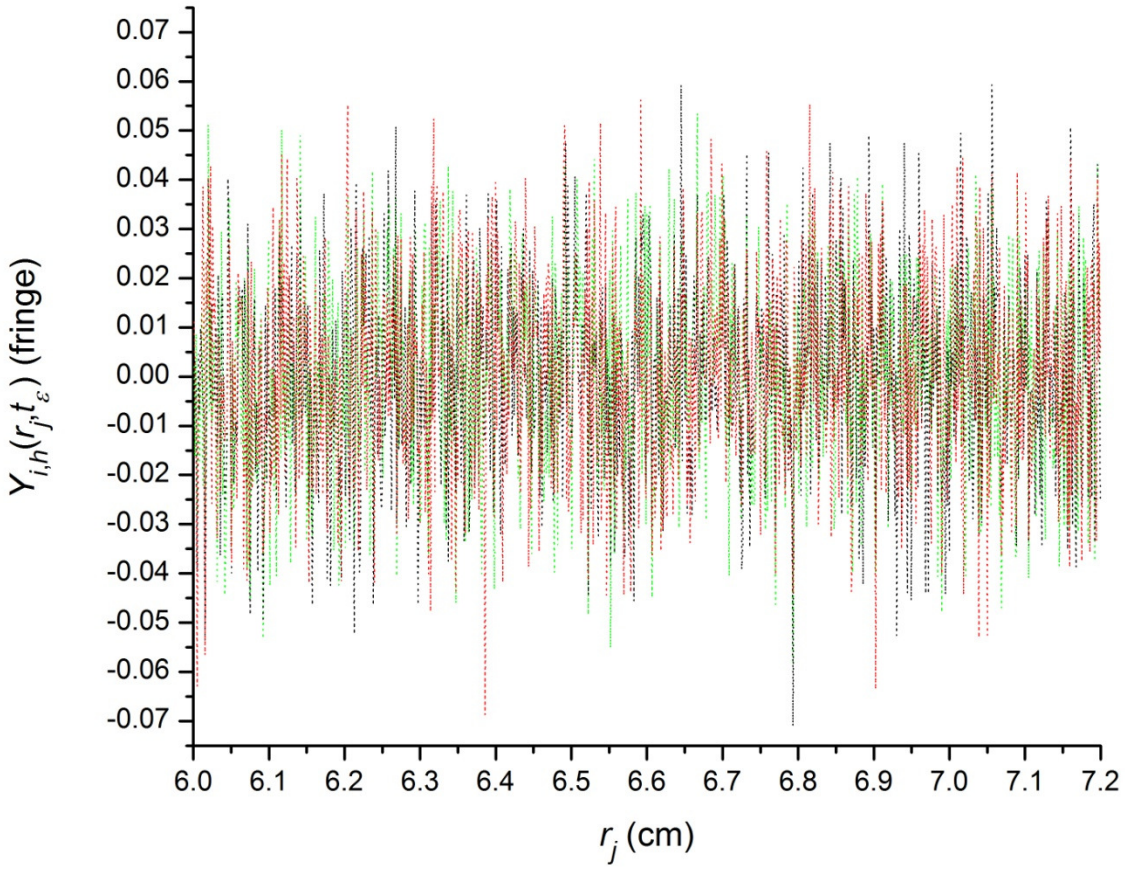

Figure 53. $Y_{i,h}(r_j,t_\epsilon) = \Delta GRN_{i,h}(r_j,t_\epsilon)$ versus r_j at $t_\epsilon = t_{36}$ (·····), $t_\epsilon = t_{51}$ (·····) and $t_\epsilon = t_{66}$ (·····), where $i = 0$ and $h = 1$. In general, $Y_{i,h}(r_j,t_\epsilon) = \Delta NFS_i(r_j,t_\epsilon) + 0 + k_{i,h,\epsilon} + \Delta GRN_{i,h}(r_j,t_\epsilon)$ (Equation 111a), or as originally cast (Equation 7), $Y_{i,h}(r_j,t_\epsilon) = NMS_{i,h}(r_j,t_\epsilon)$ - $NMS_{i,h}(r_j,t_\alpha)$. Here, $NMS_{i,h}(r_j,t_\epsilon)$ - $NMS_{i,h}(r_j,t_\alpha) = \Delta GRN_{i,h}(r_j,t_\epsilon)$, which is the randomly distributed noise of $Y_{i,h}(r_j,t_\epsilon)$. (See Equation 109.) The standard deviation of the randomly distributed noise of $Y_{i,h}(r_j,t_\epsilon)$ is about $2^{0.5}$-fold greater than that of either $NMS_{i,h}(r_j,t_\alpha)$ or $NMS_{i,h}(r_j,t_\epsilon)$, which are shown in Figure 52. (See the discussion that follows Equation 8.) Thus, to a close approximation, at any given time, each set of $Y_{i,h}(r_j,t_\epsilon) = \Delta GRN_{i,h}(r_j,t_\epsilon)$ values is normally distributed about a mean of $\langle Y_{i,h}([r_1,r_{2N}],t_\epsilon)\rangle$ $\mu_{RI} = 0$ fringe with a standard deviation of $\sigma_{i,h}\left(Y_{i,h}([r_1,r_{2N}],t_\epsilon)\right) = 2^{0.5}\sigma_{RI} =$ 1.97990E-2 fringe (Figure 5;

Table 14). More importantly, for $Y_{i,h}(r_j,t_\epsilon) = \Delta GRN_{i,h}(r_j,t_\epsilon)$, at any given time, the standard deviation (Equation 120b) of $Y_{i,h}(r_j,t_\epsilon)$ about its mean (Equation 120a) does not vary systematically from one narrow range of r_j values to another.

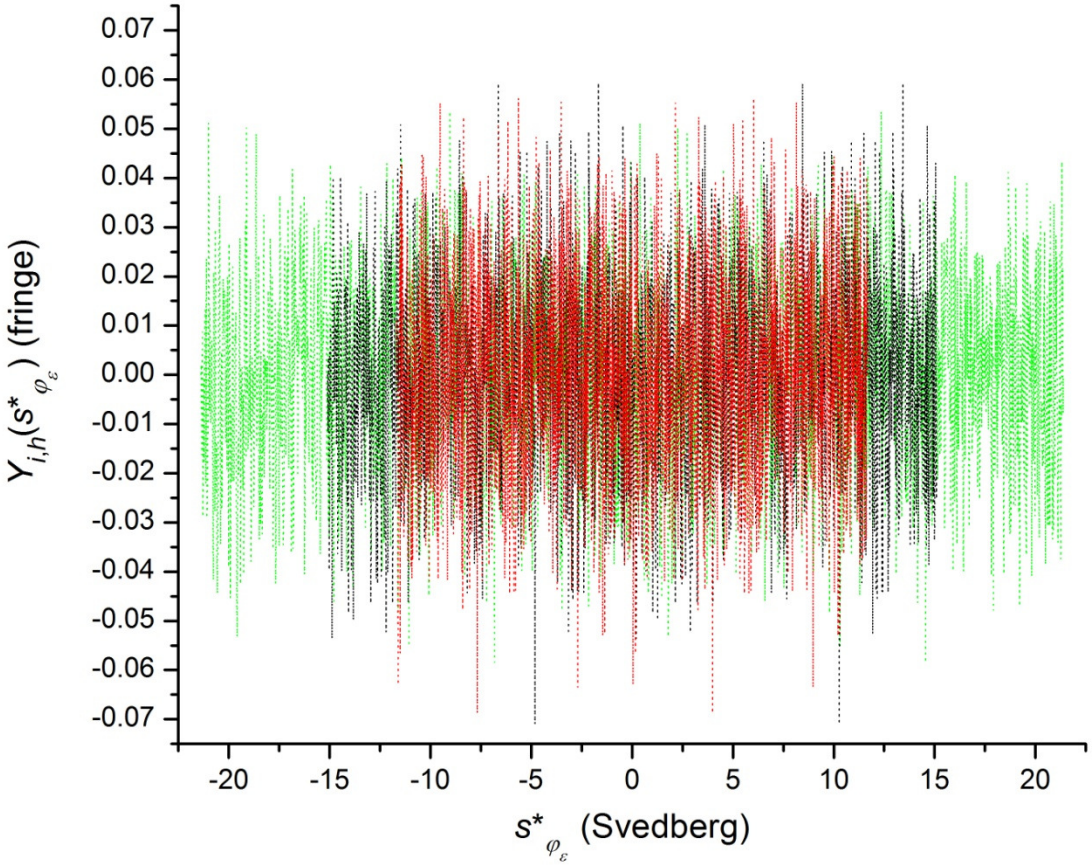

Figure 54. $Y_{i,h}(s^*_{\varphi_\epsilon}) = \Delta GRN_{i,h}(s^*_{\varphi_\epsilon})$ versus $s^*_{\varphi_\epsilon}$ at $t_\epsilon = t_{36}$ (·····), $t_\epsilon = t_{51}$ (·····) and $t_\epsilon = t_{66}$ (·····), where $i = 0$ and $h = 1$. In general (Equation 111), $Y_{i,h}(r_j,t_\epsilon)$ remapped from r_j to $s^*_{\varphi_\epsilon}$ yields $Y_{i,h}(s^*_{\varphi_\epsilon})$, where $s^*_{\varphi_\epsilon}$ is calculated from r_j and t_ϵ using Equation 5. As with $Y_{i,h}(r_j,t_\epsilon) = \Delta GRN_{i,h}(r_j,t_\epsilon)$ mapped to r_j in the previous figure, to a close approximation, at any given time, each set of $Y_{i,h}(s^*_{\varphi_\epsilon}) = \Delta GRN_{i,h}(s^*_{\varphi_\epsilon})$ values is normally distributed about a mean of $\langle Y_{i,h}([s^*_{\varphi_\epsilon=1}, s^*_{\varphi_\epsilon=2N}])\rangle = \mu_{RI} = 0$ fringe with a standard deviation of $\sigma_{i,h}\left(Y_{i,h}([s^*_{\varphi_\epsilon=1}, s^*_{\varphi_\epsilon=2N}])\right) = 2^{0.5}\sigma_{RI} = 1.97990\text{E-}2$

fringe (Figure 5; Table 14). More importantly, for $Y_{i,h}(s^*_{\varphi_\epsilon}) = \Delta GRN_{i,h}(s^*_{\varphi_\epsilon})$, at any given time, the standard deviation (Equation 121b) of $Y_{i,h}(s^*_{\varphi_\epsilon})$ about its mean (Equation 121a) does not vary systematically from one narrow range of $s^*_{\varphi_\epsilon}$ values to another.

The application of Equation 8 to $Y_{i,h}(s^*_{\varphi_\epsilon})$ yields $\Delta Y_{i,h}(s^*_{\varphi_\epsilon})/\Delta s^*_{\varphi_\epsilon}$ (Figure 55), which is an approximation of $\left(\frac{\partial Y_{i,h}(s^*_{\varphi_\epsilon})}{\partial s^*_{\varphi_\epsilon}}\right)_t$. It is really $\Delta Y_{i,h}(s^*_{\varphi_\epsilon})/\Delta s^*_{\varphi_\epsilon}$ that can be considered the apparent signal with respect to data analysis. The operations performed to obtain $\Delta Y_{i,h}(s^*_{\varphi_\epsilon})/\Delta s^*_{\varphi_\epsilon}$ extract this signal from the raw data, $NMS_{i,h}(r_j, t_\epsilon)$ and $NMS_{i,h}(r_j, t_\alpha)$ (Equation 7; Figure 52).

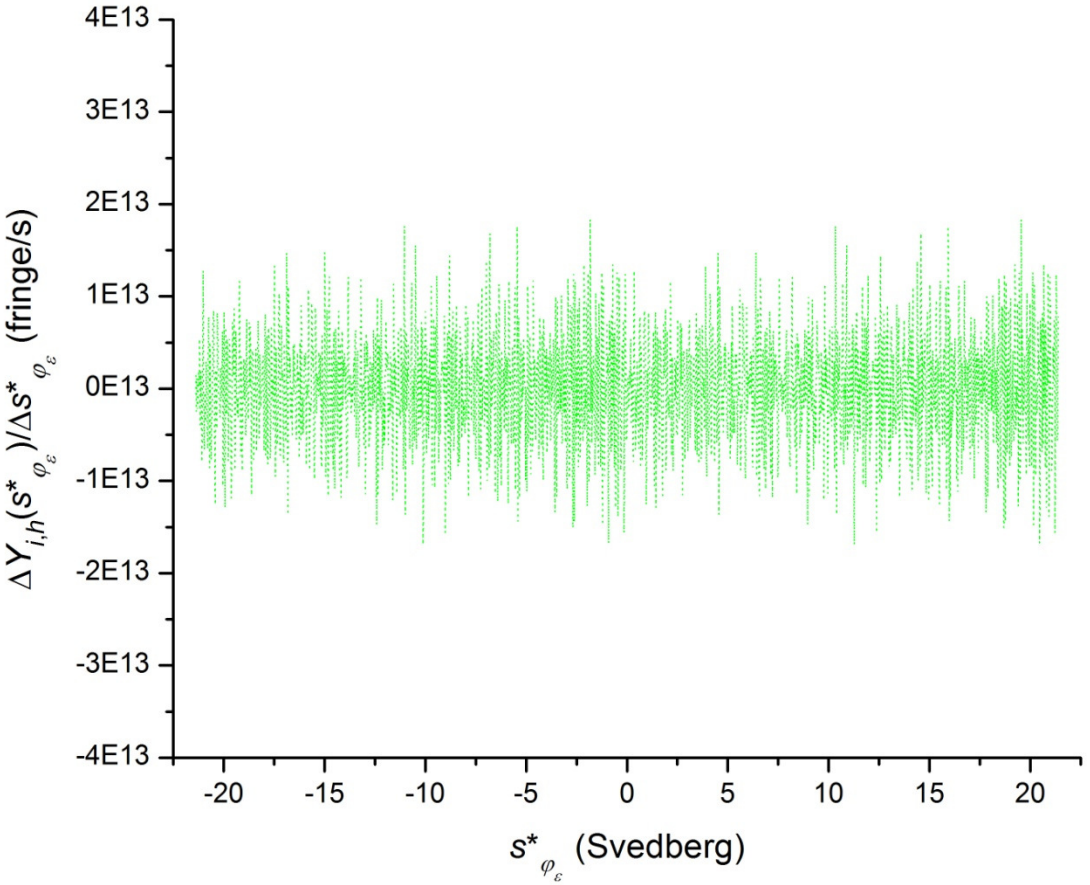

Figure 55a. $\Delta Y_{i,h}(s^*_{\varphi_\epsilon})/\Delta s^*_{\varphi_\epsilon}$ versus $s^*_{\varphi_\epsilon}$ at $t_\epsilon = t_{36}$ (·····), where $i = 0$ and $h = 1$. As $i = 0$, $Y_{i,h}(s^*_{\varphi_\epsilon}) =$

$\Delta GRN_{i,h}(s^*_{\varphi_\epsilon})$. Figure 54 shows $Y_{i,h}(s^*_{\varphi_\epsilon})$, of which $\Delta Y_{i,h}(s^*_{\varphi_\epsilon})/\Delta s^*_{\varphi_\epsilon}$ is the approximate derivative with respect to $s^*_{\varphi_\epsilon}$ (Equation 8). At any given time, the standard deviation (Equation 122b) of $\Delta Y_{i,h}(s^*_{\varphi_\epsilon})/\Delta s^*_{\varphi_\epsilon}$ about its mean (Equation 122a) varies systematically from one narrow range of $s^*_{\varphi_\epsilon}$ values to another within the entire range of $s^*_{\varphi_\epsilon}$, across which, $\Delta Y_{i,h}(s^*_{\varphi_\epsilon})/\Delta s^*_{\varphi_\epsilon}$ is proportional to $1/\Delta s^*_{\varphi_{\epsilon=j}} = 1/\Delta s^*_{\varphi_{\epsilon=N+j}} = \omega^2 t_\epsilon r_j/\Delta r_j$ (Equation 117). As in this figure, at any given time, the proportionality of $\Delta Y_{i,h}(s^*_{\varphi_\epsilon})/\Delta s^*_{\varphi_\epsilon}$ to $r_j/\Delta r_j$ produces fairly subtle effects across $s^*_{\varphi_\epsilon}$. The proportionality of $\Delta Y_{i,h}(s^*_{\varphi_\epsilon})/\Delta s^*_{\varphi_\epsilon}$ to t_ϵ produces obvious effects across time, as is shown by a comparison of Figures 55a, 55b and 55c, which apply to $t_\epsilon = t_{36}$, $t_\epsilon = t_{51}$ and $t_\epsilon = t_{66}$, respectively.

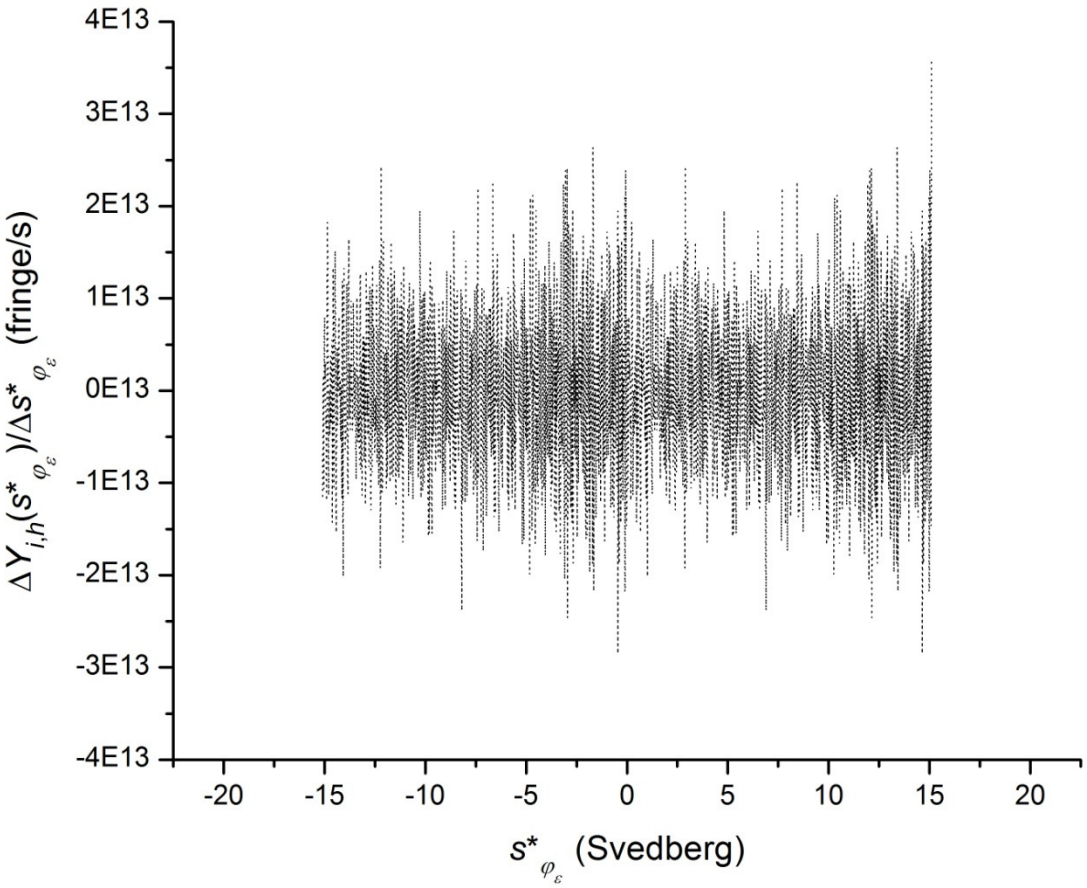

Figure 55b. $\Delta Y_{i,h}(s^*_{\varphi_\epsilon})/\Delta s^*_{\varphi_\epsilon}$ versus $s^*_{\varphi_\epsilon}$ at $t_\epsilon = t_{51}$ (·····), where $i = 0$ and $h = 1$. As $i = 0$, $Y_{i,h}(s^*_{\varphi_\epsilon}) =$

$\Delta GRN_{i,h}(s^*_{\varphi_\epsilon})$. Figure 54 shows $Y_{i,h}(s^*_{\varphi_\epsilon})$, of which $\Delta Y_{i,h}(s^*_{\varphi_\epsilon})/\Delta s^*_{\varphi_\epsilon}$ is the approximate derivative with respect to $s^*_{\varphi_\epsilon}$ (Equation 8). At any given time, the standard deviation (Equation 122b) of $\Delta Y_{i,h}(s^*_{\varphi_\epsilon})/\Delta s^*_{\varphi_\epsilon}$ about its mean (Equation 122a) varies systematically from one narrow range of $s^*_{\varphi_\epsilon}$ values to another within the entire range of $s^*_{\varphi_\epsilon}$, across which, $\Delta Y_{i,h}(s^*_{\varphi_\epsilon})/\Delta s^*_{\varphi_\epsilon}$ is proportional to $1/\Delta s^*_{\varphi_{\epsilon=j}} = 1/\Delta s^*_{\varphi_{\epsilon=N+j}} = \omega^2 t_\epsilon r_j/\Delta r_j$ (Equation 117). As in this figure, at any given time, the proportionality of $\Delta Y_{i,h}(s^*_{\varphi_\epsilon})/\Delta s^*_{\varphi_\epsilon}$ to $r_j/\Delta r_j$ produces fairly subtle effects across $s^*_{\varphi_\epsilon}$. The proportionality of $\Delta Y_{i,h}(s^*_{\varphi_\epsilon})/\Delta s^*_{\varphi_\epsilon}$ to t_ϵ produces obvious effects across time, as is shown by a comparison of Figures 55a, 55b and 55c, which apply to $t_\epsilon = t_{36}$, $t_\epsilon = t_{51}$ and $t_\epsilon = t_{66}$, respectively.

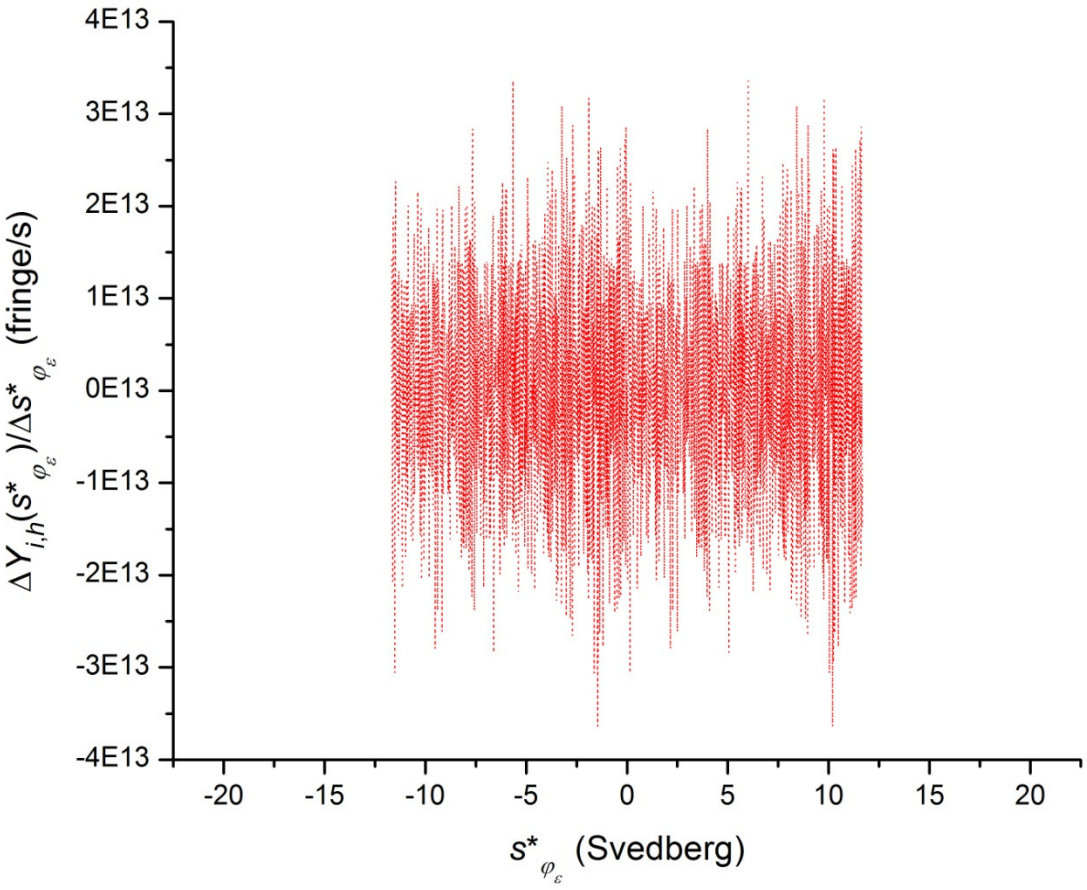

Figure 55c. $\Delta Y_{i,h}(s^*_{\varphi_\epsilon})/\Delta s^*_{\varphi_\epsilon}$ versus $s^*_{\varphi_\epsilon}$ at $t_\epsilon = t_{66}$ (·····), where $i = 0$ and $h = 1$. As $i = 0$, $Y_{i,h}(s^*_{\varphi_\epsilon}) =$

$\Delta GRN_{i,h}(s^*_{\varphi_\epsilon})$. Figure 54 shows $Y_{i,h}(s^*_{\varphi_\epsilon})$, of which $\Delta Y_{i,h}(s^*_{\varphi_\epsilon})/\Delta s^*_{\varphi_\epsilon}$ is the approximate derivative with respect to $s^*_{\varphi_\epsilon}$ (Equation 8). At any given time, the standard deviation (Equation 122b) of $\Delta Y_{i,h}(s^*_{\varphi_\epsilon})/\Delta s^*_{\varphi_\epsilon}$ about its mean (Equation 122a) varies systematically from one narrow range of $s^*_{\varphi_\epsilon}$ values to another within the entire range of $s^*_{\varphi_\epsilon}$, across which, $\Delta Y_{i,h}(s^*_{\varphi_\epsilon})/\Delta s^*_{\varphi_\epsilon}$ is proportional to $1/\Delta s^*_{\varphi_{\epsilon=j}} = 1/\Delta s^*_{\varphi_{\epsilon=N+j}} = \omega^2 t_\epsilon r_j/\Delta r_j$ (Equation 117). As in this figure, at any given time, the proportionality of $\Delta Y_{i,h}(s^*_{\varphi_\epsilon})/\Delta s^*_{\varphi_\epsilon}$ to $r_j/\Delta r_j$ produces fairly subtle effects across $s^*_{\varphi_\epsilon}$. The proportionality of $\Delta Y_{i,h}(s^*_{\varphi_\epsilon})/\Delta s^*_{\varphi_\epsilon}$ to t_ϵ produces obvious effects across time, as is shown by a comparison of Figures 55a, 55b and 55c, which apply to $t_\epsilon = t_{36}$, $t_\epsilon = t_{51}$ and $t_\epsilon = t_{66}$, respectively.

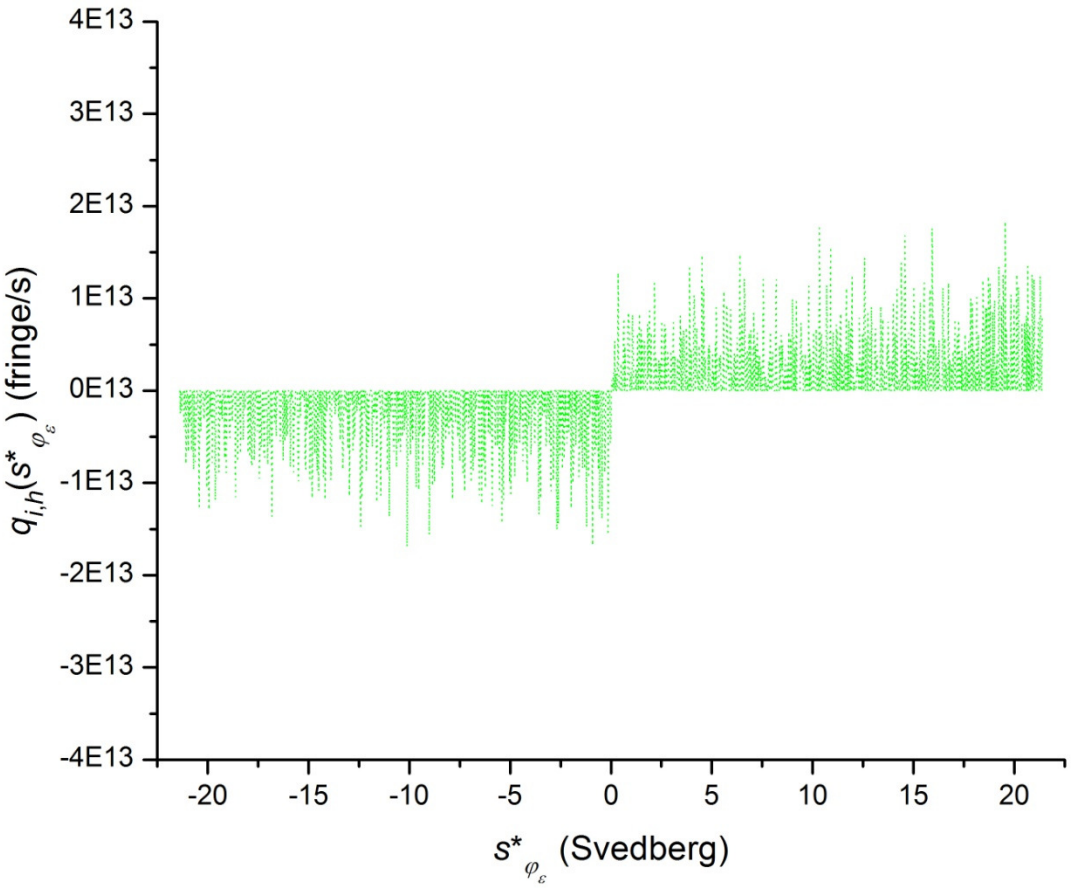

Figure 56a. $q_{i,h}(s^*_{\varphi_\epsilon})$ versus $s^*_{\varphi_\epsilon}$ at $t_\epsilon = t_{36}$ (·····), where $i = 0$ and $h = 1$. As $i = 0$, $q_{i,h}(s^*_{\varphi_\epsilon})$ in this

figure has its source in a noise-free signal (Figures 52 to 55). The nonredundant derivative of $Y_{i,h}(s^*_{\varphi_\epsilon})$ with respect to $s^*_{\varphi_\epsilon}$ at time t_ϵ for replicate h of treatment group i is $q_{i,h}(s^*_{\varphi_\epsilon}) = \left(\frac{\partial Y_{i,h}(s^*_{\varphi_\epsilon})}{\partial s^*_{\varphi_\epsilon}}\right)_t - e_{i,h}(s^*_{\varphi_\epsilon})$ (Equation 9a), in which the elimination function, $e_{i,h}(s^*_{\varphi_\epsilon})$, is equal to zero if $s^*_{\varphi_\epsilon}\left(\frac{\partial Y_{i,h}(s^*_{\varphi_\epsilon})}{\partial s^*_{\varphi_\epsilon}}\right)_t \geq 0$ and is equal to $\left(\frac{\partial Y_{i,h}(s^*_{\varphi_\epsilon})}{\partial s^*_{\varphi_\epsilon}}\right)_t$ otherwise (Equation 9a), with $\left(\frac{\partial Y_{i,h}(s^*_{\varphi_\epsilon})}{\partial s^*_{\varphi_\epsilon}}\right)_t$ being approximated as $\Delta Y_{i,h}(s^*_{\varphi_\epsilon})/\Delta s^*_{\varphi_\epsilon}$(Figure 55a). Thus, the proportionality of nonzero values of $\Delta Y_{i,h}(s^*_{\varphi_\epsilon})/\Delta s^*_{\varphi_\epsilon}$ to$1/\Delta s^*_{\varphi_{\epsilon=j}} = 1/\Delta s^*_{\varphi_{\epsilon=N+j}} = \omega^2 t_\epsilon r_j/\Delta r_j$ (Equation 117) is inherited by $q_{i,h}(s^*_{\varphi_\epsilon})$ wherever $e_{i,h}(s^*_{\varphi_\epsilon}) = 0$. As such, at any given time, the standard deviation (Equation 123b) of $q_{i,h}(s^*_{\varphi_\epsilon})$ about its mean (Equation 123a) varies systematically from one narrow range of $s^*_{\varphi_\epsilon}$ values to another.

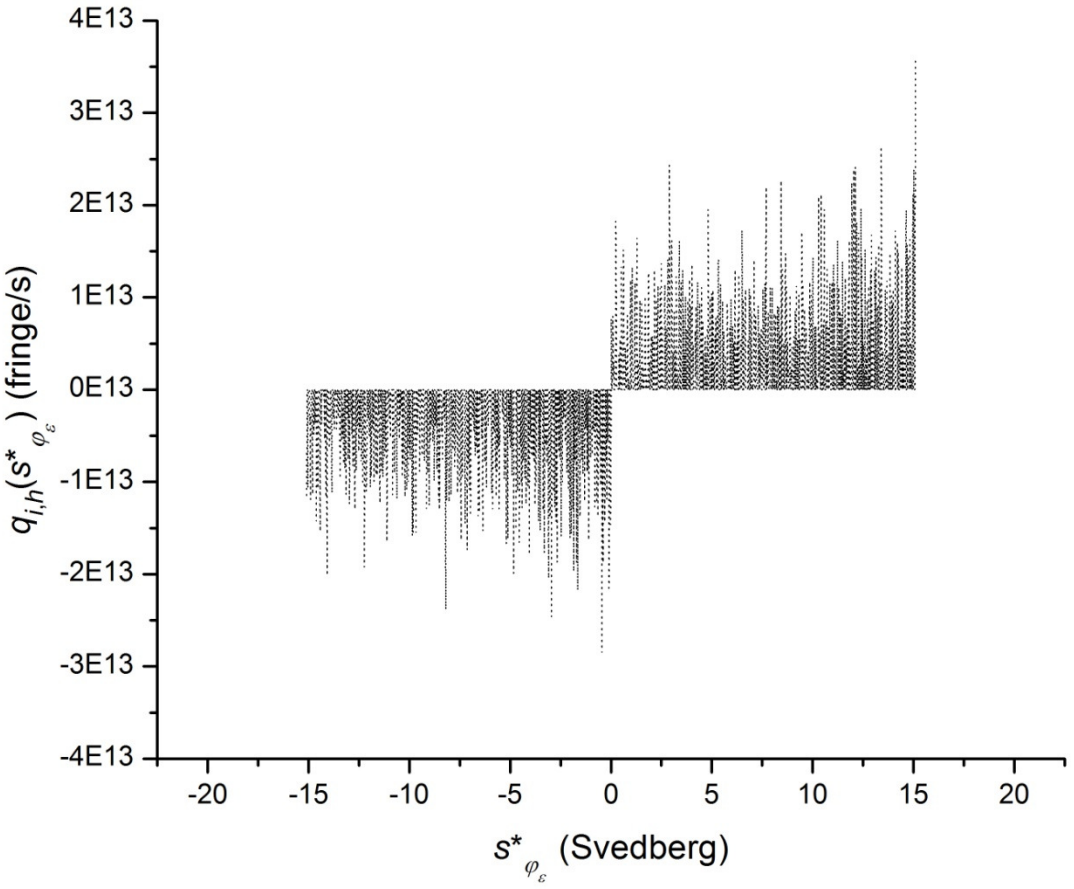

Figure 56b. $q_{i,h}(s^*_{\varphi_\epsilon})$ versus $s^*_{\varphi_\epsilon}$ at $t_\epsilon = t_{51}$ (·····), where $i = 0$ and $h = 1$. As $i = 0$, $q_{i,h}(s^*_{\varphi_\epsilon})$ in this figure has its source in a noise-free signal (Figures 52 to 55). The nonredundant derivative of $Y_{i,h}(s^*_{\varphi_\epsilon})$ with respect to $s^*_{\varphi_\epsilon}$ at time t_ϵ for replicate h of treatment group i is $q_{i,h}(s^*_{\varphi_\epsilon}) = \left(\frac{\partial Y_{i,h}(s^*_{\varphi_\epsilon})}{\partial s^*_{\varphi_\epsilon}}\right)_t - e_{i,h}(s^*_{\varphi_\epsilon})$ (Equation 9a), in which the elimination function, $e_{i,h}(s^*_{\varphi_\epsilon})$, is equal to zero if $s^*_{\varphi_\epsilon}\left(\frac{\partial Y_{i,h}(s^*_{\varphi_\epsilon})}{\partial s^*_{\varphi_\epsilon}}\right)_t \geq 0$ and is equal to $\left(\frac{\partial Y_{i,h}(s^*_{\varphi_\epsilon})}{\partial s^*_{\varphi_\epsilon}}\right)_t$ otherwise (Equation 9a), with $\left(\frac{\partial Y_{i,h}(s^*_{\varphi_\epsilon})}{\partial s^*_{\varphi_\epsilon}}\right)_t$ being approximated as $\Delta Y_{i,h}(s^*_{\varphi_\epsilon})/\Delta s^*_{\varphi_\epsilon}$(Figure 55b). Thus, the proportionality of nonzero values of $\Delta Y_{i,h}(s^*_{\varphi_\epsilon})/\Delta s^*_{\varphi_\epsilon}$ to$1/\Delta s^*_{\varphi_{\epsilon=j}} = 1/\Delta s^*_{\varphi_{\epsilon=N+j}} = \omega^2 t_\epsilon r_j/\Delta r_j$ (Equation 117) is inherited by $q_{i,h}(s^*_{\varphi_\epsilon})$ wherever $e_{i,h}(s^*_{\varphi_\epsilon}) = 0$. As such, at any given time, the standard deviation (Equation 123b) of

$q_{i,h}(s^*_{\varphi_\epsilon})$ about its mean (Equation 123a) varies systematically from one narrow range of $s^*_{\varphi_\epsilon}$ values to another.

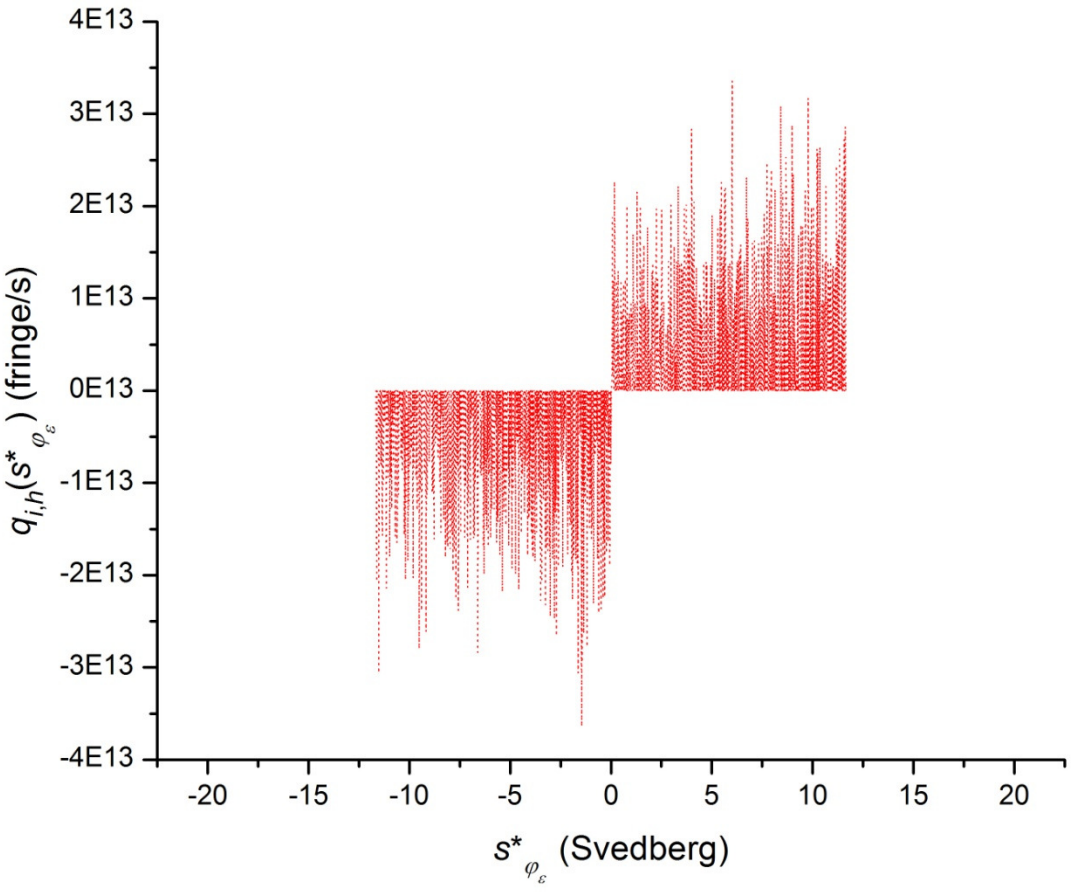

Figure 56c. $q_{i,h}(s^*_{\varphi_\epsilon})$ versus $s^*_{\varphi_\epsilon}$ at $t_\epsilon = t_{66}$ (·····), where $i = 0$ and $h = 1$. As $i = 0$, $q_{i,h}(s^*_{\varphi_\epsilon})$ in this figure has its source in a noise-free signal (Figures 52 to 55). The nonredundant derivative of $Y_{i,h}(s^*_{\varphi_\epsilon})$ with respect to $s^*_{\varphi_\epsilon}$ at time t_ϵ for replicate h of treatment group i is $q_{i,h}(s^*_{\varphi_\epsilon}) = \left(\frac{\partial Y_{i,h}(s^*_{\varphi_\epsilon})}{\partial s^*_{\varphi_\epsilon}}\right)_t - e_{i,h}(s^*_{\varphi_\epsilon})$ (Equation 9a), in which the elimination function, $e_{i,h}(s^*_{\varphi_\epsilon})$, is equal to zero if $s^*_{\varphi_\epsilon}\left(\frac{\partial Y_{i,h}(s^*_{\varphi_\epsilon})}{\partial s^*_{\varphi_\epsilon}}\right)_t \geq 0$ and is equal to $\left(\frac{\partial Y_{i,h}(s^*_{\varphi_\epsilon})}{\partial s^*_{\varphi_\epsilon}}\right)_t$ otherwise (Equation 9a), with $\left(\frac{\partial Y_{i,h}(s^*_{\varphi_\epsilon})}{\partial s^*_{\varphi_\epsilon}}\right)_t$ being approximated as $\Delta Y_{i,h}(s^*_{\varphi_\epsilon})/\Delta s^*_{\varphi_\epsilon}$ (Figure 55c). Thus, the proportionality of nonzero values of

$\Delta Y_{i,h}(s^*_{\varphi_\epsilon})/\Delta s^*_{\varphi_\epsilon}$ to$1/\Delta s^*_{\varphi_{\epsilon=j}} = 1/\Delta s^*_{\varphi_{\epsilon=N+j}} = \omega^2 t_\epsilon r_j/\Delta r_j$ (Equation 117) is inherited by $q_{i,h}(s^*_{\varphi_\epsilon})$ wherever $e_{i,h}(s^*_{\varphi_\epsilon}) = 0$. As such, at any given time, the standard deviation (Equation 123b) of $q_{i,h}(s^*_{\varphi_\epsilon})$ about its mean (Equation 123a) varies systematically from one narrow range of $s^*_{\varphi_\epsilon}$ values to another.

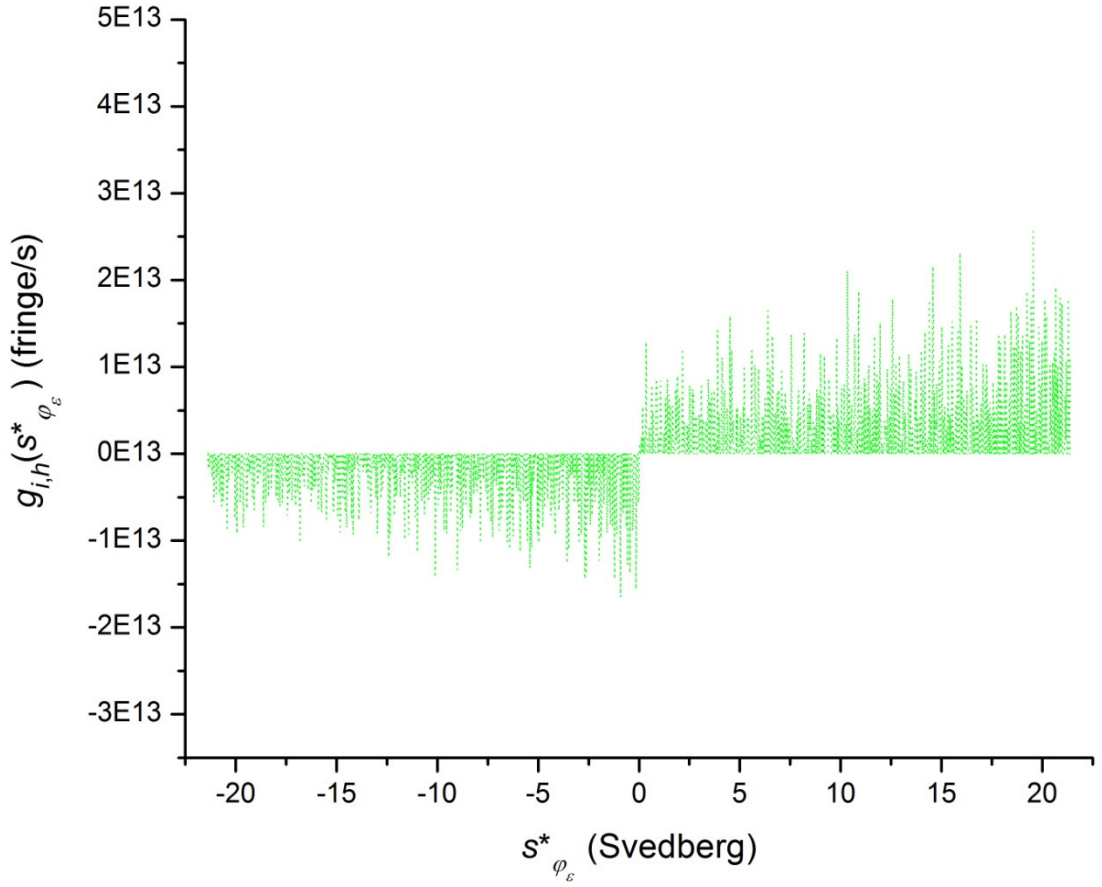

Figure 57a. $g_{i,h}(s^*_{\varphi_\epsilon})$ versus $s^*_{\varphi_\epsilon}$ at $t_\epsilon = t_{36}$ (·····), where $i = 0$ and $h = 1$. As $i = 0$, $g_{i,h}(s^*_{\varphi_\epsilon})$ in this figure has its source in a noise-free signal (Figures 52 to 56). The apparent sedimentation coefficient distribution function for replicate h of treatment group i at time t_ϵ is, by Equation 10, $g_{i,h}(s^*_{\varphi_\epsilon}) = q_{i,h}(s^*_{\varphi_\epsilon})(e^{2s^*_{\varphi_\epsilon}\omega^2 t_\epsilon})$. Multiplication of $q_{i,h}(s^*_{\varphi_\epsilon})$ by $e^{2s^*_{\varphi_\epsilon}\omega^2 t_\epsilon}$ yields a product that is normalised for the radial dilution or radial concentration effect that a hypothetical solute

characterised by $s^*_{\varphi_\epsilon}$ would have accumulated by time t_ϵ. As a consequence of being proportional to both $q_{i,h}(s^*_{\varphi_\epsilon})$ and $e^{2s^*_{\varphi_\epsilon}\omega^2 t_\epsilon}$, $g_{i,h}(s^*_{\varphi_\epsilon})$ inherits $e^{2s^*_{\varphi_\epsilon}\omega^2 t_\epsilon}$ times the systematic $s^*_{\varphi_\epsilon}$ dependence of the standard deviation of $q_{i,h}(s^*_{\varphi_\epsilon})$ about its mean. Thus, from one narrow range of $s^*_{\varphi_\epsilon}$ values to another, the systematic $s^*_{\varphi_\epsilon}$ dependence of the standard deviation (Equation 124b) about the mean (Equation 124a) is greater for $g_{i,h}(s^*_{\varphi_\epsilon})$ than it is for $q_{i,h}(s^*_{\varphi_\epsilon})$ at any given time.

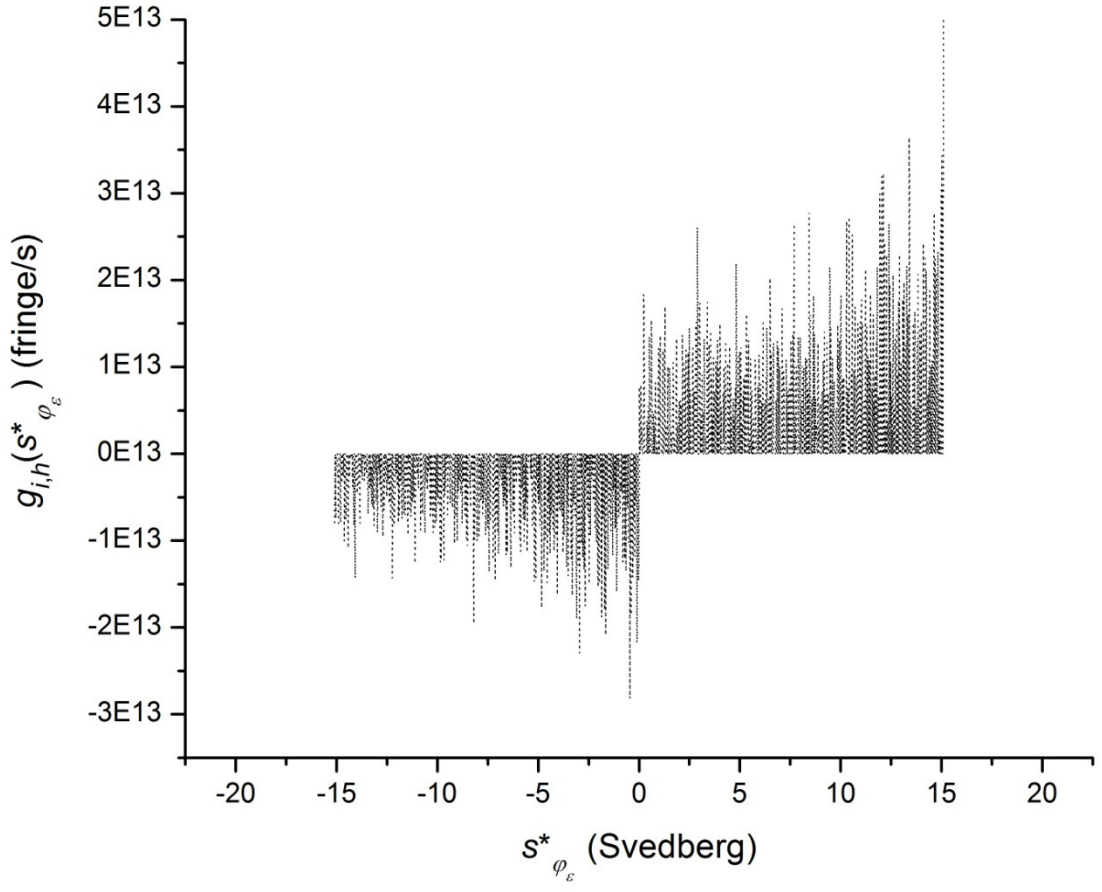

Figure 57b. $g_{i,h}(s^*_{\varphi_\epsilon})$ versus $s^*_{\varphi_\epsilon}$ at $t_\epsilon = t_{51}$ (·····), where $i = 0$ and $h = 1$. As $i = 0$, $g_{i,h}(s^*_{\varphi_\epsilon})$ in this figure has its source in a noise-free signal (Figures 52 to 56). The apparent sedimentation coefficient distribution function for replicate h of treatment group i at time t_ϵ is, by Equation 10, $g_{i,h}(s^*_{\varphi_\epsilon}) = q_{i,h}(s^*_{\varphi_\epsilon})(e^{2s^*_{\varphi_\epsilon}\omega^2 t_\epsilon})$. Multiplication of $q_{i,h}(s^*_{\varphi_\epsilon})$ by $e^{2s^*_{\varphi_\epsilon}\omega^2 t_\epsilon}$ yields a product that is

normalised for the radial dilution or radial concentration effect that a hypothetical solute characterised by $s^*_{\varphi_\epsilon}$ would have accumulated by time t_ϵ. As a consequence of being proportional to both $q_{i,h}(s^*_{\varphi_\epsilon})$ and $e^{2s^*_{\varphi_\epsilon}\omega^2 t_\epsilon}$, $g_{i,h}(s^*_{\varphi_\epsilon})$ inherits $e^{2s^*_{\varphi_\epsilon}\omega^2 t_\epsilon}$ times the systematic $s^*_{\varphi_\epsilon}$ dependence of the standard deviation of $q_{i,h}(s^*_{\varphi_\epsilon})$ about its mean. Thus, from one narrow range of $s^*_{\varphi_\epsilon}$ values to another, the systematic $s^*_{\varphi_\epsilon}$ dependence of the standard deviation (Equation 124b) about the mean (Equation 124a) is greater for $g_{i,h}(s^*_{\varphi_\epsilon})$ than it is for $q_{i,h}(s^*_{\varphi_\epsilon})$ at any given time.

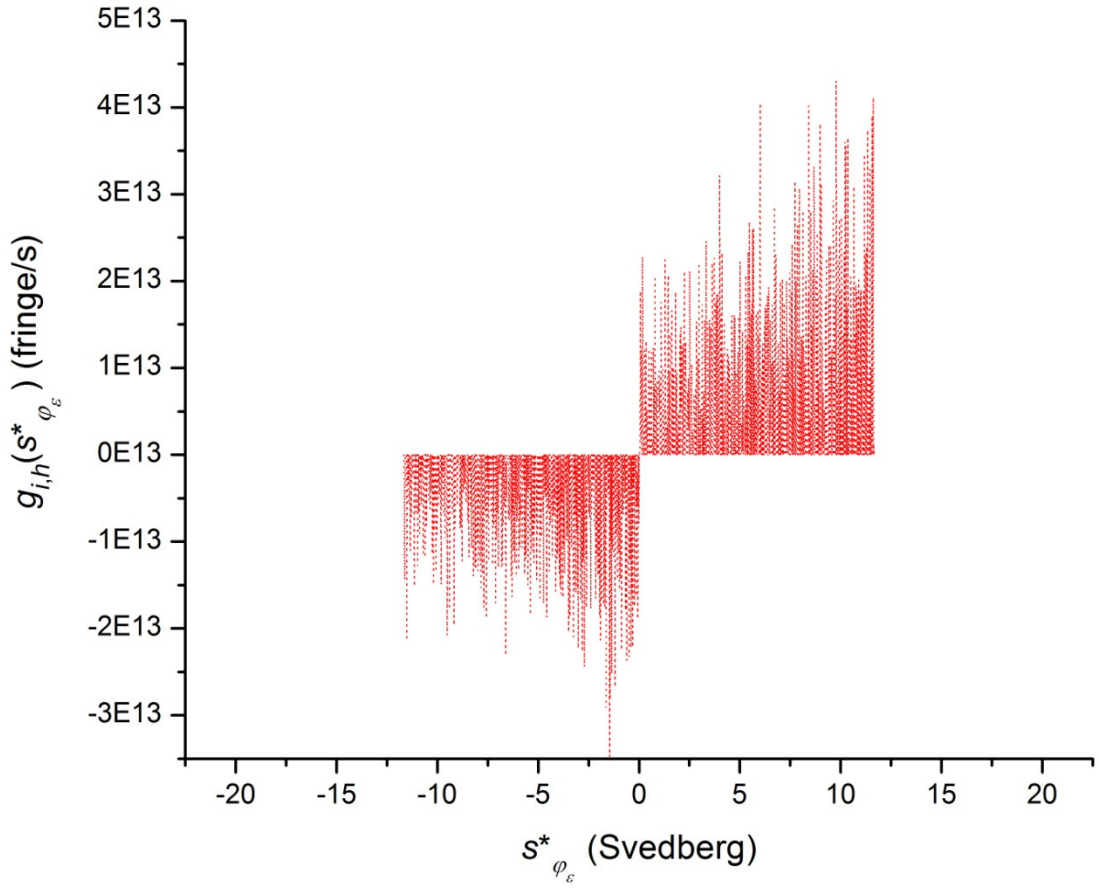

Figure 57c. $g_{i,h}(s^*_{\varphi_\epsilon})$ versus $s^*_{\varphi_\epsilon}$ at $t_\epsilon = t_{66}$ (·····), where $i = 0$ and $h = 1$. As $i = 0$, $g_{i,h}(s^*_{\varphi_\epsilon})$ in this figure has its source in a noise-free signal (Figures 52 to 56). The apparent sedimentation coefficient distribution function for replicate h of treatment group i at time t_ϵ is, by Equation 10,

$g_{i,h}\left(s^*_{\varphi_\epsilon}\right) = q_{i,h}\left(s^*_{\varphi_\epsilon}\right)\left(e^{2s^*_{\varphi_\epsilon}\omega^2 t_\epsilon}\right)$. Multiplication of $q_{i,h}\left(s^*_{\varphi_\epsilon}\right)$ by $e^{2s^*_{\varphi_\epsilon}\omega^2 t_\epsilon}$ yields a product that is normalised for the radial dilution or radial concentration effect that a hypothetical solute characterised by $s^*_{\varphi_\epsilon}$ would have accumulated by time t_ϵ. As a consequence of being proportional to both $q_{i,h}\left(s^*_{\varphi_\epsilon}\right)$ and $e^{2s^*_{\varphi_\epsilon}\omega^2 t_\epsilon}$, $g_{i,h}\left(s^*_{\varphi_\epsilon}\right)$ inherits $e^{2s^*_{\varphi_\epsilon}\omega^2 t_\epsilon}$ times the systematic $s^*_{\varphi_\epsilon}$ dependence of the standard deviation of $q_{i,h}\left(s^*_{\varphi_\epsilon}\right)$ about its mean. Thus, from one narrow range of $s^*_{\varphi_\epsilon}$ values to another, the systematic $s^*_{\varphi_\epsilon}$ dependence of the standard deviation (Equation 124b) about the mean (Equation 124a) is greater for $g_{i,h}\left(s^*_{\varphi_\epsilon}\right)$ than it is for $q_{i,h}\left(s^*_{\varphi_\epsilon}\right)$ at any given time.

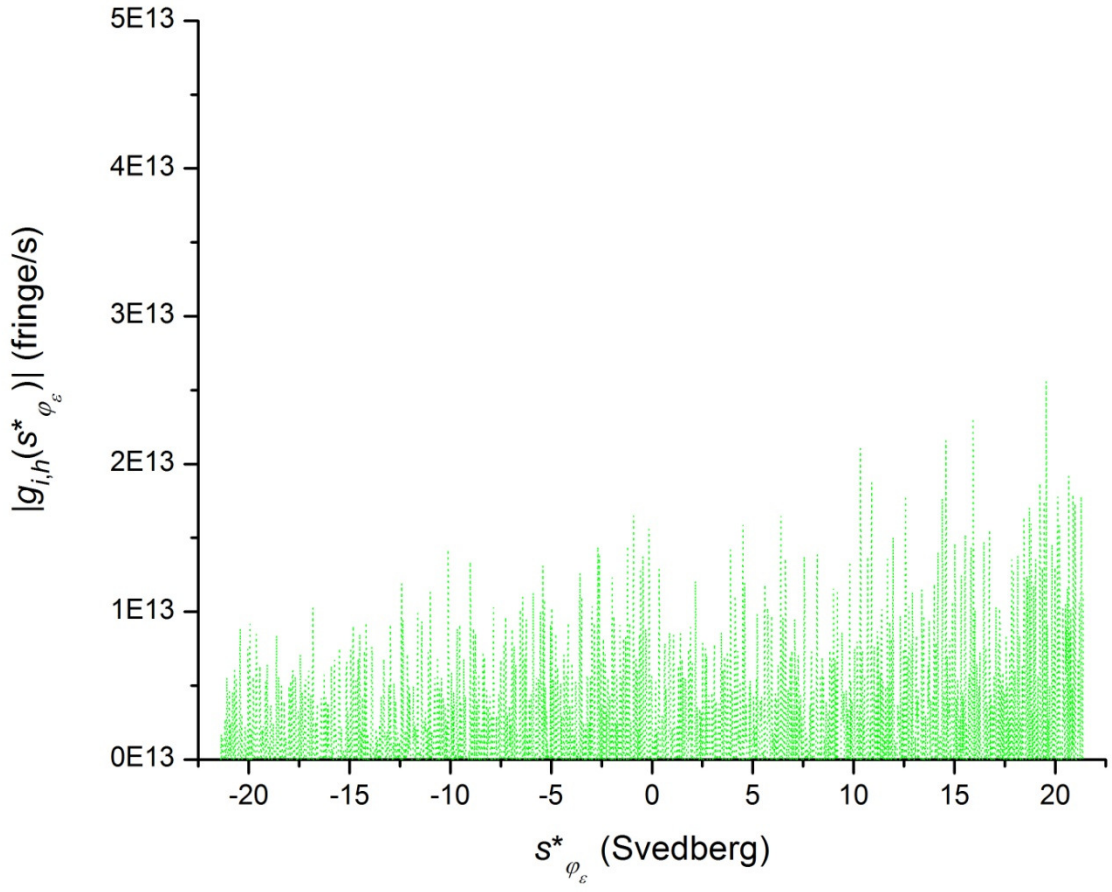

Figure 58a. $\left|g_{i,h}\left(s^*_{\varphi_\epsilon}\right)\right|$ versus $s^*_{\varphi_\epsilon}$ at $t_\epsilon = t_{36}$ (·····), where $i = 0$ and $h = 1$. As $i = 0$, $\left|g_{i,h}\left(s^*_{\varphi_\epsilon}\right)\right|$ in this figure has its source in a noise-free signal (Figures 52 to 57). At $t_\epsilon = t_{36}$, and at any other

given time, the standard deviation (Equation 125b) of $\left|g_{i,h}\left(s^*_{\varphi_\epsilon}\right)\right|$ about its mean (Equation 125a) varies systematically from one narrow range of $s^*_{\varphi_\epsilon}$ values to another. If, from one narrow range of $s^*_{\varphi_\epsilon}$ values to another, there were no systematic $s^*_{\varphi_\epsilon}$ dependence of the standard deviation about the mean of $\left|g_{i,h}\left(s^*_{\varphi_\epsilon}\right)\right|$, then $G_{i,h}\left(s^*_{\varphi_\epsilon}\right)$, the integral of $\left|g_{i,h}\left(s^*_{\varphi_\epsilon}\right)\right|$ from $s^*_{\varphi_\epsilon=1}$ to $s^*_{\varphi_\epsilon}$, would linearly approach $\left(s^*_{\varphi_\epsilon=2N} - s^*_{\varphi_\epsilon=1}\right)\langle\left|g_{i,h}\left(\left[s^*_{\varphi_\epsilon=1}, s^*_{\varphi_\epsilon=2N}\right]\right)\right|\rangle$ as $s^*_{\varphi_\epsilon}$ ranged from $s^*_{\varphi_\epsilon=1}$ to $s^*_{\varphi_\epsilon=2N}$, while $s^*_{i,h,\epsilon}\left(s^*_{\varphi_\epsilon=1}, s^*_{\varphi_\epsilon}\right)$, the weight-average sedimentation coefficient within $s^*_{\varphi_\epsilon=1}$ to $s^*_{\varphi_\epsilon}$, would linearly approach $s^*_{i,h,\epsilon}\left(s^*_{\varphi_\epsilon=1}, s^*_{\varphi_\epsilon=2N}\right) = 0$. As $\langle\left|g_{i,h}\left(\left[s^*_{\varphi_\epsilon=1}, s^*_{\varphi_\epsilon=2N}\right]\right)\right|\rangle$, the mean of all $\left|g_{i,h}\left(s^*_{\varphi_\epsilon}\right)\right|$ within the full range of $s^*_{\varphi_\epsilon}$ values at $t_\epsilon = t_{36}$ (Table 18: -21.3665E-13 s to 21.3709E-13 s), is equal to 2.49231E12 fringe/s, $\left(s^*_{\varphi_\epsilon=2N} - s^*_{\varphi_\epsilon=1}\right)\langle\left|g_{i,h}\left(\left[s^*_{\varphi_\epsilon=1}, s^*_{\varphi_\epsilon=2N}\right]\right)\right|\rangle = 10.65753$ fringe at $t_\epsilon = t_{36}$. Instead, at $t_\epsilon = t_{36}$, $G_{i,h}\left(s^*_{\varphi_\epsilon}\right)$ approaches $G_{i,h}\left(s^*_{\varphi_\epsilon=2N}\right) = 10.43303$ fringe with an approximately quadratic trend (Figure 59), while $s^*_{i,h,\epsilon}\left(s^*_{\varphi_\epsilon=1}, s^*_{\varphi_\epsilon}\right)$ approaches $s^*_{i,h,\epsilon}\left(s^*_{\varphi_\epsilon=1}, s^*_{\varphi_\epsilon=2N}\right) =$ 3.12830E-13 s with an approximately quadratic trend (Figure 62).

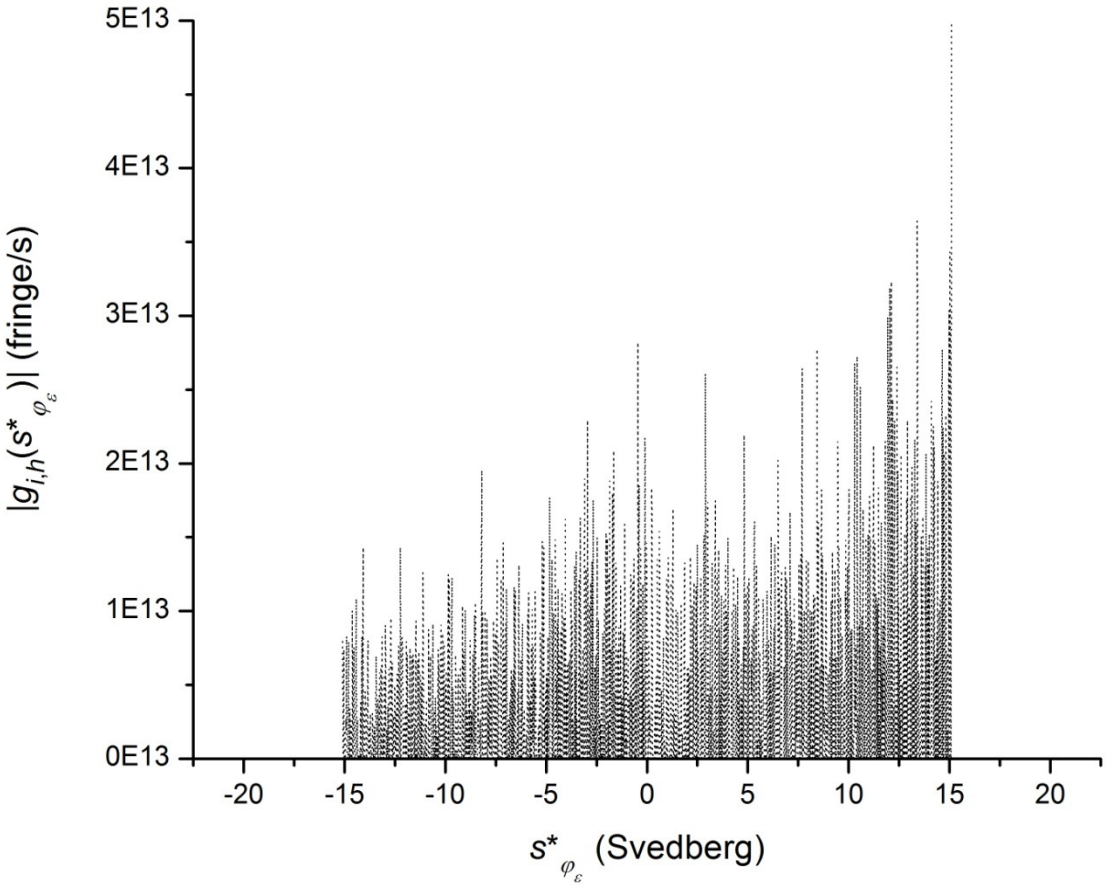

Figure 58b. $\left|g_{i,h}\left(s^*_{\varphi_\epsilon}\right)\right|$ versus $s^*_{\varphi_\epsilon}$ at $t_\epsilon = t_{51}$ (·····), where $i = 0$ and $h = 1$. As $i = 0$, $\left|g_{i,h}\left(s^*_{\varphi_\epsilon}\right)\right|$ in this figure has its source in a noise-free signal (Figures 52 to 57). At $t_\epsilon = t_{51}$, and at any other given time, the standard deviation (Equation 125b) of $\left|g_{i,h}\left(s^*_{\varphi_\epsilon}\right)\right|$ about its mean (Equation 125a) varies systematically from one narrow range of $s^*_{\varphi_\epsilon}$ values to another. If, from one narrow range of $s^*_{\varphi_\epsilon}$ values to another, there were no systematic $s^*_{\varphi_\epsilon}$ dependence of the standard deviation about the mean of $\left|g_{i,h}\left(s^*_{\varphi_\epsilon}\right)\right|$, then $G_{i,h}\left(s^*_{\varphi_\epsilon}\right)$, the integral of $\left|g_{i,h}\left(s^*_{\varphi_\epsilon}\right)\right|$ from $s^*_{\varphi_{\epsilon=1}}$ to $s^*_{\varphi_\epsilon}$, would linearly approach $\left(s^*_{\varphi_{\epsilon=2N}} - s^*_{\varphi_{\epsilon=1}}\right)\langle\left|g_{i,h}\left(\left[s^*_{\varphi_{\epsilon=1}}, s^*_{\varphi_{\epsilon=2N}}\right]\right)\right|\rangle$ as $s^*_{\varphi_\epsilon}$ ranged from $s^*_{\varphi_{\epsilon=1}}$ to $s^*_{\varphi_{\epsilon=2N}}$, while $s^*_{i,h,\epsilon}\left(s^*_{\varphi_{\epsilon=1}}, s^*_{\varphi_\epsilon}\right)$, the weight-average sedimentation coefficient within $s^*_{\varphi_{\epsilon=1}}$ to $s^*_{\varphi_\epsilon}$, would linearly approach $s^*_{i,h,\epsilon}\left(s^*_{\varphi_{\epsilon=1}}, s^*_{\varphi_{\epsilon=2N}}\right) = 0$. As $\langle\left|g_{i,h}\left(\left[s^*_{\varphi_{\epsilon=1}}, s^*_{\varphi_{\epsilon=2N}}\right]\right)\right|\rangle$, the mean of all $\left|g_{i,h}\left(s^*_{\varphi_\epsilon}\right)\right|$

within the full range of $s^*_{\varphi_\epsilon}$ values at $t_\epsilon = t_{51}$ (Table 18: -15.0822E-13 s to 15.0853E-13 s), is equal to 3.57702E12 fringe/s, $\left(s^*_{\varphi_{\epsilon=2N}} - s^*_{\varphi_{\epsilon=1}}\right)\langle\left|g_{i,h}\left(\left[s^*_{\varphi_{\epsilon=1}}, s^*_{\varphi_{\epsilon=2N}}\right]\right)\right|\rangle = 10.79711$ fringe at $t_\epsilon = t_{51}$. Instead, at $t_\epsilon = t_{51}$, $G_{i,h}\left(s^*_{\varphi_\epsilon}\right)$ approaches $G_{i,h}\left(s^*_{\varphi_{\epsilon=2N}}\right) = 10.50085$ fringe with an approximately quadratic trend (Figure 59), while $s^*_{i,h,\epsilon}\left(s^*_{\varphi_{\epsilon=1}}, s^*_{\varphi_\epsilon}\right)$ approaches $s^*_{i,h,\epsilon}\left(s^*_{\varphi_{\epsilon=1}}, s^*_{\varphi_{\epsilon=2N}}\right) =$ 2.25887E-13 s with an approximately quadratic trend (Figure 62).

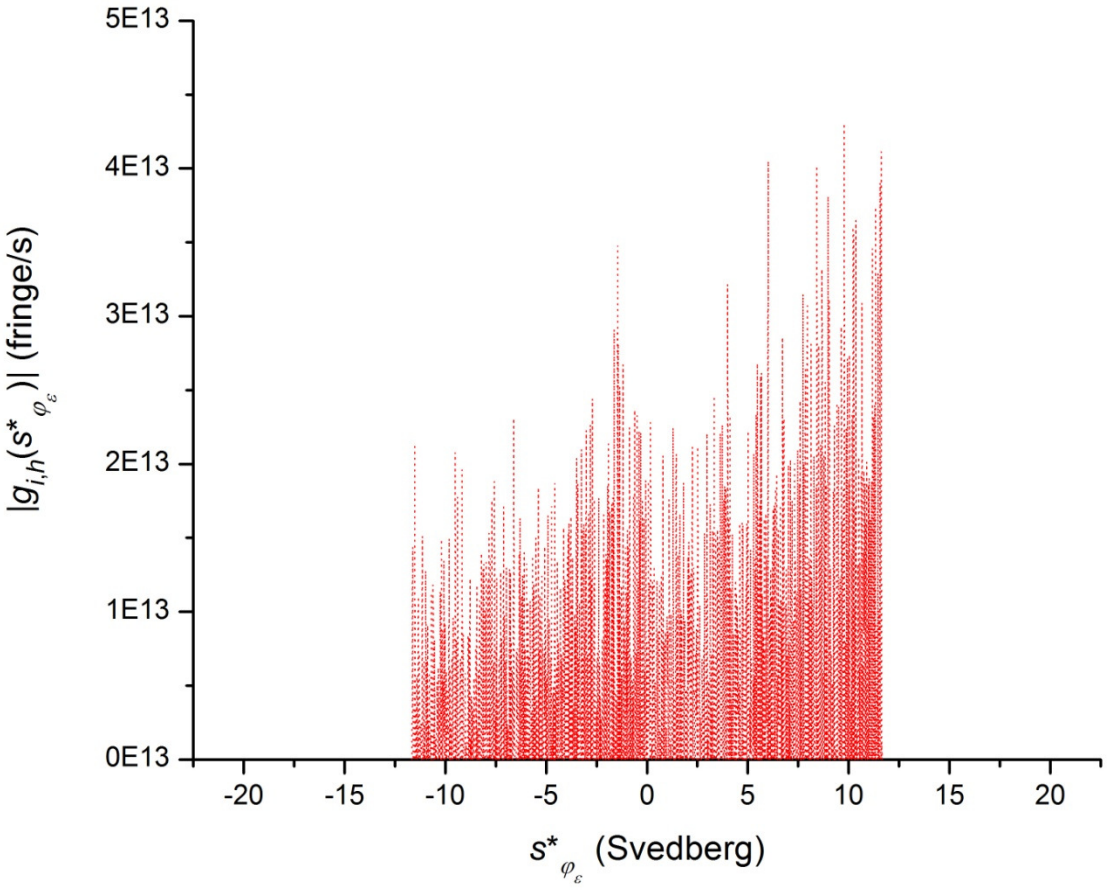

Figure 58c. $\left|g_{i,h}\left(s^*_{\varphi_\epsilon}\right)\right|$ versus $s^*_{\varphi_\epsilon}$ at $t_\epsilon = t_{66}$ (·····), where $i = 0$ and $h = 1$. As $i = 0$, $\left|g_{i,h}\left(s^*_{\varphi_\epsilon}\right)\right|$ in this figure has its source in a noise-free signal (Figures 52 to 57). At $t_\epsilon = t_{66}$, and at any other given time, the standard deviation (Equation 125b) of $\left|g_{i,h}\left(s^*_{\varphi_\epsilon}\right)\right|$ about its mean (Equation 125a) varies systematically from one narrow range of $s^*_{\varphi_\epsilon}$ values to another. If, from one narrow range

of $s^*_{\varphi_\epsilon}$ values to another, there were no systematic $s^*_{\varphi_\epsilon}$ dependence of the standard deviation about the mean of $\left|g_{i,h}\left(s^*_{\varphi_\epsilon}\right)\right|$, then $G_{i,h}\left(s^*_{\varphi_\epsilon}\right)$, the integral of $\left|g_{i,h}\left(s^*_{\varphi_\epsilon}\right)\right|$ from $s^*_{\varphi_{\epsilon=1}}$ to $s^*_{\varphi_\epsilon}$, would linearly approach $\left(s^*_{\varphi_{\epsilon=2N}} - s^*_{\varphi_{\epsilon=1}}\right)\langle\left|g_{i,h}\left(\left[s^*_{\varphi_{\epsilon=1}}, s^*_{\varphi_{\epsilon=2N}}\right]\right)\right|\rangle$ as $s^*_{\varphi_\epsilon}$ ranged from $s^*_{\varphi_{\epsilon=1}}$ to $s^*_{\varphi_{\epsilon=2N}}$, while $s^*_{i,h,\epsilon}\left(s^*_{\varphi_{\epsilon=1}}, s^*_{\varphi_\epsilon}\right)$, the weight-average sedimentation coefficient within $s^*_{\varphi_{\epsilon=1}}$ to $s^*_{\varphi_\epsilon}$, would linearly approach $s^*_{i,h,\epsilon}\left(s^*_{\varphi_{\epsilon=1}}, s^*_{\varphi_{\epsilon=2N}}\right) = 0$. As $\langle\left|g_{i,h}\left(\left[s^*_{\varphi_{\epsilon=1}}, s^*_{\varphi_{\epsilon=2N}}\right]\right)\right|\rangle$, the mean of all $\left|g_{i,h}\left(s^*_{\varphi_\epsilon}\right)\right|$ within the full range of $s^*_{\varphi_\epsilon}$ values at $t_\epsilon = t_{66}$ (Table 18: -11.6545E-13 s to 11.6568E-13 s), is equal to 4.65149E12 fringe/s, $\left(s^*_{\varphi_{\epsilon=2N}} - s^*_{\varphi_{\epsilon=1}}\right)\langle\left|g_{i,h}\left(\left[s^*_{\varphi_{\epsilon=1}}, s^*_{\varphi_{\epsilon=2N}}\right]\right)\right|\rangle = 10.84938$ fringe at $t_\epsilon = t_{66}$. Instead, at $t_\epsilon = t_{66}$, $G_{i,h}\left(s^*_{\varphi_\epsilon}\right)$ approaches $G_{i,h}\left(s^*_{\varphi_{\epsilon=2N}}\right) = 10.66301$ fringe with an approximately quadratic trend (Figure 59), while $s^*_{i,h,\epsilon}\left(s^*_{\varphi_{\epsilon=1}}, s^*_{\varphi_\epsilon}\right)$ approaches $s^*_{i,h,\epsilon}\left(s^*_{\varphi_{\epsilon=1}}, s^*_{\varphi_{\epsilon=2N}}\right) =$ 1.65244E-13 s with an approximately quadratic trend (Figure 62).

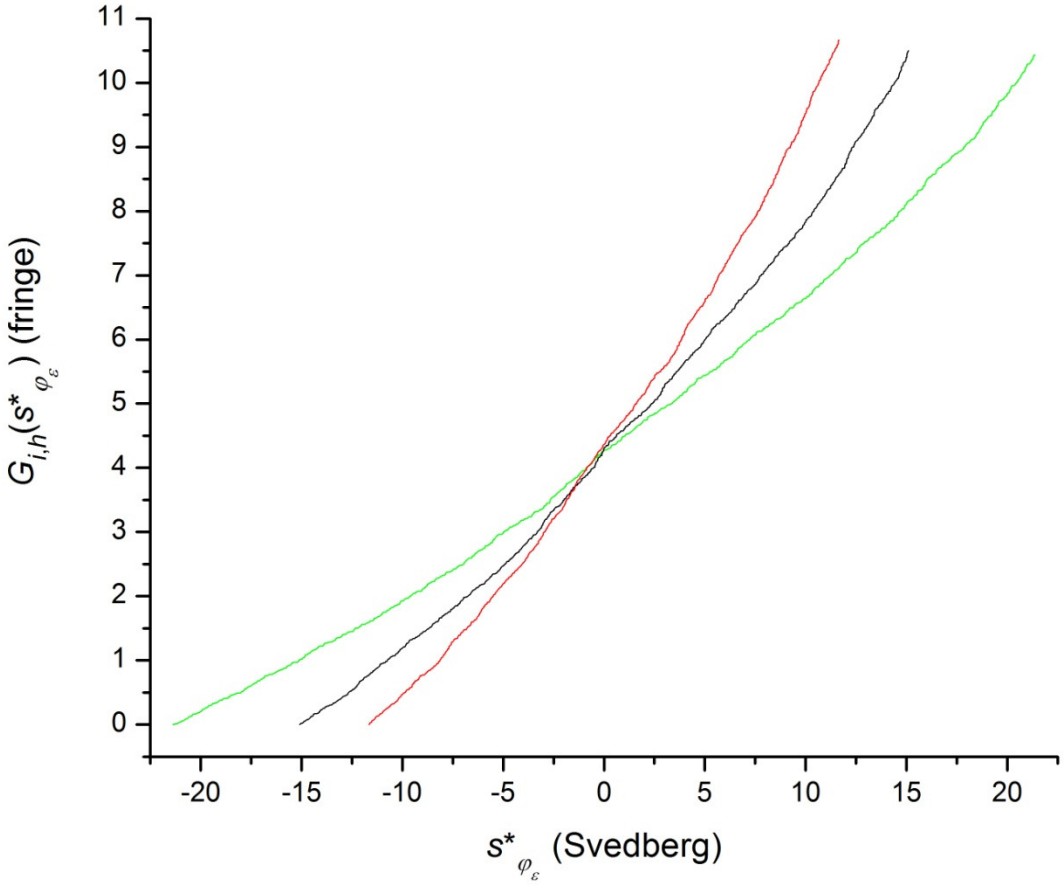

Figure 59. $G_{i,h}(s^*_{\varphi_\epsilon})$ versus $s^*_{\varphi_\epsilon}$ at $t_\epsilon = t_{36}$ (——), $t_\epsilon = t_{51}$ (——) and $t_\epsilon = t_{66}$ (——), where $i = 0$ and $h = 1$. As $i = 0$, $G_{i,h}(s^*_{\varphi_\epsilon})$, the integral with respect to $s^*_{\varphi_\epsilon}$ of $|g_{i,h}(s^*_{\varphi_\epsilon})|$ in the previous figure, has its source in a noise-free signal (Figures 52 to 58). As there are no masks (Figures 20 to 23; Figure 32) applied to the integrand, $|g_{i,h}(s^*_{\varphi_\epsilon})|$, or the data that give rise to it, $s^*_{min<0} = s^*_{\varphi_\epsilon=1}$, $s^*_{max<0} = s^*_{min>0} = 0$ and $s^*_{max>0} = s^*_{\varphi_\epsilon=2N}$ at time t_ϵ (Table 18 lists $s^*_{\varphi_\epsilon=1}$ and $= s^*_{\varphi_\epsilon=2N}$ at each time of analysis) are the limits applied to the integral that yields $G_{i,h}(s^*_{\varphi_\epsilon=2N})$ at time t_ϵ (Equation 77). For each value of $G_{i,h}(s^*_{\varphi_\epsilon})$ shown in this figure, the lower limit of integration is $s^*_{min<0} = s^*_{\varphi_\epsilon=1}$ at time t_ϵ, and the upper limit of integration ranges from $s^*_{min<0}$ to $s^*_{max>0} = s^*_{\varphi_\epsilon=2N}$ at time t_ϵ. Figures 58a, 58b and 58c show $|g_{i,h}(s^*_{\varphi_\epsilon})|$ for $t_\epsilon = t_{36}$, $t_\epsilon = t_{51}$ and $t_\epsilon = t_{66}$, respectively.

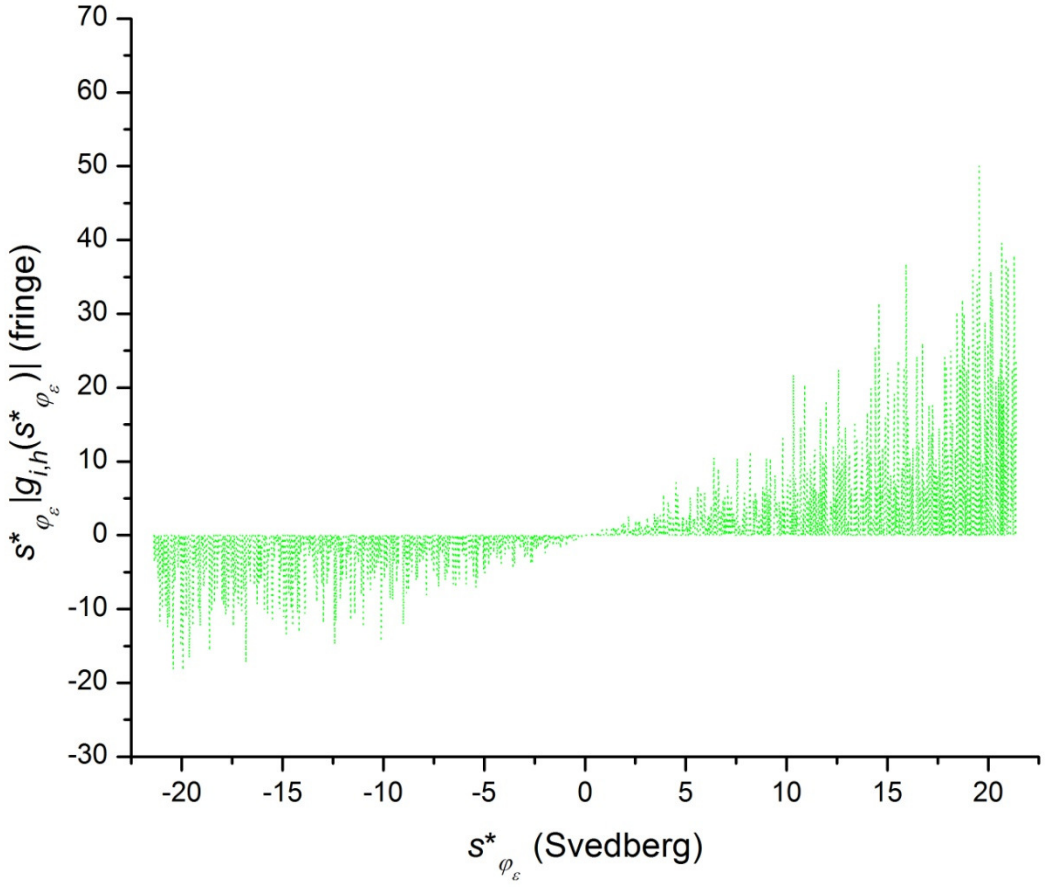

Figure 60a. $s^*_{\varphi_\epsilon}\left|g_{i,h}\left(s^*_{\varphi_\epsilon}\right)\right|$ versus $s^*_{\varphi_\epsilon}$ at $t_\epsilon = t_{36}$ (·····), where $i = 0$ and $h = 1$. Figures 60b and 60c show $s^*_{\varphi_\epsilon}\left|g_{i,h}\left(s^*_{\varphi_\epsilon}\right)\right|$ versus $s^*_{\varphi_\epsilon}$ at $t_\epsilon = t_{51}$ and $t_\epsilon = t_{66}$, respectively. Figure 61 shows the integral of $s^*_{\varphi_\epsilon}\left|g_{i,h}\left(s^*_{\varphi_\epsilon}\right)\right|$ with respect to $s^*_{\varphi_\epsilon}$ at each time of analysis, $t_\epsilon = t_{36}$, $t_\epsilon = t_{51}$ and $t_\epsilon = t_{66}$. As $i = 0$, $s^*_{\varphi_\epsilon}\left|g_{i,h}\left(s^*_{\varphi_\epsilon}\right)\right|$ in this figure has its source in a noise-free signal (Figures 52 to 58).

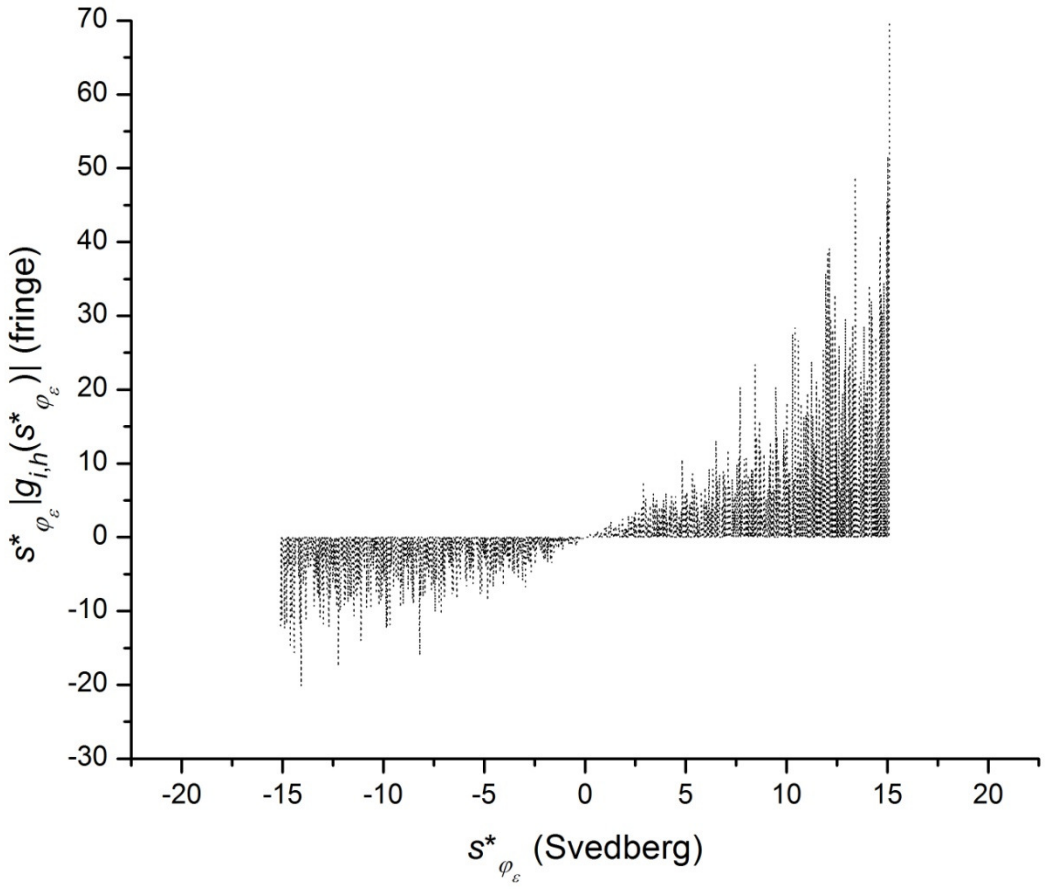

Figure 60b. $s^*_{\varphi_\epsilon}\left|g_{i,h}\left(s^*_{\varphi_\epsilon}\right)\right|$ versus $s^*_{\varphi_\epsilon}$ at $t_\epsilon = t_{51}$ (·····), where $i = 0$ and $h = 1$. Figures 60a and 60c show $s^*_{\varphi_\epsilon}\left|g_{i,h}\left(s^*_{\varphi_\epsilon}\right)\right|$ versus $s^*_{\varphi_\epsilon}$ at $t_\epsilon = t_{36}$ and $t_\epsilon = t_{66}$, respectively. Figure 61 shows the integral of $s^*_{\varphi_\epsilon}\left|g_{i,h}\left(s^*_{\varphi_\epsilon}\right)\right|$ with respect to $s^*_{\varphi_\epsilon}$ at each time of analysis, $t_\epsilon = t_{36}$, $t_\epsilon = t_{51}$ and $t_\epsilon = t_{66}$. As $i = 0$, $s^*_{\varphi_\epsilon}\left|g_{i,h}\left(s^*_{\varphi_\epsilon}\right)\right|$ in this figure has its source in a noise-free signal (Figures 52 to 58).

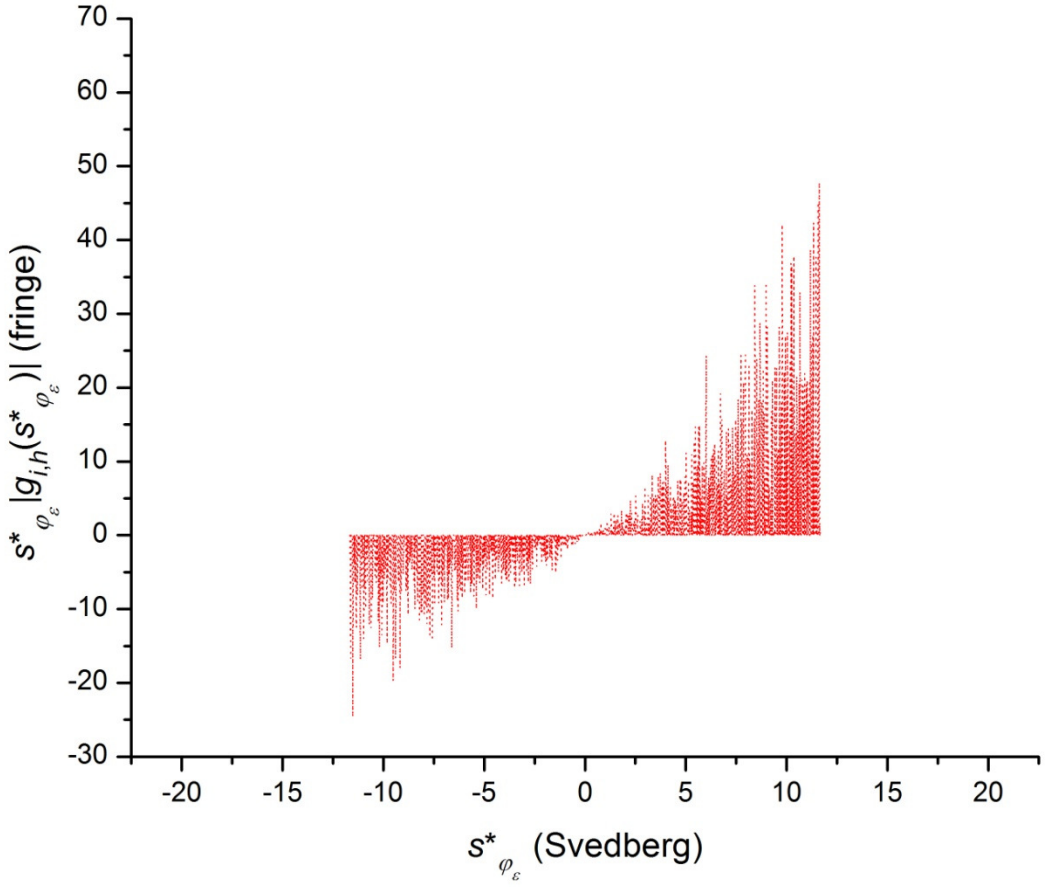

Figure 60c. $s^*_{\varphi_\epsilon}\left|g_{i,h}\left(s^*_{\varphi_\epsilon}\right)\right|$ versus $s^*_{\varphi_\epsilon}$ at $t_\epsilon = t_{66}$ (·····), where $i = 0$ and $h = 1$. Figures 60a and 60b show $s^*_{\varphi_\epsilon}\left|g_{i,h}\left(s^*_{\varphi_\epsilon}\right)\right|$ versus $s^*_{\varphi_\epsilon}$ at $t_\epsilon = t_{36}$ and $t_\epsilon = t_{51}$, respectively. Figure 61 shows the integral of $s^*_{\varphi_\epsilon}\left|g_{i,h}\left(s^*_{\varphi_\epsilon}\right)\right|$ with respect to $s^*_{\varphi_\epsilon}$ at each time of analysis, $t_\epsilon = t_{36}$, $t_\epsilon = t_{51}$ and $t_\epsilon = t_{66}$. As $i = 0$, $s^*_{\varphi_\epsilon}\left|g_{i,h}\left(s^*_{\varphi_\epsilon}\right)\right|$ in this figure has its source in a noise-free signal (Figures 52 to 58).

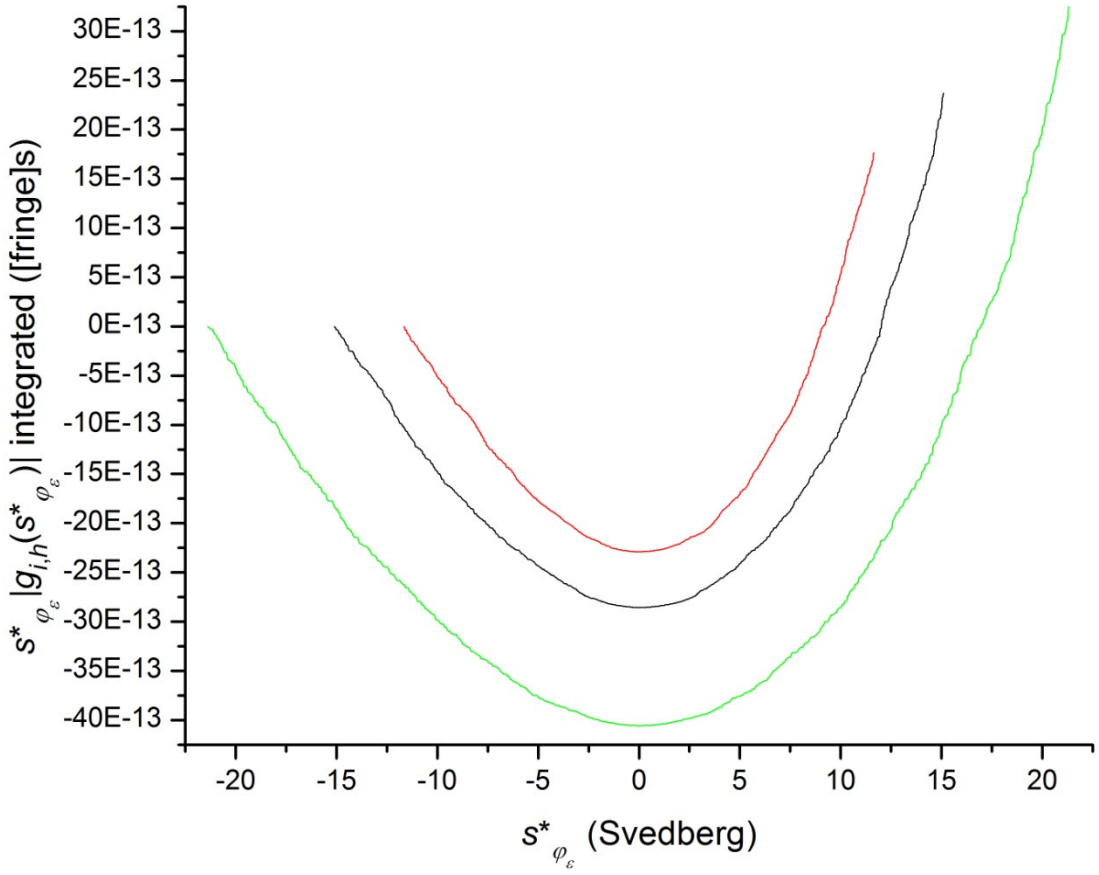

Figure 61. The integral of $s^*_{\varphi_\epsilon}\left|g_{i,h}\left(s^*_{\varphi_\epsilon}\right)\right|$ with respect to $s^*_{\varphi_\epsilon}$ at $t_\epsilon = t_{36}$ (——), $t_\epsilon = t_{51}$ (——) and $t_\epsilon = t_{66}$ (——), where $i = 0$ and $h = 1$. As $i = 0$, the integral of $s^*_{\varphi_\epsilon}\left|g_{i,h}\left(s^*_{\varphi_\epsilon}\right)\right|$ in this figure has its source in a noise-free signal (Figures 52 to 60). Figures 60a, 60b and 60c show $s^*_{\varphi_\epsilon}\left|g_{i,h}\left(s^*_{\varphi_\epsilon}\right)\right|$ for $t_\epsilon = t_{36}, t_\epsilon = t_{51}$ and $t_\epsilon = t_{66}$, respectively. As there are no masks (Figures 20 to 23; Figure 32) applied to the integrand, $s^*_{\varphi_\epsilon}\left|g_{i,h}\left(s^*_{\varphi_\epsilon}\right)\right|$, or the data that give rise to it, $s^*_{min<0} = s^*_{\varphi_{\epsilon=1}}$, $s^*_{max<0} = s^*_{min>0} = 0$ and $s^*_{max>0} = s^*_{\varphi_{\epsilon=2N}}$ at time t_ϵ (Table 18 lists $s^*_{\varphi_{\epsilon=1}}$ and $= s^*_{\varphi_{\epsilon=2N}}$ at each time of analysis) are the limits applied to the integral that, upon division by $G_{i,h}\left(s^*_{\varphi_{\epsilon=2N}}\right)$ at time t_ϵ (Equation 77; Figure 59), yields $s^*_{i,h,\epsilon}\left(s^*_{\varphi_{\epsilon=1}}, s^*_{\varphi_{\epsilon=2N}}\right)$ at time t_ϵ (Equation 81a; Figure 62). For each value of the integral (the numerator of Equation 81a) shown in this figure, the lower limit of integration is $s^*_{min<0} =$

$s^*_{\varphi_\epsilon=1}$ at time t_ϵ, and the upper limit of integration ranges from $s^*_{min<0}$ to $s^*_{max>0} = s^*_{\varphi_\epsilon=2N}$ at time t_ϵ.

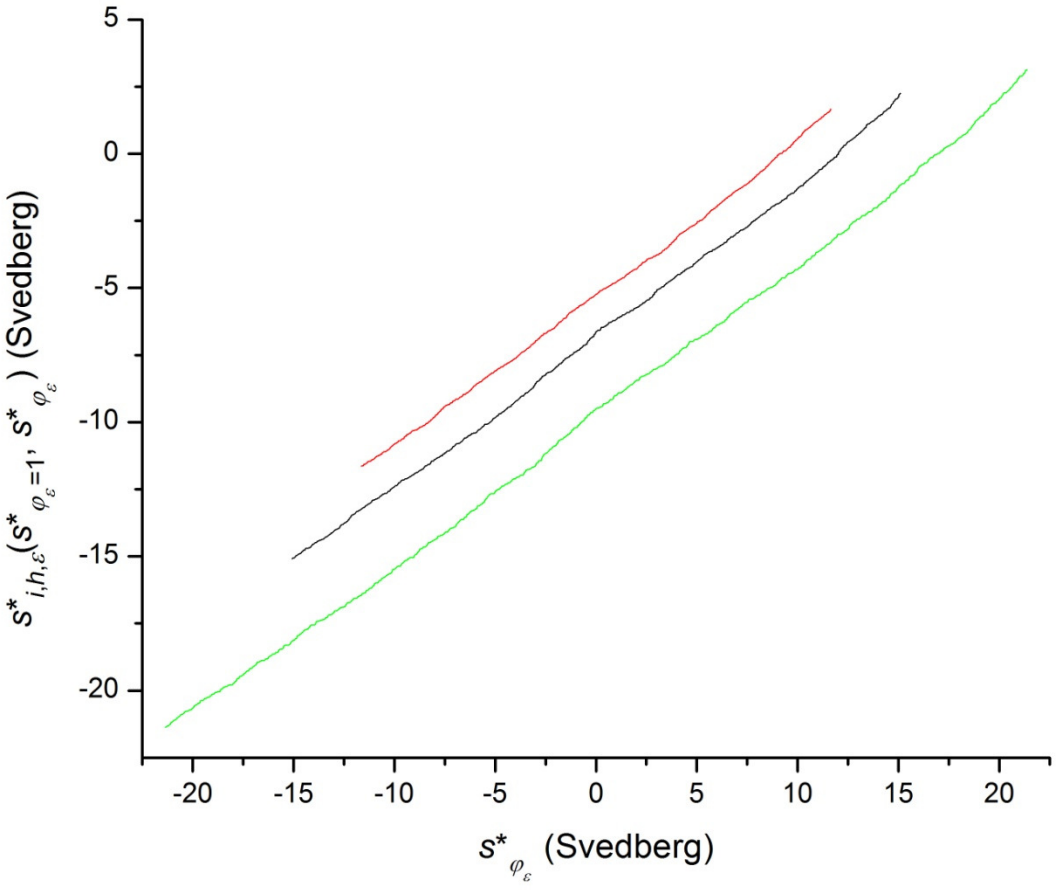

Figure 62. $s^*_{i,h,\epsilon}\left(s^*_{\varphi_\epsilon=1}, s^*_{\varphi_\epsilon}\right)$ versus $s^*_{\varphi_\epsilon}$ at $t_\epsilon = t_{36}$ (——), $t_\epsilon = t_{51}$ (——) and $t_\epsilon = t_{66}$ (——), where $i = 0$ and $h = 1$. As $i = 0$, $s^*_{i,h,\epsilon}\left(s^*_{\varphi_\epsilon=1}, s^*_{\varphi_\epsilon}\right)$ in this figure has its source in a noise-free signal (Figures 52 to 61). At any given value of $s^*_{\varphi_\epsilon}$, $s^*_{i,h,\epsilon}\left(s^*_{\varphi_\epsilon=1}, s^*_{\varphi_\epsilon}\right)$ is equal to the integral of $s^*_{\varphi_\epsilon}\left|g_{i,h}\left(s^*_{\varphi_\epsilon}\right)\right|$ (Figure 61) divided by $G_{i,h}\left(s^*_{\varphi_\epsilon}\right)$ (Figure 59). As there are no masks (Figures 20 to 23; Figure 32) applied to the integrands or the data that give rise to them, $s^*_{min<0} = s^*_{\varphi_\epsilon=1}$, $s^*_{max<0} = s^*_{min>0} = 0$ and $s^*_{max>0} = s^*_{\varphi_\epsilon=2N}$ at time t_ϵ (Table 18 lists $s^*_{\varphi_\epsilon=1}$ and $= s^*_{\varphi_\epsilon=2N}$ at each time of analysis) are the limits applied to the integrals (Equation 81a) that yield $s^*_{i,h,\epsilon}\left(s^*_{\varphi_\epsilon=1}, s^*_{\varphi_\epsilon=2N}\right)$ at each time of

analysis. For each value of $s^*_{i,h,\epsilon}\left(s^*_{\varphi_\epsilon=1}, s^*_{\varphi_\epsilon}\right)$ shown in this figure, the lower limit of integration is $s^*_{min<0} = s^*_{\varphi_\epsilon=1}$ at time t_ϵ, and the upper limit of integration ranges from $s^*_{min<0}$ to $s^*_{max>0} = s^*_{\varphi_\epsilon=2N}$ at time t_ϵ.

Changing N and r_j values to keep $\Delta s^*_{\varphi_\epsilon}$ constant

If $\Delta s^*_{\varphi_\epsilon}$, the increment between consecutive values of $s^*_{\varphi_\epsilon}$, did not change over the full range of $s^*_{\varphi_\epsilon}$, and if, as in Equation 112, $\Delta Y_{i,h}(s^*_{\varphi_\epsilon})$ were equal to $\Delta\Delta GRN_{i,h}\left(s^*_{\varphi_\epsilon}\right)$, the product, $\frac{\Delta\varphi_\epsilon}{\Delta s^*_{\varphi_\epsilon}}\left(\frac{\Delta Y_{i,h}(s^*_{\varphi_\epsilon})}{\Delta\varphi_\epsilon}\right) = \frac{\Delta Y_{i,h}(s^*_{\varphi_\epsilon})}{\Delta s^*_{\varphi_\epsilon}}$, would, to a close approximation, be normally distributed about a mean of $\mu_{RI} = 0$ fringe with a standard deviation equal to $\frac{\Delta\varphi_\epsilon}{\Delta s^*_{\varphi_\epsilon}}\sigma_{RI}$, where $\Delta\varphi_\epsilon$, being the increment in the index (Equation 6), is always and everywhere equal to 1. Instead, the spacing between values of r_j is such that, upon the application of Equation 5, $\Delta s^*_{\varphi_\epsilon}$ is a function of $s^*_{\varphi_\epsilon}$. Additionally, $\Delta s^*_{\varphi_\epsilon}$ is a function of t_ϵ. (See Figure 51.)

As shown by Equations 16 and 17, $1/\Delta s^*_{\varphi_\epsilon=j} = 1/\Delta s^*_{\varphi_\epsilon=N+j} = \omega^2 t_\epsilon r_j/\Delta r_j$. If each $\Delta s^*_{\varphi_\epsilon}$ were equal to a constant, Δs^*_0, at all times and at all values of $s^*_{\varphi_\epsilon}$, then

$$s^*_{\varphi_\epsilon} = s^*_{min_\epsilon} + \varphi_\epsilon \Delta s^*_0$$

(126a)

would always hold, but the number of $s^*_{\varphi_\epsilon}$ values, $2N_\epsilon$, would depend on t_ϵ, such that

$$2N_\epsilon + 1 = \frac{s^*_{max_\epsilon} - s^*_{min_\epsilon}}{\Delta s^*_0} - \left(\frac{s^*_{max_\epsilon} - s^*_{min_\epsilon}}{\Delta s^*_0}\ mod\ 1\right) = \frac{2s^*_{max_\epsilon}}{\Delta s^*_0} - \left(\frac{2s^*_{max_\epsilon}}{\Delta s^*_0}\ mod\ 1\right),$$

(126b)

where

$$s^*_{max_\epsilon} = \frac{1}{\omega^2 t_\epsilon} ln\left(\frac{r_b}{r_m}\right)$$

(126c)

is the highest possible value of $s^*_{\varphi_\epsilon}$ at time t_ϵ and

$$s^*_{min_\epsilon} = \frac{1}{\omega^2 t_\epsilon} ln\left(\frac{r_m}{r_b}\right)$$

(126d)

is the lowest possible value of $s^*_{\varphi_\epsilon}$ at time t_ϵ. The index, φ_ϵ, would lie within $1 \leq \varphi_\epsilon \leq 2N_\epsilon$ at time t_ϵ. By application of Equation 114, the time-dependent radial positions would be given by

$$r_{j_\epsilon} = r_0 e^{s^*_{\varphi_\epsilon}\omega^2 t_\epsilon} = r_0 e^{\left(s^*_{min_\epsilon} + \varphi_\epsilon \Delta s^*_0\right)\omega^2 t_\epsilon},$$

(127)

where the time-dependent index of r_{j_ϵ} would lie within $1 \leq j_\epsilon \leq N_\epsilon$, and where as in Equation 115,

$$r_0 = \begin{Bmatrix} r_b \; for \; \varphi_\epsilon = j_\epsilon \\ r_m \; for \; \varphi_\epsilon = j_\epsilon + N_\epsilon \end{Bmatrix} in \; r_{j_\epsilon} = r_0 e^{\left(s^*_{min_\epsilon} + \varphi_\epsilon \Delta s^*_0\right)\omega^2 t_\epsilon}.$$

(128)

Thus, at a given value of $\left(s^*_{min_\epsilon} + \varphi_\epsilon \Delta s^*_0\right)$, r_{j_ϵ} varies exponentially with $\omega^2 t_\epsilon$. As N_ϵ is inversely proportional to $\omega^2 t_\epsilon$, at a given value of Δs^*_0, the number of radial positions at which data are recorded decreases with time and the square of the angular velocity. As N_ϵ is inversely proportional to Δs^*_0, it would behove one to choose a value of Δs^*_0 that is small enough to keep N_ϵ from approaching zero before all solutes of interest have cleared the system between the radial extrema of accumulation.

In principle, to ensure that $\Delta s^*_{\varphi_\epsilon}$ is constant with time and radial position, it should be possible to collect data at the time-dependent number, N_ϵ, of time-dependent radial positions, r_{j_ϵ}, described

by Equations 126to 128. Doing so would, where $\Delta Y_{i,h}(s^*_{\varphi_\epsilon}) = \Delta\Delta GRN_{i,h}(s^*_{\varphi_\epsilon})$, render $\frac{\Delta Y_{i,h}(s^*_{\varphi_\epsilon})}{\Delta s^*_{\varphi\epsilon}}$ normally distributed about a mean of $\mu_{RI} = 0$ fringe with a standard deviation approximately equal to $\frac{\Delta\varphi_\epsilon}{\Delta s^*_{\varphi_\epsilon}}\sigma_{RI} = \frac{1}{\Delta s^*_0}\sigma_{RI}$. Doing so, however, would still result in an $s^*_{\varphi_\epsilon}$-dependent signal-to-noise ratio of $\frac{e^{2s^*_{\varphi_\epsilon}\omega^2 t_\epsilon}}{\Delta s^*_{\varphi_\epsilon}} = \frac{e^{2s^*_{\varphi_\epsilon}\omega^2 t_\epsilon}}{\Delta s^*_0}$, once $q_{i,h}(s^*_{\varphi_\epsilon})$ is multiplied by $e^{2s^*_{\varphi_\epsilon}\omega^2 t_\epsilon}$ to obtain $g_{i,h}(s^*_{\varphi_\epsilon})$, and would not solve the worse problem of data clipping.

Mitigation of data clipping

Each of the three possible outcomes for any given value of $\left(\frac{\partial Y_{i,h}(s^*_{\varphi_\epsilon})}{\partial s^*_{\varphi_\epsilon}}\right)_t$ is thoroughly described in an earlier section: *The accumulated error in $G_{i,h}(s^*_{\varphi_\epsilon=2N})$ increases in proportion to the clipping of random noise*. Data clipping is one such outcome, and is the only possible outcome for the $\left(\frac{\partial Y_{i,h}(s^*_{\varphi_\epsilon})}{\partial s^*_{\varphi_\epsilon}}\right)_t$ values of Figure 55. Following a quick review of the all possible outcomes for $\left(\frac{\partial Y_{i,h}(s^*_{\varphi_\epsilon})}{\partial s^*_{\varphi_\epsilon}}\right)_t$ values generally, a method to reduce the extent of data clipping is presented.

In general, $s^*_{\varphi_\epsilon}\left(\frac{\partial Y_{i,h}(s^*_{\varphi_\epsilon})}{\partial s^*_{\varphi_\epsilon}}\right)_t > 0$ holds for all $\left(\frac{\partial Y_{i,h}(s^*_{\varphi_\epsilon})}{\partial s^*_{\varphi_\epsilon}}\right)_t$ data that are retained, and all data that are retained are described as belonging to the data-retention category, while $s^*_{\varphi_\epsilon}\left(\frac{\partial Y_{i,h}(s^*_{\varphi_\epsilon})}{\partial s^*_{\varphi_\epsilon}}\right)_t < 0$ holds for all $\left(\frac{\partial Y_{i,h}(s^*_{\varphi_\epsilon})}{\partial s^*_{\varphi_\epsilon}}\right)_t$ data that are replaced with zeroes, and all data that are replaced with zeroes are described as belonging to the data-replacement (with zeroes) category. A value of $\left(\frac{\partial Y_{i,h}(s^*_{\varphi_\epsilon})}{\partial s^*_{\varphi_\epsilon}}\right)_t$ in the data-retention category yields, by Equation 9a, $q_{i,h}(s^*_{\varphi_\epsilon}) = \left(\frac{\partial Y_{i,h}(s^*_{\varphi_\epsilon})}{\partial s^*_{\varphi_\epsilon}}\right)_t$, which,

by Equation 10, propagates to $g_{i,h}(s^*_{\varphi_\epsilon}) = q_{i,h}(s^*_{\varphi_\epsilon})e^{2s^*_{\varphi_\epsilon}\omega^2 t_\epsilon}$ as $\left(\frac{\partial Y_{i,h}(s^*_{\varphi_\epsilon})}{\partial s^*_{\varphi_\epsilon}}\right)_t e^{2s^*_{\varphi_\epsilon}\omega^2 t_\epsilon}$, and thence, by Equation 11 or 77, contributes to the noise accumulated by $G_{i,h}(s^*_{\varphi_\epsilon})$ upon integration of $\left|g_{i,h}(s^*_{\varphi_\epsilon})\right|$. A value of $\left(\frac{\partial Y_{i,h}(s^*_{\varphi_\epsilon})}{\partial s^*_{\varphi_\epsilon}}\right)_t$ in the data-replacement category yields $q_{i,h}(s^*_{\varphi_\epsilon}) = 0$, which renders $g_{i,h}(s^*_{\varphi_\epsilon})$ equal to zero, and thence contributes nothing to $G_{i,h}(s^*_{\varphi_\epsilon})$ upon integration of $\left|g_{i,h}(s^*_{\varphi_\epsilon})\right|$, provided that, as it is often found, $g_{i,h}(s^*_{\varphi_\epsilon-1})$ and $g_{i,h}(s^*_{\varphi_\epsilon+1})$ are also equal to zero. (See *The accumulated error in* $G_{i,h}(s^*_{\varphi_\epsilon=2N})$ *increases in proportion to the clipping of random noise*.)

Over a range of $s^*_{\varphi_\epsilon}$ values throughout which $\left(\frac{\partial Y_{i,h}(s^*_{\varphi_\epsilon})}{\partial s^*_{\varphi_\epsilon}}\right)_t$ (Equation 8) is either above zero or below zero exclusively, all of the data are replaced with zeroes if $s^*_{\varphi_\epsilon}\left(\frac{\partial Y_{i,h}(s^*_{\varphi_\epsilon})}{\partial s^*_{\varphi_\epsilon}}\right)_t < 0$ holds throughout, and all of the data are retained if $s^*_{\varphi_\epsilon}\left(\frac{\partial Y_{i,h}(s^*_{\varphi_\epsilon})}{\partial s^*_{\varphi_\epsilon}}\right)_t > 0$ holds throughout. In contrast, in data clipping, which is a phenomenon restricted to ranges of $s^*_{\varphi_\epsilon}$ within which $\left(\frac{\partial Y_{i,h}(s^*_{\varphi_\epsilon})}{\partial s^*_{\varphi_\epsilon}}\right)_t$ is noise that varies randomly between positive and negative values (Figure 55), a random set of approximately half the data yield $s^*_{\varphi_\epsilon}\left(\frac{\partial Y_{i,h}(s^*_{\varphi_\epsilon})}{\partial s^*_{\varphi_\epsilon}}\right)_t > 0$ and are accordingly retained, while the rest of the data yield $s^*_{\varphi_\epsilon}\left(\frac{\partial Y_{i,h}(s^*_{\varphi_\epsilon})}{\partial s^*_{\varphi_\epsilon}}\right)_t < 0$ and are accordingly replaced with zeroes.

Over a range of $s^*_{\varphi_\epsilon}$ values throughout which $\left(\frac{\partial Y_i(s^*_{\varphi_\epsilon})}{\partial s^*_{\varphi_\epsilon}}\right)_t = 0$, the noise, $\left(\frac{\partial Y_{i,h}(s^*_{\varphi_\epsilon})}{\partial s^*_{\varphi_\epsilon}}\right)_t$ approximated as $\Delta Y_{i,h}(s^*_{\varphi_\epsilon})/\Delta s^*_{\varphi_\epsilon}$, is clipped in going from $\Delta Y_{i,h}(s^*_{\varphi_\epsilon})/\Delta s^*_{\varphi_\epsilon}$ (Figure 55) to $q_{i,h}(s^*_{\varphi_\epsilon})$ (Figure 56).

Approximately half the noise would be in the data-retention category, for which $s^*_{\varphi_\epsilon}\left(\frac{\partial Y_{i,h}(s^*_{\varphi_\epsilon})}{\partial s^*_{\varphi_\epsilon}}\right)_t > 0$, and the rest of the noise would be in the data-replacement category, for which $s^*_{\varphi_\epsilon}\left(\frac{\partial Y_{i,h}(s^*_{\varphi_\epsilon})}{\partial s^*_{\varphi_\epsilon}}\right)_t < 0$. The noise in the data-retention category would first render $q_{i,h}(s^*_{\varphi_\epsilon}) = \Delta Y_{i,h}(s^*_{\varphi_\epsilon})/\Delta s^*_{\varphi_\epsilon}$, which would then render $g_{i,h}(s^*_{\varphi_\epsilon}) = q_{i,h}(s^*_{\varphi_\epsilon})(e^{2s^*_{\varphi_\epsilon}\omega^2 t_\epsilon})$ equal to $\left(\frac{\Delta Y_{i,h}(s^*_{\varphi_\epsilon})}{\Delta s^*_{\varphi_\epsilon}}\right)(e^{2s^*_{\varphi_\epsilon}\omega^2 t_\epsilon})$ (Figure 57), and thence contribute to the noise accumulated by $G_{i,h}(s^*_{\varphi_\epsilon})$ (Figure 59) upon integration of $|g_{i,h}(s^*_{\varphi_\epsilon})|$ (Figure 58). The noise in the data-replacement category would first render $q_{i,h}(s^*_{\varphi_\epsilon})$ equal to zero, which would then render $g_{i,h}(s^*_{\varphi_\epsilon}) = q_{i,h}(s^*_{\varphi_\epsilon})(e^{2s^*_{\varphi_\epsilon}\omega^2 t_\epsilon})$ equal to zero, and thence contribute nothing to $G_{i,h}(s^*_{\varphi_\epsilon})$ upon integration of $|g_{i,h}(s^*_{\varphi_\epsilon})|$.

Values of $|g_{i,h}(s^*_{\varphi_\epsilon})|$ that are greater than zero due to noise result in nonzero values of $s^*_{\varphi_\epsilon}|g_{i,h}(s^*_{\varphi_\epsilon})|$ (Figure 60), which then contribute to the integral of $s^*_{\varphi_\epsilon}|g_{i,h}(s^*_{\varphi_\epsilon})|$ (Figure 61) with respect to $s^*_{\varphi_\epsilon}$. When divided by $G_{i,h}(s^*_{\varphi_\epsilon=b})$ (Equation 77, with limits given in the legend of Figure 59), the integral of $s^*_{\varphi_\epsilon}|g_{i,h}(s^*_{\varphi_\epsilon})|$ from $s^*_{\varphi_\epsilon=1}$ to $s^*_{\varphi_\epsilon=b}$ yields $s^*_{i,h,\epsilon}(s^*_{\varphi_\epsilon=1}, s^*_{\varphi_\epsilon=b})$ (Figure 62). Thus, values of $|g_{i,h}(s^*_{\varphi_\epsilon})|$ that are greater than zero due to noise result in nonzero values of $s^*_{i,h,\epsilon}(s^*_{\varphi_\epsilon=1}, s^*_{\varphi_\epsilon=b})$ (Equation 81a, with limits given in the legend of Figure 62).

The problem with data clipping is not that roughly half the data yield $g_{i,h}(s^*_{\varphi_\epsilon}) = 0$ over a range of $s^*_{\varphi_\epsilon}$ values throughout which $\left(\frac{\partial Y_i(s^*_{\varphi_\epsilon})}{\partial s^*_{\varphi_\epsilon}}\right)_t = 0$. The problem with data clipping is that roughly half the data yield $g_{i,h}(s^*_{\varphi_\epsilon}) = \left(\frac{\partial Y_{i,h}(s^*_{\varphi_\epsilon})}{\partial s^*_{\varphi_\epsilon}}\right)_t e^{2s^*_{\varphi_\epsilon}\omega^2 t_\epsilon}$ over a range of $s^*_{\varphi_\epsilon}$ values throughout which $\left(\frac{\partial Y_i(s^*_{\varphi_\epsilon})}{\partial s^*_{\varphi_\epsilon}}\right)_t = 0$. If instead, all the data yielded $g_{i,h}(s^*_{\varphi_\epsilon}) = 0$ over any range of $s^*_{\varphi_\epsilon}$ values

throughout which $\left(\frac{\partial Y_i(s^*_{\varphi\epsilon})}{\partial s^*_{\varphi\epsilon}}\right)_t = 0$, the net contribution of noise to $G_{i,h}(s^*_{\varphi_\epsilon})$ would be minimal. The less the net contribution of noise to $G_{i,h}(s^*_{\varphi_\epsilon})$, the less the net contribution of noise to $s^*_{i,h,\epsilon}$ (Equation 81a) is likely to be, and the more $e_{s^*_{i,\epsilon}}$ (Equation 83) should be minimised, thus bringing $\langle s^*_{i,\epsilon}\rangle$ (Equation 82) as close to $s^*_{i,\epsilon}$ (Equation 81b) as possible.

If data for which $\left(\frac{\partial Y_i(s^*_{\varphi\epsilon})}{\partial s^*_{\varphi\epsilon}}\right)_t = 0$ could be identified and set to zero before calculating $\left|g_{i,h}(s^*_{\varphi_\epsilon})\right|$ and $s^*_{\varphi_\epsilon}\left|g_{i,h}(s^*_{\varphi_\epsilon})\right|$, the net contribution of noise to $G_{i,h}(s^*_{\varphi_\epsilon})$ and $s^*_{i,h,\epsilon}(s^*_{\varphi\epsilon=1}, s^*_{\varphi_\epsilon})$ would be minimised. Thus, a method is sought to identify data that are likely to be described by $Y_{i,h}(s^*_{\varphi_\epsilon}) = \Delta GRN_{i,h}(s^*_{\varphi_\epsilon}) + k_{i,h,\epsilon}$ (Equation 111b), as $\left(\frac{\partial Y_i(s^*_{\varphi\epsilon})}{\partial s^*_{\varphi\epsilon}}\right)_t = 0$ wherever $Y_{i,h}(s^*_{\varphi_\epsilon}) = \Delta GRN_{i,h}(s^*_{\varphi_\epsilon}) + k_{i,h,\epsilon}$. As a step toward implementing such a method, the distribution of $\Delta GRN_{i,h}(s^*_{\varphi_\epsilon})$ about its mean is examined in detail.

In going from Equation 111a to Equation 111b, the difference in the randomly distributed noise is remapped from $\Delta GRN_{i,h}(r_j, t_\epsilon)$ versus r_j to $\Delta GRN_{i,h}(s^*_{\varphi_\epsilon})$ versus $s^*_{\varphi_\epsilon}$, where $s^*_{\varphi_\epsilon}$ is calculated from r_j and t_ϵ using Equation 5. Equation 111 shows that, in the absence of a noise-free signal, and with $k_{i,h,\epsilon} = 0$, $Y_{i,h}(s^*_{\varphi_\epsilon}) = \Delta GRN_{i,h}(s^*_{\varphi_\epsilon})$. Figure 54 shows that, at any given time, to a close approximation, $Y_{i,h}(s^*_{\varphi_\epsilon}) = \Delta GRN_{i,h}(s^*_{\varphi_\epsilon})$ is normally distributed about a mean (Equation 121a) of $\langle Y_{i,h}([s^*_{\varphi\epsilon=1}, s^*_{\varphi\epsilon=2N}])\rangle \cong \mu_{RI} = 0$ fringe with a standard deviation (Equation 121b) of $\sigma_{i,h}\left(Y_{i,h}([s^*_{\varphi\epsilon=1}, s^*_{\varphi\epsilon=2N}])\right) \cong 2^{0.5}\sigma_{RI}$ (Figure 5; Table 14).

In general (Equation 111b), where $\left(\frac{\partial Y_i(s^*_{\varphi\epsilon})}{\partial s^*_{\varphi\epsilon}}\right)_t = 0$, $Y_{i,h}(s^*_{\varphi_\epsilon}) = \Delta GRN_{i,h}(s^*_{\varphi_\epsilon}) + k_{i,h,\epsilon}$, where $k_{i,h,\epsilon}$

contributes an $s^*_{\varphi_\epsilon}$-independent offset in the mean value of $Y_{i,h}(s^*_{\varphi_\epsilon})$. As such, $k_{i,h,\epsilon}$ has no effect the standard deviation in $Y_{i,h}(s^*_{\varphi_\epsilon})$ about its mean. Thus, $Y_{i,h}(s^*_{\varphi_\epsilon}) = \Delta GRN_{i,h}(s^*_{\varphi_\epsilon}) + k_{i,h,\epsilon}$ is normally distributed about a mean (Equation 121a) of $\langle Y_{i,h}([s^*_{\varphi_\epsilon=1}, s^*_{\varphi_\epsilon=2N}])\rangle \cong \mu_{RI} + k_{i,h,\epsilon} = k_{i,h,\epsilon}$ with a standard deviation (Equation 121b) of $\sigma_{i,h}\left(Y_{i,h}([s^*_{\varphi_\epsilon=1}, s^*_{\varphi_\epsilon=2N}])\right) \cong 2^{0.5}\sigma_{RI}$.

By differentiating $Y_{i,h}(s^*_{\varphi_\epsilon})$ with respect to a variable on which $\Delta GRN_{i,h}(s^*_{\varphi_\epsilon})$ depends but $k_{i,h,\epsilon}$ does not, a result is obtained that is indistinguishable from that which would be found for $k_{i,h,\epsilon} = 0$. One such variable is $s^*_{\varphi_\epsilon}$, which is problematic, in that the dependence of $\Delta s^*_{\varphi_\epsilon}$ on $s^*_{\varphi_\epsilon}$ (Figure 51) renders $\sigma_{i,h}(\Delta Y_{i,h}([s^*_{\varphi_\epsilon=a}, s^*_{\varphi_\epsilon=b}])/\Delta s^*_{\varphi_\epsilon})$ proportional to $1/\Delta s^*_{\varphi_\epsilon=j} = 1/\Delta s^*_{\varphi_\epsilon=N+j} = \omega^2 t_\epsilon r_j/\Delta r_j$ (Equation 117; Figure 55), where $\sigma_{i,h}(\Delta Y_{i,h}([s^*_{\varphi_\epsilon=a}, s^*_{\varphi_\epsilon=b}])/\Delta s^*_{\varphi_\epsilon})$ is the standard deviation (Equation 122b) of $\Delta Y_{i,h}(s^*_{\varphi_\epsilon})/\Delta s^*_{\varphi_\epsilon}$ about its mean (Equation 122a) within $s^*_{\varphi_\epsilon=a} \le s^*_{\varphi_\epsilon} \le s^*_{\varphi_\epsilon=b}$ at time t_ϵ, and $\Delta Y_{i,h}(s^*_{\varphi_\epsilon})/\Delta s^*_{\varphi_\epsilon}$ is the approximation used to evaluate the partial derivative of $Y_{i,h}(s^*_{\varphi_\epsilon})$ with respect to $s^*_{\varphi_\epsilon}$ at time t_ϵ (Equation 8). Another such variable is φ_ϵ.

If the partial derivative of $Y_{i,h}(s^*_{\varphi_\epsilon}) = \Delta GRN_{i,h}(s^*_{\varphi_\epsilon}) + k_{i,h,\epsilon}$ at time t_ϵ were taken with respect to the index, φ_ϵ, for which $\Delta\varphi_\epsilon$, the increment between consecutive values, is always equal to 1, the approximated derivative, $\frac{\Delta Y_{i,h}(s^*_{\varphi_\epsilon})}{\Delta\varphi_\epsilon} = \frac{\Delta\Delta GRN_{i,h}(s^*_{\varphi_\epsilon})}{\Delta\varphi_\epsilon} \cong \left(\frac{\partial Y_{i,h}(s^*_{\varphi_\epsilon})}{\partial\varphi_\epsilon}\right)_t = \left(\frac{\partial\Delta GRN_{i,h}(s^*_{\varphi_\epsilon})}{\partial\varphi_\epsilon}\right)_t$ would, to a close approximation, be normally distributed about a mean of $\mu_{RI} = 0$ fringe with a standard deviation equal to σ_{RI}. (See discussion following Equation 8.) The evaluation of $\frac{\Delta Y_{i,h}(s^*_{\varphi_\epsilon})}{\Delta\varphi_\epsilon}$ requires further consideration of differences in $GRN_{i,h}(r_j, t_\epsilon)$ values, as such differences are the source of the $\Delta GRN_{i,h}(s^*_{\varphi_\epsilon})$ values found within $Y_{i,h}(s^*_{\varphi_\epsilon}) = \Delta GRN_{i,h}(s^*_{\varphi_\epsilon}) + k_{i,h,\epsilon}$. As $k_{i,h,\epsilon}$ solely depends on t_ϵ

(Equations 108 and 111), $\frac{\Delta k_{i,h,\epsilon}}{\Delta \varphi_\epsilon} = \left(\frac{\partial k_{i,h,\epsilon}}{\partial \varphi_\epsilon}\right)_t = \left(\frac{\partial k_{i,h,\epsilon}}{\partial s^*_{\varphi_\epsilon}}\right)_t = \left(\frac{\partial k_{i,h,\epsilon}}{\partial r_j}\right)_t = 0$. Thus, as in Figures 52 to 54, $k_{i,h,\epsilon}$ is equated to zero throughout the evaluation of $\frac{\Delta Y_{i,h}(s^*_{\varphi_\epsilon})}{\Delta \varphi_\epsilon}$ that follows.

Within r_a to r_b of replicate h of treatment group i at time t_ϵ, the mean of $GRN_{i,h}(r_j, t_\epsilon)$ is given by

$$\langle GRN_{i,h}([r_a, r_b], t_\epsilon)\rangle = \frac{1}{b-a+1}\sum_{j=a}^{j=b} GRN_{i,h}(r_j, t_\epsilon),$$

(129a)

and the standard deviation of $GRN_{i,h}(r_j, t_\epsilon)$ about its mean, $\langle GRN_{i,h}([r_a, r_b], t_\epsilon)\rangle$, is given by

$$\sigma_{i,h}\left(GRN_{i,h}([r_a, r_b], t_\epsilon)\right) = \left\{\frac{1}{b-a-1}\left[\sum_{j=a}^{j=b}\left(GRN_{i,h}(r_j, t_\epsilon) - \langle GRN_{i,h}([r_a, r_b], t_\epsilon)\rangle\right)^2\right]\right\}^{0.5},$$

(129b)

where $1 \le a < b \le N$. Thus, at time t_ϵ, within the full range of r_j values, $\sigma_{i,h}\left(GRN_{i,h}([r_1, r_N], t_\epsilon)\right)$ is equal to the standard deviation about $\langle GRN_{i,h}([r_1, r_N], t_\epsilon)\rangle$, which is equal to the mean of all $GRN_{i,h}(r_j, t_\epsilon)$.

Given a difference such as $Y_{i,h}(r_j, t_\epsilon) = NMS_{i,h}(r_j, t_\epsilon)$ - $NMS_{i,h}(r_j, t_\alpha)$ (Equation 7; Figure 53), where $NMS_{i,h}(r_j, t_\epsilon) = GRN_{i,h}(r_j, t_\epsilon)$, and $NMS_{i,h}(r_j, t_\alpha) = GRN_{i,h}(r_j, t_\alpha)$ (Figure 52), $Y_{i,h}(r_j, t_\epsilon) = \Delta GRN_{i,h}(r_j, t_\epsilon)$. For $Y_{i,h}(r_j, t_\epsilon) = \Delta GRN_{i,h}(r_j, t_\epsilon)$, Equation 120a yields $\langle Y_{i,h}([r_a, r_b], t_\epsilon)\rangle = \langle \Delta GRN_{i,h}([r_a, r_b], t_\epsilon)\rangle$ and Equation 120b yields $\sigma_{i,h}\left(Y_{i,h}([r_a, r_b], t_\epsilon)\right) = \sigma_{i,h}\left(\Delta GRN_{i,h}([r_a, r_b], t_\epsilon)\right)$. Thus, at time t_ϵ, within the full range of $s^*_{\varphi_\epsilon}$ values that apply at that time, $\sigma_{i,h}\left(\Delta GRN_{i,h}([r_1, r_N], t_\epsilon)\right)$ is equal to the standard deviation about $\langle \Delta GRN_{i,h}([r_1, r_N], t_\epsilon)\rangle$, which is equal to the mean of all $\Delta GRN_{i,h}(s^*_{\varphi_\epsilon})$. The standard deviation of $\Delta GRN_{i,h}(r_j, t_\epsilon)$ about its mean is also given by

$$\sigma_{i,h}\left(\Delta GRN_{i,h}([r_1, r_N], t_\epsilon)\right) = \sqrt{\sigma_{i,h}\left(GRN_{i,h}([r_1, r_N], t_\epsilon)\right) + \sigma_{i,h}\left(GRN_{i,h}([r_1, r_N], t_\alpha)\right)}.$$

(130)

Thus, with $\sigma_{i,h}\left(GRN_{i,h}([r_1, r_N], t_\epsilon)\right) \cong \sigma_{i,h}\left(GRN_{i,h}([r_1, r_N], t_\alpha)\right) \cong \sigma_{RI} = 0.01400$ fringe,

$\sigma_{i,h}\left(\Delta GRN_{i,h}([r_1, r_N], t_\epsilon)\right) \cong 2^{0.5}\sigma_{RI} = 1.197990\text{E-}2$ fringe.

For $Y_{i,h}(s^*_{\varphi_\epsilon}) = \Delta GRN_{i,h}(s^*_{\varphi_\epsilon})$, Equation 121a yields $\langle Y_{i,h}\left(\left[s^*_{\varphi_\epsilon=a}, s^*_{\varphi_\epsilon=b}\right]\right)\rangle =$ $\langle \Delta GRN_{i,h}\left(\left[s^*_{\varphi_\epsilon=a}, s^*_{\varphi_\epsilon=b}\right]\right)\rangle$ and Equation 121b yields $\sigma_{i,h}\left(Y_{i,h}\left(\left[s^*_{\varphi_\epsilon=a}, s^*_{\varphi_\epsilon=b}\right]\right)\right) =$ $\sigma_{i,h}\left(\Delta GRN_{i,h}\left(\left[s^*_{\varphi_\epsilon=a}, s^*_{\varphi_\epsilon=b}\right]\right)\right)$. Thus, at time t_ϵ, within the full range of $s^*_{\varphi_\epsilon}$ values that apply at that time, $\sigma_{i,h}\left(\Delta GRN_{i,h}\left(\left[s^*_{\varphi_\epsilon=1}, s^*_{\varphi_\epsilon=2N}\right]\right)\right)$ is equal to the standard deviation about $\langle \Delta GRN_{i,h}\left(\left[s^*_{\varphi_\epsilon=1}, s^*_{\varphi_\epsilon=2N}\right]\right)\rangle$, which is equal to the mean of all $\Delta GRN_{i,h}\left(s^*_{\varphi_\epsilon}\right)$.

As the sum of all $\Delta GRN_{i,h}\left(s^*_{\varphi_\epsilon}\right)$ divided by $2N$ (Equation 121a with $Y_{i,h}(s^*_{\varphi_\epsilon}) = \Delta GRN_{i,h}(s^*_{\varphi_\epsilon})$) is equal to the sum of all $\Delta GRN_{i,h}\left(r_j, t_\epsilon\right)$ divided by N (Equation 120a for $Y_{i,h}(r_j, t_\epsilon) = \Delta GRN_{i,h}(r_j, t_\epsilon)$),

$$\langle \Delta GRN_{i,h}\left(\left[s^*_{\varphi_\epsilon=1}, s^*_{\varphi_\epsilon=2N}\right]\right)\rangle = \langle \Delta GRN_{i,h}([r_1, r_N], t_\epsilon)\rangle.$$

(131a)

As the sum of all $\left(\Delta GRN_{i,h}\left(s^*_{\varphi_\epsilon}\right) - \langle \Delta GRN_{i,h}\left(\left[s^*_{\varphi_\epsilon=1}, s^*_{\varphi_\epsilon=2N}\right]\right)\rangle\right)^2$ divided by $2N$ (Equation 121b with $Y_{i,h}(s^*_{\varphi_\epsilon}) = \Delta GRN_{i,h}(s^*_{\varphi_\epsilon})$) is equal to the sum of all $\left(\Delta GRN_{i,h}\left(r_j, t_\epsilon\right) - \langle \Delta GRN_{i,h}([r_1, r_N], t_\epsilon)\rangle\right)^2$ divided by N (Equation 120b for $Y_{i,h}(r_j, t_\epsilon) = \Delta GRN_{i,h}(r_j, t_\epsilon)$),

$$\sigma_{i,h}\left(\Delta GRN_{i,h}\left(\left[s^*_{\varphi_\epsilon=1}, s^*_{\varphi_\epsilon=2N}\right]\right)\right) = \sigma_{i,h}\left(\Delta GRN_{i,h}([r_1, r_N], t_\epsilon)\right),$$

(131b)

given which, when $Y_{i,h}(r_j, t_\epsilon) = \Delta GRN_{i,h}(r_j, t_\epsilon)$ is remapped from r_j at t_ϵ to $s^*_{\varphi_\epsilon}$, the result (Figure 54),

$Y_{i,h}(s^*_{\varphi_\epsilon}) = \Delta GRN_{i,h}(s^*_{\varphi_\epsilon})$, has a standard deviation about its mean of approximately $2^{0.5}\sigma_{RI}$. (See Equation 130.)

The approximation used to evaluate the partial derivative of $Y_{i,h}(s^*_{\varphi_\epsilon})$ with respect to φ_ϵ at time t_ϵ is given by,

$$\left(\frac{\partial Y_{i,h}(s^*_{\varphi_\epsilon})}{\partial \varphi_\epsilon}\right)_t \cong \frac{1}{2}\left[\frac{Y_{i,h}(s^*_{\varphi_\epsilon}) - Y_{i,h}(s^*_{\varphi_\epsilon-1})}{\varphi_\epsilon - (\varphi_\epsilon - 1)} + \frac{Y_{i,h}(s^*_{\varphi_\epsilon+1}) - Y_{i,h}(s^*_{\varphi_\epsilon})}{(\varphi_\epsilon + 1) - \varphi_\epsilon}\right] = \frac{1}{2}\left[Y_{i,h}(s^*_{\varphi_\epsilon+1}) - Y_{i,h}(s^*_{\varphi_\epsilon-1})\right]$$

$$\equiv \frac{\Delta Y_{i,h}(s^*_{\varphi_\epsilon})}{\Delta\varphi_\epsilon}$$

(132a)

at φ_ϵ within $1 < \varphi_\epsilon < 2N$,

$$\left(\frac{\partial Y_{i,h}(s^*_{\varphi_\epsilon=1})}{\partial \varphi_\epsilon}\right)_t \cong \frac{Y_{i,h}(s^*_{\varphi_\epsilon+1}) - Y_{i,h}(s^*_{\varphi_\epsilon})}{(\varphi_\epsilon + 1) - \varphi_\epsilon} = \Delta Y_{i,h}(s^*_{\varphi_\epsilon=1}) \equiv \frac{\Delta Y_{i,h}(s^*_{\varphi_\epsilon=1})}{\Delta(\varphi_\epsilon = 1)}$$

(132b)

at $\varphi_\epsilon = 1$, and

$$\left(\frac{\partial Y_{i,h}(s^*_{\varphi_\epsilon=2N})}{\varphi_\epsilon}\right)_t \cong \frac{Y_{i,h}(s^*_{\varphi_\epsilon}) - Y_{i,h}(s^*_{\varphi_\epsilon-1})}{\varphi_\epsilon - (\varphi_\epsilon - 1)} = \Delta Y_{i,h}(s^*_{\varphi_\epsilon=2N}) \equiv \frac{\Delta Y_{i,h}(s^*_{\varphi_\epsilon=2N})}{\Delta(\varphi_\epsilon = 2N)}$$

(132c)

at $\varphi_\epsilon = 2N$.

Within $s^*_{\varphi_\epsilon=a}$ to $s^*_{\varphi_\epsilon=b}$ of replicate h of treatment group i at time t_ϵ, the mean of $\Delta Y_{i,h}(s^*_{\varphi_\epsilon})/\Delta\varphi_\epsilon$ (Equation 31) is given by

$$\langle \Delta Y_{i,h}([s^*_{\varphi_\epsilon=a}, s^*_{\varphi_\epsilon=b}])/\Delta\varphi_\epsilon \rangle = \frac{1}{b-a+1}\sum_{\varphi_\epsilon=a}^{\varphi_\epsilon=b} \Delta Y_{i,h}(s^*_{\varphi_\epsilon})/\Delta\varphi_\epsilon,$$

(133a)

and the standard deviation of $\Delta Y_{i,h}\left(s^*_{\varphi_\epsilon}\right)/\Delta\varphi_\epsilon$ about its mean, $\langle\Delta Y_{i,h}\left(\left[s^*_{\varphi_\epsilon=a}, s^*_{\varphi_\epsilon=b}\right]\right)/\Delta\varphi_\epsilon\rangle$, is given by

$$\sigma_{i,h}\left(\Delta Y_{i,h}\left(\left[s^*_{\varphi_\epsilon=a}, s^*_{\varphi_\epsilon=b}\right]\right)/\Delta\varphi_\epsilon\right) = \left\{\frac{1}{b-a-1}\left[\sum_{\varphi_\epsilon=a}^{\varphi_\epsilon=b}\left(\Delta Y_{i,h}\left(s^*_{\varphi_\epsilon}\right)/\Delta\varphi_\epsilon - \langle\Delta Y_{i,h}\left(\left[s^*_{\varphi_\epsilon=a}, s^*_{\varphi_\epsilon=b}\right]\right)/\Delta\varphi_\epsilon\rangle\right)^2\right]\right\}^{0.5},$$

(133b)

where $1 \le a < b \le 2N$. Thus, at time t_ϵ, within the full range of $s^*_{\varphi_\epsilon}$ values that apply at that time, $\sigma_{i,h}\left(\Delta Y_{i,h}\left(\left[s^*_{\varphi_\epsilon=1}, s^*_{\varphi_\epsilon=2N}\right]\right)/\Delta\varphi_\epsilon\right)$ is equal to the standard deviation about $\langle\Delta Y_{i,h}\left(\left[s^*_{\varphi_\epsilon=1}, s^*_{\varphi_\epsilon=2N}\right]\right)/\Delta\varphi_\epsilon\rangle$, which is equal to the mean of all $\Delta Y_{i,h}\left(s^*_{\varphi_\epsilon}\right)/\Delta\varphi_\epsilon$.

For $Y_{i,h}(s^*_{\varphi_\epsilon}) = \Delta GRN_{i,h}(s^*_{\varphi_\epsilon})$, it might be expected that the standard deviation in $\frac{\Delta Y_{i,h}(s^*_{\varphi_\epsilon})}{\Delta\varphi_\epsilon}$ would be approximately equal to $2\sigma_{RI}$. In the calculation of $\frac{\Delta Y_{i,h}(s^*_{\varphi_\epsilon})}{\Delta\varphi_\epsilon}$, however, all but the innermost (Equation 132b) and outermost (Equation 132c) terms reduce to $\left(Y_{i,h}\left(s^*_{\varphi_\epsilon+1}\right) - Y_{i,h}\left(s^*_{\varphi_\epsilon-1}\right)\right)/2$ (Equation 132a), which is a difference in $Y_{i,h}\left(s^*_{\varphi_\epsilon}\right)$ values divided by 2. The standard deviation of $\left(Y_{i,h}\left(s^*_{\varphi_\epsilon+1}\right) - Y_{i,h}\left(s^*_{\varphi_\epsilon-1}\right)\right)/2$ about its mean is given by

$$\frac{\sigma_{i,h}\left(\Delta Y_{i,h}\left(\left[s^*_{\varphi_\epsilon=2}, s^*_{\varphi_\epsilon=2N-1}\right]\right)\right)}{2} = \frac{\sqrt{\sigma_{i,h}\left(Y_{i,h}\left(\left[s^*_{\varphi_\epsilon=2}, s^*_{\varphi_\epsilon=2N-1}\right]\right)\right) + \sigma_{i,h}\left(Y_{i,h}\left(\left[s^*_{\varphi_\epsilon=2}, s^*_{\varphi_\epsilon=2N-1}\right]\right)\right)}}{2}$$

$$= \frac{\sqrt{2\sigma_{i,h}\left(Y_{i,h}\left(\left[s^*_{\varphi_\epsilon=2}, s^*_{\varphi_\epsilon=2N-1}\right]\right)\right)}}{2} = \frac{1}{\sqrt{2}}\sqrt{\sigma_{i,h}\left(Y_{i,h}\left(\left[s^*_{\varphi_\epsilon=2}, s^*_{\varphi_\epsilon=2N-1}\right]\right)\right)}.$$

(134)

For $Y_{i,h}(s^*_{\varphi_\epsilon}) = \Delta GRN_{i,h}(s^*_{\varphi_\epsilon})$ and $N >> 2$, by the reasoning applied to Equation 131b,

$\sigma_{i,h}\left(\Delta GRN_{i,h}\left(\left[s^*_{\varphi_\epsilon=2}, s^*_{\varphi_\epsilon=2N-1}\right]\right)\right) = \sigma_{i,h}\left(\Delta GRN_{i,h}([r_2, r_{N-1}], t_\epsilon)\right) \cong 2^{0.5}\sigma_{RI}$. Thus, for $Y_{i,h}(s^*_{\varphi_\epsilon}) = \Delta GRN_{i,h}(s^*_{\varphi_\epsilon})$ and $N >> 2$, $\sigma_{i,h}\left(\Delta Y_{i,h}\left(\left[s^*_{\varphi_\epsilon=2}, s^*_{\varphi_\epsilon=2N-1}\right]\right)\right)/2$, the standard deviation of $\left(Y_{i,h}\left(s^*_{\varphi_\epsilon+1}\right) - Y_{i,h}\left(s^*_{\varphi_\epsilon-1}\right)\right)/2$ about its mean, is approximately equal to σ_{RI}.

With $a = 2$ and $b = 2N$ - 1, $\sigma_{i,h}\left(\Delta Y_{i,h}\left(\left[s^*_{\varphi_\epsilon=a}, s^*_{\varphi_\epsilon=b}\right]\right)/\Delta\varphi_\epsilon\right)$ of Equation 133b becomes identical to $\sigma_{i,h}\left(\Delta Y_{i,h}\left(\left[s^*_{\varphi_\epsilon=2}, s^*_{\varphi_\epsilon=2N-1}\right]\right)\right)/2$ of Equation 134. Thus, for $Y_{i,h}(s^*_{\varphi_\epsilon}) = \Delta GRN_{i,h}(s^*_{\varphi_\epsilon})$ and $N >> 2$, the standard deviation in $\frac{\Delta Y_{i,h}(s^*_{\varphi_\epsilon})}{\Delta\varphi_\epsilon}$ is approximately the same as that in the raw data, for which $\sigma_{i,h}\left(NMS_{i,h}([r_1, r_{2N}], t_\epsilon)\right) \cong \sigma_{RI} = 0.01400$ fringe (Figure 5; Table 14; Equation 119b; Figure 52). As it is generally the case that $N >> 2$, it is generally the case that $\sigma_{i,h}\left(\Delta Y_{i,h}\left(\left[s^*_{\varphi_\epsilon=a}, s^*_{\varphi_\epsilon=b}\right]\right)/\Delta\varphi_\epsilon\right) \cong \sigma_{RI} = 0.01400$ fringe.

Given $\sigma_{i,h}\left(\Delta Y_{i,h}\left(\left[s^*_{\varphi_\epsilon=a}, s^*_{\varphi_\epsilon=b}\right]\right)/\Delta\varphi_\epsilon\right) \cong \sigma_{RI} = 0.01400$ fringe, setting to zero the approximately 95.45000% of $\frac{\Delta Y_{i,h}(s^*_{\varphi_\epsilon})}{\Delta\varphi_\epsilon}$ values that lie within -2σ_{RI} and 2σ_{RI} (-0.02800 fringe $< \frac{\Delta Y_{i,h}(s^*_{\varphi_\epsilon})}{\Delta\varphi_\epsilon} <$ 0.02800 fringe) removes all but approximately 4.55000% of the signal-free data, for which $\left(\frac{\partial Y_i(s^*_{\varphi_\epsilon})}{\partial s^*_{\varphi_\epsilon}}\right)_t = 0$. For times $t_\epsilon = t_{36}$, $t_\epsilon = t_{51}$ and $t_\epsilon = t_{66}$, Figure 63 shows the derivative of $Y_{i,h}\left(s^*_{\varphi_\epsilon}\right) = \Delta GRN_{i,h}\left(s^*_{\varphi_\epsilon}\right)$ with respect to φ_ϵ versus φ_ϵ. (Compare Figure 63 with Figure 55, which shows the derivative of $Y_{i,h}\left(s^*_{\varphi_\epsilon}\right) = \Delta GRN_{i,h}\left(s^*_{\varphi_\epsilon}\right)$ with respect to $s^*_{\varphi_\epsilon}$ versus $s^*_{\varphi_\epsilon}$ at the same times.) Figure 63 also distinguishes $\frac{\Delta Y_{i,h}(s^*_{\varphi_\epsilon})}{\Delta\varphi_\epsilon}$ from the approximately 4.55000% of $\frac{\Delta Y_{i,h}(s^*_{\varphi_\epsilon})}{\Delta\varphi_\epsilon}$ that lie outside the range of -2σ_{RI} to 2σ_{RI}.

Where a signal is present, $\Delta NFS_i\left(s^*_{\varphi_\epsilon}\right) \neq 0$, and thus $Y_{i,h}\left(s^*_{\varphi_\epsilon}\right) = \Delta NFS_i\left(s^*_{\varphi_\epsilon}\right) + \Delta GRN_{i,h}\left(s^*_{\varphi_\epsilon}\right) + k_{i,h,\epsilon}$ must be used to describe the data (Equation 111b). The percentage of data for which $0 < \frac{\Delta Y_{i,h}\left(s^*_{\varphi\epsilon}\right)}{\Delta\varphi_\epsilon} < 2\sigma_{RI}$ will be the percentage of data for which $\frac{\Delta Y_{i,h}\left(s^*_{\varphi\epsilon}\right)}{\Delta\varphi_\epsilon}$ is mistaken for $\frac{\Delta GRN_{i,h}\left(s^*_{\varphi\epsilon}\right)}{\Delta\varphi_\epsilon}$ and wrongly set to zero, despite $Y_{i,h}\left(s^*_{\varphi_\epsilon}\right)$ being equal to $\Delta NFS_i\left(s^*_{\varphi_\epsilon}\right) + \Delta GRN_{i,h}\left(s^*_{\varphi_\epsilon}\right) + k_{i,h,\epsilon}$, where $\Delta NFS_i\left(s^*_{\varphi_\epsilon}\right) \neq 0$.

As $\Delta\varphi_\epsilon = 1$ always and everywhere,

$$\left(\frac{\partial Y_{i,h}\left(s^*_{\varphi_\epsilon}\right)}{\partial s^*_{\varphi_\epsilon}}\right)_t = \left(\frac{\partial Y_{i,h}\left(s^*_{\varphi_\epsilon}\right)}{\partial \varphi_\epsilon}\right)_t \left(\frac{\partial \varphi_\epsilon}{\partial s^*_{\varphi_\epsilon}}\right)_t \cong \frac{\Delta Y_{i,h}\left(s^*_{\varphi_\epsilon}\right)}{\Delta\varphi_\epsilon}\frac{\Delta\varphi_\epsilon}{\Delta s^*_{\varphi_\epsilon}} = \frac{\Delta Y_{i,h}\left(s^*_{\varphi_\epsilon}\right)}{\Delta\varphi_\epsilon}\frac{1}{\Delta s^*_{\varphi_\epsilon}} = \frac{\Delta Y_{i,h}\left(s^*_{\varphi_\epsilon}\right)}{\Delta\varphi_\epsilon}\frac{r_j\omega^2 t_\epsilon}{\Delta r_j}$$

$$\equiv \frac{\Delta Y_{i,h}\left(s^*_{\varphi_\epsilon}\right)}{\Delta s^*_{\varphi_\epsilon}}$$

(135)

where $\frac{1}{\Delta s^*_{\varphi_\epsilon}}$ is given by Equation 117, and where the relationship between r_j and $s^*_{\varphi_\epsilon}$ is given by Equations 114 and 115. Using Equation 135, $\frac{\Delta Y_{i,h}\left(s^*_{\varphi\epsilon}\right)}{\Delta s^*_{\varphi_\epsilon}}$ was calculated from the values of $\frac{\Delta Y_{i,h}\left(s^*_{\varphi\epsilon}\right)}{\Delta\varphi_\epsilon}$ shown in Figure 63 as a function of φ_ϵ. Figure 64 shows the resulting values of $\frac{\Delta Y_{i,h}\left(s^*_{\varphi\epsilon}\right)}{\Delta s^*_{\varphi_\epsilon}}$ remapped from φ_ϵ to $s^*_{\varphi_\epsilon}$. The remainder of the analysis (Figures 65 to 71) proceeds as previously shown (Figures 56 to 62).

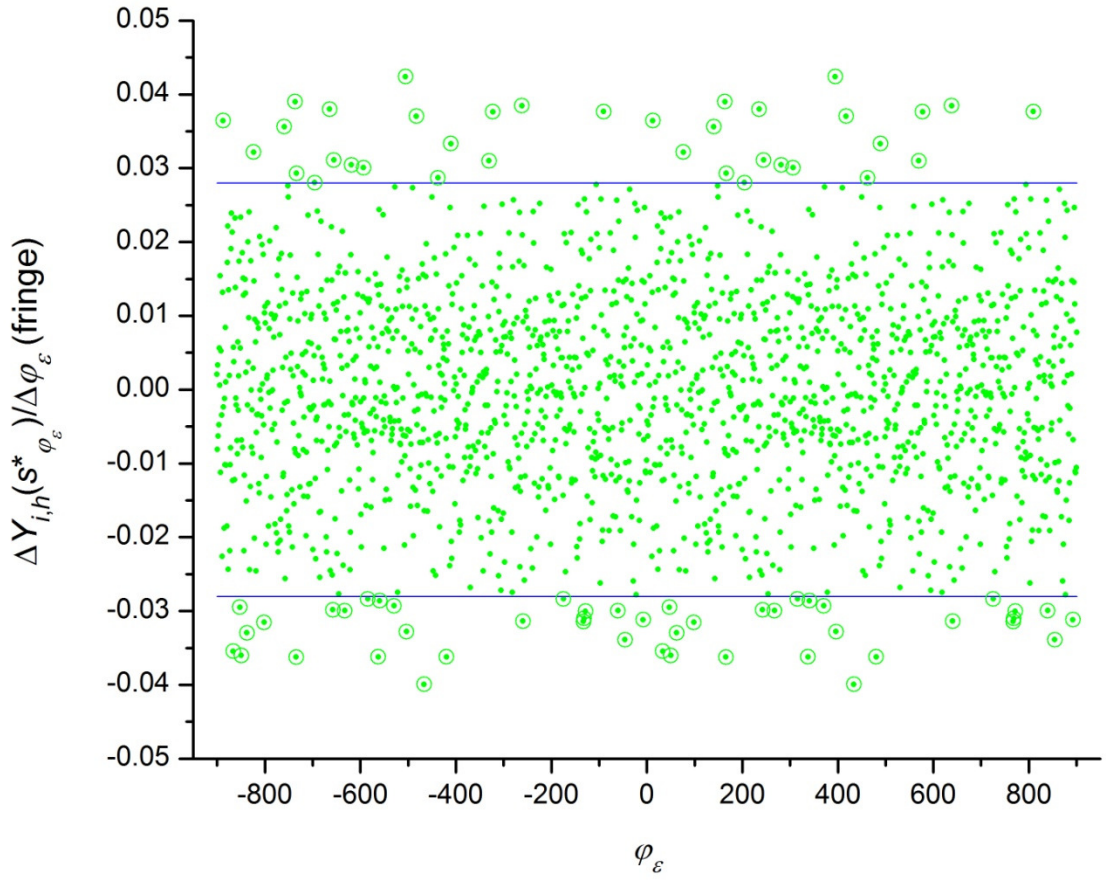

Figure 63a. The derivative of $Y_{i,h}(s^*_{\varphi_\epsilon}) = \Delta GRN_{i,h}(s^*_{\varphi_\epsilon})$ with respect to φ_ϵ (Equation 132) versus φ_ϵ at $t_\epsilon = t_{36}$. All $\frac{\Delta Y_{i,h}(s^*_{\varphi_\epsilon})}{\Delta\varphi_\epsilon}$ (·) versus φ_ϵ are shown and distinguished from the 4.55050% (○) of $\frac{\Delta Y_{i,h}(s^*_{\varphi_\epsilon})}{\Delta\varphi_\epsilon}$ that lie outside the range of -2σ_{RI} to 2σ_{RI} ($\sigma_{i,h}\left(\Delta Y_{i,h}\left(\left[s^*_{\varphi_\epsilon=a}, s^*_{\varphi_\epsilon=b}\right]\right)/\Delta\varphi_\epsilon\right) \cong \sigma_{RI} =$ 0.01400 fringe), with -2σ_{RI} and 2σ_{RI} shown as blue lines. Replacing with zero any data for which $\frac{\Delta Y_{i,h}(s^*_{\varphi_\epsilon})}{\Delta\varphi_\epsilon}$ lies within -2σ_{RI} to 2σ_{RI} reduces the frequency with which $Y_{i,h}(s^*_{\varphi_\epsilon}) = \Delta GRN_{i,h}(s^*_{\varphi_\epsilon})$ is treated as signal to approximately 4.55% of what it is when no data are replaced with zero (Figure 55a).

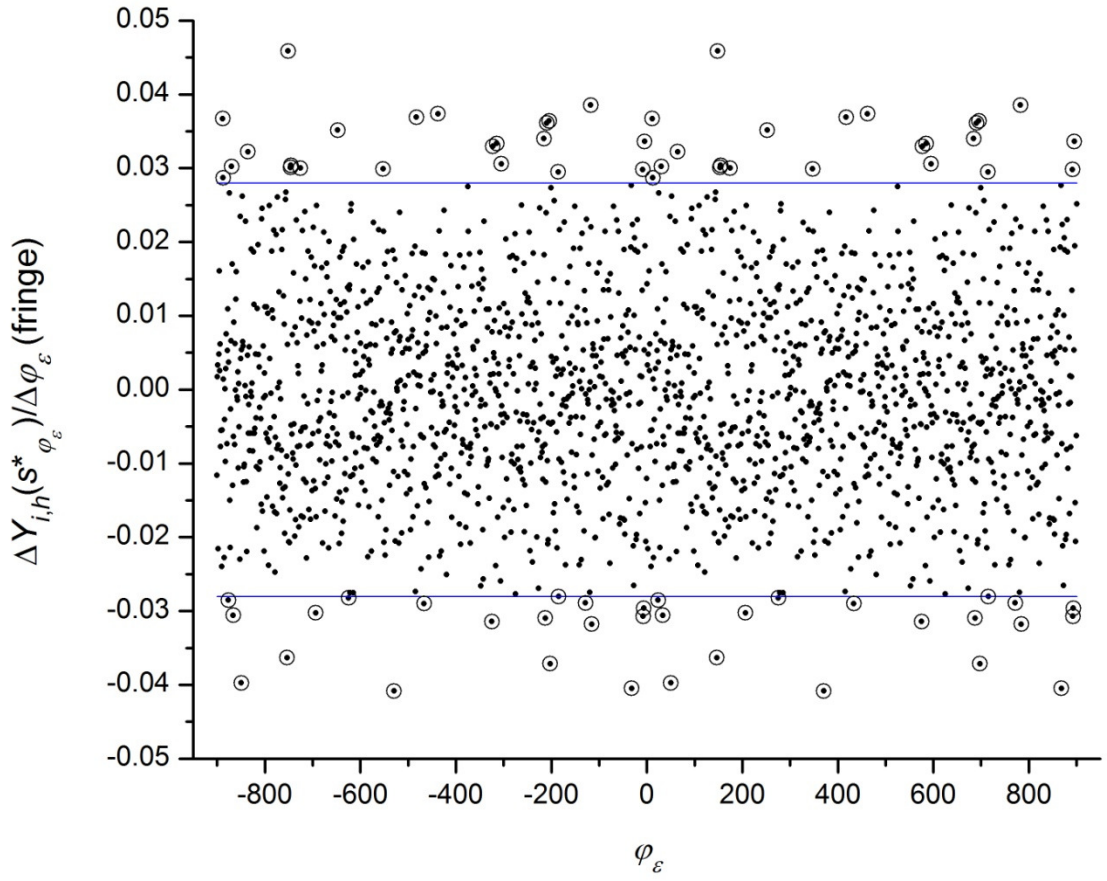

Figure 63b. The derivative of $Y_{i,h}(s^*_{\varphi_\epsilon}) = \Delta GRN_{i,h}(s^*_{\varphi_\epsilon})$ with respect to φ_ϵ (Equation 132) versus φ_ϵ at $t_\epsilon = t_{51}$. All $\frac{\Delta Y_{i,h}(s^*_{\varphi_\epsilon})}{\Delta\varphi_\epsilon}$ (·) versus φ_ϵ are shown and distinguished from the 4.32852% (○) of $\frac{\Delta Y_{i,h}(s^*_{\varphi_\epsilon})}{\Delta\varphi_\epsilon}$ that lie outside the range of -2σ_{RI} to 2σ_{RI} ($\sigma_{i,h}\left(\Delta Y_{i,h}\left(\left[s^*_{\varphi_\epsilon=a}, s^*_{\varphi_\epsilon=b}\right]\right)/\Delta\varphi_\epsilon\right) \cong \sigma_{RI} =$ 0.01400 fringe), with -2σ_{RI} and 2σ_{RI} shown as blue lines. Replacing with zero any data for which $\frac{\Delta Y_{i,h}(s^*_{\varphi_\epsilon})}{\Delta\varphi_\epsilon}$ lies within -2σ_{RI} to 2σ_{RI} reduces the frequency with which $Y_{i,h}(s^*_{\varphi_\epsilon}) = \Delta GRN_{i,h}(s^*_{\varphi_\epsilon})$ is treated as signal to approximately 4.55% of what it is when no data are replaced with zero (Figure 55b).

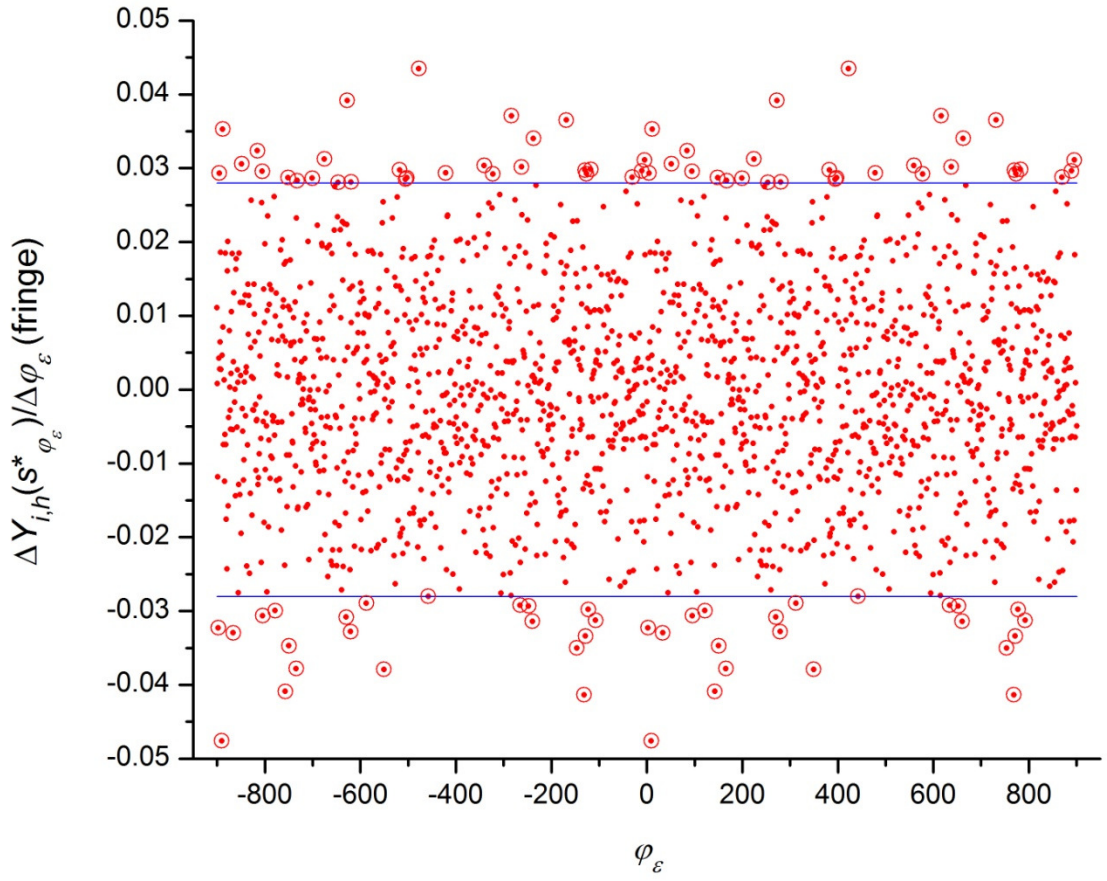

Figure 63c. The derivative of $Y_{i,h}(s^*_{\varphi_\epsilon}) = \Delta GRN_{i,h}(s^*_{\varphi_\epsilon})$ with respect to φ_ϵ (Equation 132) versus φ_ϵ at $t_\epsilon = t_{66}$. All $\frac{\Delta Y_{i,h}(s^*_{\varphi_\epsilon})}{\Delta\varphi_\epsilon}$ (·) versus φ_ϵ are shown and distinguished from the 5.54939% (○) of $\frac{\Delta Y_{i,h}(s^*_{\varphi_\epsilon})}{\Delta\varphi_\epsilon}$ that lie outside the range of -2σ_{RI} to 2σ_{RI} ($\sigma_{i,h}\left(\Delta Y_{i,h}\left(\left[s^*_{\varphi_\epsilon=a}, s^*_{\varphi_\epsilon=b}\right]\right)/\Delta\varphi_\epsilon\right) \cong \sigma_{RI} =$ 0.01400 fringe), with -2σ_{RI} and 2σ_{RI} shown as blue lines. Replacing with zero any data for which $\frac{\Delta Y_{i,h}(s^*_{\varphi_\epsilon})}{\Delta\varphi_\epsilon}$ lies within -2σ_{RI} to 2σ_{RI} reduces the frequency with which $Y_{i,h}(s^*_{\varphi_\epsilon}) = \Delta GRN_{i,h}(s^*_{\varphi_\epsilon})$ is treated as signal to approximately 4.55% of what it is when no data are replaced with zero (Figure 55c).

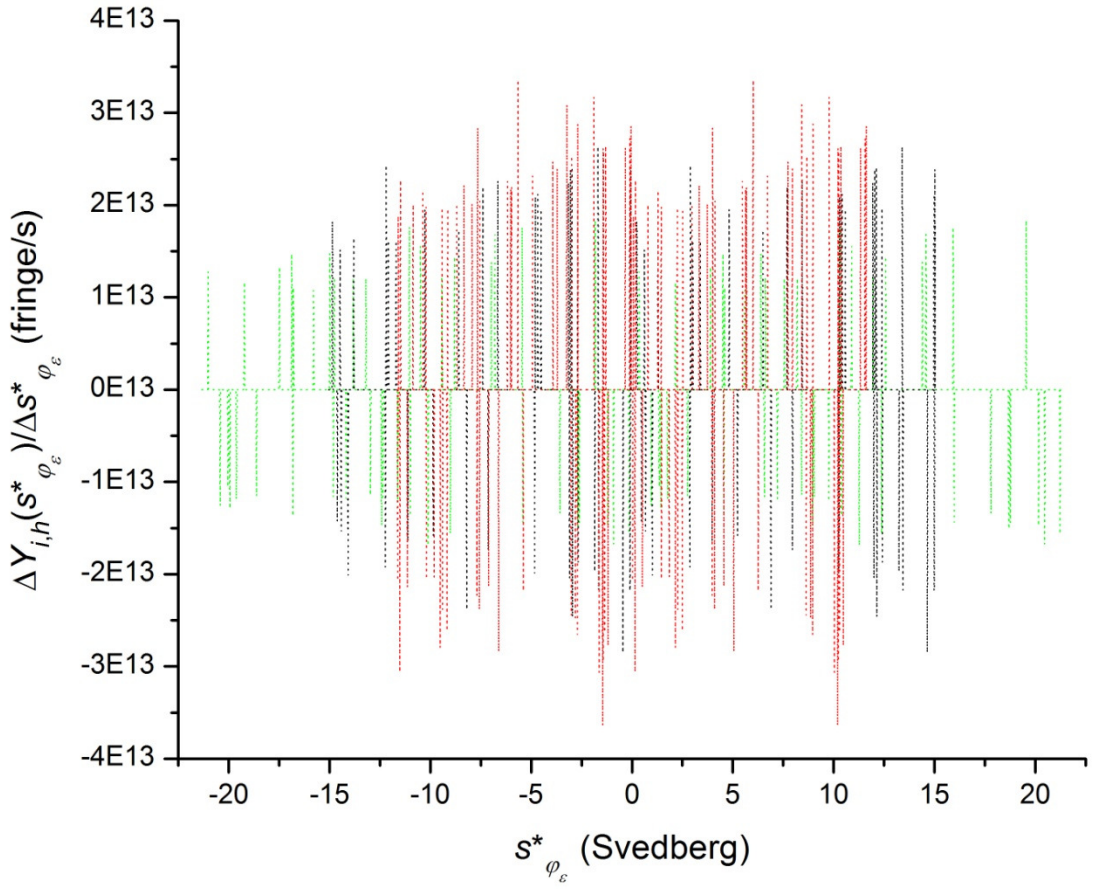

Figure 64. $\Delta Y_{i,h}(s^*_{\varphi_\epsilon})/\Delta s^*_{\varphi_\epsilon}$ versus $s^*_{\varphi_\epsilon}$ at $t_\epsilon = t_{36}$ (·····), $t_\epsilon = t_{51}$ (·····) and $t_\epsilon = t_{66}$ (·····), where $i = 0$ and $h = 1$. As $i = 0$, $Y_{i,h}(s^*_{\varphi_\epsilon}) = \Delta GRN_{i,h}(s^*_{\varphi_\epsilon})$. Figure 63 shows $\frac{\Delta Y_{i,h}(s^*_{\varphi_\epsilon})}{\Delta\varphi_\epsilon}$, the values of which were multiplied by $\frac{\Delta\varphi_\epsilon}{\Delta s^*_{\varphi_\epsilon}}$ to obtain $\Delta Y_{i,h}(s^*_{\varphi_\epsilon})/\Delta s^*_{\varphi_\epsilon}$ (Equation 135) and remapped from φ_ϵ to $s^*_{\varphi_\epsilon}$ to produce this figure. As $\Delta\varphi_\epsilon = 1$, $\frac{\Delta\varphi_\epsilon}{\Delta s^*_{\varphi_\epsilon}} = \frac{1}{\Delta s^*_{\varphi_\epsilon}}$, which Equation 117 shows is equal to $\omega^2 t_\epsilon r_j/\Delta r_j$. (The relationship between r_j and $s^*_{\varphi_\epsilon}$ is given by Equations 114 and 115.) Replacing with zero any data for which $\frac{\Delta Y_{i,h}(s^*_{\varphi_\epsilon})}{\Delta\varphi_\epsilon}$ lies within -2 σ_{RI} to 2 σ_{RI} (Figure 63), where $\sigma_{i,h}\left(\Delta Y_{i,h}\left(\left[s^*_{\varphi_\epsilon=a}, s^*_{\varphi_\epsilon=b}\right]\right)/\Delta\varphi_\epsilon\right) \cong \sigma_{RI} = 0.01400$ fringe, reduces the frequency with which $Y_{i,h}(s^*_{\varphi_\epsilon}) = \Delta GRN_{i,h}(s^*_{\varphi_\epsilon})$ is treated as signal to approximately 4.55% of what it is when no data are replaced with zero (Figure 55).

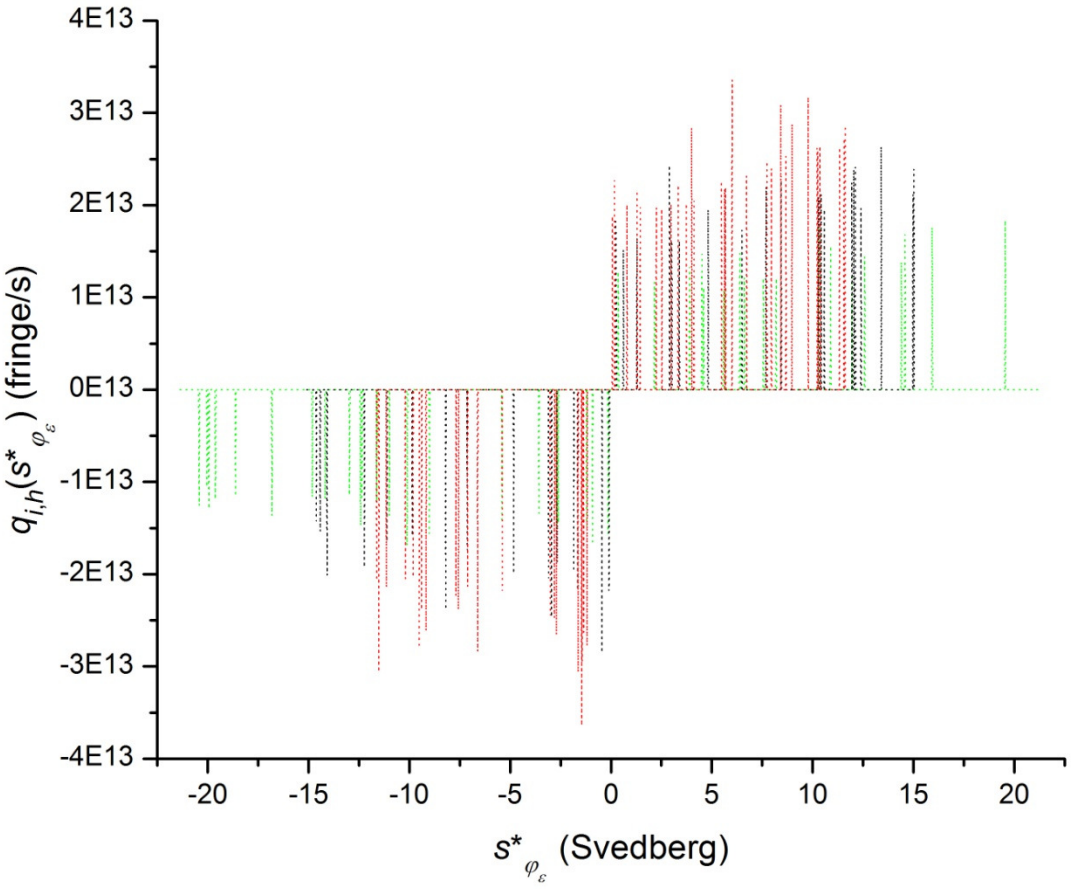

Figure 65. $q_{i,h}(s^*_{\varphi_\epsilon})$ versus $s^*_{\varphi_\epsilon}$ at $t_\epsilon = t_{36}$ (·····), $t_\epsilon = t_{51}$ (·····) and $t_\epsilon = t_{66}$ (·····), where $i = 0$ and $h = 1$. As $i = 0$, these data have their source in a noise-free signal (Figures 64). Replacing with zero any data for which $\frac{\Delta Y_{i,h}(s^*_{\varphi\epsilon})}{\Delta\varphi_\epsilon}$ lies within -2 σ_{RI} to 2 σ_{RI} (Figure 63), where $\sigma_{i,h}(\Delta Y_{i,h}([s^*_{\varphi_\epsilon=a}, s^*_{\varphi_\epsilon=b}])/\Delta\varphi_\epsilon) \cong \sigma_{RI} = 0.01400$ fringe, reduces the number of nonzero $q_{i,h}(s^*_{\varphi_\epsilon})$ values to approximately 4.55% of what it is when no data are replaced with zero (Figure 56).

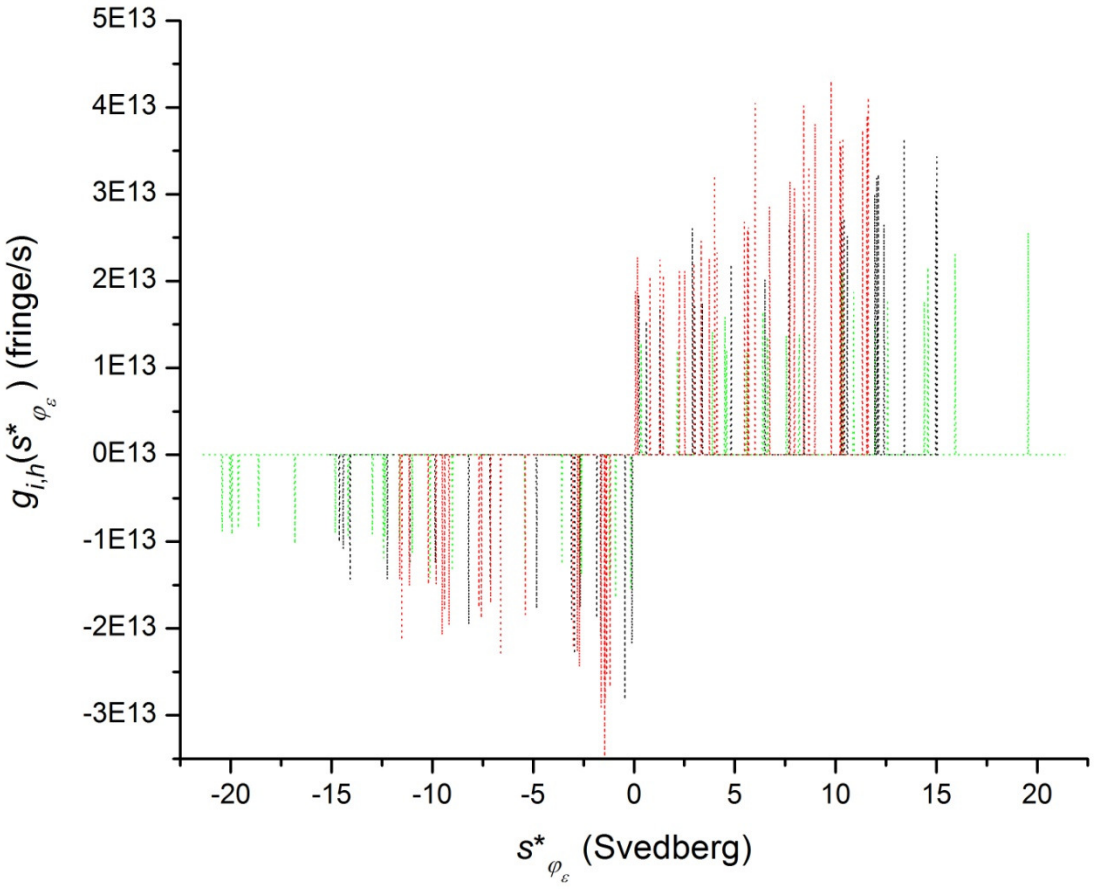

Figure 66. $g_{i,h}(s^*_{\varphi_\epsilon})$ versus $s^*_{\varphi_\epsilon}$ at $t_\epsilon = t_{36}$ (·····), $t_\epsilon = t_{51}$ (·····) and $t_\epsilon = t_{66}$ (·····), where $i = 0$ and $h = 1$. As $i = 0$, these data have their source in a noise-free signal (Figures 64). Replacing with zero any data for which $\frac{\Delta Y_{i,h}(s^*_{\varphi_\epsilon})}{\Delta\varphi_\epsilon}$ lies within -2 σ_{RI} to 2 σ_{RI} (Figure 63), where $\sigma_{i,h}(\Delta Y_{i,h}([s^*_{\varphi_\epsilon=a}, s^*_{\varphi_\epsilon=b}])/\Delta\varphi_\epsilon) \cong \sigma_{RI} = 0.01400$ fringe, reduces the number of nonzero $g_{i,h}(s^*_{\varphi_\epsilon})$ values to approximately 4.55% of what it is when no data are replaced with zero (Figure 57).

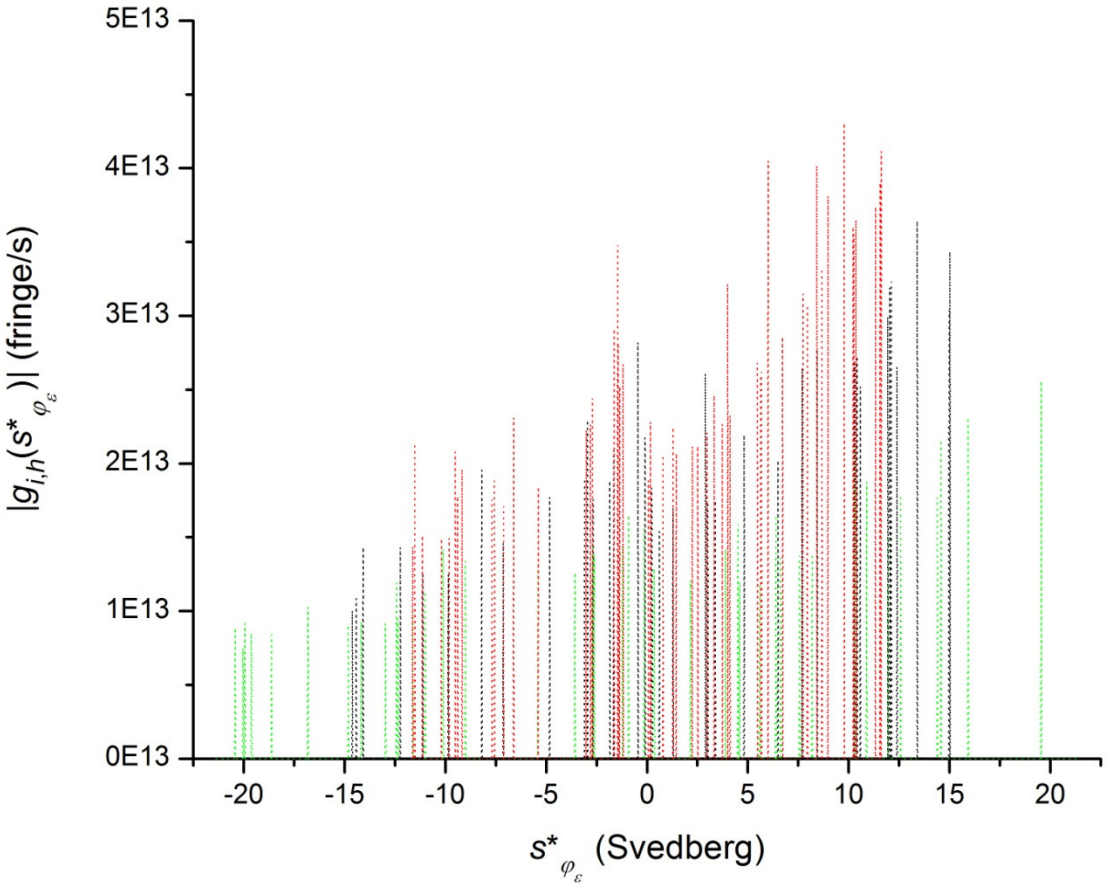

Figure 67. $\left|g_{i,h}\left(s^*_{\varphi_\epsilon}\right)\right|$ versus $s^*_{\varphi_\epsilon}$ at $t_\epsilon = t_{36}$ (·····), $t_\epsilon = t_{51}$ (·····) and $t_\epsilon = t_{66}$ (·····), where $i = 0$ and $h = 1$. As $i = 0$, these data have their source in a noise-free signal (Figures 64). Replacing with zero any data for which $\frac{\Delta Y_{i,h}(s^*_{\varphi_\epsilon})}{\Delta\varphi_\epsilon}$ lies within -2 σ_{RI} to 2 σ_{RI}, where $\sigma_{i,h}\left(\Delta Y_{i,h}\left(\left[s^*_{\varphi_\epsilon=a}, s^*_{\varphi_\epsilon=b}\right]\right)/\Delta\varphi_\epsilon\right) \cong \sigma_{RI} =$ 0.01400 fringe, reduces the number of nonzero $\left|g_{i,h}\left(s^*_{\varphi_\epsilon}\right)\right|$ values to approximately 4.55% of what it is when no data are replaced with zero (Figure 58).

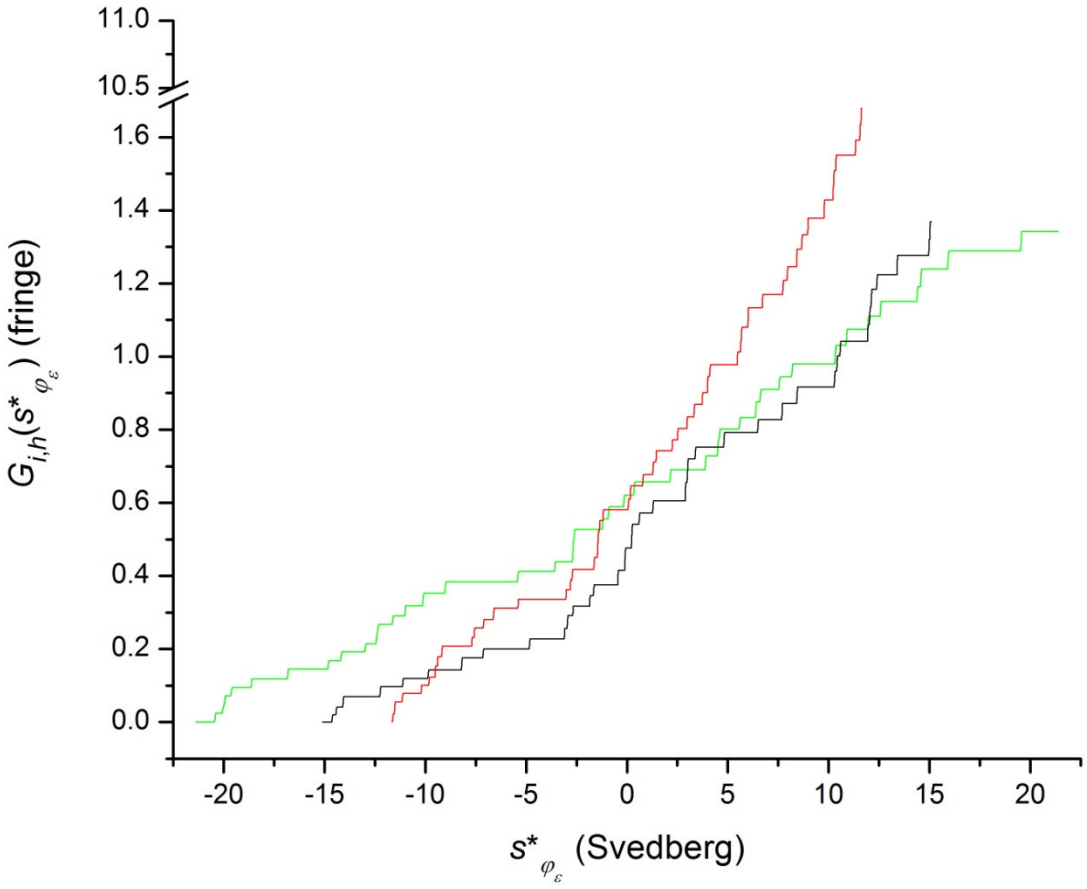

Figure 68. $G_{i,h}(s^*_{\varphi_\epsilon})$ versus $s^*_{\varphi_\epsilon}$ at $t_\epsilon = t_{36}$ (——), $t_\epsilon = t_{51}$ (——) and $t_\epsilon = t_{66}$ (——), where $i = 0$ and $h = 1$. As $i = 0$, these results have their source in a noise-free signal (Figures 64). For each value of $G_{i,h}(s^*_{\varphi_\epsilon})$ shown in this figure, the lower limit of integration is $s^*_{min<0} = s^*_{\varphi_\epsilon=1}$ at time t_ϵ, and the upper limit of integration ranges from $s^*_{min<0}$ to $s^*_{max>0} = s^*_{\varphi_\epsilon=2N}$ at time t_ϵ (Equation 77).

Replacing with zero any data for which $\frac{\Delta Y_{i,h}(s^*_{\varphi_\epsilon})}{\Delta\varphi_\epsilon}$ lies within -2σ_{RI} to 2σ_{RI} (Figure 63), where $\sigma_{i,h}(\Delta Y_{i,h}([s^*_{\varphi_\epsilon=a}, s^*_{\varphi_\epsilon=b}])/\Delta\varphi_\epsilon) \cong \sigma_{RI} = 0.01400$ fringe, reduces the number of nonzero $|g_{i,h}(s^*_{\varphi_\epsilon})|$ values integrated to approximately 4.55% of what it is when no data are replaced with zero (Figure 59, the upper limit of which is shown above the break in the ordinate axis).

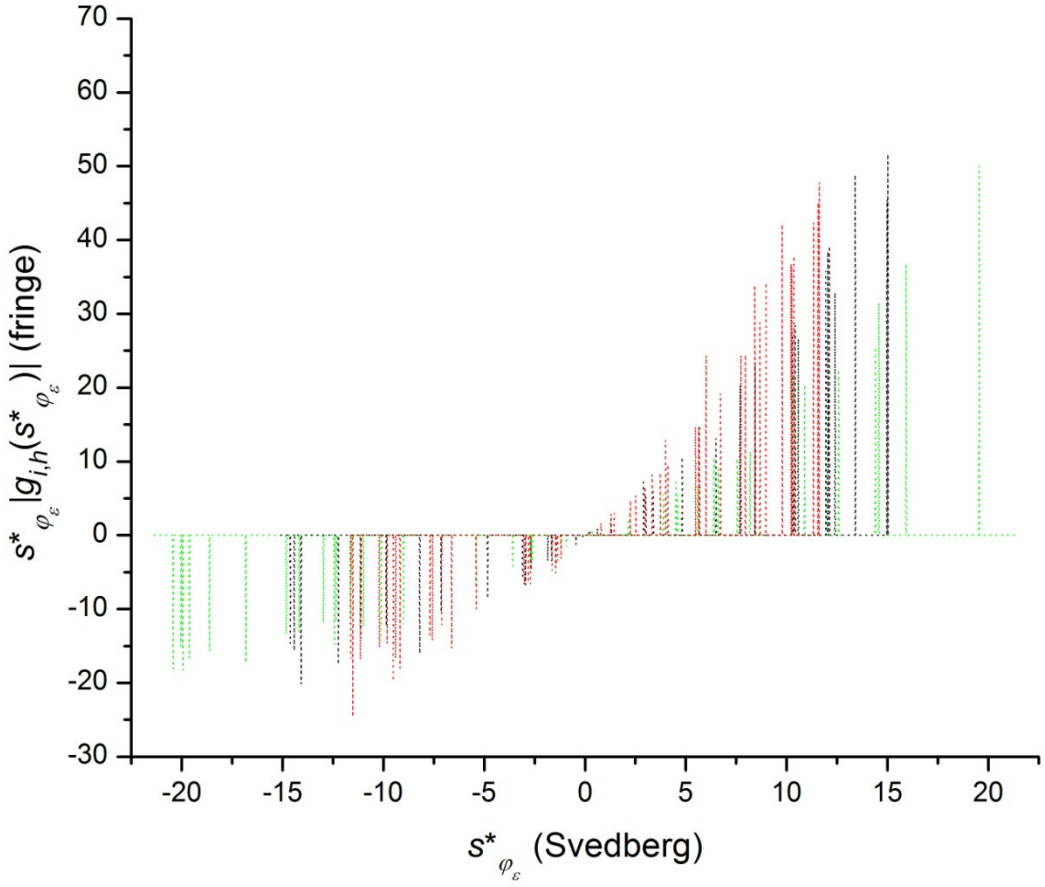

Figure 69. $s^*_{\varphi_\epsilon}\left|g_{i,h}\left(s^*_{\varphi_\epsilon}\right)\right|$ versus $s^*_{\varphi_\epsilon}$ at $t_\epsilon = t_{36}$ (·····), $t_\epsilon = t_{51}$ (·····) and $t_\epsilon = t_{66}$ (·····), where $i = 0$ and $h = 1$. As $i = 0$, these data have their source in a noise-free signal (Figures 64). Replacing with zero any data for which $\frac{\Delta Y_{i,h}\left(s^*_{\varphi_\epsilon}\right)}{\Delta\varphi_\epsilon}$ lies within -2σ_{RI} to 2σ_{RI} (Figure 63), where $\sigma_{i,h}\left(\Delta Y_{i,h}\left(\left[s^*_{\varphi_\epsilon=a}, s^*_{\varphi_\epsilon=b}\right]\right)/\Delta\varphi_\epsilon\right) \cong \sigma_{RI} = 0.01400$ fringe, reduces the number of nonzero $s^*_{\varphi_\epsilon}\left|g_{i,h}\left(s^*_{\varphi_\epsilon}\right)\right|$ values to approximately 4.55% of what it is when no data are replaced with zero (Figure 60).

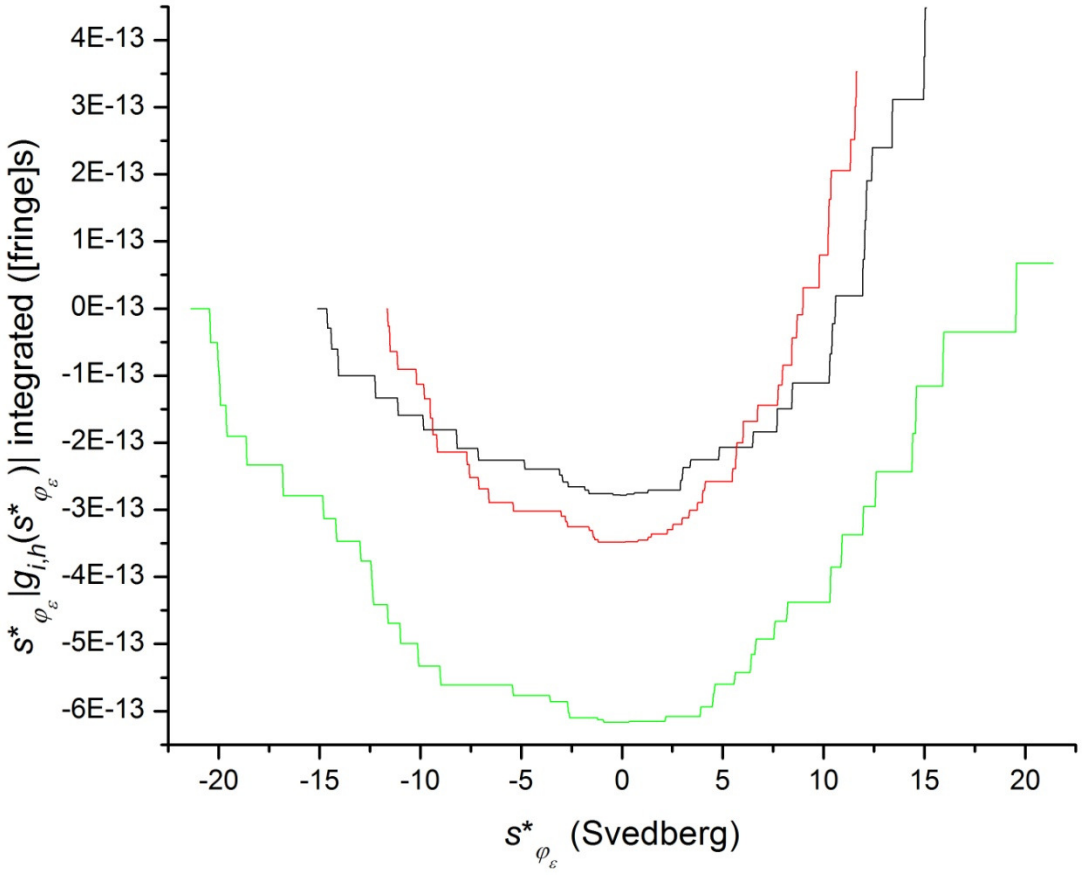

Figure 70. The integral of $s^*_{\varphi_\epsilon}\left|g_{i,h}\left(s^*_{\varphi_\epsilon}\right)\right|$ with respect to $s^*_{\varphi_\epsilon}$ at $t_\epsilon = t_{36}$ (——), $t_\epsilon = t_{51}$ (——) and $t_\epsilon = t_{66}$ (——), where $i = 0$ and $h = 1$. As $i = 0$, these results have their source in a noise-free signal (Figures 64). For each value of the integral (the numerator of Equation 81a) shown in this figure, the lower limit of integration is $s^*_{min<0} = s^*_{\varphi_\epsilon=1}$ at time t_ϵ, and the upper limit of integration ranges from $s^*_{min<0}$ to $s^*_{max>0} = s^*_{\varphi_\epsilon=2N}$ at time t_ϵ. Replacing with zero any data for which $\frac{\Delta Y_{i,h}\left(s^*_{\varphi_\epsilon}\right)}{\Delta\varphi_\epsilon}$ lies within $-2\sigma_{RI}$ to $2\sigma_{RI}$ (Figure 63), where $\sigma_{i,h}\left(\Delta Y_{i,h}\left(\left[s^*_{\varphi_\epsilon=a}, s^*_{\varphi_\epsilon=b}\right]\right)/\Delta\varphi_\epsilon\right) \cong \sigma_{RI} = 0.01400$ fringe, reduces the number of nonzero $s^*_{\varphi_\epsilon}\left|g_{i,h}\left(s^*_{\varphi_\epsilon}\right)\right|$ values integrated to approximately 4.55% of what it is when no data are replaced with zero (Figure 61).

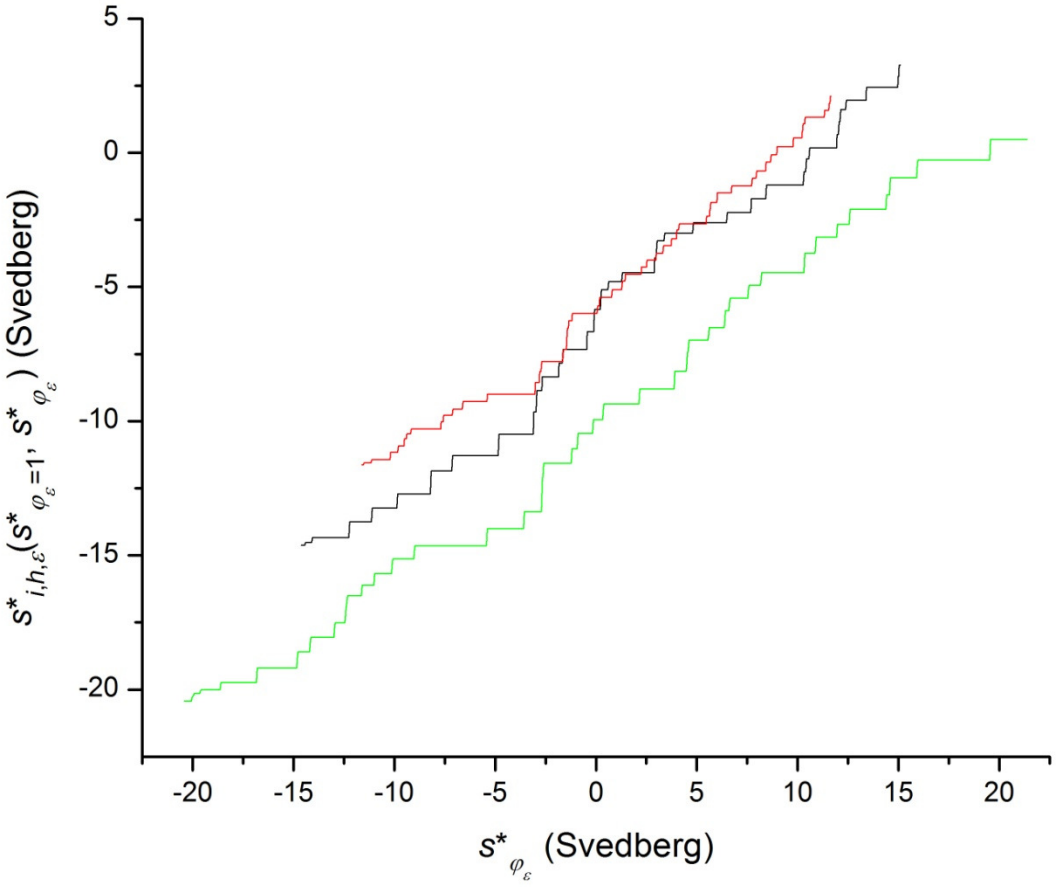

Figure 71. $s^*_{i,h,\epsilon}\left(s^*_{\varphi_\epsilon=1}, s^*_{\varphi_\epsilon}\right)$ versus $s^*_{\varphi_\epsilon}$ at $t_\epsilon = t_{36}$ (——), $t_\epsilon = t_{51}$ (——) and $t_\epsilon = t_{66}$ (——), where $i = 0$ and $h = 1$. As $i = 0$, these results have their source in a noise-free signal (Figures 64). At any given value of $s^*_{\varphi_\epsilon}$, $s^*_{i,h,\epsilon}\left(s^*_{\varphi_\epsilon=1}, s^*_{\varphi_\epsilon}\right)$ is equal to the integral of $s^*_{\varphi_\epsilon}\left|g_{i,h}\left(s^*_{\varphi_\epsilon}\right)\right|$ (Figure 70) divided by $G_{i,h}\left(s^*_{\varphi_\epsilon}\right)$ (Figure 68). The limits applied to the integrals (Equation 81a) that yield $s^*_{i,h,\epsilon}\left(s^*_{\varphi_\epsilon=1}, s^*_{\varphi_\epsilon=2N}\right)$ at each time of analysis are $s^*_{min<0} = s^*_{\varphi_\epsilon=1}$, $s^*_{max<0} = s^*_{min>0} = 0$ and $s^*_{max>0} = s^*_{\varphi_\epsilon=2N}$ at time t_ϵ (Table 18 lists $s^*_{\varphi_\epsilon=1}$ and $= s^*_{\varphi_\epsilon=2N}$ at each time of analysis). For each value of $s^*_{i,h,\epsilon}\left(s^*_{\varphi_\epsilon=1}, s^*_{\varphi_\epsilon}\right)$ shown in this figure, the lower limit of integration is $s^*_{min<0} = s^*_{\varphi_\epsilon=1}$ at time t_ϵ, and the upper limit of integration ranges from $s^*_{min<0}$ to $s^*_{max>0} = s^*_{\varphi_\epsilon=2N}$ at time t_ϵ. Replacing with zero any data for which $\frac{\Delta Y_{i,h}\left(s^*_{\varphi_\epsilon}\right)}{\Delta\varphi_\epsilon}$ lies within -2σ_{RI} to 2σ_{RI} (Figure 63), where

$\sigma_{i,h}\left(\Delta Y_{i,h}\left(\left[s^*_{\varphi_\epsilon=a}, s^*_{\varphi_\epsilon=b}\right]\right)/\Delta\varphi_\epsilon\right) \cong \sigma_{RI} = 0.01400$ fringe, reduces the number of $s^*_{\varphi_\epsilon}\left|g_{i,h}\left(s^*_{\varphi_\epsilon}\right)\right|$ values integrated (compare Figure 59 with Figure 68) and reduces the number of $s^*_{\varphi_\epsilon}\left|g_{i,h}\left(s^*_{\varphi_\epsilon}\right)\right|$ values integrated (compare Figure 61 with Figure 70) to approximately 4.55% of what they are when no data are replaced with zero (compare Figure 62 with this figure).

In going from the results in which no data are replaced with zero (Figure 55) to the results in which data are replaced with zero wherever $\frac{\Delta Y_{i,h}\left(s^*_{\varphi_\epsilon}\right)}{\Delta\varphi_\epsilon}$ lies within -2σ_{RI} to 2σ_{RI} (Figure 63), at any given $s^*_{\varphi_\epsilon}$ value, the fractional decrease in $G_{i,h}\left(s^*_{\varphi_\epsilon}\right)$ (Figures 59 and 68) is approximately the same as the fractional decrease in the value of the integral of $s^*_{\varphi_\epsilon}\left|g_{i,h}\left(s^*_{\varphi_\epsilon}\right)\right|$ (Figures 61 and 70). The fractional decrease in $G_{i,h}\left(s^*_{\varphi_\epsilon}\right)$ and the fractional decrease in the value of the integral of $s^*_{\varphi_\epsilon}\left|g_{i,h}\left(s^*_{\varphi_\epsilon}\right)\right|$ can both be attributed to the minimisation of data clipping that results from data being replaced with zero wherever $\frac{\Delta Y_{i,h}\left(s^*_{\varphi_\epsilon}\right)}{\Delta\varphi_\epsilon}$ lies within -2σ_{RI} to 2σ_{RI} or similar limits.

As $s^*_{i,h,\epsilon}\left(s^*_{\varphi_\epsilon=1}, s^*_{\varphi_\epsilon}\right)$ is equal to the integral of $s^*_{\varphi_\epsilon}\left|g_{i,h}\left(s^*_{\varphi_\epsilon}\right)\right|$ divided by $G_{i,h}\left(s^*_{\varphi_\epsilon}\right)$, at any given $s^*_{\varphi_\epsilon}$ value, $s^*_{i,h,\epsilon}\left(s^*_{\varphi_\epsilon=1}, s^*_{\varphi_\epsilon}\right)$ is approximately the same, regardless of whether data are replaced with zero (Figures 62 and 71). With respect to $s^*_{i,h,\epsilon}\left(s^*_{\varphi_\epsilon=1}, s^*_{\varphi_\epsilon}\right)$, however, the results would be dominated by any significant signal added to the data (Figure 52) from which Figures 62 and 71 arise, and the more that the data were replaced with zero wherever $\frac{\Delta Y_{i,h}\left(s^*_{\varphi_\epsilon}\right)}{\Delta\varphi_\epsilon}$ lay within such limits as -2σ_{RI} to 2σ_{RI}, the more the signal would dominate the results.

A comparison of three differential methods by which $\left(\frac{\partial Y_{i,h}\left(s^*_{\varphi_\epsilon}\right)}{\partial s^*_{\varphi_\epsilon}}\right)_t$ *can be obtained*

Rather than remapping $Y_{i,h}(r_j,t_\epsilon)$ versus r_j to $Y_{i,h}\left(s^*_{\varphi_\epsilon}\right)$ versus $s^*_{\varphi_\epsilon}$ (Equations 7 and 111) and then differentiating to obtain $\left(\frac{\partial Y_{i,h}\left(s^*_{\varphi_\epsilon}\right)}{\partial s^*_{\varphi_\epsilon}}\right)_t$ approximated as $\frac{\Delta Y_{i,h}\left(s^*_{\varphi_\epsilon}\right)}{\Delta s^*_{\varphi_\epsilon}}$ (Equation 8), $\left(\frac{\partial Y_{i,h}\left(s^*_{\varphi_\epsilon}\right)}{\partial s^*_{\varphi_\epsilon}}\right)_t$ can be obtained via

$$\left(\frac{\partial Y_{i,h}\left(s^*_{\varphi_\epsilon}\right)}{\partial s^*_{\varphi_\epsilon}}\right)_t = \left(\frac{\partial Y_{i,h}\left(r_j,t_\epsilon\right)}{\partial r_j}\right)_t \left(\frac{\partial r_j}{\partial s^*_{\varphi_\epsilon}}\right)_t \cong \frac{\Delta Y_{i,h}\left(r_j,t_\epsilon\right)}{\Delta r_j}\frac{\Delta r_j}{\Delta s^*_{\varphi_\epsilon}} = \frac{\Delta Y_{i,h}\left(r_j,t_\epsilon\right)}{\Delta r_j} r_j\omega^2 t_\epsilon \equiv \frac{\Delta Y_{i,h}\left(s^*_{\varphi_\epsilon}\right)}{\Delta s^*_{\varphi_\epsilon}},$$

(136)

where $\frac{\Delta r_j}{\Delta s^*_{\varphi_\epsilon}}$ is given by Equation 116, and where the relationship between r_j and $s^*_{\varphi_\epsilon}$ is given by Equations 114 and 115. The approach represented by Equation 136 is identical to that employed by Bridgeman (1942).

As $\left(\frac{\partial Y_{i,h}(r_j)}{\partial r_j}\right)_t$ cannot be evaluated analytically, it must be approximated. The approximation used to evaluate the partial derivative of $Y_{i,h}(s^*_{\varphi_\epsilon})$ with respect to $s^*_{\varphi_\epsilon}$ at time t_ϵ via the partial derivative of $Y_{i,h}(r_j,t_\epsilon)$ with respect to r_j is given by

$$\left(\frac{\partial Y_{i,h}\left(s^*_{\varphi_\epsilon}\right)}{\partial s^*_{\varphi_\epsilon}}\right)_t = \left(\frac{\partial Y_{i,h}\left(s^*_{\varphi_\epsilon+N}\right)}{\partial s^*_{\varphi_\epsilon}}\right)_t \cong \frac{1}{2}\left[\frac{Y_{i,h}\left(r_j,t_\epsilon\right)-Y_{i,h}\left(r_{j-1},t_\epsilon\right)}{r_j-r_{j-1}} + \frac{Y_{i,h}\left(r_{j+1},t_\epsilon\right)-Y_{i,h}\left(r_j,t_\epsilon\right)}{r_{j+1}-r_j}\right] r_j\omega^2 t_\epsilon$$

$$\equiv \frac{\Delta Y_{i,h}\left(s^*_{\varphi_\epsilon}\right)}{\Delta s^*_{\varphi_\epsilon}} = \frac{\Delta Y_{i,h}\left(s^*_{\varphi_\epsilon+N}\right)}{\Delta s^*_{\varphi_\epsilon}}$$

(137a)

at j within $1 < j < N$,

$$\left(\frac{\partial Y_{i,h}\left(s^*_{\varphi_\epsilon=1}\right)}{\partial s^*_{\varphi_\epsilon}}\right)_t = \left(\frac{\partial Y_{i,h}\left(s^*_{\varphi_\epsilon=N+1}\right)}{\partial s^*_{\varphi_\epsilon}}\right)_t \cong \left[\frac{Y_{i,h}\left(r_{j+1},t_\epsilon\right)-Y_{i,h}\left(r_j,t_\epsilon\right)}{r_{j+1}-r_j}\right] r_j\omega^2 t_\epsilon \equiv \frac{\Delta Y_{i,h}\left(s^*_{\varphi_\epsilon=1}\right)}{\Delta s^*_{\varphi_\epsilon=1}}$$

$$= \frac{\Delta Y_{i,h}\left(s^*_{\varphi_\epsilon=N+1}\right)}{\Delta s^*_{\varphi_\epsilon=N+1}}$$

(137b)

at $j = 1$, and

$$\left(\frac{\partial Y_{i,h}\left(s^*_{\varphi_\epsilon=N}\right)}{\partial s^*_{\varphi_\epsilon}}\right)_t = \left(\frac{\partial Y_{i,h}\left(s^*_{\varphi_\epsilon=2N}\right)}{\partial s^*_{\varphi_\epsilon}}\right)_t \cong \left[\frac{Y_{i,h}(r_j, t_\epsilon) - Y_{i,h}(r_{j-1}, t_\epsilon)}{r_j - r_{j-1}}\right] r_j \omega^2 t_\epsilon \equiv \frac{\Delta Y_{i,h}\left(s^*_{\varphi_\epsilon=N}\right)}{\Delta s^*_{\varphi_\epsilon=N}}$$

$$= \frac{\Delta Y_{i,h}\left(s^*_{\varphi_\epsilon=2N}\right)}{\Delta s^*_{\varphi_\epsilon=2N}}$$

(137c)

at $j = N$.

For a given set $Y_{i,h}(r_j, t_\epsilon)$ versus r_j data, applying Equation 137 yields exactly the same values of $\frac{\Delta Y_{i,h}\left(s^*_{\varphi_\epsilon}\right)}{\Delta s^*_{\varphi_\epsilon}}$ as those obtained by first remapping $Y_{i,h}(r_j, t_\epsilon)$ versus r_j to $Y_{i,h}(s^*_{\varphi_\epsilon})$ versus $s^*_{\varphi_\epsilon}$ and then applying Equation 8. Thus, regardless of whether Equation 8 or Equation 137 is used to approximate $\left(\frac{\partial Y_{i,h}\left(s^*_{\varphi_\epsilon}\right)}{\partial s^*_{\varphi_\epsilon}}\right)_t$ as $\frac{\Delta Y_{i,h}\left(s^*_{\varphi_\epsilon}\right)}{\Delta s^*_{\varphi_\epsilon}}$, all results obtained from that approximation, such as $g_{i,h}\left(s^*_{\varphi_\epsilon}\right)$, $G_{i,h}\left(s^*_{\varphi_\epsilon}\right)$ and $s^*_{i,h,\epsilon}\left(s^*_{\varphi_\epsilon=1}, s^*_{\varphi_\epsilon}\right)$, are identical.

Rather than obtaining $\left(\frac{\partial Y_{i,h}\left(s^*_{\varphi_\epsilon}\right)}{\partial s^*_{\varphi_\epsilon}}\right)_t$ by differentiating $Y_{i,h}(r_j, t_\epsilon)$ with respect to r_j and multiplying the result by $\left(\frac{\partial r_j}{\partial s^*_{\varphi_\epsilon}}\right)_t$ as in Equations 136 and 137, or simply by differentiating $Y_{i,h}\left(s^*_{\varphi_\epsilon}\right)$ with respect to $s^*_{\varphi_\epsilon}$ as in Equation 8, $\left(\frac{\partial Y_{i,h}\left(s^*_{\varphi_\epsilon}\right)}{\partial s^*_{\varphi_\epsilon}}\right)_{t_\epsilon}$ can be obtained via

$$\left(\frac{\partial Y_{i,h}\left(s^*_{\varphi_\epsilon}\right)}{\partial s^*_{\varphi_\epsilon}}\right)_{t_\epsilon} = \left[\left(\frac{\partial Y_{i,h}(r_j, t_\epsilon)}{\partial t_\epsilon}\right)_{r_j} - \left(\frac{\partial Y_{i,h}\left(s^*_{\varphi_\epsilon}\right)}{\partial t_\epsilon}\right)_{s^*_{\varphi_\epsilon}}\right]\left(\frac{\partial t_\epsilon}{\partial s^*_{\varphi_\epsilon}}\right)_{r_j},$$

(138)

in which both $Y_{i,h}(r_j, t_\epsilon)$ and $Y_{i,h}\left(s^*_{\varphi_\epsilon}\right)$ are differentiated with respect to t_ϵ, and the difference

between the derivatives is multiplied by $\left(\frac{\partial t_\epsilon}{\partial s^*_{\varphi_\epsilon}}\right)_{r_j}$, which is easily evaluated.

Equation 138 is based on Stafford's (1992, 1994, 2000) derivation of $g_{i,h}(s^*_{\varphi_\epsilon})$, which starts with the total differential of $Y_{i,h}(r_j,t_\epsilon)$ with respect to $s^*_{\varphi_\epsilon}$ and t_ϵ,

$$dY_{i,h}(r_j,t_\epsilon)=\left(\frac{\partial Y_{i,h}(r_j,t_\epsilon)}{\partial s^*_{\varphi_\epsilon}}\right)_{t_\epsilon} ds^*_{\varphi_\epsilon}+\left(\frac{\partial Y_{i,h}(r_j,t_\epsilon)}{\partial t_\epsilon}\right)_{s^*_{\varphi_\epsilon}} dt_\epsilon\,,$$

(139a)

from which, through division by an infinitesimally small change in t_ϵ at constant r_j, the partial derivative of $Y_{i,h}(r_j,t_\epsilon)$ with respect to t_ϵ at constant r_j,

$$\left(\frac{\partial Y_{i,h}(r_j,t_\epsilon)}{\partial t_\epsilon}\right)_{r_j}=\left(\frac{\partial Y_{i,h}(r_j,t_\epsilon)}{\partial s^*_{\varphi_\epsilon}}\right)_{t_\epsilon}\left(\frac{\partial s^*_{\varphi_\epsilon}}{\partial t_\epsilon}\right)_{r}+\left(\frac{\partial Y_{i,h}(r_j,t_\epsilon)}{\partial t_\epsilon}\right)_{s^*_{\varphi_\epsilon}},$$

(139b)

is obtained. Solving Equation 139b for $\left(\frac{\partial Y_{i,h}(r_j,t_\epsilon)}{\partial s^*_{\varphi_\epsilon}}\right)_{t_\epsilon}$ yields

$$\left(\frac{\partial Y_{i,h}(r_j,t_\epsilon)}{\partial s^*_{\varphi_\epsilon}}\right)_{t_\epsilon}=\left[\left(\frac{\partial Y_{i,h}(r_j,t_\epsilon)}{\partial t_\epsilon}\right)_{r_j}-\left(\frac{\partial Y_{i,h}(r_j,t_\epsilon)}{\partial t_\epsilon}\right)_{s^*_{\varphi_\epsilon}}\right]\left(\frac{\partial t_\epsilon}{\partial s^*_{\varphi_\epsilon}}\right)_{r_j}.$$

(139c)

Remapping $\left(\frac{\partial Y_{i,h}(r_j,t_\epsilon)}{\partial s^*_{\varphi_\epsilon}}\right)_{t_\epsilon}$ versus r_j to $\left(\frac{\partial Y_{i,h}(s^*_{\varphi_\epsilon})}{\partial s^*_{\varphi_\epsilon}}\right)_{t_\epsilon}$ versus $s^*_{\varphi_\epsilon}$ and remapping $\left(\frac{\partial Y_{i,h}(r_j,t_\epsilon)}{\partial t_\epsilon}\right)_{s^*_{\varphi_\epsilon}}$ versus r_j to $\left(\frac{\partial Y_{i,h}(s^*_{\varphi_\epsilon})}{\partial t_\epsilon}\right)_{s^*_{\varphi_\epsilon}}$ versus $s^*_{\varphi_\epsilon}$ yields Equation 138, which is the form of Equation 139c that is most convenient to approximate. Before presenting the approximation of $\left(\frac{\partial Y_{i,h}(s^*_{\varphi_\epsilon})}{\partial s^*_{\varphi_\epsilon}}\right)_{t_\epsilon}$, $\left(\frac{\partial t_\epsilon}{\partial s^*_{\varphi_\epsilon}}\right)_{r_j}$ is solved analytically.

Previously (Equation 114), Equation 5 was solved for r_j to obtain $r_j = r_0 e^{s^*_{\varphi_\epsilon}\omega^2 t_\epsilon}$, where, in correspondence with Equation 6, $r_0 = r_b$ for $\varphi_\epsilon = j$, while $r_0 = r_m$ for $\varphi_\epsilon = j + N$ (Equation 115). Solving Equation 114 for t_ϵ and differentiating with respect to $s^*_{\varphi_\epsilon}$ at constant r_j yields

$$\left(\frac{\partial t_\epsilon}{\partial s^*_{\varphi_\epsilon}}\right)_{r_j} = \frac{-1}{\left(\omega s^*_{\varphi_\epsilon}\right)^2} ln\left(\frac{r_j}{r_0}\right) = -\frac{t_\epsilon}{\frac{1}{\omega^2 t_\epsilon} ln\left(\frac{r_j}{r_0}\right)} = -\frac{t_\epsilon}{s^*_{\varphi_\epsilon}}.$$

(140)

As t_ϵ cannot be less than zero, Equation 140 shows that the signs of $\left(\frac{\partial t_\epsilon}{\partial s^*_{\varphi_\epsilon}}\right)_{r_j}$ and $s^*_{\varphi_\epsilon}$ are always opposite.

Equation 138 is approximated as

$$\frac{\Delta Y_{i,h}\left(s^*_{\varphi_\epsilon}\right)}{\Delta s^*_{\varphi_\epsilon}} = \left(\frac{\Delta Y_{i,h}\left(r_j, t_\epsilon\right)}{\Delta t_\epsilon} - \frac{\Delta Y_{i,h}\left(s^*_{\varphi_\epsilon}\right)}{\Delta t_\epsilon}\right)\frac{\Delta t_\epsilon}{\Delta s^*_{\varphi_\epsilon}},$$

(141)

where $\frac{\Delta t_\epsilon}{\Delta s^*_{\varphi_\epsilon}}$ is an approximation of $\left(\frac{\partial t_\epsilon}{\partial s^*_{\varphi_\epsilon}}\right)_{r_j}$ and, on the basis of Equation 5,

$$\Delta s^*_{\varphi_\epsilon} = \frac{1}{\omega^2}\left[\frac{1}{t_\epsilon} - \frac{1}{t_\delta}\right] ln\left(\frac{r_j}{r_0}\right) = \left[\frac{-\Delta t_\epsilon}{\omega^2 t_\delta t_\epsilon}\right] ln\left(\frac{r_j}{r_0}\right)$$

(142)

is the change in $s^*_{\varphi_\epsilon}$ from time t_δ to time t_ϵ at radial position r_j. The time increment, Δt_ϵ, is equal to t_ϵ - t_δ. Equation 6 shows each of the two possible values of r_0 that can apply to Equation 5. As noted with respect to Equation 7, r_j is an actual radial position where a value of $Y_{i,h}(r_j, t_\epsilon)$ is recorded at time t_ϵ. (See *Point-by-point subtraction of data recorded at one time from data recorded at a later time*.) Using Equation 142 in the denominator $\frac{\Delta t_\epsilon}{\Delta s^*_{\varphi_\epsilon}}$ and taking the limit at Δt_ϵ approaches zero yields

$$\lim_{t_\delta \to t_\epsilon} \frac{\Delta t_\epsilon}{\Delta s^*_{\varphi_\epsilon}} = \lim_{t_\delta \to t_\epsilon} \frac{\Delta t_\epsilon}{\left[\frac{-\Delta t_\epsilon}{\omega^2 t_\delta t_\epsilon}\right] ln\left(\frac{r_j}{r_0}\right)} = -\frac{t_\epsilon}{\frac{1}{\omega^2 t_\epsilon} ln\left(\frac{r_j}{r_0}\right)} = -\frac{t_\epsilon}{s^*_{\varphi_\epsilon}} = \left(\frac{\partial t_\epsilon}{\partial s^*_{\varphi_\epsilon}}\right)_{r_j},$$

(143)

which is consistent with the result obtained in Equation 140.

Signal differences, $Y_{i,h}(r_j,t_\delta)$ and $Y_{i,h}(r_j,t_\epsilon)$, at a common radial position, r_j, but different times, t_δ and t_ϵ, where $t_\delta \neq t_\epsilon$, will not generally map to a common value of the apparent sedimentation coefficient. That is, for $t_\delta \neq t_\epsilon$, in general, $s^*_{\varphi_\delta} \neq s^*_{\varphi_\epsilon}$ at $\varphi_\delta = \varphi_\epsilon = j$ or $\varphi_\delta = \varphi_\epsilon = j + N$ (Equations 5, 6 and 144a). Thus, to evaluate $\frac{\Delta Y_{i,h}(s^*_{\varphi_\epsilon})}{\Delta t_\epsilon}$ at the apparent sedimentation coefficients calculated for time t_ϵ at the actual radial positions, which are the values of r_j for which $1 \leq j \leq N$, it is necessary to calculate interpolated values of the radial position that would apply if the apparent sedimentation coefficients at time t_δ were equal to those at time t_ϵ.

The actual values of the apparent sedimentation coefficient at t_ϵ are given by

$$s^*_{\varphi_\epsilon} = \frac{1}{\omega^2 t_\epsilon} ln\left(\frac{r_j}{r_0}\right),$$

(Equation 5)

where r_j is an actual radial position where a value of $Y_{i,h}(r_j,t_\epsilon)$ is recorded at time t_ϵ. As previously stated (Equations 6 and 115), $r_0 = r_b$ for $\varphi_\epsilon = j$, while $r_0 = r_m$ for $\varphi_\epsilon = j + N$.

The actual values of the apparent sedimentation coefficient at t_δ are given by

$$s^*_{\varphi_\delta} = \frac{1}{\omega^2 t_\delta} ln\left(\frac{r_j}{r_0}\right),$$

(144a)

where r_j is an actual radial position where a value of $Y_{i,h}(r_j,t_\delta)$ is recorded at time t_δ. As at any other time (Equations 6 and 115), $r_0 = r_b$ for $\varphi_\delta = j$, while $r_0 = r_m$ for $\varphi_\delta = j + N$.

The interpolated values of $s^*_{\varphi_\epsilon}$ at t_δ are given by

$$s^*_{\varphi^*_\epsilon} = \frac{1}{\omega^2 t_\delta} ln\left(\frac{r^*_j}{r_0}\right),$$

(144b)

where r^*_j is an interpolated radial position with respect to the original $Y_{i,h}(r_j,t_\delta)$ versus r_j data at t_δ. As with φ_δ and φ_ϵ (Equations 6 and 115), $r_0 = r_b$ for $\varphi^*_\epsilon = j$, while $r_0 = r_m$ for $\varphi^*_\epsilon = j + N$. As the set of all $s^*_{\varphi^*_\epsilon}$ equals the set of all $s^*_{\varphi_\epsilon}$, the right-hand sides of Equations 5 and 144b can be equated and solved for r^*_j to obtain

$$r^*_j = \left(r_j^{t_\delta} r_0^{t_\epsilon - t_\delta}\right)^{\frac{1}{t_\epsilon}} = \left(r_j^{t_\delta} r_0^{\Delta t_\epsilon}\right)^{\frac{1}{t_\epsilon}}.$$

(145a)

Alternatively, given t_δ and $s^*_{\varphi_\epsilon}$, r^*_j Equation 114 can be used to calculate

$$r^*_j = r_0 e^{\,s^*_{\varphi_\epsilon}\omega^2 t_\delta} = r_0 e^{\,s^*_{\varphi^*_\epsilon}\omega^2 t_\delta}.$$

(145b)

The interpolated values needed to evaluate the partial derivative of $Y_{i,h}(s^*_{\varphi_\epsilon})$ with respect to t_ϵ at constant $s^*_{\varphi_\epsilon}$ are calculated as

$$Y_{i,h}\left(s^*_{\varphi^*_\epsilon}\right) = Y_{i,h}\left(r^*_j, t_\delta\right) = Y_{i,h}\left(r_j, t_\delta\right) + \left(\frac{\partial Y_{i,h}\left(r_j, t_\delta\right)}{\partial r_j}\right)_{t_\epsilon} \left(r^*_j - r_j\right),$$

(146)

for which the partial derivative of $Y_{i,h}(r_j,t_\epsilon)$ with respect to r_j is approximated as

$$\left(\frac{\partial Y_{i,h}(r_j,t_\delta)}{\partial r_j}\right)_{t_\epsilon} \cong \frac{1}{2}\left[\frac{Y_{i,h}(r_j,t_\delta)-Y_{i,h}(r_{j-1},t_\delta)}{r_j-r_{j-1}}+\frac{Y_{i,h}(r_{j+1},t_\delta)-Y_{i,h}(r_j,t_\delta)}{r_{j+1}-r_j}\right] \equiv \frac{\Delta Y_{i,h}(r_j,t_\delta)}{\Delta r_j}$$

(147a)

at j within $1 < j < N$,

$$\left(\frac{\partial Y_{i,h}(r_{j=1},t_\delta)}{\partial r_j}\right)_{t_\epsilon} \cong \frac{Y_{i,h}(r_{j+1},t_\delta)-Y_{i,h}(r_j,t_\delta)}{r_{j+1}-r_j} \equiv \frac{\Delta Y_{i,h}(r_{j=1},t_\delta)}{\Delta s^*_{\varphi_\epsilon=1}}$$

(147b)

at $j = 1$, and

$$\left(\frac{\partial Y_{i,h}(r_{j=N},t_\delta)}{\partial r_j}\right)_{t_\epsilon} \cong \frac{Y_{i,h}(r_j,t_\delta)-Y_{i,h}(r_{j-1},t_\delta)}{r_j-r_{j-1}} \equiv \frac{\Delta Y_{i,h}(r_{j=N},t_\delta)}{\Delta r_j}$$

(147c)

at $j = N$.

Within $1 \leq j \leq N$, the approximation used to evaluate the partial derivatives of $Y_{i,h}(s^*_{\varphi_\epsilon})$ with respect to t_ϵ at constant r_j and constant $s^*_{\varphi_\epsilon}$ are given, respectively, by

$$\left(\frac{\partial Y_{i,h}(r_j,t_\epsilon)}{\partial t_\epsilon}\right)_{r_j} \cong \frac{Y_{i,h}(r_j,t_\epsilon)-Y_{i,h}(r_j,t_\delta)}{t_\epsilon-t_\delta} \equiv \frac{\Delta Y_{i,h}(r_j,t_\epsilon)}{\Delta t_\epsilon}$$

(148)

and

$$\left(\frac{\partial Y_{i,h}(s^*_{\varphi_\epsilon})}{\partial t_\epsilon}\right)_{s^*_{\varphi\epsilon}} \cong \frac{Y_{i,h}(s^*_{\varphi_\epsilon})-Y_{i,h}(s^*_{\varphi^*_\epsilon})}{t_\epsilon-t_\delta} \equiv \frac{\Delta Y_{i,h}(s^*_{\varphi_\epsilon=j})}{\Delta t_\epsilon} = \frac{\Delta Y_{i,h}(s^*_{\varphi_\epsilon=j+N})}{\Delta t_\epsilon}.$$

(149)

As noted with respect to Equations 111a and 111b, the signal difference, $Y_{i,h}(r_j,t_\epsilon) =$

$NMS_{i,h}(r_j,t_\epsilon)$ - $NMS_{i,h}(r_j,t_\alpha)$, can be remapped from $Y_{i,h}(r_j,t_\epsilon)$ versus r_j (Equation 111a) to $Y_{i,h}(s^*_{\varphi_\epsilon})$ versus $s^*_{\varphi_\epsilon}$ (Equation 111b), where $s^*_{\varphi_\epsilon}$ is calculated from r_j and t_ϵ using Equation 5. In the process, the difference in the time-independent noise is remapped from $\Delta TIN_{i,h}(r_j) = 0$ versus r_j (1b, 7, 107 and 111a) to $\Delta TIN_{i,h}(s^*_{\varphi_\epsilon}) = 0$ versus $s^*_{\varphi_\epsilon}$ (Equation 111b), the difference in the radially independent noise is remapped from $\Delta RIN_{i,h}(t_\epsilon) = RIN_{i,h}(t_\epsilon)$ - $RIN_{i,h}(t_\alpha) = k_{i,h,\epsilon}$ versus r_j (Equations 1b, 7, 108 and 111a) to $\Delta RIN_{i,h}(s^*_{\varphi_\epsilon}) = k_{i,h,\epsilon}$ versus $s^*_{\varphi_\epsilon}$ (Equation 111b), the difference in the noise-free signal is remapped from $\Delta NFS_i(r_j,t_\epsilon) = NFS_i(r_j,t_\epsilon)$ - $NFS_i(r_j,t_\alpha)$ versus r_j (1b, 7, 110 and 111a) to $\Delta NFS_i(s^*_{\varphi_\epsilon})$ versus $s^*_{\varphi_\epsilon}$ (Equation 111b), and the difference in the randomly distributed noise is remapped from $\Delta GRN_{i,h}(r_j,t_\epsilon) = GRN_{i,h}(r_j,t_\epsilon)$ - $GRN_{i,h}(r_j,t_\alpha)$ versus r_j (Equations 1b, 7, 109 and 111a) to $\Delta GRN_{i,h}(s^*_{\varphi_\epsilon})$ versus $s^*_{\varphi_\epsilon}$ (Equation 111b).

Likewise, the signal difference, $Y_{i,h}(r_j,t_\delta) = NMS_{i,h}(r_j,t_\delta)$ - $NMS_{i,h}(r_j,t_\alpha)$, can be remapped from $Y_{i,h}(r_j,t_\delta)$ versus r_j to $Y_{i,h}(s^*_{\varphi_\epsilon})$ versus $s^*_{\varphi_\delta}$, where $s^*_{\varphi_\delta}$ is calculated from r_j and t_δ using Equation 144a. In the process, the difference in the time-independent noise is remapped from $\Delta TIN_{i,h}(r_j) = 0$ versus r_j to $\Delta TIN_{i,h}(s^*_{\varphi_\delta}) = 0$ versus $s^*_{\varphi_\delta}$, the difference in the radially independent noise is remapped from $\Delta RIN_{i,h}(t_\delta) = RIN_{i,h}(t_\delta)$ - $RIN_{i,h}(t_\alpha) = k_{i,h,\delta}$ versus r_j to $\Delta RIN_{i,h}(s^*_{\varphi_\delta}) = k_{i,h,\delta}$ versus $s^*_{\varphi_\epsilon}$, the difference in the noise-free signal is remapped from $\Delta NFS_i(r_j,t_\delta) = NFS_i(r_j,t_\delta)$ - $NFS_i(r_j,t_\alpha)$ versus r_j to $\Delta NFS_i(s^*_{\varphi_\delta})$ versus $s^*_{\varphi_\delta}$, and the difference in the randomly distributed noise is remapped from $\Delta GRN_{i,h}(r_j,t_\delta)$ versus r_j to $\Delta GRN_{i,h}(s^*_{\varphi_\delta})$ versus $s^*_{\varphi_\delta}$.

Similarly, the interpolated signal difference, $Y_{i,h}(r_j^*,t_\delta)$ (Equation 146), can be remapped from $Y_{i,h}(r_j^*,t_\delta)$ versus r_j^* to $Y_{i,h}(s^*_{\varphi^*_\epsilon})$ versus $s^*_{\varphi^*_\epsilon}$, where $s^*_{\varphi^*_\epsilon}$ is calculated from r_j^* and t_δ using Equation 144b. In the process, the difference in the time-independent noise is remapped from $\Delta TIN_{i,h}(r_j^*)$

$= \Delta TIN_{i,h}(r_j) = 0$ versus r_j to $\Delta TIN_{i,h}(s^*_{\varphi^*_\epsilon}) = 0$ versus $s^*_{\varphi_\delta}$, the difference in the radially independent noise is remapped from $\Delta RIN_{i,h}(t_\delta) = k_{i,h,\delta}$ versus r_j to $\Delta RIN_{i,h}(s^*_{\varphi^*_\epsilon}) = k_{i,h,\epsilon^*}$ versus $s^*_{\varphi^*_\epsilon}$, the difference in the noise-free signal is remapped from $\Delta NFS_i(r_j^*, t_\delta)$ versus r_j^* to $\Delta NFS_i(s^*_{\varphi^*_\epsilon})$ versus $s^*_{\varphi^*_\epsilon}$, and the difference in the randomly distributed noise is remapped from $\Delta GRN_{i,h}(r_j^*, t_\delta)$ $= GRN_{i,h}(r_j, t_\epsilon)$ - $GRN_{i,h}(r_j, t_\alpha)$ versus r_j^* to $\Delta GRN_{i,h}(s^*_{\varphi^*_\epsilon})$ versus $s^*_{\varphi^*_\epsilon}$.

The use of the signal differences, $Y_{i,h}(r_j, t_\epsilon)$ and $Y_{i,h}(r_j, t_\delta)$, ensures that the time-independent noise has already been eliminated before Equation 138 (approximated as Equation 141) is applied. (For $Y_{i,h}(r_j, t_\epsilon)$, $\Delta TIN_{i,h}(r_j) = 0$. For $Y_{i,h}(r_j, t_\delta)$, $\Delta TIN_{i,h}(r_j) = 0$.) As there is no time-independent noise in the signal differences, $Y_{i,h}\left(s^*_{\varphi_\epsilon}\right)$ or $Y_{i,h}(s^*_{\varphi_\delta})$, there is no interpolated time-independent noise in $Y_{i,h}\left(s^*_{\varphi^*_\epsilon}\right)$. (For $Y_{i,h}(s^*_{\varphi_\epsilon})$, $\Delta TIN_{i,h}(s^*_{\varphi_\epsilon}) = 0$. For $Y_{i,h}(s^*_{\varphi_\delta})$, $\Delta TIN_{i,h}(s^*_{\varphi_\delta}) = 0$.) Thus, the time-independent noise contributes nothing to $\left(\frac{\partial Y_{i,h}(s^*_{\varphi_\epsilon})}{\partial t_\epsilon}\right)_{s^*_{\varphi_\epsilon}}$ (Equation 138) or its approximation, $\frac{\Delta Y_{i,h}(s^*_{\varphi_\epsilon})}{\Delta s^*_{\varphi_\epsilon}}$ (Equation 141).

If $NMS_{i,h}(r_j, t_\epsilon)$ (Equation 1b) were used in place of $Y_{i,h}(r_j, t_\epsilon)$ (Equation 7), such that $\left(\frac{\partial NMS_{i,h}(s^*_{\varphi_\epsilon})}{\partial t_\epsilon}\right)_{s^*_{\varphi_\epsilon}}$ approximated as $\frac{\Delta NMS_{i,h}(s^*_{\varphi_\epsilon})}{\Delta t_\epsilon}$ took the place of $\left(\frac{\partial Y_{i,h}(s^*_{\varphi_\epsilon})}{\partial t_\epsilon}\right)_{s^*_{\varphi_\epsilon}}$ approximated as $\frac{\Delta Y_{i,h}(s^*_{\varphi_\epsilon})}{\Delta t_\epsilon}$ in Equation 141, at each value of $s^*_{\varphi_\epsilon} = s^*_{\varphi^*_\epsilon}$ (Equations 5 and 144), an interpolated value, $TIN_{i,h}(r_j^*)$, of the time-independent noise at $r_j^* = r_0 e^{s^*_{\varphi^*_\epsilon}\omega^2 t_\delta}$ would be subtracted from the actual value (Equation 107), $TIN_{i,h}(r_j)$, of the time-independent noise at $r_j = r_0 e^{s^*_{\varphi_\epsilon}\omega^2 t_\epsilon}$. As can be seen from Equation 145, the more that Δt_ϵ differs from zero, the farther r_j^* lies from r_j. The greater the distance between r_j^* and r_j, the more poorly the time-independent noise would be eliminated in

the course of calculating $\frac{\Delta NMS_{i,h}(s^*_{\varphi_\epsilon})}{\Delta t_\epsilon}$ at constant $s^*_{\varphi_\epsilon}$. Furthermore, as implemented here (Equations 138 to 150), even in the limit as Δt_ϵ approached zero (Equation 151), $\left(\frac{\partial TIN_{i,h}(r_j)}{\partial s^*_{\varphi_\epsilon}}\right)_{t_\epsilon}$ would be a component of $\left(\frac{\partial NMS_{i,h}(s^*_{\varphi_\epsilon})}{\partial s^*_{\varphi_\epsilon}}\right)_{t_\epsilon}$ if $NMS_{i,h}(r_j,t_\epsilon)$ were used in place of $Y_{i,h}(r_j,t_\epsilon)$. Thus, this method does not permit the use of $NMS_{i,h}(r_j,t_\epsilon)$ in place of $Y_{i,h}(r_j,t_\epsilon)$.

As both $\Delta RIN_{i,h}(t_\epsilon)$ and $\Delta RIN_{i,h}(t_\delta)$ are constant with r_j, the radially independent noise present in $\Delta Y_{i,h}(r_j,t_\epsilon) = Y_{i,h}(r_j,t_\epsilon) - Y_{i,h}(r_j,t_\delta)$ of Equation 141 is equal to $\Delta RIN_{i,h}(t_\epsilon) - \Delta RIN_{i,h}(t_\delta) = RIN_{i,h}(t_\epsilon) - RIN_{i,h}(t_\delta)$. As $\Delta RIN_{i,h}(s^*_{\varphi_\epsilon})$ is constant with $s^*_{\varphi_\epsilon}$, and as $\Delta RIN_{i,h}(s^*_{\varphi^*_\epsilon})$ is constant with $s^*_{\varphi^*_\epsilon} = s^*_{\varphi_\epsilon}$, the radially independent noise present in $\Delta Y_{i,h}(s^*_{\varphi_\epsilon}) = Y_{i,h}(s^*_{\varphi_\epsilon}) - Y_{i,h}(s^*_{\varphi^*_\epsilon})$ of Equation 141 is equal to $\Delta RIN_{i,h}(s^*_{\varphi^*_\epsilon}) - \Delta RIN_{i,h}(s^*_{\varphi_\epsilon}) = RIN_{i,h}(s^*_{\varphi^*_\epsilon}) - RIN_{i,h}(s^*_{\varphi_\epsilon})$, which, by Equation 111, is also equal to $RIN_{i,h}(t_\epsilon) - RIN_{i,h}(t_\delta)$. Thus, with Δt_ϵ being identical in both terms, when $\frac{\Delta Y_{i,h}(s^*_{\varphi_\epsilon})}{\Delta t_\epsilon}$ is subtracted from $\frac{\Delta Y_{i,h}(r_j,t_\epsilon)}{\Delta t_\epsilon}$ in Equation 141, the radially independent noise is eliminated.

As the finite approximation of $\left(\frac{\partial Y_{i,h}(s^*_{\varphi_\epsilon})}{\partial s^*_{\varphi_\epsilon}}\right)_{t_\epsilon}$ of Equation 141 is ultimately shown (Equation 150) to be proportional to r_j times the finite approximation of $\left(\frac{\partial Y_{i,h}(r_j,t_\delta)}{\partial r_j}\right)_{t_\epsilon}$ of Equation 137, and as that equation shows r_j times that approximation to be proportional to the finite approximation of $\left(\frac{\partial Y_{i,h}(s^*_{\varphi_\epsilon})}{\partial s^*_{\varphi_\epsilon}}\right)_{t_\epsilon}$ of Equation 8, there is neither an advantage nor a disadvantage to one of these methods of obtaining $\left(\frac{\partial Y_{i,h}(s^*_{\varphi_\epsilon})}{\partial s^*_{\varphi_\epsilon}}\right)_{t_\epsilon}$ over the other, as each, by Equation 133b, would yield $\sigma_{i,h}\left(\Delta Y_{i,h}\left(\left[s^*_{\varphi_\epsilon=a}, s^*_{\varphi_\epsilon=b}\right]\right)/\Delta\varphi_\epsilon\right) \cong \sigma_{RI}$ for $Y_{i,h}(s^*_{\varphi_\epsilon}) = \Delta GRN_{i,h}(s^*_{\varphi_\epsilon})$. (See Equations 129 to 134 in *Mitigation of data clipping*.) As previously noted (Figure 5; Table 14), $\sigma_{RI} = 0.01400$ fringe is the

approximate standard deviation in $GRN_{i,h}(r_j,t_\alpha)$, $GRN_{i,h}(r_j,t_\epsilon)$ or the generally random noise at any other time, such as t_δ.

Applying Equations 142, 148 and 149 to Equation 141 yields

$$\frac{\Delta Y_{i,h}(s^*_{\varphi_\epsilon})}{\Delta s^*_{\varphi_\epsilon}} = \left(\frac{Y_{i,h}(r_j,t_\epsilon) - Y_{i,h}(r_j,t_\delta)}{t_\epsilon - t_\delta} - \frac{Y_{i,h}(s^*_{\varphi_\epsilon}) - Y_{i,h}(s^*_{\varphi^*_\epsilon})}{t_\epsilon - t_\delta}\right)\left(\frac{-(t_\epsilon - t_\delta)}{\left[\frac{-(t_\epsilon - t_\delta)}{\omega^2 t_\delta t_\epsilon} ln\left(\frac{r_j}{r_0}\right)\right]}\right)$$

$$= \left[\frac{Y_{i,h}(s^*_{\varphi_\epsilon}) - Y_{i,h}(s^*_{\varphi^*_\epsilon}) + Y_{i,h}(r_j,t_\delta) - Y_{i,h}(r_j,t_\epsilon)}{t_\epsilon - t_\delta}\right]\frac{t_\delta}{\left[\frac{1}{\omega^2 t_\epsilon} ln\left(\frac{r_j}{r_0}\right)\right]}.$$

(150a)

Application of Equation 5 to the denominator in the right-most term of Equation 150a results in

$$\frac{\Delta Y_{i,h}(s^*_{\varphi_\epsilon})}{\Delta s^*_{\varphi_\epsilon}} = \left[\frac{Y_{i,h}(s^*_{\varphi_\epsilon}) - Y_{i,h}(s^*_{\varphi^*_\epsilon}) + Y_{i,h}(r_j,t_\delta) - Y_{i,h}(r_j,t_\epsilon)}{t_\epsilon - t_\delta}\right]\frac{t_\delta}{s^*_{\varphi_\epsilon}}.$$

(150b)

Using Equation 5 to express $Y_{i,h}(r_j,t_\epsilon)$ as $Y_{i,h}(s^*_{\varphi_\epsilon})$, Equation 150b reduces to

$$\frac{\Delta Y_{i,h}(s^*_{\varphi_\epsilon})}{\Delta s^*_{\varphi_\epsilon}} = \left[\frac{Y_{i,h}(r_j,t_\delta) - Y_{i,h}(s^*_{\varphi^*_\epsilon})}{t_\epsilon - t_\delta}\right]\frac{t_\delta}{s^*_{\varphi_\epsilon}}.$$

(150c)

Using Equation 146 to substitute for $Y_{i,h}(s^*_{\varphi^*_\epsilon})$ in Equation 150c yields, after placement of the minus sign with the right-most term,

$$\frac{\Delta Y_{i,h}(s^*_{\varphi_\epsilon})}{\Delta s^*_{\varphi_\epsilon}} = \left(\frac{\partial Y_{i,h}(r_j,t_\delta)}{\partial r_j}\right)_{t_\epsilon}\left[\frac{(r^*_j - r_j)}{t_\epsilon - t_\delta}\right]\left[-\frac{t_\delta}{s^*_{\varphi_\epsilon}}\right],$$

(150d)

where, as in Equations 6 and 115, $r_0 = r_b$ for $\varphi_\epsilon = j$, while $r_0 = r_m$ for $\varphi_\epsilon = j + N$.

In the limit as t_δ approaches t_ϵ, r_j^* approaches r_j (Equation 145b), and the application of this limit to Equation 150d yields

$$\lim_{t_\delta \to t_\epsilon} \frac{\Delta Y_{i,h}\left(s^*_{\varphi_\epsilon}\right)}{\Delta s^*_{\varphi_\epsilon}} = -\left(\frac{\partial Y_{i,h}\left(r_j, t_\epsilon\right)}{\partial r_j}\right)_{t_\epsilon} \left(\frac{\partial r_j}{\partial t_\epsilon}\right)_{s^*_{\varphi_\epsilon}} \left(\frac{\partial t_\epsilon}{\partial s^*_{\varphi_\epsilon}}\right)_{r_j} = \left(\frac{\partial Y_{i,h}\left(r_j, t_\epsilon\right)}{\partial r_j}\right)_{t_\epsilon} \left(\frac{\partial r_j}{\partial s^*_{\varphi_\epsilon}}\right)_{t_\epsilon}$$

$$= \left(\frac{\partial Y_{i,h}\left(s^*_{\varphi_\epsilon}\right)}{\partial s^*_{\varphi_\epsilon}}\right)_{t_\epsilon}.$$

(151)

That $\left(\frac{\partial r_j}{\partial s^*_{\varphi_\epsilon}}\right)_{t_\epsilon} = -\left(\frac{\partial r_j}{\partial t_\epsilon}\right)_{s^*_{\varphi_\epsilon}} \left(\frac{\partial t_\epsilon}{\partial s^*_{\varphi_\epsilon}}\right)_{r_j}$ can be shown using previously discussed Equations. By Equation 114, $r_j = r_0 e^{s^*_{\varphi_\epsilon} \omega^2 t_\epsilon}$, from which

$$\left(\frac{\partial r_j}{\partial s^*_{\varphi_\epsilon}}\right)_{t_\epsilon} = \omega^2 t_\epsilon r_0 e^{s^*_{\varphi_\epsilon} \omega^2 t_\epsilon} = \omega^2 t_\epsilon r_j$$

(152)

is obtained by differentiation with respect to $s^*_{\varphi_\epsilon}$ at constant t_ϵ. This result is also shown by Equation 116, the focus of which, however, is the finite forms of $\left(\frac{\partial r_j}{\partial s^*_{\varphi_\epsilon}}\right)_{t_\epsilon}$ and $\left(\frac{\partial s^*_{\varphi_\epsilon}}{\partial r_j}\right)_{t_\epsilon}$. Finally, Equations 140 and 143 both yield $\left(\frac{\partial t_\epsilon}{\partial s^*_{\varphi_\epsilon}}\right)_{r_j} = -\frac{t_\epsilon}{s^*_{\varphi_\epsilon}}$. Thus,

$$-\left(\frac{\partial r_j}{\partial t_\epsilon}\right)_{s^*_{\varphi_\epsilon}} \left(\frac{\partial t_\epsilon}{\partial s^*_{\varphi_\epsilon}}\right)_{r_j} = \omega^2 t_\epsilon r_j = \left(\frac{\partial r_j}{\partial s^*_{\varphi_\epsilon}}\right)_{t_\epsilon}.$$

(153)

Equation 151 shows the close correspondence between Equations 137 and 150. The equivalence of Equation 137 to Equation 8, in turn, shows the close correspondence between Equations 8 and 150. Thus, it should come as no surprise that Equations 8 and Equations 150 yield strikingly similar results when applied to comparable data sets, including the sort of signal-free data used

to produce Figures 52 to 62. Figures 72 to 82 show results obtained by application of Equation 150 to signal-free data sets that correspond as closely as possible to those used for Figures 52 to 62. All the data sets from Figures 52 to 62 are reused in Figures 72 to 82. To render Equation 150 applicable, an additional set of signal-free data is assigned a time that is 60 s prior to each of the previously used data sets associated with times t_{36}, t_{51} and t_{66} of Figures 52 to 62.

As noted in the legend of Figure 52, the sets of $GRN_{i,h}(r_j,t_\epsilon)$ previously applied to replicate $h = 1$ of treatment group $i = 4$ were equated to the sets of $NMS_{0,1}(r_j,t_\epsilon)$ shown in that figure. Thus, as for $h = 1$ of $i = 4$ in Table 14a, set ${}_6a$ was used for $NMS_{0,1}(r_j,t_\alpha)$, set ${}_7a$ was used for $NMS_{0,1}(r_j,t_{36})$, set ${}_1b$ was used for $NMS_{0,1}(r_j,t_{51})$, and set ${}_1b$ was used for $NMS_{0,1}(r_j,t_{66})$.

For the new data sets, denoted as $NMS_{0,1}(r_j,t_\delta)$, where $t_\delta = t_\epsilon$ - 60 s, three sets of $GRN_{i,h}(r_j,t_\epsilon)$ previously applied to replicate $h = 2$ of treatment group $i = 4$ were equated to three additional sets of $NMS_{0,1}(r_j,t_\delta)$ needed to obtain results via Equation 150. Thus, as for $h = 2$ of $i = 4$ in Table 14a, but with a -60-second time difference, set ${}_2b$ was used for $NMS_{0,1}(r_j,t_{35})$, set ${}_3b$ was used for $NMS_{0,1}(r_j,t_{50})$, and set ${}_3b$ was used for $NMS_{0,1}(r_j,t_{65})$, where $t_\delta = t_{35} = t_{36}$ - 60 s, $t_\delta = t_{50} = t_{51}$ - 60 s and $t_\delta = t_{65} = t_{66}$ - 60 s.

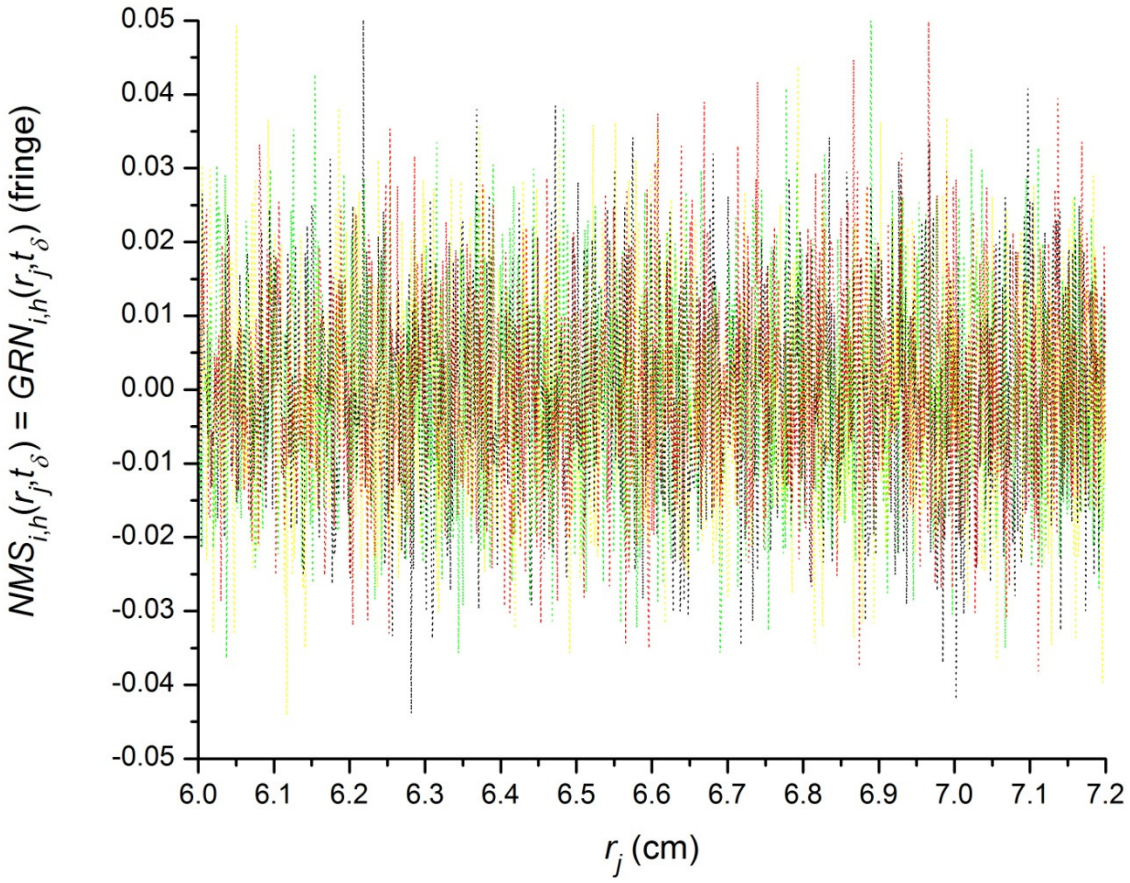

Figure 72. The sets of $NMS_{i,h}(r_j,t_\delta) = GRN_{i,h}(r_j,t_\delta)$, of which $NMS_{i,h}(r_j,t_\alpha) = GRN_{i,h}(r_j,t_\alpha)$ is a subset, versus r_j at $t_\delta = t_\alpha = t_1$ (·····), $t_\delta = t_{35}$ (·····), $t_\delta = t_{50}$ (·····) and $t_\delta = t_{65}$ (·····), where $i = 0$ and $h = 1$. The sets of $GRN_{i,h}(r_j,t_\delta)$ previously applied to replicate $h = 2$ of treatment group $i = 4$ were equated to the sets of $NMS_{0,1}(r_j,t_\delta)$ shown in this figure. Thus, as for $h = 2$ of $i = 4$ in Table 14a, but with a -60-second time difference, set ${}_2b$ was used for $NMS_{0,1}(r_j,t_{35})$, set ${}^3b$ was used for $NMS_{0,1}(r_j,t_{50})$, and set ${}_3b$ was used for $NMS_{0,1}(r_j,t_{65})$, where $t_\delta = t_{35} = t_{36}$ - 60 s, $t_\delta = t_{50} = t_{51}$ - 60 s and $t_\delta = t_{65} = t_{66}$ - 60 s. To a close approximation, each set of $NMS_{0,1}(r_j,t_\delta)$ values is normally distributed about a mean of $\langle NMS_{i,h}([r_1, r_{2N}], t_\delta)\rangle = \mu_{RI} = 0$ fringe with a standard deviation of $\sigma_{i,h}\left(NMS_{i,h}([r_1, r_{2N}], t_\delta)\right) = \sigma_{RI} = 0.01400$ fringe (Figure 5; Table 14). At any given time, the standard deviation (Equation 119b) of $NMS_{0,1}(r_j,t_\delta)$ about its mean (Equation 119a) does not

vary systematically from one narrow range of r_j values to another. Figure 52 shows the sets of $NMS_{i,h}(r_j,t_\epsilon) = GRN_{i,h}(r_j,t_\epsilon)$ versus r_j at $t_\epsilon = t_{36}, t_\epsilon = t_{51}$ and $t_\epsilon = t_{66}$, where $i = 0$ and $h = 1$.

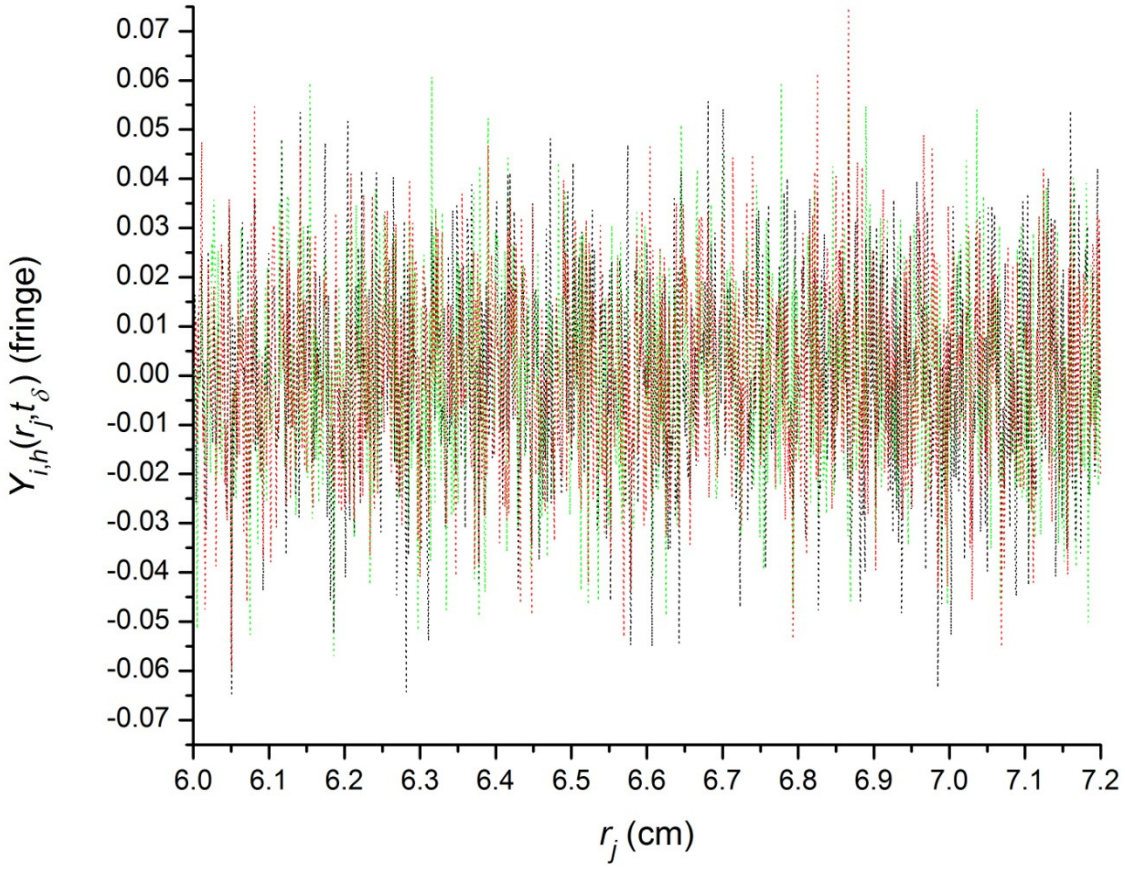

Figure 73. $Y_{i,h}(r_j,t_\delta) = \Delta GRN_{i,h}(r_j,t_\delta)$ versus r_j at $t_\delta = t_{35}$ (·····), $t_\delta = t_{50}$ (·····) and $t_\delta = t_{65}$ (·····), where $i = 0$ and $h = 1$. In general, $Y_{i,h}(r_j,t_\delta) = \Delta NFS_i(r_j,t_\delta) + 0 + k_{i,h,\,\delta} + \Delta GRN_{i,h}(r_j,t_\delta)$ (Equation 111a), or as originally cast (Equation 7), $Y_{i,h}(r_j,t_\delta) = NMS_{i,h}(r_j,t_\delta)$ - $NMS_{i,h}(r_j,t_\alpha)$. Here, $NMS_{i,h}(r_j,t_\delta)$ - $NMS_{i,h}(r_j,t_\alpha) = \Delta GRN_{i,h}(r_j,t_\delta)$, which is the randomly distributed noise of $Y_{i,h}(r_j,t_\delta)$. (See Equation 109.) The standard deviation of the randomly distributed noise of $Y_{i,h}(r_j,t_\delta)$ is about $2^{0.5}$-fold greater than that of either $NMS_{i,h}(r_j,t_\alpha)$ or $NMS_{i,h}(r_j,t_\delta)$, which are shown in Figure 72. Thus, to a close approximation, at any given time, each set of $Y_{i,h}(r_j,t_\delta) = \Delta GRN_{i,h}(r_j,t_\delta)$ values is normally distributed about a mean of $\langle Y_{i,h}([r_1, r_{2N}], t_\delta)\rangle$ $\mu_{RI} = 0$ fringe with a standard deviation of

$\sigma_{i,h}\left(Y_{i,h}([r_1, r_{2N}], t_\delta)\right) = 2^{0.5}\sigma_{RI} =$ 1.97990E-2 fringe (Figure 5; Table 14). More importantly, for $Y_{i,h}(r_j, t_\delta) = \Delta GRN_{i,h}(r_j, t_\delta)$, at any given time, the standard deviation (Equation 120b) of $Y_{i,h}(r_j, t_\delta)$ about its mean (Equation 120a) does not vary systematically from one narrow range of r_j values to another. Figure 53 shows $Y_{i,h}(r_j, t_\epsilon) = \Delta GRN_{i,h}(r_j, t_\epsilon)$ versus r_j at $t_\epsilon = t_{36}, t_\epsilon = t_{51}$ and $t_\epsilon = t_{66}$, where $i = 0$ and $h = 1$.

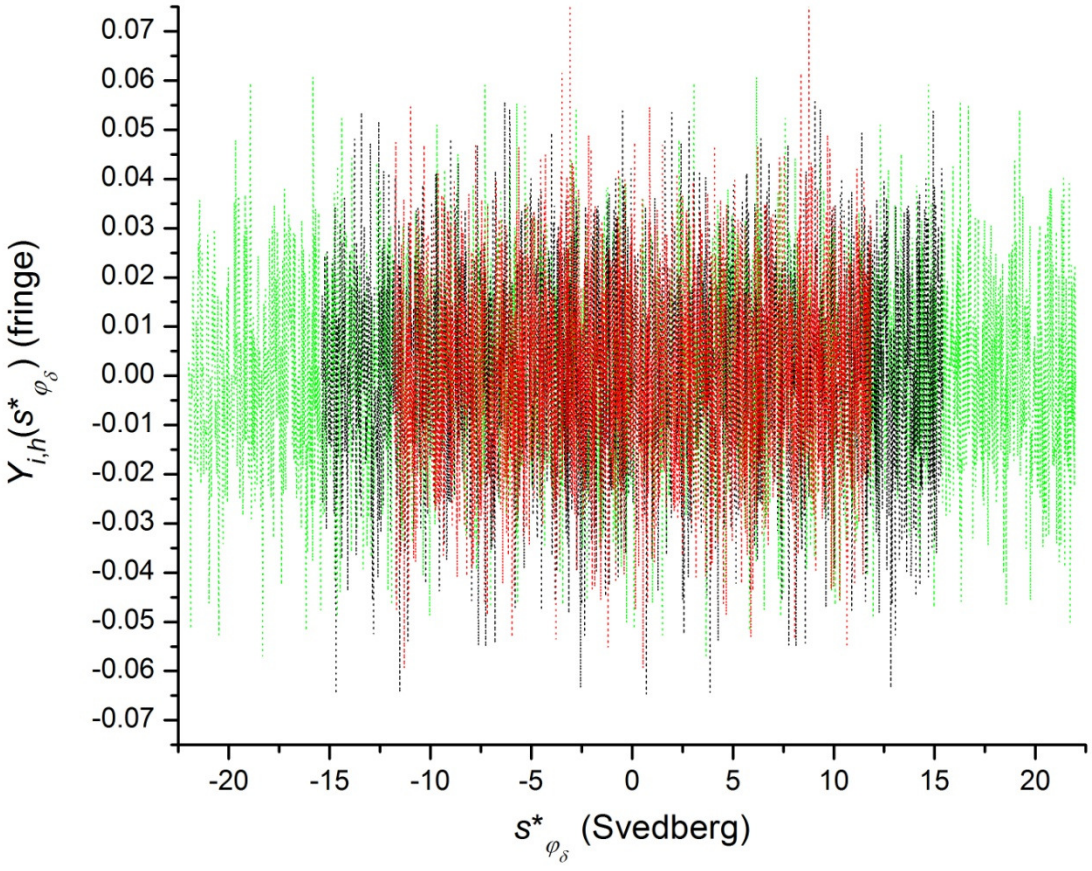

Figure 74. $Y_{i,h}(s^*_{\varphi_\delta}) = \Delta GRN_{i,h}(s^*_{\varphi_\delta})$ versus $s^*_{\varphi_\epsilon}$ at $t_\delta = t_{35}$ (·····), $t_\delta = t_{50}$ (·····) and $t_\delta = t_{65}$ (·····), where $i = 0$ and $h = 1$. In general (Equation 111), $Y_{i,h}(r_j, t_\epsilon)$ remapped from r_j to $s^*_{\varphi_\delta}$ yields $Y_{i,h}(s^*_{\varphi_\delta})$, where $s^*_{\varphi_\delta}$ is calculated from r_j and t_δ using Equation 144a. As with $Y_{i,h}(r_j, t_\epsilon) = \Delta GRN_{i,h}(r_j, t_\epsilon)$ mapped to r_j in the previous figure, to a close approximation, at any given time, each

set of $Y_{i,h}(s^*_{\varphi_\delta}) = \Delta GRN_{i,h}(s^*_{\varphi_\delta})$ values is normally distributed about a mean of $\langle Y_{i,h}([s^*_{\varphi_\delta=1}, s^*_{\varphi_\delta=2N}])\rangle = \mu_{RI} = 0$ fringe with a standard deviation of $\sigma_{i,h}\left(Y_{i,h}([s^*_{\varphi_\delta=1}, s^*_{\varphi_\delta=2N}])\right) = 2^{0.5}\sigma_{RI} = 1.97990\text{E-}2$ fringe (Figure 5; Table 14). More importantly, for $Y_{i,h}(s^*_{\varphi_\delta}) = \Delta GRN_{i,h}(s^*_{\varphi_\delta})$, at any given time, the standard deviation (Equation 121b) of $Y_{i,h}(s^*_{\varphi_\delta})$ about its mean (Equation 121a) does not vary systematically from one narrow range of $s^*_{\varphi_\delta}$ values to another. Figure 54 shows $Y_{i,h}(s^*_{\varphi_\epsilon}) = \Delta GRN_{i,h}(s^*_{\varphi_\epsilon})$ versus $s^*_{\varphi_\epsilon}$ at $t_\epsilon = t_{36}, t_\epsilon = t_{51}$ and $t_\epsilon = t_{66}$, where $i = 0$ and $h = 1$.

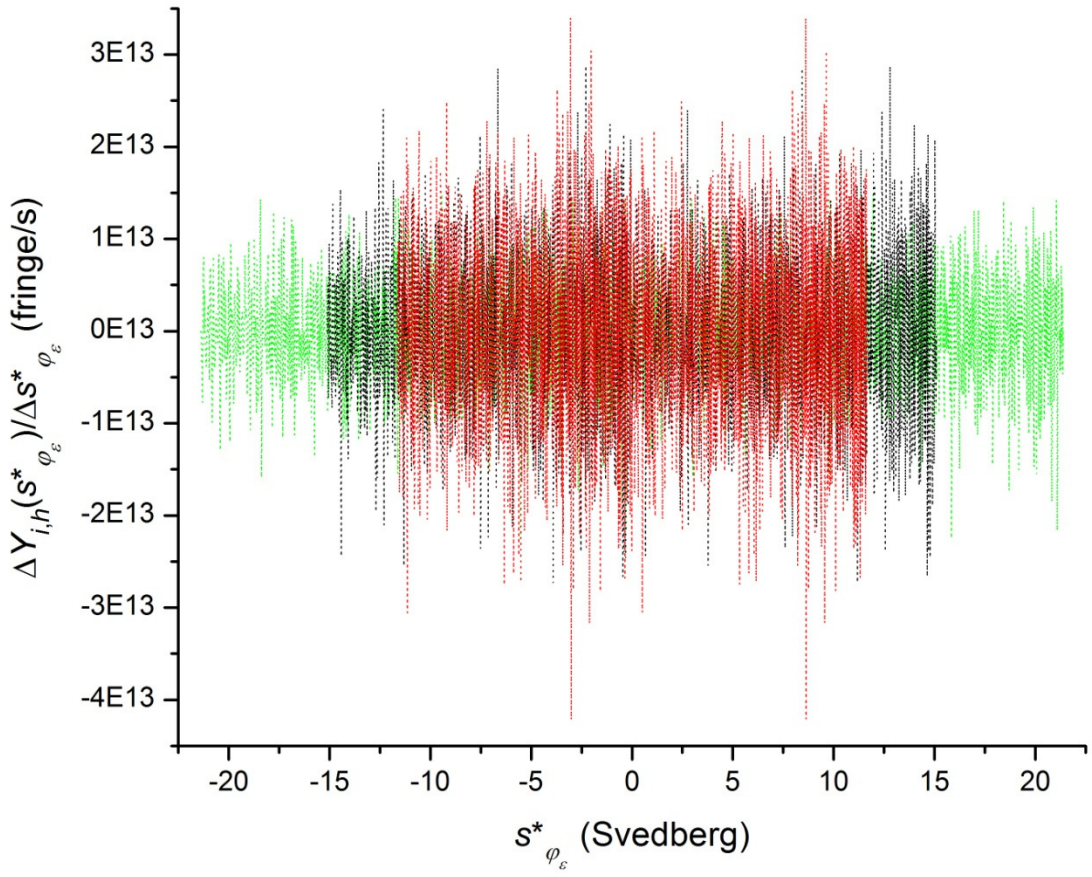

Figure 75. $\Delta Y_{i,h}(s^*_{\varphi_\epsilon})/\Delta s^*_{\varphi_\epsilon}$, determined using Equation 150, versus $s^*_{\varphi_\epsilon}$ at $t_\epsilon = t_{36}$ (·····), $t_\epsilon = t_{51}$ (·····) and $t_\epsilon = t_{66}$ (·····), where $i = 0$ and $h = 1$. As $i = 0$, $Y_{i,h}(s^*_{\varphi_\epsilon}) = \Delta GRN_{i,h}(s^*_{\varphi_\epsilon})$ (Figure 54) and $Y_{i,h}(s^*_{\varphi_\delta}) = \Delta GRN_{i,h}(s^*_{\varphi_\delta})$ (Figure 74). At any given time, the standard deviation (Equation 122b)

of $\Delta Y_{i,h}(s^*_{\varphi_\epsilon})/\Delta s^*_{\varphi_\epsilon}$ about its mean (Equation 122a) varies systematically from one narrow range of $s^*_{\varphi_\epsilon}$ values to another within the entire range of $s^*_{\varphi_\epsilon}$, across which, $\Delta Y_{i,h}(s^*_{\varphi_\epsilon})/\Delta s^*_{\varphi_\epsilon}$ is proportional to $1/\Delta s^*_{\varphi_{\epsilon=j}} = 1/\Delta s^*_{\varphi_{\epsilon=N+j}} = \omega^2 t_\epsilon r_j/\Delta r_j$ (Equation 117). Figure 55 shows $\Delta Y_{i,h}(s^*_{\varphi_\epsilon})/\Delta s^*_{\varphi_\epsilon}$, determined using Equation 8, versus $s^*_{\varphi_\epsilon}$ at $t_\epsilon = t_{36}, t_\epsilon = t_{51}$ and $t_\epsilon = t_{66}$, where $i = 0$ and $h = 1$.

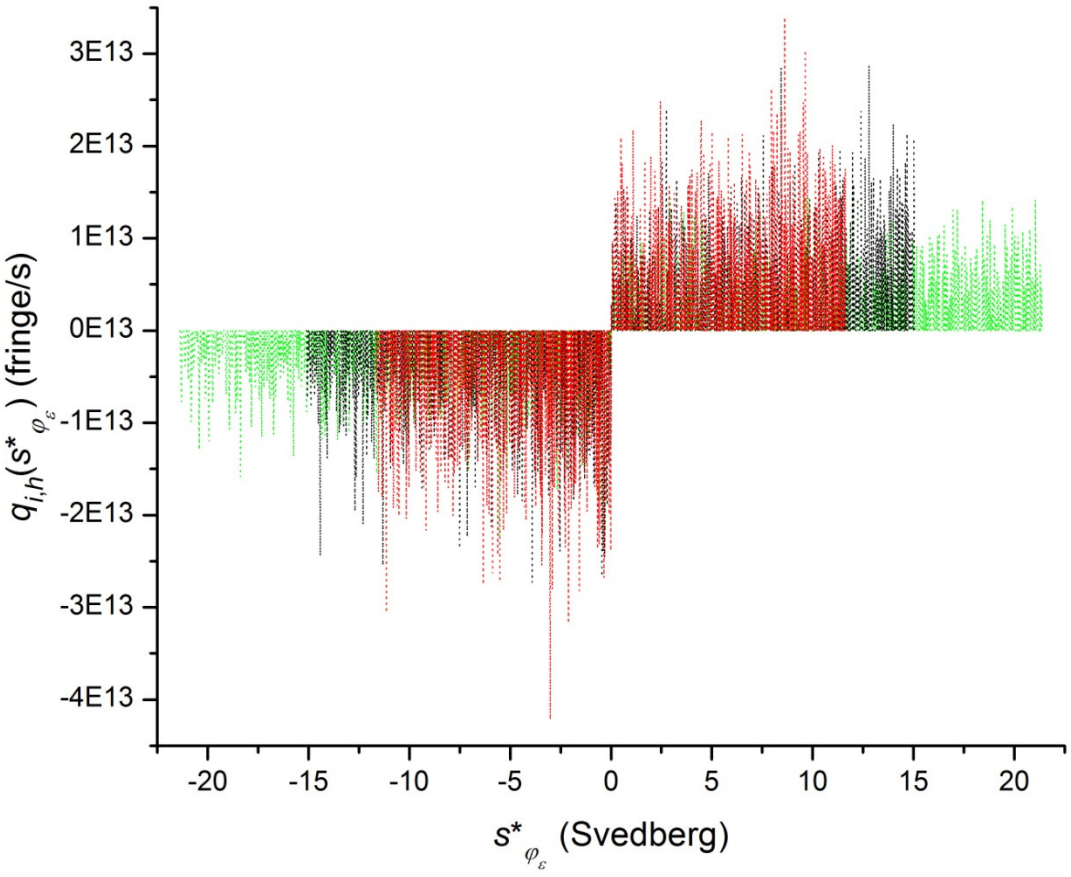

Figure 76. $q_{i,h}(s^*_{\varphi_\epsilon})$, obtained from $\Delta Y_{i,h}(s^*_{\varphi_\epsilon})/\Delta s^*_{\varphi_\epsilon}$ determined using Equation 150, versus $s^*_{\varphi_\epsilon}$ at $t_\epsilon = t_{36}$ (·····), $t_\epsilon = t_{51}$ (·····) and $t_\epsilon = t_{66}$ (·····), where $i = 0$ and $h = 1$. As $i = 0$, $q_{i,h}(s^*_{\varphi_\epsilon})$ in this figure has its source in a noise-free signal (Figures 52 to 55 and 72 to 75). The proportionality of nonzero values of $\Delta Y_{i,h}(s^*_{\varphi_\epsilon})/\Delta s^*_{\varphi_\epsilon}$ to$1/\Delta s^*_{\varphi_{\epsilon=j}} = 1/\Delta s^*_{\varphi_{\epsilon=N+j}} = \omega^2 t_\epsilon r_j/\Delta r_j$ (Equation 117; Figure

75) is inherited by $q_{i,h}(s^*_{\varphi_\epsilon})$ (Equation 9a) wherever the elimination function (Equation 9b), $e_{i,h}(s^*_{\varphi_\epsilon})$, is equal to zero. As such, at any given time, the standard deviation (Equation 123b) of $q_{i,h}(s^*_{\varphi_\epsilon})$ about its mean (Equation 123a) varies systematically from one narrow range of $s^*_{\varphi_\epsilon}$ values to another. Figure 56 shows $q_{i,h}(s^*_{\varphi_\epsilon})$, obtained from $\Delta Y_{i,h}(s^*_{\varphi_\epsilon})/\Delta s^*_{\varphi_\epsilon}$ determined using Equation 8, versus $s^*_{\varphi_\epsilon}$ at $t_\epsilon = t_{36}, t_\epsilon = t_{51}$ and $t_\epsilon = t_{66}$, where $i = 0$ and $h = 1$.

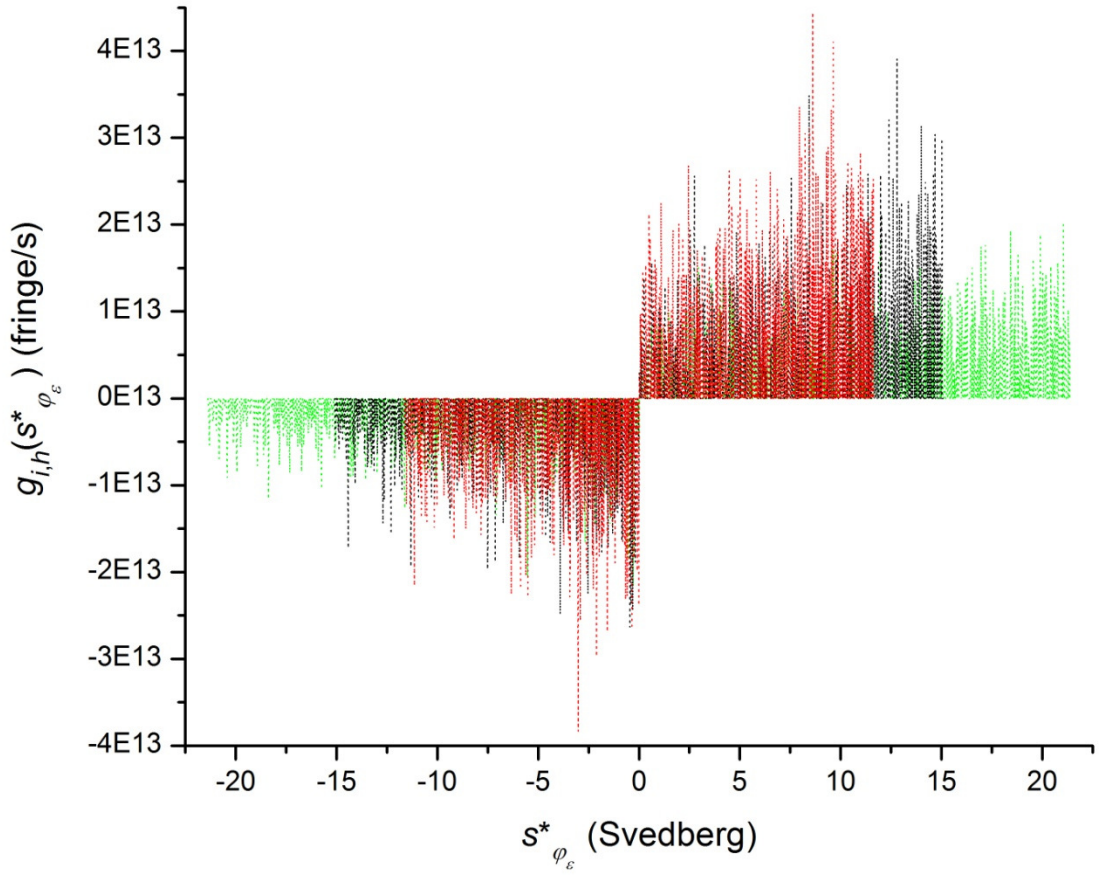

Figure 77. $g_{i,h}(s^*_{\varphi_\epsilon})$, obtained from $\Delta Y_{i,h}(s^*_{\varphi_\epsilon})/\Delta s^*_{\varphi_\epsilon}$ determined using Equation 150, versus $s^*_{\varphi_\epsilon}$ at $t_\epsilon = t_{36}$ (·····), $t_\epsilon = t_{51}$ (·····) and $t_\epsilon = t_{66}$ (·····), where $i = 0$ and $h = 1$. As $i = 0$, $g_{i,h}(s^*_{\varphi_\epsilon})$ in this figure has its source in a noise-free signal (Figures 52 to 56 and 72 to 76). The apparent sedimentation coefficient distribution function for replicate h of treatment group i at time t_ϵ is, by Equation 10,

$g_{i,h}(s^*_{\varphi_\epsilon}) = q_{i,h}(s^*_{\varphi_\epsilon})(e^{2s^*_{\varphi_\epsilon}\omega^2 t_\epsilon})$. As a consequence of being proportional to both $q_{i,h}(s^*_{\varphi_\epsilon})$ (Figure 76) and $e^{2s^*_{\varphi_\epsilon}\omega^2 t_\epsilon}$, $g_{i,h}(s^*_{\varphi_\epsilon})$ inherits $e^{2s^*_{\varphi_\epsilon}\omega^2 t_\epsilon}$ times the systematic $s^*_{\varphi_\epsilon}$ dependence of the standard deviation of $q_{i,h}(s^*_{\varphi_\epsilon})$ about its mean. Thus, from one narrow range of $s^*_{\varphi_\epsilon}$ values to another, the systematic $s^*_{\varphi_\epsilon}$ dependence of the standard deviation (Equation 124b) about the mean (Equation 124a) is greater for $g_{i,h}(s^*_{\varphi_\epsilon})$ than it is for $q_{i,h}(s^*_{\varphi_\epsilon})$ at any given time. Figure 57 shows $g_{i,h}(s^*_{\varphi_\epsilon})$, obtained from $\Delta Y_{i,h}(s^*_{\varphi_\epsilon})/\Delta s^*_{\varphi_\epsilon}$ determined using Equation 8, versus $s^*_{\varphi_\epsilon}$ at $t_\epsilon = t_{36}, t_\epsilon = t_{51}$ and $t_\epsilon = t_{66}$, where $i = 0$ and $h = 1$.

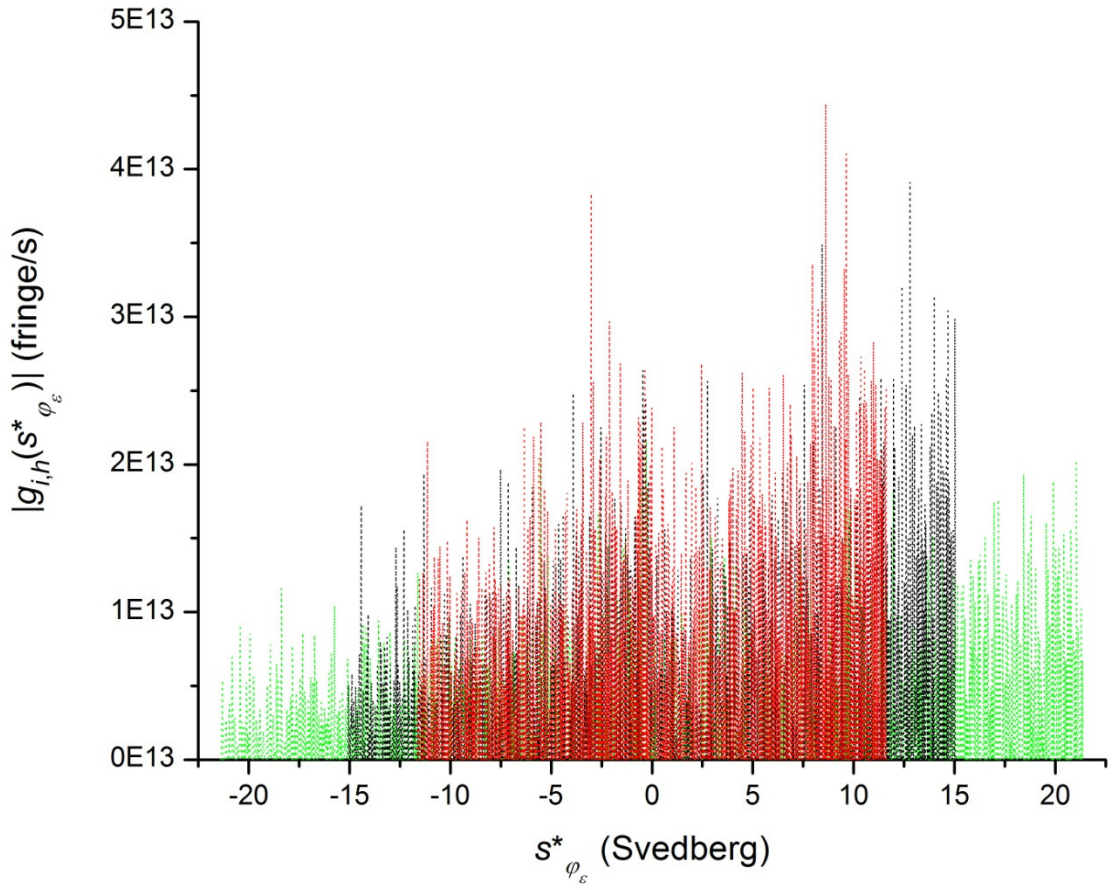

Figure 78. $|g_{i,h}(s^*_{\varphi_\epsilon})|$, obtained from $\Delta Y_{i,h}(s^*_{\varphi_\epsilon})/\Delta s^*_{\varphi_\epsilon}$ determined using Equation 150, versus $s^*_{\varphi_\epsilon}$ at $t_\epsilon = t_{36}$ (·····), $t_\epsilon = t_{51}$ (·····) and $t_\epsilon = t_{66}$ (·····), where $i = 0$ and $h = 1$. As $i = 0$, $|g_{i,h}(s^*_{\varphi_\epsilon})|$ in this

figure has its source in a noise-free signal (Figures 52 to 57 and 72 to 77). At $t_\epsilon = t_{36}$, and at any other given time, the standard deviation (Equation 125b) of $\left|g_{i,h}\left(s^*_{\varphi_\epsilon}\right)\right|$ about its mean (Equation 125a) varies systematically from one narrow range of $s^*_{\varphi_\epsilon}$ values to another. Figure 58 shows $\left|g_{i,h}\left(s^*_{\varphi_\epsilon}\right)\right|$, obtained from $\Delta Y_{i,h}\left(s^*_{\varphi_\epsilon}\right)/\Delta s^*_{\varphi_\epsilon}$ determined using Equation 8, versus $s^*_{\varphi_\epsilon}$ at $t_\epsilon = t_{36}, t_\epsilon = t_{51}$ and $t_\epsilon = t_{66}$, where $i = 0$ and $h = 1$.

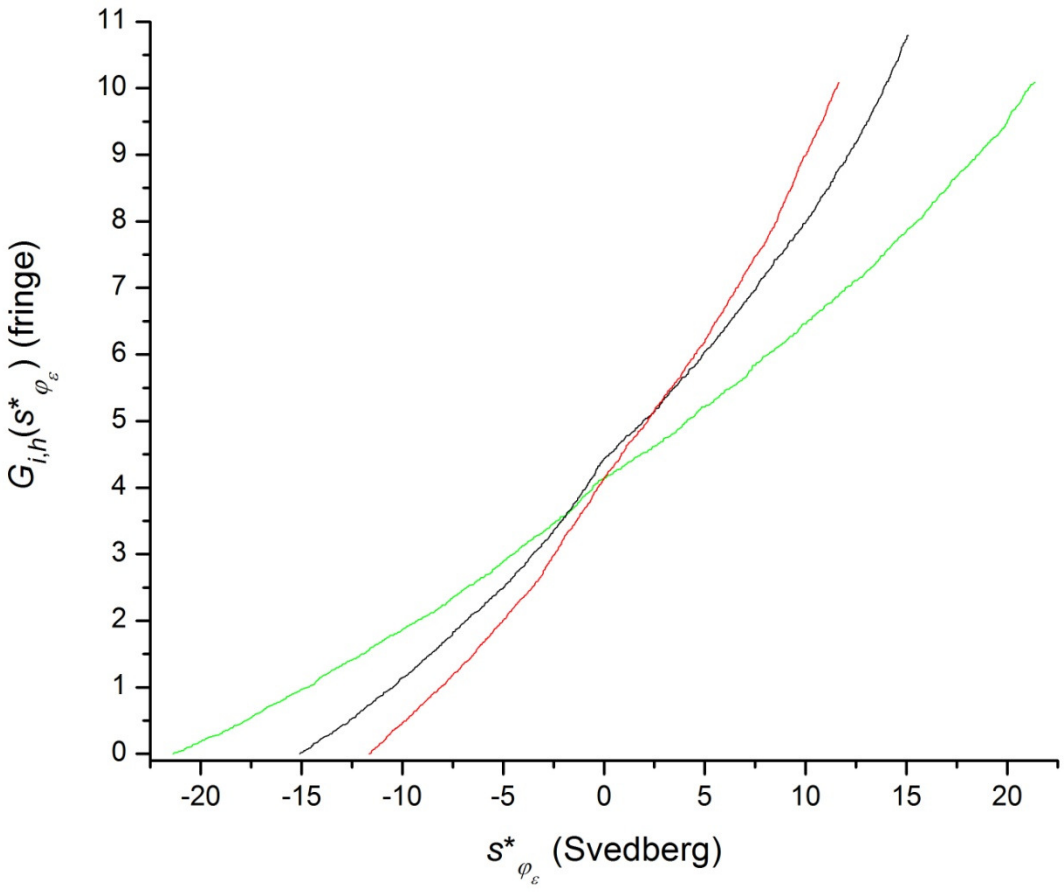

Figure 79. $G_{i,h}\left(s^*_{\varphi_\epsilon}\right)$, obtained from $\Delta Y_{i,h}\left(s^*_{\varphi_\epsilon}\right)/\Delta s^*_{\varphi_\epsilon}$ determined using Equation 150, versus $s^*_{\varphi_\epsilon}$ at $t_\epsilon = t_{36}$ (——), $t_\epsilon = t_{51}$ (——) and $t_\epsilon = t_{66}$ (——), where $i = 0$ and $h = 1$. As $i = 0$, $G_{i,h}\left(s^*_{\varphi_\epsilon}\right)$, the integral with respect to $s^*_{\varphi_\epsilon}$ of $\left|g_{i,h}\left(s^*_{\varphi_\epsilon}\right)\right|$ in the previous figure, has its source in a noise-free signal (Figures 52 to 58 and 72 to 78). For each value of $G_{i,h}\left(s^*_{\varphi_\epsilon}\right)$ shown in this figure, the lower

limit of integration is $s^*_{min<0} = s^*_{\varphi_\epsilon=1}$ at time t_ϵ, and the upper limit of integration ranges from $s^*_{min<0}$ to $s^*_{max>0} = s^*_{\varphi_\epsilon=2N}$ at time t_ϵ. Figure 59 shows $G_{i,h}(s^*_{\varphi_\epsilon})$, obtained from $\Delta Y_{i,h}(s^*_{\varphi_\epsilon})/\Delta s^*_{\varphi_\epsilon}$ determined using Equation 8, versus $s^*_{\varphi_\epsilon}$ at $t_\epsilon = t_{36}, t_\epsilon = t_{51}$ and $t_\epsilon = t_{66}$, where $i = 0$ and $h = 1$.

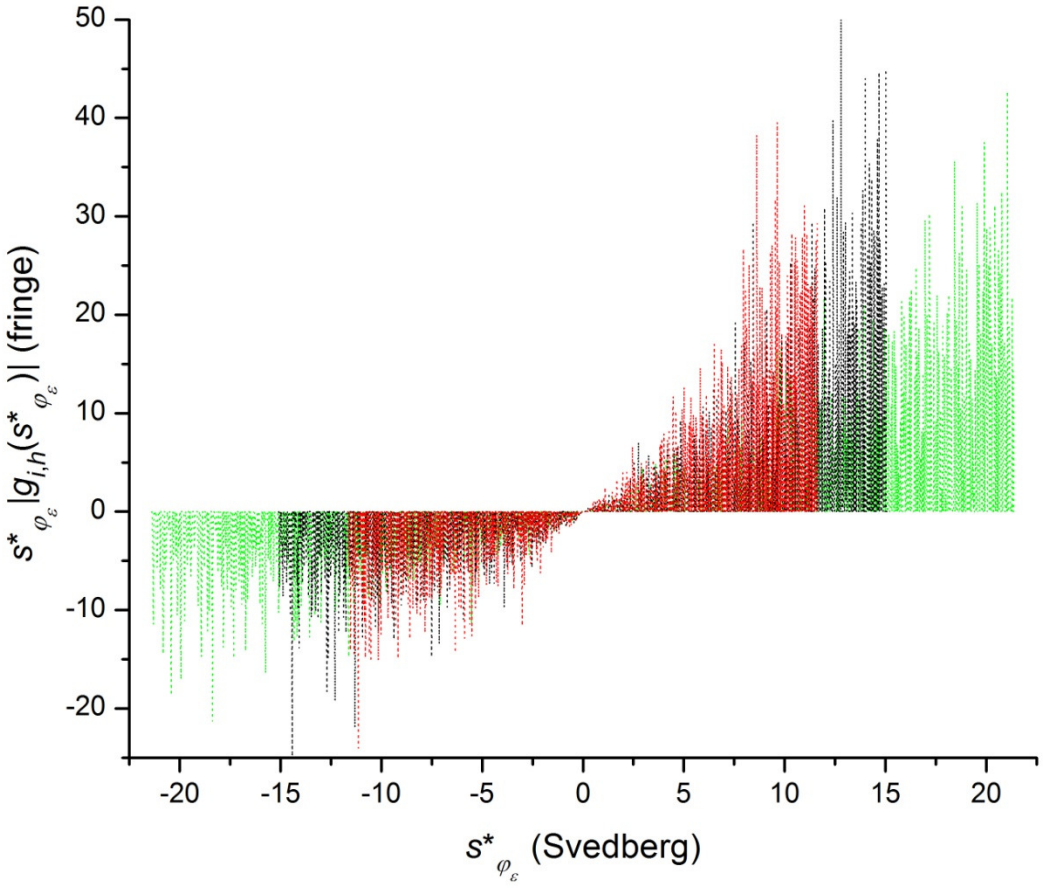

Figure 80. $s^*_{\varphi_\epsilon}|g_{i,h}(s^*_{\varphi_\epsilon})|$, obtained from $\Delta Y_{i,h}(s^*_{\varphi_\epsilon})/\Delta s^*_{\varphi_\epsilon}$ determined using Equation 150, versus $s^*_{\varphi_\epsilon}$ at $t_\epsilon = t_{36}$ (·····), $t_\epsilon = t_{51}$ (·····) and $t_\epsilon = t_{66}$ (·····), where $i = 0$ and $h = 1$. \Figure 81 shows the integral of $s^*_{\varphi_\epsilon}|g_{i,h}(s^*_{\varphi_\epsilon})|$ with respect to $s^*_{\varphi_\epsilon}$ at each time of analysis, $t_\epsilon = t_{36}, t_\epsilon = t_{51}$ and $t_\epsilon = t_{66}$. As $i = 0$, $s^*_{\varphi_\epsilon}|g_{i,h}(s^*_{\varphi_\epsilon})|$ in this figure has its source in a noise-free signal (Figures 52 to 58 and 72 to 78). Figure 60 shows $s^*_{\varphi_\epsilon}|g_{i,h}(s^*_{\varphi_\epsilon})|$, obtained from $\Delta Y_{i,h}(s^*_{\varphi_\epsilon})/\Delta s^*_{\varphi_\epsilon}$ determined using Equation 8, versus $s^*_{\varphi_\epsilon}$ at $t_\epsilon = t_{36}, t_\epsilon = t_{51}$ and $t_\epsilon = t_{66}$, where $i = 0$ and $h = 1$.

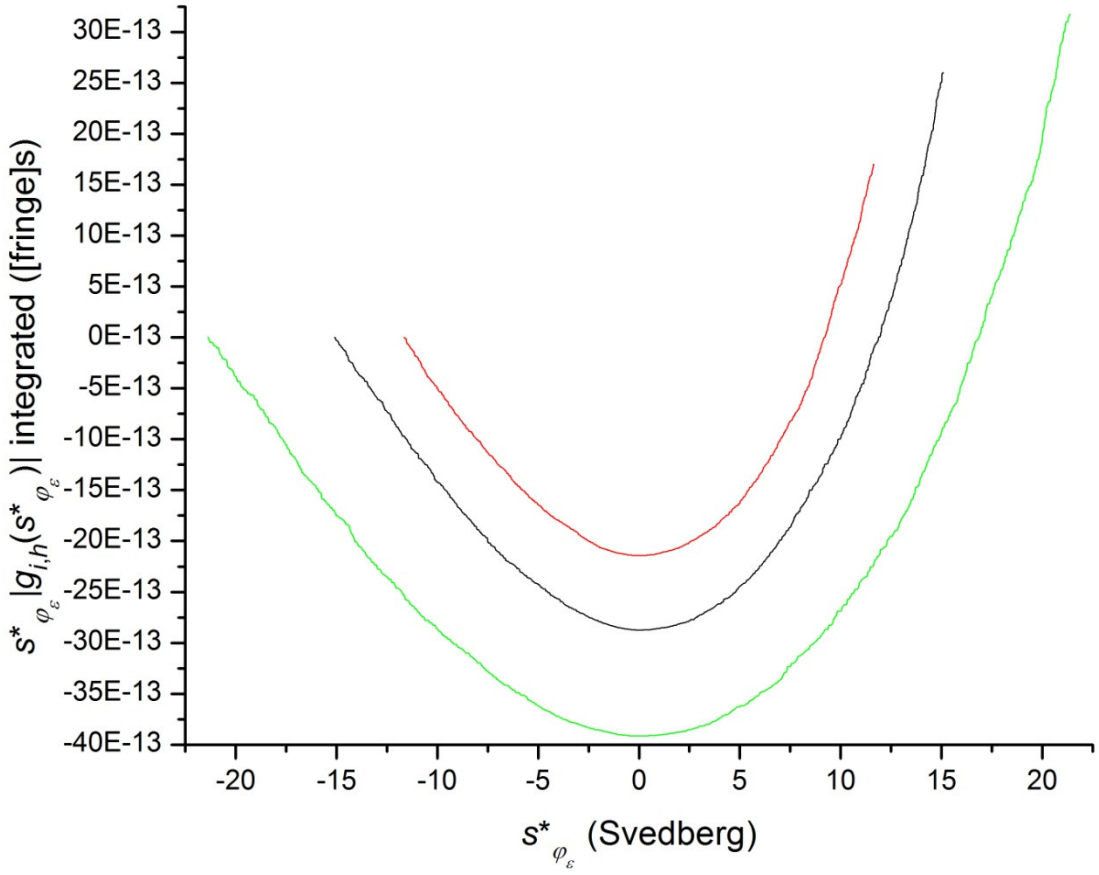

Figure 81. The integral of $s^*_{\varphi_\epsilon}\left|g_{i,h}\left(s^*_{\varphi_\epsilon}\right)\right|$, obtained from $\Delta Y_{i,h}\left(s^*_{\varphi_\epsilon}\right)/\Delta s^*_{\varphi_\epsilon}$ determined using Equation 150, with respect to $s^*_{\varphi_\epsilon}$ at $t_\epsilon = t_{36}$ (——), $t_\epsilon = t_{51}$ (——) and $t_\epsilon = t_{66}$ (——), where $i = 0$ and $h = 1$. As $i = 0$, the integral of $s^*_{\varphi_\epsilon}\left|g_{i,h}\left(s^*_{\varphi_\epsilon}\right)\right|$ in this figure has its source in a noise-free signal (Figures 52 to 60 and 72 to 80). As there are no masks (Figures 20 to 23; Figure 32) applied to the integrands or the data that give rise to them, $s^*_{min<0} = s^*_{\varphi_\epsilon=1}$, $s^*_{max<0} = s^*_{min>0} = 0$ and $s^*_{max>0} = s^*_{\varphi_\epsilon=2N}$ at time t_ϵ (Table 18 lists $s^*_{\varphi_\epsilon=1}$ and $= s^*_{\varphi_\epsilon=2N}$ at each time of analysis) are the limits applied to the integral that, upon division by $G_{i,h}\left(s^*_{\varphi_\epsilon=2N}\right)$ at time t_ϵ (Equation 77; Figure 79), yields $s^*_{i,h,\epsilon}\left(s^*_{\varphi_\epsilon=1}, s^*_{\varphi_\epsilon=2N}\right)$ at time t_ϵ (Equation 81a; Figure 82). For each value of the integral (the numerator of Equation 81a) shown in this figure, the lower limit of integration is $s^*_{min<0} = s^*_{\varphi_\epsilon=1}$

at time t_ϵ, and the upper limit of integration ranges from $s^*_{min<0}$ to $s^*_{max>0} = s^*_{\varphi_\epsilon=2N}$ at time t_ϵ.

Figure 61 shows the integral of $s^*_{\varphi_\epsilon}\left|g_{i,h}\left(s^*_{\varphi_\epsilon}\right)\right|$, obtained from $\Delta Y_{i,h}\left(s^*_{\varphi_\epsilon}\right)/\Delta s^*_{\varphi_\epsilon}$ determined using Equation 8, with respect to $s^*_{\varphi_\epsilon}$ at $t_\epsilon = t_{36}, t_\epsilon = t_{51}$ and $t_\epsilon = t_{66}$, where $i = 0$ and $h = 1$.

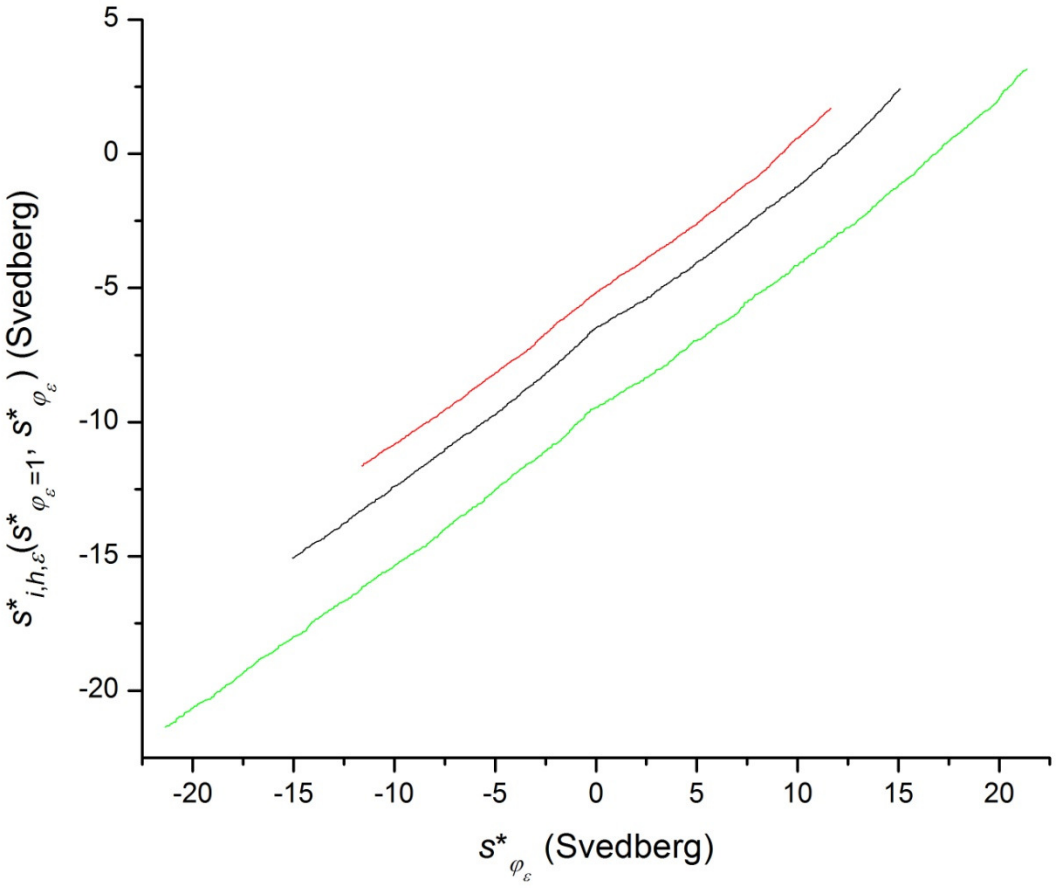

Figure 82. $s^*_{i,h,\epsilon}\left(s^*_{\varphi_\epsilon=1}, s^*_{\varphi_\epsilon}\right)$, obtained from $\Delta Y_{i,h}\left(s^*_{\varphi_\epsilon}\right)/\Delta s^*_{\varphi_\epsilon}$ determined using Equation 150, versus $s^*_{\varphi_\epsilon}$ at $t_\epsilon = t_{36}$ (——), $t_\epsilon = t_{51}$ (——) and $t_\epsilon = t_{66}$ (——), where $i = 0$ and $h = 1$. As $i = 0$, $s^*_{i,h,\epsilon}\left(s^*_{\varphi_\epsilon=1}, s^*_{\varphi_\epsilon}\right)$ in this figure has its source in a noise-free signal (Figures 52 to 61 and 72 to 81). At any given value of $s^*_{\varphi_\epsilon}$, $s^*_{i,h,\epsilon}\left(s^*_{\varphi_\epsilon=1}, s^*_{\varphi_\epsilon}\right)$ is equal to the integral of $s^*_{\varphi_\epsilon}\left|g_{i,h}\left(s^*_{\varphi_\epsilon}\right)\right|$ (Figure 81) divided by $G_{i,h}\left(s^*_{\varphi_\epsilon}\right)$ (Figure 79). As there are no masks (Figures 20 to 23; Figure 32) applied to the integrands or the data that give rise to them, $s^*_{min<0} = s^*_{\varphi_\epsilon=1}$, $s^*_{max<0} = s^*_{min>0} = 0$ and $s^*_{max>0}$

$= s^*_{\varphi_\epsilon=2N}$ at time t_ϵ (Table 18 lists $s^*_{\varphi_\epsilon=1}$ and $= s^*_{\varphi_\epsilon=2N}$ at each time of analysis) are the limits applied to the integrals (Equation 81a) that yield $s^*_{i,h,\epsilon}\left(s^*_{\varphi_\epsilon=1}, s^*_{\varphi_\epsilon=2N}\right)$ at each time of analysis. For each value of $s^*_{i,h,\epsilon}\left(s^*_{\varphi_\epsilon=1}, s^*_{\varphi_\epsilon}\right)$ shown in this figure, the lower limit of integration is $s^*_{min<0} = s^*_{\varphi_\epsilon=1}$ at time t_ϵ, and the upper limit of integration ranges from $s^*_{min<0}$ to $s^*_{max>0} = s^*_{\varphi_\epsilon=2N}$ at time t_ϵ. Figure 62 shows $s^*_{i,h,\epsilon}\left(s^*_{\varphi_\epsilon=1}, s^*_{\varphi_\epsilon}\right)$, obtained from $\Delta Y_{i,h}\left(s^*_{\varphi_\epsilon}\right)/\Delta s^*_{\varphi_\epsilon}$ determined using Equation 8, versus $s^*_{\varphi_\epsilon}$ at $t_\epsilon = t_{36}, t_\epsilon = t_{51}$ and $t_\epsilon = t_{66}$, where $i = 0$ and $h = 1$.

IMAGINARY EXPERIMENTAL PROTOCOL

A somewhat general AUC velocity protocol that might have been applied had the work been real

The AUC velocity (a.k.a. sedimentation velocity) protocol described here is somewhat general, in that much would apply to work conducted with any Beckman model XL-I analytical ultracentrifuge at some temperature of interest within such instruments' range of 4.0°C to 40.0°C, but some parts of the protocol apply specifically to the sort of instrument (www.lmb.ubc.ca/BT-xli-auc.html) maintained by the Centre for Biothermodynamics (supported by the Michael Smith Foundation for Health Research Infrastructure Grant) at the University of British Columbia. Furthermore, to strengthen the tenuous link between real AUC experiments and imaginary experiments in which data have been generated by simulations, the protocol is based on that which one might apply if one could actually conduct the simulated AUC described here (**DATA**) and in previous works (Moody, 2012a and 2012b). Hence, 20.0°C is assumed to be the temperature of interest.

It is further assumed that, for the sake of example, an imaginary experimental protocol might

serve as well as a real one. It is also assumed that no real experiment involving an analytical ultracentrifuge should ever be conducted. (For a detailed example of just a small part of the initial portion of a real AUC velocity experiment, see *Data that formed the basis of* $GRN_{i,h}(r,t)$.) Bear in mind that a preparative centrifuge is a ghastly machine that should never be connected to power, let alone operated. More dreadful still is an analytical ultracentrifuge, which is a demonic contraption that casts its users into an especially nauseating neighbourhood of a Circle of Hell that spins ever faster in all reference frames, including its own somehow. Take it from Dante Alighieri: "Lasciate ogne speranza, voi ch'intrate."

Preliminary procedures

Prior to the first experiment in the series, the radial position would, for the hypothetical experiments described here, be calibrated for the interference optical system using the 4-hole An-60 Ti rotor as described in *Common interference system settings*, below. Prior to loading the reference-and-sample-filled cells into the 4-hole An-60 Ti rotor, the rotor and optical periscope would be equilibrated to temperature at vacuum, at 0 RPM, for over an hour. (Rotor speeds are given in RPM or kRPM, where 1 kRPM = 1000 RPM.)

The An-60 Ti rotor has a maximum speed of 60 kRPM. The An-50 Ti, which is an 8-hole rotor, has a maximum speed of 50 kRPM. Methods for the two rotors are similar, but where important differences exist, they are noted below.

Personal protection equipment (PPE)

Appropriate PPE, including full-coverage footwear, full-coverage clothing, safety glasses, a lab coat and chemical-resistant gloves that do not leak, should be worn whenever solutions or centrifuge parts are handled, and whenever hazardous events, such as chemical spills or glass breakage, may occur. The materials of everything worn should be appropriate to the hazards that may be present. (Consider, with respect to fire hazards for example, that while cotton and a typical synthetic fibre will both burn, the synthetic fibre may also melt and become stuck to the skin.)

Velocity cell assembly

A velocity cell comprises a housing, two windows, two window holders, two window gaskets, two window liners, a velocity centrepiece, a screw-ring washer, a screw ring, two housing-plug gaskets and two housing plugs, plus two spacers if the centrepiece is less than full height. As the housing, the windows, the window holders, the screw ring and the spacers are cylindrical in profile, it is convenient to describe these components in terms of cylindrical coordinates. For guidance in the proper assembly of a cell, relevant diagrams in appropriate manuals should be consulted.

Each velocity cell would be assembled using 2 sapphire windows, each placed in on a window gasket in a window holder, with a window liner between the cylindrical edge of the window and the wall of the holder against which the window would press in the presence of centrifugal forces. Once in their holders, the fully accessible faces of the sapphire windows would be placed directly against the flat faces of a double-sector epon centrepiece with a 0.3 cm or 1.2 cm height along its longitudinal axis. It is this height of the centrepiece that determines the optical path-

length. (See *Cell loading*. Also see Equations 154a and 155a.) If a 0.3 cm centrepiece were used, one 0.45 cm spacer would be placed below the lower window holder and one 0.45 cm spacer would be placed above the upper window holder. In all cases, the recessed faces of the window holders would be the faces farthest from the centrepiece. After hand-tightening a Spinkote-lubricated screw ring underlain by a Spinkote-lubricated screw-ring gasket, each cell would be tightened using a torque of 125 inch-pounds. A few minutes later, the torque would be checked for each cell. A few minutes after that, the torque would again be checked for each cell. (The purpose of such checking is to minimise the chance of a solution leaking from a cell at any possible rotor speed.)

Cell identification and paired placement in the rotor

Each cell is identified by the number of the rotor position it will occupy in an experiment, and each cell placed in the rotor must be counterbalanced by a cell in the rotor position directly opposite to it.

When using a 4-hole rotor, the counterbalance/calibration cell is placed in position 4, and the cell it is balanced against is placed in rotor position 2. The cell in rotor position 2 is identified as cell 2, and the counterbalance/calibration cell in rotor position 4 can be referred to as cell 4. An additional pair of counterbalanced cells can be placed in rotor positions 1 and 3. If used, rotor positions 1 and 3 would be occupied by cells 1 and 3, respectively.

When using an 8-hole rotor, the counterbalance/calibration cell is placed in position 8, and the cell it is balanced against is placed in rotor position 4. The cell in rotor position 4 is identified as

cell 4, and the counterbalance/calibration cell in rotor position 8 can be referred to as cell 8. Additional pairs of counterbalanced cells can be paired opposite each other in rotor positions 1 versus 5, 2 versus 6, and 3 versus 7. If used, rotor positions 1 and 5 would be occupied by cells 1 and 5, respectively, rotor positions 2 and 6 would be occupied by cells 2 and 6, respectively, rotor positions 3 and 7 would be occupied by cells 3 and 7, respectively.

Cell loading

Each cell would be loaded with a replicate sample/reference pair of solutions, for which the height of the centrepiece is the optical path-length, *L*. The most commonly employed centrepiece heights are thus the most commonly employed optical path-lengths, which are $L = 1.2$ cm and $L = 0.3$ cm. On average, the solution volumes in a 0.3 cm velocity centrepiece are $(0.3\text{ cm})/(1.2\text{ cm})$ of those of a 1.2 cm velocity centrepiece. For some degree of generality, solution volumes and masses are thus given as multiples of $L/(1.2\text{ cm})$.

The reference solution, at a volume of approximately $(0.475\text{ ml})\,L/(1.2\text{ cm})$ (approximate maximum volume), would be loaded by tuberculin syringe (Becton-Dickinson ½ ml with 27 G × ½ inch, permanently attached needle) into the reference channel of each cell. *Care should be taken to avoid scratching the centrepiece or windows with the needle!* During AUC, such scratches can cause solutions to exhibit nonlaminar fluid flows that render any collected data uninterpretable.

Once filled, each reference channel would be closed with a Teflon gasket and a brass housing plug at a torque of 33 inch-pounds.

The sample solution, at a volume of approximately (0.465 ml)L/(1.2 cm), would then be loaded by sterile tuberculin syringe into the sample channel of each cell. Again, *care should be taken to avoid scratching the centrepiece or windows with the needle!*

Once filled, each sample channel would then be closed with a Teflon housing-plug gasket under a brass housing plug to which a torque of 33 inch-pounds would be applied with an appropriate device.

To ensure that each sample's meniscus position (needed to analyse the data in terms of the apparent sedimentation coefficient and its distribution function) would be determinable, each cell would be visually inspected to confirm that the volume of the reference exceeded the volume of the sample.

Cell balancing

The mass of each reference-and-sample-filled cell would be checked after loading. The masses of cells to be loaded directly opposite one another in the rotor must be within 0.5 g of each other. When working with aqueous solutions, masses typically range from approximately 39.2 g to 39.5 g for cells assembled and loaded as described above. It is preferable and usually possible to ensure that any two opposing cells that are within 0.15 g of each other. When the rotor is spinning, a difference of more than 1 g between directly opposite cells can be detected by the XL-I as a sufficient imbalance of mass to warrant a forced deceleration to 0 RPM.

If possible, the counterweight/calibration cell with a counterweight of appropriate mass would be placed and aligned in its designated rotor position (rotor position 4 for a 4-hole rotor), and it would not be removed or re-aligned until data for all replicates of all treatment groups within a set of experiments had been gathered. The rationale for this preference is presented later. (See *RI system calibration procedure*.)

Assuming a 4-hole rotor is to be loaded, the counterweight/calibration cell would, by virtue of its being already present in rotor position 4, become cell 4, and a 7 g brass counterweight would already have been used to bring its mass to approximately 38.85 g, thereby rendering it appropriate to balance against a cell with a mass of 38.35 g to 39.35 g, according to the rule above. More often than not, however, cell 4 is purposefully underbalanced against its opposite, cell 2. As such, if cell 2 were to lose all its liquid contents of approximately $(0.940 \text{ ml})\,L/(1.2 \text{ cm})$ in a leakage failure, its mass would decrease by approximately $(0.940 \text{ g})\,L/(1.2 \text{ cm})$, assuming it had been loaded with aqueous sample and reference solutions. Therefore, an excessively unbalanced rotor condition would be unlikely to occur, as, regardless of whether cell 2 leaked, the difference between the masses of cells 2 and 4 should always have been well under 1 g.

It is important to remember that, when screwing a counterweight into the calibration/counterweight cell, no part of the counterweight can be allowed to extend above or below to housing of the cell. The reason for this is that the centrifugal forces can be strong enough to shear off any overhanging part of the counterweight. The sheared bit of metal can then strike critical components of substantial mass, such as the optical periscope, at high velocity, and so wreak extremely expensive and fairly frightening havoc.

If an additional pair of counterbalanced cells is to be placed in rotor positions 1 and 3 of a 4-hole rotor, cell 1 should be balanced as well as possible against its opposite, cell 3. Thus, a complete leakage of one cell in any pair of well counterbalanced cells in rotor positions 3 and 4 would not necessarily cause an imbalance of more than 1 g between the opposing cells, and thus would not necessarily lead to an excessively unbalanced rotor condition.

Rotor and XL-I loading

Just before loading the reference-and-sample-filled cells into the 4-hole An-60 Ti rotor, The XL-I would be stopped, its vacuum would be released, the optical periscope and rotor would be removed, and the XL-I would be shut off entirely. If the associated PC were running, it, too, would be shut down at this time, and its Ethernet cable, if present, would be disconnected.

Sedimentation velocity experiments would be set up using as many as 3 sample/reference pairs in a 4-hole An-60 Ti rotor. The cells would be placed and aligned in the 4-hole An-60 Ti rotor, which would have the calibration/counterweight cell already present and aligned in rotor position 4. (To reiterate: To counterbalance a calibration cell in position 4, a cell would have to be placed opposite to it, in position 2. An additional pair of cells could be placed in positions 1 and 3.) Next, the XL-I would be turned on, the fully loaded rotor and optical periscope would be placed in its chamber, the chamber would be closed, and the contents of the chamber would be equilibrated to temperature at vacuum at 0 RPM for over an hour prior to the first step involving acceleration of the rotor. During temperature equilibration, the PC would be turned on, the XL-I operating software would be started, and the XL-I method files would be set up.

Overview of a basic velocity procedure

Each experiment would typically consist of at least 2 parts, with the 1st conducted at 3 kRPM, and the 2nd conducted at X_2 kRPM, where $X_2 \geq 3$. (At a given radial position, r, the relative centrifugal force, RCF, at 3 kRPM is $(3/X_2)^2$ less than that at X_2 kRPM. At X_2 kRPM = 60 kRPM, $(3/X_2)^2 = 1/400$. With g_E, the cgs standard acceleration due to gravity, being approximately 981 cm/s^2 at sea level on Earth, at 60 kRPM, the RCF, which is given by $(r\omega^2/g_E) \times g_E$, ranges from 233,410 $\times$ g_E at $r = 5.8$ cm, which is close to the innermost detectable point, to 289,750 $\times$ g_E at $r = 7.2$ cm, which is close to the outermost detectable point. Near the approximate mid-point of $r = 6.5$ cm, the RCF = 261,580 $\times$ g_E at 60 kRPM.) All parts of the experiment would typically utilise the interference optical system, which operates at a single wavelength, λ, that is well above from the absorbance maximum of most biological macromolecules. (By virtue of the interference optical system using a relatively long wavelength, the loss of signal to light scattering is minimised.) Additional parts of the experiment might also utilise the absorbance system, the available wavelengths of which range from $\lambda = 800$ nm to $\lambda = 190$ nm. The absorbance system can monitor optical density at up to two wavelengths.

Prior to starting the 1st method, all common XL-I settings, all interference system settings, and all absorbance system settings would be checked to ensure that they matched the intended settings.

Common XL-I settings

The type of rotor (4-hole in this case) would be specified. The temperature would be set to the chosen value (20.0°C in this case). Default settings (400 RPM/s, a.k.a. “max”) would be used for

XL-I acceleration and deceleration. Rather than specifying a shut-down after a chosen period of time had elapsed, the time setting would be kept on hold. With the probable exception of the last method used, in the scan options, "stop XL-I after last scan" would not be selected.

Common cell comment format for all scan methods

For all methods, the comment line for each cell would briefly describe the sample solution, the reference solution, and the cell (such as, "12 mm V-CP, S" for a 1.2 cm sedimentation-velocity centrepiece and sapphire windows). For all methods, "counterbalance/cal" would be used in the comment line for cell 4 when using the 4-hole rotor, as in the case. (When using the 8-hole rotor, "counterbalance/cal" would be used in the comment line for cell 8, instead.)

Common interference system settings

At any given radial position, the interference optical system is sensitive to the total mass concentration of any solute for which the concentration distribution in the sample is different from that in the reference, as would be expected in the case of a solute found solely in the sample solution at the radial position in question. Adjustments of instrument parameters are generally needed to optimise the detection of such differences.

For a solute species a, of a solute component, q, that is found in the sample solution only, and where the sample solution is at dialysis equilibrium with the reference solution, the noise-free signal at radial position r_j and time t_ϵ is given by

$$RI_{\lambda,q,a}(r_j, t_\epsilon) = k_{\lambda,q,a}\left[c_{q,a}(r_j, t_\epsilon)\right]L,$$

(154a)

where L is the optical path-length, $c_{q,a}(r_j, t_\epsilon)$ is the mass/volume concentration of solute species a of solute component q at radial position r_j of the sample solution at time t_ϵ, and $k_{\lambda,q,a}$ is the specific fringe displacement of solute species a of solute component q at the wavelength λ, of the light source, which is assumed to be monochromatic. (Compare this equation with Equation 4.) For $c_{q,a}(r_j, t_\epsilon)$ in g/cm and L in cm, $k_{\lambda,q,a}$ would be in fringe·cm^2/g.

Assuming that the sample solution is at dialysis equilibrium with the reference solution, the total noise-free signal at radial position r_j and time t_ϵ is given by

$$RI_\lambda(r_j, t_\epsilon) = \sum_{q=1}^{n} \sum_{a=1}^{n_q} RI_{\lambda,q,a}(r_j, t_\epsilon),$$

(154b)

where n_q is the number of species of component q, which is one of n components that are only found in the sample solution.

For sample materials of a given composition, the specific fringe displacement is directly proportional to the refractive index increment and inversely proportional to λ (Moody, 2011: Equation E1). The proportionality of $RI_{\lambda,q,a}(r_j, t_\epsilon)$ to L stems from the proportionality of $k_{\lambda,q,a}$ to $1/\lambda$. As the refractive index increment is a function of λ, solvent properties, and such system properties as temperature, few experimental parameters can be altered without affecting $k_{\lambda,q,a}$.

For the Rayleigh interference (RI) optical system, the optimal laser delay settings must be determined for each cell of whichever rotor is used. Denoting the laser delay of cell h as $LD_h{}^\circ$, for an H-hole rotor, it should be found that either $LD_h{}^\circ - LD_{h+1}{}^\circ = 360°/H$ or $360° + LD_h{}^\circ - LD_{h+1}{}^\circ =$

$360°/H$, where $1 \leq h < H$. For the comparison between cell H and cell 1, it should be found that either $LD_H{}^\circ - LD_1{}^\circ = 360°/H$ or $360° + LD_H{}^\circ - LD_1{}^\circ = 360°/H$.

For each cell, typical settings of the interference optical system would include 0.40° for the laser duration, 10 for the laser gain (contrast), and 127 for the laser offset (brightness). (Though the laser duration, the laser gain and the laser offset can be set to different values for each cell, the same settings for these parameters would probably work well for each cell when all cells contain optically similar solutions.) By default, no blank subtraction is applied to any cell. (A basic description of blank subtraction can be found in the manuals that apply to the instrument.)

The default settings would normally be used for the other parameters of the interference optical system, which relate to scaling factors for the images to be recorded. For each such image, horizontally oriented points (as pixel columns) can be considered those that are parallel to the radial axis, while vertically oriented points (as pixel rows) can be considered those that are perpendicular to the radial axis and perpendicular to the longitudinal axis of the cell. (Thus, the pixel rows lie in the plane of a cell window.) For the vertical scaling factor, 21.75 points (pixel rows) per fringe is the default setting. The horizontal scaling factor is equal to $(r_{last} - r_{1st})/(p_{last} - p_{1st})$, where p_{1st} is the first point (pixel column 1, by definition) of the image, p_{last} is the last point (pixel column 2020, approximately) of the image, r_{1st} is the inside radius that is assigned to p_{1st}, and r_{last} is the outside radius that is assigned to p_{last}. The default setting of the inside radius is $r_{1st} = 5.7500$ cm, and the default setting of the outside radius is $r_{last} = 7.2140$ cm. Using these default settings of r_{1st} and r_{last}, for $p_{1st} = 1$ pixel and $p_{last} = 2020$ pixel, the horizontal scaling factor would be $(r_{last} - r_{1st})/(p_{last} - p_{1st}) \cong 7.2313\text{E-}4$ cm/pixel.

For any given solute, the signal is a function of its specific fringe displacement (in fringe·cm^2/g), its concentration difference from sample to reference, and the optical path-length (Equation 154a). As previously noted, the specific fringe displacement of each solute is proportional to its refractive index increment, and is thus sensitive to such variables as solvent properties, temperature and wavelength. Consequently, it is worth knowing the wavelength of the detection system. (A laser light source with a nominal wavelength of 675 nm is usually used for the RI optical system.)

It is also worth bearing in mind that the signal-to-noise ratio will approach 1 from above as the optical density of the sample solution or reference solution approaches infinity. Ideally, then, at the wavelength of the light source of the RI optical system, the optical density of each solution would equal zero. Fortunately, the RI optical system is sufficiently robust to permit its use with solutions that exhibit fairly high optical densities at the wavelength of the light source. To achieve acceptable signal-to-noise ratios in such cases, however, painstaking adjustments of the laser delays, laser durations and laser offsets may be needed.

RI system calibration procedure

Prior to the first experiment in the series, the calibration/counterweight cell with a 6-gram counterweight (approximately 37.85 g in total) would be placed in position 4 of the 4-hole rotor, and an assembled but yet-to-be-filled cell (approximately 38.3 g) is placed in position 2 for a counterbalance. (As with any cell, even an empty cell, such as that which would be used here in position 2, should be properly aligned to avoid perpendicular centrifugal forces that could break the septum of the centrepiece.) So loaded, the rotor and the optical periscope would be

equilibrated at the temperature of interest (20.0°C in this case) in vacuum. Once the temperature and vacuum were stable, the rotor would be run at 3 kRPM. Standard XL-I procedures would then be used to set the radial reference positions for the RI system.

The pixel column corresponding to each radial reference position, $r = 5.8500$ cm for the inner reference position, r_{inner}, and $r = 7.1500$ cm for the outer reference position, r_{outer}, is likely to vary slightly from one calibration to another. (For example, after one calibration, pixel column 138 might correspond to $r_{inner} = 5.8500$ cm, and pixel column 1936 might correspond to $r_{outer} = 7.1500$ cm. After another calibration, pixel column 141 might correspond to $r_{inner} = 5.8500$ cm, and pixel column 1940 might correspond to $r_{outer} = 7.1500$ cm.)

After calibration, the empty cell in position 2 would be removed. Next, the 6 g counterweight in cell 4 would be gently removed and replaced with the 7 g counterweight without disturbing the alignment of the cell, which, unless absolutely necessary, would not be removed or repositioned until the completion of the entire set of related experiments. (With the 7 g counterweight in place, cell 4 would be expected to balance against a filled cell in position 2, provided that the cell had been constructed and loaded as described above.) Thus, one calibration of the RI system would apply to all the RI data collected in all experiments. This condition is ideal, but far from necessary, and if, by mistake or necessity, the calibration cell were removed or its alignment disturbed, the calibration procedure would be repeated.

To repeat: **It is important to remember that, when screwing a counterweight into the calibration/counterweight cell, no part of the counterweight can be allowed to extend above or below to housing of the cell.** The reason for this is that the centrifugal forces can be strong enough

to shear off any overhanging part of the counterweight. "Lasciate ogne speranza, voi ch'intrate."

Common absorbance system settings

All scans involving the absorbance system would be performed in continuous mode from radial positions 5.8 to 7.3 cm at 0.003 cm intervals for 1 replicate at one or two selected wavelengths, and in *no* case would the "No delay calibration" option be chosen, while in *each* case, the "Radial calibration before first scan" option would be chosen.

For a solute species a, of a solute component, q, that is found in the sample solution only, and where the sample solution is at dialysis equilibrium with the reference solution, the noise-free signal at radial position r_j and time t_ϵ is given by

$$OD_{\lambda,q,a}(r_j, t_\epsilon) = \epsilon_{\lambda,q,a}[c_{q,a}(r_j, t_\epsilon)]L = \left[\alpha_{\lambda,q,a} + \frac{\theta_{\lambda,q,a}}{ln(10)}\right][c_{q,a}(r_j, t_\epsilon)]L, \quad (155a)$$

where λ is the wavelength of the light source (assumed to be monochromatic), L is the optical path-length, $c_{q,a}(r_j, t_\epsilon)$ is the mass/volume concentration of solute species a of solute component q at radial position r_j of the sample solution at time t_ϵ, $\epsilon_{\lambda,q,a}$ is the apparent mass extinction coefficient of solute species a of solute component q at wavelength λ, $\alpha_{\lambda,q,a}$ is the part of $\epsilon_{\lambda,q,a}$ that applies to absorbance, and $\theta_{\lambda,q,a}/ln(10)$ is the part of $\epsilon_{\lambda,q,a}$ that applies to turbidity. (Compare this equation with Equation 154a.) For $c_{q,a}(r_j, t_\epsilon)$ in g/cm and L in cm, $\epsilon_{\lambda,q,a}$ would be in OD·cm^2/g, where 1 OD is the unit of optical density.

Assuming that the sample solution is at dialysis equilibrium with the reference solution, the total noise-free signal at radial position r_j and time t_ϵ is given by

$$OD_\lambda(r_j, t_\epsilon) = \sum_{q=1}^{n} \sum_{a=1}^{n_q} OD_{\lambda,q,a}(r_j, t_\epsilon),$$

(155b)

where n_q is the number of species of component q, which is one of n components that are only found in the sample solution.

For sample materials of a given composition, the apparent mass extinction coefficient is a function of λ, solvent properties, and such system properties as temperature. Thus, few experimental parameters can be altered without affecting $\epsilon_{\lambda,q,a}$.

1st scan method: Rotor speed = 3 kRPM; RI and OD_λ scans of all cells

The initial scan method would consist of an acceleration to 3 kRPM, followed by one set of RI scans of all cells (including the calibration cell in rotor position 4) and one set of OD_λ (absorbance system) scans of all cells (including the calibration cell in rotor position 4). The results from this scan method are useful for damage avoidance and quality control (QC). The sort of damage avoided is that caused by subjecting empty or misaligned cells to AUC at rotor speeds above 3 kRPM. The QC potential in part derives from the ability to check the data quality or radial calibrations before it is too late to do anything but abort an experiment that could have been salvaged by adjusting the settings of the detection systems and/or repeating radial calibrations. The QC potential also derives from the forensic value of the data collected.

The RI scans, absorbance system calibration and OD_λ scans for a fully loaded 4-hole rotor might take approximately 20 minutes to complete if the OD_λ scans are conducted at just 1 wavelength.

(The RI scans should take less than 1 minute. The subsequent baseline, delay and radial calibrations of the absorbance system could take up to 12 minutes at 3 kRPM. The subsequent OD_λ scans of cells 1 to 4 would probably take approximately 7 minutes at 3 kRPM.)

The method would be named 3x*mon.scn, where "3" would refer to the rotor speed (3 kRPM), "x" would refer to the extra scans (OD_λ in addition to RI), "mon" would refer to the month ("jan" for January, etc) within which the method was run, and "*" would be the date of the day of the month when the method was used. (Method file names are limited to 8 characters, not including the .scn suffix.)

After the scans were completed, and assuming that a single wavelength were used in the OD_λ scans, the XL-I would be left running at 3 kRPM until $t_1 = 30$ minutes had elapsed since the start of rotor acceleration from 0 RPM. At the $t_1 = 30$ minute mark, the 2nd scan method would be started.

2nd scan method: 1 RI scan per minute of all cells except cell 4 for t_2 minutes at X_2 kRPM

The next scan method would consist of N_2 sets of RI scans of all filled cells at X_2 kRPM. This method would be started immediately after $t_1 = 30$ minutes had elapsed since the start of rotor acceleration from 0 RPM.

The "time between scans" would be set to 1 minute, which would ensure that exactly 1 minute would elapse between the start of one set of scans and the start of the next, provided that each set of scans was completed in 1 minute or less. (As each set of RI scans normally takes less than 1 minute, the method should take exactly $t_2 = N_2$ minutes to complete.)

The method would be named X_2k*mon.scn, where "X_2k" refers to the rotor speed (X_2 kRPM), "mon" would refer to the month within which the method was run, and "*" would be the date of the day of the month when the method was used.

In the protocol for the simulated AUC described here (**DATA**) and in previous works (Moody, 2012a and 2012b), X_2 would equal 60, and N_2 would equal 116. If, as specified, exactly1 minute elapsed between the start of one set of scans and the start of the next, then, with $N_2 = 116$, t_2 would equal 116 minutes.

3rd *scan method: Rotor speed = X_3 kRPM; RI and OD_λ scans of all filled cells*

A final velocity method would consist of (up to) N_3 sets of scans at X_3 kRPM, where each set would consist of RI scans of all filled cells, followed by OD_λ scans of all filled cells. This method would start immediately after the last iteration of the 2nd scan method was done, which would be after a time of approximately ($t_1 + t_2$) had elapsed since the start of rotor acceleration from 0 RPM.

The "time between scans" would be set to 10 minutes. (With the "time between scans" set to 10 minutes, exactly 10 minutes would elapse between the start of one set of scans and the start of the next, provided that each set of scans had been completed in 10 minute or less. Thus, 10 minutes would be the minimum time between the start of one set of scans and the start of the next.)

After the first set of RI scans, the delay calibration of the absorbance system would typically require less than a minute to complete, and the radial calibration of the absorbance system would typically require less than 4 minutes to complete, after which, the first set of OD_λ scans would begin. Subsequent sets of RI and OD_λ scans require less time than the first set, as the calibration steps only occurs prior to the first OD_λ scan of any given method. The method might be stopped before completion, either after running overnight, or after just a few sets of scans.

The method would be named X_3x*mon.scn, where "X_3" would refer to the rotor speed (X_3 kRPM), "x" would refer to the extra scans (OD_λ in addition to RI), "mon" would refer to the month within which the method was run, and "*" would be the date of the day of the month when the method was used.

In the protocol for the simulated experiment described here, X_3 would equal 60, and N_3 would equal 104. If, as specified, exactly10 minutes elapsed between the start of one set of scans and the start of the next, then, with $N_3 = 104$, t_3 would equal 1,040 minutes.

Shut down

Scanning would be stopped (if it hadn't already stopped automatically), the XL-I would be stopped (if it hadn't already stopped automatically), its vacuum would be released (which could not occur until the diffusion pump had had time to cool), the rotor chamber would be opened, the optical periscope and rotor would be removed, the rotor chamber would be closed, the XL-I operating software would be closed, and the XL-I would be shut off entirely. The data collected would be zipped, and the output would be split into volumes of limited size (such as 1 Mb) to

ensure that the resulting files were not too big to be e-mailed. The Ethernet cable would be connected to the PC, the browser (very likely Opera, as of 2014, if the operating system is Windows 95) would be opened, and an accessible e-mail system would be opened. The zipped data would be saved as a draft, or would be sent if addressed to anyone beyond the sender. (Some XL-Is are operated via PCs that do not support CD or USB devices. Such XL-Is may have an RI camera system that is incompatible with computer hardware that is sufficiently new to support such devices. In such cases, the use of newer computer hardware that does supports CD or USB devices would require an upgrade to the RI camera system. As of 2012, the cost of such an upgrade was approximately 30,000 CAD. The cost of the upgrade is such that the older camera system, and thus an older PC, may still be found on an older XL-I.)

Cell cleaning

Good eye protection, such as goggles, and chemical-resistant gloves that do not leak would be especially important in this step. If disposable gloves were used, one would want to make sure that they were of good quality, and had not become brittle with age. Wearing two pairs of gloves would provide an extra margin of safety, if doing so would not unduly impair dexterity.
After AUC, the reference and sample solutions would be removed from each cell by the same type of syringe previously used to load them. *Care should be taken to avoid scratching the centrepieces or windows with the needle!* (See the *Cell loading* section, above.) This process permits the salvaged solutions to be saved for further analysis. The cells would then be disassembled, and any residual material left on the sapphire windows and epon centrepieces would be removed by washing each of these parts one at a time, by hand, three times. The first and third washes would be with water (distilled and deionised or the like, such as Milli-Q), and

the second wash would be with an appropriate alcohol (reagent grade methanol or ethanol). Laboratory squirt bottles may be used to direct a stream of liquid at each part in all washes with water. As alcohols leach plasticisers from laboratory squirt bottles, a glass dropper is a better choice for directing such liquids at each part. Washing at a short height above an appropriately sized container, such as a medium-sized weighing boat, would collect the washing fluid and would gently catch any part that might be dropped. In the case of the sapphire windows, the flat surfaces would be rubbed with the thumb and forefinger of a clean, nitrile-gloved hand while each washing solution was applied. After the third wash, all parts would be air-dried while set edge-wise on a stack of about 6 Kimwipes (or similar tissue paper) on a clean, dry surface. (*Before setting any cylindrical parts on their curved surfaces, set up physical barriers to prevent the parts from rolling!* Pyrex baking dishes or the like can provide both barriers to rolling and the clean, dry surfaces on which to stack Kimwipes.) After drying, the parts would be inspected for cleanliness, and, if necessary, washed again.

Other cell parts besides the windows and centrepieces would be cleaned, as needed, using water and either methanol or ethanol, but the last wash for any metal part would always be with methanol or ethanol. Any of these washed parts would also be air dried.

RANDOMNESS AS A FUNCTION OF THE TOTAL POPULATION OF OBSERVATIONS

The general approach of the analysis was summarised, and the main result was given, in an earlier section (**RANDOM NOISE**). In this section, results that are fairly consistent with Inequality 23 are presented. Further details regarding data generation and some results of data analysis (*One-way analyses of variance (ANOVA), Bonferroni adjusted t-test (2-tailed), and confidence*

intervals about mean values) are also included in this section.

Regarding Equations 21 and 22, it might be said that, given an infinite amount of noise in the form of real, random numbers that are normally distributed about a mean of 0 with a standard deviation of 1, an infinite amount of information would emerge if, by dint of an infinite effort lasting forever, the noise were placed in ascending order, such that the value obtained by applying the Cumulative Distribution Function (Equation 16) to each random number would be equal to, or at least infinitely difficult to distinguish from, the normalised index value (Equation 15) by which that random number would be enumerated if it were possible to enumerate an infinite number of anything.

For a population of m normally distributed random numbers, there are $m!$ equally probable orders in which they may be found, with the probability of finding them in any particular order being $1/m!$. Thus, as the population of normally distributed random numbers approaches infinity, the likelihood of those numbers appearing in any given order approaches zero. By infinitely remote chance, then, an infinitely large set of normally distributed random numbers could, prior to any sorting, appear in some particular order, such as ascending order, but betting on that set of numbers coming up in any particular order would be tantamount to playing the worst lottery in the universe. Such a lottery might ultimately be the only game in town, however, and would almost certainly have been played by the Schlemiel of Fortune of whom Mickey Katz (1957) sang, so why not you? Who or what you are, anyway, might next be called into question, but as one answer is likely to be as baseless as any other, no digression on that point need be heaped on what has already become “a crushing concatenation of detail,” which is to say, a megillah (Rosten, 2001), here. Speaking of which, the method used to construct each of the

previously mentioned five megillahs (**THE 5 MEGILLAHS**) is described next.

Four files, $Origin_{k,1}$, $Origin_{k,2}$, $Origin_{k,3}$ and $Origin_{k,4}$, each consisting of 9,750,000 normally distributed random numbers generated by Origin 6.0, were adjusted as per the data shown in Figure 1 to obtain for new files, $random_{k,1}$, $random_{k,2}$, $random_{k,3}$ and $random_{k,4}$, respectively, so that, for the data in each new file, the mean, μ, was rendered as close as possible to 0, and the standard deviation, σ, was rendered as close as possible to 1. Further manipulations on $random_{k,1}$, $random_{k,2}$, $random_{k,3}$ and $random_{k,4}$ were carried out by functions within a C++ program that was compiled using Borland C++ Builder 6.0. The precision of all the data within the C++ program was that of a long double, which, upon conversion from binary to decimal, resulted in data with 18 significant figures. (Data exported from Origin had just 13 significant figures, but the various operations performed by the C++ program led, ultimately, to data with 18 significant figures of which the last 5 did not merely consist of padding with zeroes.)

Within the C++ program, the adjusted values of the four files, $random_{k,1}$, $random_{k,2}$, $random_{k,3}$ and $random_{k,4}$, were used to create four lists. The first list, $Pforward_k$, was equated to the values of $random_{k,1}$ in their original order. The second list, $Nforward_k$, was equated to the negated values of $random_{k,2}$ in their original order. The third list, $Preverse_k$, was equated to the values of $random_{k,3}$ in reverse order. The fourth list, $Nreverse_k$, was equated to the negated values of $random_{k,4}$ in reverse order.

The values of $Pforward_k$, $Nforward_k$, $Preverse_k$ and $Nreverse_k$ were shuffled to create a new list, $Shuffle_k$, such that a list of every fourth value of $Shuffle_k$ would equal $Pforward_k$ if started from the first value of $Shuffle_k$, a list of every fourth value of $Shuffle_k$ would equal $Nforward_k$ if started

from the second value of $Shuffle_k$, a list of every fourth value of $Shuffle_k$ would equal $Preverse_k$ if started from the third value of $Shuffle_k$, and a list of every fourth value of $Shuffle_k$ would equal $Nreverse_k$ if started from the fourth value of $Shuffle_k$. The mean and standard deviation of the 39,000,000 values of $Shuffle_k$ were calculated, the mean was subtracted from each individual value, and each resulting difference was divided by the standard deviation to obtain a normalised list, $Normal_k$. The mean, the standard deviation, and the extrema of $Normal_k$ were then determined and recorded.

The above process was carried out five times to obtain, for each value of k within $1 \leq k \leq 5$, a unique set, $Normal_k$, of 39,000,000 normally distributed random numbers. Table 42 gives the mean value, μ, the standard deviation, σ, and the extrema of each set, $Normal_k$.

K	minimum value of $Normal_k$	standard deviation of $Normal_k$
	mean value of $Normal_k$	
	maximum value of $Normal_k$	
1	-4.925735296127199250	9.999999999999999445E-1
	4.637891633241242318E-21	
	4.926383972328482432	
2	-4.922139761541072794	9.999999999999999445E-1
	9.527262570387712150E-21	
	4.928536909747558450	
3	-4.927430865243476314	9.999999999999999445E-1
	-4.627784922989778083E-21	
	4.927125052925080668	
4	-4.926041521708016880	1.000000000000000000
	-3.976924458818877393E-21	
	4.924238725852489045	
5	-4.926612489984357333	1.000000000000000111
	-6.091285495499839578E-21	

	4.926477761141594544	

Table 42. The mean value, μ, the standard deviation, σ, the minimum value and the maximum of each set of 39,000,000 normally distributed random numbers, $Normal_k$. As $1 \leq k \leq 5$, there are as many sets of 39,000,000 normally distributed random numbers as there are megillahs (Rosten, 2001).

Concatenated, the five megillahs, $Normal_k$ from $k = 1$ to $k = 5$ (Table 42), form *Normal*, which consists of 195,000,000 normally distributed random numbers, 64 subsets of which constitute the treatment groups (Table 43) used to quantify the extent to which, as the population of random numbers per replicate increases, the normalised index value (Equation 15) approaches the value obtained by applying the Cumulative Distribution Function (Equation 16) to each random number.

The 195,000,000 normally distributed random numbers of *Normal* are divided into a number of equally populated subsets that constitute the replicates data sets of a treatment group, within which each value of *Normal* appears once. Thus, as a whole, each treatment group is identical with *Normal*, and one treatment group is distinguished from all others solely by the number of its equally populated replicates. The original order of the values of each replicate is identical to the order in which they appear within *Normal*, within which, the last value of one replicate would be followed by the first value of the next replicate, if any. As such, first value of the first replicate of a treatment group is always the first value of *Normal*, and the last value of the last replicate of a treatment group is always the last value of *Normal*.

As previously described (**THE 5 MEGILLAHS**), the 64 treatment groups are indexed by *i*, and

within a given treatment group, there are n_i replicate data sets that are indexed by h. Within each replicate, h, of treatment group i, there is a population of m_i random variables that are denoted as $\chi_{Z_i,h}$ when in their original order given by the integral index, Z_i, for which $1 \leq Z_i \leq m_i$. When placed in ascending order, the m_i random variables within replicate h of treatment group i are denoted as $\chi_{\zeta_i,h}$, and their place in the ascending order is given by the integral index ζ_i, for which $1 \leq \zeta_i \leq m_i$. As defined by Equations 14 and 15, respectively, the normalised index of Z_i is given by $Z_{m_i} = Z_i/(m_i + 1)$, and the normalised index of ζ_i is given by $\zeta_{m_i} = \zeta_i/(m_i + 1)$. Thus, $0 < Z_{m_i} < 1$, $0 < \zeta_{m_i} < 1$, and for any permitted value of m_i, the mean of all Z_{m_i} values and the mean of all ζ_{m_i} values are both equal to 0.5.

The defining parameter of each treatment group i, is the population, m_i, of each replicate, h. Within a given treatment group, i, the m_i values of ζ_{m_i} are identical for each replicate, h, but each replicate comprises a unique set of m_i values of $\chi_{\zeta_i,h}$ that increase monotonically as ζ_{m_i} increases, assuming $m_i > 1$. Thus, for $m_i > 1$, the set of m_i values of $CDF(\chi_{\zeta_i,h})$ (Equation 16) will increase monotonically as ζ_{m_i} increases. As with the data shown in Figure 1, within replicate h of treatment group i, the set of ordered pairs given by $(\chi_{\zeta_i,h}, CDF(\chi_{\zeta_i,h}))$ is not identical to the set of all ordered pairs given by $(\chi_{\zeta_i,h}, \zeta_{m_i})$, but according to the hypothesis being tested via the 64 treatment groups of Table 43, the two sets of ordered pairs should approach a state of indistinguishability as m_i increases to very large values, in which case, in the limit as m_i approaches infinity, the set of all ζ_{m_i} values and the set of all $CDF(\chi_{\zeta_i,h})$ values should share the same range.

For each treatment group, i, n_1/m_i is equal to the number of replicates, n_i, and is also equal to the

expected number of coincidences in which $\chi_{[Z_i=\zeta_i],h} = \chi_{[\zeta_i=Z_i],h}$, where $\chi_{[Z_i=\zeta_i],h} = \chi_{[\zeta_i=Z_i],h}$ somewhat more compactly represents an instance for which $Z_i = \zeta_i$ when $\chi_{Z_i,h} = \chi_{\zeta_i,h}$. (The random variables are denoted as $\chi_{Z_i,h}$ when in their original order given by the integral index Z_i, and the random variables are denoted as $\chi_{\zeta_i,h}$ when in their ascending order given by the integral index ζ_i.) As a population of m_i normally distributed random numbers can be ordered in any of $m_i!$ equally probable ways, the frequency of coincidences in which $\chi_{[Z_i=\zeta_i],h} = \chi_{[\zeta_i=Z_i],h}$ should approach an average value of $1/m_i$ as the number of replicate data sets, n_i, approaches infinity.

Table 43 shows the result, κ_i, which denotes the total number of actual coincidences in which $\chi_{[Z_i=\zeta_i],h} = \chi_{[\zeta_i=Z_i],h}$ within treatment group i, for which the frequency of such coincidences is equal to κ_i/n_1. Using all the κ_i values from Table 43, $\log_{10}(\kappa_i)$ plotted against $\log_{10}(n_i)$ in Figure 83a, a linear regression fit (Equation 156) yields a y-intercept close to 0 and a slope close to 1 (Table 44), as would be expected for κ_i values that are close to n_1/m_i. Figure 83b shows that the magnitude of the residuals (Equation 157) tends to increase as n_i decreases, especially from n_{33} = 30,000 to $n_{64} = 5$. Figure 83c further illustrates the increasing deviation of κ_i from its expected value of n_1/m_i as n_i decreases. When, as in Figure 84a, only the data from n_{32} = 32,500 to n_1 = 39,000,000 are included in the plot of $\log_{10}(\kappa_i)$ versus $\log_{10}(n_i)$, a linear regression fit (Equation 156) yields results (Table 45; Figure 84b) that are even more consistent with those that would be expected for κ_i values that are close to n_1/m_i.

Table 43 also shows the parameters, m_i and n_i, and the descriptive statistics, A_i and σ_i. Equations 17 through 19 define A_i, the mean of all absolute differences within treatment group i, and in the context of Table 43, σ_i is the standard deviation of those absolute differences about A_i. In the limit as n_i approaches infinity, Equation 20 yields 0.25 exactly as the expectation value of $A_{i=1}$ for $m_{i=1}$

$= 1$, while Equations 21 and 22 yield 0 exactly as the expectation value of $A_{i\equiv\infty}$ as $m_{i\equiv\infty}$ approaches infinity. According to Inequality 23, for $1 \leq m_i$, in the limit as n_i approaches infinity, $A_i \geq A_{ref}/m_i^{0.5}$, where A_{ref}, being defined as $\lim_{n_1\to\infty} A_1$, is equal to 0.25 exactly (Equation 20).

i	m_i	n_i	A_i	σ_i	κ_i
1	1	195,000,000	2.4999832837112E-1	8.7077841760457E-7	195,000,000
2	2	97,500,000	1.9757428108351E-1	1.8635324945893E-5	97,492,712
3	3	65,000,000	1.6798042603626E-1	2.6474595833294E-5	64,998,153
4	4	48,750,000	1.4851594751065E-1	2.5757421659871E-5	48,761,184
5	5	39,000,000	1.3443118968412E-1	4.8807897820465E-5	39,007,773
6	6	32,500,000	1.2368015890910E-1	2.9544023082796E-5	32,525,548
7	8	24,375,000	1.0811685932456E-1	3.4882947172934E-5	24,381,747
8	10	19,500,000	9.7282895502670E-2	3.9905732124972E-5	19,494,172
9	13	15,000,000	8.5755339287675E-2	4.5985758313039E-5	14,995,015
10	16	12,187,500	7.7525615398701E-2	4.9428854971516E-5	12,180,765
11	20	9,750,000	6.9507512834572E-2	4.5400440093546E-5	9,750,304
12	25	7,800,000	6.2313819345222E-2	4.6595967916773E-5	7,801,872
13	26	7,500,000	6.1109546878366E-2	5.4507593003812E-5	7,494,904
14	30	6,500,000	5.6947256211710E-2	4.5710359822824E-5	6,500,338
15	39	5,000,000	5.0039874443815E-2	4.7568604318033E-5	4,998,512
16	50	3,900,000	4.4252399080256E-2	6.4222941242156E-5	3,901,293
17	75	2,600,000	3.6168638701312E-2	8.1593186783161E-5	2,595,018
18	100	1,950,000	3.1310043135025E-2	1.0529491581071E-4	1,949,443
19	150	1,300,000	2.5544016580830E-2	1.2929588618458E-4	1,299,112
20	200	975,000	2.2107654677519E-2	1.6330054423301E-4	976,963
21	300	650,000	1.8048206180518E-2	2.1230027777531E-4	649,370
22	375	520,000	1.6139319626739E-2	2.3527212739276E-4	520,288
23	500	390,000	1.3959563633666E-2	2.7881214747286E-4	390,258
24	750	260,000	1.1349550386867E-2	3.1692866223891E-4	260,215
25	1,000	195,000	9.8519970889088E-3	3.6386058140381E-4	195,065
26	1,250	156,000	8.8413410086975E-3	3.9282464590836E-4	156,310
27	1,500	130,000	8.0987901167207E-3	4.2064017173392E-4	130,164
28	2,000	97,500	7.0839068722909E-3	4.5708392972472E-4	97,727
29	3,000	65,000	5.8680722742208E-3	4.9852599370067E-4	64,745
30	3,750	52,000	5.2776131419042E-3	4.9568509328944E-4	52,174
31	5,000	39,000	4.5630927623009E-3	4.7143032180050E-4	38,988
32	6,000	32,500	4.1527430956351E-3	4.5098763135801E-4	32,558

33	6,500	30,000	3.9832507768225E-3	4.3306476941954E-4	29,960
34	7,500	26,000	3.6945928028265E-3	4.4125922396121E-4	25,908
35	10,000	19,500	3.1510321755269E-3	4.3907644157880E-4	19,403
36	15,000	13,000	2.2960493397602E-3	3.0611572982081E-4	13,139
37	20,000	9,750	1.7188937905416E-3	1.8354729567972E-4	9,683
38	30,000	6,500	1.3920754637913E-3	6.1685533796389E-5	6,696
39	50,000	3,900	1.0096914278491E-3	4.6743490530242E-5	3,843
40	75,000	2,600	7.8681424888761E-4	4.0625299505745E-5	2,720
41	100,000	1,950	6.6946827360550E-4	3.9663665394563E-5	1,970
42	120,000	1,625	6.1555758475969E-4	3.5851513471463E-5	1,552
43	150,000	1,300	5.3497934266620E-4	3.0690074070817E-5	1,379
44	200,000	975	4.5117781214606E-4	3.2381842716981E-5	958
45	250,000	780	4.1306188430356E-4	2.9040751748916E-5	769
46	300,000	650	3.7994098614290E-4	2.8921684491128E-5	652
47	375,000	520	3.4380214399073E-4	2.9033617836531E-5	489
48	500,000	390	3.0971634632948E-4	3.2895805495724E-5	409
49	600,000	325	2.9128713872930E-4	3.5830995819049E-5	295
50	750,000	260	2.6986426599182E-4	3.3986384573881E-5	266
51	1,000,000	195	2.5193043199051E-4	3.3833343638270E-5	184
52	1,300,000	150	2.3489173342152E-4	3.4326467276275E-5	173
53	1,500,000	130	2.3693845515043E-4	3.6999336729738E-5	133
54	1,950,000	100	2.1411704553917E-4	2.9648183076820E-5	84
55	2,437,500	80	2.0444563000082E-4	2.7747498791131E-5	87
56	3,000,000	65	2.0557158863560E-4	3.4435172345880E-5	53
57	3,900,000	50	1.6655217989345E-4	9.9897723488307E-6	43
58	4,875,000	40	1.4873435409885E-4	3.6149787903437E-6	46
59	6,500,000	30	1.4195530630420E-4	1.1468796733719E-6	27
60	7,800,000	25	1.4561487958088E-4	1.6266842204806E-6	20
61	9,750,000	20	1.4442831300069E-4	2.0293709979472E-6	20
62	13,000,000	15	1.4030723742356E-4	4.4992018738476E-7	13
63	19,500,000	10	1.4039322734346E-4	3.8369527763469E-7	6
64	39,000,000	5	1.3985991037397E-4	4.2128548740653E-7	4

Table 43. Selected parameters and results for the $g = 64$ treatment groups indexed by i. The tabulated parameters are n_i, which is the number of replicates within treatment group i, and m_i, which is the population of random variables per replicate within treatment group i. Among the 64 treatment groups, the number of replicates ranged from a high of $n_{i=1} = 195{,}000{,}000$ at $m_{i=1} = 1$ to a low of $n_{i=64} = 5$ at $m_{i=64} = 39{,}000{,}000$. For any given treatment group, i, the relationship

between n_i and m_i is given by $n_i = n_1/m_i$. The tabulated results include κ_i, which is the total number of coincidences in which $\chi_{[Z_i=\zeta_i],h} = \chi_{[\zeta_i=Z_i],h}$ within treatment group i. In the limit as n_i approaches infinity, κ_i is expected to approach n_1/m_i, which is also equal to n_i. Another tabulated result consists of the descriptive statistic A_i, which is the mean of all absolute differences within treatment group i (Equations 17 to 19). The remaining tabulated result is the descriptive statistic σ_i, which, in the context of this table, is the standard deviation of the absolute differences about A_i within treatment group i. The values of A_i and σ_i are shown at truncated precision.

The functional relationship between n_i and coincidences in which $\chi_{[Z_i=\zeta_i],h} = \chi_{[\zeta_i=Z_i],h}$

The equation for the linear regression fit of $\log_{10}(\kappa_i)$ versus $\log_{10}(n_i)$ can be written as

$$\log_{10}(\kappa_i) = \{\log_{10}(\kappa_0) \pm [\log_{10}(\kappa_0)]_{se}\} + \{\Delta\kappa_i/\Delta n_i \pm [\Delta\kappa_i/\Delta n_i]_{se}\} \log_{10}(n_i),$$

(156)

where $\log_{10}(\kappa_0)$ is the y-intercept, $[\log_{10}(\kappa_0)]_{se}$ is the standard error in the y-intercept, $\Delta\kappa_i/\Delta n_i$ is the slope and $[\Delta\kappa_i/\Delta n_i]_{se}$ is the standard error in the slope. Thus, for a given value of i, the residual, being equal to the difference between the actual result and the central value obtained from the fit (Equation 156 with $[\log_{10}(\kappa_0)]_{se} = 0$ and $[\Delta\kappa_i/\Delta n_i]_{se} = 0$), is given by

$$\varepsilon_i = \log_{10}(\kappa_i) - [\log_{10}(\kappa_0) + (\Delta\kappa_i/\Delta n_i) \log_{10}(n_i)].$$

(157)

Table 44 shows the values of the parameters of Equation 156 in the case of $\log_{10}(\kappa_i)$ versus $\log_{10}(n_i)$ data from all $g = 64$ groups being fit, results for which are shown in Figures 83a and 83b.

On rearrangement, Equation 156 yields $\kappa_i = \left(\kappa_0 10^{\pm\lceil\log_{10}\kappa_0\rceil_{se}}\right)\left(n_i{}^{\Delta\kappa_i/\Delta n_i \pm [\Delta\kappa_i/\Delta n_i]_{se}}\right)$, where $\kappa_0 =$

$10^{\log_{10}(\kappa_0)}$ would be the fitted value of κ_i at $n_i = n_0 = 1$. A fit of κ_i versus n_i in the case of an exact conformity to the expected result yields the expected values of $\Delta\kappa_i/\Delta n_i$ and κ_0. If κ_i were equal to its expected value of $n_1/m_i = n_i$ at all values of n_i, and if $[\log_{10}(\kappa_0)]_{se}$ and $[\Delta\kappa_i/\Delta n_i]_{se}$ were both equal to 0, $\Delta\kappa_i/\Delta n_i$ would have to equal 1, and therefore κ_0 would also have to equal 1, from which it follows that m_0, being the value of m_i at $n_i = n_0 = 1$, would have to equal n_1.

With the population of data equal to N_{pop}, the upper (1 - α)% confidence limit is given by

$$\log_{10}(\kappa_i) = \{\log_{10}(\kappa_0) + t([\alpha/2], [N_{pop} - 2])[\log_{10}(\kappa_0)]_{se}\} + \{\Delta\kappa_i/\Delta n_i + t([\alpha/2], [N_{pop} - 2])[\Delta\kappa_i/\Delta n_i]_{se}\}\log_{10}(n_i),$$

(158a)

and the lower (1 - α)% confidence limit is given by

$$\log_{10}(\kappa_i) = \{\log_{10}(\kappa_0) - t([\alpha/2], [N_{pop} - 2])[\log_{10}(\kappa_0)]_{se}\} + \{\Delta\kappa_i/\Delta n_i - t([\alpha/2], [N_{pop} - 2])[\Delta\kappa_i/\Delta n_i]_{se}\}\log_{10}(n_i),$$

(158b)

where $t([\alpha/2],[N_{pop} - 2])$ is the upper critical value of Student's t-distribution at $[N_{pop} - 2]$ degrees of freedom and a significance level of $[\alpha/2]$ for a two-sided test.

Parameter	central value	standard error
y-intercept	$\log_{10}(\kappa_0)$ = -4.07348E-2	$[\log_{10}(\kappa_0)]_{se}$ = 1.07303E-2
Slope	$\Delta\kappa_i/\Delta n_i$ = 1.00692	$[\Delta\kappa_i/\Delta n_i]_{se}$ = 2.15960E-3

Table 44. Values of the parameters of Equation 156, which applies to the linear regression fit of $\log_{10}(\kappa_i)$ versus $\log_{10}(n_i)$, in the case of data from all $g = 64$ groups (Table 43) being fit. The sample correlation coefficient was $R = 0.99986$ (with less than a probability of 0.0001 that R is really zero), and the standard error of estimate obtained from the residuals (Equation 157) was

$\sigma_\varepsilon = 3.72273\text{E-}2$. With $N_{pop} = g = 64$ (Table 43) and with $\alpha = 0.05$, $t([\alpha/2],[N_{pop} - 2]) = 1.99897$ was used to calculate the upper and lower $(1 - \alpha)\%$ confidence limits (Equations 158a and 158b).

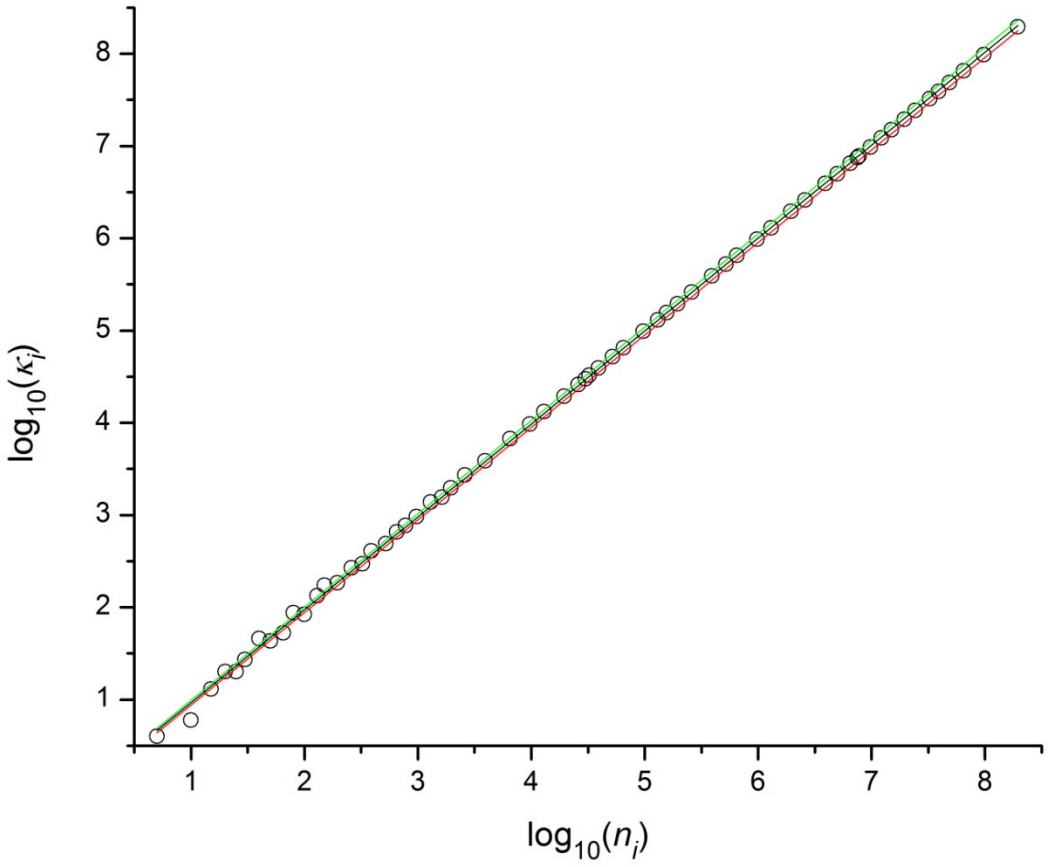

Figure 83a. The linear regression fit (——) for the complete set of $\log_{10}(\kappa_i)$ versus $\log_{10}(n_i)$ data (○), along with the upper (——) and lower (——) 95% confidence limits (Equations 158a and 158b) of that fit (Equation 156). The double-logarithmic presentation ensures that each data point is clearly visible in this figure and the figure that follows. Table 44 shows the parameters of the fit, for which data from all $g = 64$ groups in Table 43 were included. Within treatment group i, κ_i is the total number of coincidences in which $\chi_{[Z_i=\zeta_i],h} = \chi_{[\zeta_i=Z_i],h}$, and n_i is the number of replicates. The expected value of κ_i is n_1/m_i. As Figure 83b shows, the residuals (Equation 157)

are biased and heteroscedastic. As Figure 83c shows, however, κ_i lies well within 1% of n_1/m_i for $n_i > n_{33} = 30{,}000$, despite its trend toward increasing deviation from n_1/m_i as n_i decreases from n_{64} to n_1.

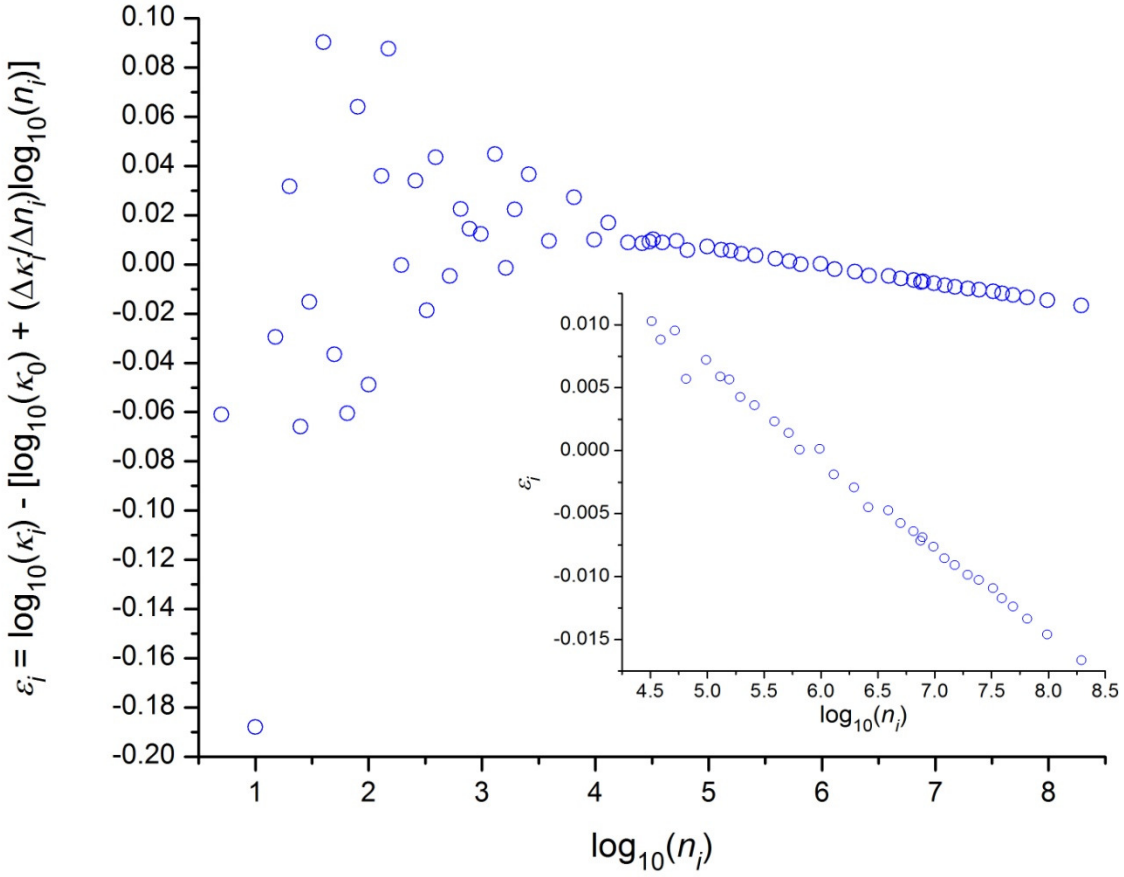

Figure 83b. The residuals (Equation 157), $\varepsilon_i = \kappa_i - [\log_{10}(\kappa_0) + (\Delta\kappa_i/\Delta n_i)\log_{10}(n_i)]$, from the linear regression fit (Equation 156), shown in Figure 83a, of the complete set of $\log_{10}(\kappa_i)$ versus $\log_{10}(n_i)$ data. The residuals are biased and heteroscedastic, but within $n_{32} = 32{,}500$ to $n_1 = 39{,}000{,}000$, they lie within a range, $-0.018 < \varepsilon_i < 0.013$, that is approximately tenfold narrower than the $-0.19 < \varepsilon_i < 0.10$ range found within $n_{64} = 5$ to $n_{33} = 30{,}000$.

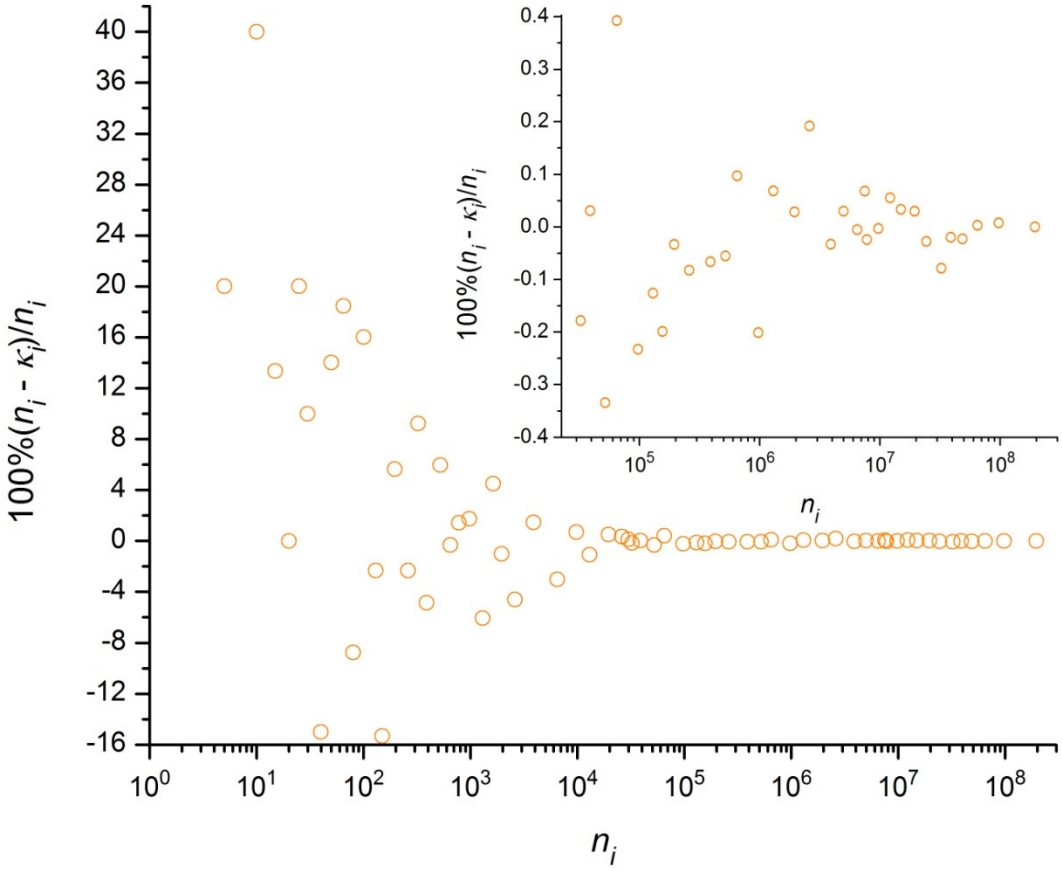

Figure 83c. The deviation of κ_i from the expected value of $n_1/m_i = n_i$, shown as $(100\%)(n_i - \kappa_i)/n_i$ (○) versus n_i, which is placed on a $\log_{10}$ scale. From $n_{64} = 5$ to $n_{33} = 30{,}000$, values of $(100\%)(n_i - \kappa_i)/n_i$ may be unbiased, but they are clearly heteroscedastic, ranging from -15.333% to 40% as n_i approaches $n_{64} = 5$ from above, and lying within -4.61538% to 4.49231% as n_i approaches $n_{33} = 30{,}000$ from below. For $n_i > n_{33} = 30{,}000$, $(100\%)(n_i - \kappa_i)/n_i$ values appear to be unbiased, but they are still heteroscedastic, ranging from -0.33462% to 0.39231% as n_i approaches $n_{32} = 32{,}500$ from above, and lying within -0.07861% to 0.05526% as n_i approaches $n_1 = 39{,}000{,}000$ from below.

Parameter	central value	standard error
y-intercept	$\log_{10}(\kappa_0) = 8.94150\text{E-}4$	$[\log_{10}(\kappa_0)]_{se} = 5.83660\text{E-}4$
Slope	$\Delta\kappa_i/\Delta n_i = 0.99987$	$[\Delta\kappa_i/\Delta n_i]_{se} = 9.05893\text{E-}5$

Table 45. Values of the parameters of Equation 156, which applies to the linear regression fit of $\log_{10}(\kappa_i)$ versus $\log_{10}(n_i)$, in the case of data from groups $i = 1$ to $i = 32$, within which n_i ranges from $n_{32} = 32{,}500$ to $n_1 = 39{,}000{,}000$ (Table 43), being fit. The sample correlation coefficient, R, was indistinguishable from 1 (with less than a probability of 0.0001 that R is really zero), and the standard error of estimate, σ_ε, obtained from the residuals (Equation 157) was 5.54797E-4. With $N_{pop} = 32$ and with $\alpha = 0.05$, $t([\alpha/2],[N_{pop} - 2]) = 2.04227$ was used to calculate the upper and lower $(1 - \alpha)$% confidence limits (Equations 158a and 158b).

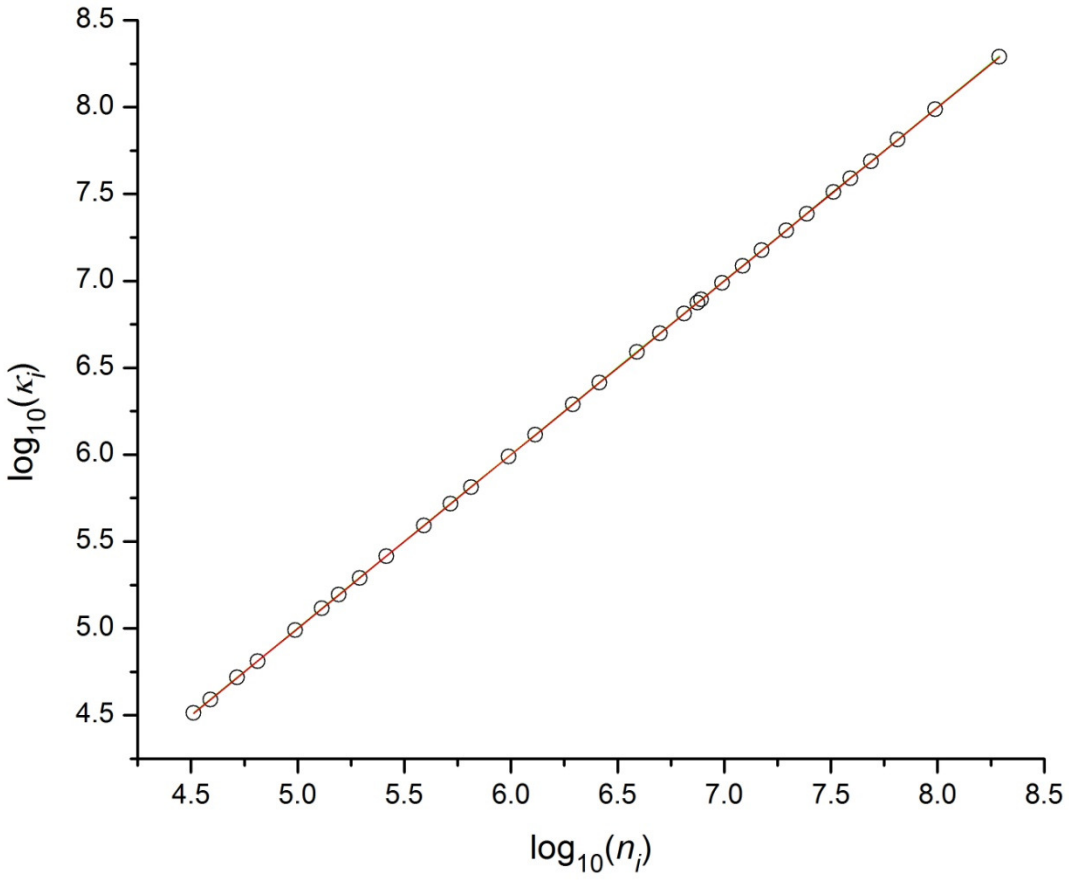

Figure 84a. The linear regression fit (——) for a truncated set of $\log_{10}(\kappa_i)$ versus $\log_{10}(n_i)$ data (○), along with the upper (——) and lower (——) 95% confidence limits (Equations 158a and 158b) of that fit (Equation 156). As with Figures 83a and 83b, the double-logarithmic presentation ensures that each data point is clearly visible in this figure and the figure that follows. The lines for the fit and the confidence limits appear to be superimposed at the scale shown. The truncated set only included data from groups $i = 1$ to $i = 32$ of Table 43. Table 45 shows the parameters of the fit to that truncated data. As Figure 84b shows, the residuals (Equation 157) are heteroscedastic but largely unbiased.

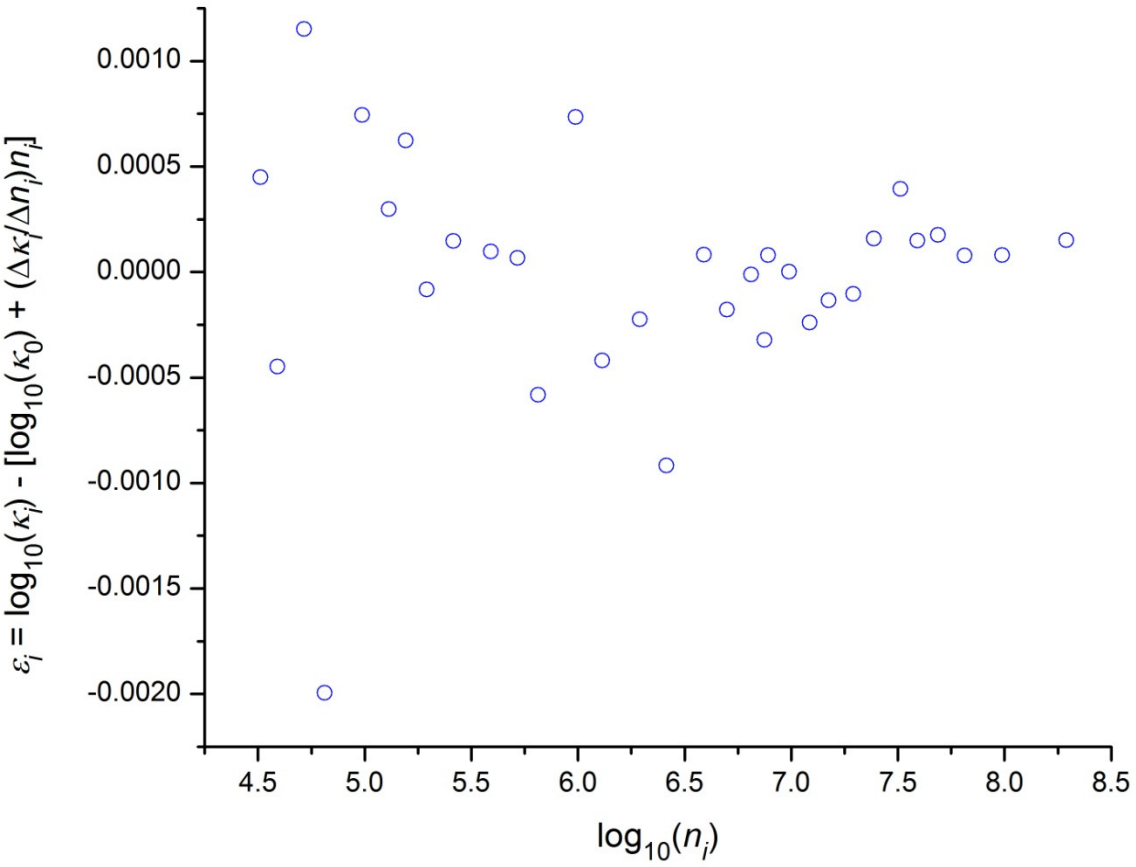

Figure 84b. The residuals (Equation 157), $\varepsilon_i = \kappa_i - [\log_{10}(\kappa_0) + (\Delta\kappa_i/\Delta n_i)\log_{10}(n_i)]$, from the linear regression fit (Equation 156), shown in Figure 84a, of the truncated set of $\log_{10}(\kappa_i)$ versus $\log_{10}(n_i)$ data.

The rarity of coincidences in which $CDF(\chi_{\zeta_i,h})$ *and* ζ_{m_i} *are exactly equal*

The set of all real numbers includes the set of all rational numbers and much else, and thus there is almost no chance that an exact equality of $CDF(\chi_{\zeta_i,h})$ to ζ_{m_i} would ever occur, though the two sets of values should become increasing indistinguishable as m_i approaches infinity. Where both the real values of $CDF(\chi_{\zeta_i,h})$ and the rational values of ζ_{m_i} are approximated as decimal

expansions, such indistinguishability might largely be an artefact of insufficient precision. Given a finite precision of the decimal expansions, at some point as m_i approaches infinity, it would even become impossible to distinguish either individual $CDF(\chi_{\zeta_i,h})$ values within clusters of consecutive $CDF(\chi_{\zeta_i,h})$ values or individual ζ_{m_i} values within clusters of consecutive ζ_{m_i} values. Despite such finite precision favouring the appearance of indistinguishability where none should be found, not even one exact equality of $CDF(\chi_{\zeta_i,h})$ to ζ_{m_i} is found among the 64 treatment groups listed in Table 43.

Values of A_i for finite values of m_i that are greater than 1

As with the plots of κ_i and ε_i versus n_i (Figures 83 and 84), double-logarithmic plots are used to present A_i, the mean of all absolute differences within treatment group i, versus m_i. In the first instance, all of the A_i versus m_i data of Table 43 are presented as $\log_{10}(A_i)$ versus $\log_{10}(m_i)$ in Figure 85. For each of the treatment groups listed in Table 43, $n_i m_i = n_1$, where n_i is the number of replicates within treatment group i, and $n_1 = n_{i=1}$. Thus, as m_i increases from its lowest value of $m_{i=1} = 1$, n_i decreases from its highest value of $n_{i=1} = 195{,}000{,}000$. It might be expected, then, that as m_i increases, n_i would eventually reach such low values that the results might cease to follow Inequality 23, according to which, in the limit as n_i approaches infinity, $A_i \geq A_{ref}/m_i^{0.5}$, where $A_{ref} = \lim_{n_1 \to \infty} A_1 = 0.25$ (Equation 20). Furthermore, even though Equations 21 and 22 yield 0 for the expected value of $A_{i \equiv \infty}$ as $m_{i \equiv \infty}$ approaches infinity, as m_i increases, the accompanying decrease in n_i might yield results that do not clearly show a trend in A_i toward zero. Such effects of low n_i values at high m_i values are evident in Figure 85.

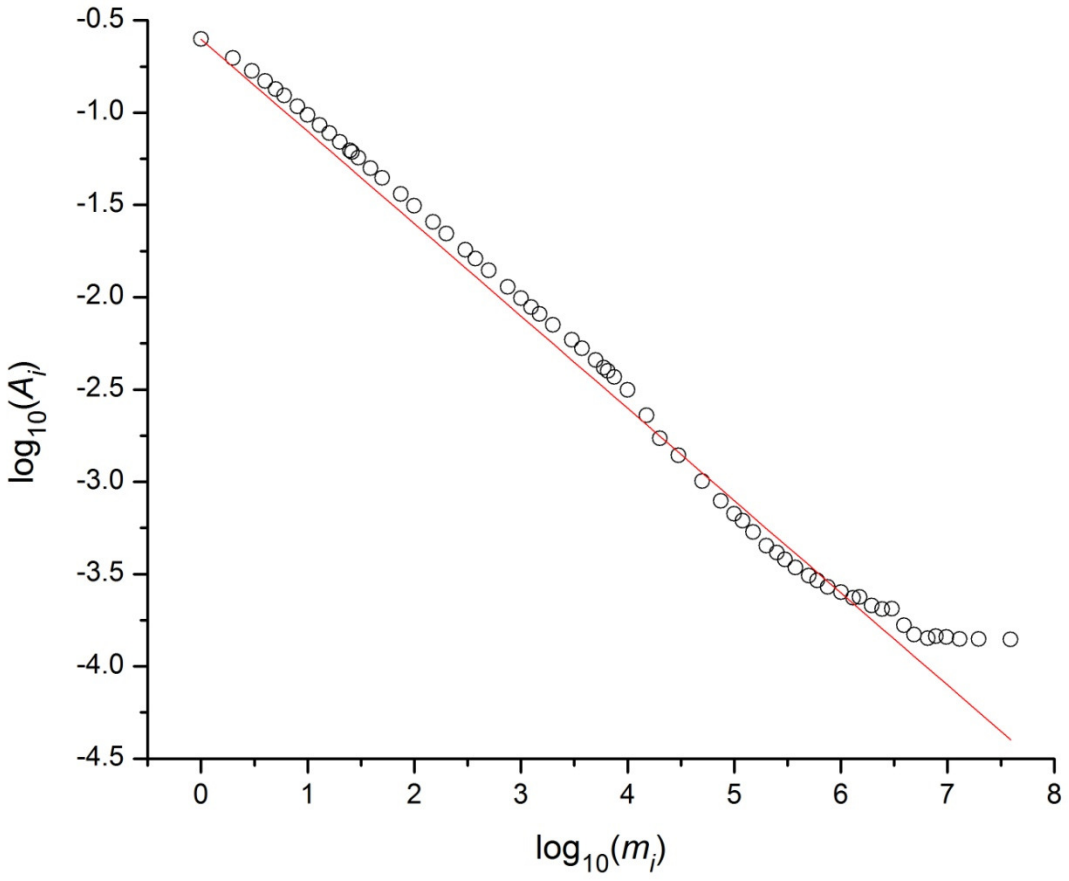

Figure 85. The set of all $\log_{10}(A_i)$ versus $\log_{10}(m_i)$ data (○) obtainable from the A_i versus m_i data of Table 43, and the line (——) obtained by plotting $\log_{10}(0.25/m_i^{0.5})$ against $\log_{10}(m_i)$. This line is the logarithmic form of the line pertaining to Inequality 23, which states that, for $1 \leq m_i$, in the limit as n_i approaches infinity, $A_i \geq A_{ref}/m_i^{0.5}$, where A_{ref}, being defined as $\lim_{n_1 \to \infty} A_1$, is equal to 0.25 (Equation 20). Presumably due to the relatively low n_i values, Inequality 23 breaks down among roughly the same treatment groups, $i = 33$ to $i = 64$, that show the greatest deviation of κ_i from the expected value of $n_1/m_i = n_i$ in Figure 83. For treatment groups $i = 33$ to $i = 64$, n_i ranges from $n_{33} = 30{,}000$ to $n_{64} = 5$, while m_i ranges from $m_{33} = 6{,}500$ to $m_{64} = 39{,}000{,}000$.

To identify which A_i values closely follow a functional trend with m_i and which do not, the

difference, $\log_{10}(A_i) - \log_{10}(0.25/m_i^{0.5})$, was plotted against $\log_{10}(m_i)$. The results, presented in Figure 86, can be interpreted as showing that $\log_{10}(A_i)$ increases with $\log_{10}(m_i)$ in the pattern of an exponential decay, but only where m_i is relatively low, so the n_i is relatively high.

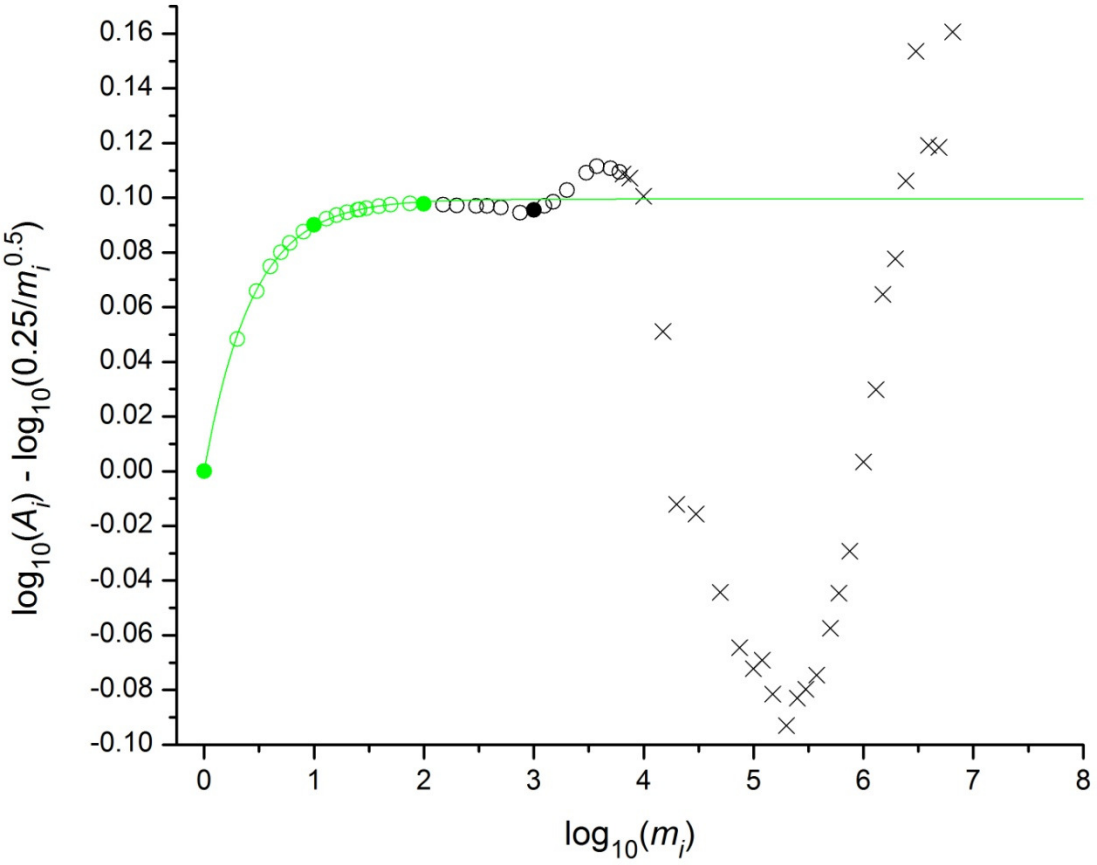

Figure 86. The difference, $\log_{10}(A_i) - \log_{10}(0.25/m_i^{0.5})$, versus $\log_{10}(m_i)$. Circles indicate the treatment groups $i = 1$ to $i = 32$, for which Inequality 23 holds consistently (Figure 85). Filled circles indicate of treatment groups $i = 1$, $i = 8$, $i = 18$ and $i = 25$, which are subjected to further statistical analysis in the next section, *Pair-wise comparisons of the A_i values for the 4 treatment groups with n_i values ≥ 195,000*. The symbol × is used for treatment groups $i = 33$ to $i = 64$, for which Inequality 23 does not hold consistently (Figure 85). Data indicated by the symbols ×, ○

or ●, are deemed to behave irregularly, relative to the trend observed where m_i is low. Data that follow the trend established where m_i is low, and thus, where n_i is high, are indicated by the symbols ○ and ●, and were fit, via the nonlinear least-squares fitting (NLSF) utility of Origin 6.0, to an exponential decay function given by $y_i = \delta\left(1 - e^{-\log_{10}(m_i)/\log_{10}(e)}\right)$. For the line (——) pertaining to the fit, $\delta = 0.09954 = \log_{10}(4/\upsilon)$, where $\upsilon = 3.180_{68}$, and where the factor $\log_{10}(4/\upsilon)$ will be used to obtain a convenient form of an equation (Equation 159a) with which to fit the high-replicate $\log_{10}(A_i)$ versus $\log_{10}(m_i)$ data.

Figure 85 shows the line that pertains to Inequality 23, and the difference between that line and $\log_{10}(A_i)$ was fit to obtain the line shown in Figure 86. The fit of the regularly behaving data of Figure 86 to $y_i = \delta\left(1 - e^{-\log_{10}(m_i)/\log_{10}(e)}\right)$ yields $\delta = (0.09954 \pm 0.00014)$, with a correlation coefficient of $R^2 = 0.99958$ and a reduced chi-squared statistic of $\chi^2/DoF = 2.4922\text{E-}7$. (A discussion of such NLSF results begins prior to Equation 30.) With respect to m_i, the data included in the fit range from $m_{i=1} = 1$ to $m_{i=25} = 1000$. With respect to n_i, the data included in the fit range from $n_{i=25} = 195{,}000$ to $n_{i=1} = 195{,}000{,}000$. The function $y_i = \delta\left(1 - e^{-\log_{10}(m_i)/\log_{10}(e)}\right)$, simplifies to $y_i = \delta\left(1 - 10^{-\log_{10}(m_i)}\right) = \delta(m_i - 1)/m_i$.

Combining the line for which $\delta = \log_{10}(4/\upsilon)$ in Figure 86 with the line pertaining to Inequality 23 in Figure 85 yields an equation,

$$\log_{10}(A_i) = \log_{10}\left(\left[\frac{1}{4\sqrt{m_i}}\right]\left[\frac{4}{\upsilon}\right]^{\frac{m_i-1}{m_i}}\right),$$

(159a)

that fits the $\log_{10}(A_i)$ versus $\log_{10}(m_i)$ data in the region where Inequality 23 holds (Figure 87), which it does among roughly the same treatment groups, $i = 1$ to $i = 32$, that show the least

deviation of κ_i from the expected value of $n_1/m_i = n_i$ in Figure 83. For treatment groups $i = 1$ to $i = 32$, n_i ranges from $n_{32} = 32{,}500$ to $n_1 = 195{,}000{,}000$, while m_i ranges from $m_1 = 1$ to $m_{32} = 6{,}000$.

As m_i approaches $m_{i=1} = 1$ from above, the results obtained from Equation 159a increasingly resemble those of

$$\lim_{m_i \to 1} \log_{10}(A_i) = \log_{10}\left(\frac{1}{4\sqrt{m_i}}\right),$$

(159b)

which is identical to the logarithmic form of Inequality 23 shown in Figure 85.

In Equation 159a, as m_i approaches infinity, the factor $[4/\upsilon]^{\frac{m_i-1}{m_i}}$ of Equation 159a approaches $4/\upsilon$. Thus, as m_i approaches infinity (Equations 21 and 22), the results obtained from Equation 159a increasingly resemble those of

$$\lim_{m_i \to \infty} \log_{10}(A_i) = \log_{10}\left(\frac{1}{\upsilon\sqrt{m_i}}\right),$$

(159c)

which gives the hypothetical values that $\log_{10}(A_i)$ approaches asymptotically as m_i increases to ever larger values.

Figure 87 shows $\log_{10}(A_i)$ versus $\log_{10}(m_i)$, obtained from the A_i versus m_i data of Table 43, and the lines given by the right-hand sides of Equations 159a, 159b and 159c.

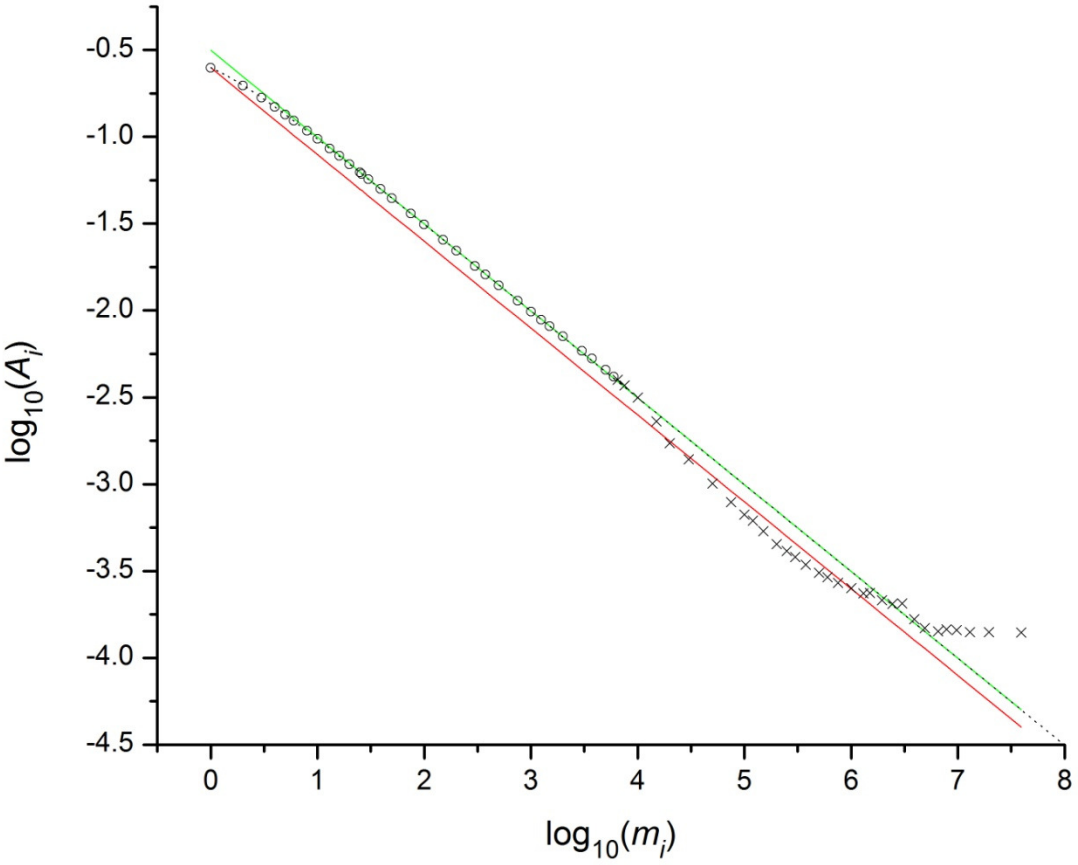

Figure 87. The $\log_{10}(A_i)$ versus $\log_{10}(m_i)$ data (O for treatment groups $i = 1$ to $i = 32$, which show the least deviation of κ_i from the expected value of $n_1/m_i = n_i$ in Figure 83; × for treatment groups $i = 33$ to $i = 64$, which show the greatest deviation of κ_i from the expected value of $n_1/m_i = n_i$ in Figure 83), obtained from the A_i versus m_i data of Table 43, and the lines given by the right-hand sides of Equations 159a (·····), 159b (——) and 159c (——), which are $\log_{10}\left(\left[1/4\sqrt{m_i}\right][4/\upsilon]^{\{m_i-1/m_i\}}\right)$, $\log_{10}\left(1/4\sqrt{m_i}\right)$ and $\log_{10}\left(1/\upsilon\sqrt{m_i}\right)$, respectively. Where υ appears, it is set equal to 3.180_{68} (Figure 86). For treatment groups $i = 1$ to $i = 32$ (O), among which Inequality 23 always holds, n_i ranges from $n_{32} = 32{,}500$ to $n_1 = 195{,}000{,}000$, while m_i ranges from $m_1 = 1$ to $m_{32} = 6{,}000$. For treatment groups $i = 33$ to $i = 64$ (×), among which Inequality 23 does not always hold, n_i ranges from $n_{33} = 30{,}000$ to $n_{64} = 5$, while m_i ranges from

$m_{33} = 6{,}500$ to $m_{64} = 39{,}000{,}000$.

Figure 87 might be viewed as a specific instance of a general test that could be applied to any set of treatment groups, such as the set to which Table 43 pertains, that are characterised by a treatment-group-specific population of random variables per replicate. In such a test, where a plot of $\log_{10}(A_i)$ versus $\log_{10}(m_i)$ data closely follows a plot of $\log_{10}\left(\left[1/4\sqrt{m_i}\right][4/\upsilon]^{\{m_i-1/m_i\}}\right)$ versus $\log_{10}(m_i)$ over a broad range of population-per-replicate values, m_i, the treatment groups, i, within such a range can be judged to have a sufficient number of replicates, n_i, to ensure that any statistics calculated for those treatment groups will approach the values that would be expected as n_i approaches infinity.

Pair-wise comparisons of the A_i values for the 4 treatment groups with n_i values ≥ 195,000

Of from the 64 treatment groups presented in Table 43, four representative treatment groups, $i = 1$, $i = 8$, $i = 18$ and $i = 25$, were selected from those that were judged to have a sufficient number of replicates, n_i, to ensure that any statistics calculated would approach the values that would be expected as n_i approaches infinity. Treatment groups $i = 1$ to $i = 32$ were deemed to have sufficient replicates to fit this criterion, as for these treatment groups, the plot of the $\log_{10}(A_i)$ versus $\log_{10}(m_i)$ data (Figure 87) closely follows the plot of $\log_{10}\left(\left[1/4\sqrt{m_i}\right][4/\upsilon]^{\{m_i-1/m_i\}}\right)$ versus $\log_{10}(m_i)$ (Equation 159a) over a broad range of population-per-replicate values, m_i.

For each of four selected treatment groups, $i = 1$, $i = 8$, $i = 18$ and $i = 25$, statistical analysis was applied to the set of all mean values, $A_{i,h}$, calculated for each replicate using Equation 18. Due to the high population of replicates within each of these four treatment groups, values of $A_{i,h}$ and

related statistics pertaining to individual replicates were deemed too numerous to tabulate. For treatment groups, $i = 1$, $i = 8$, $i = 18$ and $i = 25$, the respective number of replicates is $n_1 = 195{,}000{,}000$, $n_8 = 19{,}500{,}000$, $n_{18} = 1{,}950{,}000$ and $n_{25} = 195{,}000$.

To quantify the statistical significance of a difference between any two treatment groups, a Bonferroni-adjusted *t*-test (2-tailed) was applied to pair-wise comparisons of the population means from different treatment groups. Confidence intervals about the population means were determined and graphed to illustrate selected results from the Bonferroni-adjusted *t*-tests. (For details, see: *One-way analyses of variance (ANOVA), Bonferroni adjusted t-test (2-tailed), and confidence intervals about mean values*.)

Treatment-group-independent statistical parameters are those that apply to the set of all treatment groups being analysed. Table 46 lists treatment-group-independent the statistical parameters that would be dimensionless no matter what dimensions might apply to the mean values being compared. Table 47 lists the treatment-group-independent statistical parameters for which the dimensions depend on the dimensions of the mean values being compared. Table 48 lists descriptive statistical parameters that apply to each treatment group individually. Table 49 lists the comparative statistical parameters that apply to the (1 - α)100% confidence interval about each pair-wise mean difference, $\Delta\mu_{ij}$ (Equation 96), between treatment groups. Table 50 lists the comparative statistical parameters that constitute the $e_{\Delta\mu_{ij}}$-based (1 - α)100% confidence interval about the mean, μ_i, of each treatment group. Figure 88 shows, as a function of $P_i = m_i$, the $e_{\Delta\mu_{ij}}$-based (1 - α)100% confidence interval about the mean as $-C_{\mu_{P,P+}} < \mu_P < +C_{\mu_{P,P-}}$ (Table 50), along with the fit (Equation 159a; Figure 87).

The treatment-group-wide mean value, A_i, of Equation 19 is identical to the treatment-group-wide mean value, μ_i of Equation 85 in the section describing Bonferroni adjusted *t*-test (*One-way analyses of variance (ANOVA), Bonferroni adjusted t-test (2-tailed), and confidence intervals about mean values*). Furthermore, just prior to Equation 96, which is also in the section describing Bonferroni adjusted *t*-test, A_i was defined as the true value that must underlie each observation, $A_{i,h}$, within treatment group *i*. Finally, in Equation 105a of the section presenting the comparisons between different treatment groups of the simulated AUC results (*Statistical analysis of AUC simulation results for any given time of analysis, t_ϵ*), A_i was redefined as the expectation value of each observation, $A_{i,h}$, within treatment group *i*. Thus, to avoid confusion between the mean and either the true or the expectation value of each observation within a treatment group, and to present parameters in the same notation as that used in section describing the Bonferroni adjusted *t*-test, μ_i is used in place of A_i in the remainder of this section. Similarly, to present parameters in the same notation as that used in section describing the Bonferroni adjusted *t*-test, P_i is used to denote m_i in this section, but frequent reminders are given that $P_i = m_i$ in this context.

Table 49 gives the value of the Bonferroni adjusted *t*-test (2-tailed), p_{Bonf}, for each pair-wise mean difference, $\Delta\mu_{ij}$ at $t_\epsilon = t_{51}$. Less than (1 - α)100% confidence is accorded to the difference between any two means for which the comparison yields $p_{Bonf} > \alpha$, and by this measure, with $\alpha = 0.05$, each mean value, μ_P (identical to μ_i), is considered distinguishable from every other mean value, as each pair-wise comparison yields $p_{Bonf} < \alpha$. Likewise, in Table 50 and in Figure 88, less than (1 - α)100% confidence is accorded to the difference between any two means with overlapping confidence intervals, and by this measure as well, each mean value is considered distinguishable from every other mean value.

Statistic	notation	value
total population (of all replicates)	N_{tot}	216,645,000
number of treatment groups	g	4
degrees of freedom of error	$[N_{tot} - g]$	216,644,996
degrees of freedom of treatment	$[g - 1]$	3
pair-wise between-group comparisons	q	6
significance level	α	0.05
Bonferroni-adjusted significance level	$[\alpha/2q]$	4.16667E--3
upper critical value of Student's t-distribution	$t([\alpha/2q],[N_{tot} - g])$	3.76142

Table 46. Treatment-group-independent the statistical parameters that would be dimensionless no matter what dimensions might apply to the mean values being compared. These parameters apply to the set of all treatment groups, $i = 1$, $i = 8$, $i = 18$ and $i = 25$, being analysed. The total population is given by Equation 84. The upper critical value of Student's t-distribution at $[N_{tot} - g]$ degrees of freedom and a Bonferroni-adjusted significance level of $[\alpha/2q]$ for a two-sided test is $t([\alpha/2q],[N_{tot} - g])$, which is applied first to the $(1 - \alpha)100\%$ confidence interval about each $\Delta\mu_{ij}$ in Equation 96, and is applied later to the $e_{\Delta\mu_{ij}}$-based $(1 - \alpha)100\%$ confidence interval about μ_i in Equations 99 and 100.

Equation	Statistic		value
87	raw sum	A_{tot}	5.07097E7
88	raw sum of squares	A_{sq}	1.64771E7
89	mean of the raw sum squared	μ_{sq}	1.18696E7
90	correction term of the mean	μ_{corr}	1.23738E7

91	mean square error within groups	e_{MSw}	1.89310E-2
92	mean of the sum of squares of treatments	T_{MSb}	1.68101E5

Table 47. Treatment-group-independent statistical parameters for which the dimensions depend on the dimensions of the mean values being compared. These parameters apply to the set of all treatment groups, $i = 1$, $i = 8$, $i = 18$ and $i = 25$, being analysed. The ratio of two of these statistics, T_{MSb} and e_{MSw}, yield $F = T_{MSb}/e_{MSw} = 8.87548E6$. The results in this table are calculated using the replicate observations, which are the sets of all $A_{i,h}$ that are too numerous to tabulate.

treatment group	Population per replicate	replicates	mean	standard deviation	e_{μ_i}-based (1 - α)100% confidence interval	
i	$P_i = m_i$	n_i	$\mu_i = A_i$	σ_i	$-C_{\mu_i}$	$+C_{\mu_i}$
1	10^0	195,000,000	2.49998E-1	1.44407E-1	2.49961E-1	2.50035E-1
8	10^1	19,500,000	9.72829E-2	4.32366E-2	9.71657E-2	9.74001E-2
18	10^2	1,950,000	3.13100E-2	1.36187E-2	3.09393E-2	3.16807E-2
25	10^3	195,000	9.85200E-3	4.35057E-3	8.67974E-3	1.10243E-2

Table 48. The descriptive statistics, μ_i (Equation 85), σ_i (Equation 106) and, with $\alpha = 0.05$ (Equation 98), the 95% confidence interval about μ_i, $\pm C_{\mu_i}$, determined using the standard error of the mean, e_{μ_i} (Equation 97). In turn, the standard error of the mean was determined using e_{MSw} (Table 47). Each statistic in this table applies to just one treatment group.

P_i	n_i	P_j	n_j	$\Delta\mu_{ij} = \mu_i - \mu_j$	$e_{\Delta\mu_{ij}}$	$-C_{\Delta\mu_{ij}}$	$+C_{\Delta\mu_{ij}}$	p_{Bonf}
10^0	$n_1/10^0$	10^1	$n_1/10^1$	1.52715E-1	3.26865E-5	1.52592E-1	1.52838E-1	< 1E-6
10^0	$n_1/10^0$	10^2	$n_1/10^2$	2.18688E-1	9.90451E-5	2.18316E-1	2.19061E-1	< 1E-6

10^0	$n_1/10^0$	10^3	$n_1/10^3$	2.40146E-1	3.11809E-4	2.38973E-1	2.41319E-1	< 1E-6
10^1	$n_1/10^1$	10^2	$n_1/10^2$	6.59729E-2	1.03364E-4	6.55841E-2	6.63616E-2	< 1E-6
10^1	$n_1/10^1$	10^3	$n_1/10^3$	8.74309E-2	3.13208E-4	8.62528E-2	8.86090E-2	< 1E-6
10^2	$n_1/10^2$	10^3	$n_1/10^3$	2.14580E-2	3.26865E-4	2.02286E-2	2.26875E-2	< 1E-6

Table 49. Comparative statistical parameters, for which $P_i = m_i$, $P_j = m_j$ and $n_1 = 195{,}000{,}000$. Each statistic applies to just one pair-wise comparison between two treatment groups. Equation 95 gives the critical value, $t\left([n_i - 1], [n_j - 1]\right) = \frac{\Delta\mu_{ij}}{e_{\Delta\mu_{ij}}}$, for each pair-wise comparison. The probability obtained from the Bonferroni adjusted t-test (2-tailed) is p_{Bonf}. Less than (1 - α)100% confidence is accorded to the difference between any two means for which the comparison yields $p_{Bonf} > \alpha$. Values of p_{Bonf} that lie below 1 – $p(-5\sigma, 5\sigma) \simeq$ 1E-6 (Figure 2; Equation 26) are tabulated as $p_{Bonf} <$ 1E-6.

i	P_i	$+C_{\mu_{P,P-}} = +C_{\mu_{i,j}}$	$-C_{\mu_{P,P+}} = -C_{\mu_{i,j}}$		i	P_i	$-C_{\mu_{P,P-}} = -C_{\mu_{i,j}}$	$+C_{\mu_{P,P+}} = +C_{\mu_{i,j}}$
1	10^0	$+C_{\mu_{i=1,j=8}}$	$-C_{\mu_{i=1,j=25}}$		1	10^0		
8	10^1	$+C_{\mu_{i=8,j=18}}$	$-C_{\mu_{i=8,j=1}}$		8	10^1		
18	10^2	$+C_{\mu_{i=18,j=4}}$	$-C_{\mu_{i=18,j=8}}$		18	10^2		
25	10^3	$+C_{\mu_{i=25,j=1}}$	$-C_{\mu_{i=4,j=18}}$		25	10^3		

Table 50a. The identities of the $e_{\Delta\mu_{ij}}$-based (1 - α)100% confidence interval about μ_i, which are expressed as either $-C_{\mu_{P,P-}} < \mu_P < +C_{\mu_{P,P+}}$ or $-C_{\mu_{P,P+}} < \mu_P < +C_{\mu_{P,P-}}$, that are shown in Figure 88. In this table, $P_i = m_i$.

i	P_i	$+C_{\mu_{P,P-}}$	$-C_{\mu_{P,P+}}$		i	P_i	$-C_{\mu_{P,P-}}$	$+C_{\mu_{P,P+}}$

1	10^0	2.50585E-1	2.49937E-1		1	10^0		
8	10^1	9.73444E-2	9.70885E-2		8	10^1		
18	10^2	3.15044E-2	3.06953E-2		18	10^2		
25	10^3	1.04667E-2	9.26557E-3		25	10^3		

Table 50b. Selected values of the $e_{\Delta\mu_{ij}}$-based (1 - α)100% confidence interval about μ_i, which are expressed as either $-C_{\mu_{P,P-}} < \mu_P < +C_{\mu_{P,P+}}$ or $-C_{\mu_{P,P+}} < \mu_P < +C_{\mu_{P,P-}}$. These are the confidence intervals presented graphically in Figure 88. Less than (1 - α)100% confidence is accorded to the difference between any two means with overlapping confidence intervals. In this table, $P_i = m_i$.

j and n_j apply to $-C_{\mu_{ij}}$			i and n_i apply to both $-C_{\mu_{ij}}$ and $+C_{\mu_{ij}}$					j and n_j apply to $+C_{\mu_{ij}}$		
j	n_j	$-C_{\mu_{ij}}$	μ_i	i	P_i	n_i	fitted value	$+C_{\mu_{ij}}$	j	n_j
8	$10^{-1}n_1$	2.49937E-1	2.49998E-1	1	10^0	$10^{-0}n_1$	2.500_{00}E-1	2.50585E-1	25	$10^{-3}n_1$
18	$10^{-2}n_1$	9.70885E-2	9.72829E-2	8	10^1	$10^{-1}n_1$	9.716_{86}E-1	9.73444E-2	1	$10^{-0}n_1$
25	$10^{-3}n_1$	3.06953E-2	3.13100E-2	18	10^2	$10^{-2}n_1$	3.136_{78}E-2	3.15044E-2	8	$10^{-1}n_1$
1	$10^{-0}n_1$	9.26557E-3	9.85200E-3	25	10^3	$10^{-3}n_1$	9.939_{86}E-2	1.04667E-2	18	$10^{-2}n_1$

Table 50c. The fitted value (Figure 87; Equation 159a); the mean, μ_i; and the $e_{\Delta\mu_{ij}}$-based (1 - α)100% confidence interval about μ_i, $-C_{\mu_{i,j}} < \mu_i < +C_{\mu_{i,j}}$, shown in Figure 88. These parameters are plotted as a function of $P_i = m_i$ in Figure 88. The fit is given by $\left[1/4\sqrt{m_i}\right][4/\upsilon]^{\{m_i - 1/m_i\}}$, which is the antilog of the fit (Equation 159a) presented in Figure 87. The value of υ obtained from the fit of $\log_{10}(A_i)$ - $\log_{10}(0.25/m_i^{0.5})$ versus $\log_{10}(m_i)$ in Figure 86 was 3.180_{68}, which is the value of υ used here. In this table, $P_i = m_i$ and n_1 = 195,000,000.

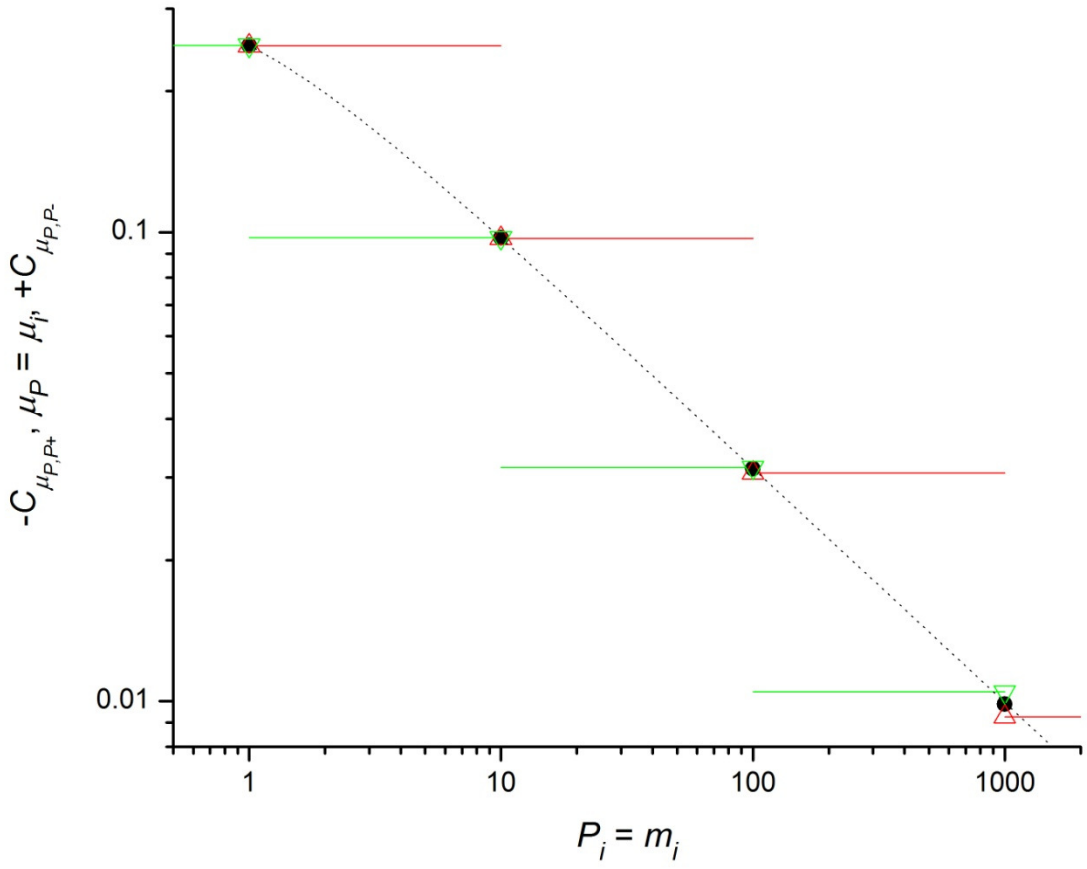

Figure 88a. The fit (·····), given by $[1/4\sqrt{m_i}][4/\upsilon]^{\{m_i-1/m_i\}}$, which is the antilog of the fit (Equation 159a) presented in Figure 87; and the $e_{\Delta\mu_{ij}}$-based (1 - α)100% confidence interval about $\mu_P = \mu_i, -C_{\mu_{P,P+}}$ (△——) < μ_P (●) < $+C_{\mu_{P,P-}}$ (——▽). Table 50 lists the values of the confidence intervals, the values of μ_i and the values of the fit for each treatment group. The value of υ obtained from the fit of $\log_{10}(A_i)$ - $\log_{10}(0.25/m_i^{0.5})$ versus $\log_{10}(m_i)$ in Figure 86 was 3.180_{68}, which is the value of υ used here.

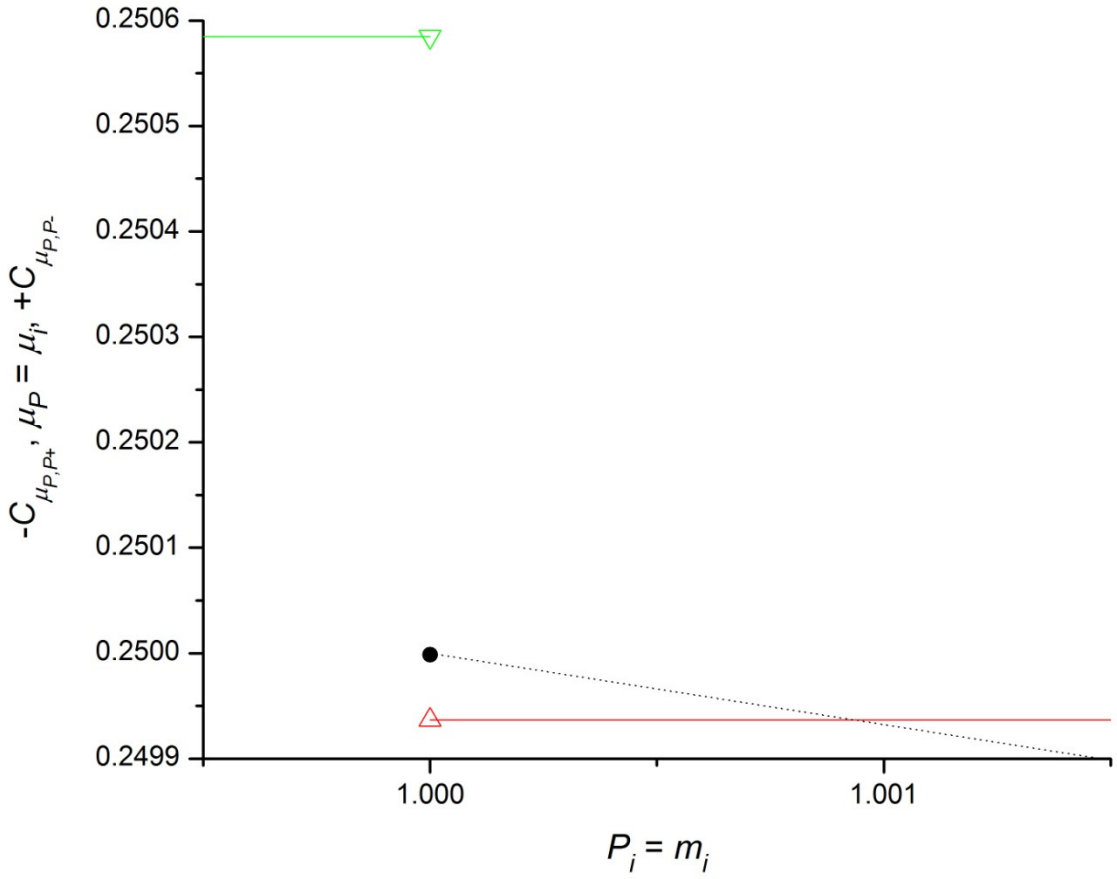

Figure 88b. A detail showing, for treatment group 1 ($P_1 = m_1 = 1$), the fit (·····), given by $[1/4\sqrt{m_i}][4/\upsilon]^{\{m_i - 1/m_i\}}$, which is the antilog of the fit (Equation 159a) presented in Figure 87; and the $e_{\Delta\mu_{ij}}$-based (1 - α)100% confidence interval about $\mu_P = \mu_i, -C_{\mu_{P,P+}}$ (△——) < μ_P (●) < $+C_{\mu_{P,P-}}$ (——▽). This plot is presented with both axes on a normal scale. Table 50 lists the values of the confidence intervals, the values of μ_i and the values of the fit for this treatment group and the other three treatment groups. The value of υ obtained from the fit of $\log_{10}(A_i)$ - $\log_{10}(0.25/m_i^{0.5})$ versus $\log_{10}(m_i)$ in Figure 86 was 3.180_{68}, which is the value of υ used here.

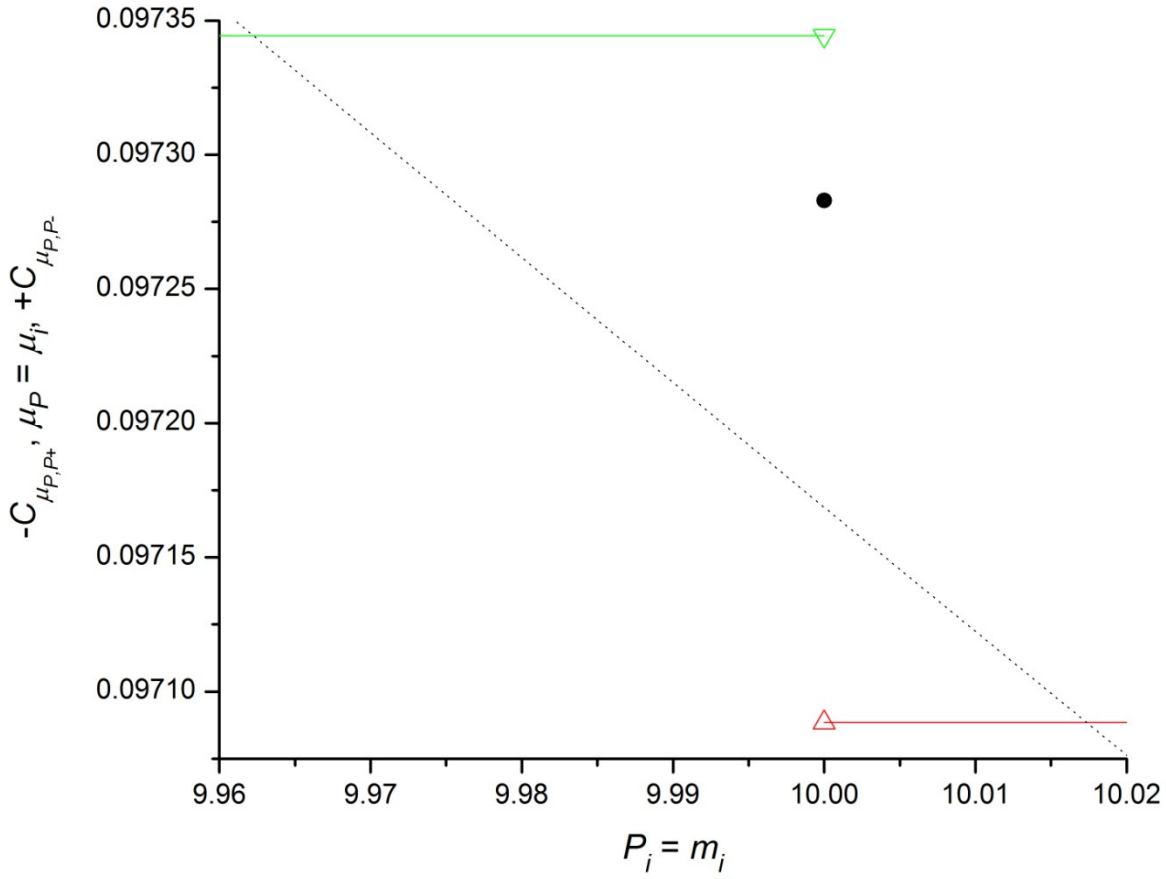

Figure 88c. A detail showing, for treatment group 8 ($P_8 = m_8 = 10$), the fit (·····), given by $[1/4\sqrt{m_i}][4/\upsilon]^{\{m_i - 1/m_i\}}$, which is the antilog of the fit (Equation 159a) presented in Figure 87; and the $e_{\Delta\mu_{ij}}$-based (1 - α)100% confidence interval about $\mu_P = \mu_i$, $-C_{\mu_{P,P+}}$ (△——) < μ_P (●) < $+C_{\mu_{P,P-}}$ (——▽). This plot is presented with both axes on a normal scale. Table 50 lists the values of the confidence intervals, the values of μ_i and the values of the fit for this treatment group and the other three treatment groups. The value of υ obtained from the fit of $\log_{10}(A_i)$ - $\log_{10}(0.25/m_i^{0.5})$ versus $\log_{10}(m_i)$ in Figure 86 was 3.180_{68}, which is the value of υ used here.

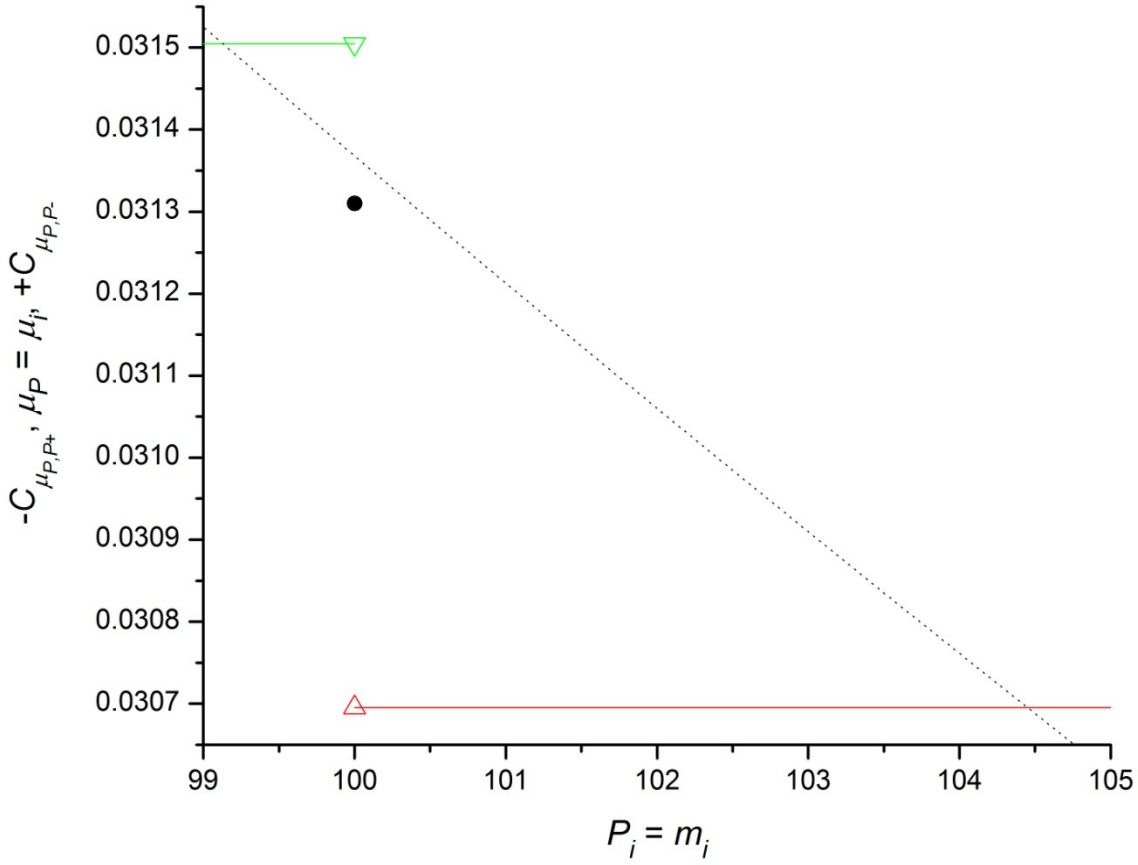

Figure 88d. A detail showing, for treatment group 18 ($P_{18} = m_{18} = 100$), the fit (·····), given by $[1/4\sqrt{m_i}][4/\upsilon]^{\{m_i - 1/m_i\}}$, which is the antilog of the fit (Equation 159a) presented in Figure 87; and the $e_{\Delta\mu_{ij}}$-based (1 - α)100% confidence interval about $\mu_P = \mu_i$, $-C_{\mu_{P,P+}}$ (△——) < μ_P (●) < $+C_{\mu_{P,P-}}$ (——▽). This plot is presented with both axes on a normal scale. Table 50 lists the values of the confidence intervals, the values of μ_i and the values of the fit for this treatment group and the other three treatment groups. The value of υ obtained from the fit of $\log_{10}(A_i)$ - $\log_{10}(0.25/m_i^{0.5})$ versus $\log_{10}(m_i)$ in Figure 86 was 3.180_{68}, which is the value of υ used here.

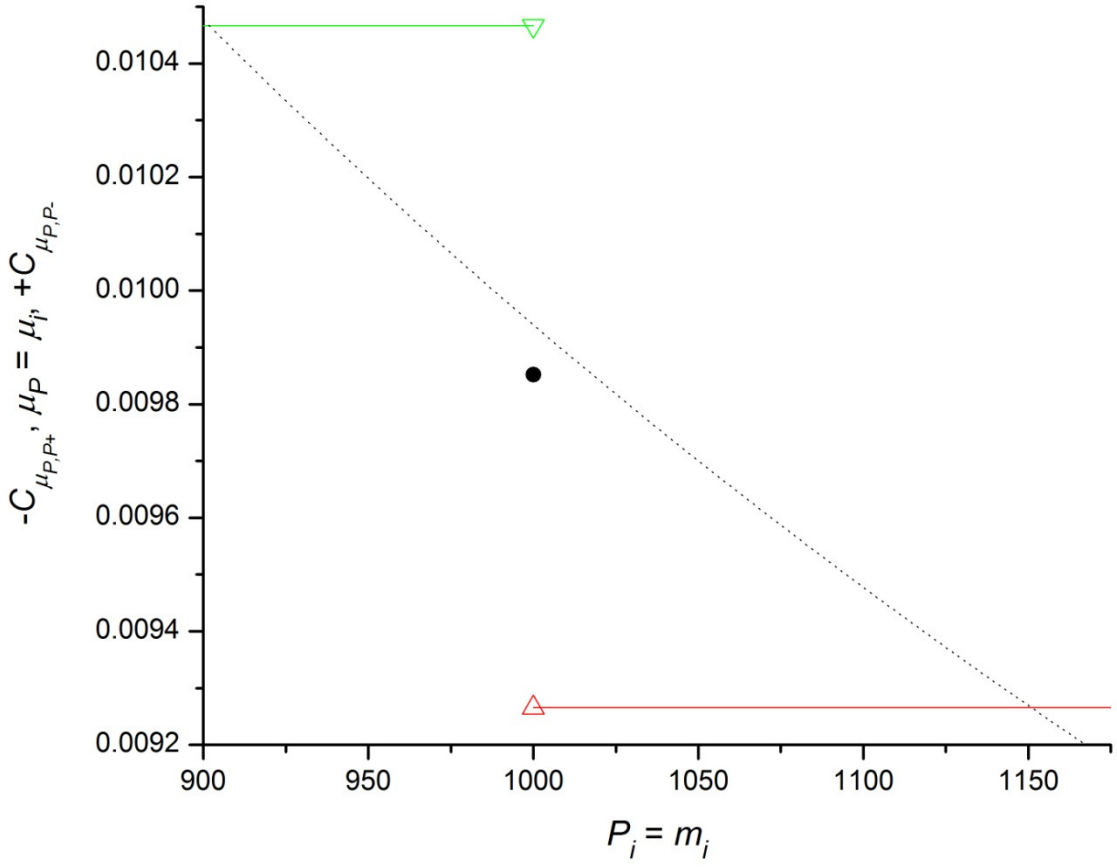

Figure 88e. A detail showing, for treatment group 25 ($P_{25} = m_{25} = 1000$), the fit (·····), given by $[1/4\sqrt{m_i}][4/\upsilon]^{\{m_i - 1/m_i\}}$, which is the antilog of the fit (Equation 159a) presented in Figure 87; and the $e_{\Delta\mu_{ij}}$-based (1 - α)100% confidence interval about $\mu_P = \mu_i$, $-C_{\mu_{P,P+}}$ (△——) < μ_P (●) < $+C_{\mu_{P,P-}}$ (——▽). This plot is presented with both axes on a normal scale. Table 50 lists the values of the confidence intervals, the values of μ_i and the values of the fit for this treatment group and the other three treatment groups. The value of υ obtained from the fit of $\log_{10}(A_i)$ - $\log_{10}(0.25/m_i^{0.5})$ versus $\log_{10}(m_i)$ in Figure 86 was 3.180_{68}, which is the value of υ used here.

The results given in Tables 46 to 50 and presented in Figure 88 show that the four treatment groups, $i = 1$, $i = 8$, $i = 18$ and $i = 25$, can be distinguished from each other with a great deal of

confidence, and also show that a fit to the mean values of the observations for these groups yields values that lie within the confidence intervals about the means. Thus, the mean values can be considered to be very precise, and the fitting results can be considered to be both precise and accurate. The results prove nothing (Kupferberg, 1965) regarding the accuracy of the mean values of the observations for these groups, however.

References

Moody, T. P. (2012a) Johnston-Ogston effects in AUC simulations of two model systems based on polystyrene beads that are polydisperse with respect to specific gravity. http://moodybiophysicalconsulting.blogspot.com/.

Moody, T. P. (2011) An irreversible thermodynamic description of analytical ultracentrifugation (AUC) applied to a solution of the time- and gravitational-potential-space-dependent Lamm equation. http://moodybiophysicalconsulting.blogspot.com/.

Claverie, J.-M., Dreux, H., and Cohen, R. (1975). Sedimentation of generalized systems of interacting particles. I. Solution of systems of complete Lamm equations. *Biopolymers*. **14**, 1685-1700.

Moody, T. P. (2012b) The apparent sedimentation coefficient, s*, and its distribution function, g(s*), within $-\infty < s^* < \infty$. http://moodybiophysicalconsulting.blogspot.com/.

Hembree, B., McCormack, D., Michelson, D., and Horrell, K. *Chapter 3. Production Process*

Characterization. (B. Hembree, Ed.) NIST/SEMATECH e-Handbook of Statistical Methods: http://www.itl.nist.gov/div898/handbook/ (created 2003, June 1; last updated 2013, October 30).

Prins, J., McCormack, D., Michelson, D., and Horrell, K. *Chapter 7. Product and Process Comparisons.* (J. Prins, Ed.) Retrieved from NIST/SEMATECH e-Handbook of Statistical Methods: http://www.itl.nist.gov/div898/handbook/ (created 2003, June 1; last updated 2013, October 30).

Bridgeman, W. B. (1942) Some physical chemical characteristics of glycogen. *J. Am. Chem. Soc.*, **64**, 2349-2356.

Stafford, W. F. (1992) Boundary analysis in sedimentation transport experiments: A procedure for obtaining sedimentation coefficient distributions using the time derivative of the concentration profile. *Anal. Biochem.*, **203**, 295-301.

Stafford, W. F. (1994) Boundary analysis in sedimentation velocity experiments. *Methods Enzymol.*, **240**, 478-501.

Stafford, W. F. (2000) Analysis of reversibly interacting macromolecular systems by time derivative sedimentation velocity. *Methods Enzymol.*, **323**, 302-325.

Katz, M. (1957) "I'm a Schlemiel of Fortune." *Mish Mosh*, Capitol Records **T-799** (track B1), Los Angeles. LP.

Rosten, L. (2001) Lexicon of Yiddish-in-English. *In*, "The new Joys of Yiddish." (Revised by Lawrence Bush.) p. 226. Three Rivers Press (Random House), New York.

Kupferberg, T. (1965) "Nothing." The Village Fugs Sing Ballads of Contemporary Protest, Point of Views, and General Dissatisfaction, Broadside Records **304**/Folkways Records **FW 05304** (track B5), New York. LP.